OPTICAL MICROSCOPIC AND SPECTROSCOPIC TECHNIQUES TARGETING BIOLOGICAL APPLICATIONS

EDITED BY: Vicente Micó, Giancarlo Pedrini, Ming Lei, Chao Zuo and Peng Gao
PUBLISHED IN: Frontiers in Physics

frontiers Research Topics

frontiers

ISSN 1664-8714
ISBN 978-2-88971-523-7
DOI 10.3389/978-2-88971-523-7

About Frontiers

Frontiers is more than just an open-access publisher of scholarly articles: it is a pioneering approach to the world of academia, radically improving the way scholarly research is managed. The grand vision of Frontiers is a world where all people have an equal opportunity to seek, share and generate knowledge. Frontiers provides immediate and permanent online open access to all its publications, but this alone is not enough to realize our grand goals.

Frontiers Journal Series

The Frontiers Journal Series is a multi-tier and interdisciplinary set of open-access, online journals, promising a paradigm shift from the current review, selection and dissemination processes in academic publishing. All Frontiers journals are driven by researchers for researchers; therefore, they constitute a service to the scholarly community. At the same time, the Frontiers Journal Series operates on a revolutionary invention, the tiered publishing system, initially addressing specific communities of scholars, and gradually climbing up to broader public understanding, thus serving the interests of the lay society, too.

Dedication to Quality

Each Frontiers article is a landmark of the highest quality, thanks to genuinely collaborative interactions between authors and review editors, who include some of the world's best academicians. Research must be certified by peers before entering a stream of knowledge that may eventually reach the public - and shape society; therefore, Frontiers only applies the most rigorous and unbiased reviews.
Frontiers revolutionizes research publishing by freely delivering the most outstanding research, evaluated with no bias from both the academic and social point of view. By applying the most advanced information technologies, Frontiers is catapulting scholarly publishing into a new generation.

What are Frontiers Research Topics?

Frontiers Research Topics are very popular trademarks of the Frontiers Journals Series: they are collections of at least ten articles, all centered on a particular subject. With their unique mix of varied contributions from Original Research to Review Articles, Frontiers Research Topics unify the most influential researchers, the latest key findings and historical advances in a hot research area! Find out more on how to host your own Frontiers Research Topic or contribute to one as an author by contacting the Frontiers Editorial Office: frontiersin.org/about/contact

OPTICAL MICROSCOPIC AND SPECTROSCOPIC TECHNIQUES TARGETING BIOLOGICAL APPLICATIONS

Topic Editors:
Vicente Micó, University of Valencia, Spain
Giancarlo Pedrini, University of Stuttgart, Germany
Ming Lei, Xi'an Jiaotong University, China
Chao Zuo, Nanjing University of Science and Technology, China
Peng Gao, Xidian University, China

Citation: Micó, V., Pedrini, G., Lei, M., Zuo, C., Gao, P., eds. (2021). Optical Microscopic and Spectroscopic Techniques Targeting Biological Applications. Lausanne: Frontiers Media SA. doi: 10.3389/978-2-88971-523-7

Table of Contents

frontiers in Physics

EDITORIAL
published: 06 September 2021
doi: 10.3389/fphy.2021.752435

Editorial: Optical Microscopic and Spectroscopic Techniques Targeting Biological Applications

Vicente Micó[1], *Giancarlo Pedrini*[2], *Ming Lei*[3], *Chao Zuo*[4] *and Peng Gao*[5]*

[1]Departamento de Óptica y de Optometría y Ciencias de la Visión, Universidad de Valencia, Burjassot, Spain, [2]Institut für Technische Optik, Universität Stuttgart, Stuttgart, Germany, [3]School of Physic, Xi'an Jiaotong University, Xi'an, China, [4]School of Electronic and Optical Engineering, Nanjing University of Science and Technology, Nanjing, China, [5]School of Physics and Optoelectronic Engineering, Xidian University, Xi'an, China

Keywords: optical microscopy, spectroscopy, super-resolution, deep-learning, quantitative phase imaging, fluorescent probe, algorithms

Editorial on the Research Topic

Optical Microscopic and Spectroscopic Techniques Targeting Biological Applications

Optical microscopy and spectroscopy are two mainstream tools for the exploration of an unknown microworld, especially in biomedical fields. Specifically, optical microscopy uses visible light and a system of lenses to magnify images of small samples [1]. It is non-invasive to live samples and has the capability to visualize specific structures once employing fluorescent labeling strategies [2]. Meanwhile, optical spectroscopy allows investigation of chemical, physical and electronic structures of matter at atomic, molecular, and macro scales [3]. In the past decades, remarkable developments of optical microscopy and spectroscopy have been witnessed, mainly in hardware implementation, algorithm performance, and innovative approaches [4–8].

We are glad to see that this special issue collects 23 articles, which report both the latest technological advances and the applications of optical microscopy and spectroscopy. Conceptually, these articles can be categorized into five classes according to the specific techniques (**Figure 1**).

The first class is fluorescence microscopy and correlation spectroscopy. These techniques can visualize the structures or the bio-molecular dynamics of samples by tagging them with fluorescence markers. Specifically, Li et al. review 3D imaging with dual-lens fluorescence microscopy, Qin and Xia present simultaneous two-photon fluorescence microscopy with two endogenous fluorescent coenzymes, entitled NADH and FAD. Yu et al. reviews fluorescence correlation spectroscopy (FCS), a powerful technique for quantification of molecular dynamics. Cui et al. fabricated a novel near-infrared fluorescent nanoparticles (NPs) for high-contrast and high-penetration *in-vivo* imaging.

The second class is quantitative phase microscopy (QPM). These techniques explore the phase of the light passing through or being reflected by a sample, providing quantitative information of 3D profiles or refractive index distributions of the sample. Picazo-Bueno et al., Guo et al., and Karako et al. propose new types of digital holographic microscopy (DHM) to quantify the thickness and refractive index distributions of samples. Meanwhile, Lima and Cojoc utilize DHM for the assessment of human neutrophil differentiation from myeloid cells. Zhou et al. propose a non-interference QPM strategy, recovering the phase from a stack of through-focus intensity images. Soto et al. present a partially coherent illumination based optical diffraction tomography (ODT) approach, allowing 3D refractive-index imaging of dynamic samples. Wu et al. propose a lens-free on-chip microscopy incorporated with a high-precision autofocusing algorithm for pixel-super-resolved QPM imaging of the sample. Sahu and Mazumder summarize some of the application of adaptive optics (AO) in two-photon fluorescence (TPF) microscopy for wavefront corrections in brain imaging and ophthalmoscopy.

OPEN ACCESS

Edited and reviewed by:
Lorenzo Pavesi,
University of Trento, Italy

***Correspondence:**
Peng Gao
peng.gao@xidian.edu.cn

Specialty section:
This article was submitted to Optics and Photonics, a section of the journal Frontiers in Physics

Received: *03 August 2021*
Accepted: *10 August 2021*
Published: *06 September 2021*

Citation:
Micó V, Pedrini G, Lei M, Zuo C and Gao P (2021) Editorial: Optical Microscopic and Spectroscopic Techniques Targeting Biological Applications. Front. Phys. 9:752435. doi: 10.3389/fphy.2021.752435

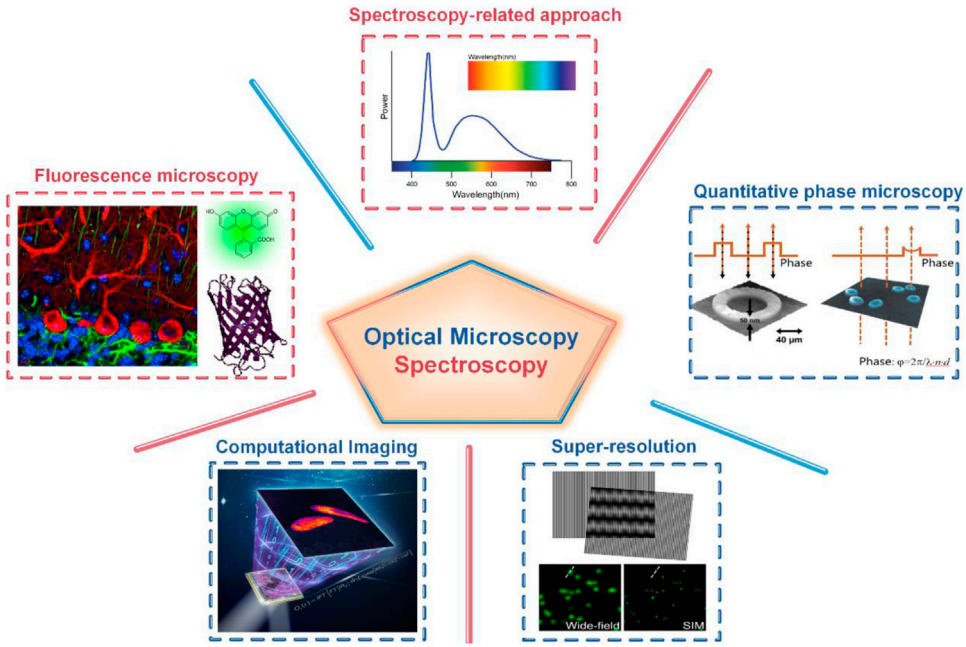

FIGURE 1 | Topical classification of the articles in the special issue [9][10].

The third class is super-resolution optical microscopy. The techniques of this class are far-field, minimally invasive, and they can image samples with a resolution surpassing the diffraction limit. Yong et al. present a high-dynamic-range structured illumination microscopy (HDR-SIM) using a multi-exposure acquisition strategy. With HDR-SIM, microspheres and vesicles with 420 intensity levels can be visualized in the same scene. Wen et al. demonstrate a digital micromirror device (DMD) based optical microscopic apparatus for dual-modality imaging, including quantitative differential phase contrast (qDIC) imaging and coherent SIM imaging. Zhao et al. review recent advances in high-speed SIM that include both hardware and software improvements, including reduction of the number of raw images, GPU acceleration, deep learning, and spatial domain reconstruction. Chen et al. present a super-resolution optical microscopy entitled expansion microscopy (ExM). This technique immobilizes the fluorescent molecules of interest in a polyacrylamide hydrogel. Then, the structure of the sample is spatially amplified as the hydrogel physically expands isotopically, thus indirectly improving resolution. This paper also present the applications of super resolution expansion microscopy in yeast.

The fourth class is deep-learning based computational imaging techniques. These techniques brought about new revolutionary computational power in optical microscopy. Zhang et al. present deep learning (DL) based adaptive optics (AO) to correct optical aberrations. They utilize a revised ResNet-34 network to infer the phase distortions of all the 224 valid zones on a SLM in one shot. Zhang et al. present a new deep-learning-based approach for recovering halo-free white-light diffraction phase images. The neural network-based method can accurately and rapidly remove the halo artifacts, not relying on any a-priori knowledge. Di et al. present an optimized structural convolution neural network PhaseNet for the reconstruction of digital holograms for DHM.

The fifth class is spectroscopy-related techniques. These techniques can non-invasively probe the structure, properties, and dynamics of molecules in different environments or different physico-chemical conditions. Hence, they are widely used in physics, astronomy, chemistry, biology, and related research fields. Here, Li et al. review the principle, configuration, and applications of coherent anti-stokes Raman scattering (CARS) microscopy, which can provide high-resolution, high-sensitivity, and non-invasive imaging of specific biomolecules without fluorescent labeling. Poulen et al. review the application of CARS in the identification and characterization of myelin in the mammalian nervous system of different species. Duadi et al. investigate near-infrared (NIR) measurements of turbid media using different size detectors at different positions. García-Martínez et al. propose a supercontinuum (SC) laser source from 450 to 1,600 nm with programmable spectrum by using liquid-crystal on silicon (LCoS) spatial light modulators (SLM).

To sum up, this research topic features 23 excellent articles encompassing the start-of-art developments and applications of optical microscopy and spectroscopy. This collection should be of interest to readers in the areas of optics, biophysics, and chemistry orientated subjects. It is our

hope that this special research topic will contribute to the scientific advancements of optical microscopy and spectroscopy, as well as to their practical applications in biology and medicine.

REFERENCES

1. Girkin J. *A Practical Guide to Optical Microscopy*. 1st ed. Boca Raton, FL: CRC Press (2019).
2. Dean KM, and Palmer AE. Advances in Fluorescence Labeling Strategies for Dynamic Cellular Imaging. *Nat Chem Biol* (2014) 10:512–23. doi:10.1038/nchembio.1556
3. Atkin JM, and Raschke MB. Optical Spectroscopy Goes Intramolecular. *Nature* (2013) 498:44–5. doi:10.1038/498044a
4. Bacia K, Kim SA, and Schwille P. Fluorescence Cross-Correlation Spectroscopy in Living Cells. *Nat Methods* (2006) 3:83–9. doi:10.1038/nmeth822
5. Cheng J-X, Volkmer A, and Xie XS. Theoretical and Experimental Characterization of Coherent Anti-Stokes Raman Scattering Microscopy. *J Opt Soc Am B* (2002) 19:1363–75. doi:10.1364/JOSAB.19.001363
6. Lippincott-Schwartz J, and Manley S. Putting Super-Resolution Fluorescence Microscopy to Work. *Nat Methods* (2009) 6:21–3. doi:10.1038/nmeth.f.233
7. Lichtman JW, and Conchello J-A. Fluorescence Microscopy. *Nat Methods* (2005) 2:910–9. doi:10.1038/nmeth817
8. Micó V, Zheng J, Garcia J, Zalevsky Z, and Gao P. Resolution Enhancement in Quantitative Phase Microscopy. *Adv Opt Photon* (2019) 11:135–214. doi:10.1364/AOP.11.000135
9. Kemper B, and von Bally G. Digital Holographic Microscopy for Live Cell Applications and Technical Inspection. *Appl Opt* (2008) 47:A52–A61. doi:10.1364/AO.47.000A52
10. Lyncée tec. Available at: https://www.lynceetec.com/types/downloads/

AUTHOR CONTRIBUTIONS

All authors listed have made a substantial, direct, and intellectual contribution to the work, and approved it for publication.

Conflict of Interest: The authors declare that the research was conducted in the absence of any commercial or financial relationships that could be construed as a potential conflict of interest.

frontiers in Physics

REVIEW
published: 07 December 2020
doi: 10.3389/fphy.2020.606217

A Review on Dual-Lens Fluorescence Microscopy for Three-Dimensional Imaging

Xiaoyan Li[1], Yubing Han[1], Wenjie Liu[1], Cuifang Kuang[1,2,3], Xu Liu[1,2,3] and Xiang Hao[1]**

[1]State Key Laboratory of Modern Optical Instrumentation, College of Optical Science and Engineering, Zhejiang University, Hangzhou, China, [2]Ningbo Research Institute, Zhejiang University, Ningbo, China, [3]Collaborative Innovation Center of Extreme Optics, Shanxi University, Taiyuan, China

Three-dimensional (3D) imaging using dual-lens fluorescence microscopies is popular in observing fluorescently labeled biological samples, such as mammalian/model animal cells, tissues, and embryos. Specifically, dual-lens super-resolution fluorescence microscopy methods using two opposing objective lenses allow significantly higher axial resolution and better signal to noise ratio than traditional single-lens counterparts, and thus distinguish more details in 3D images of fine intracellular structures. For 3D imaging of thick tissues and entire embryos, dual-lens light-sheet fluorescence microscopy methods using two objective lenses, either orthogonal or non-orthogonal, to achieve selective plane illumination, can meet the requirements, and thus can be used to observe embryo development and structures of interest in thick tissues. This review summarizes both dual-lens fluorescence microscopy methods, including their principles, configurations, and 3D imaging applications, providing a guideline for biological laboratories with different 3D imaging needs.

Keywords: three-dimensional imaging, dual lens, axial resolution, light-sheet illumination, super-resolution, fluorescence microscopy

OPEN ACCESS

Edited by:
Ming Lei,
Xi'an Jiaotong University, China

Reviewed by:
Xiangping Li,
Jinan University, China
Jianming Wen,
Kennesaw State University, United States

****Correspondence:***
Yubing Han
hanyubing@zju.edu.cn
Xiang Hao
haox@zju.edu.cn

Specialty section:
This article was submitted to Optics and Photonics, a section of the journal Frontiers in Physics

Received: *14 September 2020*
Accepted: *05 November 2020*
Published: *07 December 2020*

Citation:
Li X, Han Y, Liu W, Kuang C, Liu X and Hao X (2020) A Review on Dual-Lens Fluorescence Microscopy for Three-Dimensional Imaging. Front. Phys. 8:606217. doi: 10.3389/fphy.2020.606217

INTRODUCTION

In the past decades, far-field fluorescence microscopy was widely used for observing regions of interest noninvasively in life science. These studies focusing on biological samples, especially mammalian/model animal cells, tissues, and embryos, have tremendously promoted human's understanding of some important structures and mechanisms. In the process, three-dimensional (3D) imaging is popular and often essential because of the 3D entity characteristics of biological samples, which provides more information than two-dimensional (2D) imaging to resolve the practical structure of the samples.

Comparing with conventional epifluorescence microscopy whose 3D resolution is ~250 nm laterally and ~600 nm axially, traditional single-lens 3D super-resolution fluorescence microscopy (SRFM) methods, which can be divided into laser scanning confocal fluorescence microscopy [1] and widefield 3D structured illumination microscopy (3D-SIM) [2] according to their illumination modalities, can provide ~ $\sqrt{2}$- and 2-fold resolution improvement, respectively. However, irrespective of scanning or widefield modality, their resolutions in 3D are still restricted to the diffraction limit [3]. As a further step, SRFM methods with diffraction-unlimited 3D resolution called fluorescence nanoscopy were developed, whose underneath basis is the use of a bright ("on") and a dark ("off") state of the fluorophores to record sub-wavelength features sequentially in time [4].

Similarly, fluorescence nanoscopy can be classified into two modalities by distinguishing different illumination modality: the scanning modality, such as stimulated emission depletion (STED) [5], ground state depletion [6], and reversible saturable optical fluorescence transition (RESOLFT) [7], which record the fluorescent marker molecule by molecule sequentially; the widefield modality, such as photoactivated localization microscopy (PALM) [8], stochastic optical reconstruction microscopy (STORM) [9], and fluorescence PALM (fPALM) [10], whose sequential recordings occur in molecular ensembles. Both modalities had achieved impressive works since they were proposed [11].

However, the traditional single-lens configurations cannot avoid the problem of resolution anisotropy, by which the axial resolution is substantially ~2.5-fold worse than the lateral counterpart. The inferior axial resolution severely limits the precise 3D imaging and corresponding image-based data analysis. For this, dual-lens axial SRFM methods which sandwich the sample between two opposing objective lenses (**Figure 1**) to break the axial diffraction limit were developed. In the dual-lens axial SRFM configurations, there are two symmetric illumination wave fronts that interfere in the common focal region and/or two symmetric detection wave fronts that interfere on the detector when the optical lengths of the illumination arm and detection arm are both within the coherent length. The interference results into three- to seven-fold resolution improvement in the axial direction in both scanning and widefield modalities of dual-lens axial SRFM methods without (**Figures 1A-C**) or with (**Figures 1D,E**) relying on fluorescence nanoscopy. Furthermore, because the detected fluorescence photons are doubled in the dual-lens configurations, the signal-to-noise ratio (SNR) of their 3D images is improved. However, the more faithful 3D imaging results come at the expense of experimental difficulties in alignment and interference maintaining, that is, the two critically chosen objective lenses need to be aligned with a large number of parameters in parallel, and the illumination/detection arms (each >10 cm long) have to be maintained with sub-wavelength scale stability to insure interference. The two experiment requirements cause their sensitivity to refractive index inhomogeneity. As a result, the dual-lens axial SRFM methods are limited to observe subcellular structures of fixed and some living mammalian cells, and their 3D imaging of thicker samples, for example, mammalian/model animal tissues or embryos, have almost not been explored.

For thick biological samples like tissues or embryos, their 3D images can be obtained by dual-lens light-sheet fluorescence microscopy (LSFM), which is another dual-lens 3D imaging method reviewed here. In the dual-lens LSFM configurations, there are one illumination objective lens (IO) and one detection objective lens (DO) which are arranged either orthogonally or non-orthogonally to achieve selective plane illumination. The IO focuses a thin light sheet just in the position of the focal plane of the DO and thus causes no out-of-focus fluorescence distraction inherently, which results into remarkable optical sectioning capability and accompanying low phototoxicity and photobleaching, and its widefield detection mechanism is beneficial to living imaging. As a result, the dual-lens LSFM methods are widely used for longtime 3D imaging of large biological samples, such as recording the embryogenesis and early embryo development of mammalian/model animals [12]. Further combined with SR methods, they can also be used to observe fine intracellular structures in thick tissues. In fact, on top of the dual-lens LSFM configurations, some LSFM methods using three or four objective lenses were developed. Although their two-sided illumination and/or detection by adding an objective lens opposite the existing IO and/or DO achieve better 3D imaging performances to some extent, the experimental complexity is increased. These LSFM methods will not be discussed in this review, readers can refer to other publications for further details [13–15].

The present review focuses on two complementary advanced dual-lens fluorescence microscopy methods called dual-lens axial SRFM and LSFM, respectively. Specifically, the dual-lens axial SRFM with superior axial super resolution can image fine subcellular structures at a penetration depth comparable with an entire mammalian cell, but its 3D imaging capability for thicker biological samples like mammalian/model animal tissues and embryos is limited, which can be compensated by dual-lens LSFM, a type of microscopy with inherent optical sectioning capability arising from selective plane illumination, but inferior axial resolution despite the introduction of SR methods. In the following sections, we introduce the dual-lens axial SRFM and LSFM methods, including their principles, configurations, and applications, and then, we summarize this review and make a discussion and brief outlook around dual-lens 3D imaging methods.

DUAL-LENS AXIAL SUPER-RESOLUTION FLUORESCENCE MICROSCOPY METHODS FOR 3D IMAGING

Dual-Lens Super-Resolution Fluorescence Microscopy Methods Without Relying on Nanoscopy

Scanning Modality

In 1992, Hell *et al.* first proposed dual-lens axial SRFM called 4Pi microscopy because its full solid angle is nearly 4π [16]. In the first 4Pi microscopy configuration, there was only the interference between two symmetric illumination wave fronts around the focal region that was exploited, which is called the 4Pi-type-A mode. Similarly, the mode which combines the fluorescence emitted from the two opposing objective lenses coherently is called 4Pi-type-B [17]. Although the two modes are sufficient for a three- to five-fold sharpened 4Pi point spread function (4Pi-PSF) [18], a seven-fold sharpened 4Pi-PSF can be achieved by combining both modes simultaneously, which is referred to as 4Pi-type-C mode [19], and the initial left and right arrangement of the two opposing objective lenses [20] was replaced by a modified upper and lower arrangement for more convenient sample mounting [21], as shown in **Figure 2**.

Most applications of 4Pi microscopy in 3D imaging of biological samples were based on the 4Pi-type-C mode. In

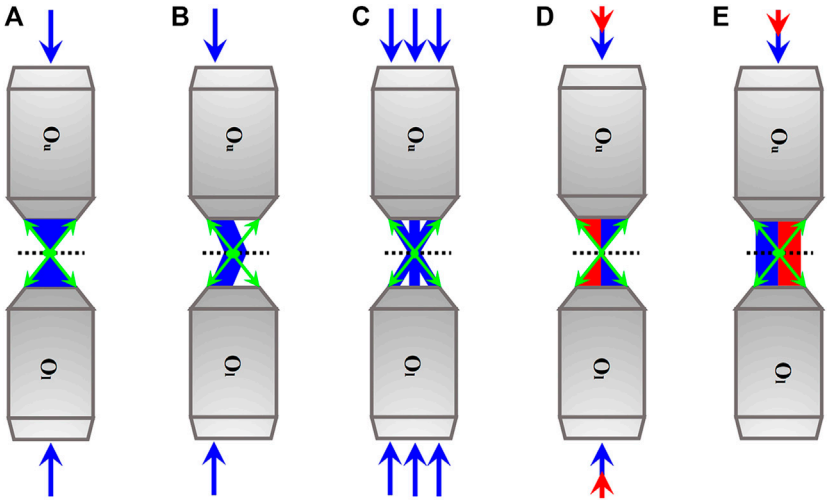

FIGURE 1 | Simplified schematics of axial SRFM methods. **(A)**–**(C)** Axial SRFM methods without relying on nanoscopy. According to their illumination modalities, they can be divided into scanning modality **(A)**, widefield modality without **(B)** and with **(C)** laterally structured illumination. **(D)** and **(E)** Axial SRFM methods relying on nanoscopy. According to their illumination modalities, they can also be divided into scanning modality in which synchronized excitation light (blue) and STED light (red) are used for sharpening focal spot **(D)** and widefield modality in which synchronized excitation light (blue) and activation light (red) are used for localizing the individual fluorescent molecule sequentially **(E)**. Blue and green arrows indicate the directions of the excitation beam and fluorescence. The directions of the STED light and activation light are both indicated by red arrows. The dotted line is at the sample plane. Ou, the upper objective lens; O_l, the lower objective lens.

combination with two-photon excitation (2PE) which can suppress "ghost images" arising from interference effectively, 4Pi microscopy was used to observe the mitochondrial network of living *Saccharomyces cerevisiae* cells [21] and reveals H2AX chromatin structures and their response to DNA damage in fixed HeLa cells [22] at an axial resolution of ~100 nm. Furthermore, mitochondrial oxidative phosphorylation and energetic status can be reflected by observing the disintegration of the mitochondrial network. For example, the tubules or their branching or bifurcation points in the interconnected mitochondrion of optimum insulinoma 1NS-1E cells will be transferred into flat cisternae when cultivated at decreased glucose condition (**Figures 3A,B**) [23], and type-2 diabetes islet β-cells isolated from diabetic Goto-Kakizaki rats exhibit a more disintegrated mitochondrial network than those from control Wistar rats (**Figures 3C,D**) [24]. The standardization of these patterns may lead to the development of morphological diagnostics for Langerhans islets before their transplantations.

Widefield Modality

In 1995, Gustafsson *et al.* first developed dual-lens axial SRFM adopting widefield illumination and detection [25], which is called I^5M later [26], as shown in **Figures 4A and 4C**. The concept of "I^5" equals to a combination of "I^3" (incoherent interference illumination, an analogy to 4Pi-type-A) and "I^2" (image interference, an analogy to 4Pi-type-B), and thus, the I^5M method also achieved up to seven-fold axial resolution improvement [27]. However, its lateral resolution is unchanged as in epifluorescence microscopy. For this, an extension of I^5M called I^5S which adds structured illumination in the lateral direction for lateral super resolution was proposed [28], as shown in **Figures 4B and 4D**. The I^5S method achieved 100 nm scale near-isotropic 3D resolution and was used to image microtubule cytoskeleton in HeLa cells [29].

The initial I^5S implementation used gratings to split the illumination light into three diffracted beams (order 0th and ±1st), and the interference between them produced a 3D sinusoidal pattern. In contrast to the diffraction grating, ferroelectric liquid crystal spatial light modulator [30, 31] and scanning galvanometer mirror (SGM) [32–34] can satisfy the demands of faster and more flexible pattern generation. As a result, a combination of SGM-based I^5S and fluorescence saturation [35] termed as saturated I^5S or SI^5S [36] was developed in theory and obtained near-isotropic 3D resolution below 60 nm. Its superior imaging capability can be seen from **Figures 5**. Furthermore, the grating- and SGM-based I^5S implementations can both be provided optionality of a second camera at the detection end for higher fluorescence efficiency [37].

Dual-Lens Super-Resolution Fluorescence Microscopy Methods Relying on Nanoscopy

Scanning Modality

Dual-lens axial SRFM methods relying on nanoscopy which are called 4Pi nanoscopies uniformly can also be classified into scanning modality and widefield modality. In scanning modality (**Figure 6A**), it is the illumination light in the sample space that matters. Specifically, the sample is scanned by a sharpened scanning focal spot which is formed by superimposing diffraction-limited excitation spot and doughnut-shaped STED pattern. The synchronized excitation

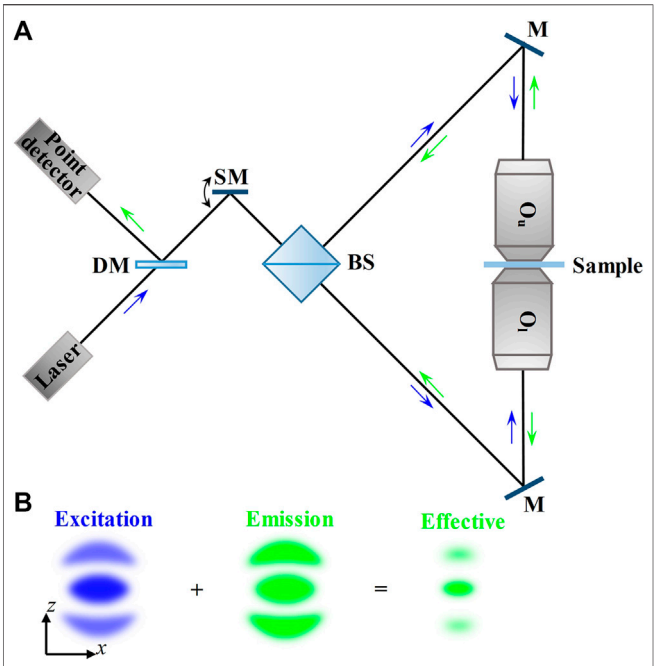

FIGURE 2 | Schematic and principle of 4Pi-type–C microscopy. **(A)** Schematic of 4Pi-type–C microscopy. The excitation beam from the laser is fed through a scanning mirror and a 50/50 beam splitter into the 4Pi cavity. The fluorescence emitted from the sample is inversely collected by the same objective lenses and reflected by a dichroic mirror, and finally collected by a point detector. **(B)** PSFs in 4Pi-type–C microscopy in the axial (xz) plane. The effective PSF is obtained by the superimposition of excitation PSF and emission PSF. Blue and green arrows indicate the directions of the excitation beam and fluorescence. DM, dichroic mirror; SM, scanning mirror; BS, 50/50 beam splitter; M, mirror; Ou, the upper objective lens; O_l, the lower objective lens.

beam (visible laser pulse on the sub-picosecond scale) and STED beam (near-infrared laser pulse on the scale of tens of picoseconds) should be aligned carefully to achieve the most effective depletion.

In 2002, Hell *et al.* first implemented two concepts of STED and 4Pi synergistically [38]. The so-called STED–4Pi (4Pi-type-A in effect) nanoscopy obtained an oblate focal spot whose full width at half maximum is ~33 nm in the axial direction but unchanged in the lateral direction. The method was used for imaging bacteria membranes [38] and microtubules in fixed HEK cells [39]. As a spherical spot is more desired to unfold the sample's full 3D potential in most biological imaging applications, Roman *et al.* proposed isoSTED (4Pi-type-C in effect) nanoscopy [40]. The method exploited the polarization of illumination beams, that is, the polarization directions of two symmetric lateral depletion ($STED_{xy}$) beams and two symmetric axial depletion ($STED_z$) beams were perpendicular to each other so that their interferences were constructive and destructive, respectively. Meanwhile, two symmetric excitation beams interfered constructively and rendered a focal volume cut down by half. As a result, the isoSTED nanoscopy obtained an isotropic focal spot of 40–45 nm in diameter, and its 3D imaging capability was demonstrated by dissecting the distribution of the mitochondrial outer membrane proteins (**Figures 7A,B**) and quantifying 3D dynamics of inner membrane cristae (**Figure 7C**) in living PtK2 cell [41]. However, the superior imaging performance of isoSTED comes at the expense of complex implementation, including counter alignment of the two objective lenses and co-alignment of the three beams. To reduce the overall alignment effort, a segmented wave plate with chromatic selectivity was introduced into isoSTED to remain the constructive interference of the excitation beams and achieve interference between two symmetric polarization-modified STED beams [42]. The single-beam isoSTED nanoscopy achieved an isotropic 3D resolution of 20–50 nm and was used to image vimentin network and nuclear pore complex in Vero cells.

Nevertheless, the applications of isoSTED in living cell imaging are always limited because it requires extremely high STED laser intensity to guarantee effective depletion. For this, a STED-derivative named RESOLFT, which operates reversibly switchable fluorescent proteins with low light levels to provide mandatory bright and dark states, was developed as 4Pi architecture to image living cells genteelly [43]. The 4Pi-RESOLFT nanoscopy achieved imaging of microfilaments and intermediate filaments in living HeLa cells at a 3D resolution of 30 nm.

Widefield Modality

In widefield modality, it is the emitted fluorescence detected by the camera that matters. Specifically, the sample is widefield illuminated by synchronized excitation light and activation light through the two opposing objective lenses, but the emitted fluorescence is divided into two symmetric coherent wave fronts and interfere at the camera, as shown in **Figure 6A**. The self-interference of individual fluorescence molecules generates three or four interference phases which are sensitive to their axial positions within the 0–2π interval, and thus the 3D coordinates of individual fluorescence molecules can be localized using localization algorithms. Therefore, the widefield modality can also be called 4Pi single-molecule localization microscopy (4Pi-SMLM).

The first realization of 4Pi-SMLM was a three-phase interferometric PALM (iPALM) in 2009 [44]. The method achieved sub-20-nm 3D resolution and was used for imaging microtubules in PtK1 cell, dorsal and ventral plasma membranes in COS7 cell, and endoplasmic reticulum/adhesion complexes in U2OS cell. Further, it performed well in multicolor imaging, such as deciphering the 3D organization of endosomal sorting complexes required for transport (ESCRT) components at human immunodeficiency virus (HIV) assembly sites in two color [45] (**Figure 8A**) and understanding the mechanism of recruitment of viral envelope glycoprotein (Env) to HIV type 1 (HIV-1) assembly sites in three color [46] (**Figure 8B**). Furthermore, the problem of its imaging of mammalian cell samples thicker than 250 nm was limited because of the axial localization ambiguity that was solved by using hyperbolic mirrors to introduce ellipticity into scanning spot [47]. The modified iPALM extended its imaging depth to 750 nm and was used to visualize the mitochondrial nucleoids in 500-nm–thick mouse fibroblasts.

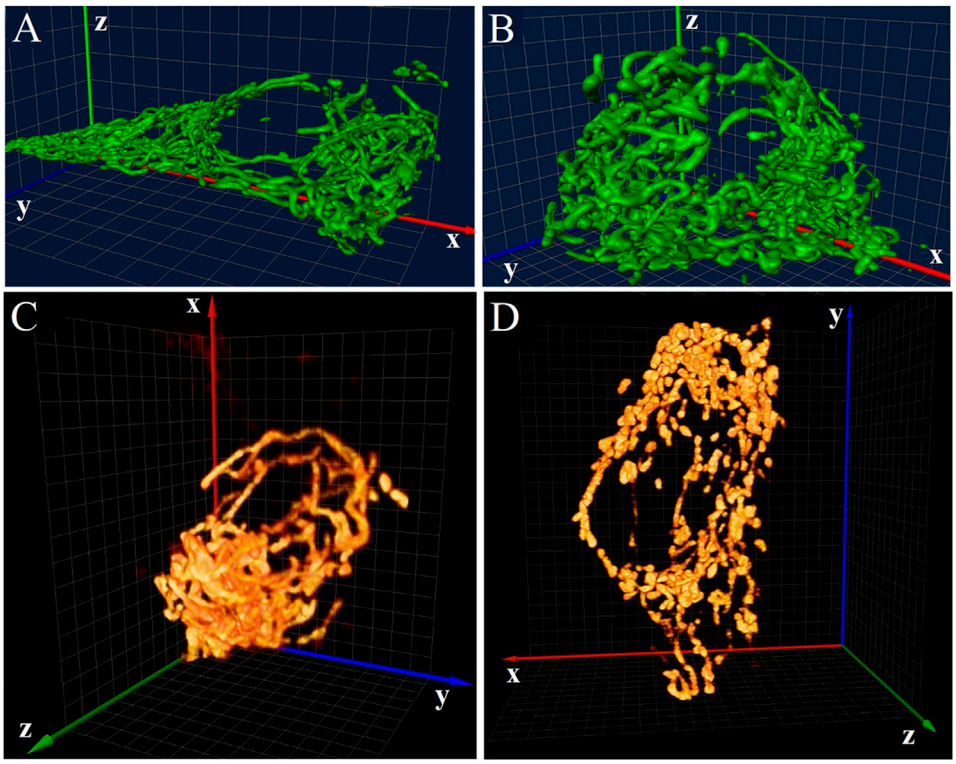

FIGURE 3 | Applications of 4Pi microscopy in 3D imaging. **(A)** and **(B)** 4Pi images of the mitochondrial network in 1NS-1E cells cultivated at optimum **(A)** and decreased **(B)** glucose conditions. Figures are modified with permission from Ref. 23. Copyright © 2008 Elsevier. **(C)** and **(D)** 4Pi images of the mitochondrial network in islet β-cells of control Wistar rats **(C)** and diabetic Goto-Kakizaki rats **(D)**. Figures are modified with permission from Ref. 24. Copyright © 2010 Elsevier. The size of all 3D grids shown in the background is 1 μm.

Besides, the axial localization ambiguity even at 1-μm imaging depth can be eliminated by analyzing image moments, which was first operated on four-phase 4Pi single-molecule switching (4Pi-SMS) microscopy [48]. The method achieved a 3D resolution of 5.4–6.6 nm axially and 8.3–22.3 nm laterally, and its capability for 3D imaging of biological samples thicker than 250 nm was demonstrated by observing human platelet activation and microtubules in Vero cells. Further, two-color imaging of peroxysomes (Atto 532 labeled) and microtubules (Atto 565 labeled) in a PtK2 cell was achieved through classifying Atto 532 and Atto 565 by the ratio of the combined s-polarization vs. the p-polarization components. On top of the 4Pi-SMS microscopy, a modified implementation named 4Pi-SMSN with a penetration depth up to 10 μm was achieved in 2016 [49]. The 4Pi-SMSN introduced adaptive optical elements in the "4Pi cavity" to compensate for sample-induced aberrations and replaced an electron multiplying charge-coupled device (EMCCD) with scientific complementary metal-oxide semiconductor (sCMOS) for higher quantum efficiency. Further, coupled with the optimized higher precision axial localization algorithm, the 4Pi-SMSN achieved a 3D resolution in the range of 10–20 nm and could be used to resolve almost any subcellular structure throughout a whole mammalian cell, as shown in **Figure 8C**. Furthermore, the 4Pi-SMSN was applied to visualize the type III protein secretion machines in living bacteria [50] and observe the Golgi apparatus in three-color at nanoscale lateral super resolution for the first time [51].

DUAL-LENS LIGHT-SHEET FLUORESCENCE MICROSCOPY METHODS FOR 3D IMAGING

For 3D imaging of biological samples like mammalian/model animal tissues and embryos which are thicker than mammalian cells, dual-lens LSFM performs well. Because its general configurations use two orthogonal or non-orthogonal objectives to achieve selective plane illumination, that is, placing the IO before a cylindrical lens [52] (**Figure 9A**) or laser scanner [53] (**Figure 9B**) to focus a static or dynamic light sheet in the focal plane of the DO, so the LSFM can also be called selective plane illumination microscopy (SPIM) [54].

In the traditional dual-lens LSFM with a horizontal IO and a vertical DO, as shown in **Figure 10A**, the sample is embedded in a cylinder of agarose gel held in a glass capillary or a syringe which can be inserted from above into an aqueous-medium-filled chamber placed in the center of the illumination and detection paths. This arrangement is beneficial to the alignment of the illumination and detection axes, but the preparation and

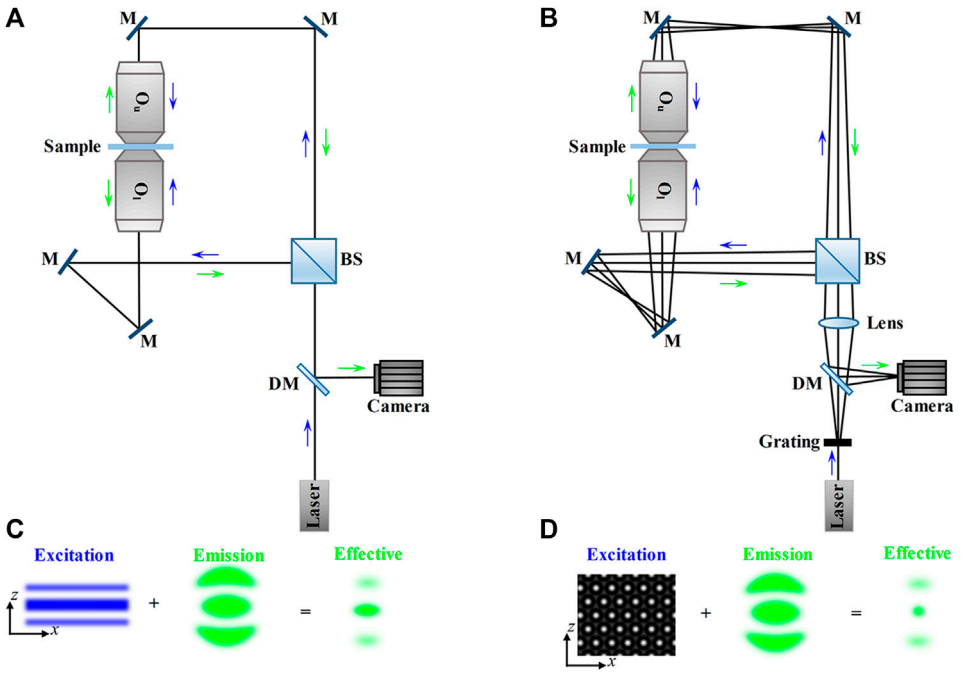

FIGURE 4 | Schematic and principle of I^5M and I^5S. **(A)** Schematic of I^5M. The excitation beam from the laser is fed through a beam splitter and four mirrors into the interference cavity. The fluorescence emitted from the sample is inversely collected by the same objective lenses, reflected by a dichroic mirror, and finally collected by a camera. **(B)** Schematic of I^5S. The excitation beam from the laser is split by a grating into three diffracted beams, which is the only difference between I^5S and I^5M. **(C)** PSFs in I^5M in the axial (xz) plane. The effective PSF is obtained by the superposition of excitation PSF and emission PSF. **(D)** The excitation pattern and PSFs in the axial (xz) plane. The effective PSF is obtained by the superimposition of the 3D interference pattern produced by the three diffracted beams and the emission PSF. Blue and green arrows indicate the directions of the excitation beam and fluorescence. DM, dichroic mirror; SM, scanning mirror; BS, 50/50 beam splitter; M, mirror; Ou, the upper objective lens; O_l, the lower objective lens.

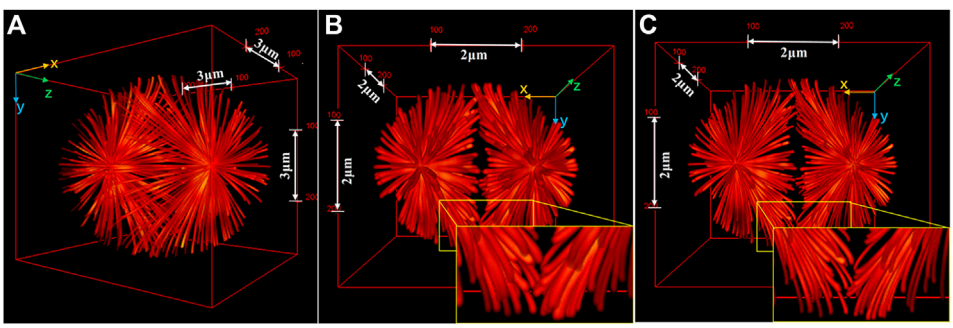

FIGURE 5 | Comparison of 3D images of a complex sample reconstructed by I^5S and SI^5S. **(A)** Ground truth image. **(B)** and **(C)** 3D perspectives of the images reconstructed by I^5S **(B)** and SI^5S **(C)**. The image reconstructed by SI^5S shows more distinct structures. The insets show expansions of the yellow outlined regions of the images. Figures are modified with permission from Ref. 36. Copyright © 2020 Elsevier.

positioning of the sample are challenging. For this, some variants of dual-lens LSFM compatible with sample formats used in traditional inverted microscope appeared, such as inverted SPIM [55] and open-top SPIM [56], which use oblique orthogonally arranged IO and DO above (**Figure 10B**) and beneath (**Figure 10C**) the sample stage of a traditional inverted microscope, respectively. However, the orthogonal arrangements still require the sum of access angles of IO and DO to be less than 90°, which limits the choice of their respective numerical apertures (NA).

To solve the problem, some dual-lens LSFM configurations with non-orthogonally arranged high-NA IO and/or DO were developed. For example, πSPIM [57] whose sum of the NA opening angles of IO and DO is close to π uses a high-NA IO to produce an oblique light sheet, as shown in **Figure 10D**. The method was used to image endocytosis in living yeast. Besides,

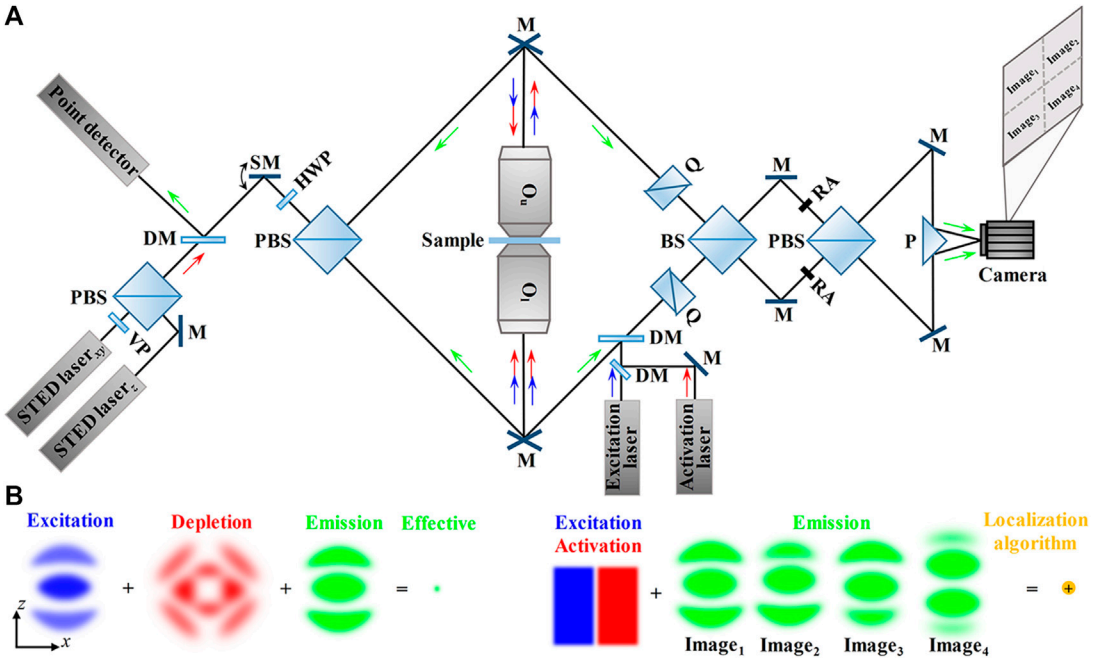

FIGURE 6 | Schematic and principle of dual-lens SRFM methods relying on nanoscopy. **(A)** Schematic of scanning modality (left, such as isoSTED/4Pi-RESOLFT) and widefield modality (right, 4Pi-SMLM). Left: in isoSTED, the beams for STEDxy (lateral) and STEDz (axial) are combined by a polarizing beam splitter and then fed through a scanning mirror and a second polarizing beam splitter into the 4Pi cavity. The fluorescence from the sample is inversely collected by the same objective lenses and reflected by a dichroic mirror, and finally collected by a point detector. Right: in 4Pi-SMLM, the synchronized excitation beam and activation beam are fed into the interference cavity so that only individual fluorescence molecules are bright at a time. The fluorescence is divided and recombined by a beam splitter and a polarizing beam splitter to create four interference patterns with different phases, and then, the four interference patterns are imaged by the four-quadrant camera simultaneously. **(B)** PSFs in isoSTED (left) and 4Pi-SMLM (right) in the axial (xz) plane. Left: the isotropic effective PSF is obtained by the superimposition of excitation PSF, depletion PSF (the superimposition of STEDxy beam and STEDz beam), and emission PSF. Right: the synchronized excitation beam and activation beam make sure only individual fluorescence molecules are bright at a time. The four emission PSF images obtained by the self-interference of individual fluorescence molecules are processed by the localization algorithm to localize the individual molecules. Blue and green arrows indicate the directions of the excitation beam and fluorescence. VP, 0–2π vortex phase plate; DM, dichroic mirror; SM, scanning mirror; Q, quartz wedges; BS, 50/50 beam splitter; PBS, polarizing beam splitter; RA, rectangle aperture; M, mirror; P, prism; Ou, the upper objective lens; O_l, the lower objective lens.

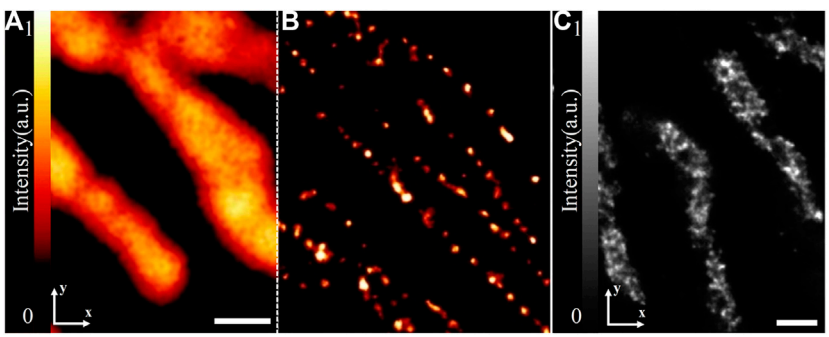

FIGURE 7 | Applications of isoSTED in 3D imaging. **(A)** and **(B)** Confocal image **(A)** and isoSTED image **(B)** of the translocase on the outer membrane of mitochondria complexes. **(C)** isoSTED image of mitochondrial inner membrane cristae protein complexes F1F0ATPase. There are pronounced heterogeneous cristae arrangements within individual mitochondrial tubules in which some regions are absent of cristae. Figures are modified with permission from Ref. 41. Copyright © 2009 American Chemical Society. All scale bars: 500 nm.

reflected light-sheet microscopy (RLSM) [58], in which the vertical light sheet focused by IO on the surface of atomic force microscopy (AFM), cantilever is reflected by 90° off to produce a horizontal light sheet, and the fluorescence is detected by a high-NA DO, as shown in **Figure 10E**. The method was used to monitor the binding properties of the glucocorticoid receptor and estrogen receptor-α to DNA in living MCF-7 cells. Combining the RLSM with individual molecule localization

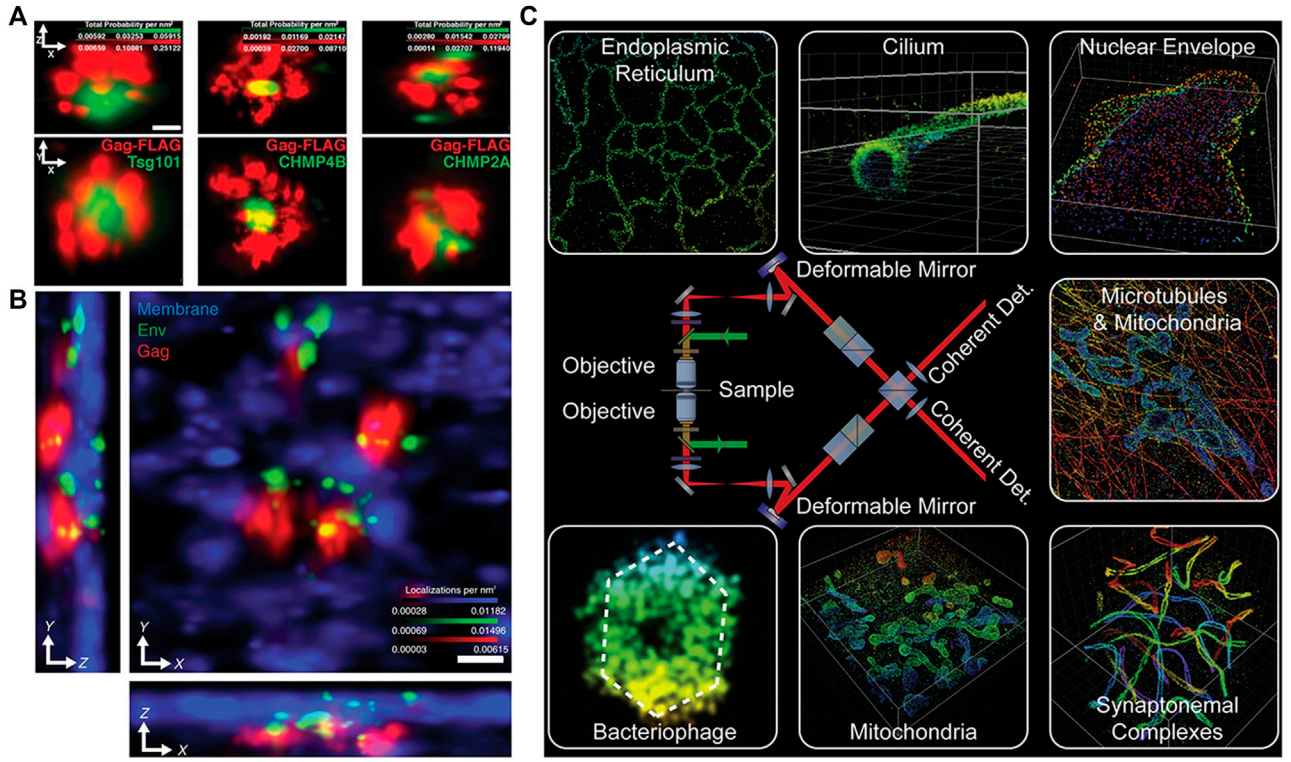

FIGURE 8 | Applications of 4Pi-SMLM in 3D imaging. **(A)** Two-color iPALM imaging of Gag-FLAG (red) and PSCFP2-ESCRT probes (including Tsg101, CHMP4B, and CHMP2A) (green). Axial (top) and lateral (bottom) views show localization of PSCFP2-ESCRT probes with the HIV Gag lattice. The figure is modified with permission from Ref. 45. Copyright © 2018 Springer Nature. **(B)** Three-color iPALM imaging of subviral angular distributions of Env at HIV-1 assembly sites. Lateral (center) and axial (lower and left) views show individual Env clusters (green) with four assembly sites (red) protruding from the plasma membrane (blue). The figure is modified with permission from Ref. 46. Copyright © 2014 American Association for the Advancement of Science. **(C)** A sketch of 4Pi-SMSN and some imaging results. The figure is modified with permission from Ref. 49. Copyright © 2016 Elsevier. Scale bars: 50 nm **(A)** and 100 nm **(B)**.

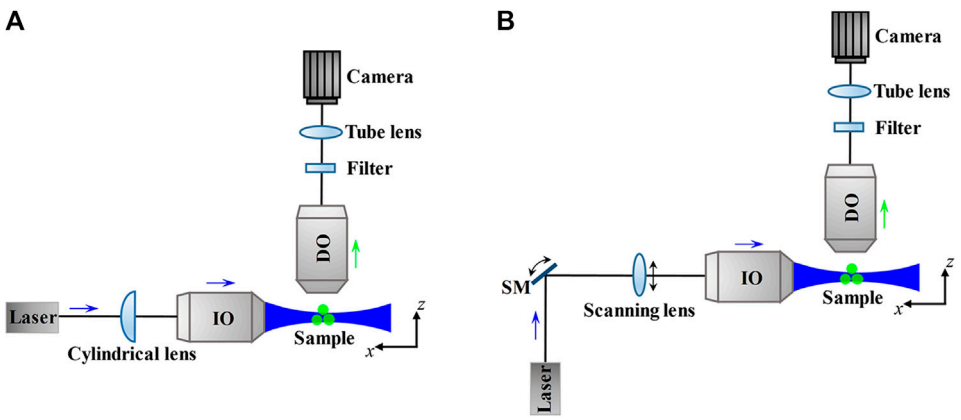

FIGURE 9 | Schematic and principle of dual-lens LSFM. **(A)** and **(B)** The thin excitation light sheet produced by a cylindrical lens **(A)** or a laser scanner (including a scanning mirror and a scanning lens) **(B)** only illuminate the focal plane of the detection objective lens, which reduces photobleaching and phototoxicity to the sample. The fluorescence emitted from the sample is through the filter and tube lens and then detected by the camera. Blue and green arrows indicate the directions of the excitation beam and fluorescence. SM, scanning mirror; IO, illumination objective lens; DO, detection objective lens.

(IML) algorithms, 3D imaging of the spatial organization of RNA polymerase II in the nucleus of U2OS cells was achieved [59]. In addition to them, a configuration called light-sheet Bayesian microscopy (LSBM) [60] whose angle between IO and DO is approximately 120° uses a prism-coupled IO to produce a horizontal light sheet at the focal plane of a high-NA DO, as

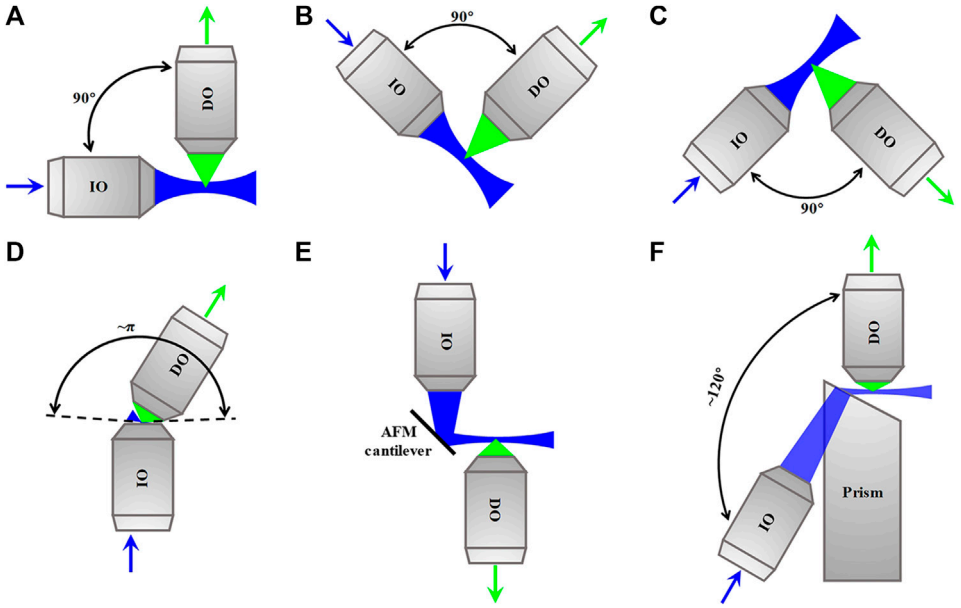

FIGURE 10 | Schematics of dual-lens LSFM methods. **(A)–(C)** Dual-lens LSFM methods with two orthogonal objective lenses. **(D)–(F)** Dual-lens LSFM methods with two non-orthogonal objective lenses. Blue and green arrows indicate the directions of the excitation beam and fluorescence. IO, illumination objective lens; DO, detection objective lens; AFM, atomic force microscopy.

shown in **Figure 10F**. The LSBM adopted localization-based Bayesian algorithm and achieved 50–60 nm lateral resolution, and it was applied to image heterochromatin in the nucleus of human embryonic stem cells.

In addition to RLSM and LSBM, the SR method of IML was also introduced to traditional dual-lens LSFM configuration and achieved imaging an entire 150-μm–thick human mammary MCF10A cell spheroid at a 3D resolution of 63 nm laterally and 140 nm axially [61]. To maximize the advantage of the remarkable optical sectioning capability of LSFM, some other SR methods had also been introduced into it to resolve fine intracellular structures of thick samples. For example, SIM can be combined with dual-lens LSFM to understand some dynamic cellular and subcellular processes, such as lattice-SIM [62], which achieves structured illumination by scanning a hexagonal lattice obtained a 3D resolution of 150 nm laterally and 280 nm axially, and Bessel-SIM [63], which scans parallel Bessel beams for structured illumination, obtaining a 3D resolution of 180, 230, and 350 nm in *x*-, *y*-, and *z*-directions, respectively. Besides, the integration of STED and SPIM can obtain 30% and 17% resolution improvements in the axial direction and lateral direction, respectively [64]. The method was used to observe actin in zebrafish embryos, and the STED–SPIM image showed more details than its SPIM counterpart, as shown in **Figures 11A and 11B**. Besides, a combination of 2PE and dual-lens LSFM called two-photon three-axis digital scanned light-sheet microscopy (DSLM) [65] achieved a 3D resolution of 350 nm laterally and 600 nm axially. Further introducing stochastic optical fluctuation imaging (SOFI) into it [66], the method achieved a 3D resolution of 200 nm laterally and 500 nm axially and was used for imaging mitochondria of HeLa cells in a volume of about 25 × 30 × 11.5 μm^3, as shown in **Figures 11C and 11D**.

DISCUSSION AND OUTLOOK

All 3D imaging methods reviewed here are based on dual-lens axial SRFM and LSFM which use two opposing and orthogonal/non-orthogonal objective lenses, respectively. We summarized their principles, configurations, and 3D imaging applications. We can conclude that, in 3D imaging of biological samples covering mammalian/model animal cells, tissues, and embryos, the two methods have their advantages and disadvantages but complement each other meanwhile. Specifically, the dual-lens axial SRFM methods have superior axial super resolution but are sensitive to the aberrations induced by the refractive index inhomogeneities within the sample, so they are limited to image fine intracellular structures of relatively thin biological samples like mammalian cells, and the dual-lens LSFM methods have an inferior axial resolution but inherent optical sectioning capability arising from selective plane illumination, and thus can be used for 3D imaging thicker biological samples like mammalian/model animal tissues and embryos. There are other dual-lens fluorescence microscopy methods [67] besides the ones reviewed here, for example, confocal theta fluorescence microscopy [68, 69], whose angle between illumination axis and detection axis is typically set to be 90° to improve the axial resolution and thus obtain isotropic 3D resolution. However,

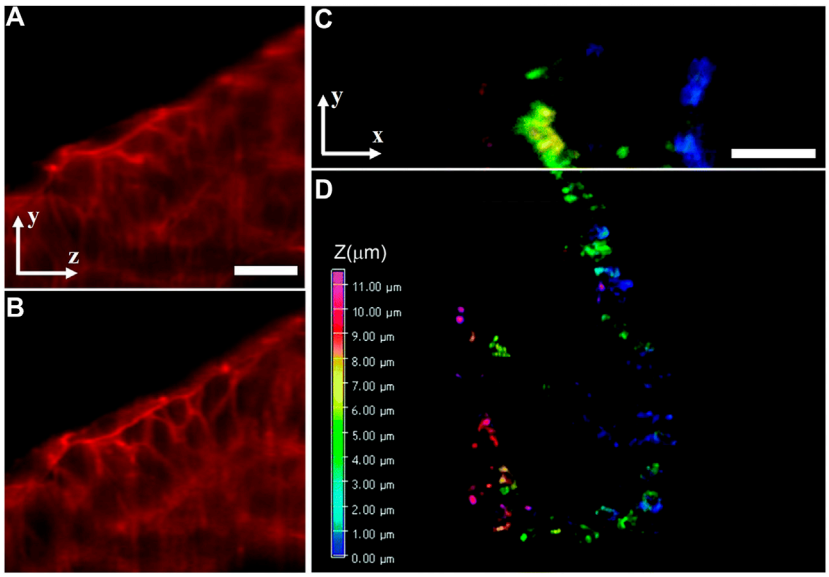

FIGURE 11 | Dual-lens LSFM methods for 3D imaging of intracellular structures of thick biological samples. **(A)** and **(B)** SPIM image **(A)** and STED–SPIM image **(B)** of the actin cytoskeleton in developing zebrafish embryos. Figures are modified with permission from Ref. 64. Copyright © 2011 Elsevier. **(C)** and **(D)** 3D images of mitochondrial structures of fixed HeLa cell taken with two-photon three-axis DSLM **(C)** and its SOFI counterpart **(D)**. Figures are modified with permission from Ref. 66. Copyright © 2016 The Royal Society of Chemistry. Scale bars: 20 μm **(A)** and 5 μm **(C)**.

its axial resolution can only be increased by 3–4 times, and its lateral resolution is slightly reduced because the effective NA of the two objective lenses is less than that of a single objective lens. Besides, there is an analog of I^5M called standing wave fluorescence microscopy (SWFM) [70] which also uses a pair of objective lenses positioned on opposite sides of the sample to improve the axial resolution. Differently, in the focal region of SWFM, the standing wave fringes formed by interference between two symmetric illumination wave fronts have periodic axial intensity distribution, which causes multiple fluorophores across several periods to not be distinguished because they emit the same intensity. As a result, the thickness of the observed samples in SWFM is limited to an axial extension comparable to one light wavelength which is thinner than most mammalian cells.

Furthermore, considering the experimental complexity of dual-lens axial SRFM, there are some virtual axial SRFM configurations that were developed to give access to this promising method to more laboratories. Specifically, one of the two opposing objective lenses is replaced by a flat mirror to make the incident and back-reflected illumination wave fronts interfere in the sample. These configurations provide comparable axial resolution enhancement that can be readily implemented on both scanning modality and widefield modality of the dual-lens axial SRFM methods, for example, isotropic single-objective focusing microscopy [71], axial-resolution–extended SIM through mirrored illumination [72], and mirror-enhanced axial-narrowing super-resolution STED technique [73], which can be regarded as virtual configurations of 4Pi microscopy, I^5S, and isoSTED, respectively. Besides, a virtual 4Pi-SMLM configuration can be achieved by combining the single-objective reflected interference scheme with 3D particle localization [74]. Similarly, there are also some simplified setups of dual-lens LSFM for reduced experimental difficulties but unchanged imaging effect. For example, single-objective SPIM (soSPIM) in which the illumination light from a high NA objective lens is reflected by a 45° micromirror cavity to create a horizontal light sheet and the emitted fluorescence is collected through the same objective lens [75], and single-objective light-sheet microscopy (SO-LSM) which uses a 45° mirror sidewall of a microfluidic channel instead to create a horizontal light sheet [76].

Moreover, for 3D imaging of some challenging intracellular structures and structures of the eukaryotic cell nucleus, a nanoscale or even atomic-scale super resolution is essential. Recently, an advanced combination of STED and SMLM called minimal photon fluxes (MINFLUX) microscopy [77], which localizes individual switchable fluorophores with a doughnut-shaped excitation beam minimum, achieved imaging of nuclear pore complexes of mammalian cells and dual-color imaging of DNA origami at a 3D resolution in the range of 1–3 nm [78]. It was also used to image the challenging quasi-one-dimensional lattice structured spectrin tetramers which connect the adjacent actin/adducin rings along the cytoskeleton of an axon, and the MINFLUX image showed a more realistic continuous spiral structure [79] than an earlier end-to-end and side-by-side organizations revealed by STORM [80] and polarized SIM [81], respectively. Although the MINFLUX is primarily operated on the single-lens configuration to date, there is no

fundamental barrier that rejects its integration into the dual-lens axial SRFM architecture to gain better SNR. Besides, 3D imaging of biological samples thicker than mammalian/model animal tissues and embryos, like the entire mouse brain and body, will contribute to a better understanding of some severe diseases related to human beings, such as Alzheimer's and Parkinson's. To do this, LSFM is a good choice. Meanwhile, the biological samples have to be transparent by optical clearing which uses organic solvents to make the refractive indexes of different layers matching the solvent [82, 83]. We can make a reasonable prediction that with the advent of more advanced optical clearing techniques, its combination with LSFM can lead to more unexpected discoveries.

AUTHOR CONTRIBUTIONS

XiL conceived the idea and finished the manuscript. YH, WL, and XH gave guidance. XH, CK, and XuL supervised the project. All the authors contributed to the discussion on this manuscript.

FUNDING

This work was financially supported by the grants from National Key R&D Program of China (2018YFA0701400, 2018YFE0119000), the Fundamental Research Funds for the Central Universities (2019QNA5006), and Zhejiang Provincial Natural Science Foundation (LR18H180001).

REFERENCES

1. White JG, Amos WB, Fordham M. An evaluation of confocal versus conventional imaging of biological structures by fluorescence light microscopy. *J Cell Biol* (1987) 105(1):41–8. doi:10.1083/jcb.105.1.41
2. Gustafsson MG, Shao L, Carlton PM, Wang CJ, Golubovskaya IN, Cande WZ, et al. Three-dimensional resolution doubling in wide-field fluorescence microscopy by structured illumination. *Biophys J* (2008) 94(12):4957–70. doi:10.1529/biophysj.107.120345
3. Abbe E. Beiträge zur Theorie des Mikroskops und der mikroskopischen Wahrnehmung. *Arch Mikrosk Anatat* (1873) 9:413–8. doi:10.1007/BF02956173
4. Hell SW. Far-field optical nanoscopy. *Science* (2007) 316(5828):1153. doi:10.1126/science.1137395
5. Hell SW Wichmann J. Breaking the diffraction resolution limit by stimulated emission: stimulated-emission-depletion fluorescence microscopy. *Optic Lett* (1994) 19(19):780–2. doi:10.1364/ol.19.000780
6. Hell SW Kroug M. Ground-state-depletion fluorscence microscopy: a concept for breaking the diffraction resolution limit. *Appl Phys* (1995) 60(5):495–7. doi:10.1007/BF01081333
7. Hofmann M, Eggeling C, Jakobs S, Hell SW. Breaking the diffraction barrier in fluorescence microscopy at low light intensities by using reversibly photoswitchable proteins. *Proc Natl Acad Sci USA* (2005) 102(49):17565. doi:10.1073/pnas.0506010102
8. Betzig E, Patterson GH, Sougrat R, Lindwasser OW, Olenych S, Bonifacino JS, et al. Imaging intracellular fluorescent proteins at nanometer resolution. *Science* (2006) 313(5793):1642. doi:10.1126/science.1127344
9. Rust MJ, Bates M, Zhuang X. Sub-diffraction-limit imaging by stochastic optical reconstruction microscopy (STORM). *Nat Methods* (2006) 3(10):793–6. doi:10.1038/nmeth929
10. Hess ST, Girirajan TPK, Mason MD. Ultra-high resolution imaging by fluorescence photoactivation localization microscopy. *Biophys J* (2006) 91(11):4258–72. doi:10.1529/biophysj.106.091116
11. Eggeling C, Willig KI, Sahl SJ, Hell SW. Lens-based fluorescence nanoscopy. *Q Rev Biophys* (2015) 48(2):178–243. doi:10.1017/S0033583514000146
12. Girkin JM Carvalho MT. The light-sheet microscopy revolution. *J Optic* (2018) 20(5):053002. doi:10.1088/2040-8986/aab58a
13. Swoger J, Huisken J, Stelzer EHK. Multiple imaging axis microscopy improves resolution for thick-sample applications. *Optic Lett* (2003) 28(18):1654–6. doi:10.1364/OL.28.001654
14. Huisken J Stainier DYR. Even fluorescence excitation by multidirectional selective plane illumination microscopy (mSPIM). *Optic Lett* (2007) 32(17):2608–10. doi:10.1364/OL.32.002608
15. Tomer R, Khairy K, Amat F, Keller PJ. Quantitative high-speed imaging of entire developing embryos with simultaneous multiview light-sheet microscopy. *Nat Methods* (2012) 9(7):755–63. doi:10.1038/nmeth.2062
16. Hell S Stelzer EHK. Properties of a 4Pi confocal fluorescence microscope. *J Opt Soc Am A* (1992) 9(12):2159–66. doi:10.1364/JOSAA.9.002159
17. Hell SW, Stelzer EHK, Lindek S, Cremer C. Confocal microscopy with an increased detection aperture: type-B 4Pi confocal microscopy. *Opt Lett* (1994) 19(3):222–4. doi:10.1364/OL.19.000222
18. Cremer A, Verrier S, Goroshkov A, Söling H-D, Hell SW. 4Pi-microscopy of the Golgi apparatus in live mammalian cells. *J Struct Biol* (2004) 147(1):70–6. doi:10.1016/j.jsb.2003.10.006
19. Hell SW, Lindek S, Cremer C, Stelzer EHK. Measurement of the 4Pi-confocal point spread function proves 75 nm axial resolution. *Appl Phys Lett* (1994) 64(11):1335. doi:10.1063/1.111926
20. Egner A, Jakobs S, Hell SW. Fast 100-nm resolution 3D-microscope reveals structural plasticity of mitochondria in live yeast. *Proc Natl Acad Sci USA* (2002) 99(6):3370–5. doi:10.1073/pnas.052545099
21. Gugel H, Bewersdorf J, Jakobs S, Engelhardt J, Storz R, Hell SW. Cooperative 4Pi excitation and detection yields sevenfold sharper optical sections in live-cell microscopy. *Biophys J* (2004) 87(6):4146–52. doi:10.1529/biophysj.104.045815
22. Bewersdorf J, Bennett BT, Knight KL. H2AX chromatin structures and their response to DNA damage revealed by 4Pi microscopy. *Proc Natl Acad Sci USA* (2006) 103(48):18137–42. doi:10.1073/pnas.0608709103
23. Plecitá-Hlavatá L, Lessard M, Šantorová J, Bewersdorf J, Ježek P. Mitochondrial oxidative phosphorylation and energetic status are reflected by morphology of mitochondrial network in INS-1E and HEP-G2 cells viewed by 4Pi microscopy. *Biochim Biophys Acta* (2008) 1777(7-8):834–46. doi:10.1016/j.bbabio.2008.04.002
24. Dlasková A, Spacek T, Santorova J, Plecita-Hlavata L, Berkova Z, Saudek F, et al. 4Pi microscopy reveals an impaired three-dimensional mitochondrial network of pancreatic islet β-cells, an experimental model of type-2 diabetes. *Biochim Biophys Acta* (2010) 1797(6-7):1327–41. doi:10.1016/j.bbabio.2010.02.003
25. Gustafsson MGL, Agard DA, Sedat JW. Sevenfold improvement of axial resolution in 3D wide-field microscopy using two objective-lenses. *Proc SPIE* (1995) 2412:147–56. doi:10.1117/12.205334
26. Gustafsson M, Agard D, Sedat J. 3D widefield microscopy with two objective lenses: experimental verification of improved axial resolution. *Proc SPIE* (1996) 2655:62–6. doi:10.1117/12.237489
27. Gustafsson MGL, Agard DA, Sedat JW. I^5M: 3D widefield light microscopy with better than 100 nm axial resolution. *J Microsc* (1999) 195(1):10–6. doi:10.1046/j.1365-2818.1999.00576.x
28. Gustafsson MGL. Surpassing the lateral resolution limit by a factor of two using structured illumination microscopy. *J Microsc* (2000) 198(2):82–7. doi:10.1046/j.1365-2818.2000.00710.x
29. Shao L, Isaac B, Uzawa S, Agard DA, Sedat JW, Gustafsson MG. I5S: wide-field light microscopy with 100-nm-scale resolution in three dimensions. *Biophys J* (2008) 94(12):4971–83. doi:10.1529/biophysj.107.120352
30. Shao L, Kner P, Rego EH, Gustafsson MG. Super-resolution 3D microscopy of live whole cells using structured illumination. *Nat Methods* (2011) 8(12):1044–6. doi:10.1038/nmeth.1734
31. Fiolka R, Shao L, Rego EH, Davidson MW, Gustafsson MG. Time-lapse two-color 3D imaging of live cells with doubled resolution using structured

illumination. *Proc Natl Acad Sci USA* (2012) 109(14):5311–5. doi:10.1073/pnas.1119262109
32. Chen Y, Cao R, Liu W, Zhu D, Zhang Z, Kuang C, et al. Widefield and total internal reflection fluorescent structured illumination microscopy with scanning galvo mirrors. *J Biomed Optic* (2018) 23(4):1–9. doi:10.1117/1.JBO.23.4.046007
33. Chen Y, Liu W, Zhang Z, Zheng C, Huang Y, Cao R, et al. Multi-color live-cell super-resolution volume imaging with multi-angle interference microscopy. *Nat Commun* (2018) 9(1):4818. doi:10.1038/s41467-018-07244-4
34. Liu W, Liu Q, Zhang Z, Han Y, Kuang C, Xu L, et al. Three-dimensional super-resolution imaging of live whole cells using galvanometer-based structured illumination microscopy. *Optic Express* (2019) 27(5):7237–48. doi:10.1364/OE.27.007237
35. Mats GLG. Nonlinear structured-illumination microscopy: wide-field fluorescence imaging with theoretically unlimited resolution. *Proc Natl Acad Sci USA* (2005) 102(37):13081–6. doi:10.1073/pnas.0406877102
36. Liu Q, Yuan Y, Liu W, Li X, Kuang C, Hao X, et al. Sub-60-nm 3D super-resolution imaging via saturated I5S. *Optic Commun* (2020) 473:125981. doi:10.1016/j.optcom.2020.125981
37. Shao L, Winoto L, Agard DA, Gustafsson MG, Sedat JW. Interferometer-based structured-illumination microscopy utilizing complementary phase relationship through constructive and destructive image detection by two cameras. *J Microsc* (2012) 246(3):229–36. doi:10.1111/j.1365-2818.2012.03604.x
38. Dyba M Hell SW. Focal spots of size λ/23 open up far-field fluorescence microscopy at 33 nm axial resolution. *Phys Rev Lett* (2002) 88(16):163901. doi:10.1103/PhysRevLett.88.163901
39. Dyba M, Jakobs S, Hell SW. Immunofluorescence stimulated emission depletion microscopy. *Nat Biotechnol* (2003) 21(11):1303–4. doi:10.1038/nbt897
40. Schmidt R, Wurm CA, Jakobs S, Engelhardt J, Egner A, Hell SW. Spherical nanosized focal spot unravels the interior of cells. *Nat Methods* (2008) 5(6):539–44. doi:10.1038/nmeth.1214
41. Schmidt R, Wurm CA, Punge A, Egner A, Jakobs S, Hell SW. Mitochondrial cristae revealed with focused light. *Nano Lett* (2009) 9(6):2508–10. doi:10.1021/nl901398t
42. Curdt F, Herr SJ, Lutz T, Schmidt R, Engelhardt J, Sahl SJ, et al. isoSTED nanoscopy with intrinsic beam alignment. *Optic Express* (2015) 23(24):30891–903. doi:10.1364/OE.23.030891
43. Bohm U, Hell SW, Schmidt R. 4Pi-RESOLFT nanoscopy. *Nat Commun* (2016) 7:10504. doi:10.1038/ncomms10504
44. Shtengel G, Galbraith J, Galbraith C, Lippincott-Schwartz J, Gillette JM, Manley S, et al. Interferometric fluorescent super-resolution microscopy resolves 3D cellular ultrastructure. *Proc Natl Acad Sci USA* (2009) 106(9):3125–30. doi:10.1073/pnas.0813131106
45. Van Engelenburg SB, Shtengel G, Sengupta P, Waki K, Jarnik M, Ablan SD, et al. Distribution of ESCRT machinery at HIV assembly sites reveals virus scaffolding of ESCRT subunits. *Science* (2014) 343(6171):653–6. doi:10.1126/science.1247786
46. Buttler CA, Pezeshkian N, Fernandez MV, Aaron J, Norman S, Freed EO, et al. Single molecule fate of HIV-1 envelope reveals late-stage viral lattice incorporation. *Nat Commun* (2018) 9(1):1861. doi:10.1038/s41467-018-04220-w
47. Brown TA, Tkachuk AN, Shtengel G, Kopek BG, Bogenhagen DF, Hess HF, et al. Superresolution fluorescence imaging of mitochondrial nucleoids reveals their spatial range, limits, and membrane interaction. *Mol Cell Biol* (2011) 31(24):4994–5010. doi:10.1128/MCB.05694-11
48. Aquino D, Schonle A, Geisler C, Middendorff CV, Wurm CA, Okamura Y, et al. Two-color nanoscopy of three-dimensional volumes by 4Pi detection of stochastically switched fluorophores. *Nat Methods* (2011) 8(4):353–9. doi:10.1038/nmeth.1583
49. Huang F, Sirinakis G, Allgeyer ES, Schroeder LK, Duim WC, Kromann EB, et al. Ultra-high resolution 3D imaging of whole cells. *Cell* (2016) 166(4):1028–40. doi:10.1016/j.cell.2016.06.016
50. Zhang Y, Lara-Tejero M, Bewersdorf J, Galan JE. Visualization and characterization of individual type III protein secretion machines in live bacteria. *Proc Natl Acad Sci USA* (2017) 114(23):6098–103. doi:10.1073/pnas.1705823114
51. Zhang Y, Schroeder LK, Lessard MD, Kidd P, Chung J, Song Y, et al. Nanoscale subcellular architecture revealed by multicolor three-dimensional salvaged fluorescence imaging. *Nat Methods* (2020) 17(2):225–31. doi:10.1038/s41592-019-0676-4
52. Greger K, Swoger J, Stelzer EHK. Basic building units and properties of a fluorescence single plane illumination microscope. *Rev Sci Instrum* (2007) 78(2):023705. doi:10.1063/1.2428277
53. Keller PJ, Schmidt AD, Wittbrodt J, Stelzer EHK. Reconstruction of zebrafish early embryonic development by scanned light sheet microscopy. *Science* (2008) 322(5904):1065–9. doi:10.1126/science.1162493
54. Huisken J, Swoger J, Del Bene F, Wittbrodt J, Stelzer EH. Optical sectioning deep inside live embryos by selective plane illumination microscopy. *Science* (2004) 305(5686):1007–9. doi:10.1126/science.1100035
55. Wu Y, Ghitani A, Christensen R, Santella A, Du Z, Rondeau G, et al. Inverted selective plane illumination microscopy (iSPIM) enables coupled cell identity lineaging and neurodevelopmental imaging in *Caenorhabditis elegans*. *Proc Natl Acad Sci USA* (2011) 108(43):17708. doi:10.1073/pnas.1108494108
56. McGorty R, Liu H, Kamiyama D, Dong Z, Guo S, Huang B. Open-top selective plane illumination microscope for conventionally mounted specimens. *Optic Express* (2015) 23(12):16142–53. doi:10.1364/OE.23.016142
57. Theer P, Dragneva D, Knop M. πSPIM: high NA high resolution isotropic light-sheet imaging in cell culture dishes. *Sci Rep* (2016) 6(1):32880. doi:10.1038/srep32880
58. Gebhardt JC, Suter DM, Roy R, Zhao ZW, Chapman AR, Basu S, et al. Single-molecule imaging of transcription factor binding to DNA in live mammalian cells. *Nat Methods* (2013) 10(5):421–6. doi:10.1038/nmeth.2411
59. Zhao ZW, Roy R, Gebhardt JC, Suter DM, Chapman AR, Xie XS. Spatial organization of RNA polymerase II inside a mammalian cell nucleus revealed by reflected light-sheet superresolution microscopy. *Proc Natl Acad Sci USA* (2014) 111(2):681–6. doi:10.1073/pnas.1318496111
60. Hu YS, Zhu Q, Elkins K, Tse K, Li Y, Fitzpatrick JAJ, et al. Light-sheet Bayesian microscopy enables deep-cell super-resolution imaging of heterochromatin in live human embryonic stem cells. *Opt Nanoscopy* (2013) 2(1):7. doi:10.1186/2192-2853-2-7
61. Cella Zanacchi F, Lavagnino Z, Perrone Donnorso M, Del Bue A, Furia L, Faretta M, et al. Live-cell 3D super-resolution imaging in thick biological samples. *Nat Methods* (2011) 8(12):1047–9. doi:10.1038/nmeth.1744
62. Chen BC, Legant WR, Wang K, Shao L, Milkie DE, Davidson MW, et al. Lattice light-sheet microscopy: imaging molecules to embryos at high spatiotemporal resolution. *Science* (2014) 346(6208):1257998. doi:10.1126/science.1257998
63. Gao L, Shao L, Chen BC, Betzig E. 3D live fluorescence imaging of cellular dynamics using Bessel beam plane illumination microscopy. *Nat Protoc* (2014) 9(5):1083–101. doi:10.1038/nprot.2014.087
64. Friedrich M, Gan Q, Ermolayev V, Harms GS. STED-SPIM: stimulated emission depletion improves sheet illumination microscopy resolution. *Biophys J* (2011) 100(8):L43–5. doi:10.1016/j.bpj.2010.12.3748
65. Zong W, Zhao J, Chen X, Lin Y, Ren H, Zhang Y, et al. Large-field high-resolution two-photon digital scanned light-sheet microscopy. *Cell Res* (2015) 25(2):254–7. doi:10.1038/cr.2014.124
66. Chen X, Zong W, Li R, Zeng Z, Zhao J, Xi P, et al. Two-photon light-sheet nanoscopy by fluorescence fluctuation correlation analysis. *Nanoscale* (2016) 8(19):9982. doi:10.1039/C6NR00324A
67. Liu W, Toussaint KC, Okoro C, Zhu D, Chen Y, Kuang C, et al. Breaking the axial diffraction limit: a guide to axial super-resolution fluorescence microscopy. *Laser Photon Rev* (2018) 12(8):1700333. doi:10.1002/lpor.201700333
68. Stelzer EHK Lindek S. Fundamental reduction of the observation volume in far-field light microscopy by detection orthogonal to the illumination axis: confocal theta microscopy. *Optic Commun* (1994) 111(5-6):536–47. doi:10.1016/0030-4018(94)90533-9
69. Stelzer EHK, Lindek S, Albrecht S, Pick R, Stricker R. A new tool for the observation of embryos and other large specimens: confocal theta fluorescence microscopy. *J Microsc* (1995) 179(1):1–10. doi:10.1111/j.1365-2818.1995.tb03608.x
70. Bailey B, Farkas DL, Taylor DL, Lanni F. Enhancement of axial resolution in fluorescence microscopy by standing-wave excitation. *Nature* (1993) 366(6450):44–8. doi:10.1038/366044a0

71. Mudry E, Le Moal E, Ferrand P, Chaumet PC, Sentenac A. Isotropic diffraction-limited focusing using a single objective lens. *Phys Rev Lett* (2010) 105(20):203903. doi:10.1103/PhysRevLett.105.203903
72. Manton JD, Ströhl F, Fiolka R, Kaminski CF, Rees EJ. Concepts for structured illumination microscopy with extended axial resolution through mirrored illumination. *Biomed Optic Express* (2020) 11(4):2098–108. doi:10.1364/BOE.382398
73. Yang X, Xie H, Alonas E, Liu Y, Chen X, Santangelo PJ, et al. Mirror-enhanced super-resolution microscopy. *Light Sci Appl* (2016) 5(6):e16134. doi:10.1038/lsa.2016.134
74. Schnitzbauer J, McGorty R, Huang B. 4Pi fluorescence detection and 3D particle localization with a single objective. *Optic Express* (2013) 21(17): 19701–8. doi:10.1364/OE.21.019701
75. Galland R, Grenci G, Aravind A, Viasnoff V, Studer V, Sibarita J-B. 3D high- and super-resolution imaging using single-objective SPIM. *Nat Methods* (2015) 12(7):641–4. doi:10.1038/nmeth.3402
76. Meddens MBM, Liu S, Finnegan PS, Edwards TL, James CD, Lidke KA. Single objective light-sheet microscopy for high-speed whole-cell 3D super-resolution. *Biomed Optic Express* (2016) 7(6):2219–36. doi:10.1364/BOE.7.002219
77. Balzarotti F, Eilers Y, Gwosch KC, Gynna AH, Westphal V, Stefani FD, et al. Nanometer resolution imaging and tracking of fluorescent molecules with minimal photon fluxes. *Science* (2017) 355(6325):606–12. doi:10.1126/science.aak9913
78. Gwosch KC, Pape JK, Balzarotti F, Hoess P, Ellenberg J, Ries J, et al. MINFLUX nanoscopy delivers 3D multicolor nanometer resolution in cells. *Nat Methods* (2020) 17(2):217–24. doi:10.1038/s41592-019-0688-0
79. abberior-instruments. abberior-instruments.com (2018). Available from: https://www.abberior-instruments.com/products/minflux [Accessed October 30, 2020].
80. Xu K, Zhong G, Zhuang X. Actin, spectrin, and associated proteins form a periodic cytoskeletal structure in axons. *Science* (2013) 339(6118):452–6. doi:10.1126/science.1232251
81. Zhanghao K, Chen X, Liu W, Li M, Liu Y, Wang Y, et al. Super-resolution imaging of fluorescent dipoles via polarized structured illumination microscopy. *Nat Commun* (2019) 10(1):4694. doi:10.1038/s41467-019-12681-w
82. Ertürk A, Becker K, Jährling N, Mauch CP, Hojer CD, Egen JG, et al. Three-dimensional imaging of solvent-cleared organs using 3DISCO. *Nat Protoc* (2012) 7(11):1983–95. doi:10.1038/nprot.2012.119
83. Pan C, Cai R, Quacquarelli FP, Ghasemigharagoz A, Lourbopoulos A, Matryba P, et al. Shrinkage-mediated imaging of entire organs and organisms using uDISCO. *Nat Methods* (2016) 13(10):859–67. doi:10.1038/nmeth.3964

Conflict of Interest: The authors declare that the research was conducted in the absence of any commercial or financial relationships that could be construed as a potential conflict of interest.

frontiers in Physics

REVIEW
published: 17 December 2020
doi: 10.3389/fphy.2020.598420

Coherent Anti-Stokes Raman Scattering Microscopy and Its Applications

*Shaowei Li, Yanping Li, Rongxing Yi, Liwei Liu and Junle Qu**

College of Physics and Optoelectronic Engineering, Shenzhen University, Shenzhen, China

Coherent anti-Stokes Raman scattering (CARS) microscopy can provide high resolution, high speed, high sensitivity, and non-invasive imaging of specific biomolecules without labeling. In this review, we first introduce the principle of CARS microscopy, and then discuss its configuration, including that of the laser source and the multiplex CARS system. Finally, we introduce the applications of CARS in biomedicine and materials, and its future prospects.

Keywords: Raman scattering, coherent anti-Stokes Raman scattering, nonlinear optical microscopy, label-free imaging, biomedical imaging

OPEN ACCESS

Edited by:
Ming Lei,
Xi'an Jiaotong University, China

Reviewed by:
Kebin Shi,
Peking University, China
Ping Wang,
Huazhong University of Science and Technology, China

****Correspondence:***
Junle Qu
jlqu@szu.edu.cn

Specialty section:
This article was submitted to Optics and Photonics, a section of the journal Frontiers in Physics

Received: *24 August 2020*
Accepted: *06 October 2020*
Published: *17 December 2020*

Citation:
Li S, Li Y, Yi R, Liu L and Qu J (2020) Coherent Anti-Stokes Raman Scattering Microscopy and Its Applications. Front. Phys. 8:598420. doi: 10.3389/fphy.2020.598420

INTRODUCTION

Raman scattering was named after its discoverer C. V. Raman, the celebrated Indian scientist, in 1928 [1]. The discovery of Raman scattering not only proved that the energy level of light is discrete but also opened up a new research area for the study of the chemical characteristics of molecules. First, Raman scattered photons in the mid-infrared range carry information about molecular vibration. The switch from infrared to visible light circumvents the strong optical absorption of water in the infrared region, which is of great significance in the field of biomedical science. Second, Raman spectroscopy obviates the need for chemical labeling when obtaining chemical information, so that the biological functional characteristics of the sample can be studied without chemical interference.

Although it has many advantages, spontaneous Raman scattering is a very weak second-order radiative process. The cross-section of Raman scattering is approximately 10–30 cm^2 per molecule, which is 10^{11} times smaller than the corresponding cross-section of infrared absorption. The small cross-section of the scattering leads to a low spontaneous Raman scattering efficiency and consequently necessitates a long integration time. This is acceptable for Raman spectroscopy, but for imaging, it is not feasible to collect real-time data with such a long integration time. The development of the femtosecond laser with high peak power has enabled the observation of many nonlinear processes, and promoted the study of coherent Raman scattering.

As a new nonlinear optical microscopy technique, coherent Raman scattering microscopy overcomes the limitation of the imaging speed of spontaneous Raman micro-imaging [2–8]. In coherent Raman scattering microscopy, typically, two beams of light are used to simultaneously excite the sample, one beam is referred to as the pump beam and the other is the Stokes beam. When the frequency difference between the two beams of light corresponds to a chemical bond vibrational frequency of the target sample, four simultaneous coherent Raman processes will occur. These processes are coherent anti-Stokes Raman scattering at the frequency $(\omega_p - \omega_s) + \omega_p$, coherent Stokes Raman scattering at the frequency $\omega_p - (\omega_p - \omega_s)$, stimulated Raman gain at ω_s, and stimulated Raman loss at ω_p. The CARS signal is generated at a frequency that is different from the excitation light. Stimulated Raman gain and stimulated Raman loss are both employed in another

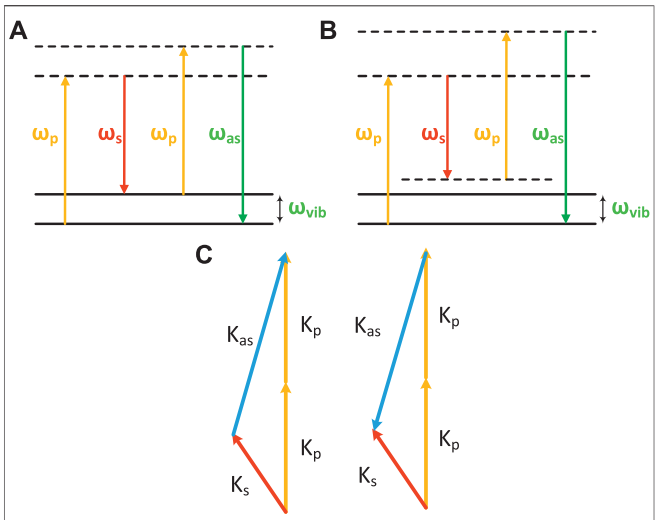

FIGURE 1 | Energy diagrams of the CARS process. Energy diagram of the **(A)** resonant condition and **(B)** non-resonant condition. **(C)** Phase-matching condition of CARS.

coherent Raman microscopy technique referred to as Stimulated Raman Scattering (SRS) Microscopy.

The first observation of CARS was reported by Terhune and Maker [9], as a third-order nonlinear effect in 1965 at Ford Motor Company, the car manufacturer. However, the official name of CARS was not coined until 10 years later by Begley [10]. Begley and his co-workers used CARS to study the chemical reaction kinetics of combustion. CARS microscopy was first implemented by Duncan [11] in 1982 using a non-collinear geometry to match the phase and obtain two-dimensional images. In 1999, Zumbusch [12] changed the excitation light configuration to overlap collinearly with the Stokes beam, and used a femtosecond laser for close focusing to achieve fast three-dimensional imaging. This work greatly promoted the rapid development of modern CARS microscopy technologies. Over the next few years, a systematic study of CARS was performed by Cheng and co-workers [2, 13–16]. In 2001, Cheng exploited polarization-CARS by using the difference between the polarizations of resonant and non-resonant CARS signals to eliminate the non-resonant background. Laser scanning CARS microscopy based on the picosecond pulsed laser was developed for high-speed imaging of biomedical samples [16], and the imaging speed of CARS reached the level of video-rate (20 frames/s) in 2005 [17]. Many strategies, including frequency modulation [18], nonlinear interferometric vibrational imaging [19], and spectral mixing [20] were used to suppress the non-resonant background or extract the pure Raman responses from the CARS spectrum.

In this review, the history and early development of CARS are introduced, as well as the implementation of both single frequency and multiplex CARS. Subsequently, recent applications in biomedical and material science are presented. Finally, the future directions of CARS are discussed.

CARS PRINCIPLE

CARS is a third-order nonlinear optical process. Under the interaction of $E(p)$, $E(s)$ of the Stokes light field and $E'(p)$ of the probe light field, the sample molecules will produce an anti-Stokes field E (as) with a frequency of $\omega_{as} = 2\omega_p - \omega_s$. **Figure 1** shows the energy diagram of the CARS process. **Figures 1A,B** show the generation process of the resonant CARS and non-resonant CARS signals, respectively, under the action of the pump light. In most cases, both the pump and probe light originate from the same laser beam; thus, in the above process, I_{CARS} describes the intensity of the CARS signal and is given by

$$I_{\mathrm{CARS}} \propto \left|\chi^{(3)}\right|^{(2)} I_p^2 I_s \left|\frac{\sin(\Delta kz/2)}{\Delta \mathrm{k}/2}\right|^2 \tag{1}$$

Where $k_i = 2\pi/\lambda_i$ is the wavevector, z is the thickness of the sample, and the wavevector mismatch Δk is defined as $\Delta k = k_{as} - (2K_p - k_s)$. When Δk z is close to zero, the sinc function is maximized. This condition is known as the phase-matched condition. **Figures 1C** exhibits the phase-matched conditions for forward- and epi-detected CARS signals. Here $\chi^{(3)}$ is the third-order polarizability which is usually expressed in the following form:

$$\chi^{(3)} = \chi_{NR}^{(3)} + \frac{\chi_R^{(3)}}{\Delta - i\Gamma} \tag{2}$$

where Δ is the Raman shift, which can be described as $\Delta = \omega_p - \omega_s - \Omega_R$, and Ω_R is the center frequency of a Raman line with bandwidth Γ. Hence, the CARS signal can be written as

$$I_{CARS} \propto \left|\chi_{NR}^{(3)}\right|^2 + \left|\chi_R^{(3)}(\Delta)\right|^2 + 2\chi_{NR}^{(3)} Re\chi_R^{(3)}(\Delta) \tag{3}$$

As can be seen from **Eq. 3**, the CARS intensity is determined by three terms: the first term is known as the non-resonant

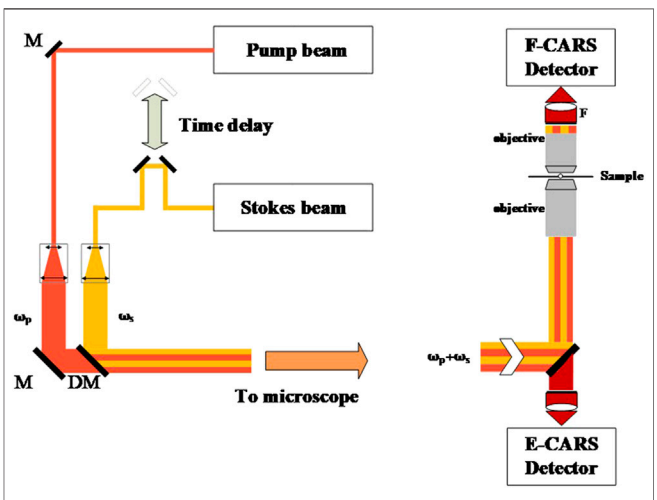

FIGURE 2 | (A) Spatio-temporal combination of pump and Stokes beams. **(B)** CARS signal collection: forward-CARS (F-CARS) and backward (epi)-CARS (E-CARS).

background and is independent of the Raman shift. The second term is the dominant contribution to probing strong resonant scatterers. The third term includes a mixture of resonant and non-resonant contributions, which contains the real part of the vibrational response.

CARS MICROSCOPY

Two pulsed laser trains at different frequencies, i.e., ω_p and ω_s, are necessary to build a CARS microscope (**Figure 2A**). One beam of the lasers is tunable to adjust the desired Raman shift, $\omega_p - \omega_s$. A pair of mirrors on a motorized linear stage is used to adjust the time delay between the pump and Stokes beams. Expanded beams are combined in a collinear geometry, and then directed to an inverted or upright microscope. Finally, the two temporally and spatially overlapped beams are focused onto the sample using a water/oil immersion objective lens. The strong CARS signals are generated both in the forward and backward direction, and are referred to as F-CARS and E-CARS, respectively (**Figure 2B**). Each signal is collected by a photomultiplier tube (PMT) or an avalanche photodiode after filtering the useless fluorescence with a bandpass filter, and focused by a lens. CARS images are obtained by a laser scanning system similar to that of a laser scanning confocal fluorescence microscope.

The cost and complexity of coherent Raman microscopy are mainly due to the laser light source. The two excitation beams must accurately control the absolute wavelength and linewidth. Although a pulsed dye laser in the visible band was used in the first coherent Raman microscopy system in history [11], the current mainstream light source for CARS is the Ti: sapphire laser or optical parametric oscillator (OPO) [17, 21]. Although the newly developed fiber laser-based coherent Raman microscopy can greatly reduce cost, it still cannot surpass solid-state lasers in performance [22, 23].

At least two excitation light sources are required for coherent Raman microscopy, one of which must be tunable to match the Raman frequency difference of different molecular vibration frequencies. For laser pulse width, a balance must be established; femtosecond has a shorter pulse width, higher peak power, and stronger nonlinear effect, while picosecond laser has narrower linewidth (l–10 cm^{-1} for a similar molecular vibration width) and can excite coherent Raman scattering more efficiently. Experiments show that pulses of 1–10 picoseconds can ideally achieve this balance [24]. For high-speed imaging, a repetition rate of at least 10 MHz is required, and ideally a higher rate. In addition, the laser excitation of the spectrum in the near infrared region can minimize the generation of the non-resonant background in CARS [12], providing less light-induced damage than visible light, and deeper penetration into the tissue. Further, because near-infrared light has a low transmission efficiency in a coherent Raman microscopy system (typically 10%–20% from excitation light to the sample), the power of the excitation source is approximately at the milliwatt level. Several groups have reported that they employed 50–200 fs pulse widths rather than a 2–6 picosecond pulse width [22, 25–27]. In spite of the fact that coherent Raman scattering processes could be excited by femtosecond pulses, this resulted in decreased signal levels, broader spectral resolution, and higher intensity non-resonant background signals.

CARS microscopy offers many unique advantages, including 1) nondestructive molecular imaging without labeling, 2) ease of spectral separation from the single-photon fluorescence background, and 3) 3D sectioning capability. Despite all of its advantages, however, the non-resonant background that limits the sensitivity of CARS is a major disadvantage.

MULTICOLOR CARS MICROSCOPY

Multicolor CARS microscopy refers to a method that can detect all or part of the vibration spectrum information on a sample at the same time. Multicolor CARS microscopy can be understood as a technique that can acquire a certain vibration spectrum such as a spontaneous Raman spectrum, but which has good imaging speed and spatial resolution. Although the imaging speed of multicolor CARS microscopy is still not as fast as that of single-color CARS, it has two essential advantages. The first is that multi-color CARS can obtain a full range of spectral information, while single-color can only obtain information at a certain frequency. The second is that multicolor CARS can better achieve quantitative analysis. Most microscopy techniques endeavor to achieve qualitative analysis at a certain point of the sample; however, in the fields of biology and material science, quantitative analysis of the composition of the sample is often required.

There are several common methods of implementing multicolor CARS microscopy, as shown in **Figure 3**. **Figures 3A** shows multicolor CARS microscopy using picosecond pump and femtosecond Stokes pulses [28, 29], in which a 100-fs Stokes pulse is used to provide a frequency domain window of approximately 400 cm^{-1}, which is sufficient to obtain the spectrum of the entire CH stretching range. In addition, by adjusting the center wavelength of the Stokes pulse, other regions of the vibration spectrum can also be studied, although not simultaneously. Using a 10-ps pump pulse can achieve a high spectral resolution of 2–3 cm^{-1}. **Figures 3B** shows multicolor CARS microscopy using picosecond pump and supercontinuum Stokes pulse [30–37]. Although a femtosecond Stokes pulse can include 400 cm^{-1} of spectral information in one-shot, this is still not sufficient for a vibrational frequency domain of 4,000 cm^{-1}. With the rapid development of photonic crystal fiber-based supercontinuum light sources, it has become feasible to use supercontinuum light sources as Stokes sources for CARS microscopy and to achieve a window of 4,000 cm^{-1}. Femtosecond and nanosecond sources are used to generate the supercontinuum spectrum. **Figures 3C** shows multicolor CARS using a femtosecond pump and Stokes pulse with spectral focusing [30, 38–44], and **Figures 3D** shows the principle of the spectral focusing method. In general, by using broadband pump and broadband Stokes pulses, the spectral resolution of the CARS signal is reduced. Hellerer [38] proposed the method of spectral focusing in 2004,

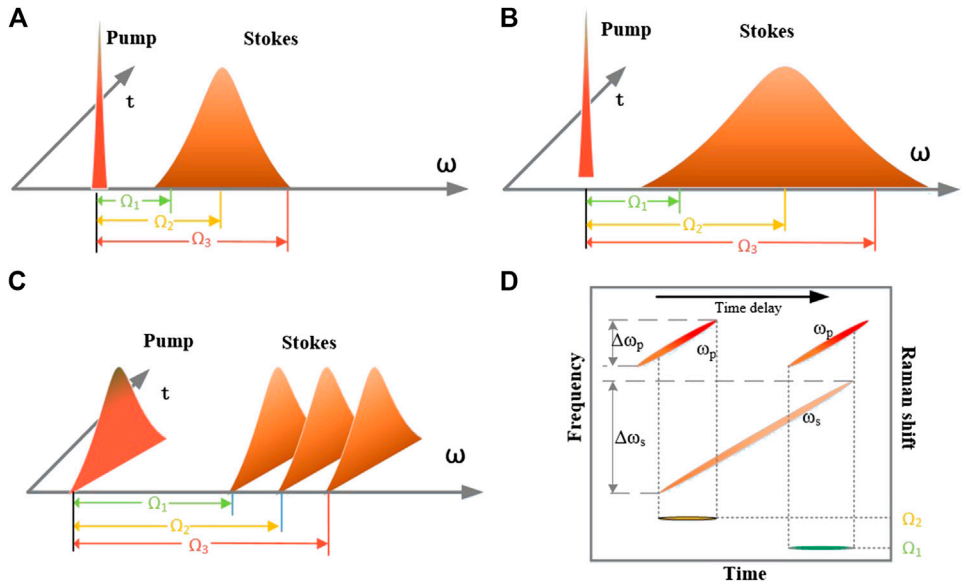

FIGURE 3 | Several common methods of multicolor CARS microscopy. **(A)** Picosecond pump and femtosecond Stokes pulses. **(B)** Picosecond pump and supercontinuum Stokes pulses. **(C)** Femtosecond pump and Stokes pulses with spectral focusing. **(D)** Principle of the spectral focusing method.

which can obtain a high spectral resolution when excited by a broadband light source. In this method, a dispersive medium is used to linearly chirp the light source. Although the linewidth of the chirped source remains the same, the instantaneous linewidth of the interaction between the two beams becomes very narrow. This instantaneous linewidth determines the spectral resolution of the system. The desired CARS spectrum can be obtained easily and quickly by adjusting the time delay between the pump and Stokes beams. In addition to being ingenious, this method has the advantage of being simple and fast. The disadvantages are the same as that of the ps-pump–fs-Stokes pulse method, i.e., it is not feasible to obtain a wide range of spectral signals simultaneously.

Over the past few years, it has become possible to study complex samples obtaining more detailed information for both biological and material science samples by multiplex CARS microscopy. Multiplex CARS microscopy confers the two key advantages of the full spectrum being available, and of being quantitative. The full spectrum is essential when studying complex samples with many overlapping peaks and the quantitative nature of the spectrum makes multiplex CARS microscopy a particularly useful technique for probing such complex samples. The extremely rich information obtained from imaging and spectral information constitutes a hyperspectral dataset. With the advent of phase retrieval techniques such as the maximum entropy method (MEM) and time-domain Kramers–Kronig (TD–KK) transformation, such spectra become amenable to analysis by multivariate techniques such as principal component analysis and related approaches. Therefore, the different components in the sample can be distinguished based on their vibrational information in an unlabeled manner, and the sensitivity of each component can be increased to the mM–μM level by using electronic resonance enhancement. Coupled with rapid spectral acquisition, these sophisticated algorithms should make it possible for researchers to investigate phenomena in the biological and material science fields that manifest as only subtle changes in the vibrational spectrum and occur on sub-micrometer length scales at sub-ms timescales.

APPLICATIONS OF CARS MICROSCOPY

Cell Imaging

CARS microscopy has been widely used for cell imaging [36, 45–53]. The strong CARS signal in the C-H stretching region can provide rich and unexpected chemical information, such as that related to lipids and proteins. For example, Nan et al. [54] used the CH_2 stretching vibration to map neutral lipid droplets in living fibroblasts. There was a significant process of disappearance of the lipid droplets in the cells in the early stage of differentiation, after which differentiation and accumulation began again. Paar et al. [55] used CARS microscopy to study the metabolism of intracellular lipid droplets during lipid decomposition. Experiments have shown that lipid droplet growth is achieved through the transfer of lipids between one organelle and another. This lipid transfer is not a rapid spontaneous process but completed within a few hours. Experimental data show that the growth of lipid droplets is a highly regulated process, and the decomposition and production of lipids occur in parallel in cells to prevent cell acid overflow. In another work [56], cancer cells *in vivo* and *in vitro* were monitored by CARS microscopy to assess the effect of diet on the metastasis of cancer cells. The results show that the physical disturbance of free fatty acids to the cancer cell membrane in lipid rich tumors is related to tumor metastasis. CARS has also been used to study prostate circulating carcinoma cells, and the results show that prostate circulatory carcinoma cells have a CARS signal

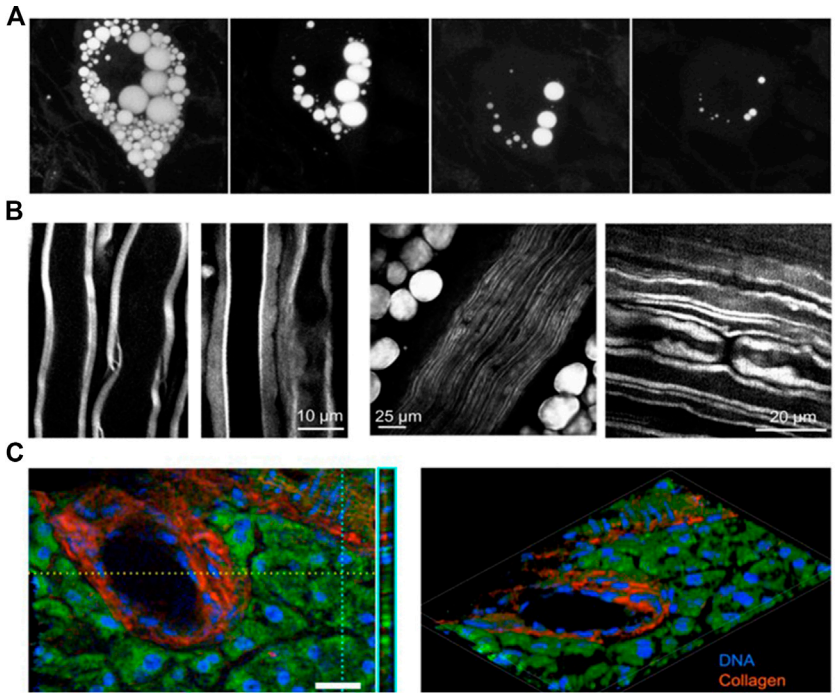

FIGURE 4 | (A) Adipocyte cellular lipid disintegration induced by forskolin [55]. **(B)** Imaging myelin sheath *ex vivo* and *in vivo* by CARS microscopy. **(C)** Extremely broadband, 785 cm^{-1} (nuclei) to 1,665 cm^{-1} (protein), CARS imaging of a murine pancreatic duct and 3D reconstruction imaging [60].

intensity seven times stronger than leukocytes [57]. The absorption and decomposition of surfactants in mammalian cells were studied by CARS spectroscopy [58]. The results show that living cells retain surfactants not only on the cell membrane but also throughout the intracellular membrane system. Label-free chemical mapping of cells by hyperspectral CARS microscopy has led to promising results. In another work, Di Napoli [59] fed different ratios of Palmitic acid and α-linolenic acid to human adipose derived stem cells and the results showed good contrast between cellular components and the corresponding CARS spectra.

Tissue Imaging

CARS has also been posited as a unique tool for label free tissue imaging. Visualization and characterization of the myelin sheath in the peripheral nervous system [61, 62] and central nervous system [63–67] is an important application. The sciatic nerve is a perfect candidate for *in vivo* CARS imaging since it is the largest single nerve in mammals and located in the peripheral nervous system isolated from the movement induced by breathing and the heartbeat. By 3D imaging of fat cells that surround the nerve, the underlying contrast mechanisms of *in vivo* CARS are found to arise from both interfaces and back reflection of the forward CARS signal [61]. Longitudinal *in vivo* CARS imaging of the spinal cord has been demonstrated through a careful experimental design to overcome complexities induced by laminectomy surgery [64]. To reduce the amount of tissue to be removed and improve the survivability and recovery time of the animals, the spine was exposed by making an incision through the skin and muscle tissue at T10, where the natural curvature of the spinal cord makes this region more superficial to the skin than at other locations [64]. The myelin sheath [63], myelinated axons [61], and the node of Ranvier [64] were distinguished clearly by CARS microscopy, as shown in **Figures 4B** left, middle, and right, respectively. The lipid metabolism in the atherosclerotic tissue of mouse and human subjects has been studied by CARS microscopy. Employing picosecond lasers, Wang et al. explored the imaging capabilities of CARS-based multimodal microscopy imaging of atherosclerosis. The study first demonstrated the capability to identify different atherosclerotic types [68] based on the scheme of atherosclerosis classification suggested by the American Heart Association (AHA) by imaging. Furthermore, Wang et al. [68] showed that a multimodal approach employing CARS and sum-frequency generation (SFG) signals allows quantitation of collagen and lipid content in lesions from early to advanced stages. Additional studies have shown increasing interest in using CARS microscopy for the studies of atherosclerotic lesions in animal models. Lim et al. utilized multimodal NLO microscopy to quantitatively measure the impact of a high-fat, high-cholesterol Western diet on the composition of atherosclerotic plaques in ApoE-deficient mice [69]. Using photonic crystal fiber-based CARS microscopy, the capability of multimodal imaging was demonstrated by an alternative femtosecond system to study lesion development in myocardial infarction-prone, hyperlipidemic rabbits [70]. Moreover, CARS has been used to skin biopsy [17, 71–74] and for stain-free histopathology. An imaging platform based on broadband coherent anti-Stokes Raman scattering (BCARS)

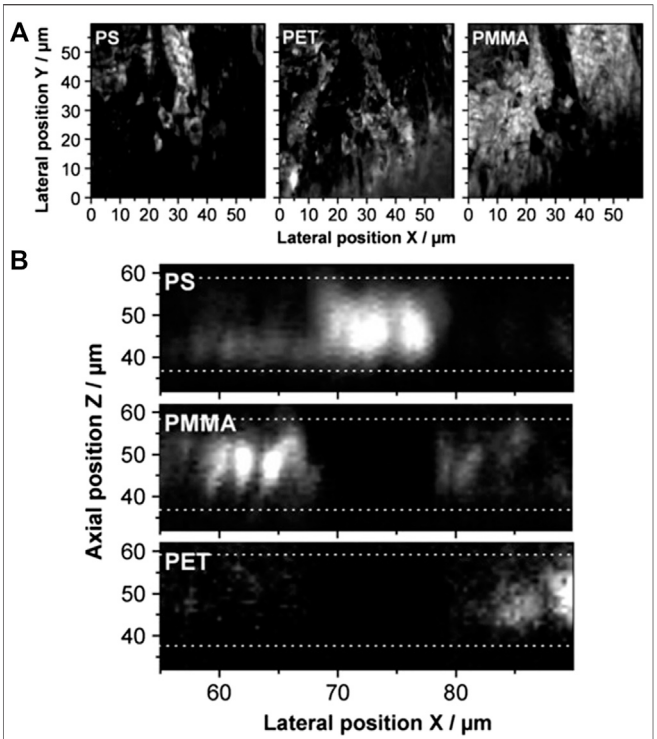

FIGURE 5 | CARS imaging of a polymer blend consisting of PS, PET, and PMMA. **(A)** Lateral and **(B)** axial views.

was developed by Camp et al. [60], and demonstrated 3D tissue imaging of a murine pancreatic duct showing the distributions of DNA, collagen, protein and lipids, as shown in **Figures 4C**. Recently, Wei-Wen [75] studied lipid particles in *Caenorhabditis elegans* by using this BCARS platform. The results show that fat particles in the adult intestine are diverse, and most are destined for the next generation. In comparison, fat particles in skin-like *epidermis* are similar and less dynamic.

Material Science

CARS microscopy lends itself well to the study of polymer films, thanks to the intrinsic sectioning capability of CARS and the intensity of the polymer peaks. Von Vacano et al. [35] were able to discriminate between the different polymers in tertiary blends of polystyrene (PS), polyethylene terephthalate (PET) and polymethylmethacrylate (PMMA), as well as to construct a virtual section of an adhesive and its carrier film, as shown in **Figure 5**. Jeoung group has also used the sectioning capability of multiplex CARS microscopy to quantitatively determine the thickness of sub-micron polymeric films [76, 77].

CARS microscopy has also been used to study reactions in zeolite crystals. CARS is an ideal tool to study the interplay between catalyst architecture and reactivity and hence obtain previously inaccessible information about fundamental processes of catalysts. Specifically, the precursor states of thiophene conversion over individual H-ZSM-5 zeolite crystals have been studied [78]. Maps of the catalyst loaded with thiophene revealed a heterogeneous, diffusion-limited distribution of thiophene throughout the zeolite, with the analytes accumulating at the center of the crystal and along defect sites.

More recently, Kotaro [79] developed a high-throughput flow cytometry system based on a Fourier-transform CARS spectrometer, enabling a high throughput of 2000 events/s. High chemical specificity and classification accuracy without labeling is demonstrated by the differentiation of polymer beads and *Euglena gracilis*. Super-resolution vibration imaging by higher-order CARS microscopy that detects higher-order anti-stokes Raman signals, such as six-wave mixing (SWM) at $\omega_{SWM} = 3\omega_p - 2\omega_S$ and eight-wave mixing (EWM) at $\omega_{EWM} = 4\omega_p - 3\omega_S$, increasing the respective lateral resolutions to 230 and 196 nm is reported by Li [80]. To increase the signal-to-noize radio and imaging speed, the wide-field CARS implementation was improved. Duarte [81] developed wide-field Fourier-transform coherent anti-Stokes Raman scattering microscopy with high-contrast, and outline detail of the wide-field FT-CARS signal. Heuke [82] implemented wide-field CARS by using a rotating disk with an imprinted modulation pattern and a PMT detector, referred to as spatial frequency modulated imaging (SPIFI). The results demonstrate that SPIFI-CARS could detect a much larger number of photons than that of laser-scanning microscopy (LSM)-CARS, and further, could be operated in ambient light.

OUTLOOK

Although the technological development of CARS is close to maturity, its application has just begun; however, the results are encouraging. Although CARS has broad application prospects, it will not replace other imaging methods in all fields. Because the cost of the spontaneous Raman system is relatively low and the system is relatively simple, it will likely be chosen when imaging speed is not a priority or there are technical difficulties (such as sample environment) to apply the coherent method. However, if the sample does not have second harmonic generation (SHG) characteristics, and fast acquisition is important, CARS or coherent Raman microscopy is the best label-free optical imaging method.

The clinical translation of CARS microscopy has long been hindered by traditional solid-state lasers that are sensitive to the environment. Ultrafast fiber lasers can potentially overcome these shortcomings but have not yet been fully exploited for CARS microscopy, as previous implementations have suffered from high intensity noise, a narrow tuning range, and low power, resulting in low image quality and slow imaging speed [23, 83–90]. Therefore, high-performance fiber lasers are highly required.

Another recent trend has been focusing on label-free multimodal nonlinear microscopy based on CARS, two-photon excited fluorescence (TPEF), and SHG [91–94]. The coupling of two-photon fluorescence, second-harmonic generation, and coherent anti-Stokes Raman scattering has allowed for investigation of a broad range of biological phenomena concerning lipid metabolism, cancer development, cardiovascular disease, and skin biology. By integrating the strengths of each non-linear optical (NLO) imaging modality, different structures and their interactions in a complex biological system can be simultaneously visualized.

Overall, as a label-free optical imaging method, CARS has a bright future with the development of other technologies such as laser light source and detection devices.

AUTHOR CONTRIBUTIONS

SL, LL and JQ wrote and edited the manuscript. SL, YL, RY, LL and JQ conceived the work and organized the manuscript.

FUNDING

This work was supported in part by National Natural Science Foundation of China (61525503/61620106016/61835009/61722508/61961136005/11904241), (Key) Project of Department of Education of Guangdong Province (2016KCXTD007), China Postdoctoral Science Foundation funded project (2018M643159) and Shenzhen Science and Technology Funding (JCYJ20180305124902165).

REFERENCES

1. Raman CV, Krishnan KS. A new type of secondary radiation. *Nature* (1928) 121(3048):501–2. doi:10.1038/121501c0
2. Cheng J-X, Volkmer A, Xie XS. Theoretical and experimental characterization of coherent anti-Stokes Raman scattering microscopy. *J Opt Soc Am B* (2002) 19(6):1363–75. doi:10.1364/josab.19.001363
3. Evans CL, Xie XS. Coherent anti-Stokes Raman scattering microscopy: chemical imaging for biology and medicine. *Annu Rev Anal Chem* (2008) 1:883–909. doi:10.1146/annurev.anchem.1.031207.112754
4. P Matousek M Morris, eds. *Emerging Raman applications and techniques in biomedical and pharmaceutical fields*. New York, NY: Springer Science & Business Media (2010)
5. Cheng JX, Xie XS. Vibrational spectroscopic imaging of living systems: an emerging platform for biology and medicine. *Science* (2015) 350(6264):aaa8870. doi:10.1126/science.aaa8870
6. Zhang C, Cheng J-X. Perspective: coherent Raman scattering microscopy, the future is bright. *APL Photonics* (2018) 3(9):090901. doi:10.1063/1.5040101
7. Rigneault H, Berto P. Tutorial: coherent Raman light matter interaction processes. *APL Photonics* (2018) 3(9):091101. doi:10.1063/1.5030335
8. Mazumder N, Balla NK, Zhuo GY, Kistenev YV, Kumar R, Kao FJ, et al. Label-free non-linear multimodal optical microscopy-basics, development, and applications. *Front Phys* (2019) 7:170. doi:10.3389/fphy.2019.00170
9. Terhune RW, Maker PD, Savage CM. Measurements of nonlinear light scattering. *Phys Rev Lett* (1965) 14(17):681–4. doi:10.1103/PhysRevLett.14.681
10. Begley RF, Harvey AB, Byer RL. Coherent anti-Stokes Raman spectroscopy. *Appl Phys Lett* (1974) 25(7):387–90
11. Duncan MD, Reintjes J, Manuccia TJ. Scanning coherent anti-Stokes Raman microscope. *Opt Lett* (1982) 7(8):350–2. doi:10.1364/ol.7.000350
12. Zumbusch A, Holtom GR, Xie XS. Three-dimensional vibrational imaging by coherent anti-Stokes Raman scattering. *Phys Rev Lett* (1999) 82(20):4142–5. doi:10.1103/PhysRevLett.82.4142
13. Djaker N, Lenne P-F, Marguet D, Colonna A, Hadjur C, Rigneault H. Coherent anti-Stokes Raman scattering microscopy (CARS): instrumentation and applications. *Nucl Instrum Methods Phys Res Sect A Accel Spectrom Detect Assoc Equip* (2007) 571(1-2):177–81. doi:10.1016/j.nima.2006.10.057
14. Cheng J-X. Coherent anti-Stokes Raman scattering microscopy. *Appl Spectrosc* (2007) 61(9):197–208. doi:10.1366/000370207781746044
15. Cheng J-X, Xie XS. Coherent anti-Stokes Raman scattering microscopy: instrumentation, theory, and applications. *J Phys Chem B* (2004) 108(3):827–40. doi:10.1021/jp035693v
16. Cheng JX, Jia YK, Zheng G, Xie XS. Laser-scanning coherent anti-Stokes Raman scattering microscopy and applications to cell biology. *Biophys J* (2002) 83(1):502–9. doi:10.1016/S0006-3495(02)75186-2
17. Evans CL, Potma EO, Puoris'haag M, Côté D, Lin CP, Xie XS. Chemical imaging of tissue *in vivo* with video-rate coherent anti-Stokes Raman scattering microscopy. *Proc Natl Acad Sci USA* (2005) 102(46):16807–12. doi:10.1073/pnas.0508282102
18. Ganikhanov F, Evans CL, Saar BG, Xie XS. High-sensitivity vibrational imaging with frequency modulation coherent anti-Stokes Raman scattering (FM CARS) microscopy. *Opt Lett* (2006) 31(12):1872–4. doi:10.1364/ol.31.001872
19. Marks DL, Boppart SA. Nonlinear interferometric vibrational imaging. *Phys Rev Lett* (2004) 92(12):123905. doi:10.1103/PhysRevLett.92.123905
20. Liu Y, Lee YJ, Cicerone MT. Broadband CARS spectral phase retrieval using a time-domain Kramers-Kronig transform. *Opt Lett* (2009) 34(9):1363–5. doi:10.1364/OL.34.001363
21. Ganikhanov F, Carrasco S, Sunney Xie X, Katz M, Seitz W, Kopf D. Broadly tunable dual-wavelength light source for coherent anti-Stokes Raman scattering microscopy. *Opt Lett* (2006) 31(9):1292–4. doi:10.1364/OL.31.001292
22. Murugkar S, Brideau C, Ridsdale A, Naji M, Stys PK, Anis H. Coherent anti-Stokes Raman scattering microscopy using photonic crystal fiber with two closely lying zero dispersion wavelengths. *Optic Express* (2007) 15(21):14028–37. doi:10.1364/OE.15.014028
23. Kieu K, Saar BG, Holtom GR, Xie XS, Wise FW. High-power picosecond fiber source for coherent Raman microscopy. *Opt Lett* (2009) 34(13):2051–3. doi:10.1364/ol.34.002051
24. Cheng J-X, Volkmer A, Book LD, Xie XS. An epi-detected coherent anti-Stokes Raman scattering (E-CARS) microscope with high spectral resolution and high sensitivity. *J Phys Chem B* (2001) 105(7):1277–80. doi:10.1021/jp003774a
25. Pegoraro AF, Ridsdale A, Moffatt DJ, Jia Y, Pezacki JP, Stolow A. Optimally chirped multimodal CARS microscopy based on a single Ti:sapphire oscillator. *Optic Express* (2009) 17(4):2984–96. doi:10.1364/OE.17.002984
26. Chen H, Wang H, Slipchenko MN, Jung Y, Shi Y, Zhu J, et al. A multimodal platform for nonlinear optical microscopy and microspectroscopy. *Optic Express* (2009) 17(3):1282–90. doi:10.1364/OE.17.001282
27. Ozeki Y, Dake F, Kajiyama S, Fukui K, Itoh K. Analysis and experimental assessment of the sensitivity of stimulated Raman scattering microscopy. *Optic Express* (2009) 17(5):3651–8. doi:10.1364/OE.17.003651
28. Cheng J-X, Volkmer A, Book LD, Xie XS. Multiplex coherent anti-Stokes Raman scattering microspectroscopy and study of lipid vesicles. *J Phys Chem B* (2002) 106(34):8493–8. doi:10.1021/jp025771z
29 Müller M, Schins JM. Imaging the thermodynamic state of lipid membranes with multiplex CARS microscopy. *J Phys Chem B* (2002) 106(14):3715–23. doi:10.1021/jp014012y
30. Chen BC, Sung J, Wu X, Lim SH. Chemical imaging and microspectroscopy with spectral focusing coherent anti-Stokes Raman scattering. *J Biomed Optic* (2011) 16(2):021112. doi:10.1117/1.3533315
31. Hashimoto K, Omachi J, Ideguchi T. Ultra-broadband rapid-scan Fourier-transform CARS spectroscopy with sub-10-fs optical pulses. *Optic Express* (2018) 26(11):14307–14. doi:10.1364/OE.26.014307
32. Kano H, Hamaguchi H-O. Ultrabroadband (> 2500 cm^{-1}) multiplex coherent anti-Stokes Raman scattering microspectroscopy using a supercontinuum generated from a photonic crystal fiber. *Appl Phys Lett* (2005) 86(12):121113. doi:10.1063/1.1883714
33. Kee TW, Cicerone MT. Simple approach to one-laser, broadband coherent anti-Stokes Raman scattering microscopy. *Opt Lett* (2004) 29(23):2701–3. doi:10.1364/ol.29.002701
34. Parekh SH, Lee YJ, Aamer KA, Cicerone MT. Label-free cellular imaging by broadband coherent anti-Stokes Raman scattering microscopy. *Biophys J* (2010) 99(8):2695–704. doi:10.1016/j.bpj.2010.08.009
35. von Vacano B, Meyer L, Motzkus M. Rapid polymer blend imaging with quantitative broadband multiplex CARS microscopy. *J Raman Spectrosc* (2007) 38(7):916–26. doi:10.1002/jrs.1704
36. Okuno M, Kano H, Leproux P, Couderc V, Day JP, Bonn M, et al. Quantitative CARS molecular fingerprinting of single living cells with the use of the maximum entropy method. *Angew Chem Int Ed Engl* (2010) 49(38):6773–7. doi:10.1002/anie.201001560

37. Okuno M, Kano H, Leproux P, Couderc V, Hamaguchi HO. Ultrabroadband multiplex CARS microspectroscopy and imaging using a subnanosecond supercontinuum light source in the deep near infrared. *Opt Lett* (2008) 33(9):923–5. doi:10.1364/ol.33.000923
38. Hellerer T, Annika MK, Zumbusch A. Spectral focusing: high spectral resolution spectroscopy with broad-bandwidth laser pulses. *Appl Phys Lett* (2004) 85(1):25–7. doi:10.1063/1.1768312
39. Rocha-Mendoza I, Langbein W, Borri P. Coherent anti-Stokes Raman microspectroscopy using spectral focusing with glass dispersion. *Appl Phys Lett* (2008) 93(20):201103. doi:10.1063/1.3028346
40. Langbein W, Rocha-Mendoza I, Borri P. Coherent anti-Stokes Raman microspectroscopy using spectral focusing: theory and experiment. *J Raman Spectrosc* (2009) 40(7):800–8. doi:10.1002/jrs.2264
41. Langbein W, Rocha-Mendoza I, Borri P. Single source coherent anti-Stokes Raman microspectroscopy using spectral focusing. *Appl Phys Lett* (2009) 95(8):081109. doi:10.1063/1.3216073
42. Gu M, Satija A, Lucht RP. Impact of moderate pump–Stokes chirp on femtosecond coherent anti-Stokes Raman scattering spectra. *J Raman Spectrosc* (2020) 51(1):115–24. doi:10.1002/jrs.5754
43. Fu D, Holtom G, Freudiger C, Zhang X, Xie XS. Hyperspectral imaging with stimulated Raman scattering by chirped femtosecond lasers. *J Phys Chem B* (2013) 117(16):4634–40. doi:10.1021/jp308938t
44. Rocha-Mendoza I, Langbein W, Watson P, Borri P. Differential coherent anti-Stokes Raman scattering microscopy with linearly chirped femtosecond laser pulses. *Opt Lett* (2009) 34(15):2258–60. doi:10.1364/ol.34.002258
45. Segawa H, Okuno M, Kano H, Leproux P, Couderc V, Hamaguchi HO. Label-free tetra-modal molecular imaging of living cells with CARS, SHG, THG and TSFG (coherent anti-Stokes Raman scattering, second harmonic generation, third harmonic generation and third-order sum frequency generation). *Optic Express* (2012) 20(9):9551–7. doi:10.1364/OE.20.009551
46. Kano H. Molecular spectroscopic imaging using a white-light laser source. *Bull Chem Soc Jpn* (2010) 83(7):735–43. doi:10.1246/bcsj.20100004
47. Chen BC, Sung J, Lim SH. Chemical imaging with frequency modulation coherent anti-Stokes Raman scattering microscopy at the vibrational fingerprint region. *J Phys Chem B* (2010) 114(50):16871–80. doi:10.1021/jp104553s
48. Brackmann C, Norbeck J, Åkeson M, Bosch D, Larsson C, Gustafsson L, et al. CARS microscopy of lipid stores in yeast: the impact of nutritional state and genetic background. *J Raman Spectrsc* (2009) 40(7):748–56. doi:10.1002/jrs.2356
49. Vartiainen EM, Rinia HA, Müller M, Bonn M. Direct extraction of Raman line-shapes from congested CARS spectra. *Optic Express* (2006) 14(8):3622–30. doi:10.1364/OE.14.003622
50. Shimada R, Kano H, Hamaguchi HO. Hyper-Raman microspectroscopy: a new approach to completing vibrational spectral and imaging information under a microscope. *Opt Lett* (2006) 31(3):320–2. doi:10.1364/OL.31.000320
51. Ivleva NP, Niessner R, Panne U. Characterization and discrimination of pollen by Raman microscopy. *Anal Bioanal Chem* (2005) 381(1):261–7. doi:10.1007/s00216-004-2942-1
52. van Manen H-J, Kraan YM, Roos D, Otto C. Intracellular chemical imaging of heme-containing enzymes involved in innate immunity using resonance Raman microscopy. *J Phys Chem B* (2004) 108(48):18762–71. doi:10.1021/jp046955b
53. McConnell G, Riis E. Photonic crystal fibre enables short-wavelength two-photon laser scanning fluorescence microscopy with fura-2. *Phys Med Biol* (2004) 49(20):4757. doi:10.1088/0031-9155/49/20/007
54. Nan X, Cheng JX, Xie XS. Vibrational imaging of lipid droplets in live fibroblast cells with coherent anti-Stokes Raman scattering microscopy. *J Lipid Res* (2003) 44(11):2202–8. doi:10.1194/jlr.D300022-JLR200
55. Paar M, Jüngst C, Steiner NA, Magnes C, Sinner F, Kolb D, et al. Remodeling of lipid droplets during lipolysis and growth in adipocytes. *J Biol Chem* (2012) 287(14):11164–73. doi:10.1074/jbc.M111.316794
56. Le TT, Huff TB, Cheng JX. Coherent anti-Stokes Raman scattering imaging of lipids in cancer metastasis. *BMC Canc* (2009) 9(1):42. doi:10.1186/1471-2407-9-42
57. Mitra R, Chao O, Urasaki Y, Goodman OB, Le TT. Detection of lipid-rich prostate circulating tumour cells with coherent anti-Stokes Raman scattering microscopy. *BMC Canc* (2012) 12(1):540. doi:10.1186/1471-2407-12-540
58. Okuno M, Kano H, Fujii K, Bito K, Naito S, Leproux P, et al. Surfactant uptake dynamics in mammalian cells elucidated with quantitative coherent anti-Stokes Raman scattering microspectroscopy. *PloS One* (2014) 9(4):e93401. doi:10.1371/journal.pone.0093401
59. Di Napoli C, Pope I, Masia F, Watson P, Langbein W, Borri P. Hyperspectral and differential CARS microscopy for quantitative chemical imaging in human adipocytes. *Biomed Optic Express* (2014) 5(5):1378–90. doi:10.1364/BOE.5.001378
60. Camp CH, Jr, Lee YJ, Heddleston JM, Hartshorn CM, Hight Walker AR, Rich JN, et al. High-speed coherent Raman fingerprint imaging of biological tissues. *Nat Photon* (2014) 8(8):627–34. doi:10.1038/nphoton.2014.145
61. Huff TB, Cheng JX. *In vivo* coherent anti-Stokes Raman scattering imaging of sciatic nerve tissue. *J Microsc* (2007) 225(2):175–82. doi:10.1111/j.1365-2818.2007.01729.x
62. Jung Y, Ng JH, Keating CP, Senthil-Kumar P, Zhao J, Randolph MA, et al. Comprehensive evaluation of peripheral nerve regeneration in the acute healing phase using tissue clearing and optical microscopy in a rodent model. *PloS One* (2014) 9(4):e94054. doi:10.1371/journal.pone.0094054
63. Fu Y, Wang H, Huff TB, Shi R, Cheng JX. Coherent anti-Stokes Raman scattering imaging of myelin degradation reveals a calcium-dependent pathway in lyso-PtdCho-induced demyelination. *J Neurosci Res* (2007) 85(13):2870–81. doi:10.1002/jnr.21403
64. Shi Y, Zhang D, Huff TB, Wang X, Shi R, Xu XM, et al. Longitudinal *in vivo* coherent anti-Stokes Raman scattering imaging of demyelination and remyelination in injured spinal cord. *J Biomed Optic* (2011) 16(10):106012. doi:10.1117/1.3641988
65. Bélanger E, Henry FP, Vallée R, Randolph MA, Kochevar IE, Winograd JM, et al. *In vivo* evaluation of demyelination and remyelination in a nerve crush injury model. *Biomed Optic Express* (2011) 2(9):2698–708. doi:10.1364/BOE.2.002698
66. Shi Y, Kim S, Huff TB, Borgens RB, Park K, Shi R, et al. Effective repair of traumatically injured spinal cord by nanoscale block copolymer micelles. *Nat Nanotechnol* (2010) 5(1):80–7. doi:10.1038/nnano.2009.303
67. Wang H, Fu Y, Zickmund P, Shi R, Cheng JX. Coherent anti-Stokes Raman scattering imaging of axonal myelin in live spinal tissues. *Biophys J* (2005) 89(1):581–91. doi:10.1529/biophysj.105.061911
68. Wang HW, Langohr IM, Sturek M, Cheng JX. Imaging and quantitative analysis of atherosclerotic lesions by CARS-based multimodal nonlinear optical microscopy. *Arterioscler Thromb Vasc Biol* (2009) 29(9):1342–8. doi:10.1161/ATVBAHA.109.189316
69. Lim RS, Suhalim JL, Miyazaki-Anzai S, Miyazaki M, Levi M, Potma EO, et al. Identification of cholesterol crystals in plaques of atherosclerotic mice using hyperspectral CARS imaging. *J Lipid Res* (2011) 52(12):2177–86. doi:10.1194/jlr.M018077
70. Mostaço-Guidolin LB, Sowa MG, Ridsdale A, Pegoraro AF, Smith MS, Hewko MD, et al. Differentiating atherosclerotic plaque burden in arterial tissues using femtosecond cars-based multimodal nonlinear optical imaging. *Biomed Optic Express* (2010) 1(1):59–73. doi:10.1364/BOE.1.000059
71. Kiss N, Krolopp Á, Lőrincz K, Bánvölgyi A, Szipőcs R, Wikonkál N. Stain-free histopathology of basal cell carcinoma by dual vibration resonance frequency cars microscopy. *Pathol Oncol Res* (2018) 24(4):927–30. doi:10.1007/s12253-017-0356-6
72. Breunig HG, Bückle R, Kellner-Höfer M, Weinigel M, Lademann J, Sterry W, et al. Combined *in Vivo* multiphoton and cars imaging of healthy and disease-affected human skin. *Microsc Res Tech* (2012) 75(4):492–8. doi:10.1002/jemt.21082
73. König K, Breunig HG, Bückle R, Kellner-Höfer M, Weinigel M, Büttner E, et al. Optical skin biopsies by clinical CARS and multiphoton fluorescence/SHG tomography. *Laser Phys Lett* (2011) 8(6):465. doi:10.1002/lapl.201110014
74. Vogler N, Meyer T, Akimov D, Latka I, Krafft C, Bendsoe N, et al. Multimodal imaging to study the morphochemistry of basal cell carcinoma. *J Biophot* (2010) 3(10-11):728–36. doi:10.1002/jbio.201000071
75. Chen W-W, Lemieux GA, Camp CH, Chang T-C, Ashrafi K, Cicerone MT. Spectroscopic coherent Raman imaging of *Caenorhabditis elegans* reveals lipid particle diversity. *Nat Chem Biol* (2020) 16:1087–95. doi:10.1038/s41589-020-0565-2
76. Choi DS, Jeoung SC, Chon BH. Thickness dependent CARS measurement of polymeric thin films without depth-profiling. *Optic Express* (2008) 16(4):2604–13. doi:10.1364/oe.16.002604

77. Yahng JS, Jeoung SC. Thickness determination with chemical identification of double-layered polymeric thin film by using multiplex CARS. *Optic Laser Eng* (2011) 49(1):66–70. doi:10.1016/j.optlaseng.2010.08.016
78. Kox MH, Domke KF, Day JP, Rago G, Stavitski E, Bonn M, et al. Label-free chemical imaging of catalytic solids by coherent anti-Stokes Raman scattering and synchrotron-based infrared microscopy. *Angew Chem Int Ed Engl* (2009) 48(47):8990–4. doi:10.1002/anie.200904282
79. Hiramatsu K, Ideguchi T, Yonamine Y, Lee S, Luo Y, Hashimoto K, et al. High-throughput label-free molecular fingerprinting flow cytometry. *Sci Adv* (2019) 5(1):eaau0241. doi:10.1126/sciadv.aau0241
80. Gong L, Zheng W, Ma Y, Huang Z. Higher-order coherent anti-Stokes Raman scattering microscopy realizes label-free super-resolution vibrational imaging. *Nat Photon* (2019) 14:115–22. doi:10.1038/s41566-019-0535-y
81. Duarte AS, Schnedermann C, Kukura P. Wide-field detected fourier transform CARS microscopy. *Sci Rep* (2016) 6:37516. doi:10.1038/srep37516
82. Heuke S, Sivankutty S, Scotte C, Stockton P, Bartels RA, Sentenac A, et al. Spatial frequency modulated imaging in coherent anti-Stokes Raman microscopy. *Optica* (2020) 7(5):417–24. doi:10.1364/Optica.386526
83. Kong C, Pilger C, Hachmeister H, Wei X, Cheung TH, Lai CSW, et al. High-contrast, fast chemical imaging by coherent Raman scattering using a self-synchronized two-colour fibre laser. *Light Sci Appl* (2020) 9(1):25. doi:10.1038/s41377-020-0259-2
84. Tai B. *Fiber-based high energy ultrafast sources for nonlinear microscopy*. [PhD thesis]. Ann Arbor (MI): Boston University (2019).
85. Xu C, Wise FW. Recent advances in fiber lasers for nonlinear microscopy. *Nat Photon* (2013) 7(11):875–82. doi:10.1038/nphoton.2013.284
86. Baumgartl M, Gottschall T, Abreu-Afonso J, Díez A, Meyer T, Dietzek B, et al. Alignment-free, all-spliced fiber laser source for CARS microscopy based on four-wave-mixing. *Optic Express* (2012) 20(19):21010–8. doi:10.1364/OE.20.021010
87. Wang K, Freudiger CW, Lee JH, Saar BG, Xie XS, Xu C. All fiber, 1064-nm time-lens source for coherent anti-Stokes Raman scattering and stimulated Raman scattering microscopy. *Proc SPIE* (2011) Xi7903:79030. doi:10.1117/12.875898
88. Selm R, Winterhalder M, Zumbusch A, Krauss G, Hanke T, Sell A, et al. Ultrabroadband background-free coherent anti-Stokes Raman scattering microscopy based on a compact Er:fiber laser system. *Opt Lett* (2010) 35(19):3282–4. doi:10.1364/OL.35.003282
89. Pegoraro AF, Ridsdale A, Moffatt DJ, Pezacki JP, Thomas BK, Fu L, et al. All-fiber CARS microscopy of live cells. *Optic Express* (2009) 17(23):20700–6. doi:10.1364/OE.17.020700
90. Andresen ER, Nielsen CK, Thøgersen J, Keiding SR. Fiber laser-based light source for coherent anti-Stokes Raman scattering microspectroscopy. *Optic Express* (2007) 15(8):4848–56. doi:10.1364/oe.15.004848
91. Yarbakht M, Pradhan P, Köse-Vogel N, Bae H, Stengel S, Meyer T, et al. Nonlinear multimodal imaging characteristics of early septic liver injury in a mouse model of peritonitis. *Anal Chem* (2019) 91(17):11116–21. doi:10.1021/acs.analchem.9b01746
92. Meyer T, Bae H, Hasse S, Winter J, Woedtke TV, Schmitt M, et al. Multimodal nonlinear microscopy for therapy monitoring of cold atmospheric plasma treatment. *Micromachines* (2019) 10(9). doi:10.3390/mi10090564
93. Li R, Wang X, Zhou Y, Zong H, Chen M, Sun M. Advances in nonlinear optical microscopy for biophotonics. *J Nanophotonics* (2018) 12(3):033007. doi:10.1117/1.JNP.12.033007
94. Pegoraro AF, Slepkov AD, Ridsdale A, Moffatt DJ, Stolow A. Hyperspectral multimodal CARS microscopy in the fingerprint region. *J Biophot* (2014) 7(1-2):49–58. doi:10.1002/jbio.201200171

Conflict of Interest: The authors declare that the research was conducted in the absence of any commercial or financial relationships that could be construed as a potential conflict of interest.

frontiers in Physics

ORIGINAL RESEARCH
published: 14 January 2021
doi: 10.3389/fphy.2020.621966

Deep Learning Assisted Zonal Adaptive Aberration Correction

Biwei Zhang[1,2], *Jiazhu Zhu*[1,2], *Ke Si*[1,2,3] *and Wei Gong*[1,3]*

[1]Department of Neurology of the Second Affiliated Hospital, State Key Laboratory of Modern Optical Instrumentation, Zhejiang University School of Medicine, Hangzhou, China, [2]College of Optical Science and Engineering, Zhejiang University, Hangzhou, China, [3]NHC and CAMS Key Laboratory of Medical Neurobiology, MOE Frontier Science Center for Brain Research and Brain–Machine Integration, School of Brain Science and Brain Medicine, Zhejiang University, Hangzhou, China

Deep learning (DL) has been recently applied to adaptive optics (AO) to correct optical aberrations rapidly in biomedical imaging. Here we propose a DL assisted zonal adaptive correction method to perform corrections of high degrees of freedom while maintaining the fast speed. With a trained DL neural network, the pattern on the correction device which is divided into multiple zone phase elements can be directly inferred from the aberration distorted point-spread function image in this method. The inference can be completed in 12.6 ms with the average mean square error 0.88 when 224 zones are used. The results show a good performance on aberrations of different complexities. Since no extra device is required, this method has potentials in deep tissue imaging and large volume imaging.

Keywords: deep learning, microscopy, biomedical imaging, aberration correction, deep tissue focusing

OPEN ACCESS

Edited by:
Ming Lei,
Xi'an Jiaotong University, China

Reviewed by:
Puxiang Lai,
Hong Kong Polytechnic University, Hong Kong
Hui Li,
Suzhou Institute of Biomedical Engineering and Technology (CAS), China

***Correspondence:**
Wei Gong
weigong@zju.edu.cn

Specialty section:
This article was submitted to Optics and Photonics, a section of the journal Frontiers in Physics

Received: *27 October 2020*
Accepted: *03 December 2020*
Published: *14 January 2021*

Citation:
Zhang B, Zhu J, Si K and Gong W (2021) Deep Learning Assisted Zonal Adaptive Aberration Correction. Front. Phys. 8:621966. doi: 10.3389/fphy.2020.621966

INTRODUCTION

Biomedical imaging often suffers from the optical aberrations caused by the highly scattering characteristic of the biological tissue [1]. As the imaging target goes deeper, more complex aberrations with increasing high-order components will come into existence because of the multiple scattering process, which may severely distort the imaging focus and thus greatly undermine the performance of deep tissue imaging [2]. Adaptive optics (AO) is one of the most common used techniques to correct the aberrations [3]. In this technique, the aberrations are directly measured by a wavefront sensor or detected in an indirect way, and then accordingly corrected by a spatial light modulator (SLM) or a deformable mirror (DM) [4]. Mostly, the pattern on the AO corrector needs to be inferred through a series of calculating operations [5,6] or multiple measurements [7–9]. As a result, the AO process can be time-consuming and therefore limits the imaging speed.

Recently, deep learning (DL) has been applied to find direct mapping relations by training neural networks on large datasets in various researches [10–13]. For the purpose of accelerating the AO process, there have also been works that take advantage of DL to simplify some conventional steps. Among these works, Hu et al. presented a learning-based Shark–Hartmann wavefront sensor (SHWS) to implement a fast AO with direct aberration measurement [14]. The Zernike coefficients controlling correction pattern were predicted by a revised AlexNet [15]—one of the most used DL networks—from a single SHWS pattern. Other works include Suárez Gómez et al. [16], Swanson et al. [17] and DuBose et al. [18]. Similar with most other direct AO methods, these work can be effectively adopted in retinal imaging [19] or to relatively transparent samples as zebrafish [20]. However, their further applications to most biological samples are inevitably limited by the fact that the SHWS can hardly be placed within the sample and the utilization of backscattered light is likely to lead highly degree of inaccuracy [21,22]. Since a large part of biological sample induced aberrations

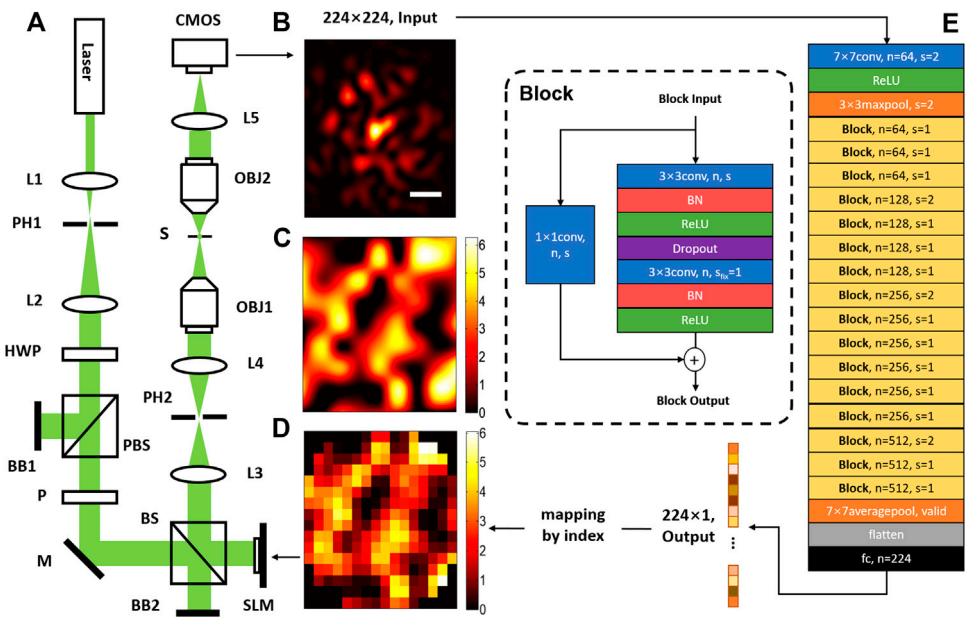

FIGURE 1 | The schematic diagram of DLZAC. **(A)** An optical system for DLZAC: L1-L5, lens; PH1-PH2, pinhole; HWP, half-wave plate; PBS, polarized beam splitter; BB1-BB2, beam block; P, linear polarizer plate; M, mirror; BS, beam splitter, 50:50 (R:T); SLM(256 × 256), spatial light modulator; OBJ1-OBJ2, objective lens (Nikon, 20X/0.75 NA); S, sample plane; CMOS, complementary metal oxide semiconductor camera. **(B)** The 224 × 224 input PSF image (scale bar: 1 μm). **(C)** The phase mask. **(D)** The correction pattern. **(E)** The architecture of the DL network.

should be measured through an indirect way [9], DL assisted sensor-less AO techniques have been developed at the same time. One representative work was carried out by Paine et al. They trained an adapted Inception v3 network (another well-known DL network) to determine a desirable starting estimate for gradient-based wavefront optimization from the point-spread function (PSF) image so that less iterations were required to achieve convergence [23]. Jin et al. moved forward to generate the correction pattern directly from the AlexNet calculated Zernike coefficients with the PSF image as the input [24]. With this method, the time consumption caused by the iterations can be completely eliminated, so the running speed of these techniques got further promoted. However, because it will be increasingly difficult to implement the measurement as well as the correction precisely when the number of Zernike modes gets bigger, this modal AO approach is only able to correct low-order aberrations [25]. Though Cumming et al. predicted the aberration function instead of Zernike coefficients, it is still limited to correct simple aberrations of the first 14 Zernike polynomials [26]. Since high-order aberrations severely degrade a large proportion of biomedical imaging results [2], new AO method is needed to achieve the correction of more complex aberrations while keeping the fast speed.

In this article, we propose a DL assisted zonal adaptive correction (DLZAC) method. Instead of correcting aberrations by Zernike modes, we equally divide the distorted wavefront into a number of zones and correct the aberration in each zone independently. In this way, correction with much more degrees of freedom can be easily achieved with most local-element based active devices and thus deal with complex aberrations effectively. It is noted that this sort of zonal adaptive correction method has already been used in multiple researches to overcome complex aberrations from biomedical imaging. Some typical examples include the pupil-segmentation based AO method by Ji et al. [9] and multidither coherent optical adaptive technique by Liu et al. [25]. However, all these former methods require repeated measurements to decide how to correct different wavefront zones, and thereby slow down the speed by a large scale. Here we creatively utilize a revised ResNet-34 network [27] to infer the correction phases of all the 224 valid zones on a SLM from a single PSF image in one shot. With the acceleration of a graphic processing unit (GPU), the whole inference process can be even much faster than the DL assisted modal adaptive correction (DLMAC) method mentioned above [24]. We introduce complex aberrations by phase masks to test the inference accuracy of the network as well as the correction ability of our method. Furthermore, the performance of DLZAC is compared with that of DLMAC on aberrations of different complexities to demonstrate the superiority of our method.

METHODS

Optical System

The optical system for DLZAC is illustrated in **Figure 1A**. In this system, a 488 nm wavelength laser beam is applied as the light source. Two lenses (L1 and L2) are located immediately after the source to serve as a beam expander. The pinhole (PH1) between L1 and L2 is used to collimate the beam. Then the expanded beam

passes through a half-wave plate (HWP) and a polarized beam splitter (PBS) to adjust its power into an appropriate range. The PBS only allows horizontally polarized light to pass, so it also controls the beam polarization into the right state for SLM modulation together with a linear polarizer (P). After this, the beam is directed into a SLM for phase modulation. When the SLM is utilized for correction, it will be equally divided into 16 × 16 square zones with 224 of them is valid because of the round pupil. Each zone on the SLM is treated as one phase element to implement correction by a single ensemble phase. The SLM is further conjugated to the back-pupil plane of the objective (OBJ1) by two relay lenses (L3 and L4). Another pinhole is placed between the relay lenses to block out the unwanted diffraction light generated by SLM. When the modulated beam reaches the objective, it is then focused on the sample plane. In order to obtain the PSF image, here another objective (OBJ2) is straightly mounted on the other side of the focal plane for detection. The light collected by OBJ2 is finally focused by a lens (L5) and recorded by a CMOS camera.

Deep Learning Network

To acquire the mapping relation between the PSF image and the zonal correction phases in DLZAC, the architecture of the neural network is correspondingly designed and shown in **Figure 1E**. To adapt the possible PSF of larger area as well as more complicated distribution induced by complex aberrations, the whole network architecture is based on ResNet-34, which is a powerful DL network with 34 weighted layers proposed by He et al. in 2016 [27]. The input of the network is a normalized 224 × 224 PSF image as shown in **Figure 1B**. The input size is set based on three considerations. First, the PSF should be covered as much as possible to minimize the margin feature loss; Second, the resolution of the PSF image should be as high as possible to minimize the fine feature loss; Third, the input size should be as small as possible to minimize the network computing cost. The network starts with a 7 × 7 convolutional layer of 64 kernels followed by a 3 × 3 max-pooling layer. Both of these two layers down-sampling the input by a stride of 2. Afterwards, the down-sampled feature maps are encoded by a series of layer blocks. In these blocks, the block input is filtered by two stacked 3 × 3 convolutional layers. Batch Normalization (BN) is adopted on both of the two convolutional layers before the activation and dropout is used after the first convolutional layer. To obtain the final block output, a special shortcut connection is implemented on every block by adding the block input to the output of the last block layer in an element-wise manner channel by channel. To make sure that the input dimension matches the dimension of the output, a 1 × 1 convolutional layer is used to operate the input before the addition. There are 16 blocks in total which can be further divided into four sequential groups by the channel number. The four groups consist of three blocks with 64 channels, four blocks with 128 channels, six blocks with 256 channels and three blocks with 512 channels respectively. It is noted that every time when the channel number doubles, the size of feature maps is halved to keep the time complexity. The output of the last block is further converted into a vector by a 7 × 7 average-pooling layer without padding. At the end of the network, a fully-connected layer is applied to perform a 224-variable regression. In the whole network, the activation is realized by Rectified Linear Unit (ReLU) function and padding is used to preserve the size of each layer with default stride as one if not specified. Finally, the network output is a 224 × 1 vector, of which each element corresponds to the correction phase of a fixed index SLM zone. Compared with AlexNet previously used by DLMAC, this revised ResNet-34 possesses larger depth and complexity, hence the high-level features brought by high-order aberrations can be better extracted and the correction phases are likely to be deduced more accurately. The possible degradation problem of deeper network is addressed by the shortcut connections in ResNet-34, which further ensure the superiority. Moreover, this revised ResNet-34 has significantly lower time complexity than most other deep networks so that the fast speed of DLZAC can be guaranteed.

To support the supervised learning of the network, datasets containing 220 thousand input-output pairs are built for training and testing [28–30]. In order to prepare these datasets, a large number of phase masks as shown in **Figure 1C** are randomly generated and added on the SLM respectively to introduce different aberrations. To make these phase masks fluctuate with a certain local smoothness, which is a common characteristic of actual aberration-distorted wavefront, we down-sample every phase mask before assign a random phase value between 0 and 2π to each pixel of it and then restore the original size by bicubic interpolation during the generation. According to different phase masks, corresponding PSF images can be obtained from the CMOS as the input part of the datasets. To get the reference zonal correction phases for the output vectors, we calculate the ensemble phase by vector averaging the phases of all the pixels within each SLM zone on every phase mask and arrange them by zone index. Finally, by matching each input with its corresponding output to form pairs, the datasets preparation can be accomplished.

For the training of the network, we allocate 200 thousand data as the training set and 10 thousand data for validation. Owing to the regression task, the loss is defined by mean square error (MSE). An L2 regularization term with the coefficient being 0.002 is further added on the loss to avoid the overfitting. To realize the training, the network weights are initialized by Xavier initialization and then trained for 200 epochs. We use Adam for optimization during the training with a mini-batch size of 32. To improve the training efficiency, the learning rate (LR) is decayed to 0.8 times of its former value every 10 epochs from 0.0001. The dropout ratio is set to 0.5 for the whole training process. To implement the network training, we apply Tensorflow framework (GPU version 1.12.0) based on Python 3.6.8 on a personal computer (PC, Intel Core i7 4770K 3.50 GHz, Kingston 16GB, NVIDIA GeForce GTX970).

Workflow of DLZAC

With the optical system presented in **Figure 1A** as well as the well-trained DL network mentioned above, the workflow of DLZAC can be divided into four steps. First of all, the distorted PSF is caused by a given aberration and recorded by the CMOS. Secondly, the PSF image from the CMOS is cropped

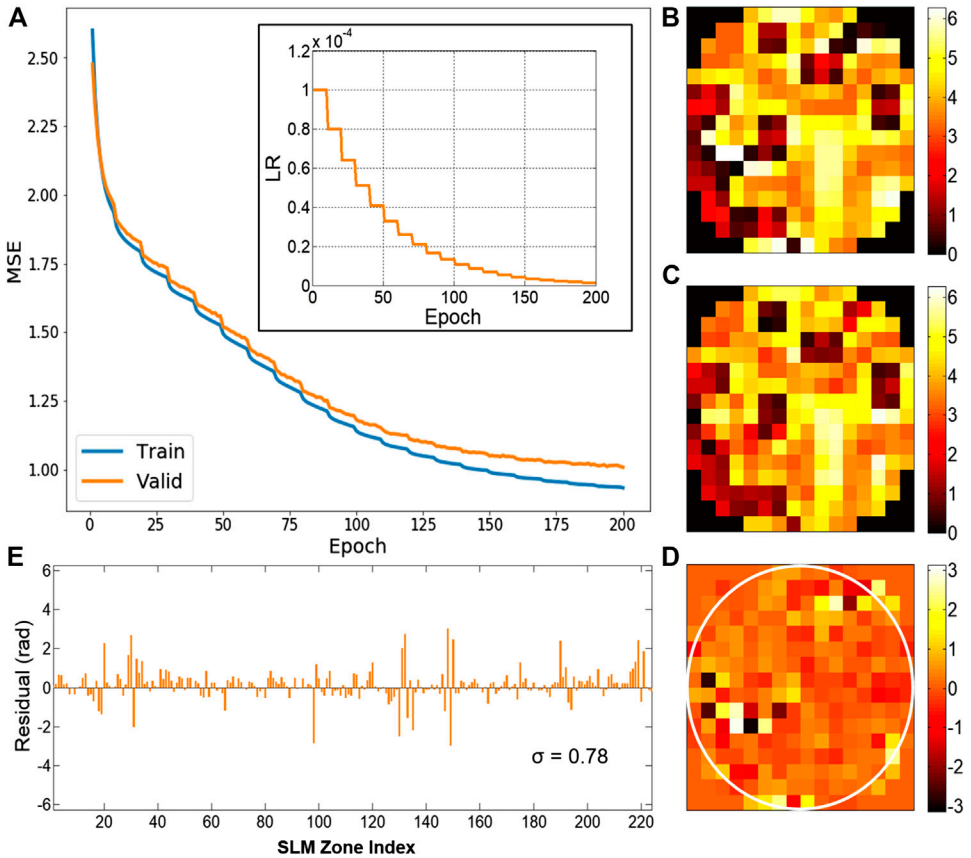

FIGURE 2 | (A) The descent curve of MSE during the training process. Subfigure: the LR decay curve. **(B)** The ideal correction phase pattern. **(C)** The phase pattern predicted by the trained network. **(D)** The phase difference pattern between (**B**) and (**C**). **(E)** The bar chart of the phase difference on every SLM zone from (**D**), with the standard deviation σ being 0.78.

and fed into the trained DL network to calculate the output by forward propagation. Thirdly, the output, namely the 224-element zonal correction phase vector, is mapped to a correction pattern as shown in **Figure 1D** by the index of SLM zones. Finally, the correction pattern is loaded onto the SLM to perform adaptive correction. In this way, DLZAC is capable of the fast correction of complex aberrations.

RESULTS

The DLZAC performance largely depends on the inference accuracy of zonal correction phases. **Figure 2A** gives the descent curve of MSE on the training set as well as the validation set during the overall training process. The inset at the upper right corner shows the LR variation as the number of epochs increases. It can be seen that MSE on both datasets has been lower than 1.0 without obvious overfitting after the training of 200 epochs. To test the inference accuracy of the trained network, here we use the leftover 10 thousand data as the test set. **Figure 2B** presents the ideal correction phase pattern of an example in the test set. The pattern predicted by the trained network from the input PSF image corresponding to **Figure 2B** is displayed in **Figure 2C**. By comparison between these two patterns, we can find that they are in good agreement despite some tolerable differences. The phase differences are shown in **Figure 2D** with a white circle used to mark out the border of the pupil. It is obvious that the average difference of all the SLM zones within the pupil is quite small. Furthermore, we plot the phase difference of each zone in a bar chart shown in **Figure 2E**. It is easy to observe from the chart that most of the differences are around 0, which means a good accuracy of the network inference. The standard deviation σ of all the differences in **Figure 2E** is computed to be 0.78. It is noted from the figures that the comparatively obvious errors tend to appear at the locations where there are phase jumps among adjacent zones. After implementing tests throughout the whole set, we calculate the mean MSE to be 0.88. The time cost of a single test is 12.6 ms on average based on the PC we previously utilized for the training. These results demonstrate that the proposed method is able to deduce the correction patterns with desirable precision in a rather fast speed.

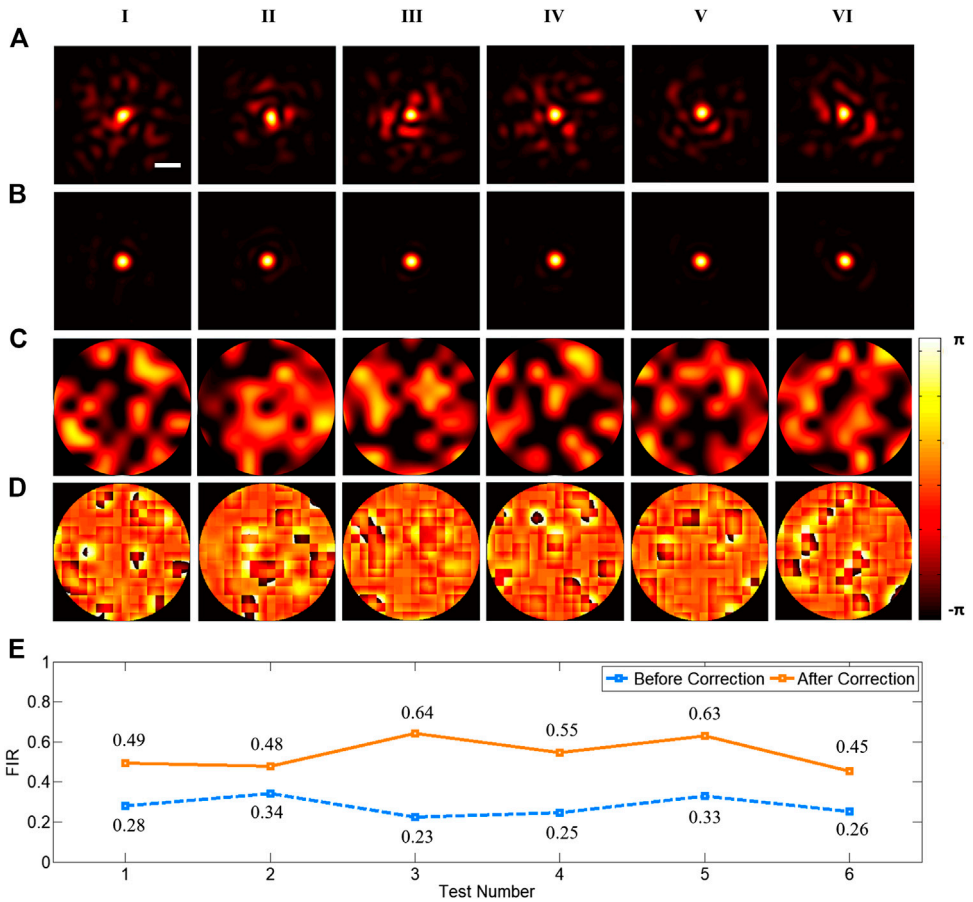

FIGURE 3 | (A) The six distorted PSFs before correction (scale bar: 1 μm). **(B)** The six corrected PSFs after DLZAC. **(C)** The six phase wavefronts before DLZAC. **(D)** The six residual phase wavefronts within the pupil after DLZAC. Each column of (**A**–**D**) corresponds to one of the six test examples. **(E)** The FIR statistics of the PSFs in (**A**) and (**B**).

In order to verify the ability of DLZAC to correct aberrations, we randomly choose six examples from the test set and compare the PSFs before and after DLZAC. In **Figure 3**, each column corresponds to one of the six examples. The distorted PSFs before the correction are presented in the first row of **Figure 3**. It can be seen that these PSFs are severely distorted by complex aberrations. Here we introduce focal intensity ratio (FIR) as an indicator to quantify the distortion level of PSFs. The FIR is defined as the ratio between the intensity calculus within the Airy disk radius of the distorted PSF and that of ideal PSF with no distortion. All the six chosen PSFs are with a FIR below 0.34, which means that at least two-thirds of the light is scattered out of the focal area in these PSFs because of the complex aberrations. The second row of **Figure 3** gives the corrected PSFs after DLZAC. Obviously, all the distorted PSFs are recovered to approximate diffraction-limited state, which represents that DLZAC is reliable on complex aberration correction. The third row of **Figure 3** shows the phase wavefronts before DLZAC of the examples. The fourth row of **Figure 3** shows the residual phase wavefronts within the pupil of the six test examples after DLZAC. The residual phase wavefront is obtained by adding the correction phase pattern to the phase mask. It can be observed that these corrected wavefronts all have fairly good flatness, which further demonstrates that the complex aberrations can be well compensated by our newly proposed AO method. To support our results quantitatively, we calculate and summarize the FIR of the PSFs before and after DLZAC in **Figure 3E**. Every FIR has enhanced significantly to about twice of its former value because of the highly effective correction.

For the purpose of comparing the correction effect of our DLZAC with that of DLMAC on aberrations of different complexities, here we produce four kinds of aberrations by phase masks to control the FIR of distorted PSFs to form a gradient. In **Figure 4**, the distorted PSFs are shown in descending order of FIR from the top to the bottom of the first column, with each row corresponding to a kind of aberration complexity. It can be easily observed that the distortion extent of these PSFs is gradually increased as the FIR drops from 0.6 to 0.1. When the FIR of the

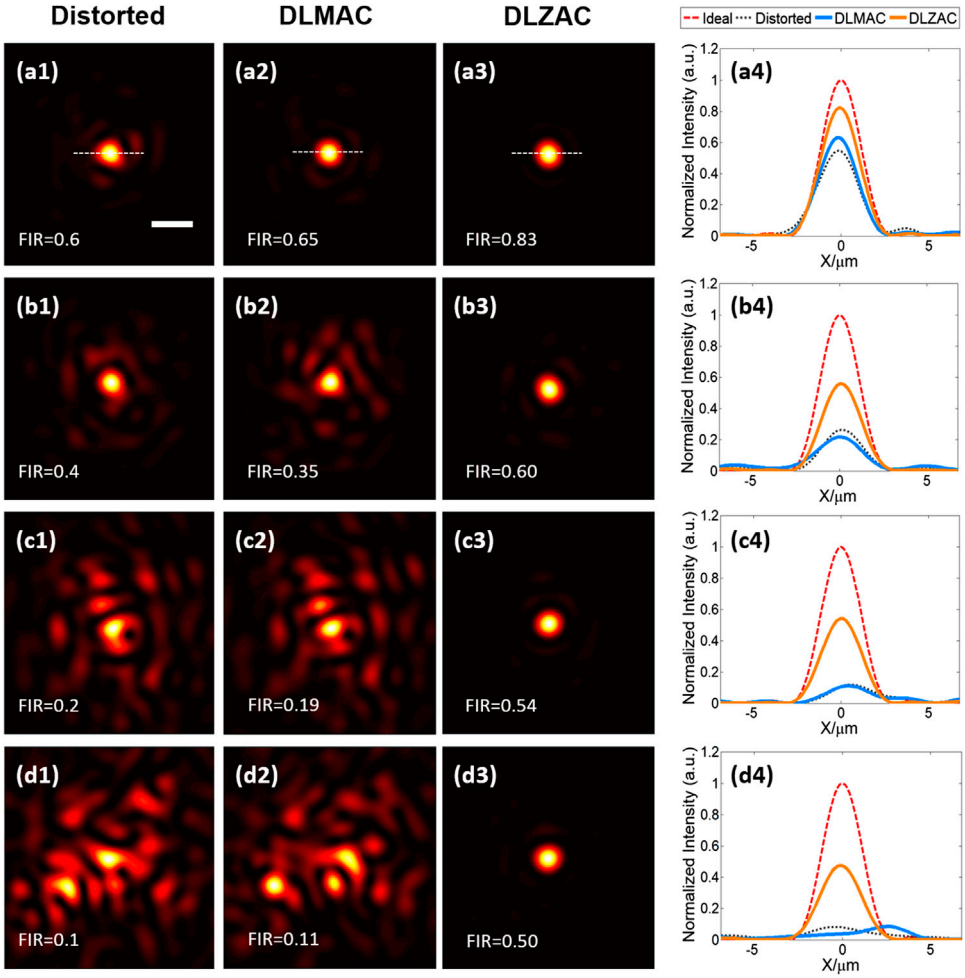

FIGURE 4 | (A1) The distorted PSF whose FIR equals 0.6 (scale bar: 1 μm). **(A2)** The corrected PSF from **(A1)** by DLMAC. **(A3)** The corrected PSF from (**A1**) by DLZAC. **(A4)** The intensity profiles along the white dashed lines in (**A1–3**), with an extra profile of the ideal PSF. **(B1–4)** The equivalents of (**A1–4**) when the FIR of the distorted PSF equals 0.4. **(C1–4)** The equivalents of (**A1–4**) when the FIR of the distorted PSF equals 0.2. **(D1–4)** The equivalents of (**A1–4**) when the FIR of the distorted PSF equals 0.1.

distorted PSF equals 0.6, we can notice from **Figure 4A1** that the aberration is relatively simple. **Figures 4A2,3** display the corrected PSFs after DLMAC and DLZAC respectively. Apparently, both of the two methods have a certain effect of correction, while DLZAC achieves a better performance. We further calculate the FIR of two corrected PSFs. The FIR of DLZAC equals 0.83, which is much higher than that of DLMAC being 0.65. To compare different PSFs more intuitively, we plot the intensity profiles along the white dashed lines representing the central axis shown in **Figures 4A1–3** and gather them in **Figure 4A4**. The red dashed line shown in **Figure 4A4** gives the profile of the ideal PSF. It can be seen here that the two profiles belonging to the corrected PSFs have higher peak than that of distorted PSF and the profile corresponding to DLZAC is closer to the ideal profile than that of DLMAC. Based on these results, we can prove the fact that DLZAC is able to correct simple aberrations better than DLMAC. Afterwards, we then conduct DLMAC as well as DLZAC on the other three distorted PSFs of lower FIR. Since more complex aberrations need to be corrected in these circumstances, it is easy to tell from the comparisons between **Figures 4B1,2,C1,2,D1,2** that the PSFs remain distinctly distorted after DLMAC. On the other hand, we can see from **Figures 4B3,C3,D3** that the PSFs can still be recovered to a degree of satisfaction after DLZAC. Even to the highly distorted PSF with multiple peaks presented in **Figure 4D1**, DLZAC can still successfully enhance the FIR to 0.5. Similarly, we compare different PSFs by intensity profile along the central axis in **Figures 4B4,C4,D4**. It can be seen that the profiles of DLZAC in these three figures all have much more desirable shape and higher peak, whereas basically no improvement can be found in the profiles of DLMAC, compared to the distorted profiles. Therefore, it is verified that DLZAC can keep its remarkable correction performance, while DLMAC loses its correction effect with regard to complex aberrations.

DISCUSSION

We present a DLZAC method in this article to achieve complex aberration AO correction for biomedical imaging in fast speed. Since the previous DLMAC method can only work on low-order simple aberrations, our method successfully overcomes this restriction by conducting the aberration measurement as well as the correction in a zonal way. To implement our method, we train a revised ResNet-34 network to infer the vector of 224 zonal correction phases from the PSF image and realize the correction by a SLM. With the acceleration of a GPU, the inference can be finished in 12.6 ms, which is even much faster than DLMAC, merely on a PC (Intel Core i7 4770K 3.50 GHz, Kingston 16 GB, NVIDIA GeForce GTX970) with the average MSE being 0.88. As for complex aberrations introduced by phase masks, which severely distort the PSF, DLZAC can recover the distorted PSF to near diffraction-limited state and significantly enhance the FIR. Compared with DLMAC, DLZAC presents even better correction on relatively simple aberrations. When the aberrations become highly complex and far beyond the correction capacity of DLMAC, DLZAC can still preserve its desirable correction performance. Since no extra device is required to implement DLZAC, our method is highly compatible with most of existing AO systems for biomedical imaging. The outstanding correction effect of kinds of aberrations, especially complex aberrations, makes DLZAC able to applied on a large range of imaging tasks. For deep living tissue imaging, DLZAC can bring benefits to remove dynamic complex aberrations caused by tissue movements and optimize the imaging result. Besides, with the rapid correction speed, DLZAC can also help to obtain the high imaging quality while keeping the efficiency as well as the photodamage level of large volume imaging.

DATA AVAILABILITY STATEMENT

The original contributions presented in the study are included in the article, further inquiries can be directed to the corresponding author.

AUTHOR CONTRIBUTIONS

BZ conceived the idea, did the simulation. JZ did additional experiments and data analysis. KS and WG supervised the project. BZ, JZ, KS, and WG wrote the paper. All the authors contributed to the discussion on the results for this manuscript.

FUNDING

National Natural Science Foundation of China (61735016, 81771877, 61975178); Natural Science Foundation of Zhejiang Province (LZ17F050001).

REFERENCES

1. Ji N. Adaptive optical fluorescence microscopy. *Nat. Methods* (2017) 14:374–80. doi:10.1038/nmeth.4218
2. Gigan S. Optical microscopy aims deep. *Nat. Photon* (2017) 11:14–6. doi:10.1038/nphoton.2016.257
3. Booth M. Adaptive optical microscopy: the ongoing quest for a perfect image. *Light Sci. Appl.* (2014) 3:e165. doi:10.1038/lsa.2014.46
4. Booth M. Adaptive optics in microscopy. *Philos. Trans. Ser. A. Math. Phys. Eng. Sci.* (2008) 365:2829–43. doi:10.1098/rsta.2007.0013
5. Cha JW, Ballesta J, So PTC. Shack-Hartmann wavefront-sensor-based adaptive optics system for multiphoton microscopy. *J. Biomed. Optic.* (2010) 15(4): 046022. doi:10.1117/1.3475954
6. Tao X, Azucena O, Fu M, Zuo Y, Chen D, Kubby J. Adaptive optics microscopy with direct wavefront sensing using fluorescent protein guide stars. *Opt. Lett.* (2011) 36:3389–91. doi:10.1364/OL.36.003389
7. Sherman L, Ye JY, Albert O, Norris TB. Adaptive correction of depth-induced aberrations in multiphoton scanning microscopy using a deformable mirror. *J. Microsc.* (2002) 206(1):65–71. doi:10.1046/j.1365-2818.2002.01004.x
8. Marsh P, Burns D, Girkin J. Practical implementation of adaptive optics in multiphoton microscopy. *Opt. Exp.* (2003) 11:1123–30. doi:10.1364/OE.11.001123
9. Ji N, Milkie D, Betzig E. Adaptive optics via pupil segmentation for high-resolution imaging in biological tissues. *Nat. Methods* (2010) 7:141–7. doi:10.1038/nmeth.1411
10. Schmidhuber J. Deep learning in neural networks: an overview. *Neural Netw.* (2015) 61:85–117. doi:10.1016/j.neunet.2014.09.003
11. Guo Y, Liu Y, Oerlemans A, Lao S, Wu S, Lew MS. Deep learning for visual understanding: a review. *Neurocomputing* (2016) 187:27–48. doi:10.1016/j.neucom.2015.09.116
12. Min S, Lee B, Yoon S. Deep learning in bioinformatics. *Briefings Bioinf.* (2016) 18(5):851–69. doi:10.1093/bib/bbw068
13. Barbastathis G, Ozcan A, Situ G. On the use of deep learning for computational imaging. *Optica* (2019) 6:921–43. doi:10.1364/OPTICA.6.000921
14. Hu L, Hu S, Gong W, Si K. Learning-based Shack-Hartmann wavefront sensor for high-order aberration detection. *Opt. Exp.* (2019) 27:33504. doi:10.1364/OE.27.033504
15. Krizhevsky A, Sutskever I, Hinton GE. ImageNet classification with deep convolutional neural networks. Commun ACM (2017) 60(6):84–90. doi:10.1145/3065386
16. SL Suárez Gómez, C González-Gutiérrez, E Díez Alonso, JD Santos Rodríguez, ML Sánchez Rodríguez, J Carballido Landeira, et al. editors. *Improving adaptive optics reconstructions with a deep learning approach*. Cham: Springer (2018).
17. Swanson R, Kutulakos K, Sivanandam S, Lamb M, Correia C. *Wavefront reconstruction and prediction with convolutional neural networks*. Washington, DC: OSA Publishing (2018). p 52.
18. DuBose TB, Gardner DF, Watnik AT. Intensity-enhanced deep network wavefront reconstruction in Shack–Hartmann sensors. *Opt. Lett.* (2020) 45(7):1699–702. doi:10.1364/OL.389895
19. Porter J, Awwal A, Lin J, Queener H, Thorn K. *Adaptive optics for vision science: principles, practices, design and applications*. New York, NY: Wiley (2006).
20. Wang K, Sun W, Richie C, Harvey B, Betzig E, Ji N. Direct wavefront sensing for high-resolution *in vivo* imaging in scattering tissue. *Nat. Commun.* (2015) 6:7276. doi:10.1038/ncomms8276
21. Liang J, Williams D, Miller D. Supernormal vision and high-resolution retinal imaging through adaptive optics. *J. Opt. Soc. Am. A Opt. Image Sci. Vision* (1997) 14:2884–92. doi:10.1364/JOSAA.14.002884
22. Rückel M, Mack-Bucher J, Denk W. Adaptive wavefront correction in two-photon microscopy using Coherence-Gated Wavefront Sensing. *Proc. Natl. Acad. Sci. USA.* (2006) 103:17137–42. doi:10.1073/pnas.0604791103

23. Paine S, Fienup J. Machine learning for improved image-based wavefront sensing. *Opt. Lett.* (2018) 43:1235. doi:10.1364/OL.43.001235
24. Jin Y, Zhang Y, Hu L, Huang H, Xu Q, Zhu X, et al. Machine learning guided rapid focusing with sensor-less aberration corrections. *Opt. Exp.* (2018) 26: 30162. doi:10.1364/OE.26.030162
25. Liu R, Milkie D, Kerlin A, Maclennan B, Ji N. Direct phase measurement in zonal wavefront reconstruction using multidither coherent optical adaptive technique. *Opt. Exp.* (2014) 22:1619–28. doi:10.1364/OE.22.001619
26. Cumming BP, Gu M. Direct determination of aberration functions in microscopy by an artificial neural network. *Opt. Exp.* (2020) 28(10): 14511–21. doi:10.1364/OE.390856
27. He K, Zhang X, Ren S, Sun J. Deep residual learning for image recognition. *CVPR* (2016) 770–8. doi:10.1109/CVPR.2016.90
28. Cheng S, Li H, Luo Y, Zheng Y, Lai P. Artificial intelligence-assisted light control and computational imaging through scattering media. *J. Innov. Opt. Health Sci.* (2019) 12(04):1930006. doi:10.1142/s1793545819300064
29. Luo Y, Yan S, Li H, Lai P, Zheng Y. Focusing light through scattering media by reinforced hybrid algorithms. *APL Photonics* (2020) 5(1):016109. doi:10.1063/1.5131181
30. Lai P, Wang L, Wang L. Photoacoustically guided wavefront shaping for enhanced optical focusing in scattering media. *Nat. Photon* (2015) 9(2): 126–32. doi:10.1038/nphoton.2014.322.

Conflict of Interest: The authors declare that the research was conducted in the absence of any commercial or financial relationships that could be construed as a potential conflict of interest.

frontiers in Physics

BRIEF RESEARCH REPORT
published: 29 January 2021
doi: 10.3389/fphy.2020.630350

Transmission Structured Illumination Microscopy for Quantitative Phase and Scattering Imaging

*Kai Wen[1†], Ying Ma[1†], Min Liu[1], Jianlang Li[1], Zeev Zalevsky[2] and Juanjuan Zheng[1]**

[1]School of Physics and Optoelectronic Engineering, Xidian University, Xi'an, China, [2]Faculty of Engineering and the Nano Technology Center, Bar-Ilan University, Ramat-Gan, Israel*

In this paper, we demonstrate a digital micromirror device (DMD) based optical microscopic apparatus for quantitative differential phase contrast (qDIC) imaging, coherent structured illumination microscopy (SIM), and dual-modality (scattering/fluorescent) imaging. For both the qDIC imaging and the coherent SIM, two sets of fringe patterns with orthogonal orientations and five phase-shifts for each orientation, are generated by a DMD and projected on a sample. A CCD camera records the generated images in a defocusing manner for qDIC and an in-focus manner for coherent SIM. Both quantitative phase images and super-resolved scattering/fluorescence images can be reconstructed from the recorded intensity images. Moreover, fluorescent imaging modality is integrated, providing specific biochemical structures of the sample once using fluorescent labeling.

Keywords: quantitative phase microscopy, structured illumination, phase gradient, resolution enhancement, multimodality imaging

OPEN ACCESS

Edited by:
Vicente Micó,
University of Valencia, Spain

Reviewed by:
Dahi Ibrahim,
National Institute of Standards and Technology, United States
Jianglei Di,
Northwestern Polytechnical University, China
Rongli Guo,
Tel Aviv University, Israel

****Correspondence:***
Juanjuan Zheng
jjzheng@xidian.edu.cn

†These authors have contributed equally to this work

Specialty section:
This article was submitted to Optics and Photonics, a section of the journal Frontiers in Physics

Received: *17 November 2020*
Accepted: *24 December 2020*
Published: *29 January 2021*

Citation:
Wen K, Ma Y, Liu M, Li J, Zalevsky Z and Zheng J (2021) Transmission Structured Illumination Microscopy for Quantitative Phase and Scattering Imaging. Front. Phys. 8:630350. doi: 10.3389/fphy.2020.630350

INTRODUCTION

Quantitative phase microscopy (QPM) utilizing the phase information of the object wave can provide not only phase-contrast images but also quantitative information about the three-dimensional morphology and refractive index distribution of the samples [1–8]. Recently, a more compact module, nominated as quadriwave lateral shearing interferometry (QWLSI), was proved for quantitative phase imaging with one-shot. The QWLSI splits an object wave into four copies, two of which are sheared along the *-x* and *-y* directions respectively [9–11].

Most of the phase imaging techniques, or the coherent imaging techniques in more general cases, utilize monochromatic plane-wave illumination and consequently, the resolution of imaging systems is limited by wavelength (λ) and numerical aperture (NA) of the system [12]. A higher spatial resolution is favorable to resolve the finer details of the sample for everyone. However, when designing a microscopic objective, a higher spatial resolution often needs to be traded with a smaller field of view (FOV). People appeal an approach that can enhance spatial resolution and at the same time, maintain a large field of view. To meet this demand, synthetic aperture approaches in QPM have been reported, for instance, oblique illumination [13–15], structured illumination [16–19], and speckle illumination [20–22] (just to cite a few) have been proposed to improve the spatial resolution (or the space-bandwidth product) in QPM. Of note, structured illumination microscopy (SIM) [23–25], is a wide-field, minimally-invasive, super-resolution imaging technique, which utilizes moiré patterns created by illuminating the sample with periodic stripes. The structured illumination can downshift unresolvable high-frequency information into low-frequency falling in the supporting area of the system, as illustrated in **Figure 1C**, [26]. Furthermore, SIM was demonstrated having an

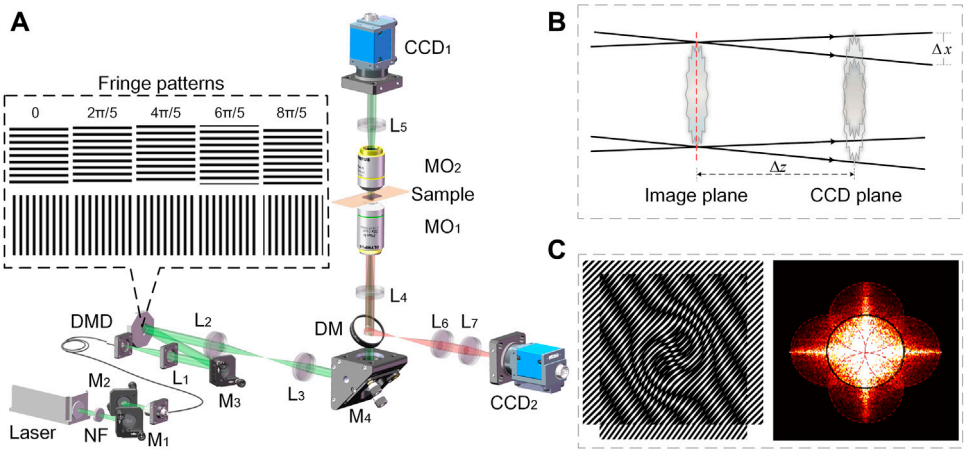

FIGURE 1 | The schematic diagram of DMD-based SIM apparatus for multi-modality imaging. **(A)** Experimental setup. Insets: structured illumination patterns **(B)** lateral shearing of the ±1 orders in qDIC modality; **(C)** resolution enhancement upon structured illumination. DM, dichroic mirrors; L_1-L_7, achromatic lens; MO_1-MO_2, microscopic objectives; M_1-M_4, mirrors; NF, neutral density filter.

optical sectioning capability comparable with confocal microscopy [27]. Hence, SIM has found widespread applications in biomedical imaging [28, 29], and notably long-term observing dynamics in living cells [25, 30]. Recently, SIM was applied to phase imaging of transparent samples when being combined with digital holographic microscopy [31] or reference-less phase retrieval approaches [18, 32]. Till yet, QPM with structured illumination has been implemented using gratings or spatial light modulator (SLM), and the phase imaging modality is often isolated from other imaging modalities such as fluorescence imaging. Therefore, the value of QPM is limited due to the lack of multi-dimensional information for the same sample.

In this paper, we propose a DMD based optical microscope that integrate multiple imaging modalities. At first, structured illumination based QPM enables to providing quantitative phase image of a sample without fluorescent labeling. Second, coherent SIM provides absorption/scattering images of unlabeled samples with resolution-enhancement. Third, this system is integrated with a fluorescence imaging modality, providing additional (functional/biochemical) information on the same sample.

METHODS

The schematic diagram of the system is shown in **Figure 1A**, of which a diode laser with a wavelength of 561 nm (MLL-U-561, Changchun New Industries Optoelectronics Technology Co., Ltd., China) is used as the illumination source. After being reflected by the mirrors M_1 and M_2 sequentially, the laser beam is coupled into a fiber and sent to the setup. In the output end, the light from the fiber is collimated by the lens L_1 and guided by the mirror M_3 to a DMD (1920 × 1080 pixels, pixel size 7.56 μm, DLP F6500, UPOLabs, China) at an incidence angle of 24°. On DMD, two groups of fringe patterns with orthogonal orientations and five-phase shifts (δ_m = 2 (m-1)π/5, m = 1, . . . , 5.) for each orientation are loaded to the DMD in sequence (as shown in the inset of **Figure 1A**). The fringe patterns displayed on the DMD are further relayed by the telescope systems L_2-L_3 and L_4-MO_1, and eventually projected onto the sample placed on the common focal plane of MO_1 and MO_2. Preferably, the illumination beam is filtered before entering the sample plane: the illumination light is Fourier transformed by the lens L_2 and its spectrum appears in the focal plane of L_2. A mask is located in the Fourier plane and blocks the unwanted diffraction orders except the ±1st orders. As a consequence, the fringe patterns on the sample plane are of ideal cosine distribution. Upon the fringe illumination, the sample is then imaged by the telescope system MO_2-L_5 to the image plane with a distance Δz apart from the CCD plane (CCD_1, 4000 × 3000 pixels, pixel size 1.85 μm, DMK 33UX226, The Imaging Source Asia Co., Ltd., China). The camera CCD_1 records diffraction images for different imaging modes, defocused images in qDIC and focused images in coherent SIM. Meanwhile, the emission light (fluorescence) from the sample will propagate along the opposite direction of the illumination light, and is then collected by the camera CCD_2. It is worth mentioning that the camera CCD_1 and CCD_2 are synchronized with the DMD, yielding an acquisition speed of 15 frames per second, providing a sub-second imaging speed for every channel.

Quantitative Differential Phase-Contrast (qDIC) Microscopy With Structured Illumination

The structured illumination for qDIC microscopy (**Figure 1B**) can be expressed as $A_m^{\xi} = 2\cos(2r/\Lambda+\delta_m)$ with m = 1, 2, . . . , 5, and ξ indicates the orientation indices of x and y, respectively. r is the spatial position vector, Λ is the stripe's period, and δ_m is the phase shift. Passing through the sample, the object wave under A_m^{ξ} is diffracted and relayed by the telescope system MO_2-L_5 to the image plane. After diffraction of a distance of Δz, the

diffraction patterns are recorded by the CCD_1 camera. The waves along the ±1st orders of A_m^ξ at the camera plane are U_1^ξ and U_{+1}^ξ. These two waves interfere with each other at the camera plane and the intensity distribution of the interferogram captured by the camera can be written as:

$$I_m^\xi(r) = \left|U_{+1}^\xi(r)\right|^2 + \left|U_{-1}^\xi(r)\right|^2 + U_{+1}^\xi(r)U_{-1}^{\xi*}(r) + U_{-1}^\xi(r)U_{+1}^{\xi*}(r) = \alpha_0^\xi + \alpha_1^\xi \exp(i2\delta_m) + \alpha_2^\xi \exp(-i2\delta_m) \quad (1)$$

where, α_0^ξ equals to $\left|U_{+1}^\xi(r)\right|^2 + \left|U_{-1}^\xi(r)\right|^2$, α_1^ξ equals to $[I_{+1}^\xi(r)I_{-1}^\xi(r)]^{1/2} exp[i(\varphi_{diff}^\xi + 2\pi r/\Lambda)]$, and α_2^ξ equals to $[I_{+1}^\xi(r)I_{-1}^\xi(r)]^{1/2} exp[-i(\varphi_{diff}^\xi + 2\pi r/\Lambda)]$. Here, φ_{diff}^ξ denotes the phase difference between U_1^ξ and U_{-1}^ξ which is generated by the lateral shearing. And $\delta_m = 2\ (m\text{-}1)\pi/5$ (m = 1, 2, . . . , 5.) is the phase shift induced by laterally translating the fringe on DMD. Despite three-step phase-shifting is enough to solve these three terms α_0^ξ, α_1^ξ, and α_2^ξ, we use the five-step phase shifting to achieve a better reconstruction immune to phase shift error and environmental instability [33]. Accordingly, **Eq. 1** can be rewritten as:

$$\begin{pmatrix} 1 & \exp(i2\delta_1) & \exp(-i2\delta_1) \\ 1 & \exp(i2\delta_2) & \exp(-i2\delta_2) \\ 1 & \exp(i2\delta_3) & \exp(-i2\delta_3) \\ 1 & \exp(i2\delta_4) & \exp(-i2\delta_4) \\ 1 & \exp(i2\delta_5) & \exp(-i2\delta_5) \end{pmatrix} \cdot \begin{pmatrix} \alpha_0^\xi \\ \alpha_1^\xi \\ \alpha_2^\xi \end{pmatrix} = \begin{pmatrix} I_1^\xi(r) \\ I_2^\xi(r) \\ I_3^\xi(r) \\ I_4^\xi(r) \\ I_5^\xi(r) \end{pmatrix} \quad (2)$$

Here α_0^ξ, α_1^ξ, and α_2^ξ can be solved in a least-square manner via multiplying both sides of **Eq. 2** with the transpose of the coefficient matrix. Therefore, α_0^ξ, α_1^ξ, and α_2^ξ along the ξ-direction can be achieved, respectively. In order to compensate for the linear phase terms in α_1^ξ and α_2^ξ induced by the oblique illumination of the ±1st orders of the structured illuminations, an accurate calibration was performed. Actually, the calibration was performed with the same procedure but in the absence of any samples, and we can get new terms α_{b0}^ξ, α_{b1}^ξ, and α_{b2}^ξ. Eventually, the pure phase difference of the sample can be obtained by $\varphi_{diff}^\xi = \mathrm{Ang}\{\alpha_1^\xi/\alpha_{b1}^\xi\}$, where Ang{·} denotes the argument retrieval operator. Similarly, the phase difference φ_{diff}^ξ along the x- and y-axes can be obtained by rotating the fringe 90° with the same calculation procedure. Ultimately, the phase distribution $\varphi(r)$ can be obtained by integrating φ_{diff}^x and φ_{diff}^y [34]:

$$\varphi(r) = IFT\left\{\frac{-i\left[\nu^x FT\left\{\varphi_{\mathrm{diff}}^x\right\} + \nu^y FT\left\{\varphi_{\mathrm{diff}}^y\right\}\right]}{2\pi(\nu^x)^2 + (\nu^y)^2}\right\} \quad (3)$$

where ν^x and ν^y are the coordinates in the Frequency domain, respectively. $FT\{\cdot\}$ and $IFT\{\cdot\}$ represent the Fourier transform and inverse Fourier transform, respectively.

Super-Resolution Scattering Imaging With Coherent Structured Illumination

Using the same stripes projection method as in phase imaging, a resolution enhancement in non-fluorescent imaging can be realized by using coherent structured illumination. The key to enhancing the spatial resolution in non-fluorescent/scattering imaging is the synthetic-aperture effect, as shown in **Figure 1C**, which can bring unobservable high-frequency information into the low-frequency supporting area through oblique illumination. Different from the phase imaging, the scattering imaging here records the diffraction patterns in an in-focus manner. Mathematically, the intensity images in the CCD_1 plane can be written as $I_m^\xi(r) = |h_c(r) \otimes [O(r) \cdot A_m^\xi]|^2$, where $h_c(r)$ is the coherent point spread function of the system, ⊗ is the convolution operator, $O(r)$ is the object transmittance function, and A_m^ξ is the structured illumination filed in the sample plane. After a Fourier transform, we can obtain the spectrum distribution of $I_m^\xi(r)$:

$$\tilde{I}_m^\xi(\nu) = \left[G_0^\xi(\nu) + \exp(i2\delta_m) \cdot G_{+1}^\xi\left(\nu - \nu_0^\xi\right) + \exp(-i2\delta_m) \cdot G_{-1}\left(\nu + \nu_0^\xi\right)\right] \quad (4)$$

where $\tilde{I}_m^\xi(\nu)$ is the Fourier transform of $I_m^\xi(r)$, ν is the spatial frequency vector, and G_m^ξ (m = 0, ±1) represent the spectral components along x- and y-directions. Notably, $G_{+1}^\xi(\nu - \nu_0^\xi)$ and $G_{-1}(\nu + \nu_0^\xi)$ have the high-frequency spectrum surpassing the supporting pupil of the imaging system, which was downshifted by the oblique illumination and therefore passing through the imaging system. To acquire these three spectral components, five-step phase-shifting was performed with the phase shifts $\delta_m = 2\ (m\text{-}1)\pi/5$. After similar mathematical operations as described in Quantitative Differential Phase-Contrast (qDIC) Microscopy With Structured Illumination different spectra along with the 0th, and ±1st orders of the structured illuminations can be solved, and an extended-spectrum can be synthesized with:

$$G_{SI}(\nu) = \frac{1}{2} \cdot \left[G_0^x(\nu) + G_0^y(\nu)\right] + G_1^x\left(\nu - \nu_0^x\right) + G_{-1}^x\left(\nu + \nu_0^x\right) + G_1^y\left(\nu - \nu_0^y\right) + G_{-1}^y\left(\nu + \nu_0^y\right) \quad (5)$$

Afterward, the resolution-enhanced image can be achieved using an inverse Fourier transform on **Eq. 5** and multiplying weight factor. It is worth noting that in such a coherent imaging system the phase distribution of different G_m^ξ (m = 0, ±1) should be compensated e.g., with the experiment without any samples, making sure that there are no additional phase shifts between different terms in **Eq. 5**.

EXPERIMENTS AND RESULTS

qDIC Microscopy Imaging of Living Cells

In the first experiment, a confirmatory experiment is carried out to demonstrate qDIC for live samples imaging without fluorescent labeling. For this purpose, live mouse adipose stem cells were used as phase samples. The magnification and numerical aperture of the imaging system MO_2-L_5 are 10× and 0.32, respectively. Two groups of binary patterns with the orientation along the x- and y-directions were loaded on the DMD, of which the period was set as ten pixels and the modulation depth is 1. The x- and y- orientated patterns were shifted by five times and each time had a phase shift $\delta_m = 2\ (m\text{-}1)\pi/5$ (m = 1, 2, . . . , 5.). The generated diffraction patterns were

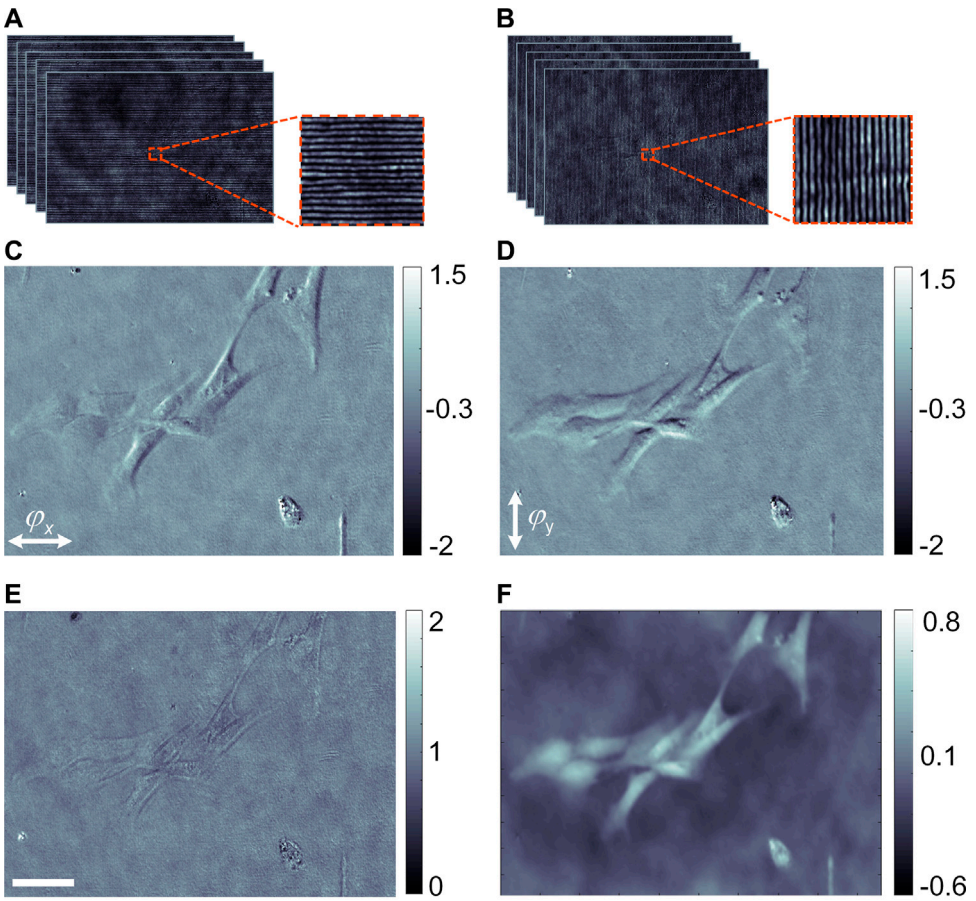

FIGURE 2 | qDIC imaging of mouse adipose stem cells. **(A,B)** The diffraction patterns along the *x*- and *y*-directions; **(C,D)** reconstructed phase derivatives of the cells along the *x*- and *y*- orientations, respectively; **(E,F)** reconstructed amplitude and phase distribution of the mouse adipose stem cells, respectively. The scale bar in **(E)**, 40 μm.

recorded by the CCD_1 camera, and shown in **Figures 2A,B** respectively. Using the reconstruction method described with **Eqs. 1**, **2**, both the amplitude and phase derivatives of the sample are obtained. **Figures 2C,D** show the phase gradients along the *x*- and *y*- orientations, respectively. Despite the contours of the cells become visible in **Figures 2C,D**, the result is a mixture of amplitude and phase-gradient in a nonlinear manner. The final phase distribution of the sample is then obtained by integrating the phase derivatives along the *x*- and *y*-orientations, as shown in **Figure 2F**. Compared to the amplitude image of the sample shown in **Figure 2E**, where the structures of the cells are nearly invisible, the phase image (**Figure 2F**) visualizes clearly the structures of the cells, and notably in a quantitative manner. The comparison reveals that qDIC can not only visualize the transparent samples with high contrast but also provide us the quantitative information on the optical path difference (OPD) of the sample.

Coherent SIM Imaging of SiO_2 Particles

In the second experiment, resolution-enhanced nonfluorescent/scattering imaging using coherent structured illumination was proved by imaging SiO_2 beads (diameter: 500-nm). Binary fringe patterns were loaded on DMD to generate sinusoidal fringe stripes at the sample plane after being filtered in the Fourier plane. The period of the binary patterns was set as five pixels, and after the de-magnification, the period of the sinusoidal fringe stripes was 0.95 μm at the sample plane. As explained in **Super-Resolution Scattering Imaging With Coherent Structured Illumination**, the binary fringe patterns were shifted by five times (yielding the phase shifts $\delta_m = 2\ (m\text{-}1)\pi/5$, $m = 1, 2, \ldots, 5$) along the *x*- and *y*-direction, and the generated diffraction patterns are recorded in sequence by CCD_1 located at the image plane. The super-resolution reconstruction is then realized with the method elaborated in **Super-Resolution Scattering Imaging With Coherent Structured Illumination**. The reconstructed image of SiO_2 beads is shown in **Figures 3A,B** shows the conventional wide-field image obtained using a perpendicular plane-wave illumination. It is clear that the coherent structured illumination provides a high-resolution image on the SiO_2 beads.

The numerical aperture (NA_{detect} = 0.32) of the detection objective MO_2 limits the lateral resolution to δ_{plan} = 1.44 μm for

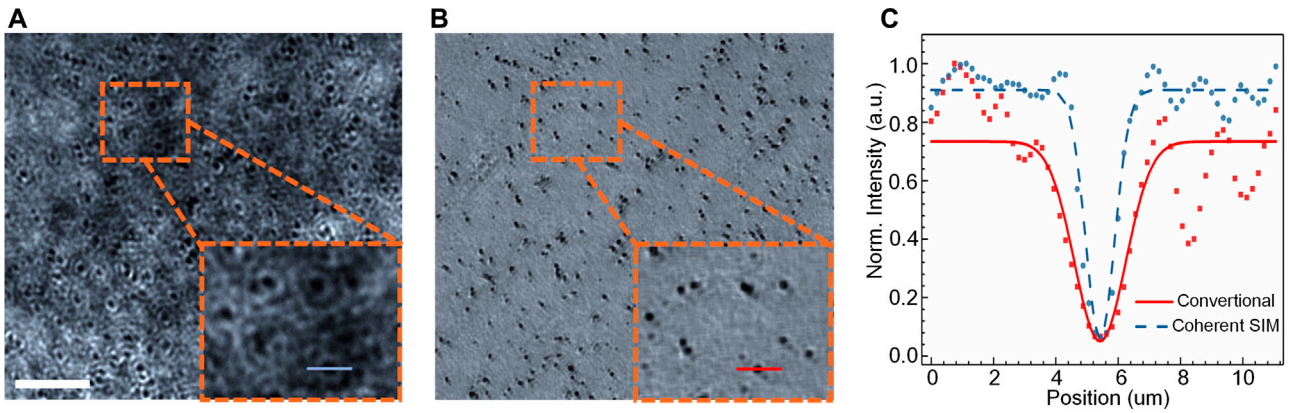

FIGURE 3 | Coherent SIM imaging of 500 nm SiO_2 beads. The images obtained using the convention al optical microscope under plane-wave illumination **(A)** and coherent SIM **(B)**. **(C)** The intensity profiles along the blue/red solid lines in **(A)** and **(B)**. The scale bar in **(A)**, 30 μm.

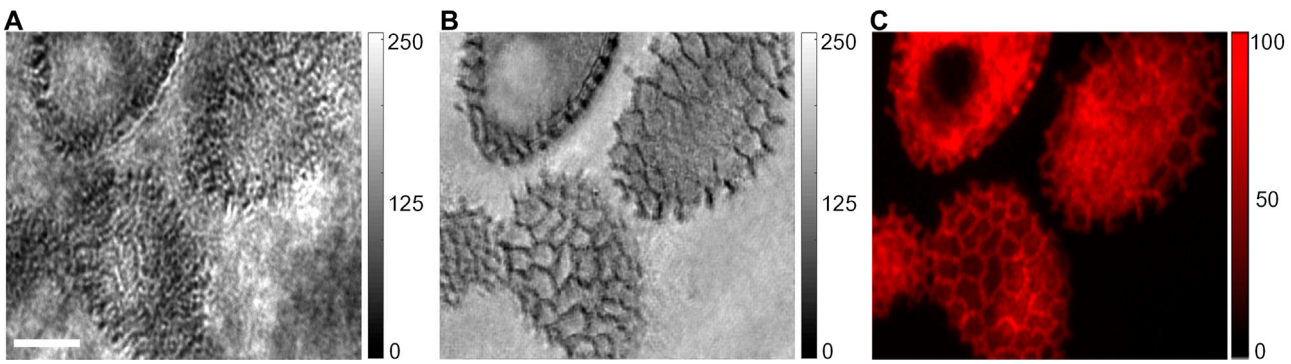

FIGURE 4 | Dual-modality imaging of lily anther. The image obtained using the conventional optical microscope under plane-wave illumination **(A)** and coherent SIM **(B)**. **(C)** Fluorescence image (spectrum band: 600/50 nm) of the same pollens. The scale bar in **(A)**, 30 μm.

the conventional imaging using a perpendicular plane wave illumination. When the structured illumination is used, the illumination angle of the ±1st diffraction orders of the fringe stripes is θ_{illum} = 0.30 rad, and thus the theoretical lateral resolution can be estimated with $\delta_{\text{str}} = 0.82\lambda/(\sin(\theta_{\text{illum}})+NA_{\text{detect}})$ = 0.75 μm [35]. For a quantitative evaluation of the lateral resolution, ten random SiO_2 beads were randomly chosen, and the intensity distributions along the line crossing the center of each bead are analyzed, as shown in **Figure 3C**. The statistics on the ten beads tells that the averaged full widths at half maximum (FWHM) under these two illuminations are 1.86 ± 0.20 μm for perpendicular uniform illumination while 1.10 ± 0.10 μm for coherent structured illumination. When considering the non-negligible size (the diameter d = 500 nm) of the SiO_2 beads, the final resolution can be calculated by $\delta_{res} = [(\delta_{plan/\text{str}})^2 - d^2]^{1/2}$, yielding the lateral resolution δ_{res} = 1.80 ± 0.20 μm and 0.98 ± 0.10 μm for the conventional wide-field imaging mode and coherent structured illumination mode, respectively. It should be noted that there is a mismatch between the measured and theoretical resolutions due to the system's aberration and other uncertain factors.

Dual-Modality (Scattering/Fluorescence) Imaging of Lily Anther

In the third experiment, the dual-modality (non-fluorescent scattering/fluorescent) imaging capability of the proposed SIM apparatus was demonstrated with lily anther as the sample. The coherent SIM image was shown in **Figure 4B**, and the fluorescence image was captured by the camera CCD_2 after being filtered by a color filter (600/50 nm, central wavelength/full-width at half maximum) and is shown in **Figure 4C**. Compared with the wide-field image in **Figure 4A** obtained by using a uniform illumination, the SIM image in **Figure 4B** shows more detailed structures and clearer background. Moreover, the fluorescent image in **Figure 4C** shows clear pollen structures (having autofluorescence) in the context of a clean background. It is also distinct that the SIM image (transmission) and the

fluorescent image (reflection) have the opposite contrast for the same sample.

DISCUSSION

In this paper, we have proposed a DMD based transmission SIM apparatus, which can be exploited for multi-modality imaging, including quantitative differential phase-contrast (qDIC) imaging, coherent SIM with resolution enhancement, fluorescence imaging. Structured illumination based qDIC is immune to environmental disturbances, compared with interferometric approaches. Coherent SIM provides super-resolved, scattering images of non-fluorescent samples. Fluorescent imaging furnishes specific, biochemical structures of samples once using fluorescent labeling. For both qDIC and coherent SIM, a DMD is used to generate structured illumination, and therefore, it has the features of high speed and high flexibility. It is worth noting that the qDIC is only applicable to continuous samples since the integration of phase derivatives are used. Moreover, both qDIC and coherent SIM cannot be realized in a real-time manner since both need to record multiple raw images once a sample is illuminated with structured patterns of different orientations and phase shifts. We believe such a simple and versatile apparatus will be widely applied for biomedical fields and life science.

In the proposed approach periodic patterns were projected to obtain the resolution enhancement and/or the phase information. As future prospective non periodic patterns (e.g., Walsh functions) can be projected and by that practically obtain the decomposing of the spatial information of the inspected sample. Projecting such functions can also be connected to compressed sensing and it may allow high resolution extraction of the spatial information in the inspected sample with smaller number of projected patterns (i.e., having faster process of information extraction).

This work is supported by National Natural Science Foundation of China (NSFC 62075177); Natural Science Foundation of Shaanxi Province (2020JM-193, 2020JQ-324); the Fund of State Key Laboratory of Transient Optics and Photonics (SKLST201804) and Key Laboratory of Image Processing and Pattern Recognition, Jiangxi Province.

DATA AVAILABILITY STATEMENT

The original contributions presented in the study are included in the article/Supplementary Material, further inquiries can be directed to the corresponding author.

AUTHOR CONTRIBUTIONS

JZ conceived and supervised the project. KW and YM performed experiments and data analysis. ML, JL, and ZZ contributed to data analysis. KW, YM, and JZ wrote the draft of the manuscript; All the authors edited the manuscript.

REFERENCES

1. Micó V, Zheng J, Garcia J, Zalevsky Z, Gao P. Resolution enhancement in quantitative phase microscopy. *Adv Optic Photon* (2019) 11:135–214. doi:10.1364/AOP.11.000135
2. Zhang M, Ma Y, Wang Y, Wen K, Zheng J, Liu L, et al. Polarization grating based on diffraction phase microscopy for quantitative phase imaging of paramecia. *Optic Express* (2020) 28:29775–87. doi:10.1364/OE.404289
3. Zernike F. Phase contrast, a new method for the microscopic observation of transparent objects. *Physica* (1942) 9:974–86. doi:10.1016/S0031-8914(42)80035-X
4. Ma Y, Guo S, Pan Y, Fan R, Smith Z, Lane SM, et al. Quantitative phase microscopy with enhanced contrast and improved resolution through ultra-oblique illumination (UO-QPM). *J Biophot* (2019) 12:e201900011. doi:10.1002/jbio.201900011
5. Shribak M, Larkin K, Biggs D. Mapping of optical path length and image enhancement using orientation-independent differential interference contrast microscopy. *J Biomed Optic* (2017) 22:016006. doi:10.1117/1.JBO.22.1.016006
6. Ding C, Li C, Deng F, Simpson GJ. Axially-offset differential interference contrast microscopy via polarization wavefront shaping. *Optic Express* (2019) 27:3837–50. doi:10.1364/OE.27.003837
7. Vishnyakov G, Levin G, Minaev V, Latushko M, Nekrasov N, Pickalov V. Differential interference contrast tomography. *Opt Lett* (2016) 41:3037–40. doi:10.1364/OL.41.003037
8. Arnison MR, Larkin KG, Sheppard CJ, Smith NI, Cogswell CJ. Linear phase imaging using differential interference contrast microscopy. *J Microsc* (2004) 214:7–12. doi:10.1111/j.0022-2720.2004.01293.x
9. Primot J. Theoretical description of Shack–Hartmann wave-front sensor. *Optic Commun* (2003) 222:81–92. doi:10.1016/S0030-4018(03)01565-7
10. Aknoun S, Bon P, Savatier J, Wattellier B, Monneret S. Quantitative retardance imaging of biological samples using quadriwave lateral shearing interferometry. *Optic Express* (2015) 23:16383–406. doi:10.1364/OE.23.016383
11. Bon P, Maucort G, Wattellier B, Monneret S. Quadriwave lateral shearing interferometry for quantitative phase microscopy of living cells. *Optic Express* (2009) 17:13080–94. doi:10.1364/OE.17.013080
12. Heintzmann R, Cremer C. Laterally modulated excitation microscopy: improvement of resolution by using a diffraction grating. *Proc SPIE* (1999) 3568:185–96. doi:10.1117/12.336833
13. Alexandrov SA, Hillman TR, Gutzler T, Sampson DD. Synthetic aperture Fourier holographic optical microscopy. *Phys Rev Lett* (2006) 97:168102. doi:10.1103/physrevlett.97.168102
14. Ou X, Horstmeyer R, Zheng G, Yang C. High numerical aperture Fourier ptychography: principle, implementation and characterization. *Optic Express* (2015) 23:3472–91. doi:10.1364/OE.23.003472
15. Lee K, Kim H-D, Kim K, Kim Y, Hillman TR, Min B, et al. Synthetic Fourier transform light scattering. *Optic Express* (2013) 21:22453–63. doi:10.1364/OE.21.022453
16. Littleton B, Lai K, Longstaff D, Sarafis V, Munroe P, Heckenberg N, et al. Coherent super-resolution microscopy via laterally structured illumination. *Micron* (2007) 38:150–7. doi:10.1016/j.micron.2006.07.010
17. Chowdhury S, Izatt J. Structured illumination diffraction phase microscopy for broadband, subdiffraction resolution, quantitative phase imaging. *Opt Lett* (2014) 39:1015–8. doi:10.1364/OL.39.001015
18. Gao P, Pedrini G, Osten W. Phase retrieval with resolution enhancement by using structured illumination. *Opt Lett* (2013) 38:5204–7. doi:10.1364/OL.38.005204
19. Mudassar AA, Hussain A. Super-resolution of active spatial frequency heterodyning using holographic approach. *Appl Optic* (2010) 49:3434–41. doi:10.1364/AO.49.003434

20. Park Y, Choi W, Yaqoob Z, Dasari R, Badizadegan K, Feld MS. Speckle-field digital holographic microscopy. *Optic Express* (2009) 17:12285–92. doi:10.1364/OE.17.012285
21. Zhang H, Jiang S, Liao J, Deng J, Liu J, Zhang Y, et al. Near-field Fourier ptychography: super-resolution phase retrieval via speckle illumination. *Optic Express* (2019) 27:7498–512. doi:10.1364/OE.27.007498
22. Zheng J, Pedrini G, Gao P, Yao B, Osten W. Autofocusing and resolution enhancement in digital holographic microscopy by using speckle-illumination. *J Optic* (2015) 17:085301. doi:10.1088/2040-8978/17/8/085301
23. Gustafsson MG. Surpassing the lateral resolution limit by a factor of two using structured illumination microscopy. *J. Microsc.* (2000) 198:82–7. doi:10.1046/j.1365-2818.2000.00710.x
24. Kim Y-D, Ahn M, Kim T, Yoo H, Gweon D. Design and analysis of a cross-type structured-illumination confocal microscope for high speed and high resolution. *Meas Sci Technol* (2012) 23:105403. doi:10.1088/0957-0233/23/10/105403
25. Shao L, Kner P, Rego EH, Gustafsson MG. Super-resolution 3D microscopy of live whole cells using structured illumination. *Nat Methods* (2011) 8:1044–6. doi:10.1038/nmeth.1734
26. Gustafsson MG. Nonlinear structured-illumination microscopy: wide-field fluorescence imaging with theoretically unlimited resolution. *Proc Natl Acad Sci U.S.A.* (2005) 102:13081–6. doi:10.1073/pnas.0406877102
27. Neil MA, Juškaitis R, Wilson T. Method of obtaining optical sectioning by using structured light in a conventional microscope. *Opt Lett* (1997) 22:1905–7. doi:10.1364/OL.22.001905
28. Schermelleh L, Carlton PM, Haase S, Shao L, Winoto L, Kner P, et al. Subdiffraction multicolor imaging of the nuclear periphery with 3D structured illumination microscopy. *Science* (2008) 320:1332–6. doi:10.1126/science.1156947
29. Fitzgibbon J, Bell K, King E, Oparka K. Super-resolution imaging of plasmodesmata using three-dimensional structured illumination microscopy. *Plant Physiol* (2010) 153:1453–63. doi:10.1104/pp.110.157941
30. Keller PJ, Schmidt AD, Santella A, Khairy K, Bao Z, Wittbrodt J, et al. Fast, high-contrast imaging of animal development with scanned light sheet–based structured-illumination microscopy. *Nat Methods* (2010) 7:637–42. doi:10.1038/nmeth.1476
31. Gao P, Pedrini G, Osten W. Structured illumination for resolution enhancement and autofocusing in digital holographic microscopy. *Opt Lett* (2013) 38:1328–30. doi:10.1364/OL.38.001328
32. Gao P, Wen K, Liu L, Zheng J. Computational phase microscopy with modulated illumination. *Proc SPIE* (2020) 11438:1143813. doi:10.1117/12.2551362
33. Abdelsalam DG, Kim D. Two-wavelength in-line phase-shifting interferometry based on polarizing separation for accurate surface profiling. *Appl Optic* (2011) 50:6153–61. doi:10.1364/AO.50.006153
34. Frankot RT, Chellappa R. A method for enforcing integrability in shape from shading algorithms. *IEEE T. Pattern Anal* (1988) 10:439–51. doi:10.1109/34.3909
35. Born M, Wolf E. *Principles of optics: electromagnetic theory of propagation, interference and diffraction of light*. New York: Cambridge University Press (2013). 417 p.

Conflict of Interest: The authors declare that the research was conducted in the absence of any commercial or financial relationships that could be construed as a potential conflict of interest.

frontiers in Physics

BRIEF RESEARCH REPORT
published: 18 February 2021
doi: 10.3389/fphy.2020.611679

Low-Coherence Shearing Interferometry With Constant Off-Axis Angle

Rongli Guo, Itay Barnea and Natan T. Shaked*

Department of Biomedical Engineering, Faculty of Engineering, Tel Aviv University, Tel Aviv, Israel

We present a wide-field interferometric imaging module for biomedical and metrological measurements, employing shearing interferometry with constant off-axis angle (SICA) that can work, for the first time, with a low-coherence light source. In the SICA module, the shearing distance between the interfering beams can be fully controlled without a direct relation with the off-axis angle. In contrast to our previous SICA module, here we use a low-coherence illumination source, providing quantitative phase profiles with significantly lower spatial coherent noise. Although a low-coherence source is used, we obtain off-axis interference on the entire camera sensor, where the optical path difference between the two beams is compensated by using a glass window positioned in the confocal plane. This highly stable, common-path, low-coherence, single-shot interferometric module can be used as an add-on unit to a conventional bright-field microscope illuminated by a low-coherence source. We demonstrate the advantages of using the module by quantitative phase imaging of a polymer bead, fluctuations in a human white blood cell, and dynamics of human sperm cells.

Keywords: quantitative phase imaging, low-coherence interferometry, shearing interferometry, microscopic imaging, digital holography

OPEN ACCESS

Edited by:
Peng Gao,
Xidian University, China

Reviewed by:
Junwei Min,
Xian Institute of Optics and Precision Mechanics (CAS), China
YongKeun Park,
Korea Advanced Institute of Science and Technology, South Korea

****Correspondence:***
Rongli Guo
guolee946@gmail.com

Specialty section:
This article was submitted to Optics and Photonics, a section of the journal Frontiers in Physics

Received: *29 September 2020*
Accepted: *23 October 2020*
Published: *18 February 2021*

Citation:
Guo R, Barnea I and Shaked NT (2021) Low-Coherence Shearing Interferometry With Constant Off-Axis Angle. Front. Phys. 8:611679. doi: 10.3389/fphy.2020.611679

INTRODUCTION

Wide-field interferometric phase microscopy (IPM), also called digital holographic microscopy, is a method that can render quantitative phase images of micro-scale samples by recording their complex fields [1–6]. Since it does not require exogenous labeling or special sample preparation for imaging transparent biological samples, IPM has shown to be a potent tool for studying cell biology [7–11], pathophysiology of cells [12–14] and in some other biomedical applications. [15, 16].

Off-axis IPM can reconstruct a quantitative phase image from a single interferogram or hologram, which is captured in a single shot. Thus, it is capable of monitoring dynamic changes of biological cells at the same frame rate of the digital camera used. There are different optical systems to implement IPM, and all of them generate a reference beam that does not contain the sample spatial modulation, to be interfere with the sample beam. The conventional Mach–Zehnder and Michelson interferometers split the beam at the exit of the laser to sample and reference beams, whereas self-referencing interferometers [17–33] typically create the reference beam externally, at the exit of the imaging system. Self-referencing interferometry includes, for example, τ interferometry [23, 33], flipping interferometry [24, 25], diffraction phase microscopy [27], shearing interferometry [28, 29], the quantitative phase imaging unit [30], quadriwave shearing interferometry [31]. All of these interferometers have a nearly common-path interferometric geometry, and hence inherently have a higher temporal phase sensitivity than the conventional Michelson and Mach–Zehnder

interferometers [23–33]. In order to decrease the amount of spatial coherent noise and parasitic interferences, low-coherence light sources can be used, which requires meticulous beam-path matching to obtain interference on the camera, so that the path difference between the sample and reference beams is smaller than the coherence length of the source. However, across the off-axis hologram obtained with a low-coherence source, the fringe visibility might be low in certain regions on the camera, decreasing the signal to noise ratio in the final quantitative phase profile, and thus limiting the interferometric imaging field of view. To overcome this limitation, white-light diffraction phase microscopy [34, 35] can be used. However, to generate a clean reference beam, this technique requires performing low-pass spatial filtering by a pinhole, which requires a precise alignment. In addition, white-light diffraction phase microscopy also demonstrated impairing halo effect [35].

Shearing interferometry, on the other hand, can create the reference beam externally by simply assuming the sample is sparse enough. Then, we can interfere two sheared copies of the same beam, and hopefully there is no overlap between sample details. Biological cells from the sheared beam appear as ghost images with negative phase values, and thus should be avoided. However, since in regular shearing interferometry the off-axis angle and the shearing distance between the beams are coupled, it is hard to avoid these ghost images. To solve this problem, we have lately introduced the shearing interferometry with constant off axis angle (SICA) module, as a simple add-on imaging unit to an existing imaging system illuminated with a highly coherent light [36]. The module employs the principle of shearing interferometry by generating two laterally shifted sample beams. The magnified image at the exit of the imaging system is split using a diffracting grating. In contrast to regular shearing interferometers, in SICA we can fully control the shearing distance by the axial position of the grating, whereas the off-axis angle is determined by the grating period, independently. This way, we can easily avoid overlaps with ghost images. Due to its off-axis nature and common-path configuration, the SICA module has benefits of real-time measurement capability and high temporal stability. However, it still suffers from spatial coherent noise due to the fact that it requires highly coherent illumination, to allow high-visibility off-axis interference on the entire field of view.

In the current paper, we introduce a low-coherence SICA (LC-SICA) module that allows single-shot quantitative phase imaging with both high spatial and temporal phase sensitivities, with high-visibility off-axis interference over the whole field of view. The new setup is an important modification to the previous SICA module, but at the same time, it inherited all its advantages i.e., easy alignment, simplicity, and an off-axis interference angle that can be controlled independently of the shearing distance.

EXPERIMENTAL SETUP

Figure 1 shows an inverted microscope, where the proposed LC-SICA module is connected to its output, and is indicated by the dashed rectangle. The module consists of diffraction grating G, two achromatic lenses L1 and L2, and optical path difference (OPD) compensator C (a glass plate). The two lenses are positioned in a 4f imaging configuration. The module is designed as an add-on unit, and is located at the output image from a conventional microscope. To generate two laterally shifted sample beams, grating G is placed behind IP at an axial distance z. The diffracted beams are Fourier transformed to get their spatial spectra in the back focal plane of lens L1. The zeroth and first diffraction orders are selected by mask M at the Fourier plane, whereas the other diffraction orders are blocked. The two orders are then projected by lens L2, so that the two laterally shifted sample beams overlap on the sensor plane at the selected off-axis angle, which is controlled by the grating period d, independently of the shearing distance, controlled by the grating axial location z [36].

In contrast to the previous design, presented in Ref. [36], here we use a low-coherence illumination and an OPD compensator. The low-coherence illumination is implemented by using a supercontinuum laser (SuperK EXTREME, NKT), followed by a computer-controlled acousto-optical tunable filter (AOTF, SuperK SELECT, NKT). The emitted light is at a central wavelength of 638 nm and a full-width-at-half-maximum bandwidth of 44 nm (as measured by a spectrometer, USB4000-VISNIR, Ocean Optics). As the spectrum has a nearly rectangle shape, the coherence length is calculated by $l_c = \lambda^2/\Delta\lambda = 9.2\,\mu$m. For ensuring a full-field interference, the OPD between two beams should be smaller than the coherence length of the source, across the entire camera sensor. Let us consider the OPD at point O on the image plane, where the two beams meet at an angle α. The conjugate point of point O at IP is point O_1; hence, the two beams, denoted by solid red line (zeroth-order beam) and dashed red line (first-order beam), have the same optical path length. However, the two interfering beams are originally emitted from points A and B, where the two red lines intercept with grating G. Hence, the OPD at point O is determined by:

$$\begin{aligned} OPD &= O_1B - O_1A \\ &= z\left(\frac{1}{\cos\theta} - 1\right), \\ &\cong 0.5 \cdot z \cdot \sin\theta \tan\theta \end{aligned} \tag{1}$$

where $\theta = \lambda/d$ is the diffraction angle of the first-order beam, which is determined by the grating period d and the wavelength λ. Usually, an OPD compensator should be inserted to minimize the mismatch of optical paths between two beams. In our experiment, as an OPD compensator we used a glass plate, placed in the first order beam path, at the Fourier plane. Although the interference angle is wavelength-dependent: $\alpha = \lambda f_1/f_2 d$, the period of the fringes at different wavelengths is independent of wavelength and equals $f_2 d/f_1$. Thus, it is an achromatic interferometer.

In our experiment, as shown in **Figure 1**, the light is steered into an inverted microscope (Olympus, IX83) to illuminate the sample S. The beam transmitted through the sample is magnified by microscope objective MO and projected by tube lens TL on IP. The intermediate image is further magnified by a factor of 2 in the

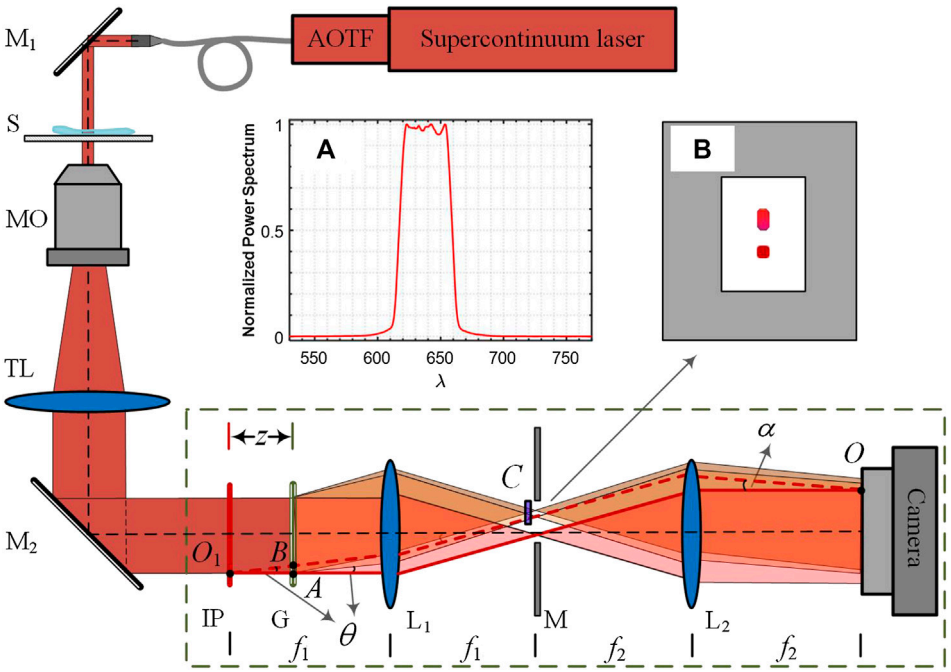

FIGURE 1 | An inverted microscope with the LC-SICA module (marked by dashed rectangle), connected to its output. M_1, M_2, mirrors; S, sample; MO, microscope objective; TL, tube lens; IP, image plane; G, diffraction grating (100 lines/mm); L_1, L_2, lenses with focal lengths of f_1 = 150 mm and f_2 = 300 mm; z, distance of IP to G; M, mask that selects only two diffraction orders; C, compensating plate; α, interference angle; θ, diffraction angle of the grating. Inset **(A)** normalized power spectrum of the light source with central wavelength of 638 nm and bandwidth of 44 nm. Inset **(B)** schematic of the filtered Fourier spectrum distribution in the focal plane.

module as $f_2/f_1 = 2$, and finally recorded by a CMOS camera (Thorlabs, DCC1545M). The period of the grating is $d = 10\ \mu m$, which is smaller than the microscopic diffraction spot magnified on IP. By choosing the grating axial distance z, the shearing distance between two beams can be tuned so that no overlap with ghost images occurs. The thickness of the compensating glass plate is dependent on distance z. We used a cover slip ($n = 1.52$) with thickness of $h = 0.17$-mm as the OPD compensator. The OPD induced by the coverslip is $(n - 1) \times h = 88.4\ \mu m$. Substituting this value into **Eq. 1** results in a grating optimal position of $z = 43$ mm. Note that working with a significantly wider spectral bandwidth results in OPDs that differ greatly, so that we cannot compensate for all of them using a constant thickness coverslip. Thus, realistically, LC-SICA is limited to using a spectral bandwidth of several tens of nanometers, which still allows a significant improvement in the spatial noise, compared with the coherent illumination scenario.

RESULTS

First, experiments were carried out to demonstrate the speckle noise suppressing capability with the proposed LC-SICA module. We measured a 5-μm polymer bead with a 100× objective under highly coherent illumination (He–Ne laser) and under low-coherence illumination (as described above). The bead ($n = 1.59$) is immersed in oil ($n = 1.52$) and sandwiched between two cover slips. The shearing distance between the interfering beams is controlled by the axial distance of the diffraction grating, and is set to be large enough so that no overlap occurs with ghost images containing negative phase values. Therefore, the full quantitative phase profile of the sample is obtained, rather than its gradient in the shearing direction. The off-axis angle is determined by the diffraction grating period, affecting the fringe spatial frequency of the hologram obtained on the digital camera. This captured off-axis hologram is processed using the Fourier transform method [20]. This includes a digital Fourier transform, cropping one of the cross-correlation terms, and an inverse Fourier transform, resulting in the complex wavefront of the sample. Then, we apply a phase unwrapping algorithm on the angle argument of the complex wavefront to solve 2π ambiguities. **Figures 2A,B** show two holograms obtained under coherent illumination and low-coherence illumination, respectively, demonstrating that although the LC-SICA module uses a low-coherence source, there is no loss in the fringe visibility along the entire field of view in comparison to using high coherent illumination.

The resulting quantitative phase images are shown in **Figures 2C,D**, respectively. It can be seen that the phase profile in **Figure 2C** is much nosier, as speckle noise ripples and abrupt fluctuations are obvious over the whole field. In contrast, these spatial noises are significantly suppressed when

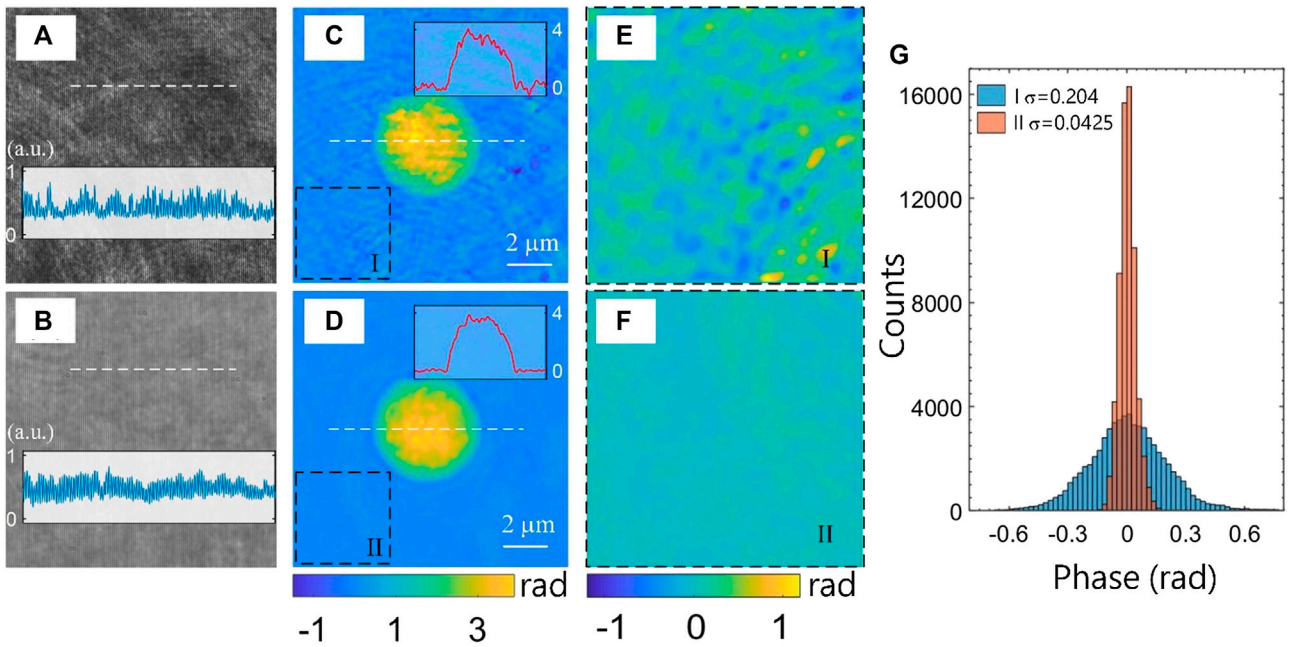

FIGURE 2 | Comparing the SICA and LC-SICA modules by quantitative phase imaging of a polymer bead. **(A, C)** Hologram and quantitative phase map from the SICA module, with highly coherent illumination (He–Ne, 633 nm). **(B, D)** Hologram and quantitative phase map from the LC-SICA module, with low-coherence illumination (638 ± 22 nm). The same 5-μm polystyrene bead immersed in index-matching oil was imaged in both cases. The two background regions, marked as I and II in **(C)** and **(D)** at the same location, are magnified in **(E)** and **(F)**, respectively. **(G)** Histogram of the phase values of the two background regions I and II, demonstrating a significantly lower spatial noise in the LC-SICA module in comparison to the regular SICA module. σ denotes spatial standard deviation of the quantitative phase values.

low-coherence illumination is used, as shown in **Figure 2D**. To further compare the spatial phase noises in both images, the two little marked regions I and II are enlarged, and shown in **Figures 2E,F**, respectively. This background phase profile is almost uniform in **Figure 2F**, whereas it has noticeable undulation in **Figure 2E**, even in the base-plane background region, due to the use of highly coherent illumination. To quantify the spatial phase noise levels, the phase distribution histograms of regions I and II are shown in **Figure 2G**. The standard deviation of the phase values in these regions are 0.204 and 0.0425 rad, respectively, which means that the phase noise level in the LC-SICA module is only approximatively a fifth of that of the SICA module. Under coherent illumination, the noise may come from scattering of dust particles or scratches on the optics surfaces, from parasitic fringes due to multiple reflections between coverslips, as well as from inherent laser noise. However, such noise can be greatly reduced when using low-coherence illumination, so that the proposed LC-SICA module can render quantitative phase images with higher spatial phase sensitivity.

Second, to show our high temporal stability and real-time imaging capability, we acquired 150 holograms over 10 s in presence of no samples, representing the case of a stationary sample. The holograms were processed to get coinciding phase profiles by subtraction the phase profile obtained from a pre-recorded hologram. The average standard deviation of 10,000 randomly selected pixels across the stack of these phase profiles, representing the temporal stability of the system, is 8.3 mrad, which indicates the high temporal stability of the setup.

We then measured the fluctuations of a human white blood cell. Human blood was provided by the Israeli blood bank (Magen David Adom) after obtaining an ethical approval from Tel Aviv University's institutional review board. Peripheral blood mononuclear cells (PBMCs), a type of white blood cells, were isolated from the whole blood using Ficoll-Paque Premium isolation kit (GE17-5442-02 Sigma-Aldrich), according to the manufacturer instructions. After centrifugation, PBMCs were collected from the buffy coat, and cleaned by centrifugation at 1250 RPM for 5 min in phosphate buffered saline (PBS) solutions supplemented with 1 mM EDTA. The supernatant was discarded, and the pellet was resuspended in 1 ml PBS-EDTA. A live PBMC was imaged for 10 s at a frame rate of 15 Hz. **Figure 3A** presents the quantitative phase image of the cell at $t = 0$. **Figure 3B** shows the temporal standard deviations of 150 phase images, which indicates the fluctuations over the cell. We also examined the phase fluctuations at the three marked points during this period, and the results are presented in **Figure 3C**. As indicated in **Figures 3A,B**, the three selected points are at the background, at the border of the cell, and at the interior region. The phase values of the point at the border has the largest fluctuations and the standard deviation was calculated to be 78.5 mrad. The point at interior area of the cell exhibits

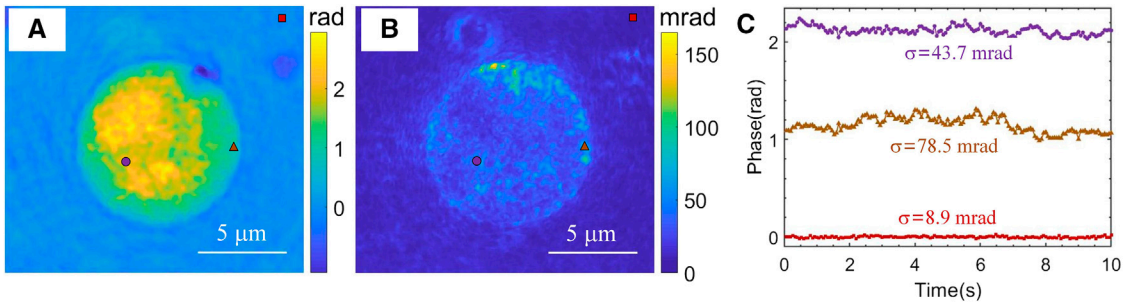

FIGURE 3 | Dynamic quantitative phase imaging of a human white blood cell at frame rate of 15 Hz, as acquired with the LC-SICA module. **(A)** Quantitative phase profile. **(B)** Quantitative phase temporal standard deviation profile over 150 frames (fluctuation map). **(C)** Quantitative phase values at the three different points marked in **(B)**. σ denotes the temporal standard deviations of the quantitative phase values at those points.

mild fluctuations and has a standard deviation value of 43.7 mrad. The background point has flat phase values with standard deviation of 8.9 mrad. This low background standard deviation value is due to using a common-path configuration in our add-on module, and is comparable with that of a white-light illuminated quantitative phase imaging unit [37]. However, the later unit is not suitable for measuring the highly dynamic phenomena, as it implements temporal phase-shifting interferometry to record multiple holograms for obtaining a single quantitative phase image.

At last, to demonstrate the flexibility of controlling the shearing distance without affecting the off-axis angle, to avoid ghost images in dynamic samples, we measured swimming sperm cells at two different shearing distances. Here, a 60×

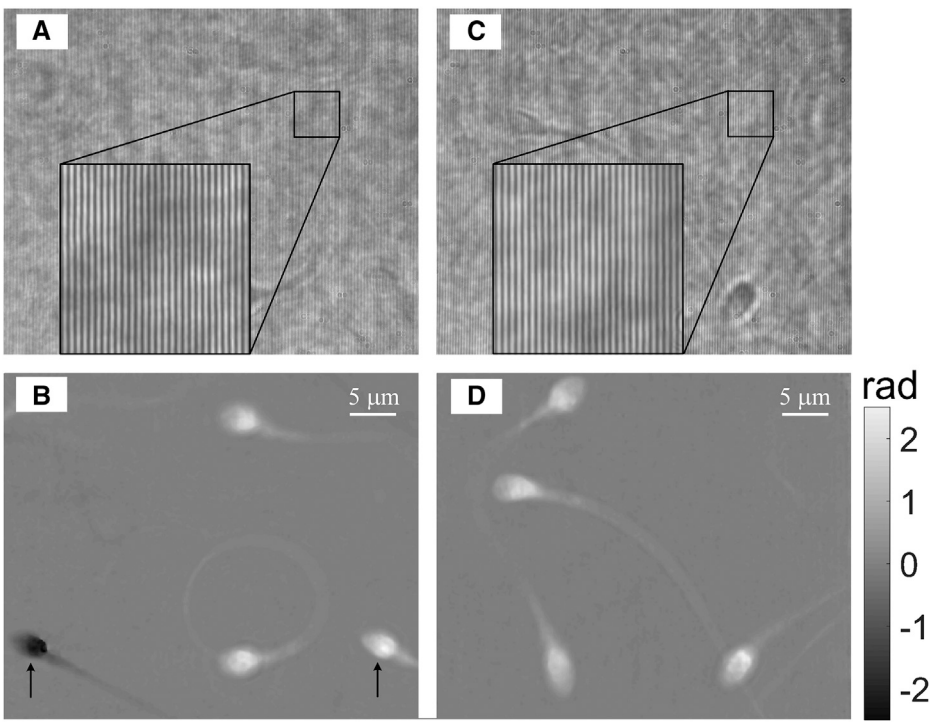

FIGURE 4 | Dynamic quantitative phase imaging of human sperm cells swimming in 80% PureCeption medium. **(A, B)** Off-axis hologram **(A)** and quantitative phase profile **(B)** with a small lateral shearing distance, as acquired by the LC-SICA module. See dynamic quantitative phase profile in **Supplementary Video S1**. **(C, D)** Off-axis hologram **(C)** and quantitative phase profile **(D)** with a large lateral shearing distance, acquired by the LC-SICA module. See dynamic quantitative phase profile in **Supplementary Video S2**. The black arrows in **(B)** indicate two conjugate images of the same cell: one image has positive phase values while the other image has negative values (ghost image), which might overlap with the positive-value cells, as demonstrated in **Supplementary Video S1**. This unwanted effect can be avoided if the shearing distance is fully controlled without direct relation to the off-axis angle. This off-axis angle is chosen to be optimal and constant, as can be seen in both holograms **(A)** and **(C)**, both having the same spatial frequency of the interference fringes, in spite of the fact that the shearing distance is different.

objective (Plan, N.A. 1.3, Olympus) was used for imaging. After obtaining an ethical approval from Tel Aviv University's institutional review board, the semen sample from a human donor was left in room temperature for 30 min to liquefy, and then the spermatozoa were separated through density gradient-based centrifugation by using a PureCeption bilayer kit (ART-2024 ORIGIO, Malov, Denmark), according to the manufacturer instructions. After centrifugation, the pellet was placed in a new tube and washed with HTF medium (#90125, Irvine Scientific, CA, United States). In the first case, 5 µl of the cell solution was placed between two cover slips. A small shearing of 5.5 mm is employed along the horizontal direction, as calculated with formula $\lambda z f_2 / f_1 d$ [36], where the grating is placed at $z = 43$ mm. **Figure 4A** shows one of the off-axis holograms from the dynamic sequence, and **Figure 4B** shows the reconstructed phase image (see full dynamic swimming in **Supplementary Video S1**). From **Figure 4B**, two inverse-contrast quantitative phase images of the same cell can be observed, due to the small shearing distance, which are marked by two arrows. As the sperm cells swim freely, the positive phase image of one cell may overlap with a negative phase image of another cell, as shown in **Supplementary Video S1**. In this case, the cells cannot be correctly reconstructed. To solve this, a large shearing can be applied, while a blank region containing no sample, located outside the field of view, is used to generate a reference beam. In this second case, the grating G was placed at a distance of $z = 130$ mm. Thus, the shearing distance was 16.5 mm, three times of that of the previous one and much longer than the lateral dimension of the sensor (6.6 mm). Three pieces of stacked coverslips were used as an OPD compensator. **Figure 4C** shows one hologram from this sequence, and **Figure 4D** shows the reconstructed phase image. In **Figure 4D**, there are only positive phase images over the entire field of view, and the dynamic swimming of the cells can be precisely monitored. It should be noted that although the shearing distance was changed in both cases, the off-axis angle was constant, and thus the interference fringe period was constant as well, as shown in the enlarged insets in **Figures 4A, C**. The adjustable shearing distance with a constant interference angle between two beams is an obvious advantage of the LC-SICA module, which benefits from convenience in choosing a clean part of the beam to act as the reference beam, according to the density of samples in a shearing interferometric setup. While in most other shearing interferometry setups [24–26, 28–30], the shearing distance is fixed, i.e., they can only image scenarios in which either the sample are sparse, or half of the field of view need to be empty [24–26], the proposed LC-SICA module can fully control the shearing distance based on the sparsity of the sample. This is even more beneficial when imaging dynamic movements of cells, as the samples may move randomly around the whole field of view, or the concentrations of cells may change over time.

CONCLUSION

We presented the LC-SICA module for dynamic phase imaging with high temporal and spatial phase sensitivities. This portable common-path module is made of simple off-the-shelf components: a diffraction grating, two lenses and a glass compensator, and has the advantages of simplicity and easy usage. The grating is used to generate two shifted sample beams on the camera sensor. Each of the two beams is the reference beam to the other beam, as in all shearing interferometer. However, in our case, the off-axis interference angle is uncoupled from the shearing distance, as opposite to other shearing interferometers. A low-coherence source is used to minimize spatial phase noise. The OPD between the two beams as a function of grating position is analyzed based on ray optics, and it is compensated with a glass plate. Thus, the full-field off-axis holograms can be obtained easily with a low-coherence light source, with no decrease in the fringe visibility. The comparative measurements of a polymer bead indicated that the spatial phase noise level was reduced significantly when compared to the results obtained with the coherently illuminated module. Measurement of a human white blood cell demonstrated the high temporal phase sensitivity imaging capability of the module. Experiments of different shearing distances were carried out, demonstrating that ghost-free imaging of swimming sperm cells can be achieved, by selecting a proper shearing distance based on sample density, as controlled by the grating axial location, and without changing the interference fringe frequency. The LC-SICA module is expected to be a useful tool empowering conventional microscopy in low-noise quantitative phase imaging.

DATA AVAILABILITY STATEMENT

The raw data supporting the conclusions of this article will be made available by the authors, without undue reservation.

AUTHOR CONTRIBUTIONS

RG and NS conceived the project. IB prepared the biological samples, and RG performed the experiments. RG and NS wrote the manuscript.

FUNDING

H2020 European Research Council (ERC) 678316.

SUPPLEMENTARY MATERIAL

The Supplementary Material for this article can be found online at: https://www.frontiersin.org/articles/10.3389/fphy.2020.611679/full#supplementary-material

REFERENCES

1. Shaked NT, Satterwhite LL, Bursac N, Wax A. Whole-cell analysis of live cardio myocytes using wide-field interferometric phase microscopy. *Biomed Opt Express.* (2010). 1:706–19. doi:10.1364/BOE.1.000706
2. Shaked NT, Zhu Y, Badie N, Bursac N, Wax A. Reflective interferometric chamber for quantitative phase imaging of biological sample dynamics. *J Biomed Opt.* (2010). 15:030503. doi:10.1117/1.3420179
3. Kemper B, von Bally G. Digital holographic microscopy for live cell applications and technical inspection. *Appl Opt.* (2008). 47:A52–61. doi:10.1364/AO.47.000A52
4. Popescu G, Park Y, Lue N, Best-Popescu C, Deflores L, Dasari RR, et al. Optical imaging of cell mass and growth dynamics. *Am J Physiol.* (2008). 295:C538–44. doi:10.1152/ajpcell.00121.2008
5. Micó V, Zheng J, Garcia J, Zalevsky Z, Gao P. Resolution enhancement in quantitative phase microscopy. *Adv Opt Photon.* (2019). 11:135–214. doi:10.1364/AOP.11.000135
6. Picazo-Bueno JA, Trusiak M, García J, Patorski K, Micó V. Hilbert-Huang single-shot spatially multiplexed interferometric microscopy. *Opt Lett.* (2018). 43:1007–10. doi:10.1364/OL.43.001007
7. Memmolo P, Miccio L, Merola F, Gennari O, Netti PA, Ferraro P. 3D morphometry of red blood cells by digital holography. *Cytometry A* (2014). 85:1030–6. doi:10.1002/cyto.a.22570
8. Park Y, Best CA, Auth T, Gov NS, Safran SA, Popescu G, et al. Metabolic remodeling of the human red blood cell membrane. *Proc Natl Acad Sci USA.* (2010). 107:1289–94. doi:10.1073/pnas.0910785107
9. Jacob Eravuchira P, Mirsky SK, Barnea I, Levi M, Balberg M, Shaked NT. Individual sperm selection by microfluidics integrated with interferometric phase microscopy. *Methods* (2018). 136:152–9. doi:10.1016/j.ymeth.2017.09.009
10. Min J, Yao B, Ketelhut S, Engwer C, Greve B, Kemper B. Simple and fast spectral domain algorithm for quantitative phase imaging of living cells with digital holographic microscopy. *Opt Lett.* (2017). 42:227–30. doi:10.1364/OL.42.000227
11. Eldridge WJ, Sheinfeld A, Rinehart MT, Wax A. Imaging deformation of adherent cells due to shear stress using quantitative phase imaging. *Opt Lett.* (2016). 41:352–5. doi:10.1364/OL.41.000352
12. Park H, Hong SH, Kim K, Cho SH, Lee WJ, Kim Y, et al. Characterizations of individual mouse red blood cells parasitized by Babesia microti using 3-D holographic microscopy. *Sci Rep.* (2015). 5:10827. doi:10.1038/srep10827
13. Shaked NT, Satterwhite LL, Telen MJ, Truskey GA, Wax A. Quantitative microscopy and nanoscopy of sickle red blood cells performed by wide field digital interferometry. *J Biomed Opt.* (2011). 16:030506. doi:10.1117/1.3556717
14. Hu C, Santi M, Adelaja O, Kajdacsy-Balla A, Popescu G, Kobak W. Imaging collagen properties in the uterosacral ligaments of women with pelvic organ prolapse using spatial light interference microscopy (SLIM). *Front Physiol.* (2019). 7:72. doi:10.3389/fphy.2019.00072
15. Haifler M, Girshovitz P, Band G, Dardikman G, Madjar I, Shaked NT. Interferometric phase microscopy for label-free morphological evaluation of sperm cells. *Fertil Steril.* (2015). 104:43–7. doi:10.1016/j.fertnstert.2015.04.013
16. Pavillon N, Kühn J, Moratal C, Jourdain P, Depeursinge C, Magistretti PJ, et al. Early cell death detection with digital holographic microscopy. *PLoS ONE.* (2012). 7:e30912. doi:10.1371/journal.pone.0030912
17. Guo RL, Wang F. Compact and stable real-time dual-wavelength digital holographic microscopy with a long-working distance objective. *Optic Express.* (2017). 25:24512–20. doi:10.1364/OE.25.024512
18. Bai H, Zhong Z, Shan M, Liu L, Guo L, Zhang Y. Interferometric phase microscopy using slightly-off axis reflective point diffraction interferometer. *Optic Laser Eng.* (2017). 90:155–60. doi:10.1016/j.optlaseng.2016.10.011
19. Chowdhury S, Eldridge WJ, Wax A, Izatt JA. Structured illumination multimodal 3D-resolved quantitative phase and fluorescence sub-diffraction microscopy. *Biomed Optic Express.* (2017). 8:2496–518. doi:10.1364/BOE.8.002496
20. Guo RL, Wang F, Hu X, Yang W. Off-axis low coherence digital holographic interferometry for quantitative phase imaging with an LED. *J Optic.* (2017). 19:115702. doi:10.1088/2040-8986/aa8887
21. Hosseini P, Zhou R, Kim YH, Peres C, Diaspro A, Kuang C, et al. Pushing phase and amplitude sensitivity limits in interferometric microscopy. *Optic Lett.* (2016). 41:1656–9. doi:10.1364/OL.41.001656
22. Gao P, Pedrini G, Osten W. Structured illumination for resolution enhancement and autofocusing in digital holographic microscopy. *Optic Lett.* (2013). 38:1328–30. doi:10.1364/OL.38.001328
23. Shaked NT. Quantitative phase microscopy of biological samples using a portable interferometer. *Optic Lett.* (2012). 37:2016–8. doi:10.1364/OL.37.002016
24. Roitshtain D, Turko NA, Javidi B, Shaked NT. Flipping interferometry and its application for quantitative phase microscopy in a micro-channel. *Optic Lett.* (2016). 41:2354–7. doi:10.1364/OL.41.002354
25. Rotman-Nativ N, Turko NA, Shaked NT. Flipping interferometry with doubled imaging area. *Optic Lett.* (2018). 43:5543–6. doi:10.1364/OL.43.005543
26. Kemper B, Vollmer A, Rommel CE, Schnekenburger J, von Bally G. Simplified approach for quantitative digital holographic phase contrast imaging of living cells. *J Biomed Optic.* (2011). 16:026014. doi:10.1117/1.3540674
27. Popescu G, Ikeda T, Dasari RR, Feld MS. Diffraction phase microscopy for quantifying cell structure and dynamics. *Opt Lett.* (2006). 31:775–7. doi:10.1364/OL.31.000775
28. Ma C, Li Y, Zhang J, Li P, Xi T, Di J, et al. Lateral shearing common-path digital holographic microscopy based on a slightly trapezoid Sagnac interferometer. *Optic Express.* (2017). 25:13659–67. doi:10.1364/OE.25.013659
29. Singh AS, Anand A, Leitgeb RA, Javidi B. Lateral shearing digital holographic imaging of small biological specimens. *Optic Express.* (2012). 20:23617–22. doi:10.1364/OE.20.023617
30. Lee K, Park Y. Quantitative phase imaging unit. *Optic Lett.* (2014). 39:3630–3. doi:10.1364/OL.39.003630
31. Bon P, Maucort G, Wattellier B, Monneret S. Quadriwave lateral shearing interferometry for quantitative phase microscopy of living cells. *Optic Express.* (2009). 17:13080–94. doi:10.1364/OE.17.013080
32. Majeed H, Ma L, Lee YJ, Kandel M, Min E, Jung W, et al. Magnified Image Spatial Spectrum (MISS) microscopy for nanometer and millisecond scale label-free imaging. *Optic Express.* (2018). 26:5423–40. doi:10.1364/OE.26.005423
33. Girshovitz P, Shaked NT. Compact and portable low-coherence interferometer with off-axis geometry for quantitative phase microscopy and nanoscopy. *Optic Express.* (2013). 21:5701–14. doi:10.1364/OE.21.005701
34. Bhaduri B, Pham H, Mir M, Popescu G. Diffraction phase microscopy with white light. *Optic Lett.* (2012). 37:1094–6. doi:10.1364/OL.37.001094
35. Edwards C, Bhaduri B, Nguyen T, Griffin BG, Pham H, Kim T, et al. Effects of spatial coherence in diffraction phase microscopy. *Optic Express.* (2014). 22:5133–46. doi:10.1364/OE.22.005133
36. Guo RL, Mirsky SK, Barnea I, Dudaie M, Shaked NT. Quantitative phase imaging by wide-field interferometry with variable shearing distance uncoupled from the off-axis angle. *Optic Express.* (2020). 28:5617–28. doi:10.1364/OE.385437
37. Baek Y, Lee K, Yoon J, Kim K, Park Y. White-light quantitative phase imaging unit. *Optic Express.* (2016). 24:9308–15. doi:10.1364/OE.24.009308

Conflict of Interest: The authors declare that the research was conducted in the absence of any commercial or financial relationships that could be construed as a potential conflict of interest.

frontiers in Physics

ORIGINAL RESEARCH
published: 10 March 2021
doi: 10.3389/fphy.2021.648174

High Dynamic Range Structured Illumination Microscope Based on Multiple Exposures

*Yong Liang[1,2], Xiaohu Chen[2], Zhenglong Sun[2], Gang Wen[2], Chong Chen[1], Libo Wang[2], Xin Jin[2], Jie Zhang[2], Guang Yang[2], Jing Gao[2], Hui Li[1,2] and Simin Li[1,2]**

[1]University of Science and Technology of China, Hefei, China, [2]Jiangsu Key Laboratory of Medical Optics, CAS Center for Excellence in Molecular Cell Science, Suzhou Institute of Biomedical Engineering and Technology, Chinese Academy of Sciences, Suzhou, China

Structured illumination microscope (SIM) can double the spatial resolution by using fringed pattern illumination. However, for samples with large intra-scene dynamic ranges, such as clustered objects, SIM fails to reconstruct high-quality images and often exhibits strong artifacts. Herein, we present a high dynamic range SIM (HDR-SIM) method using a multi-exposure acquisition strategy. With HDR-SIM, individual and clustered microspheres and vesicles with 420 times intensity differences can be visualized in the same scene while the delicate structures of the sample were preserved effectively.

Keywords: super-resolution, structured illumination microscopy, high dynamic range imaging, fusion algorithm, multiple exposures

OPEN ACCESS

Edited by:
Ming Lei,
Xi'an Jiaotong University, China

Reviewed by:
Zhaojun Wang,
Xi'an Jiaotong University, China
Fu Wang,
Shanghai Jiao Tong University, China

****Correspondence:***
Simin Li
lism@sibet.ac.cn

Specialty section:
This article was submitted to Optics and Photonics, a section of the journal Frontiers in Physics

Received: *31 December 2020*
Accepted: *01 February 2021*
Published: *10 March 2021*

Citation:
Liang Y, Chen X, Sun Z, Wen G, Chen C, Wang L, Jin X, Zhang J, Yang G, Gao J, Li H and Li S (2021) High Dynamic Range Structured Illumination Microscope Based on Multiple Exposures. Front. Phys. 9:648174. doi: 10.3389/fphy.2021.648174

INTRODUCTION

SIM is a super-resolution fluorescence imaging method that can provide adequate structure information two times beyond the Diffraction-Limit [1]. Compared with other super-resolution methods [2], SIM stands out for low-photon bleaching and compatibility for most fluorescence labeling protocols. SIM's wide-field nature makes it fit for live-cell imaging at high speed. As a result, SIM is now widely applied in studying subcellular structures [3, 4], organelle interactions [5], endocytic dynamics [6]. However, the limited dynamic range has prevented SIM from being used for biological samples like clustered vesicles or actin filaments.

In addition to imaging resolution and speed, the dynamic range is another essential factor to be concerned with when selecting imaging modalities for particular applications. An imaging system's dynamic range determines the darkest and brightest signals that it can detect [7]. When the dynamic range of an imaging system cannot cover the intra-scene dynamic range (IDR) of samples, a trade-off must be made between the loss of weak signal and intense signal saturation. It becomes even more challenging for SIM imaging. The large IDR can lead to spatial variations in the optimal values of SIM reconstruction parameters and eventually apparent artifacts. Notably, the side-lobe artifacts of structures with strong signals might overwhelm the delicate structures with weak signals. Several attempts were proposed to eliminate the artifacts in SIM, such as Wiener filtering [8], Least-Squares solver [9], Richardson-Lucy deconvolution [10], and Hessian deconvolution [11]. But they are not sufficient for samples with large IDR. Another approach to solve the problem is to divide the whole image into several subregions and apply different reconstruction parameters for each one, as in Tiled-SIM [12]. But it is hard to tile into suitable subregions when the strong signals and weak signals are mixed irregularly. As a result, SIM is considered to be not suitable for imaging samples with large IDR.

Several approaches were developed in the photography field for high dynamic range (HDR) imaging [13]. A commonly used method is the multiple exposure technique [14]. A set of low

dynamic range (LDR) images is taken with progressively increased exposure and then mathematically fused into an HDR image. The multi-exposure method was recently introduced into confocal laser scanning microscopy and two-photon microscopy [15, 16]. Another useful approach is adaptive illumination that uses a spatial light modulator to spatially control the light intensity distribution so that all points can be exposed reasonably [17, 18]. Yang et al. reported an approach to extend the dynamic of multiphoton microscopy based on a non-uniform illumination pattern by real-time negative feedback to modulate the illumination [19]. But by now, there is no prior report about extending SIM's dynamic range to our knowledge.

In this study, we introduce an HDR-SIM method based on the multi-exposure strategy. The 8-bit spatial light modulator (SLM) grating patterns are used to illuminate the sample with different intensity and fringe patterns. Sets of LDR-SIM raw images are recorded and fused into a set of HDR raw images using a pixel-wise weighting algorithm. Finally, the HDR-SIM image is achieved by using a Wiener-filter-based reconstruction algorithm. With the proposed approach, single and clustered fluorescent beads with 420 times intensity differences can be distinguished. HDR–SIM was also used to study vesicles in live osteosarcoma cells, in which the individual dim vesicles and inter-structures of bright vesicle clusters can be visualized simultaneously.

PRINCIPLE OF HDR-SIM

In SIM imaging, the measured intensity $D(\boldsymbol{r})$ of a fluorescence specimen $S(\boldsymbol{r})$ can be expressed as

$$D(\boldsymbol{r}) = [S(\boldsymbol{r}) \cdot I(\boldsymbol{r})] \otimes PSF(\boldsymbol{r}) \tag{1}$$

where $I(\boldsymbol{r})$ stands for the structured illumination intensity distribution, $\otimes$ denotes the convolution operator, $PSF(\mathbf{r})$ is the point spread function. When cosine fringe patterned light fields are used to excite fluorescence, $I(\boldsymbol{r})$ can be expressed as

$$\mathrm{I}(\mathbf{r}) = I_0 \cdot \left[1 + m\cos\left(\mathbf{k}_0 \cdot \mathbf{r} + \phi\right)\right] \tag{2}$$

where I_0 is the average illumination intensity, m is the modulation depth, $\mathbf{k}_0$ and ϕ is the spatial frequency and the bias phase, respectively. Generally, nine raw images are captured with three spatial frequencies rotated by 60°, and three phases shifted by 2π/3 for each spatial frequency. The average intensity I_0 is constant for traditional SIM. Here, to achieve HDR-SIM imaging, a set of SIM raw images $LDR_n(\boldsymbol{r})$ are captured with varying average illumination intensities I_n. The manipulation of illumination intensity is realized by changing the grayscale of fringe patterns for a laser-interference SIM. Similar to the HDR method used in photography field [14], the combined HDR image from n exposures can be calculated by a weighted sum:

$$HDR(\boldsymbol{r}) = \frac{\sum_n \rho_n(\boldsymbol{r}) \cdot LDR_n(\boldsymbol{r})}{\sum_n \rho_n(\boldsymbol{r})} \tag{3}$$

In which, the coefficient matrix $\rho(\boldsymbol{r})$ is defined as a hat function:

$$\rho(\boldsymbol{r}) = \begin{cases} D(\boldsymbol{r}) - \alpha, & for \quad D(\boldsymbol{r}) \le (\alpha + \beta)/2 \\ \beta - D(\boldsymbol{r}), & for \quad D(\boldsymbol{r}) > (\alpha + \beta)/2 \end{cases} \tag{4}$$

where α, β are the minimum and maximum brightness values in all images LDR_n. For most cases, three exposures with average intensity ratio $\eta = (0.25 : 0.5 : 1)$ allow reasonable HDR-SIM reconstruction. Taking more exposure to data processing might improve HDR performance but decrease the imaging speed.

Since $LDR_n(\boldsymbol{r})$ are recorded with the same spatial frequency and the same initial phase but with different average illumination intensities, $HDR(\boldsymbol{r})$ can also be expressed as

$$HDR(\mathbf{r}) = [S_{HDR}(\boldsymbol{r}) \cdot I(\boldsymbol{r})] \otimes PSF(\boldsymbol{r}) \tag{5}$$

$$S_{HDR}(\mathbf{r}) = \frac{\sum_n \rho_n(\boldsymbol{r}) \cdot \eta_n}{\sum_n \rho_n(\boldsymbol{r})} S(\mathbf{r}) \tag{6}$$

Now we consider $S_{HDR}(\mathbf{r})$ as the new unknown sample structure information. Noting that **Eq. 5** and **Eq. 1** are expressed approximately in the same form, so the corresponding HDR-SIM image can be reconstructed by following the state-of-the-art SIM reconstruction procedures [20] as

$$\tilde{S}_{HDR-SIM}(\mathbf{K}) = \frac{\sum_{d,n} \widetilde{\mathrm{OTF}}^{*}(\mathbf{k} + n\mathbf{k}_{\mathrm{d}}) \tilde{S}_{HDR}(\mathbf{k} + \mathrm{n}\mathbf{k}_d)}{\sum_{d,n} \left|\widetilde{\mathrm{OTF}}(\mathbf{k} + n\mathbf{k}_{\mathrm{d}})\right|^2 + w^2} A(\mathbf{k}) \tag{7}$$

where $\tilde{S}_{HDR-SIM}(\mathbf{K})$ is the HDR-SIM reconstruction result in Fourier space, $\widetilde{\mathrm{OTF}}(\mathbf{k})$ is the optical transfer function, w is the Wiener parameter and $A(\mathbf{k})$ is the anodization function [21].

EXPERIMENTAL SETUP AND SAMPLE PREPARATION

HDR-SIM Setup

As is shown in **Figure 1A**, the excitation laser beam, coupled into a single-mode polarization-maintaining optical fiber, illuminates a ferroelectric SLM with 1,280 × 1,024 pixels (SXGA-3DM, Fourth Dimension Displays). Grating patterns are stored onboard and are then activated with defined timings. The grating diffracts the incoming laser beam into different diffraction orders. Only the ±1 diffraction components are allowed to pass through a spatial filter placed at the Fourier plane of lens L2, and finally form interference light fields at the sample plane. A liquid crystal variable retarders (LCVR-200-VIS, Meadowlark) and a quarter-wave plate are used to ensure that the incoming beams' polarizations are maintained s-polarized at the sample plane. Fluorescence emitted from the sample is collected by a 100×NA1.49 oil objective (UAPON, Olympus Life Science, Japan). Images are captured using a scientific complementary metal-oxide-semiconductor camera (ORCA-Flash4.0 V2, Hamamatsu).

We use a constant camera exposure time for each image acquisition while manipulating equivalent illumination intensity to record sets of LDR-SIM raw images with multi-exposure. Typically three sets of excitation intensities are used, corresponding to under-, middle-, and over-exposure, respectively, as shown in **Figure 1B**. The manipulation of

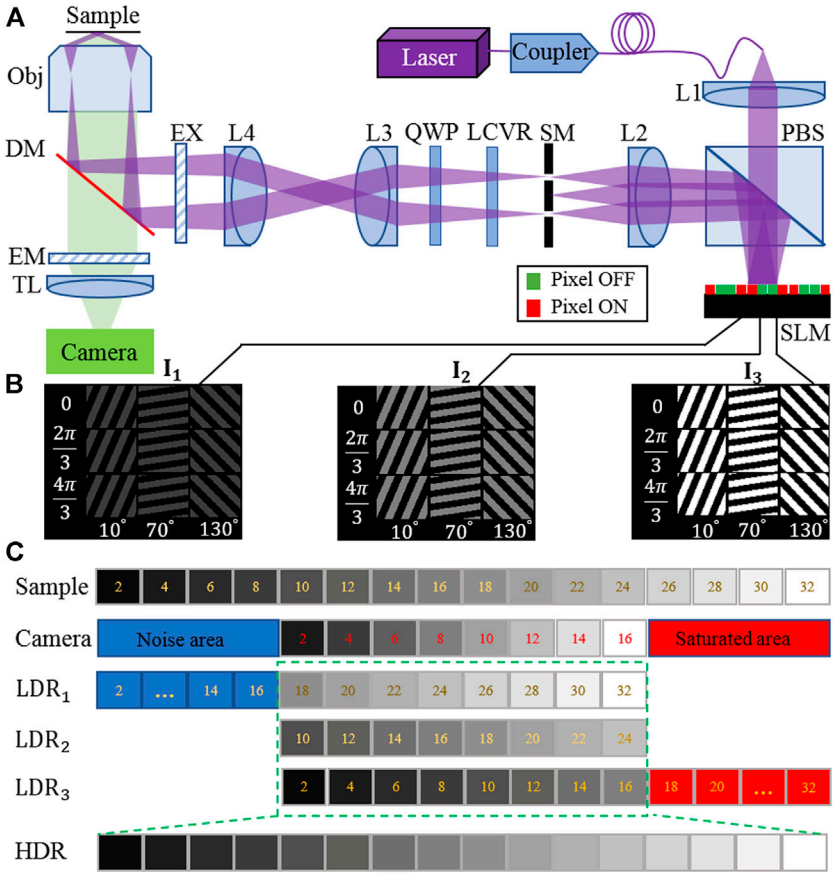

FIGURE 1 | (A) Layout of the high dynamic range structured illumination microscopy (HDR-SIM) setup. PBS, polarization beam splitter; L1–L4, lenses; SM, spatial mask; LCVR, liquid crystal variable retarders; QWP, quarter-wave plate; EX, excitation filter; DM, dichroic mirror; EM, emission filter; TL, tube lens; SLM, spatial light modulator. **(B)** Three sets of illumination patterns with different orientation angles, phase, and intensity were loaded on the SLM, corresponding to 0.25, 0.5, and 1 time the maximum incident light intensity. **(C)** Principle of the fusing process of raw images into HDR raw data. With the camera's limited dynamic range, only a portion of the sample information can be used effectively for each illumination set (green rectangle).

equivalent illumination intensity is realized by operating the SLM on grayscale mode. **Figure 1C** shows the limitation of LDR imaging and the fusing process into an HDR image.

Sample Preparation

Carboxylate-modified beads (yellow-green-fluorescent 505/515, diameter 100 nm) are purchased from Thermo Fisher Scientific (F8803). The solution of yellow-green beads was diluted 50 times and was dispensed onto a coverslip. The coverslip was left in the air and dried in ambient conditions. As a result, some beads aggregated together with very high fluorescence intensity while some beads were separated as an individual bead with low fluorescence intensity.

For cell imaging, the U2OS osteosarcoma cell line was purchased from the Stem Cell Bank at the Chinese Academy of Sciences. The U2OS cells were cultured in McCoy's 5A (modified) medium (Thermo Fisher), supplemented with 1% penicillin G, streptomycin (Sangon), and 10% fetal bovine serum (Thermo Fisher) at 37°C in a 5% (v/v) CO_2 environment. Cells were transfected using Lipofectamine 2000 (Invitrogen), following the manufacturer's protocol. The cell vesicle was labeled by the CD63-EGFP vector constructed by inserting the homo species CD63 gene into the pEGFP-n1 vector (Clonetech). Twelve hours after transfection, the cells were detached using trypsin-EDTA, seeded onto poly-L-lysine-coated 35 mm glass-bottom dishes (Cellvis), and cultured in an incubator at 37°C with 5% CO_2 for an additional 24 h before the experiments.

RESULTS AND DISCUSSION

Extending of the Dynamic Range by HDR-SIM

To validate HDR-SIM, we first created a large IDR sample with fluorescent beads. In the sample, some beads aggregated to form clusters that yielded intense fluorescence, while some individual beads scattered at other regions that showed weak fluorescence signals. The intensity ratio of the strong and weak signals can be estimated by $\boldsymbol{r} = (\boldsymbol{I}_1 \cdot \boldsymbol{I}_4)/(\boldsymbol{I}_2 \cdot \boldsymbol{I}_3)$, where $\boldsymbol{I}_1$ is the peak fluorescence intensity of clustered beads in the under-exposure image, $\boldsymbol{I}_2$ is the peak fluorescence intensity of single beads in the

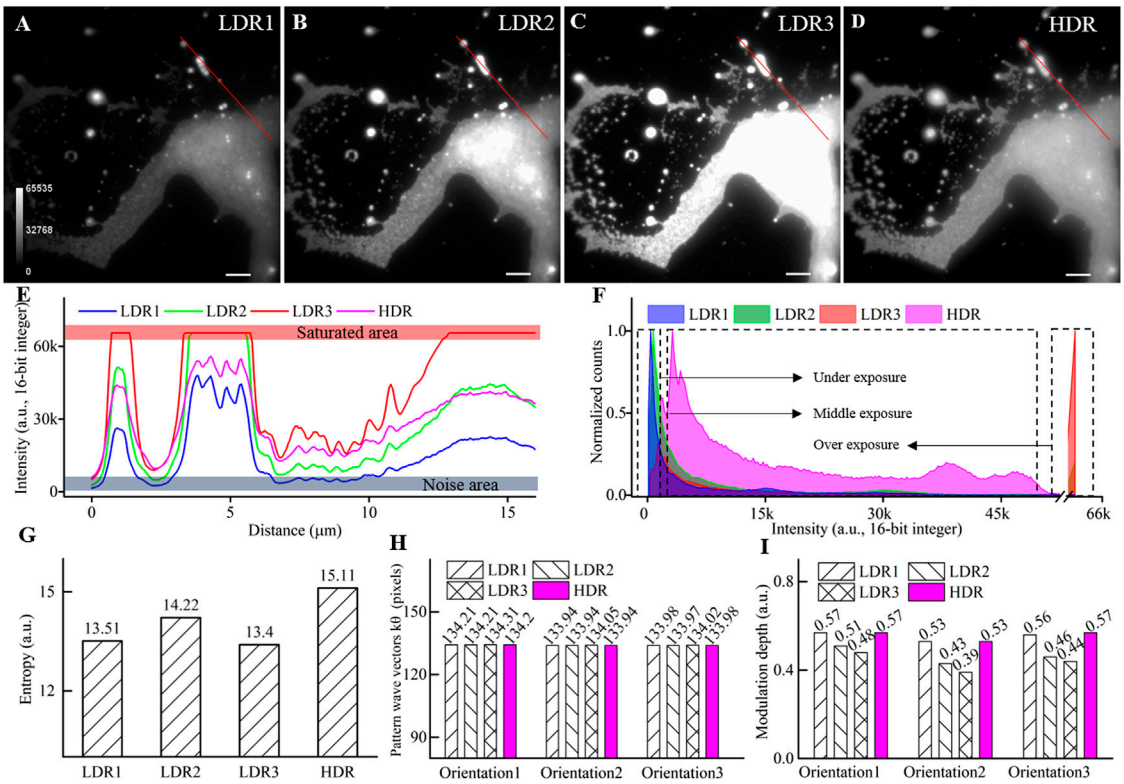

FIGURE 2 | Performance of the HDR fusing to widen the dynamic range. **(A–C)** LDR images of clustered fluorescent beads acquired with different excitation intensities corresponding to under, middle, and overexposure. **(D)** HDR image by fusing the above three LDR images. **(E)** Intensity profiles along the red lines in **(A–D)**. **(F)** The normalized histogram. **(G)** The entropy of the LDR and the HDR image. **(H)** Period of illumination pattern wave vector (**k**) at three orientations. **(I)** The modulation depth of illumination pattern at three orientations. Scale bar: 3 μm for **(A–D)**.

over-exposure image, $\boldsymbol{I}_3$ and $\boldsymbol{I}_4$ represent the average illumination intensity of under-exposure image and over-exposure image, respectively. The measured intensity ratio of the strong and weak signals can reach as high as 420:1. Three sets of SIM images (**Figures 2A–C**) were captured with different average excitation intensities (0.25: 0.5: 1) respectively and then fused into a composite HDR image (**Figure 2D**). With low excitation intensity, clustered beads in bright regions can be distinguished, but the signals from individual beads are submerged in noise. At high-excitation intensities, individual beads have improved signal-to-noize ratio (SNR), but the clustered beads' signals were saturated. In comparison, the combined HDR image maintained all the scene details (**Figure 2E**).

The histograms of the LDR images and the combined HDR image are plotted in **Figure 2F**. For LDR images, the histogram's primary domain is either at the low-intensity range or the saturated range. The broad middle part of the histogram makes minor contributions to the image details. In comparison, the combined HDR image shows significantly improved uniformity on the histogram. To quantitative compare the contained information, we further calculated the entropy of each image [22], which is defined as

$$H(x) = -\sum_{i=1}^{N} p(x_i) log_2 p(x_i) \tag{8}$$

where x_i represents the lightness value, and $p(x_i)$ is the normalized probability of x_i. **Figure 2G** shows that the fused HDR image has the highest entropy value, indicating that our multiple exposures strategy and fusion algorithm can produce SIM raw data with more sample structure details.

We further compared the estimated fringe pattern parameters from LDR raw data and fused HDR data using the cross-correlation method [23]. As is shown in **Figures 2H,I**, both the period of the illumination pattern |**k**| and modulation depth m remained the same within <1% at each orientation, which suggests that the same spatial frequency and same phase shifts were maintained during image acquisition.

HDR-SIM Imaging of Individual and Clustered Fluorescent Beads

Figures 3A–C show the equivalent wide-field image, LDR-SIM image with middle excitation intensity, and HDR-SIM image, respectively. Compared with LDR-SIM, the HDR-SIM image has a higher contrast and more detailed information. **Figures 3D–F**

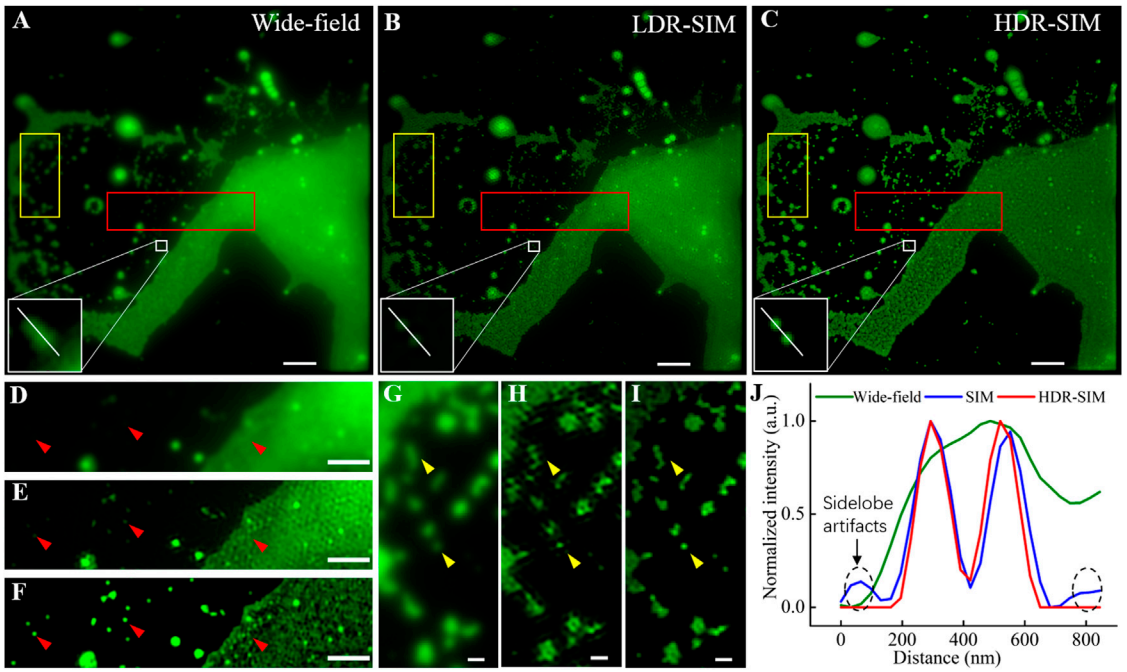

FIGURE 3 | Comparative images of fluorescent beads, 100 nm in diameter, in wide-field, traditional SIM, and HDR-SIM. **(A)** Wide-field image. **(B)** SIM image reconstructed by fairSIM [21], corresponding to middle-exposure images (reconstruction parameters: strength 0.995, full-width-at-half-maximum (FWHM) of 3 cycles/μm, Wiener parameter = 0.2). **(C)** HDR-SIM image, the reconstruction parameters are the same as **(B)**. **(D–F)** Zoom-in images corresponding to the region marked by the red boxes. **(G–I)** Zoom-in images corresponding to the region marked by the yellow boxes. **(J)** Intensity profiles along the white lines in **(A–C)**. Scale bar: **(A–C)** 3 μm, **(D–F)** 1.5 μm, and **(G–I)** 0.5 μm. Gamma value: 0.5 for images in **(A–C)**.

show the corresponding zoomed-in image of a region with large intensity differences (red box). The fluorescent intensity of clustered beads on the right is far higher than that of the individual beads on the left. These two types of features are hard to be imaged appropriately at the same time. **Figure 3D** also suggested that there is a strong out-of-focus signal along with heavy background noise. By carefully adjusting the OTF attenuation parameters, the LDR-SIM image **Figure 3E** effectively mitigates the out-of-focus signal. It turns out to be much clearer than the wide-field image. However, in the clustered area, there are obvious artifacts most likely result from background noise. Similar scenes frequently appear when imaging actin or vesicles. In contrast, HDR-SIM image **Figure 3F** shows it is still possible to recognize useful structural information such as spots consisting of a small number of individual beads or lines consisting of beads huddled in one direction.

In traditional SIM imaging, several issues, such as low SNR, symmetry-broken of SIM-PSF, and imperfect reconstruction parameters, could induce artifacts in the reconstructed image. For samples with a large dynamic range, the estimated reconstruction parameters were mostly determined by the bright region, which may not be perfect for the dim regions. The proposed HDR-SIM can effectively mitigate the reconstruction artifacts for two reasons. First, the combined HDR image contains information from all exposures (**Figure 2G**), and the resulted SNR is higher than any single-shot image. Second, the fusion algorithm greatly enhances the uniformity of intensity distribution (**Figure 2F**), which makes estimated reconstruction parameters optimal for the entire field of view. **Figures 3G–I** show the zoomed-in images of another region with more scattered individual beads (yellow boxes). The arrows point to typical individual beads. LDR-SIM images show obvious artifacts, especially in the dim region shown in **Figure 3H**. By contrast, HDR-SIM enhanced the weak signals and suppressed the strong signals. Thus, even in the weak signal region of the reconstructed image, no obvious artifacts were observed, and the individual beads demonstrated clear round shapes, as shown in **Figure 3I**. **Figure 3J** presents the intensity profiles along the white line on the two adjacent beads in **Figures 3A–C**. It demonstrates that HDR-SIM has the same super-resolution capability and performs better in reducing side-lobe artifacts than LDR-SIM. We counted the full width at half maximum of 60 individual beads, and the estimated resolution for HDR-SIM is 102 ± 5 nm.

HDR-SIM Imaging of Vesicles in Live Osteosarcoma Cells

Vesicles serve as the carrier of matters and signals in live cells [24, 25], and they might exist as individual moieties or join together to form a large cluster, known as multivesicular bodies (MVBs) inside cells [26, 27]. The MVBs can contain small intraluminal vesicles that would be released into the extracellular space in response to different cell signals. To image the individual vesicles and MVBs at the same scene is always a challenging problem owing to the large IDR.

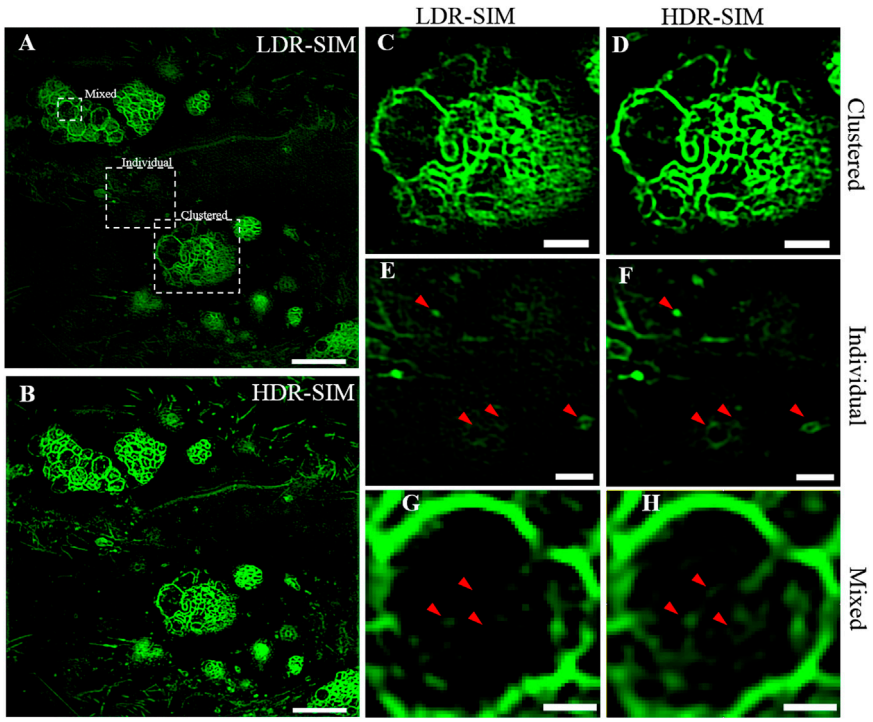

FIGURE 4 | Imaging of individual and clustered vesicles in live osteosarcoma cells. **(A)** The LDR-SIM imaging with middle excitation intensity. **(B)** HDR-SIM imaging of the same sample. **(C,D)** Zoomed-in view of a bright region showing clustered vesicles by LDR- and HDR-SIM. **(E,F)** Zoomed-in view of a dim region showing individual vesicles by LDR- and HDR-SIM. **(G,H)** Zoomed-in view of a large vesicle with an inner structure by LDR- and HDR-SIM. Color maps are scaled identically for each pair of images. Scale bar: **(A,B)** 5 μm, **(C–E)** 1.5 μm, and **(F)** 0.5 μm. Gamma value: 0.5 for images in **(A,B)**.

We applied HDR-SIM to image vesicles in live osteosarcoma cells. **Figures 4A,B** show the LDR-SIM image with moderate excitation intensity and the HDR-SIM image of the vesicles, respectively. In these images, MVBs show high brightness that dulls the fluorescence signals of individual ones. As shown in **Figures 4C,D**, the imaging quality of the LDR-SIM image and HDR-SIM image are similar for bright MVBs areas, and both exhibit high resolution and high contrast. In areas with weaker signals (**Figures 4E,F**), the HDR-SIM image maintains a high-SNR response. In contrast, the LDR-SIM image contains significant artifacts wherein the signals are almost submerged in noise. Importantly, we can now directly intraluminal vesicles inside MVBs, which are lost in LDR-SIM (**Figure 4G**), which can be visualized by HDR-SIM (**Figure 4H**). This will help a better understanding of the biochemical process and physiological function of MVBs.

CONCLUSION

In conclusion, we introduced an HDR-SIM imaging method for samples with a high dynamic range. It alleviates SIM reconstruction artifacts and enables visualization of detailed structures for both dim and bright regions at the same scene. The proposed method uses a set of grayscale periodic patterns loaded to SLM to achieve multiple excitation exposure. It can be easily implemented in any SLM-based SIM system without additional hardware costs. We believe that our HDR-SIM technique can be extensively adopted where dynamic range matters, such as studies with vesicles, mitochondria, neuron cell bodies, and their interactions in cell and molecular biology.

DATA AVAILABILITY STATEMENT

The raw data supporting the conclusions of this article will be made available by the authors, without undue reservation.

AUTHOR CONTRIBUTIONS

SL conceived the idea of this work. YL accomplished the experiment, performed the analysis of results, and wrote the manuscript. HL, JG, and XH gave the guide for analysis. ZL, JZ, and XJ prepared the biological samples. GW, LW, and CC did the simulation and analysis. All authors contributed to the discussion and manuscript revision.

FUNDING

National Key Research and Development Program of China (2017YFC0110100); Natural Scientific Research Foundation of China (NSFC) (61805272); Scientific Research Equipment Development Project of the Chinese Academy of Sciences (YJKYYQ20200074).

REFERENCES

1. Heintzmann R, Huser T. Super-resolution structured illumination microscopy. *Chem Rev* (2017) 117(23):13890–908. doi:10.1021/acs.chemrev.7b00218
2. Schermelleh L, Ferrand A, Huser T, Eggeling C, Sauer M, Biehlmaier O, et al. Super-resolution microscopy demystified. *Nat Cell Biol* (2019) 21(1):72–84. doi:10.1038/s41556-018-0251-8
3. Qian J, Lei M, Dan D, Yao B, Zhou X, Yang Y, et al. Full-color structured illumination optical sectioning microscopy. *Sci Rep* (2015) 5(1):14513. doi:10.1038/srep14513
4. Fiolka R, Shao L, Rego E, Davidson MW, Gustafsson MG. Time-lapse two-color 3D imaging of live cells with doubled resolution using structured illumination. *Proc Natl Acad Sci USA* (2012) 109(14):5311–5. doi:10.1073/pnas.1119262109
5. Guo Y, Li D, Zhang S, Yang Y, Liu JJ, Wang X, et al. Visualizing intracellular organelle and cytoskeletal interactions at nanoscale resolution on millisecond timescales. *Cell* (2018) 175(5):1430–42.e17. doi:10.1016/j.cell.2018.09.057
6. Li D, Shao L, Chen BC, Zhang X, Zhang M, Moses B, et al. ADVANCED IMAGING. Extended-resolution structured illumination imaging of endocytic and cytoskeletal dynamics. *Science* (2015) 349(6251):aab3500. doi:10.1126/science.aab3500
7. Adeyemi A, Barakat N, Darcie TE. Applications of digital micro-mirror devices to digital optical microscope dynamic range enhancement. *Opt Express* (2009) 17(3):1831–43. doi:10.1364/OE.17.001831
8. Christian K, Smedh M, Förster R, Deschout H, Fernandez-Rodriguez J, Heintzmann R. Successful optimization of reconstruction parameters in structured illumination microscopy – a practical guide. *Opt Commun* (2019) 436:69–75. doi:10.1016/j.optcom.2018.12.005
9. Luo J, Li C, Liu Q, Wu J, Li H, Kuang C, et al. Super-resolution structured illumination microscopy reconstruction using a least-squares solver. *Front Phys* (2020) 8:118. doi:10.3389/fphy.2020.00118
10. Perez V, Chang BJ, Stelzer EH. Optimal 2D-SIM reconstruction by two filtering steps with Richardson-Lucy deconvolution. *Sci Rep* (2016) 6(1):37149. doi:10.3389/fphy.2020.0011810.1038/srep37149
11. Huang X, Fan J, Li L, Liu H, Wu R, Wu Y, et al. Fast, long-term, super-resolution imaging with hessian structured illumination microscopy. *Nat Biotechnol* (2018) 36(5):451–9. doi:10.1038/nbt.4115
12. Hoffman David P, Betzig E. Tiled reconstruction improves structured illumination microscopy. *bioRxiv* (2020). doi:10.1101/895318
13. Feng W, Zhang F, Wang W, Xing W, Qu X. Digital micromirror device camera with per-pixel coded exposure for high dynamic range imaging. *Appl Opt* (2017) 56(13):3831–40. doi:10.1364/AO.56.003831
14. Debevec Paul E, Malik. J. Recovering high dynamic range radiance maps from photographs. In: Proceedings of the 24th ACM annual conference on computer graphics and interactive techniques. Proc. SIGGRAPH 1997: 369–378 (Los Angeles, CA, USA). doi:10.1145/258734.258884
15. Vinegoni C, Leon Swisher C, Fumene Feruglio P, Giedt RJ, Rousso DL, Stapleton S, et al. Real-time high dynamic range laser scanning microscopy. *Nat Commun* (2016) 7(1):11077. doi:10.1038/ncomms11077
16. Vinegoni C, Feruglio PF, Weissleder R. High dynamic range fluorescence imaging. *IEEE J Sel Top Quan Electron* (2019) 25(1):6801507. doi:10.1109/JSTQE.2018.2881608
17. Krishnaswami V, Van Noorden CJF, Manders EMM, Hoebe RA. Spatially-controlled illumination microscopy: for prolonged live-cell and live-tissue imaging with extended dynamic range. *Q Rev Biophys* (2016) 49:e19. doi:10.1017/S0033583516000135
18. Chu Kengyeh K, Lim D, Jerome M. Enhanced weak-signal sensitivity in two-photon microscopy by adaptive illumination. *Opt Lett* (2017) 32(19):2846–8. doi:10.1364/OL.32.002846
19. Yang R, Weber TD, Witkowski ED, Davison IG, Mertz J. Neuronal imaging with ultrahigh dynamic range multiphoton microscopy. *Sci Rep* (2017) 7(1):5817. doi:10.1038/s41598-017-06065-7
20. Gustafsson MG, Shao L, Carlton PM, Wang CJ, Golubovskaya IN, Cande WZ, et al. Three-dimensional resolution doubling in wide-field fluorescence microscopy by structured illumination. *Biophys J* (2008) 94(12):4957–70. doi:10.1529/biophysj.107.120345
21. Marcel M, Mönkemöller V, Hennig S, Hübner W, Huser TR. Open-source image reconstruction of super-resolution structured illumination microscopy data in ImageJ. *Nat Commun* (2016) 7(1):10980. doi:10.1038/ncomms10980
22. Tsai DY, Lee Y, Matsuyama E. Information entropy measure for evaluation of image quality. *J Digit Imaging* (2008) 21(3):338–47. doi:10.1007/s10278-007-9044-5
23. Wicker K. Non-iterative determination of pattern phase in structured illumination microscopy using auto-correlations in fourier space. *Opt Express* (2013) 21(21):24692–701. doi:10.1364/OE.21.024692
24. Piper RC, Katzmann DJ. Biogenesis and function of multivesicular bodies. *Annu Rev Cell Dev Biol* (2007) 23(1):519–47. doi:10.1146/annurev.cellbio.23.090506.123319
25. Hessvik NP, Llorente A. Current knowledge on exosome biogenesis and release. *Cell Mol Life Sci* (2018) 75(2):193–208. doi:10.1007/s00018-017-2595-9
26. Bian S, Zhang L, Duan L, Wang X, Min Y, Yu H. Extracellular vesicles derived from human bone marrow mesenchymal Stem cells promote angiogenesis in a rat myocardial infarction model. *J Mol Med* (2014) 92(4):387–97. doi:10.1007/s00109-013-1110-5
27. Bobrie A, Colombo M, Raposo G, Théry C. Exosome secretion: molecular mechanisms and roles in immune responses. *Traffic* (2011) 12(12):1659–68. doi:10.1111/j.1600-0854.2011.01225.x

Conflict of Interest: The authors declare that the research was conducted in the absence of any commercial or financial relationships that could be construed as a potential conflict of interest.

frontiers in Physics

ORIGINAL RESEARCH
published: 10 March 2021
doi: 10.3389/fphy.2021.642302

Simultaneous Two-Photon Fluorescence Microscopy of NADH and FAD Using Pixel-to-Pixel Wavelength-Switching

Yifan Qin[1]* *and Yuanqin Xia*[2]*

[1]National Key Laboratory of Science and Technology on Tunable Laser, Harbin Institute of Technology, Harbin, China, [2]Center for Advanced Laser Technology, Hebei University of Technology, Tianjin, China

OPEN ACCESS

Edited by:
Ming Lei,
College of Science, Xi'an Jiaotong University, China

Reviewed by:
Shaowei Wang,
National University of Singapore, Singapore
Yang Yanlong,
State Key Laboratory of Transient Optics and Photonics, China

***Correspondence:**
Yifan Qin
qinyifanhit@gmail.com
Yuanqin Xia
xiayq@hebut.edu.cn

Specialty section:
This article was submitted to Optics and Photonics, a section of the journal Frontiers in Physics

Received: 15 December 2020
Accepted: 11 January 2021
Published: 10 March 2021

Citation:
Qin Y and Xia Y (2021) Simultaneous Two-Photon Fluorescence Microscopy of NADH and FAD Using Pixel-to-Pixel Wavelength-Switching. Front. Phys. 9:642302. doi: 10.3389/fphy.2021.642302

Two-photon fluorescence (TPF) microscopy of intrinsic fluorophores provides physiological and pathological information from biological tissues. Reduced nicotinamide adenine dinucleotide (NADH) and flavin adenine dinucleotide (FAD) are two endogenous fluorescent coenzymes existing on the intracellular scale. Autofluorescence images of NADH and FAD have been applied to noninvasively record changes during metabolism, according to their distributions and concentrations. However, the widely used sequential (non-simultaneous) excitation scheme results in artifacts caused by sample motion or laser power fluctuation. The single-wavelength illumination scheme suffers from low excitation efficiency and spectral bleed-through. In this paper, we demonstrate a new imaging system simultaneously capturing autofluorescence images from NADH and FAD, with high excitation efficiency and negligible spectral bleed-through. Two temporally multiplexed and spatially overlapped excitation beams were achieved with fast-switching light paths based on an electro-optic modulator. The switching beams were centered at 750 and 860 nm, enabling independent excitations of NADH and FAD. Autofluorescence images of NADH and FAD were acquired at the wavelength ranges of 415–455 nm and 500–550 nm, respectively. The electro-optic modulator was synchronized with the pixel clock from the microscope, achieving pixel-to-pixel wavelength-switching. The capability of the system was demonstrated by performing TPF imaging of freshly excised mouse colon tissues. The microenvironment of the colon wall was depicted by the distributions of colonocytes, goblet cells, and crypts of Lieberkühn, and the relative concentrations of NADH and FAD were estimated. The experimental results show that the system can effectively perform simultaneous imaging of NADH and FAD, and is considered a promising tool for investigations into metabolism-associated processes and diseases.

Keywords: nonlinear optical microscopy, label-free microscopy, NADH, FAD, two-photon fluorescence

INTRODUCTION

Two-photon fluorescence (TPF) microscopy has been proven to be a powerful technique for imaging in biological tissues [1]. In TPF, the emission intensity depends quadratically on the excitation intensity, which minimizes the signal gained out of the sample volume [2]. TPF microscopy has submicron three-dimensional spatial resolution, high signal-to-noize ratio, weak out-of-focus photobleaching, and good penetration ability, which are significant for biomedical applications. Meanwhile, TPF microscopy is a label-free technique because the existence of endogenous fluorophores in biological tissues eliminates the need for exogenous biomarkers for imaging.

Reduced nicotinamide adenine dinucleotide (NADH) and flavin adenine dinucleotide (FAD) are metabolic coenzymes, which are also the most widely used endogenous fluorophores [3, 4]. During metabolism, enzymes bind to NADH and FAD, and their relative concentrations and distributions change at the same time. TPF imaging of NADH and FAD enables noninvasively monitoring of metabolism-related physiological and pathological processes, such as cell differentiation, cancer development. One imaging scheme is sequential (non-simultaneous) excitation, which switches between two wavelengths (e.g., 755 and 860 nm) by using a tunable laser [5–7]. The advantage is that autofluorescence signals of NADH and FAD can be completely separated, and misinterpretation can be avoided during analysis. However, it suffers from low acquisition speed and artifacts from sample motion or laser power fluctuation when tuning between two wavelengths. Another scheme using single-wavelength (e.g., 800 nm) excitation can excite NADH and FAD simultaneously at the cost of unavoidable spectral bleed-through (SBT) and low excitation efficiency [8].

To overcome the shortages of the aforementioned two schemes, we demonstrate a novel TPF microscopy capable of exciting NADH and FAD simultaneously by using pixel-to-pixel wavelength-switching. The concept was proposed for nonlinear optical microscopy in our previous works [9, 10]. During pixel-to-pixel wavelength-switching, two temporally multiplexed excitation beams, centered at 750 and 860 nm, are achieved by using an electro-optic modulator (EOM). Since the EOM is synchronized with the pixel clock, the wavelengths and pixels switch simultaneously. The major advantages of the imaging system are as follows.

- Simultaneous excitations of NADH and FAD ensure high acquisition speed and eliminate possible artifacts from sample motion or laser power fluctuation.
- SBT is negligible and excitation efficiency is high because of the independent excitations and separated detections.
- The pixel-to-pixel wavelength-switching strategy doesn't require any complex demultiplexing algorithm to collect signal or internal modification to commercial microscopes (e.g., FV1000, Olympus, Japan).

We will describe the system construction step by step, and demonstrate the capability of the system by performing simultaneous TPF imaging in NADH and FAD solutions as well as in freshly excised mouse colon tissues.

EXPERIMENTAL SETUP

Figure 1A shows the experimental setup. The excitation source for the simultaneous TPF microscopy of NADH and FAD is a broadband (>100-nm spectral bandwidth) mode-locked Ti: Sapphire laser, which generates femtosecond pulses with ~80-MHz repetition rate. The laser beam is delivered to a liquid-crystal spatial light modulator (SLM, SLM-640-D-VN, CRi, United States)-based pulse shaper with a 4*f* configuration. The laser beam is dispersed by a grating onto a concave mirror and focused on an SLM placed at the Fourier plane. By setting the mask of the SLM, the laser beam is tailored to a double-peak spectrum, which is centered at 750 and 860 nm. These wavelengths are selected according to the cross-sections of NADH and FAD (**Figure 1B**). The cross-section spectra indicate that the 860-nm wavelength can only excite FAD, while the 750-nm wavelength can excite both substances.

A long-pass dichroic mirror (DM1, DMLP805R, Thorlabs, United States) splits the laser beam into two arms, i.e., the transmitted 860-nm arm (shown in red) and the reflected 750-nm arm (shown in blue). Both arms are initially p-polarized. In the 860-nm arm, a polarizing beam splitter (PBS1, PBS102, Thorlabs, United States) and a half-wave plate (HWP1, WPH05M-850, Thorlabs, United States) are combined to adjust the optical power. Fine-tuning the relative position of lenses L1 and L2 (AD408-B, LBTEK, China, $f_{L1} = f_{L2} = 100$ mm) along the optical axis can compensate for the axial displacement between the two arms derived from chromatic aberration [11]. In the 750-nm arm, a polarizing beam splitter (PBS2, PBS102, Thorlabs, United States) and a half-wave plate (HWP2, WPH05M-780, Thorlabs, United States) are paired to rotate the polarization by 90° (to s-polarized) and adjust the optical power. A long-pass dichroic mirror (DM2, DMLP805R, Thorlabs, United States) recombines the two arms. Spatial synchronization of the two arms is achieved by using the same method described in [10]. A quarter-wave plate (QWP, WPQ05M-808, Thorlabs, United States) and an EOM (EO-AM-NR-C1, Thorlabs, United States) are located after DM2. The modulation signal of the EOM is from a function generator (SDG1032X, Siglent, China). When applying a $4/\lambda$ voltage, the EOM and QWP work as a half-wave plate, which rotates the polarizations of incoming beams by 90°. When applying a $-4/\lambda$ voltage, the polarizations will stay the same. A polarizing beam splitter (PBS3, PBS102, Thorlabs, United States) located after the EOM removes s-polarized components. The voltages applied to the EOM rapidly switch between $\pm 4/\lambda$ (the frequency is 125 kHz, the duty cycle is 50%). Thus the 860- and 750-nm beams are spatially overlapped and temporally multiplexed. Proper dispersion management are performed for both arms. All the optical elements mentioned above comprise the EOM-based fast-switching light paths.

A dual-axis galvanometer-scanner (GVS002, Thorlabs, United States) scans the beams at the focal plane of a scan lens (AC254-045-B, Thorlabs, $f_{SL} = 45$ mm). The beams are

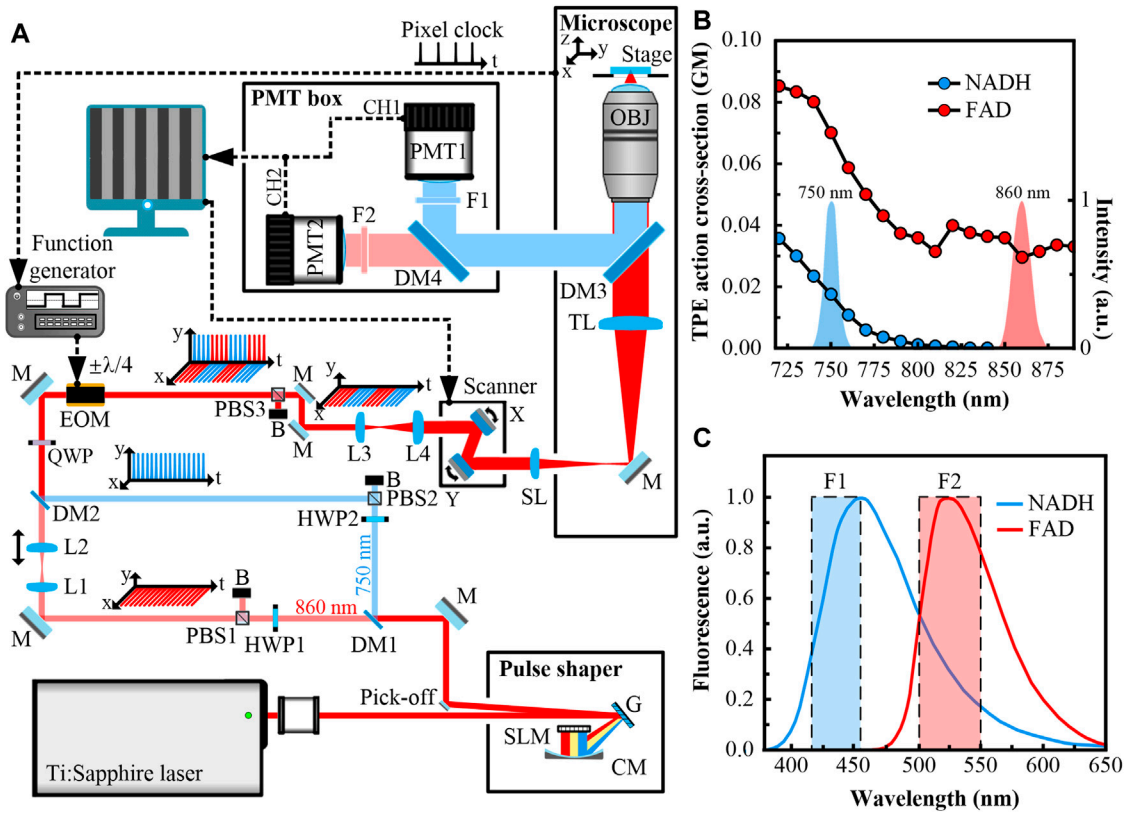

FIGURE 1 | (A) Experimental setup of the simultaneous two-photon fluorescence (TPF) microscopy of NADH and FAD. The laser beams are mainly shown in red, except that the 750-nm beam is shown in blue. Signals collected by CH1 are indicated in blue, and those collected by CH2 are indicated in red. The electrical paths are depicted in dashed black lines. HWP1, HWP2, half-wave plates; SLM, spatial light modulator; G, grating; CM, concave mirror; M, mirror; DM1, DM2, DM3, DM4, long pass dichroic mirrors; PBS1, PBS2, PBS3, polarizing beam splitters; B, blocker; L1, L2, L3, L4, lenses; QWP, quarter-wave plate; EOM, electro-optic modulator; SL, scan lens; TL, tube lens; OBJ, objective; F1, F2, bandpass filters; PMT1, PMT2, photomultiplier tubes. This figure is not to scale. **(B)** Spectra of shaped pulses overlaid with two-photon excitation (TPE) action cross-section spectra of reduced nicotinamide adenine dinucleotide (NADH) and flavin adenine dinucleotide (FAD). The cross-section is shown in GM unit (1 GM = 10^{-50} $cm^4 \cdot s \cdot photon^{-1} \cdot molecule^{-1}$). The spectra show that both substances can be excited at 750 nm, but only FAD can be excited at 860 nm. **(C)** The emission spectra of NADH and FAD. The filters are chosen to collect the emissions of NADH and FAD with minimum crosstalk.

focused by the scan lens, and delivered into a modified inverted microscope (IX71, Olympus, Japan). The scan lens, a tube lens (f_{TL} = 180 mm), and lenses L3 and L4 (AD406-B, AD408-B, LBTEK, China, f_{L3} = 50 mm, f_{L4} = 100 mm, placed before the scanner) expand the beams to fit the back-aperture of a 20× 1.00NA water immersion objective lens (XLUMPLFLN, Olympus, Japan). The scan lens and the tube lens constitute a 4*f* optical system, imaging the middle plane of the scanner to the entrance pupil of the objective. The objective collects and focuses the incoming beams into samples, which sit on a three-dimensional motorized stage.

Autofluorescence from samples is collected by the objective in the epi-direction, filtered from the fundamental beams by a long-pass dichroic mirror (DM3, FF660-Di02, Semrock, United States). Another long-pass dichroic mirror (DM4, FF470-Di01, Semrock, United States) is combined with two bandpass filters (F1, F2, FF02-435/40, FF03-525/50, Semrock, United States) to separate autofluorescence at different emission bands and minimize SBT (**Figure 1C**). Signals are detected by two channels (CH1, CH2), which are equipped with two photomultiplier tubes (PMT1, PMT2, R6357, Hamamatsu, Japan). The achieved wavelength ranges for CH1 and CH2 are 415–455 nm and 500–550 nm, respectively. As shown in **Figure 1C**, CH1 only collects autofluorescence from NADH, while CH2 collects autofluorescence from both NADH and FAD. However, using the excitation/detection combination of 860/500–550 nm ensures that only CH2 gains autofluorescence from FAD. Imaging software simultaneously drives the scanner and restores images from different detection channels with noises subtracted.

Meanwhile, the pixel clock from the microscope with a 4-μs period serves as the external trigger for the function generator (**Figure 2A**). The generated pulse train has an 8-μs period with a 50% duty cycle (**Figure 2B**). As mentioned above, the EOM is modulated by the function generator. Fine-tuning the time-delay of the modulation pulse train will ensure that only the 860- or 750-nm arm is turned on in each pixel time. This method is called pixel-to-pixel wavelength-switching. **Figure 2C** shows a stripe pattern image obtained by this method. The signal was derived from FAD in

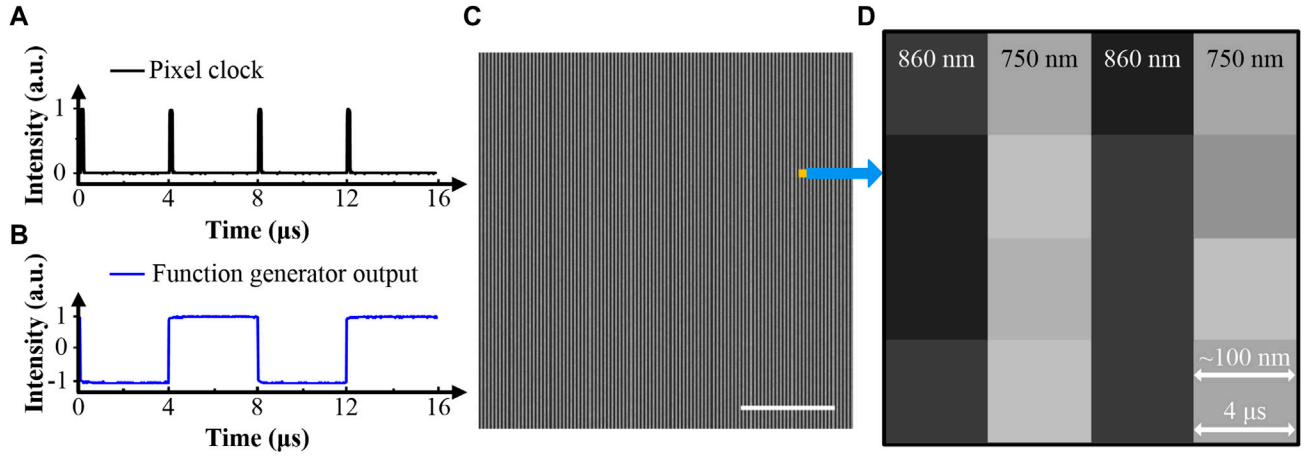

FIGURE 2 | (A) The pixel clock from the microscope. **(B)** The pulse train from the function generator. **(C)** Demonstration of TPF imaging using pixel-to-pixel wavelength-switching, 4 μs/pixel, 200×200 pixels. The stripe pattern image is acquired from FAD in a buffered solution. **(D)** Zoomed-in view of **(C)**, 4×4 pixels. Signals gained with different excitation wavelengths are displayed in different columns. The scale bar is 5 μm.

solution, and only CH2 was turned on. **Figure 2D** is a zoomed-in view of **Figure 2C**. It shows the odd columns corresponding to the 860-nm excitation appear dark, and the even columns corresponding to the 750-nm excitation are bright. The results are consistent with the cross-section spectrum of FAD shown in **Figure 1B**. The stability of the imaging system is mainly determined by the performance of pixel-to-pixel wavelength-switching. Recording the contrast between bright and dark columns in stripe pattern images provides a direct way to evaluate the system stability. We acquired three stacks of stripe pattern images from the FAD solution. During the acquisition of a stack, the excitation beams kept scanning the same region of interest (ROI). Five images were captured with 15-s intervals. The three stacks had 30-min intervals. The excitation beams were blocked between acquisitions of different stacks. These images show that the fluctuation of the contrast between bright and dark columns is within ±1%. The system is considered stable in both short- and long-term runs. Note that all electrical devices equipped in the setup are commercially available. Wiring can be operated by researchers without plentiful knowledge of electrical engineering.

RESULTS AND DISCUSSION

We first demonstrate the capability of the imaging system in NADH and FAD solutions. The NADH and FAD solutions used in the experiments had the same concentrations. Both CH1 and CH2 were turned on. **Figure 3A** shows the TPF images of NADH and FAD solutions, corresponding to different excitation/detection combinations. When imaging the NADH solution, both CH1 (415–455 nm) and CH2 (500–550 nm) channels can gain signal with 750-nm excitation, but all pixels appear dark in images acquired with 860-nm excitation. **Figure 3B** depicts the average intensities of these images, which are consistent with the cross-section spectrum of NADH (**Figure 1B**). Note that all four images of NADH were simultaneously acquired because of the utilization of pixel-to-pixel wavelength-switching. When imaging the FAD solution, CH2 can gain signal at both excitation wavelengths, but pixels appear dark in images obtained in CH1. **Figure 3C** shows the average intensities of these images. The results show that the bandpass filter of CH1 can effectively avoid SBT from CH2. Note that all four images of FAD were simultaneously acquired. If a mixture of both NADH and FAD is applied as the specimen, the excitation/detection combination of 750/500–550 nm is not suitable for imaging NADH or FAD anymore, because of severe SBT. The final excitation/detection combinations for NADH and FAD are as follows.

- NADH: 750/415–455 nm (excitation/detection), marked by * in **Figure 3A.**
- FAD: 860/500–550 nm (excitation/detection), marked by † in **Figure 3A.**

The capability of the imaging system is then demonstrated by using freshly excised mouse colon tissues. The mouse was sacrificed by applying cervical dislocation. The colon was removed immediately, and a segment was obtained. The segment was dissected longitudinally and kept in chilled phosphate-buffered saline until imaging. The animal study was reviewed and approved by the Institutional Animal Care and Use Committee of Hebei University of Technology.

The murine gastrointestinal tract, along the proximal-distal axis, comprises the mouth, esophagus, stomach, small intestine, large intestine (including the cecum, colon, and rectum), and anus. The primary functions of the stomach along with the small intestine are enzymatic digestion and absorption of nutrients [12]. The cecum occupies a large proportion of the murine abdominal cavity. It ferments digesta and produces vitamins and fatty acids by bacteria [13]. The colon can be further divided into the proximal colon, mid colon, and distal colon. It is mainly responsible for reabsorbing electrolytes and dehydrating. The stool from the colon will be pushed out of the body through the rectum and anus [14]. The colonic wall

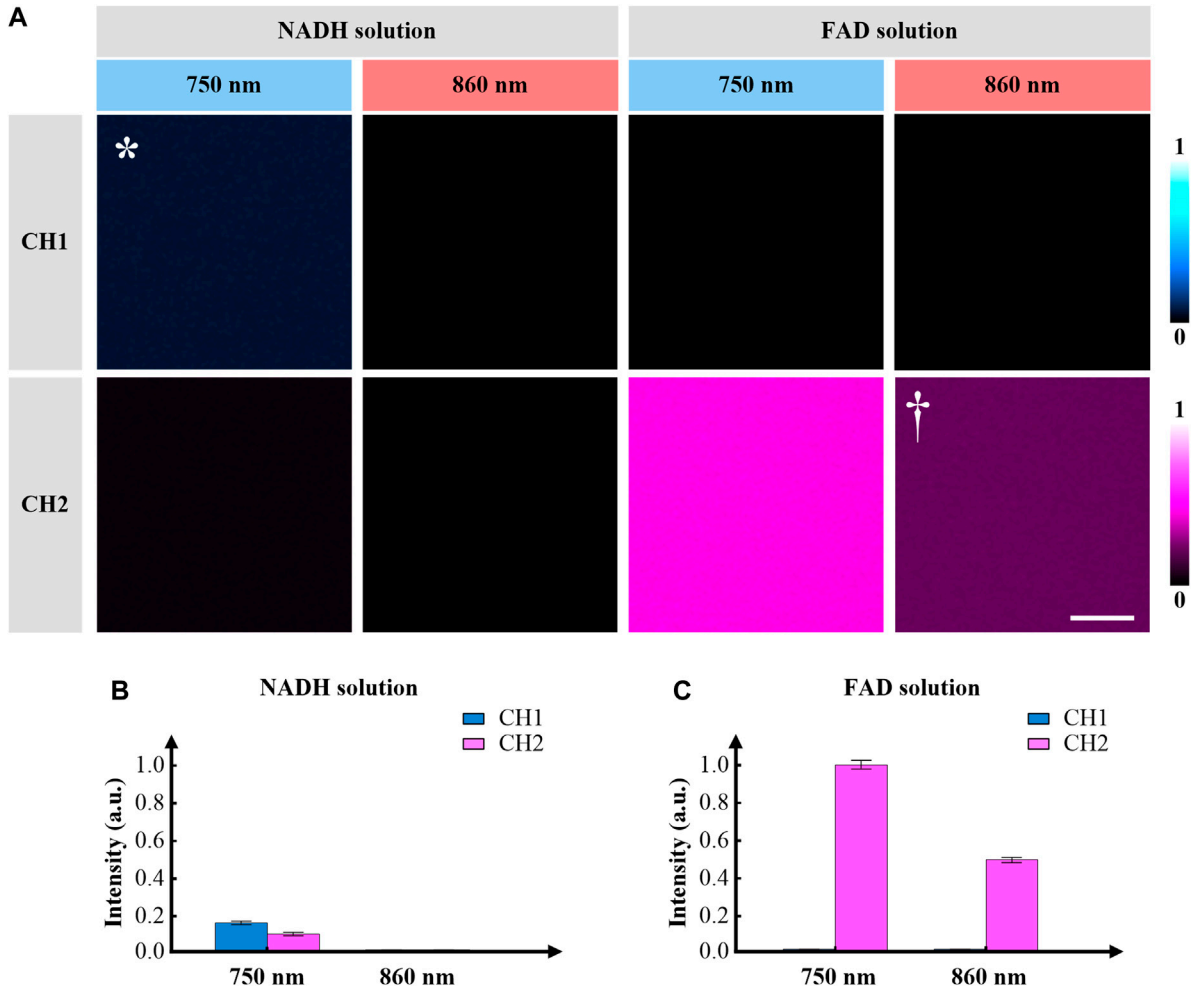

FIGURE 3 | (A) Representative TPF images of NADH and FAD solutions using pixel-to-pixel wavelength-switching, equivalent 8 μs/pixel, 100×100 pixels. The solutions are excited at 750 and 860 nm, and the signals are collected at the wavelength ranges of 415–455 nm (CH1) and 500–550 nm (CH2). The excitation/detection combinations of 750/415–455 nm and 860/500–550 nm are used to collect TPF images of NADH (marked by *) and FAD (marked by †), respectively. **(B)** Fluorescence intensities of different excitation/detection combinations, when imaging the NADH solution. **(C)** Fluorescence intensities of different excitation/detection combinations, when imaging the FAD solution. Error bars represent standard error. The scale bar is 5 μm.

consists of four tissue layers, which are the mucosa, submucosa, muscular tunic, and serosa [15]. The mucosa consists of closely packed crypts of Lieberkühn and intercryptal epithelial surfaces. The predominant cells in the mucosa are columnar absorptive colonocytes and mucus-secreting goblet cells. Investigations into colonic diseases, e.g., inflammatory and cancer, can be performed by analyzing autofluorescence derived from NADH and FAD in the cytoplasm of these cells.

Figure 4 shows the simultaneously acquired TPF images of NADH and FAD into mouse colonic mucosa. The pixel time was adjusted to improve signal level. **Figure 4A** is an autofluorescence image of NADH, which shows that the colonic mucosa comprises a prominent population of colonocytes (identified by the fluorescent cytoplasm) and the crypts of Lieberkühn. The cells indicated by the white arrows are probably goblet cells, whose mucus is usually nonfluorescent. The white oval marks a crypt of Lieberkühn. The image confirms that the system reveals the microenvironment of the mouse colonic mucosa. **Figure 4B** is an autofluorescence image of FAD in the same ROI. **Figures 4A,B** were obtained simultaneously at the depth of 15 μm. According to the similar morphological features and boundaries shown in **Figures 4A,B**, the axial displacement between the 750- and 860-nm arms, which originated from chromatic aberration, was negligible. **Figures 4C,D** are autofluorescence images of NADH and FAD simultaneously obtained at the depth of 20 μm. In **Figures 4A,C,** the white ovals outline the same crypt, and the white arrows denote the same cells (probably goblet cells). It indicates that the focal plane moves in the axial direction without tilt.

It is known that the autofluorescence intensity is proportional to the concentration of substances [16]. In our experiment, NADH has a smaller cross-section than FAD, but the fluorescence is stronger in NADH images (**Figure 4**). We consider that FAD in mouse colonic mucosa is relatively sparse comparing with NADH, which is consistent with

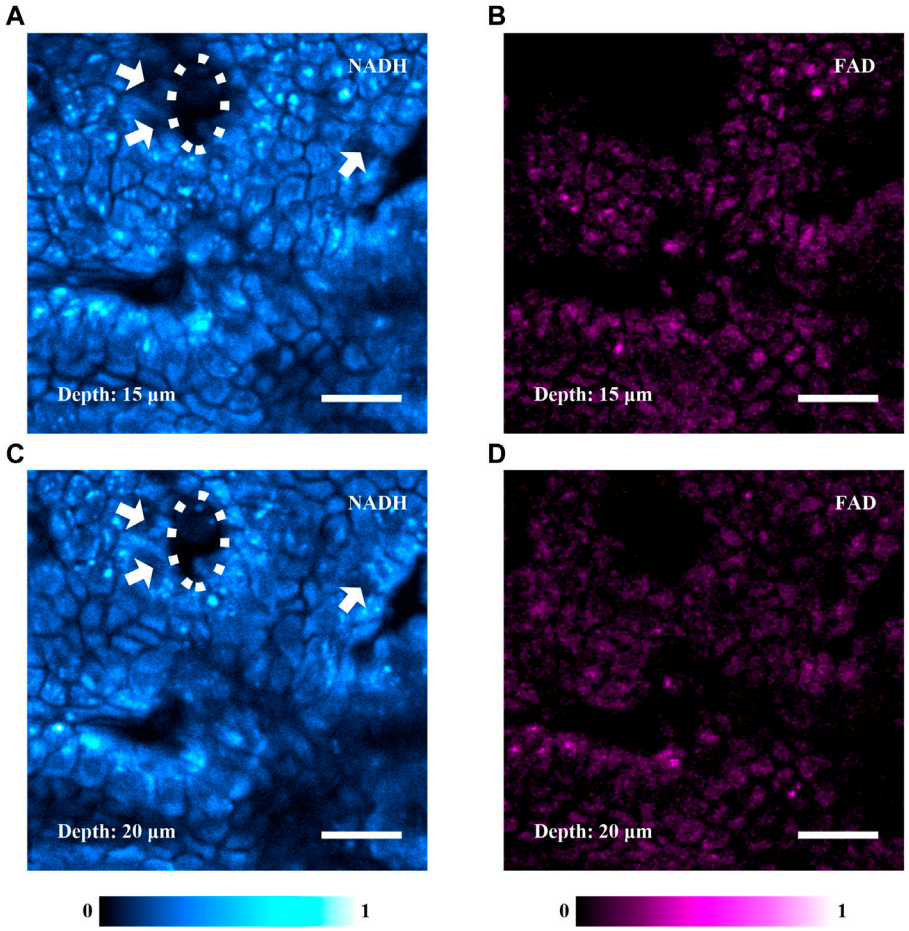

FIGURE 4 | Simultaneously acquired TPF images of NADH and FAD in mouse colonic mucosa, equivalent 20 μs/pixel, 512×512 pixels. **(A)** A TPF image of NADH acquired at the depth of 15 μm into the colonic mucosa. It shows that the colonic mucosa predominantly comprises colonocytes and crypts of Lieberkühn. The white arrows indicate a few cells, which are probably goblet cells. The white oval denotes a crypt. **(B)** A TPF image of FAD simultaneously acquired at the same region of **(A)** in the colonic mucosa. **(C,D)** TPF images of NADH and FAD simultaneously acquired at the depth of 20 μm. The white arrows in **(C)** indicate the same cells in **(A)**. The white oval in **(C)** denotes the same crypt in **(A)**. The scale bars are 20 μm.

previously published data [17, 18]. The experimental results show that the system can effectively perform simultaneous imaging of NADH and FAD, and metabolism-related quantitative analysis may be carried out with sufficient prior knowledge of tissues. Adding photon-counting modules will enable the imaging system to perform two-photon fluorescence lifetime imaging microscopy (FLIM) for studying complicated pathological processes.

Although the pixel size is set to ~100 nm in the experiments, different values can be selected upon the intensity point spread function (IPSF), which describes the spatial intensity near the focus. Since the intensity of TPF is proportional to the square of the excitation intensity, $IPSF^2$ can define the optical resolution. According to the $IPSF^2$ formulas in [1], the lateral resolutions of our system are theoretically 290 and 330 nm with 750- and 860-nm excitations, respectively. With pixel sizes smaller than 145 nm, two adjacent pixels will fall in the same resolution volume in the focal plane, ensuring high imaging performance. In practice, it's usual to find that lateral resolution may reduce to >600 nm with similar configurations [2]. Thus, a pixel size up to 300 nm will still be able to avoid mismatches between NADH and FAD images.

CONCLUSION

Simultaneous TPF microscopy of NADH and FAD is achieved by using pixel-to-pixel wavelength-switching. It provides negligible SBT and high excitation efficiency using simultaneous excitations of NADH and FAD, without the need to modify commercial microscopes. What's more, comprehensive knowledge in the field of electrical engineering is not necessary to set up the imaging system. Autofluorescence images of mouse colonic mucosa reveal the distributions and the relative concentrations of NADH and FAD, which provides a promising tool for investigations into metabolism-associated diseases in excised tissues. Note that the excitation intensities of NADH and FAD can be controlled independently with each other. Even though FAD is sparse in some tissues, its signal

level can still be comparable with that of NADH by properly increasing the average power of the 860-nm arm. Although only *in vitro* experiments are demonstrated, the imaging system has the potential to perform *in vivo* investigations. The frame rate is restricted to the order of seconds by using a galvanometer-scanner [19], which seems inadaptable for many *in vivo* applications [20]. However, the size of an ROI (e.g., accumulation of mitochondria) is usually around 10×10 pixels in a standard image of 512×512 pixels. By using pixel-to-pixel wavelength-switching, the acquisition time to obtain simultaneous local images of NADH and FAD in an ROI is on the order of one hundred microseconds, which is sufficiently short to track cellular dynamics of *in vivo* metabolic activity without image blur.

DATA AVAILABILITY STATEMENT

The original contributions presented in the study are included in the article/Supplementary Material, further inquiries can be directed to the corresponding authors.

ETHICS STATEMENT

The animal study was reviewed and approved by the Institutional Animal Care and Use Committee of Hebei University of Technology.

AUTHOR CONTRIBUTIONS

Conception, YQ and YX; investigation, YQ; design, YQ; software, YQ; data acquisition, YQ; analysis, YQ; original draft, YQ; review and editing, YQ, YX; supervision, YX; project administration, YX; funding acquisition, YX. All authors approved the submitted version.

FUNDING

This research was funded by the National Natural Science Foundation of China, grant numbers 61975050, 61675057.

REFERENCES

1. Zipfel WR, Williams RM, Webb WW. Nonlinear magic: multiphoton microscopy in the biosciences. *Nat Biotechnol* (2003) 21:1369–77. doi:10.1038/nbt899
2. Lefort C. A review of biomedical multiphoton microscopy and its laser sources. *J Phys D Appl Phys* (2017) 50:423001. doi:10.1088/1361-6463/aa8050
3. Denk W, Strickler JH, Webb WW. Two-photon laser scanning fluorescence microscopy. *Science* (1990) 248:73–76. doi:10.1126/science.2321027
4. Heikal AA. Intracellular coenzymes as natural biomarkers for metabolic activities and mitochondrial anomalies. *Biomark. Med* (2010) 4:241–263. doi:10.2217/BMM.10.1
5. Skala MC, Riching KM, Gendron-Fitzpatrick A, Eickhoff J, Eliceiri KW, White JG., et al. *In vivo* multiphoton microscopy of NADH and FAD redox states, fluorescence lifetimes, and cellular morphology in precancerous epithelia. *Proc Natl Acad Sci USA* (2007) 104:19494–9. doi:10.1073/pnas.0708425104
6. Quinn KP, Bellas E, Fourligas N, Lee K, Kaplan DL, Georgakoudi I. Characterization of metabolic changes associated with the functional development of 3D engineered tissues by non-invasive, dynamic measurement of individual cell redox ratios. *Biomaterials* (2012) 33:5341–8. doi:10.1016/j.biomaterials.2012.04.024
7. Varone A, Xylas J, Quinn KP, Pouli D, Sridharan G, McLaughlin-Drubin ME., et al. Endogenous two-photon fluorescence imaging elucidates metabolic changes related to enhanced glycolysis and glutamine consumption in precancerous epithelial tissues. *Cancer Res* (2014) 74:3067–75. doi:10.1158/0008-5472.can-13-2713
8. Huang S, Heikal AA, Webb WW. Two-photon fluorescence spectroscopy and microscopy of NAD(P)H and flavoprotein. *Biophys J* (2002) 82:2811–25. doi:10.1016/s0006-3495(02)75621-x
9. Wang S, Qin Y, Guo M, Zhang S, Xia Y. High speed 3D two-photon fluorescence microscopy by femtosecond laser pulses. *Proc. SPIE* (2017) 10605:106053J. doi:10.1117/12.2295704
10. Qin Y, Chen D, Xia Y. Real-time multidepth multiphoton microscopy using pixel-to-pixel focus-switching. *Appl Sci* (2020) 10:7173. doi:10.3390/app10207173
11. Filippi A, Dal Sasso E, Iop L, Armani A, Gintoli M, Sandri M., et al. Multimodal label-free *ex vivo* imaging using a dual-wavelength microscope with axial chromatic aberration compensation. *J Biomed Opt* (2018) 23:1–9. doi:10.1117/1.jbo.23.9.091403
12. Nishiyama K, Sugiyama M, Mukai T. Adhesion properties of lactic acid bacteria on intestinal mucin. *Microorganisms* (2016) 4:34. doi:10.3390/microorganisms4030034
13. Williams JM, Duckworth CA, Vowell K, Burkitt MD, Pritchard DM. Intestinal preparation techniques for histological analysis in the mouse. *Curr Protoc Mouse Biol* (2016) 6:148–68. doi:10.1002/cpmo.2
14. Nguyen TL, Vieira-Silva S, Liston A, Raes J. How informative is the mouse for human gut microbiota research? *Dis Model Mech* (2015) 8:1–16. doi:10.1242/dmm.017400
15. Hugenholtz F, de Vos WM. Mouse models for human intestinal microbiota research: a critical evaluation. *Cell Mol Life Sci* (2018) 75:149–60. doi:10.1007/s00018-017-2693-8
16. Qin Y, Li Q, Xia Y, Liu B, Zhang S. Construction and application of femtosecond laser two-photon fluorescence microscopy system. *J Harbin Inst Technol* (2015) 47:1–5. doi:10.11918/j.issn.0367-6234.2015.11.001
17. Ma N, Digman MA, Malacrida L, Gratton E. Measurements of absolute concentrations of NADH in cells using the phasor FLIM method. *Biomed Opt Express* (2016) 7:2441–52. doi:10.1364/boe.7.002441
18. Kimata S, Mochizuki D, Satoh J, Kitano K, Kanesaki Y, Takeda K., et al. Intracellular free flavin and its associated enzymes participate in oxygen and iron metabolism in *Amphibacillus xylanus* lacking a respiratory chain. *FEBS Open Bio* (2018) 8:947–61. doi:10.1002/2211-5463.12425
19. Deng Y, Qin Y, Zhang Z, Zhang Z, Xia Y. Simultaneous label-free two-photon fluorescence and second-harmonic generation microscopy for visualization of mouse pulmonary alveoli. *Proc SPIE* (2020) 11549:1154916. doi:10.1117/12.2573614
20. Goto A, Otomo K, Nemoto T. Real-time polarization-resolved imaging of living tissues based on two-photon excitation spinning-disk confocal microscopy. *Front Phys* (2019) 7:56. doi:10.3389/fphy.2019.00056

Conflict of Interest: The authors declare that the research was conducted in the absence of any commercial or financial relationships that could be construed as a potential conflict of interest.

frontiers in Physics

BRIEF RESEARCH REPORT
published: 11 March 2021
doi: 10.3389/fphy.2021.647281

Influence of Detector Size and Positioning on Near-Infrared Measurements and Iso-pathlength Point of Turbid Materials

*Hamootal Duadi, Idit Feder and Dror Fixler**

Faculty of Engineering and the Institute of Nanotechnology and Advanced Materials, Bar Ilan University, Ramat Gan, Israel

Measuring physical phenomena in an experimental system is commonly limited by the detector. When dealing with spatially defined behaviors, the critical parameter is the detector size. In this work, we examine near-infrared (NIR) measurements of turbid media using different size detectors at different positions. We examine cylindrical and semi-infinite scattering samples and measure their intensity distribution. An apparent crossing point between samples with different scatterings was previously discovered and named the iso-pathlength point (IPL). Monte Carlo simulations show the expected changes due to an increase in detector size or similarly as the detector's location is distanced from the turbid element. First, the simulations show that the intensity profile changes, as well as the apparent IPL. Next, we show the average optical pathlength, and as a result, the differential pathlength factor, are mostly influenced by the detector size in the range close to the source. Experimental measurements using different size detectors at different locations validate the influence of these parameters on the intensity profiles and apparent IPL point. These findings must be considered when assessing optical parameters based on multiple scattering models. In cases such as NIR assessment of tissue oxygenation, size and location may cause false results for absorption or optical path.

Keywords: Monte Carlo simulations, near-infrared measurements, turbid media, scattering measurements, light-tissue interactions

OPEN ACCESS

Edited by:
Vicente Micó,
University of Valencia, Spain

Reviewed by:
Kaikai Xu,
University of Electronic Science and Technology of China, China
Abraham Hirshberg,
Tel Aviv University, Israel

****Correspondence:***
Dror Fixler
Dror.Fixler@biu.ac.il

Specialty section:
This article was submitted to Optics and Photonics, a section of the journal Frontiers in Physics

Received: *29 December 2020*
Accepted: *18 January 2021*
Published: *11 March 2021*

Citation:
Duadi H, Feder I and Fixler D (2021) Influence of Detector Size and Positioning on Near-Infrared Measurements and Iso-pathlength Point of Turbid Materials. Front. Phys. 9:647281. doi: 10.3389/fphy.2021.647281

INTRODUCTION

Visible and near-infrared (NIR) light are commonly used to non-invasively study diffusive media, such as biological tissues [1, 2], wood [3], fruit [4], and more. The interaction of NIR light with human tissue allows the assessment of hemodynamics and oxidative metabolism for diagnosis purposes [5]. Quantitatively finding the relative concentration of chromophores within the tissue requires an estimation of the optical properties, namely the absorption coefficient (μ_a) and reduced scattering coefficient (μ_s'). This is achieved by studying the diffusion profile compared to physical models derived from the radiative transfer theory under the diffusion approximation [6]. However, these solutions are inaccurate close to the light source [7, 8]. Alternatively, Monte Carlo (MC) simulations model photon migration and predict diffusion profiles as a function of geometry and components [9].

Even though it is possible to estimate the optical properties in ideal systems, non-idealities in real measurement systems can cause variations [10–12]. From a theoretical standpoint, the accuracy of the measurement system depends strongly, but not solely, on how well the solution of the theoretical

problem fits the experimental setup. Hence, curve-shape fitting methods mostly rely on calibration by phantoms with known optical properties to improve accuracy [5, 13]. However, while solving the practical problem, efforts still need to be made to understand the differences between theoretical and practical systems [14, 15].

During the last decade, many technological advancements for sources and detectors have been achieved [14, 16–18]. The signal to noise ratio is maximized by either increasing the detector size or positioning the detector close to the light source, since the maximal laser power is defined by the safety limits for skin. Further understanding of the influence of detector size and positioning when measuring diffused light could bridge the gap between theory and practice.

In this work, we test the influence of these parameters in NIR measurements. Specifically, we examine the change in the scattered light profile of cylindrical and semi-infinite scattering media. Previously we have demonstrated theoretically [19], numerically [20], and experimentally, first by phantoms [21] and then in human fingers [22], a unique optical phenomenon. This is the existence of an angle with minimal impact of the reduced scattering coefficient, named the iso-pathlength (IPL) point, dependent only on geometry. It also exists in semi-infinite geometry, more relevant in clinical applications of NIR spectroscopy on the head, arm, leg, etc. [23]. This phenomenon was demonstrated in a range of scatterings that fulfills the multiple scattering condition [24]. We have also shown that even though anisotropy also varies between different tissues, it does not change the IPL point [20]. Furthermore, absorption does not change the position of this point; it only attenuates the intensity [24]. It is therefore the optimal point for absorption measurements since it minimizes changes in optical pathlength [25]. Despite the fact that theoretical and numerical simulations are highly agreed, a consistent difference exists over experimental results [19]. This study explains this difference by examining experimental detector conditions and exploring the influence of the detector's size or equivalent position on three measurables: the angular intensity distribution, i.e. full scattering profile (FSP); the IPL point; and the optical pathlength (OPL).

METHODS

Monte Carlo Simulations

First, MC simulations are used to find the influence of detector size on the intensity profile and OPL. The medium is characterized by the reduced scattering coefficient and anisotropy factor *g*. All photons enter the medium at ($Z = -D/2$, $X = 0$), and change their direction after a distance of dr according to the scattering coefficient with a probability of $1-\exp(-\mu_s' \, \mathrm{dr})$. If the photon was scattered, its direction is varied by an angle of arccos(g) in either the polar or azimuthal angle. Once the photon reencounters the air-tissue interface, it exits the tissue. This MC simulation was previously validated by diffusion theory [19] and experimental results [26]. Our first MC simulation defines the air-tissue interface by a circle equation with a diameter D centered on the XZ surface, while Y is the longitudinal axis of the cylinder (**Figure 1A**). Photons accumulate in the FSP, which is the angular intensity distribution. In this study, the FSPs were collected with an angular accuracy $d\theta = 2^{\circ}$ and from a 1 mm thick slice in the *Y* axis. The number of steps it took for the photon to exit the cylinder was then used to calculate the OPL. MC simulations for varying cylinder tissue diameter D (between 6 and 14 mm) of different scatterings ($\mu_s' = 10$, 16 and 26 cm^{-1}) were carried out for different detector sizes. Taking into account these different diameters, we decided to set the maximum angular accuracy to 2° and look at detector sizes between one to 20 times larger than the length defined by this angular accuracy.

We then simulated a scenario where the collection of photons takes place some distance from the air-tissue interface since this also effectively increases the detection area. Since most tissues are a half-infinite medium, we also carried out simulations of this kind. Each simulation launched 2^{18} photons, and for simplicity, there was no absorption ($\mu_a = 0$).

Experimental Setup

To validate our findings, an experimental system for FSP measurements was established [21]. A continuous wave (CW) He-Ne laser with a wavelength of 632.8 nm, and 0.8 mW power (Thorlabs, Japan) was used as an input source. A rail was placed on a rotation stage and a post was mounted on a rail carrier to allow adjustments of the distance between the sample and the detector. Different detectors were placed on the post holder. Samples were aligned to the center of the rotation stage and measured in two ways. First, a silicon photodetector (PD, SM05PD2B, Thorlabs), with an active area of 13 mm^2, was placed close to the sample (not touching). Next, a multimode fiber, with a core diameter of 1.5 mm (M107L02, Thorlabs) was placed on the post at a similar distance.

The cylindrical samples were prepared from Intralipid (IL) in different concentrations as a scattering component and 1% agarose for solidification [27]. After heating the agarose, the IL was added and poured into glass cylindrical tubes with a diameter of 13 mm. The liquid was cooled under vacuum to avoid bubbles.

RESULTS

MC Study of the Influence on Intensity Profile

In the following results, the solid, dashed, and dotted lines of the intensity profiles correspond to reduced scattering coefficients of μ_s' = 10,16 and 26 cm^{-1}. First, we examined the influence of detector size (defined in **Figure 1A**). For example, two selected diameters, 10 mm (**Figure 1B**) and 12 mm (**Figure 1C**), show a loss in accuracy. A small detector (black lines in **Figures 1B,C**) shows different IPL points for each diameter (171°, for D = 10 mm, and 173° for D = 12 mm). However, when increasing the detector size by a factor of two or more, there is a change in the FSPs and the apparent IPL point seems the same. For example, when increasing the detector by a factor of eight (red lines in **Figures 1B,C**) the apparent IPL points for both diameters are identical (157° for both diameters) and shift to a lower angle

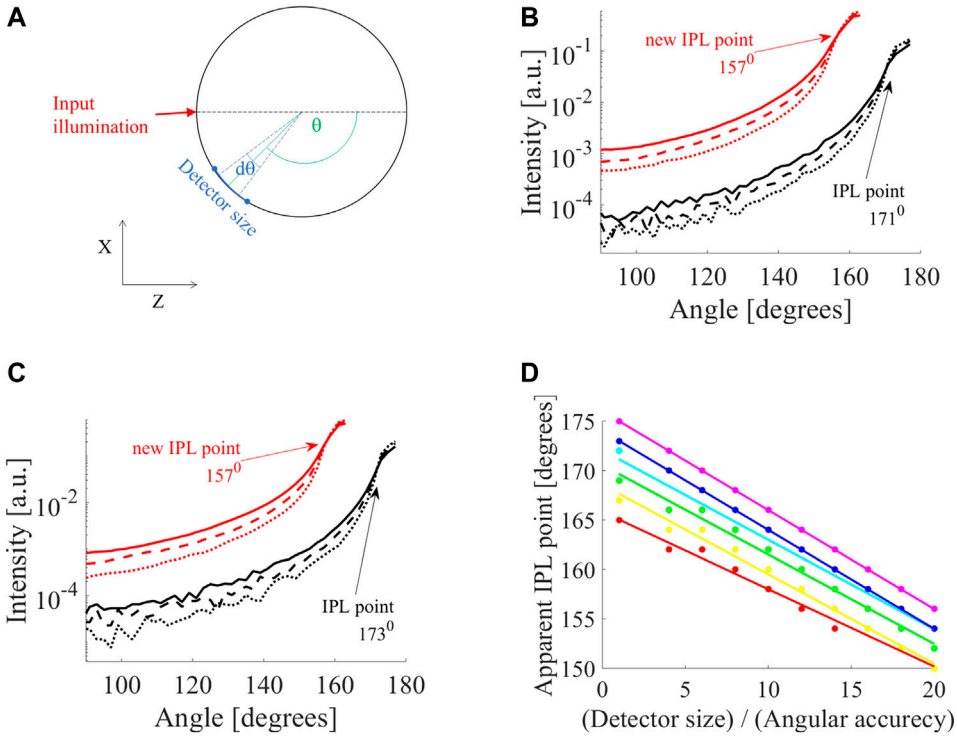

FIGURE 1 | Influence of detector on apparent iso-pathlength point (IPL) point. **(A)** MC simulation of cylinder tissue of different scatterings (μ_s' = 10, 16 and 26 cm^{-1} represented by solid, dashed and dotted lines). FSPs of cylinder diameter: **(B)** D = 10 mm and **(C)** D = 12 mm. Due to the large detector size, in both diameters, the IPL point looks as if it is at 157°. (red lines) compared to their original position (black lines: 171° for D=10 mm and 173° for D=12 mm) **(D)** Decrease in apparent IPL point as the detector size increases for different diameters (red, yellow, green, cyan, blue and violet lines correspond to a diameter of D = 6, 7, 8, 10, 12 and 14 mm).

(moving away from the light source). This emphasizes that this is not just an attenuation or linear shift, but rather a loss of spatial information and accuracy. To fully understand this, we looked at the change in apparent IPL point as the detector size increases for different diameters (D = 6,7,8,10,12 and 14 mm are red, yellow, green, cyan, blue and violet lines in **Figure 1D**). Each diameter presents a different slope of decrease so that as the detector size increases, the range of apparent IPL points decreases as well.

The influence of the location of the detector in respect to the air-tissue interface was also examined (**Figure 2A**). While moving away from the interface of an 8 mm diameter cylinder (**Figure 2B**) the IPL point moves from 168° (black lines) to 166° at a distance of 0.5 mm from the surface (blue lines), and 165° at a distance of 1 mm from the surface (red lines).

Since many clinical applications involve large tissue dimensions, MC simulations of a semi-infinite medium were examined (**Figure 2C**). As in the cylindrical geometry, the IPL point moves away from the source (**Figure 2D**). Given a step size of 30 μm, the IPL point measured for a 30 μm detector is r = 0.22 mm (black lines), compared to a 360 μm detector where the IPL point is at r = 0.28 mm (blue lines). The change in the apparent IPL point of the semi-infinite geometry (**Figure 2E**) has a similar linear behavior as the cylindrical geometry (**Figure 1D**). Note that a decrease in angle is an increase in distance from the light source (according to the definition of the angle in **Figure 1A**).

MC Study of the Influence on Optical Pathlength

Next, we looked at the change in OPL (**Figure 3A**) and consequently differential pathlength factor (DPF) (**Figure 3B**), defined as DPF = OPL/ (D sin (($\pi - \theta$)/2)). Note, that D sin ($\pi - \theta$)/2 is the length of the cord between the angle θ and the light source point of entry. As before, we see evidence of a significant change in OPL, and as a direct outcome DPF at the shorter distances (r) from the light source (corresponding to high angles), while the influence reduces in farther distances. The high sensitivity of NIR measurements in close range to the light source has been previously discussed [14, 28–30]. A summary of the simulated effect of shift and accuracy of IPL point, as well as change in DPF, is presented (**Figure 3C**). For example, an increase of factor four in detector size - will result in a 3° ± 1°, change in IPL point and a change of factor 0.87 in OPL and DPF.

Experimental Results

The experimental system (**Figure 4A**) was used to measure the FSPs of the different scatterings (solid squares, dashed circles, and

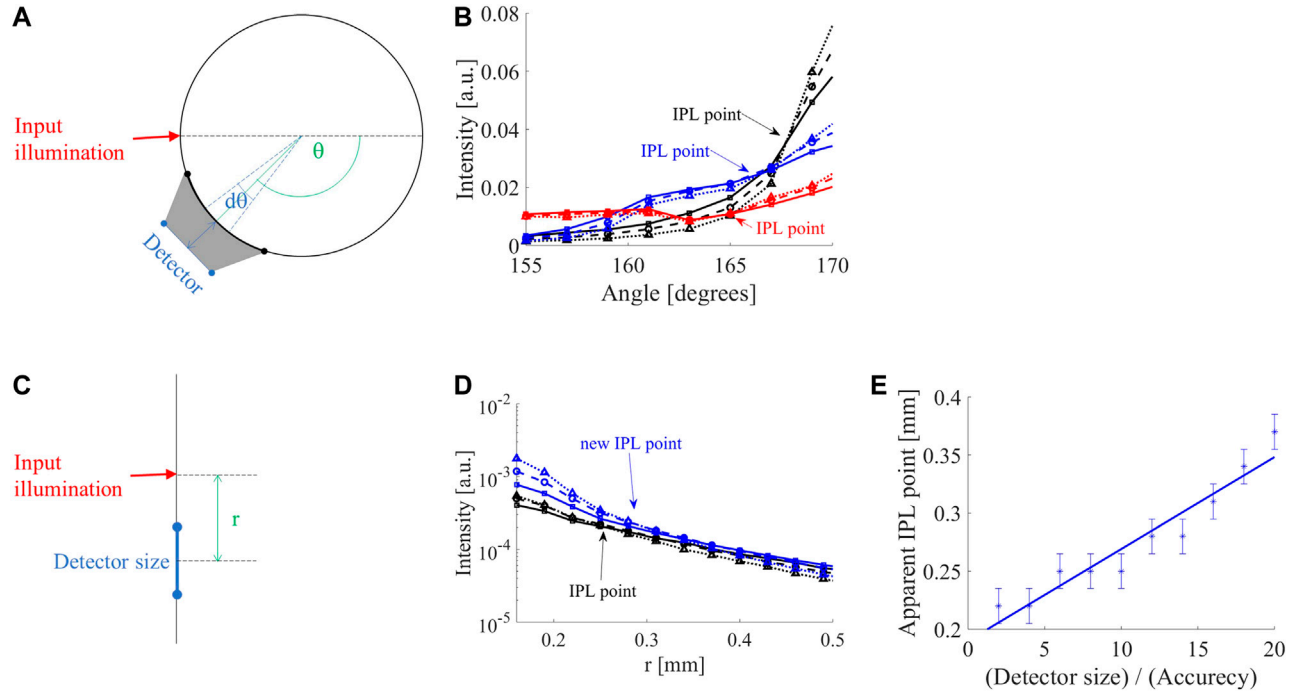

FIGURE 2 | Influence of detector position and size. **(A)** In case the detector is distant from the surface of a cylindrical sample, the detector collects from a larger angular range (gray area), hence the detector acts as if it was larger than its physical size. **(B)** FSPs of 8 mm diameter cylinder adjacent to the air-tissue interface (black lines) in comparison to 0.5 mm (blue lines) and 1 mm (red lines) away from the interface. The original iso-pathlength point (IPL) point of 168° (black lines) moves to 166° at a distance of 0.5 mm (blue lines) and 165° at a distance of 1 mm (red lines). **(C)** MC simulation of the semi-infinite geometry demonstrate a similar behavior of the intensity as a function of distance (*r*), i.e., diffusion reflection profile. **(D)** While increasing the detector size, the IPL point moves from its original location (0.22 mm) further away from the input; for a 12-fold increase in detector size, the new IPL is at 0.28 mm (blue lines). **(E)** The apparent IPL point linearly increases with the detector size in the semi-infinite case.

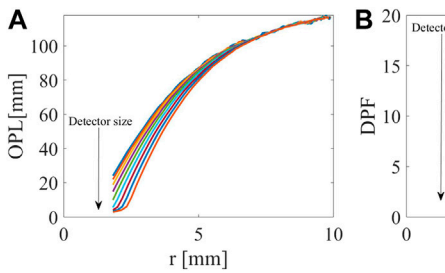

C

Factor of increasement in detector size	Shift in apparent IPL point	Angular accuracy	Corection factor of DPF @ r=2mm
4	3^0	$\pm1^0$	0.87
6	4^0	$\pm1^0$	0.81
8	6^0	$\pm1^0$	0.72
10	8^0	$\pm1^0$	0.61
12	10^0	$\pm1^0$	0.47
14	12^0	$\pm1^0$	0.32
16	13^0	$\pm2^0$	0.18
18	15^0	$\pm2^0$	0.13
20	17^0	$\pm2^0$	0.11

FIGURE 3 | Influence of detector on OPL and DPF. At the closer distances from the light source, related to the higher angles in the FSPs, **(A)** the OPL and **(B)** the PDF decrease as the detector size increases. **(C)** Table summarizing the influence of detector size on both IPL point and DPF.

dotted triangles in **Figure 4B** represent μ_s' = 10, 16, and 26°cm^{-1}). An IPL point appeared at 115° (blue lines) when a PD was used to collect photons from the sample. When using the fiber (black lines) at the same distance from the sample as the PD, the apparent IPL point was much closer to the laser input, at 160°. The higher angle is closer to the expected IPL point in the ideal theoretical case (~174°), since the fiber collects from a smaller angular range. However, since the fiber is not touching the surface, it is effectively acting as a larger detector (**Figure 2A**). The fiber was then moved on the rail so that it was further away from the sample surface (2 cm). The apparent IPL point, after moving the fiber (green lines in **Figure 4B**) was smaller (135° instead of 160°) than the previous position (black lines).

Let us consider the fiber from the experiment, which has a core diameter of 1.5 mm and a NA of 0.5. After moving the position of the fiber 2 cm away from its original position - the apparent IPL point moved 25°. Given the NA of the fiber (0.5 corresponds to an angle of 30°), a 2 cm distance translates to a factor of 4.85 of collected angular range compared to the core

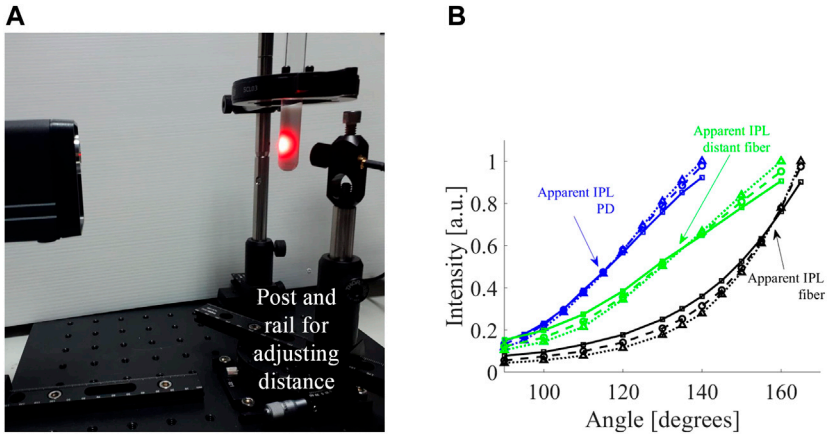

FIGURE 4 | Experimental measurement of influence of detector on apparent IPL point. **(A)** The optical system includes a rail placed on a rotation stage and a post was mounted on the rail carrier to allow adjustments of the distance between the sample and the detector. **(B)** The FSPs of cylindrical tissue mimicking phantoms with different scatterings ($\mu_s' = \mu_s\,(1-g)$ = 10, 16, and 26 cm^{-1} represented by solid squares, dashed circles, and dotted triangles). While using a fiber with a core of 1.5 mm (black lines) the IPL is at 160°, and when a larger photodetector (with an active area of 13 mm^2) is used (blue lines) the IPL point seems to be at 115°. The IPL point also moves further away from the input (from 160° to 135°) when the detector is distanced 2 cm from the phantom surface (green lines).

diameter. This translates to a factor of 24 increase in the detection area. The experimental data shows a shift of 25° ± 5°, which is consistent with the values from the simulation (Table in **Figure 3C**).

DISCUSSION

In this work, we examined the influence of the detector size and positioning on measurements of cylindrical and semi-infinite scattering samples. We performed a MC study of the averaging effect increasing the detector size compared to the angular accuracy in different cylinder diameters. The increased detection range changed the FSPs and shifted the apparent IPL point further away from the light source. This also occurred when moving the detector away from the surface of the media, since this similarly increases the collection area. The increase in the detector indicates a loss in angular or special resolution. Furthermore, we simulated the influence of detector size on apparent OPL. Since the OPL is directly related to the DPF, both demonstrated a similar behavior. At closer distances to the light source, r, the OPL, and DPF decreased with the increase in detector size. This type of behavior, of the higher sensitivity of experimental measurements of OPL in the close range from the light source, is supported by previous reports [14, 28–30]. To further validate these findings, we performed CW measurements of the FSPs of cylindrical scattering phantoms. First, we measured the same phantoms by two detectors: by a PD and using a fiber. Since these detectors have different geometries, the apparent IPL point shifted from a theoretical one according to size. While the PD is larger and hence has improved signal to noise ratio and dynamic range, the fiber presents an IPL closer to the theoretical one. Nonetheless, using the larger detector, while considering the influence it has on the diffused light seems optimal in our opinion, giving the best of all worlds. Note that in the MC simulations the detector size was increased in one axis only, hence the experimental change in detector size in two dimensions had a stronger effect. As simulated, for a similar reason, while using the same detector and moving it further away from the sample surface, the apparent IPL point shifted further from the light source.

CONCLUSION

The findings of this work help the transition of NIR methods from research to clinical settings. Clinical applications of photoplethysmography, NIR diffuse optical imaging, and spectroscopy are increasingly adopted in the medical community as multimodal imaging has become more popular in recent years [10, 11, 14]. However, the diversity of responses of different medical instruments and the need for calibration complicates their use. This study highlights factors that should be considered in such instruments to allow quantitative, reliable, and sensitive physiological measurements.

DATA AVAILABILITY STATEMENT

The original contributions presented in the study are included in the article, further inquiries can be directed to the corresponding author.

AUTHOR CONTRIBUTIONS

This research conceptualization was formed by DF and HD. DF was responsible for the project administration, funding acquisition and research supervision methodology. The software, investigation, and formal analysis were done by HD The experiments were performed by IF and final validation was conducted by HD. The writing of the original draft was performed by HD, and DF was responsible for the review and editing for improving the paper.

REFERENCES

1. Wang L, Ayaz H, Izzetoglu M, Onaral B. Evaluation of light detector surface area for functional Near Infrared Spectroscopy. *Comput Biol Med* (2017) 89:68–75. doi:10.1016/j.compbiomed.2017.07.019
2. Durduran T, Choe R, Baker WB, Yodh AG. Diffuse optics for tissue monitoring and tomography. *Rep Prog Phys* (2010) 73:076701. doi:10.1088/0034-4885/73/7/076701
3. Bargigia I, Nevin A, Farina A, Pifferi A, D'Andrea C, Karlsson M, et al. Diffuse optical techniques applied to wood characterization. *J Near Infrared Spectrosc* (2013) 21:259–68. doi:10.1255/jnirs.1068
4. Bellincontro A, Taticchi A, Servili M, Esposto S, Farinelli D, Mencarelli F. Feasible application of a portable NIR-AOTF tool for on-field prediction of phenolic compounds during the ripening of olives for oil production. *J Agric Food Chem* (2012) 60:2665–73. doi:10.1021/jf203925a
5. Re R, Pirovano I, Contini D, Spinelli L, Torricelli A. Time domain near infrared spectroscopy device for monitoring muscle oxidative metabolism: custom probe and *in vivo* applications. *Sensors* (2018) 18:264. doi:10.3390/s18010264
6. Cheong WF, Prahl SA, Welch AJ. A review of the optical properties of biological tissues. *IEEE J Quan Electron* (1990) 26:2166–85. doi:10.1109/3.64354
7. Piao D, Patel S. Simple empirical master–slave dual-source configuration within the diffusion approximation enhances modeling of spatially resolved diffuse reflectance at short-path and with low scattering from a semi-infinite homogeneous medium. *Appl Opt* (2017) 56:1447–52. doi:10.1364/AO.57.007942
8. Bhatt M, Ayyalasomayajula KR, Yalavarthy PK. Generalized Beer-Lambert model for near-infrared light propagation in thick biological tissues. *J Biomed Opt* (2016) 21:76012. doi:10.1117/1.JBO.21.7.076012
9. Wang L, Jacques SL, Zheng L. MCML--Monte Carlo modeling of light transport in multi-layered tissues. *Comput Methods Programs Biomed* (1995) 47:131–46. doi:10.1016/0169-2607(95)01640-f
10. Pirovano I, Re R, Candeo A, Contini D, Torricelli A, Spinelli L. Instrument response function acquisition in reflectance geometry for time-resolved diffuse optical measurements. *Biomed Opt Express* (2020) 11:240–50. doi:10.1364/BOE.380996
11. Cubeddu R, Pifferi A, Taroni P, Torricelli A, Valentini G. Experimental test of theoretical models for time-resolved reflectance. *Med Phys* (1996) 23:1625–33. doi:10.1118/1.597739
12. Pifferi A, Torricelli A, Bassi A, Taroni P, Cubeddu R, Wabnitz H, et al. Performance assessment of photon migration instruments: the MEDPHOT protocol. *Appl Opt* (2005) 44:2104–14. doi:10.1364/ao.44.002104
13. Wabnitz H, Taubert DR, Mazurenka M, Steinkellner O, Jelzow A, Macdonald R, et al. Performance assessment of time-domain optical brain imagers, part 1: basic instrumental performance protocol. *J Biomed Opt* (2014) 19:086010. doi:10.1117/1.JBO.19.8.086010
14. Behera A, Di Sieno L, Pifferi A, Martelli F, Mora A. Instrumental, optical and geometrical parameters affecting time-gated diffuse optical measurements: a systematic study. *Biomed Opt Express* (2018) 9:5524–42. doi:10.1364/BOE.9.005524
15. Ntziachristos V, Chance B. Accuracy limits in the determination of absolute optical properties using time-resolved NIR spectroscopy. *Med Phys* (2001) 28:1115–24. doi:10.1118/1.1373674
16. Ohlídal I, Franta D, Ohlídal M, Navrátil K. Optical characterization of nonabsorbing and weakly absorbing thin films with the wavelengths related to extrema in spectral reflectances. *Appl Opt* (2001) 40:5711–7. doi:10.1364/ao.40.005711
17. Xu K, Chen Y, Okhai TA, Snyman LW. Micro optical sensors based on avalanching silicon light-emitting devices monolithically integrated on chips. *Opt Mater Express* (2019) 9:3985–97. doi:10.1364/OME.9.003985
18. Xu K. Silicon MOS optoelectronic micro-nano structure based on reverse-biased PN junction. *Phys. Status Solidi A* (2019) 216:1800868. doi:10.1002/pssa.201800868
19. Duadi H, Piao D, Fixler D. Self calibration iso-pathlength point in cylindrical tissue geometry: solution of steady-state photon diffusion based on the extrapolated zero-boundary. *OSA Continuum* (2019) 2:92–8. doi:10.1364/OSAC.2.000092
20. Duadi H, Feder I, Fixler D. Linear dependency of full scattering profile isobaric point on tissue diameter. *J Biomed Opt* (2014) 19:026007. doi:10.1117/1.JBO.19.2.026007
21. Feder I, Duadi H, Fixler D. Experimental system for measuring the full scattering profile of circular phantoms. *Biomed Opt Express* (2015) 6:2877–86. doi:10.1364/BOE.6.002877
22. Duadi H, Feder I, Fixler D. Near-infrared human finger measurements based on self-calibration point: simulation and *in vivo* experiments. *J Biophotonics* (2018) 11:e201700208. doi:10.1002/jbio.201700208
23. Feder I, Duadi H, Chakraborty R, Fixler D. Self-calibration phenomenon for near-infrared clinical measurements: theory, simulation, and experiments. *ACS Omega* (2018) 3:2837–44. doi:10.1021/acsomega.8b00018
24. Duadi H, Fixler D. Influence of multiple scattering and absorption on the full scattering profile and the isobaric point in tissue. *J Biomed Opt* (2015) 20:56010. doi:10.1117/1.JBO.20.5.056010
25. Feder I, Duadi H, Fixler D. Single wavelength measurements of absorption coefficients based on iso-pathlength point. *Biomed Opt Express* (2020) 11:5760–71. doi:10.1364/BOE.401591
26. Ankri R, Duadi H, Motiei M, Fixler D. *In-vivo* tumor detection using diffusion reflection measurements of targeted gold nanorods - a quantitative study. *J Biophotonics* (2012a) 5:263–73. doi:10.1002/jbio.201100120
27. Ankri R, Duadi H, Motiei M, Fixler D. *In-vivo* Tumor detection using diffusion reflection measurements of targeted gold nanorods - a quantitative study. *J Biophotonics* (2012b) 5:263–73. doi:10.1002/jbio.201100120
28. Ultman JS, Piantadosi CA. Differential pathlength factor for diffuse photon scattering through tissue by a pulse-response method. *Math Biosci* (1991) 107:73–82. doi:10.1016/0025-5564(91)90072-q
29. Kohl M, Nolte C, Heekeren HR, Horst S, Scholz U, Obrig H, et al. Determination of the wavelength dependence of the differential pathlength factor from near-infrared pulse signals. *Phys Med Biol* (1998) 43:1771. doi:10.1088/0031-9155/43/6/028
30. Van der Zee P, Arridge S, Cope M, Delpy D. "The effect of optode positioning on optical pathlength in near infrared spectroscopy of brain," In: *Oxygen transport to tissue XII*. Vol. 277. Boston, MA: Springer (1990). p. 79–84.

Conflict of Interest: The authors declare that the research was conducted in the absence of any commercial or financial relationships that could be construed as a potential conflict of interest.

frontiers in Physics

BRIEF RESEARCH REPORT
published: 22 March 2021
doi: 10.3389/fphy.2021.639607

Single-Element Reflective Digital Holographic Microscopy

José Ángel Picazo-Bueno, Javier García and Vicente Micó*

Department of Optics and Optometry and Vision Sciences, University of Valencia, Burjassot, Spain

Digital holographic microscopy (DHM) is a well-known microscopy technique using an interferometric architecture for quantitative phase imaging (QPI) and it has been already implemented utilizing a large number of interferometers. Among them, single-element interferometers are of particular interest due to its simplicity, stability, and low cost. Here, we present an extremely simple common-path interferometric layout based on the use of a single one-dimensional diffraction grating for both illuminating the sample in reflection and generating the digital holograms. The technique, named single-element reflective digital holographic microscopy (SER-DHM), enables QPI and topography analysis of reflective/opaque objects using a single-shot operation principle. SER-DHM is experimentally validated involving different reflective samples.

OPEN ACCESS

Edited by:
Xinping Zhang,
Beijing University of Technology, China

Reviewed by:
Ana Doblas,
University of Memphis, United States
Randy Bartels,
Colorado State University, United States

****Correspondence:***
José Ángel Picazo-Bueno
j.angel.picazo@uv.es

Specialty section:
This article was submitted to Optics and Photonics, a section of the journal Frontiers in Physics

Received: *09 December 2020*
Accepted: *22 February 2021*
Published: *22 March 2021*

Citation:
Picazo-Bueno JÁ, García J and Micó V (2021) Single-Element Reflective Digital Holographic Microscopy. Front. Phys. 9:639607. doi: 10.3389/fphy.2021.639607

Keywords: digital holographic microscopy, quantitative phase imaging (QPI), interference microscopy, reflective microscopy, diffraction grating, phase measurememnt, nanometric topography

INTRODUCTION

Digital holographic microscopy (DHM) raises from the application of digital holography to microscopy. Thus, DHM merges high-quality imaging (microscopy), whole-object wavefront recovery (holography), and numerical processing capabilities (digital domain) [1–4]. In addition, DHM allows quantitative phase imaging (QPI) using a non-invasive, full-field, real-time, non-contact, and static working principle, at the same time that provides major advantages with respect to other microscopy techniques as the removal of the limited depth of focus in high NA lenses [5]. When DHM is implemented in a reflection modality, the phase delays of the light reflected or scattered by the sample are recovered. Those delays are directly related to the topography of the sample surface. The possibility of inspecting the topography of technical microscopic objects, which often are reflective or opaque, is of great significance in fields as important as science, technology, and industry.

In DHM, many different interferometric configurations have been implemented to work in reflection, such as modified Mach-Zehnder [6–9], Michelson [10–13], Linnik [14], Twyman-Green [15], Sagnac [16], and common-path interferometers [17–23], among others. Perhaps the modified Mach-Zehnder and Michelson interferometers are the most common used layouts. However, common-path interferometers (CPIs) enhance the performance in terms of robustness, simplicity, and stability. In CPIs, both imaging and reference beams pass through the same optical elements, thus minimizing both the required optical elements and the instabilities of the system (mechanical and thermal changes) allowing a more compact assembly. Inside CPIs category, we can find several types according to the way of generating the reference beam.

For instance, such a beam can be created: (1) by the reflection of the light in a reference mirror inside a Mirau interferometric objective [18]; (2) by a spatial filtering at the Fourier plane in diffraction phase microscopy [17, 19]; by using the clear regions near to sparse samples in lateral shearing interferometry [24–27], (3) by spatially-multiplexing the field of view (FOV) [23], or (4) by using a modulator mask in single pixel phase imaging [21, 22].

Among all CPIs described in the literature, there are some of them that employ just one optical element to produce interferences, such as a Lloyd's mirror [28], a thick glass plate [26], a diffraction grating [29], a beam splitter cube [30], or a Fresnel's biprism [31–34]. Those reduce even more the price and the complexity of CPIs and present a very simple usability. Nevertheless, all those single-element CPIs were mostly implemented in a transmission modality, being therefore limited to the analysis of transmissive/transparent objects.

In order to expand the applicability of such single-element interferometers to the obtention of the topography of reflective/opaque samples, this contribution reports on a reflective interferometric configuration based on a single one-dimensional (1D) diffraction grating. The grating is used to simultaneously illuminate the sample in reflection mode and defines a single-element CPI architecture. In this configuration, the reference beam is generated by spatially multiplexing the FOV at the input plane as spatially multiplexed interferometric microscopy (SMIM) does [23, 35–38]. The technique, named single-element reflective DHM (SER-DHM), is presented as an extremely simple, highly-stable, and robust way to provide topography analysis in reflecting surfaces with a nanometric accuracy and in a non-invasive manner. The main difference with previously reported reflective SMIM technique [23] is that, now, we are using a single element to provide both illumination and interferometric recording in the layout as well as the proposed implementation is validated outside a microscope embodiment.

The paper is organized as follows. Experimental setup describes the technique including the setup implemented for validation. Results includes three experimental validations of SER-DHM involving different reflective objects (negative USAF test target, silicon wafer, and Ronchi grating). And finally, Discussion and conclusions provides a discussion of the contribution and concludes the paper.

EXPERIMENTAL SETUP

The experimental setup of the proposed technique is depicted in **Figure 1**. The layout is a reflective CPI configuration assembled on an optical table at the lab. It utilizes a 1D diffraction grating for both illuminating the sample and producing interferences. For better understanding, we can divide the setup into illumination and interferometric/imaging arms.

The system is illuminated with a quasi-monochromatic point light source provided by a laser diode, whose wavefront curvature is properly modified by a focusing lens. Such a beam arrives to a 1D diffraction grating providing several beams diffracted at different directions according to the diffraction order. In such a way, we can take advantage of one of those diffraction orders to illuminate the sample in reflection after passing through the microscope lens (**Figure 1A**). Note that the focusing lens serves to focus the beam at the back focal plane of the objective in order to illuminate the sample with a collimated beam, thus optimizing the illuminated FOV at the input plane. It is also worthy to point out that the spatial frequency of the grating as well as the distance between such a grating and the microscope lens must be properly selected in order to have no additional diffraction orders passing through the objective lens. In that sense, Ronchi gratings are suitable for such a purpose since they present many odd orders that can be used for epi-illumination while their even orders have zero diffraction efficiency. Thus, in order to redirect the light toward the microscope lens, the illumination system must form an angle of incidence θ_i with respect to the optical axis of the objective, which is given by the diffraction grating equation,

$$sin\,(\theta_i) = sin\,(\theta_m) + m\,\lambda\,N \tag{1}$$

where N is the spatial frequency of the grating, λ is the wavelength of the light source, and m is the diffraction order. θ_m is therefore the diffracted beam corresponding with the m diffraction order. In our case, interferometric recording needs the diffraction orders at angles coming from $m = -1, 0, +1$, so that the illumination angle must be coupled with higher diffraction orders ($m = 3$ in our case) to avoid overlap with the imaging scheme. In addition, assuming a Ronchi grating (+2nd and +4th orders efficiency equal to 0) and paraxial approximation [$\tan(\theta) \approx \sin(\theta) \approx \theta$], only the +3rd order will pass through the microscope lens when the distance between the grating and the rear aperture of the objective d is higher than

$$d > \frac{r}{2\lambda N} \tag{2}$$

being r the radius of the rear aperture of the microscope lens.

On the other hand, the interferometric arm is very similar to the one implemented in the recently proposed SMIM technique [23, 35–38]. Briefly, the FOV is spatially multiplexed into two regions, object (O) and reference (R) regions, and the diffraction grating provides an interference pattern coming from the coherent overlapping of such regions, coming from the 0th and +1st orders, respectively, at the recording plane (**Figure 1B**). Thus, an off-axis hologram is recorded by the digital sensor. As we can see at **Figure 1B**, the size of the imaged FOV exceeds the dimensions of the digital sensor at the output plane. That situation is common in microscopy and can be used in our system to optimize the recording process, that is, to only record the useful interferogram. It would nevertheless be worthwhile to mention that different technical aspects such as the spatial frequency of the grating, the magnification of the system, the pixel size of the digital sensor, and the axial distances between the grating, the microscope lens and the digital sensor must be properly adjusted when implementing the technique [29, 39, 40].

The key element for the design of the system layout is the diffraction grating, since it provides illumination of the sample in reflection mode as well as it allows the off-axis holographic

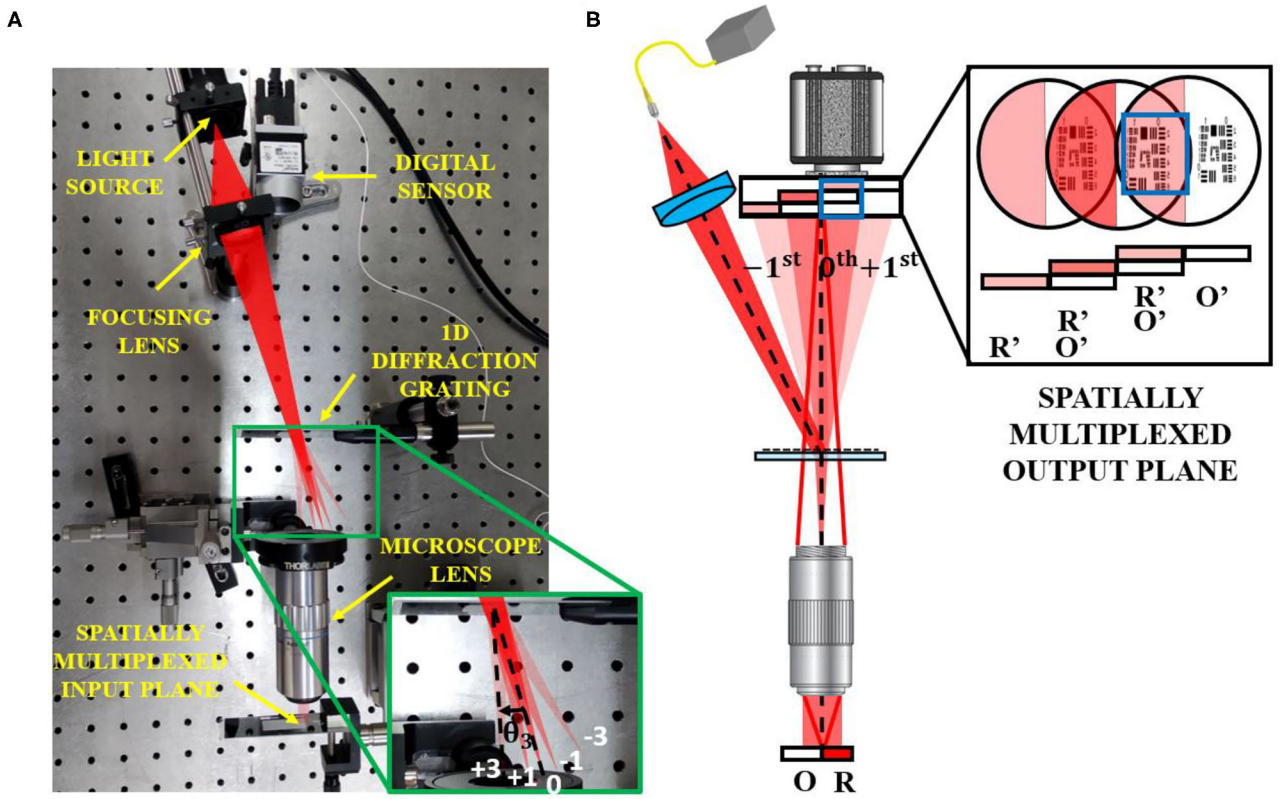

FIGURE 1 | SER-DHM layout. **(A)** Picture of the experimental setup where the illumination arm is highlighted, and the green rectangle magnifies the diffraction order's direction for clarity. **(B)** Optical scheme and ray tracing of both illumination and interferometric arms, including a frame with the output plane (black rectangle) and the recording region (blue rectangle) where the digital sensor is placed.

recording. Perhaps more important is the second issue to finally achieve a proper image reconstruction. Hence, in order to allow off-axis holographic recording and leaving aside aliasing problems, the angle between overlapping beams (R' and O') at the output plane should be high enough to allow separation of the diffraction orders of the digital hologram at the Fourier domain. Assuming a perfectly-coherent imaging system, the cutoff frequency defined in the image spectral domain is given by $f_c = \mathrm{NA}/\lambda\mathrm{M}$, being NA and M the numerical aperture and the magnification, respectively, of the imaging layout [41]. Since in our system θ corresponds to the propagation angle of the +1st diffraction order given by Equation (1), we can therefore deduce a minimum frequency $N_{\min}$ equal to 3 times such cutoff frequency:

$$N_{min} = \frac{3NA}{\lambda M} \tag{3}$$

In addition, there must be appropriate overlapping at the spatial domain between the FOV replicas provided by the diffraction grating to assure that the replicas are overlapping at FOV halves. Once the diffraction grating is properly selected, the shift between the different FOV replicas can be experimentally adjusted by displacing the camera in the axial direction, thus providing the needed shift to overlap FOV halves. This procedure will slightly modify the NA and M values of the imaging setup, but it will introduce minimal impact in the setup.

Regarding the reconstruction process, a Fourier filtering method is implemented in order to extract the complex amplitude information of the imaging beam (O') from the off-axis hologram. Briefly, this method can be summarized in the following steps: (1) Fourier transform of the off-axis hologram, (2) object spectrum filtering, (3) linear phase compensation, and (4) inverse Fourier transform [42].

RESULTS

The experimental validation of the proposed SER-DHM consists of three steps involving different reflective/opaque targets. In those experiments, we use red (R) illumination (638 nm) provided by a fiber-optic coupled laser diode source (OSI Laser Diode, TCW RGBS-400R) focused by a lens with a focal length of 60 mm. In addition, a 50X microscope lens (Mitutoyo Plan Apo, 0.55NA), a Ronchi ruling glass slides (120 lp/mm spatial frequency), and a complementary metal-oxide-semiconductor (CMOS) sensor (Basler acA1300-200uc, 1280 × 1024 px, 4.8 μm px size, 10 bits/px, 203 fps) are used to provide image plane off-axis digital holograms. We utilize the light coming from the +3rd diffraction order to illuminate the sample in reflection because

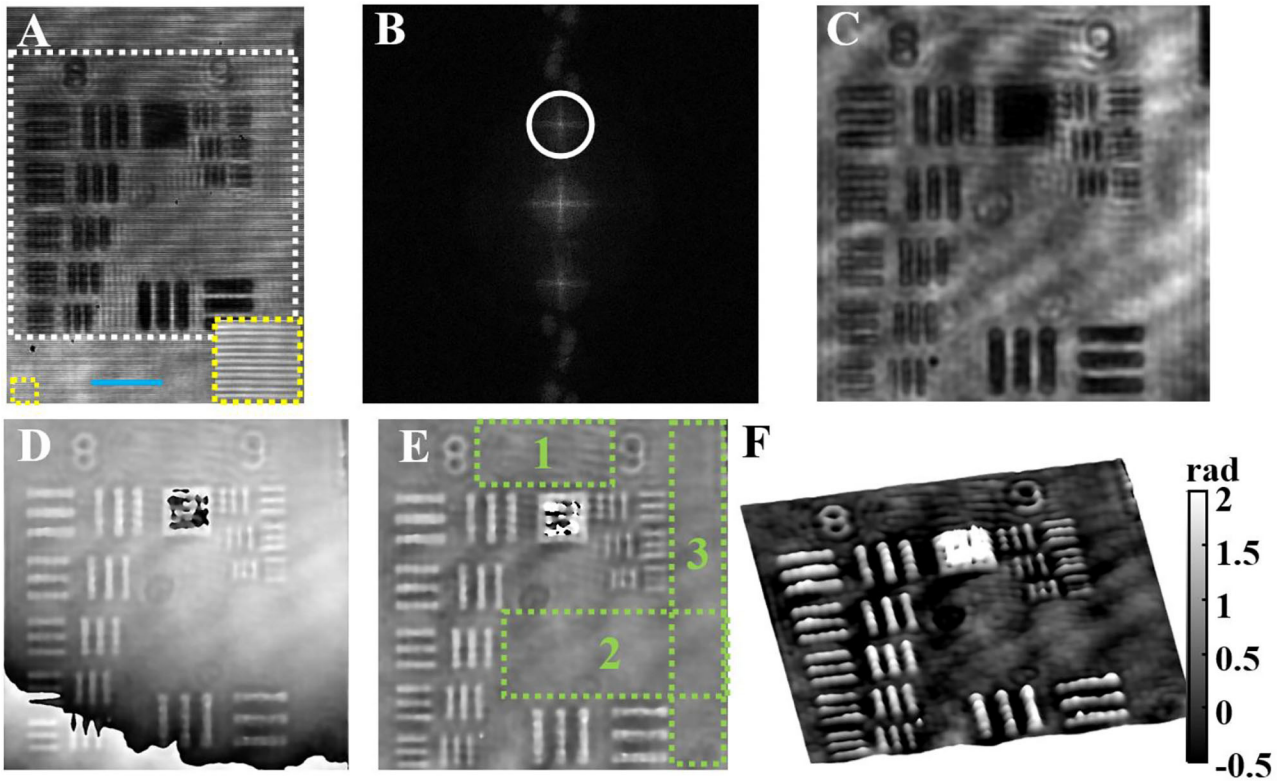

FIGURE 2 | Experimental validation of SER-DHM involving a negative USAF test target. **(A)** Off-axis digital hologram. **(B)** Fourier transform of **(A)** including the filter applied for Fourier filtering. **(C)** Retrieved amplitude distribution. **(D)** Retrieved phase distribution. **(E)** Phase map after spherical wavefront compensation. **(F)** 3D phase visualization. Blue scale bar in **(A)** means 20 μm.

the +1st order does not present a big enough angle to arrange the illumination (close proximity with the digital sensor) and to save central order for the interferometric recording. Thus, according to Equation (1), the illumination forms an angle of $\theta_i = 13.3^\circ$ with respect to the optical axis of the imaging system. Notice that, in all the included experiments, we do not have included any mirrored surface to generate the R region, but we benefit from the reflecting areas present in the surroundings of the object regions for such a purpose.

Validation of the SER-DHM Operation Principle

In order to show full reconstruction process and to provide an analysis of the system performance, results coming from a negative USAF resolution test target are included through **Figure 2**: the recorded hologram is shown in **Figure 2A**, including a magnified region (yellow rectangle) to clearly show the fringes, the Fourier transform of the off-axis hologram at **Figure 2B,** the amplitude (**Figure 2C**), and phase (**Figure 2D**) of the recovered complex amplitude distribution after Fourier filtering method (white circle at **Figure 2B**). Note that if the imaging system does not operate in telecentric mode, then there is a spherical wavefront distorting the reconstructed phase that must be canceled out (see **Figure 2D**). Once compensated, the resulting phase distribution is shown at **Figure 2E**, whose three-dimensional (3D) visualization is included at **Figure 2F**.

In order to measure the magnification and imaged FOV set in the experimental validations, let us consider the Element 1 of Group 8 (G8-E1) of the USAF test (period of 3.91 μm). The image of G8-E1 spreads over 48 pixels or, equivalently, 230 μm, thus defining a lateral magnification of $M = 58.8$ X, which is higher than the nominal magnification of the microscope objective. This is because we had to move the sensor away from the microscope lens for practical reasons (the presence of the focusing lens). Thus, since the length and width of the CMOS area are [6.14, 4.92] mm, the FOV imaged at the output plane will be [104.5, 83.6] μm.

As we can see in the reconstructions, all elements of the high-resolution USAF test target are well-resolved. In fact, the theoretical resolution of the system is $\rho = k\lambda/NA \approx 1\mu m$, being $k = 0.82$ for coherent imaging systems with circular apertures [43]. On the other hand, in order to quantify the accuracy in the phase values, that is, the phase resolution, we compute the standard deviation (STD) values in the three regions enclosed in green rectangles in **Figure 2E**. The values obtained in regions 1, 2, and 3 are, respectively, 0.23, 0.24, and 0.21 rad, thus providing a phase estimation error of 0.23 rad. The fact that these values are really close one another demonstrates that the phase error does

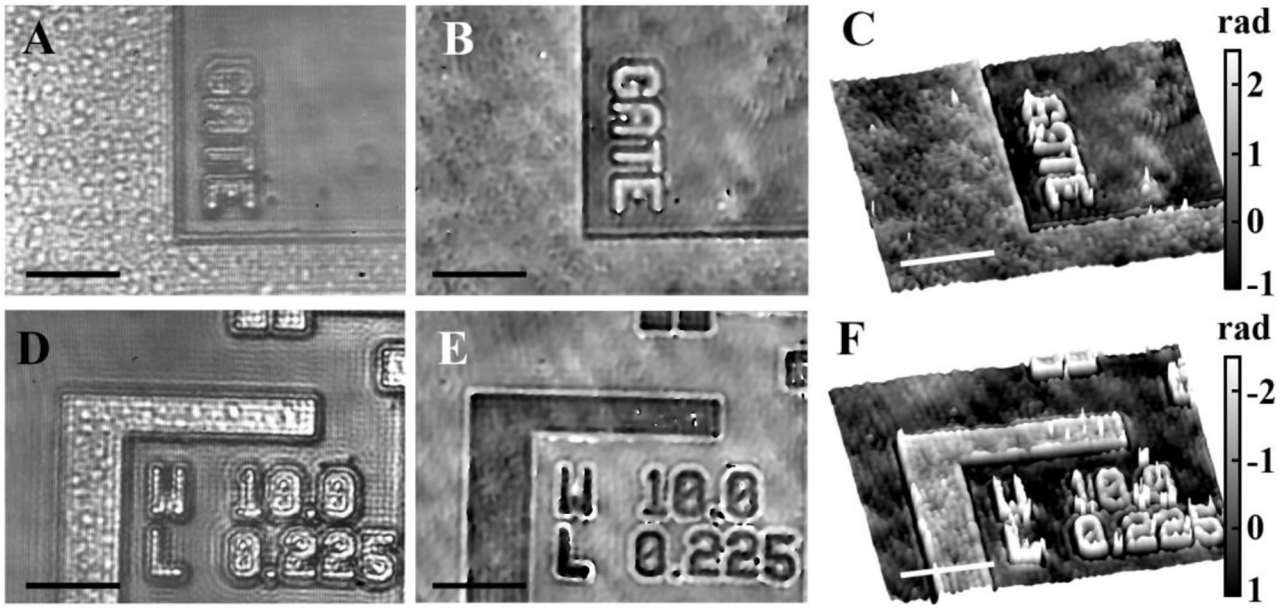

FIGURE 3 | Inspection of a microchip silicon wafer using SER-DHM. **(A,D)** Off-axis digital holograms involving two different areas. **(B,E)** Retrieved phase distributions. **(C,F)** 3D phase distributions. Scale bars in images are 20 μm.

not depend on the location in the FOV, so that the system is shift-invariant after spherical wavefront compensation. Note that the presence of noise in the phase images comes from speckle noise and coherent artifacts due to the use of a coherent light source.

Inspection of Microelectronic Components

As second target, SER-DHM is used for the inspection of different regions in a semiconductor silicon wafer containing a matrix of microchips. **Figure 3** includes the results for two different regions of a microchip, where **Figures 3A,D** depict the off-axis holograms, **Figures 3B,E** show the retrieved phase maps, and **Figures 3C,F** illustrate the 3D phase distributions of the microchip in such areas.

Single-Shot Topography Validation

Finally, the capability of SER-DHM to provide topography analysis in real-time is demonstrated by making a scanning of an object. The object is a 1D Ronchi grating with a spatial frequency of 20 lp/mm. Thus, the scanning process is performed along one of its borders by moving the object using a motorized linear translation stage (Newport, model ESP300). In this case, we characterize 1 mm of the grating by recording 330 images in a time of 30 s. That means we perform the scanning with a grating motion step of 3 μm to analyze a total of 20 grating periods. **Figure 4** includes the results concerning this characterization. We first record a set of off-axis digital holograms (**Supplementary Video 1**), from which we extract the complex amplitude of the light reflected by the object by applying Fourier filtering. Then, the recovered information is properly relocated and averaged (by performing correlation between contiguous images and averaging them) in order to increase the signal-to-noise ratio (SNR) of the phase images. The resulting phase distributions are presented in **Supplementary Video 2** from which we can directly obtain the information of the thickness distribution $t(x, y)$ of the coating chromium layer of the grating (C) (**Supplementary Video 3**), using the following expression defined in Picazo-Bueno and Micó [23].

$$t(x,y) = \frac{\lambda}{4\pi}\left[\triangle\,\varphi(x,y) + \phi_t - \pi\right] \tag{4}$$

In this expression, $\triangle\,\varphi(x, y)$ is the phase distribution, ϕ_t is the phase change introduced by the reflection in the chromium layer, and the π rad value corresponds to the phase step in reflected light at dielectric interfaces (air-glass in our case). The ϕ_t value is obtained from the website www.refractiveindex.info which is based on Johnsonand and Christy [44]: $\phi_t = -161.507^\circ = 3.4644$ rad.

The thickness distribution of the entire scanned region of the grating is included in **Figure 4D**. In order to quantitatively validate our approach for topography analysis, we have analyzed the average value of the thickness of the chromium layer by computing a plot of the height profile (**Figure 4E**) considering the average thickness values computed along the dashed blue line included in **Figure 4D**. Subsequently, we estimate the average thickness difference in each period of the grating considering a total of 20 grating periods, achieving a thickness value of $t_{mean} = 84$ nm. On the other hand, we quantitatively assess the robustness (stability in time) of our system by studying the phase stability during the scanning process. For such purpose,

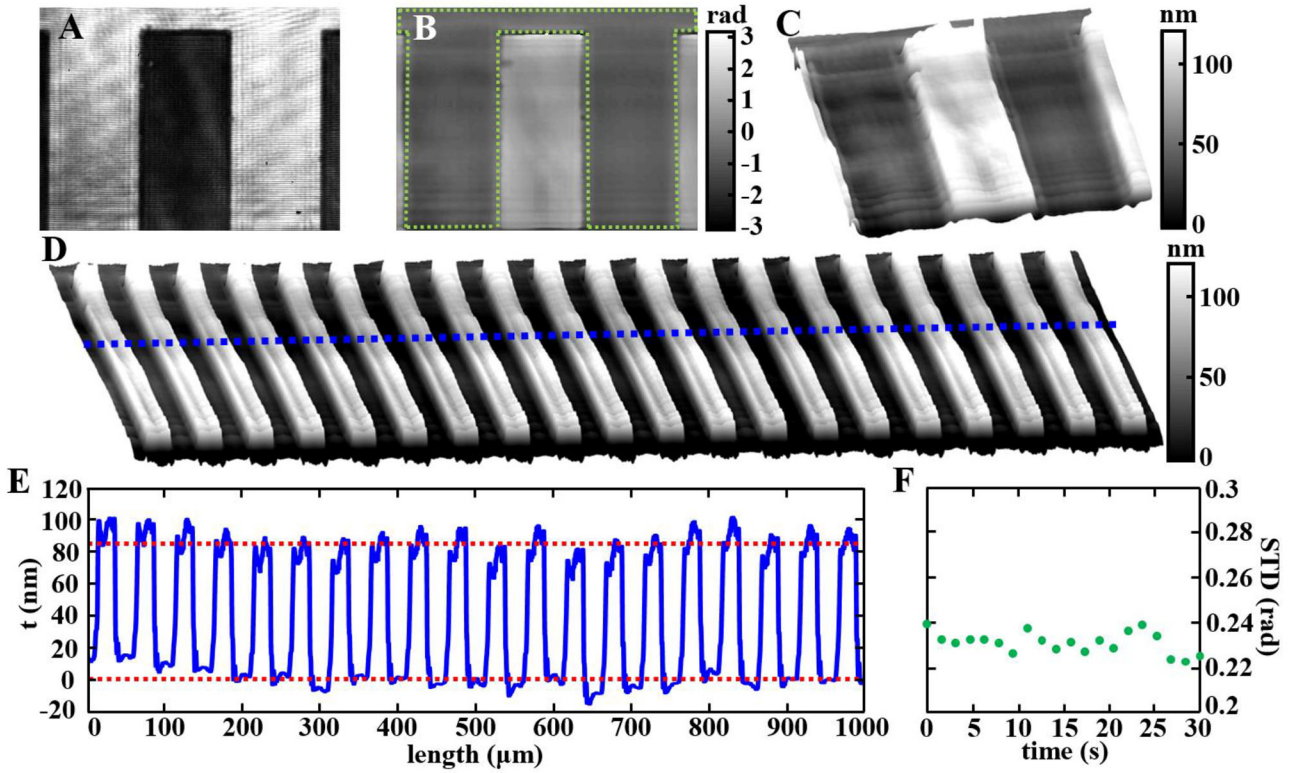

FIGURE 4 | Experimental results of SER-DHM for the case of a 20 lp/mm Ronchi grating. **(A)** Off-axis digital holograms (**Supplementary Video 1**). **(B)** Averaged phase distributions (**Supplementary Video 2**). **(C)** 3D thickness distributions (**Supplementary Video 3**). **(D)** Total scanned thickness distribution along 20 grating periods. **(E)** Height profile along blue line included in **(D)**. **(F)** STD values of the green region included in **(B)** before phase averaging.

we have computed the STD values of the phase images (after spherical wavefront compensation) in the mirrored chromium region of the grating (dotted green area in **Figure 4B**) for every period which is reconstructed during the scanning. That is, a similar area of the grating is reconstructed every 1.5 s and we have extracted the STD values of the retrieved phase distribution for a total of 20 periods, meaning a total analysis time of 30 s. STD values before phase averaging are shown at **Figure 4F** where the computed mean value is 0.23 rad. As it can be seen, the system behaves in a very stable way providing STD phase values that perfectly matches with the obtained in Validation of the SER-DHM operation principle for the case of the negative USAF test target. In addition, the averaging process performed to the phase images during the scanning process drops such value until 0.13 rad. From this value, we can obtain a thickness estimation uncertainty by simply error propagation with the expression $\delta t\left(x,y\right) = \delta \triangle \varphi(x,y)\lambda/4\pi = 6.6\ nm$. Hence, the experimental thickness is $t_{mean} = 84 \pm 7$ nm, so that the SNR is 12.

Finally, we compare this value against the thickness values provided by the characterization of such a grating performed in Picazo-Bueno and Micó [23]. There, the AFM characterization of one of those grating profiles provided a thickness value of around 85 nm, whereas the holographic setup presented at Picazo-Bueno and Micó [23] provides a value of 82 nm for the thickness of the chromium layer. As we can see, these values are in the interval defined by the experimental error, so that the values in good agreement one another, thus validating our SER-DHM approach for topography measurements.

DISCUSSION AND CONCLUSIONS

We have proposed SER-DHM as a valid technique for QPI and topography analysis in reflective objects. SER-DHM uses a single 1D diffraction grating for both illuminating the sample in a reflection mode and providing holographic imaging needed for the quantitative analysis. The technique implements a CPI architecture in which: (1) the different diffraction orders of the grating are utilized for different purposes (+3rd order for reflective illumination, and 0th and +1st orders for off-axis holographic recording), and (2) the input plane is spatially multiplexed into two regions (O + R regions), using a flat uniform region to generate the back reflected reference beam. SER-DHM has been successfully validated for a 50X/0.50NA microscope objective using different reflective objects (negative USAF test target, microchip silicon wafer, and Ronchi grating). Note that, despite being the technique successfully validated for a single microscope lens, our approach can be nonetheless implemented using other microscope objectives.

The strong point of SER-DHM comes from the use of a single optical element—a 1D Ronchi grating—to simultaneously illuminate the sample and define a CPI layout. That makes the proposed interferometric configuration be inherently more stable with respect to mechanical or thermal changes than the standard ones, e.g., Michelson, because the imaging and reference beams follow nearly the same optical path. This fact also gives the possibility to illuminate the sample using light sources with low coherence lengths, in order to reduce the coherent noise present in phase images. In addition, as SER-DHM only involves a single element, both the complexity and price of the system become significantly reduced when compared to conventional interferometers, since those usually employ a larger number of optical elements.

The proposed SER-DHM can be seen as an evolution of previous SMIM approach working in reflection mode [23], evolution in the sense of simplification because the beam splitter cube at Picazo-Bueno and Micó [23] is no longer needed in the actual configuration. However, SER-DHM has been validated on optical table instead of using the microscope embodiment where SMIM approaches were validated [23, 35–38] because it was not possible to integrate the laser source at the specific illumination angle at the same microscope body.

As main drawback, the use of diffraction gratings for such purposes means to lose a significant amount of light since we only consider the light coming from one diffraction order (+3rd order is not the most efficient one) as illumination beam as well as just two diffraction orders (0th and +1st orders) for the generation of the digital holograms. Nevertheless, this is not a big issue because illumination sources are nowadays powerful enough to perform the experiments. In addition, part of the light that arrives to the grating is reflected back and may fall into the sensor area, thus strongly deteriorating or even destroying the quality of the recorded holograms. To avoid that, we can slightly tilt the Ronchi grating in the other direction (vertical) than the multiplexing is performed; thus, all reflected light will fall out of the sensor area. Finally, the proposed SER-DHM approach also becomes restricted by the main limitation of SMIM methods the reduction of the useful FOV to one half of the available one as payment for reference beam generation. However, the FOV defined by the microscope lens is normally larger than the recorded one by the digital sensor, and we can therefore use a region outside of the recorded area as reference region.

In conclusion, our proposed SER-DHM is presented as a very simple, cost-effective, and robust technique that enables the study of the topography of reflective objects with a nanometric accuracy, in a non-invasive way, and using a single-shot operation principle. To the best knowledge, this is the first time that only a single element is used in DHM to provide both reflective illumination and holographic detection. SER-DHM could be specifically useful in, for instance, microelectronic applications, where topography measurements of the microchips (or integrated circuits) could provide extremely helpful information such as manufacturing defects.

DATA AVAILABILITY STATEMENT

The raw data supporting the conclusions of this article will be made available by the authors, without undue reservation.

AUTHOR CONTRIBUTIONS

JP-B, JG, and VM conceived and designed the research. JP-B performed the experiments. JG and VM supervised the project. All the authors wrote the manuscript and revised the results.

FUNDING

This work was supported by the Spanish Ministerio de Economía y Competitividad and the Fondo Europeo de Desarrollo Regional (FIS2017-89748-P).

SUPPLEMENTARY MATERIAL

The Supplementary Material for this article can be found online at: https://www.frontiersin.org/articles/10.3389/fphy.2021.639607/full#supplementary-material

Supplementary Video 1 | Set of recorded off-axis holograms for the scanning of the Ronchi grating.

Supplementary Video 2 | Set of retrieved and averaged phase distributions in the scanning of the Ronchi grating.

Supplementary Video 3 | Set of thickness distributions computed showing the topography of Ronchi grating.

REFERENCES

1. Marquet P, Rappaz B, Magistretti PJ, Cuche E, Emery Y, Colomb T, et al. Digital holographic microscopy: a noninvasive contrast imaging technique allowing quantitative visualization of living cells with subwavelength axial accuracy. *Opt Lett.* (2005) 30:468. doi: 10.1364/OL.30.000468
2. Ferraro P, Grilli S, Alfieri D, De Nicola S, Finizio A, Pierattini G, et al. Extended focused image in microscopy by digital holography. *Opt Express.* (2005) 13:6738–49. doi: 10.1364/OPEX.13.006738
3. Charrière F, Marian A, Montfort F, Kuehn J, Colomb T, Cuche E, et al. Cell refractive index tomography by digital holographic microscopy. *Opt Lett.* (2006) 31:178–80. doi: 10.1364/OL.31.000178
4. Kemper B, von Bally G. Digital holographic microscopy for live cell applications and technical inspection. *Appl Opt.* (2008) 47:A52–61. doi: 10.1364/AO.47.000A52
5. Kim MK. Digitalholographic microscopy. In: *Principles, Techniques, and Applications*, Vol. 162. New York, NY: Springer (2011). p. 1–240. doi: 10.1007/978-1-4419-7793-9
6. Cuche E, Marquet P, Depeursinge C. Simultaneous amplitude-contrast and quantitative phase-contrast microscopy by numerical reconstruction of Fresnel off-axis holograms. *Appl Opt.* (1999) 38:6994–7001. doi: 10.1364/AO.38.006994
7. De Nicola S, Ferraro P, Finizio A, Grilli S, Coppola G, Iodice M, et al. Surface topography of microstructures in lithium niobate

by digital holographic microscopy. *Meas Sci Technol.* (2004) 15:961–8. doi: 10.1088/0957-0233/15/5/026
8. Kühn J, Colomb T, Montfort F, Charrière F, Emery Y, Cuche E, et al. Real-time dual-wavelength digital holographic microscopy with a single hologram acquisition. *Opt Express.* (2007) 15:7231–42. doi: 10.1364/OE.15.007231
9. Castañeda R, Garcia-Sucerquia J. Single-shot 3D topography of reflective samples with digital holographic microscopy. *Appl Opt.* (2018) 57:A12. doi: 10.1364/AO.57.000A12
10. Cuche E, Bevilacqua F, Depeursinge C. Digital holography for quantitative phase-contrast imaging. *Opt Lett.* (1999) 24:291–3. doi: 10.1364/OL.24.000291
11. Iwai H, Fang-Yen C, Popescu G, Wax A, Badizadegan K, Dasari RR, et al. Quantitative phase imaging using actively stabilized phase-shifting low-coherence interferometry. *Opt Lett.* (2004) 29:2399. doi: 10.1364/OL.29.002399
12. Massatsch P, Charrière F, Cuche E, Marquat P, Depeursinge CD. Time-domain optical coherence tomography with digital holographic microscopy. *Appl Opt.* (2005) 44:1806–12. doi: 10.1364/AO.44.001806
13. Khmaladze A, Restrepo-Martínez A, Kim M, Castañeda R, Blandón A. Simultaneous dual-wavelength reflection digital holography applied to the study of the porous coal samples. *Appl Opt.* (2008) 47:3203–10. doi: 10.1364/AO.47.003203
14. Kemper B, Stürwald S, Remmersmann C, Langehanenberg P, von Bally G. Characterisation of light emitting diodes (LEDs) for application in digital holographic microscopy for inspection of micro and nanostructured surfaces. *Opt Lasers Eng.* (2008) 46:499–507. doi: 10.1016/j.optlaseng.2008.03.007
15. Reichelt S, Zappe H. Combined Twyman-Green and Mach-Zehnder interferometer for microlens testing. *Appl Opt.* (2005) 44:5786–92. doi: 10.1364/AO.44.005786
16. Běhal J. Quantitative phase imaging in common-path cross-referenced holographic microscopy using double-exposure method. *Sci Rep.* (2019) 9:1–7. doi: 10.1038/s41598-019-46348-9
17. Edwards C, Arbabi A, Popescu G, Goddard LL. Optically monitoring and controlling nanoscale topography during semiconductor etching. *Light Sci Appl.* (2012) 1:e30. doi: 10.1038/lsa.2012.30
18. León-Rodríguez M, Rodríguez-Vera R, Rayas JA, Calixto S. Digital holographic microscopy through a Mirau interferometric objective. *Opt Lasers Eng.* (2013) 51:240–5. doi: 10.1016/j.optlaseng.2012.10.006
19. Edwards C, Zhou R, Hwang S-W, McKeown SJ, Wang K, Bhaduri B, et al. Diffraction phase microscopy: monitoring nanoscale dynamics in materials science [Invited]. *Appl Opt.* (2014) 53:G33–43. doi: 10.1364/AO.53.000G33
20. Finkeldey M, Göring L, Brenner C, Hofmann M, Gerhardt NC. Depth-filtering in common-path digital holographic microscopy. *Opt Express.* (2017) 25:1939–8. doi: 10.1364/OE.25.019398
21. Stockton PA, Field JJ, Bartels RA. Single pixel quantitative phase imaging with spatial frequency projections. *Methods.* (2018) 136:24–34. doi: 10.1016/j.ymeth.2017.10.007
22. Worts N, Field J, Bartels R, Jones J, Broderick J, Squier J. Interferometric spatial frequency modulation imaging. *Opt Lett.* (2018) 43:5351–4. doi: 10.1364/OL.43.005351
23. Picazo-Bueno JA, Micó V. Opposed-view spatially multiplexed interferometric microscopy. *J Opt.* (2019) 21:3570–1. doi: 10.1088/2040-8986/ab000e
24. Bon P, Maucort G, Wattellier B, Monneret S. Quadriwave lateral shearing interferometry for quantitative phase microscopy of living cells. *Opt Express.* (2009) 17:1308–0. doi: 10.1364/OE.17.013080
25. Singh ASG, Anand A, Leitgeb RA, Javidi B. Lateral shearing digital holographic imaging of small biological specimens. Opt Express. (2012) 20:2361–7. doi: 10.1364/OE.20.023617
26. Di J, Li Y, Xie M, Zhang J, Ma C, Xi T, et al. Dual-wavelength common-path digital holographic microscopy for quantitative phase imaging based on lateral shearing interferometry. *Appl Opt.* (2016) 55:7287–93. doi: 10.1364/AO.55.007287
27. Ma C, Li Y, Zhang J, Li P, Xi T, Di J, et al. Lateral shearing common-path digital holographic microscopy based on a slightly trapezoid Sagnac interferometer. *Opt Express.* (2017) 25:1365–9. doi: 10.1364/OE.25.013659
28. Chhaniwal V, Singh ASG, Leitgeb RA, Javidi B, Anand A. Quantitative phase-contrast imaging with compact digital holographic microscope employing Lloyd's mirror. *Opt Lett.* (2012) 37:5127–9. doi: 10.1364/OL.37.005127
29. Mico V, Zalevsky Z, García J. Superresolution optical system by common-path interferometry. *Opt Express.* (2006) 14:5168–77. doi: 10.1364/OE.14.005168
30. Ferrari JA, Frins EM. Single-element interferometer. *Opt Commun.* (2007) 279:235–9. doi: 10.1016/j.optcom.2007.07.038
31. Ebrahimi S, Dashtdar M, Sánchez-Ortiga E, Martínez-Corral M, Javidi B. Stable and simple quantitative phase-contrast imaging by Fresnel biprism. *Appl Phys Lett.* (2018) 112:1–5. doi: 10.1063/1.5021008
32. Singh V, Tayal S, Mehta DS. Highly stable wide-field common path digital holographic microscope based on a Fresnel biprism interferometer. *OSA Contin.* (2018) 1:48–55. doi: 10.1364/OSAC.1.000048
33. Singh V, Joshi R, Tayal S, Mehta DS. Speckle-free common-path quantitative phase imaging with high temporal phase stability using a partially spatially coherent multi-spectral light source. *Laser Phys Lett.* (2019) 16:256–01. doi: 10.1088/1612-202X/aaf179
34. Hayes-Rounds C, Bogue-Jimenez B, Garcia-Sucerquia J, Skalli O, Doblas A. Advantages of Fresnel biprism-based digital holographic microscopy in quantitative phase imaging. *J Biomed Opt.* (2020) 25:865–01. doi: 10.1117/1.JBO.25.8.086501
35. Mico V, Ferreira C, Zalevsky Z, García J. Spatially-multiplexed interferometric microscopy (SMIM): converting a standard microscope into a holographic one. *Opt Express.* (2014) 22:1492–9. doi: 10.1364/OE.22.014929
36. Picazo-Bueno JÁ, Zalevsky Z, García J, Ferreira C, Micó V. Spatially multiplexed interferometric microscopy with partially coherent illumination. *J Biomed Opt.* (2016) 21:1060–07. doi: 10.1117/1.JBO.21.10.106007
37. Picazo-Bueno JÁ, Zalevsky Z, García J, Micó V. Superresolved spatially multiplexed interferometric microscopy. *Opt Lett.* (2017) 42:927. doi: 10.1364/OL.42.000927
38. Picazo-Bueno JÁ, Trusiak M, García J, Patorski K, Micó V. Hilbert–Huang single-shot spatially multiplexed interferometric microscopy. *Opt Lett.* (2018) 43:1007. doi: 10.1364/OL.43.001007
39. Mico V, Zalevsky Z, García J. Common-path phase-shifting digital holographic microscopy: a way to quantitative phase imaging and superresolution. *Opt Commun.* (2008) 281:4273–81. doi: 10.1016/j.optcom.2008.04.079
40. Mico V. Quantitative phase imaging by common-path interferometric microscopy: application to super-resolved imaging and nanophotonics. *J Nanophotonics.* (2009) 3:317–80. doi: 10.1117/1.3155822
41. Goodman JW. *Introduction to Fourier Optics*. Englewood, CO: Roberts (2005).
42. Kim MK. Principles and techniques of digital holographic microscopy. *SPIE Rev.* (2010) 1:018005. doi: 10.1117/6.0000006
43. Born M, Wolf E. Principles of optics 7th edition. *Principles of Optics Electromagnetic Theory of Propagation Interference and Diffraction of Light.* (1999). p. 1–95.
44. Johnson PB, Christy RW. Optical constants of transition metals. *Phys Rev B.* (1974) 9:5056–70. doi: 10.1103/PhysRevB.9.5056

Conflict of Interest: The authors declare that the research was conducted in the absence of any commercial or financial relationships that could be construed as a potential conflict of interest.

frontiers in Physics

BRIEF RESEARCH REPORT
published: 22 March 2021
doi: 10.3389/fphy.2021.651313

Quantitative Phase Imaging Using Deep Learning-Based Holographic Microscope

Jianglei Di, Ji Wu, Kaiqiang Wang, Ju Tang, Ying Li and Jianlin Zhao**

MOE Key Laboratory of Material Physics and Chemistry Under Extraordinary Conditions, and Shaanxi Key Laboratory of Optical Information Technology, School of Physical Science and Technology, Northwestern Polytechnical University, Xi'an, China

Digital holographic microscopy enables the measurement of the quantitative light field information and the visualization of transparent specimens. It can be implemented for complex amplitude imaging and thus for the investigation of biological samples including tissues, dry mass, membrane fluctuation, etc. Currently, deep learning technologies are developing rapidly and have already been applied to various important tasks in the coherent imaging. In this paper, an optimized structural convolution neural network PhaseNet is proposed for the reconstruction of digital holograms, and a deep learning-based holographic microscope using above neural network is implemented for quantitative phase imaging. Living mouse osteoblastic cells are quantitatively measured to demonstrate the capability and applicability of the system.

Keywords: digital holographic microscopy, digital holography, deep learning, quantitative phase imaging, convolution neural network

OPEN ACCESS

Edited by:
Peng Gao,
Xidian University, China

Reviewed by:
Wenjing Zhou,
Shanghai University, China
Yongfu Wen,
Beijing Institute of Technology, China

****Correspondence:***
Jianglei Di
jiangleidi@nwpu.edu.cn
Jianlin Zhao
jlzhao@nwpu.edu.cn

Specialty section:
This article was submitted to Optics and Photonics, a section of the journal Frontiers in Physics

Received: *09 January 2021*
Accepted: *15 February 2021*
Published: *22 March 2021*

Citation:
Di J, Wu J, Wang K, Tang J, Li Y and Zhao J (2021) Quantitative Phase Imaging Using Deep Learning-Based Holographic Microscope. Front. Phys. 9:651313. doi: 10.3389/fphy.2021.651313

INTRODUCTION

Optical microscope is an effective diagnostic tool in modern healthcare which allows pathologists to clearly and qualitatively observe the details of cells and tissues, and make judgments based on experience. This technique is sufficient in most cases. However, a bright field optical microscope records the intensity information of the specimen and suffers from low contrast for transparent biological cells which presents minimal light absorption. Various labeling methods, including staining and fluorescent tagging, are designed to enhance the imaging effect of the microscope, but the dyes may cross-react with the biological processes and affect the objectivity of medical diagnosis [1]. Although phase contrast microscopy or differential interference contrast microscopy, which converts the sightless phase shifts introduced by the specimen of interest into observable intensity variations, provide an approach to survey phase specimens without labeling, they cannot provide quantitative phase information on the specimen-induced phase shifts for subsequent accurate diagnosis. Furthermore, their inherent contrast mechanism makes automated cell segmentation hardly robust.

In comparison, quantitative phase imaging techniques enable quantitative light field information and the visualization of transparent specimens [2–4]. As a typical representative of this technique, digital holographic microscopy (DHM) can be implemented for complex amplitude imaging and be used to investigate transparent specimens, such as biological samples including tissues, dry mass, membrane fluctuation, etc [5–8]. In DHM, a hologram that carries specimen information is recorded digitally first, and then the hologram is numerically reconstructed to extract the amplitude or phase of the specimens' complex field [9–13]. After that, the quantitative phase information can be converted to dry mass density of the cell with extremely high accuracy which has been demonstrated

so far as a valuable tool in hematological or cancer diagnosis. The label-free, submicron scale sensitivity, full-field, non-destructive, real-time, quantitative and three-dimensional imaging abilities of DHM present a variety of advantages for biomedical applications, especially for live cell imaging [14–16]. Nowadays, DHM has been an important and powerful tool for medical diagnoses.

In our previous work, a common-path digital holographic microscopy based on a beam displacer unit was proposed for quantitative and dynamic phase imaging of biological cells [17]. This implementation reduces the system requirement for the light source coherence, realizes the convenient adjustment of the light beams and achieves an excellent temporal stability. However, its hologram reconstruction algorithms are often time consuming for obtaining satisfactory complex amplitude information of the specimen, which usually has certain requirements for computer hardware and need complicated tuning of user-defined parameters, such as the reconstruction distance, area and position in the frequency domain, etc. It is necessary to develop a new holographic reconstruction algorithm to improve the efficiency of common-path digital holographic microscopy.

In recent years, deep learning technology has developed rapidly, and very significant achievements have been made in areas such as autonomous driving, natural language processing, computer vision and many more. Currently, deep learning has also made remarkable achievements in computational imaging, and it has already been applied to various important tasks in coherent imaging, such as phase unwrapping [18], phase recovery [19–22], holograms reconstruction [23–27], and so on.

In this paper, an optimized structural convolution neural network PhaseNet is proposed for the reconstruction of digital holograms, and a deep learning-based holographic microscope (DLHM) using PhaseNet is implemented for quantitative phase imaging. Living mouse osteoblastic cells are quantitatively measured to demonstrate the capability and applicability of the system.

METHODS

Suppose the intensity of the recorded digital hologram in DHM is $I(x,y)$, the complex amplitude of the object light field $U(\xi,\eta)$ can be numerically reconstructed by using the scalar diffraction theory,

$$U(\xi,\eta) = \int_{-\infty}^{\infty}\int_{-\infty}^{\infty} I(x,y)R(x,y)g(\xi,\eta,x,y)\mathrm{d}x\mathrm{d}y, \quad (1)$$

where $R(x,y)$ is the reconstruction reference light field and $g(\xi,\eta;x,y)$ is the impulse response function [28–30].

The hologram is usually reconstructed using convolution algorithm, corresponding reconstructed object light field $U(\xi,\eta)$ can be expressed as

$$U(\xi,\eta) = IFFT\{FFT\{I(x,y)R(x,y)\}\cdot FFT\{g(\xi,\eta,x,y)\}\}, \quad (2)$$

where FFT and IFFT represent the Fourier and inverse Fourier transform operations, respectively.

And then, the intensity and phase information of the specimen can be calculated subsequently by

$$I(\xi,\eta) = \left|U(\xi,\eta)\right|^2 \quad (3)$$

and

$$\varphi(\xi,\eta) = \arctan\frac{\mathrm{Im}[U(\xi,\eta)]}{\mathrm{Re}[U(\xi,\eta)]}\ (\mathrm{mod}2\pi) \quad (4)$$

where Re and Im represent the real and imaginary parts of the object light field, respectively. Further by eliminating the 2π ambiguity due to the argument operation, the true phase information of the original object wavefield can be obtained.

After the object beam passes through the biological specimen, the optical path difference ΔOPD will be introduced due to the phase difference $\Delta\varphi$ and the difference of refractive index (RI) between the cells and the culture medium, which is dependent on the laser wavelength λ, the RI of the surrounding medium n_{medium}, the cell thickness d and integral mean RI $n_{specimen}$. Therefore, the ΔOPD can be calculated as

$$\Delta\mathrm{OPD} = \left(n_{specimen} - n_{medium}\right)\cdot d = \frac{\lambda}{2\pi}\cdot\Delta\varphi. \quad (5)$$

The ΔOPD is an integral effect of the optical path along the optical axis. Different parts of the cell have different RI resulting in different ΔOPD. Thus, in a certain sense, the ΔOPD represents the thickness of the cell.

DEEP LEARNING-BASED HOLOGRAPHIC MICROSCOPE

The proposed deep learning-based holographic microscope includes a set of digital holographic microscope for the hologram recording and a deep neural network PhaseNet for the numerical reconstruction of digital holograms.

Digital Holographic Microscope

The main body of the proposed DLHM is a common-path digital holographic microscope as shown in **Figure 1**, which is modified based on a commercial microscope. The light source of the microscope was replaced by a fiber-coupled DPSS laser (Cobolt Samba, 532 nm). Then the laser beam is focused by a lens L to illuminate the specimen and magnified by a ×20 long working distance microscope objective MO. The transmitted light beam travels through a polarizer P1 and enters into the beam displacer BD, in which it's separated into two orthogonally polarized beams with a small displacement. The two output beams pass through a polarizer P2 and interfere with each other at the lateral shearing region of BD. The polarization direction of P2 is set at 45° with the two output polarized beams, respectively. Thus, the two output beams interfere with each other in their overlap part and an off-axis digital hologram is recorded by a white-black CCD camera (target size of 5.95 mm × 4.46 mm, 1,280 × 960 pixels, pixel size 4.65 μm × 4.65 μm). The BD and two polarizers are assembled together as a simple, low-cost and compact beam displacer unit, as shown in **Figure 1B**. In

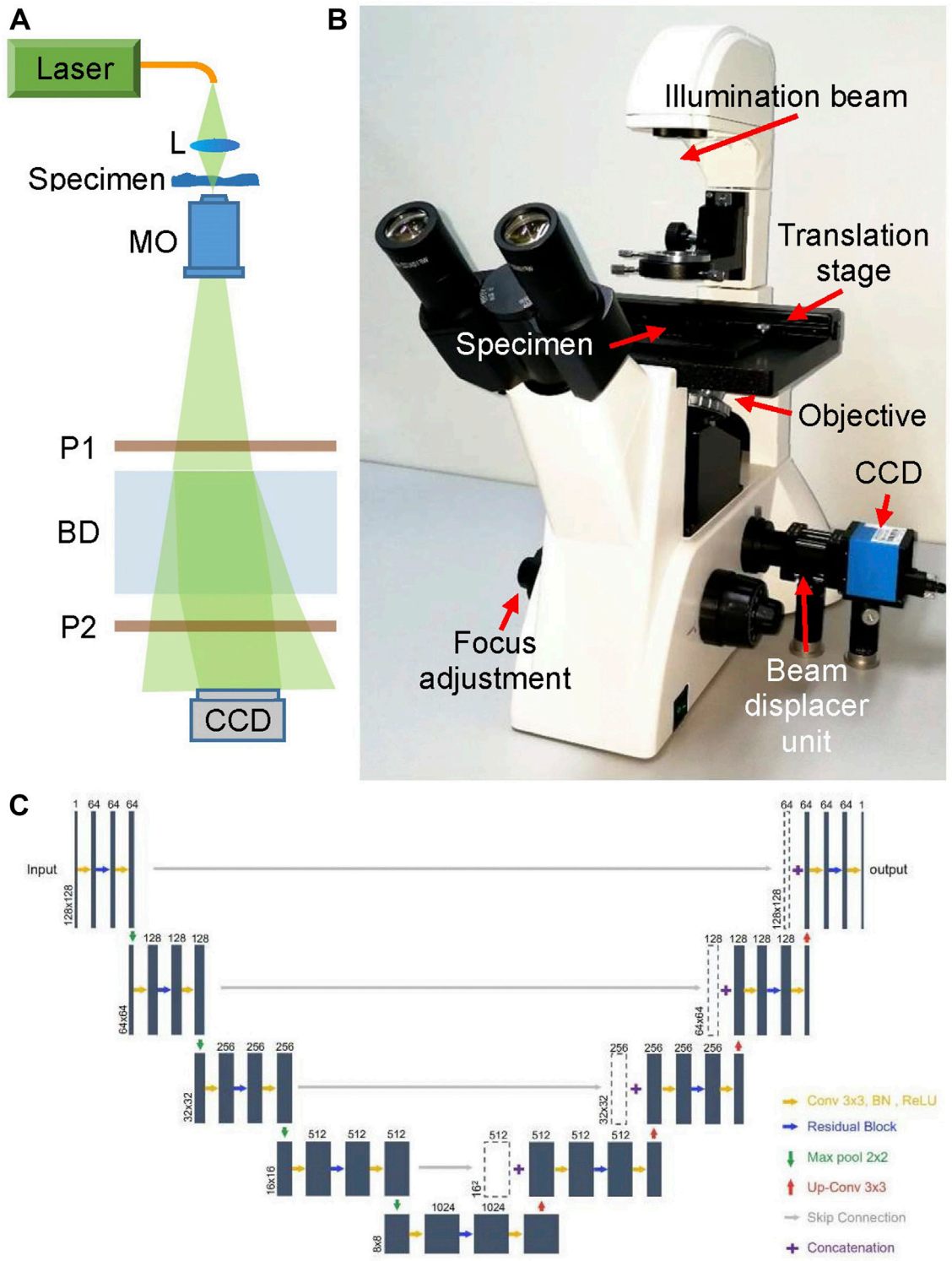

FIGURE 1 | Deep learning-based holographic microscope and PhaseNet architecture. **(A)** Optical schematic of the common-path digital holographic microscope based on a beam displacer unit; **(B)** deep learning-based holographic microscope; **(C)**. Detailed schematic of PhaseNet architecture. Each blue box corresponds to a multi-channel feature map. The number of channels is provided on top of the box. The *x*–*y*-size is denoted at the lower left edge of the box. White boxes represent copied feature maps.

fact, benefiting from the simple optical structure and common-path design, the commercial microscope has been improved to a digital holographic microscope for promising and potential applications in quantitative phase measurement.

PhaseNet

PhaseNet is one of the core components of data processing system of DLHM. It completes the intelligent reconstruction of the hologram and obtains the three-dimensional phase information of the specimens replacing the traditional convolution algorithm or the Fresnel transform algorithm in DHM. **Figure 1C** shows the detailed schematic of PhaseNet architecture which is an optimized structural CNN proposed for phase unwrapping [18]. This architecture contains three parts: down-sampling, bridge and up-sampling paths. The down-sampling path consists of five repeated use of two 3 × 3 convolutions followed by a BN and a ReLU, a residual block [31], and a 2-stride 2 × 2 max pooling operation for downsampling. The feature channels are increased by the first convolution of each repeat (first from 1 to 64 channels, the rest for double channels). By removing the max pooling from the down-sampling path, the bridge path is obtained. Each step in up-sampling consists of a transposed convolution for upsampling, a concatenation with the corresponding feature map from the down-sampling path by skip connection, two 3 × 3 convolutions followed by a BN and a ReLU, and a residual block between the two convolutions. The first two convolutions in each repeat decrease the number of feature channels (the last from 64 to 1 channel, the rest for halving channels). The residual blocks include two repeated use of 3 × 3 convolution followed by a BN and a ReLU. The skip connection is introduced to prevent the network performance degradation by summing the input and output. The down-sampling path extracts and advances the features of the sinogram, while the up-sampling path reconstructs the phase from the high-level features. The channels from the first two layers are increased from 1 to 64, which is to ensure that a sufficient number of low-level features are extracted for use in the later layers. The skip connections are added to improve the efficiency of gradient transmission.

Work Procedure

The work procedure of the proposed DLHM are as follows:

1. Hologram recording and reconstruction. Using DLHM to record off-axis digital holograms of the biological cells.
2. Phase information acquisition. Reconstructing the holograms by use of convolution algorithm to calculate the phase information of the biological cells.
3. PhaseNet training and testing. The holograms and phase results of each cell are used as input and ground truth, respectively, to train the PhaseNet. 9,000 pairs images are used for training, 1,000 pairs images for testing. Gaussian noise with random standard deviations from 0 to 25 is added into the holograms of the training dataset for better robustness. The ADAM-based optimization with an initial learning rate of 0.001 (dropping to the previous 0.75 every five epochs) is adopted to update PhaseNet's parameters. The network is trained for 200 epochs.
4. Network output obtaining. In the network training process, the PhaseNet output is calculated according to the input of the network.
5. Loss function calculation. The mean squared error (MSE) of the PhaseNet output with ground truth (the phase information of biological cells) is calculated and used as the loss function. And the loss function is back-propagated through the network.
6. Quantitatively phase imaging of the biological cells. After finishing the above operations, the network training can be finally completed, and a neural network PhaseNet matching this DLHM can be obtained. Then, the digital hologram recorded by DLHM can be randomly input PhaseNet and the quantitative phase images of the specimen can be rapidly output. The network reconstruction time for a phase image is ~0.014 s.

For PhaseNet implementing, Pytorch framework based on Python 3.6.1 is used. The network training and testing are performed on a PC with Core i7-8700K CPU, using NVIDIA GeForce GTX 1080Ti GPU. The training process takes ~4 h for 100 epochs (~10,000 pairs images size of 128 × 128 pixels in a batch size of 48).

EXPERIMENT RESULTS AND DISCUSSIONS

The living mouse osteoblastic cells are measured by the DLHM. These mouse osteoblastic cells IDG-SW3 are cultured in Alpha minimum essential medium (αMEM, gibco by life technologies). They stick to the bottom of the petri dish while maintaining activity and are placed on the DLHM for measurement in room temperature environment.

Figure 2 shows the numerical reconstruction results of one mouse osteoblastic cell. **Figure 2A** is one of the recorded digital holograms of the cells in which its partially enlarged view clearly shows the interference fringes. In order to reconstruct the hologram numerically, Fourier transform is required to complete the spectral filtering. The spectrum of the hologram is shown in **Figure 2B**. After completing the numerical reconstruction and phase unwrapping, we can finally obtain the mouse osteoblastic cells' intensity and phase information. **Figure 2C** shows the quantitative two-dimensional phase map of one mouse osteoblastic cell during the mitotic phase. This phase map represents the ΔOPD caused by the cell thickness, and it can also be called optical thickness of cells. In **Figure 2C**, some synapses are surrounding the cell. At this time, the cell is about to finish dividing and has become two cells. The biggest phase value in the central part of the two cells represents a maximum cell thickness and it's where the nucleuses are located. These are shown very clearly in the three-dimensional phase map of **Figure 2D**. The RI of the αMEM is n_{medium} = 1.3377 calibrated by an Abbe refractometer, and by assuming a constant and homogeneous cellular RI $n_{specimen}$ = 1.375, we can estimate that a phase difference of 1 rad corresponds to a cellular

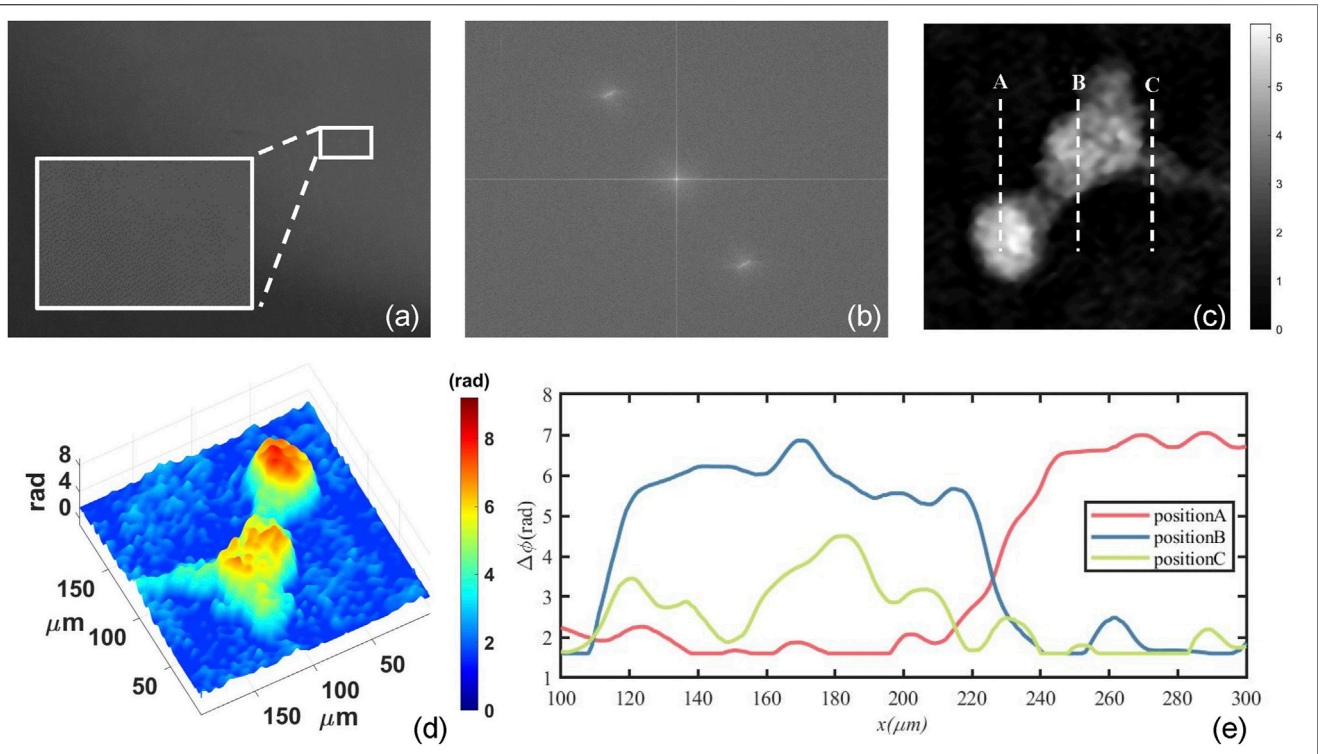

FIGURE 2 | Numerical reconstruction results of mouse osteoblastic cells by use of convolution algorithm. **(A)** The digital holograms of a living mouse osteoblastic cell; **(B)** The spectrum of the hologram; **(C)** The quantitative two-dimensional phase map of one mouse osteoblastic cell; **(D)** three-dimensional phase map; **(E)** The profile map along with the dash lines A, B and C in **(C)**.

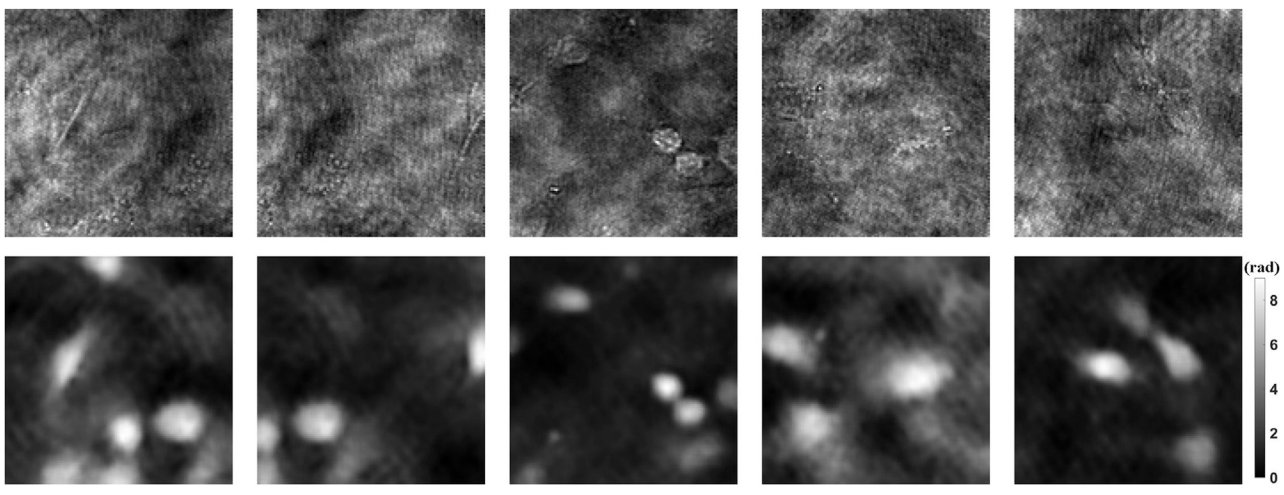

FIGURE 3 | Dataset examples. The upper part shows the holograms as input, and the lower part shows the phase results as ground truth.

thickness of 2.27 μm according to **Eq. 5**. **Figure 2E** shows the profile map along with the dash lines A, B and C in **Figure 2C**. The maximum phase difference is about 7 rad which can be translated to an optical thickness of 15.89 μm.

1990 holograms of mouse osteoblastic cells are taken with DLHM. Then the phase images are recovered by traditional convolution algorithm. In order to improve the generalization ability of the neural network, data augmentation is a standard method. The dataset including 1990 holograms and corresponding phase images is expanded to 10,000 by flipping, rotating, etc. After that, the holograms and phase images of each cell are used as input and ground truth, respectively. **Figure 3**

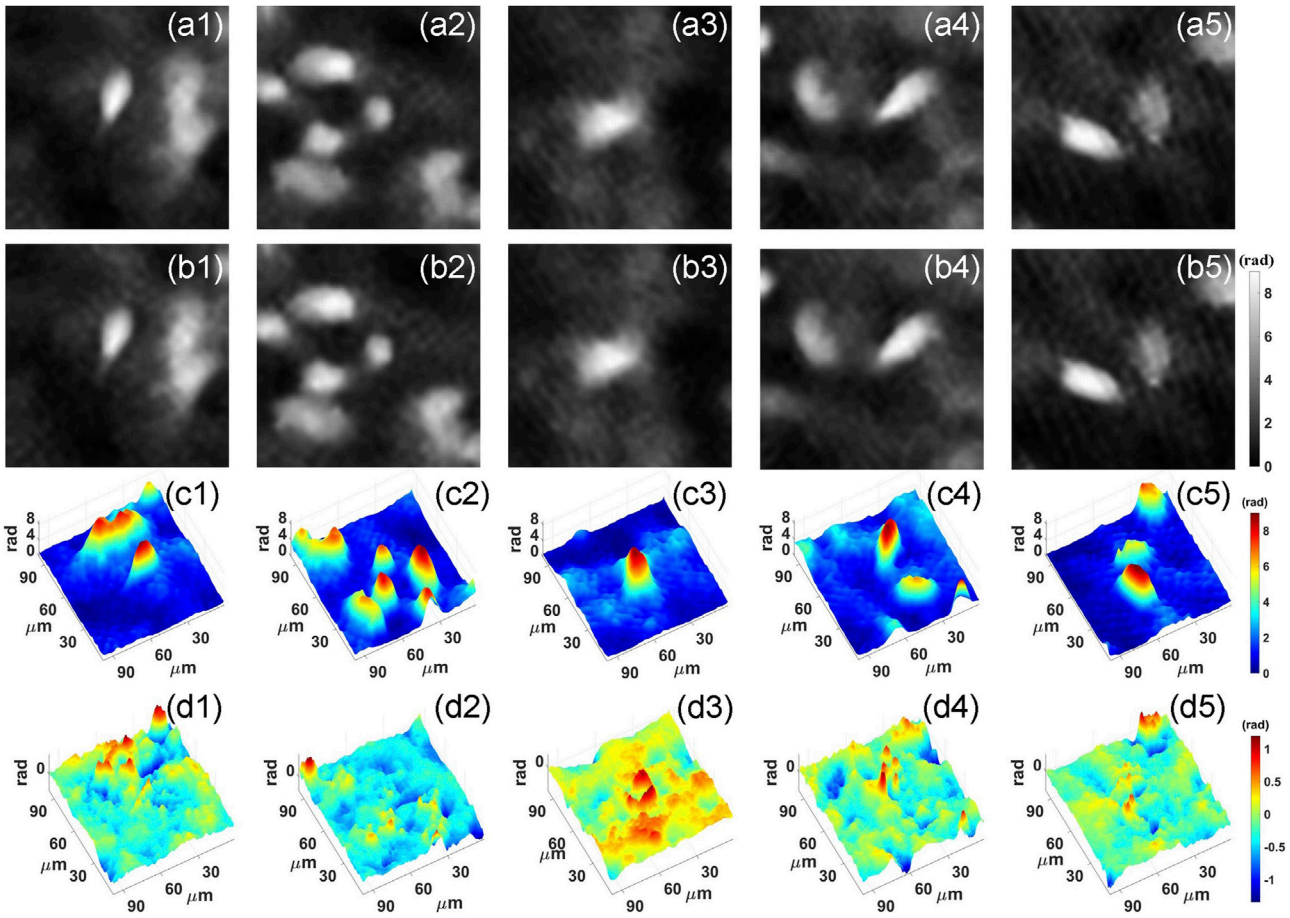

FIGURE 4 | Neural network reconstruction results. **(A)** Ground truth; **(B)** PhaseNet reconstruction result; **(C)** Three-dimensional image of PhaseNet reconstruction result; **(D)** Three-dimensional image of error maps between Ground truth and PhaseNet reconstruction result.

shows part of the dataset. Among all the data, 90% are used for training, 10% for testing. Then we can use the prepared dataset to train the neural network PhaseNet.

As the training progresses, the MSE of the ground truth and the output are back-propagated to the network, and parameters such as weights are updated by gradient descent. After 100 epoch training, the network reaches the convergence state. In the beginning, the loss function drops the fastest, as the epoch progresses, it becomes slower and slower, and the speed is close to zero at 100 epochs.

After training, we feed the holograms in the test set to PhaseNet, and the corresponding phase results are quickly reconstructed. Part of the results is visualized in **Figure 4**. **Figures 4A**,**B** are the ground truth and corresponding reconstruction results, respectively. From the two-dimensional phase images of the cell, we can see that the results of the network reconstruction are very close to the ground truth. More quantitatively, we calculated its structural similarity index measure (SSIM), which is used for measuring the similarity between two images and is a perception-based model that considers image degradation as perceived change in structural information, while also incorporating important perceptual phenomena, including both luminance masking and contrast masking terms. Finally, the SSIM of the phase results obtained using PhaseNet can reach 0. 9404. This shows that PhaseNet can replace traditional algorithms to achieve the numerical reconstruction of holograms. **Figure 4C** shows the three-dimensional phase images of the cells obtained by PhaseNet.

After completing the network training, the deep learning-based holographic microscope is feasible for quantitative phase measurement of living biological cells. It can completely replace the traditional digital holographic microscope for label-free cell imaging. At the same time, due to the use of neural networks, the acquisition of three-dimensional information of specimens can be completed more quickly.

In conclusion, we proposed PhaseNet for the reconstruction of digital holograms, based on which the DLHM is implemented for quantitative phase imaging of biological specimens. In order to verify the capability and applicability of DLHM, we used the living mouse osteoblastic cells as samples to generate dataset and train PhaseNet. The testing results show that the average SSIM index of DLHM can reach 0.9404.

DATA AVAILABILITY STATEMENT

The raw data supporting the conclusions of this article will be made available by the authors, without undue reservation.

AUTHOR CONTRIBUTIONS

JD and JZ conceived and supervised the project. YL and KW performed experiments and data analysis. KW, JW and JT contributed to data analysis. KW, JW and JD wrote the draft of the manuscript; All the authors edited the manuscript.

FUNDING

This work was supported by National Natural Science Foundation of China (NSFC) (62075183, 61927810) and NSAF (U1730137).

REFERENCES

1. Park Y, Depeursinge C, Popescu G. Quantitative phase imaging in biomedicine. *Nat Photon* (2020) 12:578–89. doi:10.1364/cleo_si.2012.ctu3j.5
2. Ahmad A, Dubey V, Singh G, Singh V, Mehta DS. Quantitative phase imaging of biological cells using spatially low and temporally high coherent light source. *Opt Lett* (2016) 41:1554–7. doi:10.1364/ol.41.001554
3. Creath K, Goldstein G. Dynamic quantitative phase imaging for biological objects using a pixelated phase mask. *Biomed Opt Express* (2012) 3:2866–80. doi:10.1364/boe.3.002866
4. Popescu G, Quantitative phase imaging of nanoscale cell structure and dynamics, BP Jena. Quantitative phase imaging of nanoscale cell structure and dynamics. *Methods Cel Biol* (2008) 90:87. doi:10.1016/S0091-679X(08)00805-4
5. Fan X, Healy JJ, O'Dwyer K, Hennelly BM. Label-free color staining of quantitative phase images of biological cells by simulated Rheinberg illumination. *Appl Opt* (2019) 58:3104–14. doi:10.1364/ao.58.003104
6. Doblas A, Sanchez-Ortiga E, Martinez-Corral M, Saavedra G, Garcia-Sucerquia J. Accurate single-shot quantitative phase imaging of biological specimens with telecentric digital holographic microscopy. *J Biomed Opt* (2014) 19:29. doi:10.1117/1.jbo.19.4.046022
7. Marquet P, Rappaz B, Magistretti PJ, Cuche E, Emery Y, Colomb T, et al. Digital holographic microscopy: a noninvasive contrast imaging technique allowing quantitative visualization of living cells with subwavelength axial accuracy. *Opt Lett* (2005) 30:468–70. doi:10.1364/ol.30.000468
8. Rong L, Latychevskaia T, Chen C, Wang D, Yu Z, Zhou X, et al. Terahertz in-line digital holography of human hepatocellular carcinoma tissue. *Scientific Rep* (2015) 5:33. doi:10.1038/srep08445
9. Gao P, Yao B, Min J, Guo R, Ma B, Zheng J, et al. Autofocusing of digital holographic microscopy based on off-axis illuminations. *Opt Lett* (2012) 37:3630–2. doi:10.1364/ol.37.003630
10. Ma J, Yuan C, Situ G, Pedrini G, Osten W. Resolution enhancement in digital holographic microscopy with structured illumination. *Chin Opt Lett* (2013) 11:124. doi:10.3788/col201311.090901
11. Guo R, Yao B, Gao P, Min J, Zhou M, Han J, et al. Off-axis digital holographic microscopy with LED illumination based on polarization filtering. *Appl Opt* (2013) 52:8233–8. doi:10.1364/ao.52.008233
12. Gao P, Pedrini G, Osten W. Structured illumination for resolution enhancement and autofocusing in digital holographic microscopy. *Opt Lett* (2013) 38:1328–30. doi:10.1364/ol.38.001328
13. Weng J, Zhong J, Hu C. Digital reconstruction based on angular spectrum diffraction with the ridge of wavelet transform in holographic phase-contrast microscopy. *Opt Express* (2008) 16:21971–81. doi:10.1364/oe.16.021971
14. Di J, Li Y, Xie M, Zhang J, Ma C, Xi T, et al. Dual-wavelength common-path digital holographic microscopy for quantitative phase imaging based on lateral shearing interferometry. *Appl Opt* (2016) 55:7287–93. doi:10.1364/ao.55.007287
15. Min J, Yfao B, Ketelhut S, Engwer C, Greve B, Kemper B. Simple and fast spectral domain algorithm for quantitative phase imaging of living cells with digital holographic microscopy. *Opt Lett* (2017) 42:227–30. doi:10.1364/ol.42.000227
16. Zhong Z, Zhao HJ, Cao LC, Shan MG, Liu B, Lu WL, et al. Automatic cross filtering for off-axis digital holographic microscopy. *Results Phys* (2020) 16:6. doi:10.1016/j.rinp.2019.102910
17. Di J, Li Y, Wang K, Zhao J. Quantitative and dynamic phase imaging of biological cells by the use of the digital holographic microscopy based on a beam displacer unit. *IEEE Photon J* (2018) 10(4):6900510. doi:10.1109/jphot.2018.2839878
18. Wang K, Li Y, Kemao Q, Di J, Zhao J. One-step robust deep learning phase unwrapping. *Opt Express* (2019) 27:15100–15. doi:10.1364/oe.27.015100
19. Rivenson Y, Zhang Y, Gnaydin H, Teng D, Ozcan A. Phase recovery and holographic image reconstruction using deep learning in neural networks. *Light-Science Appl* (2018) 7:127. doi:10.1038/lsa.2017.141
20. Wang K, Di J, Li Y, Ren Z, Kemao QJ. Transport of intensity equation from a single intensity image via deep learning. *Opt Lasers Eng* (2020) 134:106233. doi:10.1016/j.optlaseng.2020.106233
21. Zhao F, Bian Y, Wang H, Lyu M, Pedrini G, Osten W, et al. Phase imaging with an untrained neural network. *Light-Science Appl* (2020) 9:127. doi:10.1038/s41377-020-0302-3
22. Zhou W-J, Guan X, Liu F, Yu Y, Zhang H, Poon T-C, et al. Phase retrieval based on transport of intensity and digital holography. *Appl Opt* (2018) 57:A229–A234. doi:10.1364/ao.57.00a229
23. Rivenson Y, Wu Y, Ozcan A. Deep learning in holography and coherent imaging. *Light-Science Appl* (2019) 8:44. doi:10.1038/s41377-019-0196-0
24. Wang K, Dou J, Kemao Q, Di J, Zhao J. Y-Net: a one-to-two deep learning framework for digital holographic reconstruction. *Opt Lett* (2019) 44:4765–8. doi:10.1364/ol.44.004765
25. Wang K, Kemao Q, Di J, Zhao J. Y4-Net: a deep learning solution to one-shot dual-wavelength digital holographic reconstruction. *Opt Lett* (2020) 45:4220–3. doi:10.1364/ol.395445
26. Yan K, Yu Y, Huang C, Sui L, Qian K, Asundi A. Fringe pattern denoising based on deep learning. *Opt Commun* (2019) 437:148–52. doi:10.1016/j.optcom.2018.12.058
27. Ren Z, So HK-H, Lam EY. Fringe pattern improvement and super-resolution using deep learning in digital holography. *IEEE Trans Ind Inf* (2019) 15:6179–86. doi:10.1109/tii.2019.2913853
28. Di J, Zhao J, Sun W, Jiang H, Yan X. Phase aberration compensation of digital holographic microscopy based on least squares surface fitting. *Opt Commun* (2009) 282(19):3873–7. doi:10.1016/j.optcom.2009.06.049
29. Sun W, Zhao J, Di J, Wang Q, Wang L. Real-time visualization of Karman vortex street in water flow field by using digital holography. *Opt Express* (2009) 17(22):20342–8. doi:10.1364/oe.17.020342
30. Di J, Yu Y, Wang Z, Qu W, Cheng CY, Zhao J. Quantitative measurement of thermal lensing in diode-side-pumped Nd:YAG laser by use of digital holographic interferometry. *Opt Express* (2016) 24(25):28185–93. doi:10.1364/oe.24.028185
31. He K, Zhang X, Ren S, Sun J. Deep residual learning for image recognition. *IEEE Conf. Comput. Vis. Pattern Recognit* (2016) 14:770–8. doi:10.1109/cvpr.2016.90

Conflict of Interest: The authors declare that the research was conducted in the absence of any commercial or financial relationships that could be construed as a potential conflict of interest.

frontiers in Physics

MINI REVIEW
published: 26 March 2021
doi: 10.3389/fphy.2021.654868

Improving the Way We See: Adaptive Optics Based Optical Microscopy for Deep-Tissue Imaging

Pranoy Sahu[1] *and Nirmal Mazumder*[2]*

[1] Insitute of Biochemistry and Cell Biology, National Research Council, Naples, Italy, [2] Department of Biophysics, Manipal School of Life Sciences, Manipal Academy of Higher Education, Manipal, India

With the recent developments in optical imaging tools and techniques, scientists are now able to image deeper regions of the tissue with greater resolution and accuracy. However, light scattering while imaging deeper regions of a biological tissue remains a fundamental issue. Presence of lipids, proteins and nucleic acids in the tissue makes it inhomogeneous for a given wavelength of light. Two-photon fluorescence (TPF) microscopy supplemented with improved invasive optical tools allows functional imaging in awake behaving mammals in an unprecedented manner. Similarly, improved optical methods conjugated with previously existing scanning laser ophthalmoscopy (SLO) has paved diffraction-limited retinal imaging. With the evolving technology, scientists are now able to resolve biological structures and function at the sub-cellular level. Wavefront correcting methods like adaptive optics (AO) has been implemented in correcting tissue or optical-based distortions, shaping the excitation beam in 3D-holography to target multiple neurons. And more recently, AO-based SLO is implemented for eye imaging both in research and clinical settings. In this review, we discuss some of the recent improvements in TPF microscopy with the application of AO for wavefront corrections and its recent application in brain imaging as well as ophthalmoscopy.

Keywords: adaptive optics, two-photon fluorescence, ophthalmoscopy, tissue imaging, brain

OPEN ACCESS

Edited by:
Vicente Micó,
University of Valencia, Spain

Reviewed by:
Jianming Wen,
Kennesaw State University, United States
Venugopal Rao Soma,
University of Hyderabad, India

***Correspondence:**
Nirmal Mazumder
nirmaluva@gmail.com

Specialty section:
This article was submitted to Optics and Photonics, a section of the journal Frontiers in Physics

Received: *17 January 2021*
Accepted: *03 March 2021*
Published: *26 March 2021*

Citation:
Sahu P and Mazumder N (2021) Improving the Way We See: Adaptive Optics Based Optical Microscopy for Deep-Tissue Imaging. Front. Phys. 9:654868. doi: 10.3389/fphy.2021.654868

INTRODUCTION

In confocal microscopy the 3D resolution is mainly achieved from the light originating from focus and not from the scattered light, a common problem associated mainly while imaging deep tissues [1–3]. Light scattering could be reduced using longer excitation wavelengths [4–6], however, it is limited to certain wavelengths. Linear (one-photon) excitation microscopy is mainly suited for near-surface ($<100\,\mu m$) imaging. While non-linear (two-photon fluorescence) microscopy provides the advantage of imaging brain regions $>100\,\mu m$ with minimal scattering and better resolution. Deep tissue imaging at the single-cell level has provided adequate information on synaptic activity and function. **Table 1** compares the with and without adaptive optics based confocal and two photon fluorescence microscopy. Conventional functional visualization neuroimaging techniques such as magnetic resonance imaging (MRI), positron emission tomography (PET), computerized tomography (CT) is currently used for imaging the human brain *in vivo* are usually expensive and have a poor spatial and temporal resolution [7]. The improvements in the optical approach have developed techniques that allow non-labeled imaging of tissues with high sensitivity, specificity, and spatial resolution under *in vivo* and *in vitro* conditions. Non-linear microscopy, in particular, TPF supplemented by the recent advances in optical labeling of deep tissues has become the method

TABLE 1 | Comparison of microscopy techniques with and without Adaptive optics.

	Confocal Microscopy	TPF-AO Microscopy
Principle	• Focuses excitation light to the diffraction-limited spot. • A detector uses a pinhole to collect only focussed signal photon and not out-of-focus photons.	• In AO based TPM, aberration for the excitation light is corrected (direct or indirect AO) since imaging performance depends on the quality of excitation focus.
Imaging depth	• Applicable for thin specimens or near surface tissue regions (<100 μm)	• Can be applicable for imaging much deeper regions when used with Ti:Al_2O_3 regenerative amplifier (up to 1,000 μm)
Sample type	• Mostly applicable for less scattering samples like monolayer cultures	• Due to use of less-scattering long wavelength light, it is widely applicable for imaging deeper brain regions
Advantages	• Sensitivity of fluorescence detection is very high in presence of non-fluorescent molecules • It is best suited for gaining cellular level information from monolayer cultures	• Captures even out-of-focus photons emanating from the specimen thereby increasing fluorescence sensitivity • Best suitable for deep tissue imaging as the type of aberration due to tissue heterogeneity can be corrected • Applicable for imaging heterogeneously labeled neuronal circuits
Limitations	• Only ballistic photons from the specimen arrives the detector. • Tissue elucidation from deeper regions (>100 μm) of the brain is limited mainly by the penetration of the exciting laser caused by scattering from tissue heterogeneity	• The increase in excitation necessary to compensate for signal loss compared to fluorescence microscopy further leads to photobleaching and photodamage. • Not applicable for studying complex brain functions in live behaving mammals

of choice for imaging intact tissues and live animals [4, 5, 8]. Principally, the TPF technique utilizes near-infrared wavelength and ultrashort pulses where the interaction of two photons usually of higher-order is responsible for contrast generation [9, 10]. Due to its high fluorescence intensity and depth resolution [2], TPF has drawn substantial attention for the study of deeper structures and vital functions of the brain and eye. Indeed, TPF coupled with fluorescence lifetime imaging (FLIM) has shown promising data on vitamin A metabolism in the eye to study the early onset of retinal diseases [11]. Owing to the heterogeneity of biological samples under investigation and the optical setup used, wavefront distortions limit the fluorescence signal-to-noise ratio and resolution with increasing depth [12]. AO based TPF overcomes such a loss in resolution by detecting and correcting the type of wavefront aberration generated while imaging scattering samples [13]. In the following sections, we will discuss some of the applications of AO in TPF based brain imaging.

Over the past decades, there have been great improvements in the field of ophthalmoscopy which has not only allowed scientists to successfully resolve fine retinal structures but also improved the clinical interventions for different eye diseases. This was mainly possible from the development of optical systems and recent advances in aberration correcting systems. However, when augmented with existing ophthalmoscopes such as conventional fundus imaging, SLO and spectral domain-optical coherence tomography (SD-OCT), AO enhances both structural and functional retinal imaging. First developed by David Williams and coworkers at the University of Rochester, AO-fundus imaging was used to overcome wavefront aberrations in <0.5 s and to obtain dynamic correction of fluctuations in Zernike mode [14]. SLO was first applied in the 1980s and is known to be the method of choice for clinical imaging with superior contrast and resolution. In SLO, retinal images are generated over time by measuring the scattered light as the focused beam scans across the retina surface. SLO provides enhanced image contrast mainly due to the "confocality" wherein light not originating from focus is rejected *via* a pinhole. Reflectance imaging is an application of SLO where the scattered light within an optically aberrated biological sample like an eye is measured. Such a technique, when used along with different wavelength lasers, could be used in clinical settings for multicolour imaging like fundus autofluorescence (FAF) [15]. Although, being routinely used in clinical imaging of the eye, contrast and depth of imaging obtained in conventional SLO methods are limited. In the later part of the review, we highlight some of the recent advances in AO based retinal imaging.

Optical imaging is the foremost important method of choice for imaging biological specimens. With the recent developments in optical methods, three-dimensional and highly resolved structures from biological samples can be achieved. One of the limitations of deep brain imaging is the scattering of light through the heterogeneous tissues, which affects the penetration depth and image resolution. The advances in the TPF microscopy techniques provide a powerful tool for overcoming scattering of light, for *in vivo* neuro-imaging with sub-cellular resolution, endogenous contrast specificity, pinhole less optical sectioning capability, high penetration depth, and so on. The NIR light source is usually the choice for excitation source as it avoids water absorption, thus, reducing photo-bleaching and photo-toxicity in the biological optical window, and also increases the penetration depth within the thick tissue [2, 3, 16]. Ability to image deeper brain regions with the single-cell resolution has refined the establishment of synaptic activity and its functions. The high fluorescence intensity and depth resolution assist in studying the structure and vital functions of the brain.

An optical system incorporates three major components, the laser system (pulsed), optical modalities (lenses, mirrors and objective etc.) and the specimen under investigation. Each of these components contributes toward the optical aberrations which in turn affects the imaging time and resolution. Although using aberration-corrected optical components reduce the imaging limitations when scanning deeper regions of a biological specimen, sample induced aberrations and scattering yet remains substantial. One such tool very quickly realized and

implemented in optical imaging of biological samples is AO. For thick biological specimens, the optical signal strength reduces due to the aberration caused by the scattering medium (sample) and optical components used in the system [17, 18]. The ability to correct the aberration and improve the signal strength has been demonstrated using adaptive optics integrated into a wavefront sensor (WS) or sensor-less AO [19]. In the case of sensor-based AO, a WS estimates the aberration present in the imaging system and either a liquid crystal spatial light modulator (LC-SLM) or deformable membrane mirror membrane (DMM) corrects the aberration. Whereas, in sensor-less AO, the wavefront of the excitation beam is modulated and the optimal wavefront is determined through quantifying the properties of the acquired image in the form of intensity or sharpness in a feedback loop [18]. Sensorless corrections have particularly suffered from long optimization time and the introduction of fluorescent fiducial markers. In the following sections, we will briefly discuss the applications of AO in biological imaging using TPF and SLO.

APPLICATION OF TPF-AO IN BIOLOGICAL IMAGING

AO in Brain Imaging

Biological information from 3D structures such as the mammalian brain has consistently intrigued scientists over decades. However, it is quite challenging to achieve higher-resolution images with optimum spatial and temporal resolution. Light from deeper regions of the brain often suffers aberration due to tissue heterogeneity or the optical setup. In recent years, scientists have successfully measured and overcome such aberrations using special optical elements, such as a deformable mirror (DM) or liquid crystal spatial light modulators (LC-SLM), along with Shack-Hartmann wavefront sensor (SH-WS) [20–22]. Wavefront distortions could be corrected directly by measuring the wavefront of the emanating signals using WS and SLM before allowing it to enter the detector [19, 23]. Direct wavefront corrections serve well for *in vitro* cell models or transparent samples due to an ample amount of unscattered light reaching the wavefront sensor. More recently, a multi-actuator based adaptive lens (AL) was implemented in specimens derived from wavefront corrections [24]. Comparing the image quality between SLM based multiphoton imaging and AL-based imaging, Bueno and colleagues demonstrated an alternative AO-based approach to improve two-photon deep-tissue imaging. DM and LC-SLM used for wavefront correction when combined with algorithms provide ample opportunities for scientists to obtain better images using TPF. AO based TPF is a versatile tool that not only improves the optical distortions but can improve the image quality from sparsely labeled samples at greater depths. Recently, Champelovier *et al.* demonstrated that AO can be applied to heterogeneously labeled cell populations such as CA1 neurons of the hippocampus to measure neuronal activity effectively. Using axial-lock modality authors were able to measure neuronal activity from hippocampal neurons that were conveniently filtered based on low or high fluorescence intensity [18]. Liu et al. investigated *in vivo* TPF imaging of fine dendritic structures in deep cortical layers of adult mice making use of a closed cranial window and a two-photon microscope. The full AO correction of TPF images of neurons with a yellow fluorescent protein (YFP) (Thy1-YFP SLICK A mice) was obtained at a depth of 690 and 770 μm below the pia mater in the brain. This method efficiently corrects all aberrations including that of the microscope, cover glass, and brain tissue [25]. TPF serves as a valuable tool for the analysis of neuronal structures and functions, like long term potentiation, calcium signaling pathway, microglial movement, calcium dysregulation, synaptic plasticity, etc., which can all be used to study neurodegenerative disorders such as AD. TPM supplemented with improved invasive optical tools further allows imaging in awake behaving mammals in an unprecedented manner [4, 5]. Use of high numerical aperture GRIN lens along with TPF-AO allows resolving minute synaptic structures from CA1 hippocampal neurons enabling recovery of diffraction-limited resolution. Moreover, AO based TPF enabled simultaneous calcium imaging from different hippocampal cells with a greater spatiotemporal resolution [26]. Two-photon Ca^{2+} imaging with the subcellular and temporal resolution is an important platform providing neuroscientists to visualize the cellular changes upon brain stimulation. To achieve greater resolution while imaging complex brain regions in brain slices or live mammals are challenging. Indeed, AO based TPF has been applied for Ca^{2+} imaging in live animals or fixed samples.

AO corrections have shown to improve *in vivo* Ca^{2+} imaging for monitoring neural activity [27]. Ca^{2+} imaging of neurons in the primary visual cortex of the mouse brain was performed without and with AO corrections (**Figure 1**) through a cranial window. An increase of 5-fold and 3-fold signal enhancement was observed while imaging fine structures and neuronal functionality, respectively. AO-based TPF benefits the studies of densely packed and labeled neuronal populations due to the ability to improve the signal-to-noise ratio and reduce the excitation volume at a depth. Being able to resolve brain structure and function not only by correcting wavefront distortions with AO but also shaping the excitation beam in 3D (holography) to target different neuronal populations in the intact brain is vital. Using TPF-AO based holography, Yang and Yuste developed a method wherein using SLMs to generate hologram to optically manipulate and image multiple neurons in 3D [21]. In TPF based brain imaging, sequential scanning of a laser beam across the entire sample slows down the imaging speed. This issue could be resolved by computer-generated holograms to image multiple cells at any given time. More importantly, AO can be now applied to achieve a lateral resolution which was not possible before to resolve individual rod and cone cells in the retina.

AO-Based Retinal Imaging

The human eye is an optical system where aberration is generated from the difference between a reference wavefront and an actual wavefront from every individual point on the pupil [28]. Since the human eye suffers from optical monochromatic aberrations, developing optical strategies to enhance the spatial resolution in retinal imaging became inevitable. Some of the early *in vivo* retinal imaging techniques were based on spectral and directional reflectance averaged 1–2 degrees of the retina which allowed

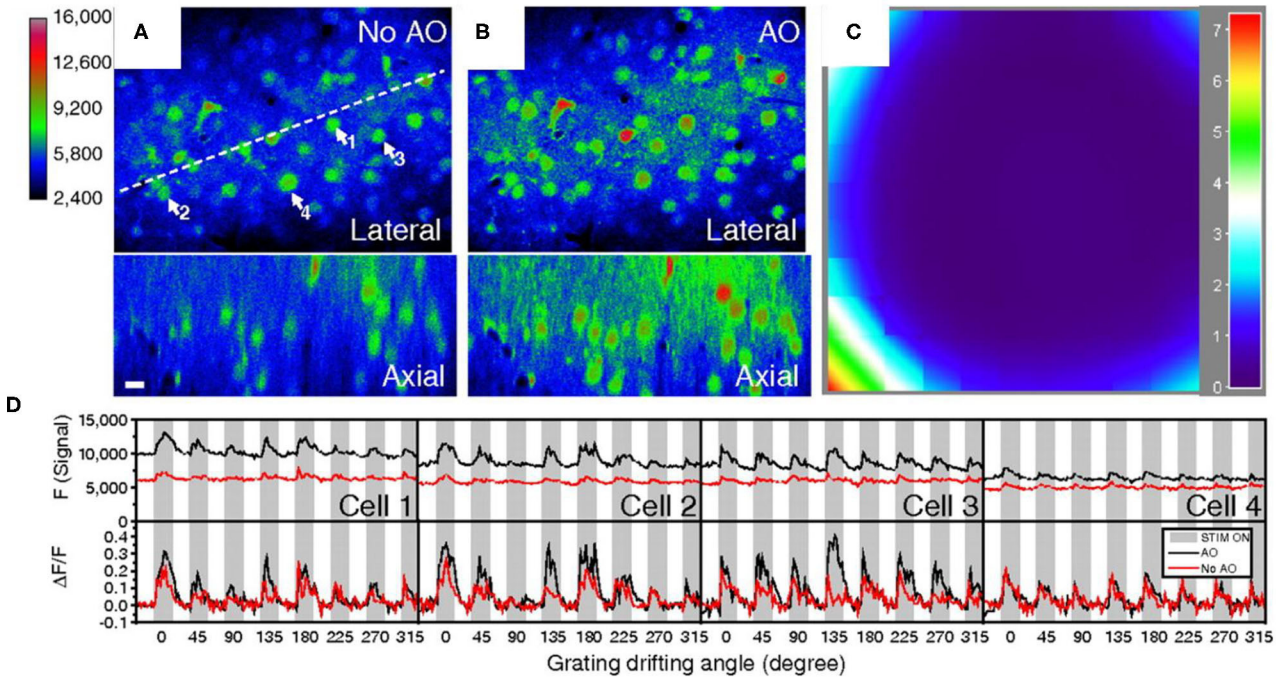

FIGURE 1 | Adaptive optics (AO) based image correction *in vivo*. **(A)** Two photon fluorescence lateral and axial images of OGB-1 AM labeled neurons at 155 μm below the brain surface in absence of AO correction. **(B)** With AO correction. **(C)** Shows the measured aberration of excitation wavelength. **(D)** Fluorescence signal (black) and its percentage change (red) for four cells indicated in Figure **(A)** without and with AO correction. Time periods are denoted wit gray bars. Black-and-white gratings drift in eight different directions, from left to right, 0, 45, 90, 135, 180, 225, 270, and 315°. This image is adapted with permission from [27].

studying structural and physiological aspects of the retina [29]. The first imaging modality developed to study retinal reflectance was the use of multi-wavelength video reflectometers [30] and scanning laser ophthalmoscopes developed by Robert Webb and coworkers [31]. Direct imaging of the retina at the cellular level (restricted only to sparsely distributed cones) was possible with a basic flood illuminated fundus camera. However, to achieve images of rods and cones with greater resolution from a broader population was only possible through AO based optical corrections. The first evidence of AO based retinal imaging came from a group in Heidelberg where SLO was previously developed [32]. Using deformable mirrors along with SLO, scientists were able to obtain much improved retinal images. Although the resolution generated by conventional SLO is hindered by the ocular aberrations, AO-SLO is the method of choice for overcoming ocular generated wavefront aberrations to enhance the imaging resolution of the mammalian eye (**Figure 2**). Conventional fundus imaging techniques such as fundus fluorescein angiography (FFA), optical coherence tomography (OCT) and fundus autofluorescence are insufficient in resolving fine structures like individual rods and cones or vessel and capillaries [34]. AO-SLO overcomes this limitation to resolve fine structures due to enhanced transverse resolution (∼2.5 μm) while imaging the retina [35]. Studies have shown that while using a 50 μm confocal pinhole axial resolution as low as 71 μm could be achieved [36]. Moreover, the axial and lateral resolution in AO-SLO can be refined by adjusting the pinhole size of the system. Owing to its confocal nature, AO-SLO is widely used for visualizing different layers within the retina such as photoreceptors, nerve fibers, retinal pigment epithelium (RPE) [37].

Retinal ganglion cells are the primary cells that process visual information and conveys it to the brain. In clinical settings, loss or death of ganglion cells is the major cause of glaucoma. AO-SLO provides a crucial imaging modality thus improving retinal ganglion cell imaging both for research and clinical purposes in a non-invasive manner [35]. Split-detector is a modality used in AO-SLO to image retinal structures such as rods and cones in the living eye of the patient and healthy control [38]. Alternatively, *in vivo* TPF used for functional retinal imaging has turned out to be an important tool to study individual retinal cells in primates when supplemented with an AO-based ophthalmoscope. It is now evident that TPF-AO-SLO could be implemented to detect fluorescence from retinal cells of a live animal with minimal photodamage to the fundus [39]. Thus, the AO based SLO approach is now widely applied for studying and monitoring age-related macular degeneration and vascular diseases with ease (reviewed elsewhere by [40]). Pinhas et al., applied AO-SLO in combination with both oral (7 mg/mL) and intravenous (500 mg) fluorescein to investigate microvasculature in humans at different retinal depths [41]. This study, one of many shows the clinical application of AO-SLO in improved lateral resolution to resolve fine retinal capillaries (average eye focal length of ∼17 mm; pupil diameter of 7.75 mm and axial resolving limit of 20 μm).

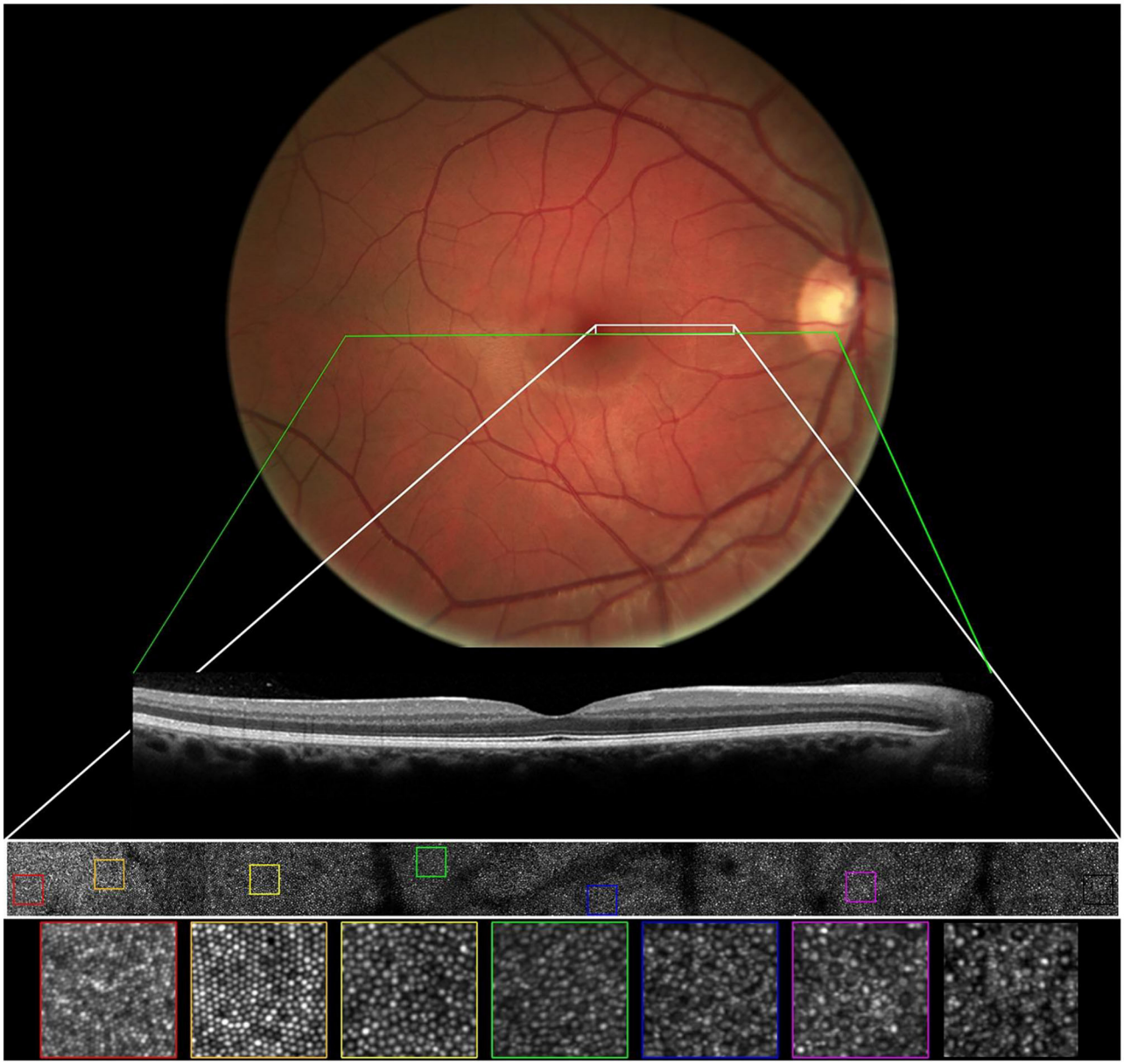

FIGURE 2 | Comparison of a conventional fundus photograph. SD-OCT cross sectional image obtained (green line) was overlaid on the fundus photograph and a montage of confocal AO-SLO images acquired (white box) was overlaid on the fundus image in the right eye of a 31 year old normal male. Magnified photoreceptor mosaic images from AO-SLO montage has been represented in colored boxes. This images has been adapted from [33] with permission.

AO-based OCT on the other hand is a label-free technique that improves lateral resolution ($\sim 4\,\mu m$) of the human eye while maintaining axial resolution ($\sim 6\,\mu m$) of the OCT alone. Huang and colleagues first showed the application of OCT in optical sectioning of biological samples such as the retina, which thereafter revolutionized the ophthalmoscopy field [42]. Importantly, in AO-OCT the axial and lateral resolution are decoupled, unlike SLO. The axial resolution of OCT is theoretically limited by the coherence properties of the imaging light source. As the human eye suffers from significant longitudinal aberration, i.e., different wavelengths focus on different planes, AO provides a way out to improve lateral resolution and sensitivity of OCT [43]. Such an improvement within the optical system has been widely used in 3D-imaging of photoreceptors and other cellular components within the retina [44, 45]. Recently, a group from the School of Engineering Science in Canada implemented sensorless adaptive optics (SAO) guided by low-coherence gated OCT to improve two-photon excitation fluorescence image brightness and sharpness of mouse retina *in vivo* [46]. Using low-coherence guided optical plane

selection, scientists were able to optimize the system in 60 s followed by TPF image acquisition at 100 ms per frame. A short optimisation protocol and improved image quality after aberration correction allowed imaging mouse retina *in vivo* in an unprecedented manner. Such AO based applications of optical imaging modalities are now paving their way into clinical settings to better understand the biological processes involved in disease generation and eventually improving existing therapeutic interventions.

CONCLUSION AND FUTURE PERSPECTIVES

The introduction of AO-based optical imaging has greatly improved deep-tissue imaging which was previously unattainable using conventional optical imaging microscopes. Since its usage in correcting atmospheric aberrations in telescopes, AO-based optical imaging has now paved its way into biological imaging. With AO, the diffraction-limited resolution could be easily achieved by correcting deep-tissue mediated aberrations. More importantly, the technology has improved the imaging quality and speed at which fine structural and functional aspects of living biological samples can be studied. The direct wavefront corrections (using SH wavefront sensors) provides a rapid and effective imaging modality compared to indirect wavefront sensing methods. Although the latter could be easily applied to any existing microscopes and is suitable for both scattering and transparent samples. Imaging deeper regions within a biological tissue have mostly been overcome by the implementation of AO based corrections. Although imaging complex neuronal populations with an AO-based optical system needs further improvements, there has been considerable improvement in retinal imaging irrespective of the differences arising from refractive index or age. Yet, imaging deeper neuronal populations with enhanced spatial-temporal resolution in a freely moving animal remain challenging. While recording neural activity in awake animals, brain movement remains a serious concern and are corrected by post image processing of 2D images. However, this approach is slow and cannot correct axial movements in a small region of interest and photostimulation. In 2016 Nadella and coworkers developed a 3D random-access two-photon laser scanning microscope using a rapid closed-loop system and acousto-optic lens (AOL). This system improves motion-mediated artifacts and monitors real-time 3D brain tissue movement at up to 1 kHz with submicrometer spatial resolution in behaving mice and zebrafish [47]. In another study, a compact AOL two-photon microscope was used for high-speed line scanning within an imaging volume at 35–50 kHz up to hundreds of micrometers. It was able to monitor cerebellar interneurons sparsely distributed neuronal activity over large depth ranges in awake animals [48].

Miniaturized fluorescence microscopes or miniscopes are becoming a key tool in neuroscience research owing to their high-resolution deep brain imaging in freely behaving animals. Owing to their lightweight, miniscopes utilizing one-photon or two-photon excitation modalities have been reported in the study of cellular activity when coupled to a freely moving animal [49, 50]. Miniscopes provides convenient *in vivo* deep-tissue imaging in an awake free moving animal due to, *i)* it's decreased footprint and weight *ii)* easy mounting on small animals *iii)* ability to record multiple neuronal activities simultaneously, thereby aiding in better understanding inter-regional signaling in behaving animal models [51].

Two-photon microscopy serves as a method of choice over conventional microscopy techniques for deep-tissue imaging. However, due to the scattering of ballistic photons from deeper samples, an optical method that could limit photon loss is necessary. TPF augmented with AO provides the advantage of limiting photon loss from deep biological samples such as the human brain [3] and eye [35]. AO-TPF has been incorporated in neurobiology and ophthalmology labs across the globe to achieve diffraction-limited contrast in biological imaging [14, 52, 53]. The use of AO-based optical imaging in ophthalmology has greatly changed the way we see the human eye both at the cellular and metabolic level. Integrating sensorless AO along with dispersion compensation of ultrashort laser pulse can improve TPF intensity of endogenous retinal fluorophores. Indeed, the use of ultrashort laser (20-fs pulse) did not show any modifications in function as well as the structure of the retina *in vivo*. Interestingly, the broad bandwidth of short pulses excites multiple fluorophores which provides better applications while studying cellular metabolism [11]. AO-based ophthalmoscopes also provide a platform to study several genetic diseases of the eye. AO-SLO has not only improved eye imaging but also facilitated its application in clinics for studying and monitoring retina-related conditions such as macular degeneration and Stargardt disease [54]. Above all, with the current advances in the filed of AO and TPF scientists can effortlessly image different regions within the brain or eye of a live organism which was impossible previously. With further improvements in the existing fluorescent probes, AO-based biological imaging modalities would further improve our way of seeing things *in vivo*.

AUTHOR CONTRIBUTIONS

PS wrote the manuscript. NM structure the manuscript and wrote the manuscript. Both authors contributed to the article and approved the submitted version.

FUNDING

NM thank the Department of Science and Technology (DST), Government of India (Project Number - DST/INT/BLG/P-03/2019) for financial support. We thank Manipal School of Life Sciences (MSLS), Manipal Academy of Higher Education (MAHE), Manipal, Karnataka, India, for providing the infrastructure needed. PS thank Euro Bioimaging for the financial support.

REFERENCES

1. Lu L, Gutruf P, Xia L, Bhatti DL, Wang X, Vazquez-Guardado A, et al. Wireless optoelectronic photometers for monitoring neuronal dynamics in the deep brain. *Proc Natl Acad Sci.* (2018) 115:E1374–83. doi: 10.1073/pnas.1718721115
2. Matsumoto N, Inoue T, Matsumoto A, Okazaki S. Correction of depth-induced spherical aberration for deep observation using two-photon excitation fluorescence microscopy with spatial light modulator. *Biomed Opt Expr.* (2015) 6:2575–87. doi: 10.1364/BOE.6.002575
3. Helmchen F, Denk W. Deep tissue two-photon microscopy. *Nat Methods.* (2005) 2:932–40. doi: 10.1038/nmeth818
4. Barretto RP, Ko TH, Jung JC, Wang TJ, Capps G, Waters AC, et al. Time-lapse imaging of disease progression in deep brain areas using fluorescence microendoscopy. *Nat Med.* (2011) 17:223–8. doi: 10.1038/nm.2292
5. Resendez SL, Stuber GD. *In vivo* calcium imaging to illuminate neurocircuit activity dynamics underlying naturalistic behavior. *Neuropsychopharmacology.* (2015) 40:238. doi: 10.1038/npp.2014.206
6. Nimmerjahn A, Kirchhoff F, Helmchen F. Resting microglial cells are highly dynamic surveillants of brain parenchyma *in vivo*. *Science.* (2005) 308:1314–8. doi: 10.1126/science.1110647
7. Ross CA, Poirier MA. Protein aggregation and neurodegenerative disease. *Nat Med.* (2004) 10:S10–7. doi: 10.1038/nm1066
8. Mertz J, Nonlinear microscopy: new techniques and applications. *Curr Opin Neurobiol.* (2004) 14:610–6. doi: 10.1016/j.conb.2004.08.013
9. Periasamy A, Mazumder N, Sun Y, Christopher KG, Day RN. *FRET Microscopy: Basics, Issues and Advantages of FLIM-FRET Imaging, Advanced Time-Correlated Single Photon Counting Applications*. Cham: Springer (2015). p. 249–76. doi: 10.1007/978-3-319-14929-5_7
10. Mazumder N, Lyn RK, Singaravelu R, Ridsdale A, Moffatt DJ, Hu C-W, et al. Fluorescence lifetime imaging of alterations to cellular metabolism by domain 2 of the hepatitis C virus core protein. *PLoS ONE.* (2013) 8:e66738. doi: 10.1371/journal.pone.0066738
11. Palczewska G, Stremplewski P, Suh S, Alexander N, Salom D, Dong Z, et al. Two-photon imaging of the mammalian retina with ultrafast pulsing laser. *JCI Insight.* (2018) 3:e121555. doi: 10.1172/jci.insight.121555
12. Sahu P, Mazumder N. Advances in adaptive optics–based two-photon fluorescence microscopy for brain imaging. *Lasers Med Sci.* (2020) 35:317–28. doi: 10.1007/s10103-019-02908-z
13. Débarre D, Botcherby EJ, Watanabe T, Srinivas S, Booth MJ, Wilson T. Image-based adaptive optics for two-photon microscopy. *Opt Lett.* (2009) 34:2495–7. doi: 10.1364/OL.34.002495
14. Hofer H, Chen L, Yoon G-Y, Singer B, Yamauchi Y, Williams DR. Improvement in retinal image quality with dynamic correction of the eye's aberrations. *Opt Express.* (2001) 8:631–43. doi: 10.1364/OE.8.000631
15. Calvo-Maroto AM, Esteve-Taboada JJ, Pérez-Cambrodí RJ, Madrid-Costa D, Cerviño A. Pilot study on visual function and fundus autofluorescence assessment in diabetic patients. *J Ophthalmol.* (2016) 2016:1287847. doi: 10.1155/2016/1287847
16. Lu J, Li C, Singh-Alvarado J, Zhou ZC, Fröhlich F, Mooney R, et al. MIN1PIPE: a miniscope 1-photon-based calcium imaging signal extraction pipeline. *Cell Rep.* (2018) 23:3673–84. doi: 10.1016/j.celrep.2018.05.062
17. Yang W, Miller J-EK, Carrillo-Reid L, Pnevmatikakis E, Paninski L, Yuste R, et al. Simultaneous multi-plane imaging of neural circuits. *Neuron.* (2016) 89:269–84. doi: 10.1016/j.neuron.2015.12.012
18. Champelovier D, Teixeira J, Conan J-M, Balla N, Mugnier L, Tressard T, et al. Image-based adaptive optics for in vivo imaging in the hippocampus. *Sci Rep.* (2017) 7:42924. doi: 10.1038/srep42924
19. Galwaduge P, Kim S, Grosberg L, Hillman E. Simple wavefront correction framework for two-photon microscopy of in-vivo brain. *Biomed Opt Expr.* (2015) 6:2997–3013. doi: 10.1364/BOE.6.002997
20. Dal Maschio M, Donovan JC, Helmbrecht TO, Baier H. Linking neurons to network function and behavior by wo-photon holographic optogenetics and volumetric imaging. *Neuron.* (2017) 94:774–89.e5. doi: 10.1016/j.neuron.2017.04.034
21. Yang W, Yuste R. Holographic imaging and photostimulation of neural activity. *Curr Opin Neurobiol.* (2018) 50:211–21. doi: 10.1016/j.conb.2018.03.006
22. Yang W, Carrillo-Reid L, Bando Y, Peterka DS, Yuste R. Simultaneous two-photon imaging and two-photon optogenetics of cortical circuits in three dimensions. *Elife.* (2018) 7:e32671. doi: 10.7554/eLife.32671
23. Facomprez A, Beaurepaire E, Débarre D. Accuracy of correction in modal sensorless adaptive optics. *Opt Express.* (2012) 20:2598–612. doi: 10.1364/OE.20.002598
24. Bueno JM, Skorsetz M, Bonora S, Artal P. Wavefront correction in two-photon microscopy with a multi-actuator adaptive lens. *Opt Express.* (2018) 26:14278–87. doi: 10.1364/OE.26.014278
25. Liu R, Li Z, Marvin JS, Kleinfeld D. Direct wavefront sensing enables functional imaging of infragranular axons and spines. *Nat Methods.* (2019) 16:615–8. doi: 10.1038/s41592-019-0434-7
26. Qin Z, He S, Yang C, Yung JS-Y, Chen C, Leung CK-S, et al. Adaptive optics two-photon microscopy enables near-diffraction-limited and functional retinal imaging in vivo. *Light Sci Appl.* (2020) 9:1–11. doi: 10.1038/s41377-020-0317-9
27. Ji N, Sato TR, Betzig E. Characterization and adaptive optical correction of aberrations during in vivo imaging in the mouse cortex. *Proc Natl Acad Sci.* (2012) 109:22–7. doi: 10.1073/pnas.1109202108
28. Venkateswaran N, Galor A, Wang J, Karp CL. Optical coherence tomography for ocular surface and corneal diseases: a review. *Eye Vision.* (2018) 5:1–11. doi: 10.1186/s40662-018-0107-0
29. Delori FC, Noninvasive technique for oximetry of blood in retinal vessels. *Appl Opt.* (1988) 27:1113–25. doi: 10.1364/AO.27.001113
30. Faulkner D, Kemp C. Human rhodopsin measurement using a TV-based imaging fundus reflectometer. *Vision Res.* (1984) 24:221–31. doi: 10.1016/0042-6989(84)90124-X
31. Webb RH, Hughes GW, Pomerantzeff O. Flying spot TV ophthalmoscope. *Appl Opt.* (1980) 19:2991–7. doi: 10.1364/AO.19.002991
32. Dreher AW, Bille JF, Weinreb RN. Active optical depth resolution improvement of the laser tomographic scanner. *Appl Opt.* (1989) 28:804–8. doi: 10.1364/AO.28.000804
33. Morgan JI, The fundus photo has met its match: optical coherence tomography and adaptive optics ophthalmoscopy are here to stay. *Ophthalmic Physiol Opt.* (2016) 36:218–39. doi: 10.1111/opo.12289
34. Zhang B, Li N, Kang J, He Y, Chen X-M. Adaptive optics scanning laser ophthalmoscopy in fundus imaging, a review and update. *Int J Ophthalmol.* (2017) 10:1751. doi: 10.18240/ijo.2017.11.18
35. Rossi EA, Granger CE, Sharma R, Yang Q, Saito K, Schwarz C, et al. Imaging individual neurons in the retinal ganglion cell layer of the living eye. *Proc Natl Acad Sci.* (2017) 114:586–91. doi: 10.1073/pnas.1613445114
36. Romero-Borja F, Venkateswaran K, Roorda A, Hebert T. Optical slicing of human retinal tissue in vivo with the adaptive optics scanning laser ophthalmoscope. *Appl Opt.* (2005) 44:4032–40. doi: 10.1364/AO.44.004032
37. Godara P, Dubis AM, Roorda A, Duncan JL, Carroll J. Adaptive optics retinal imaging: emerging clinical applications. *Optom Vis Sci.* (2010) 87:930. doi: 10.1097/OPX.0b013e3181ff9a8b
38. Sun LW, Johnson RD, Langlo CS, Cooper RF, Razeen MM, Russillo MC, et al. Assessing photoreceptor structure in retinitis pigmentosa and Usher syndrome. *Invest Ophthalmol Vis Sci.* (2016) 57:2428–42. doi: 10.1167/iovs.15-18246
39. Hunter JJ, Masella B, Dubra A, Sharma R, Yin L, Merigan WH, et al. Images of photoreceptors in living primate eyes using adaptive optics two-photon ophthalmoscopy. *Biomed Opt Expr.* (2011) 2:139–48. doi: 10.1364/BOE.2.000139
40. Paques M, Meimon S, Rossant F, Rosenbaum D, Mrejen S, Sennlaub F, et al. Adaptive optics ophthalmoscopy: application to age-related macular degeneration and vascular diseases. *Prog Retin Eye Res.* (2018) 66:1–16. doi: 10.1016/j.preteyeres.2018.07.001
41. Pinhas A, Dubow M, Shah N, Chui TY, Scoles D, Sulai YN, et al. In vivo imaging of human retinal microvasculature using adaptive optics scanning light ophthalmoscope fluorescein angiography. *Biomed Opt Expr.* (2013) 4:1305–17. doi: 10.1364/BOE.4.001305
42. Huang D, Swanson EA, Lin CP, Schuman JS, Stinson WG, Chang W, et al. Optical coherence tomography. *Science.* (1991) 254:1178–81. doi: 10.1126/science.1957169

43. Hermann B, Fernández E, Unterhuber A, Sattmann H, Fercher A, Drexler W, et al. Adaptive-optics ultrahigh-resolution optical coherence tomography. *Opt Lett.* (2004) 29:2142–4. doi: 10.1364/OL.29.002142
44. Zawadzki RJ, Cense B, Zhang Y, Choi SS, Miller DT, Werner JS. Ultrahigh-resolution optical coherence tomography with monochromatic and chromatic aberration correction. *Opt Express.* (2008) 16:8126–43. doi: 10.1364/OE.16.008126
45. Torti C, PovaŽay B, Hofer B, Unterhuber A, Carroll J, Ahnelt PK, et al. Adaptive optics optical coherence tomography at 120,000 depth scans/s for non-invasive cellular phenotyping of the living human retina. *Opt Express.* (2009) 17:19382–400. doi: 10.1364/OE.17.019382
46. Cua M, Wahl DJ, Zhao Y, Lee S, Bonora S, Zawadzki RJ, et al. Coherence-gated sensorless adaptive optics multiphoton retinal imaging. *Sci Rep.* (2016) 6:1–9. doi: 10.1038/srep32223
47. Nadella KNS, Roš H, Baragli C, Griffiths VA, Konstantinou G, Koimtzis T, et al. Random-access scanning microscopy for 3D imaging in awake behaving animals. *Nat Methods.* (2016) 13:1001–4. doi: 10.1038/nmeth.4033
48. Griffiths VA, Valera AM, Lau JY, Roš H, Younts TJ, Marin B, et al. Real-time 3D movement correction for two-photon imaging in behaving animals. *Nat Methods.* (2020) 17:741–8. doi: 10.1038/s41592-020-0851-7
49. Helmchen F, Fee MS, Tank DW, Denk W. A miniature head-mounted two-photon microscope: high-resolution brain imaging in freely moving animals. *Neuron.* (2001) 31:903–12. doi: 10.1016/S0896-6273(01)00421-4
50. Heo CH, Sarkar AR, Baik SH, Jung TS, Kim JJ, Kang H, et al. A quadrupolar two-photon fluorescent probe for in vivo imaging of amyloid-β plaques. *Chem Sci.* (2016) 7:4600–6. doi: 10.1039/C6SC00355A
51. de Groot A, van den Boom BJ, van Genderen RM, Coppens J, van Veldhuijzen J, Bos J, et al. NINscope, a versatile miniscope for multi-region circuit investigations. *Elife.* (2020) 9:e49987. doi: 10.7554/eLife.49987
52. Wang C, Liu R, Milkie DE, Sun W, Tan Z, Kerlin A, et al. Multiplexed aberration measurement for deep tissue imaging in vivo. *Nat Methods.* (2014) 11:1037–40. doi: 10.1038/nmeth.3068
53. Ruminski D, Palczewska G, Nowakowski M, Zielińska A, Kefalov VJ, Komar K, et al. Two-photon microperimetry: sensitivity of human photoreceptors to infrared light. *Biomed Opt Expr.* (2019) 10:4551–67. doi: 10.1364/BOE.10.004551
54. Song H, Rossi EA, Latchney L, Bessette A, Stone E, Hunter JJ, et al. Cone and rod loss in Stargardt disease revealed by adaptive optics scanning light ophthalmoscopy. *JAMA Ophthalmol.* (2015) 133:1198–203. doi: 10.1001/jamaophthalmol.2015.2443

Conflict of Interest: The authors declare that the research was conducted in the absence of any commercial or financial relationships that could be construed as a potential conflict of interest.

frontiers in Physics

ORIGINAL RESEARCH
published: 29 March 2021
doi: 10.3389/fphy.2021.651316

Autofocusing Algorithm for Pixel-Super-Resolved Lensfree On-Chip Microscopy

Yumin Wu[1,2,3,4], *Linpeng Lu*[1,2,3,4], *Jialin Zhang*[1,2,3,4], *Zhuoshi Li*[1,2,3,4] *and Chao Zuo*[1,2,3,4]*

[1] School of Electronic and Optical Engineering, Nanjing University of Science and Technology, Nanjing, China, [2] Jiangsu Key Laboratory of Spectral Imaging and Intelligent Sense, Nanjing University of Science and Technology, Nanjing, China, [3] Smart Computational Imaging Laboratory, Nanjing University of Science and Technology, Nanjing, China, [4] Institute of Smart Computational Imaging, Nanjing University of Science and Technology, Nanjing, China

In recent years, lensfree on-chip microscopy has developed into a promising and powerful computational optical microscopy technique that allows for wide-field, high-throughput microscopic imaging without using any lenses. However, due to the limited pixel size of the state-of-the-art image sensors, lens-free on-chip microscopy generally suffers from low imaging resolution, which is far from enough to meet the current demand for high-resolution microscopy. Many pixel super-resolution techniques have been developed to solve or at least partially solve this problem by acquiring a series of low-resolution holograms with multiple lateral sub-pixel shifting or axial distances. However, the prerequisite of these pixel super-resolution techniques is that the propagation distance of each low-resolution hologram can be obtained precisely, which faces two major challenges. On the one hand, the captured hologram is inherent pixelated and of low resolution, making it difficult to determine the focal plane by evaluating the image sharpness accurately. On the other hand, the twin-image is superimposed on the backpropagated raw hologram, further exacerbating the difficulties in accurate focal plane determination. In this study, we proposed a high-precision autofocusing algorithm for multi-height pixel-super-resolved lensfree on-chip microscopy. Our approach consists of two major steps: individual preliminary estimation and global precise estimation. First, an improved critical function that combines differential critical function and frequency domain critical function is proposed to obtain the preliminary focus distances of different holograms. Then, the precise focus distances can be determined by further evaluating the global offset of the averaged, low-noise reconstruction from all backpropagated holograms with preliminary focus distances. Simulations and experimental results verified the validity and effectiveness of the proposed algorithm.

Keywords: lensfree on-chip imaging, autofocusing, super-resolution, phase retrieval, computational imaging

OPEN ACCESS

Edited by:
Peng Gao,
Xidian University, China

Reviewed by:
Shaohui Zhang,
Beijing Institute of Technology, China
Lihong Ma,
Zhejiang Normal University, China

***Correspondence:**
Chao Zuo
zuochao@njust.edu.cn

Specialty section:
This article was submitted to Optics and Photonics, a section of the journal Frontiers in Physics

Received: *09 January 2021*
Accepted: *03 March 2021*
Published: *29 March 2021*

Citation:
Wu Y, Lu L, Zhang J, Li Z and Zuo C (2021) Autofocusing Algorithm for Pixel-Super-Resolved Lensfree On-Chip Microscopy. Front. Phys. 9:651316. doi: 10.3389/fphy.2021.651316

1. INTRODUCTION

In recent years, high-resolution wide-field optical imaging has become a valuable tool in various biomedical applications such as cell counting [1], cell morphology measurement [2], and optical microscopy techniques that require low-cost and compact imaging systems [3–5]. Nevertheless, it is difficult for traditional microscopic imaging technology to satisfy the large field-of-view and high-resolution at the same time. The recently developed lensfree on-chip microscopy provides a new opportunity to process high-resolution and large field-of-view images, which has the advantages of small size, low cost, and excellent performance [6–14]. Lensfree on-chip microscopy reconstructed the image of a specimen based on the interference patterns created by the diffracted object. To achieve wide-field imaging, the samples are placed as close as possible to the imaging sensor [13, 14]. In this case, the resolution of the reconstructed image is limited by the pixel size of the sensor instead of the system numerical aperture, which results in the system resolution does not meet the needs of current applications. In order to solve this problem, super-resolution algorithms that process a series of low-resolution holograms have been applied to lensfree imaging [15–18]. Many related studies have been proposed and can be classified as: two-dimensional movement of light sources by mechanical structures [19], tightly distributed fiber arrays [14], multi-height super-resolution algorithm [11], different illumination wavelengths [18], different illumination angles [20], and so on.

Furthermore, to improve the data processing efficiency of super-resolution and twin-image removal, related research has been proposed. Luo et al. [12] proposed a propagation phasor approach, which combines pixel super-resolution and phase retrieval techniques. Zhang et al. [8] proposed an adaptive pixel-super-resolved lensfree imaging (APLI) method based on the Z-axis scanning holograms. Both of these methods require a series of holograms of different heights. In the process, the sample-to-sensor distances must be accurately determined, otherwise, it will directly affect the final super-resolution image resolution. For example, an error of 1 μm in the reconstruction distance directly results in the absence of information corresponding to group 9 of 1951 USAF resolution test target for typical lensfree on-chip systems [8]. Therefore, accurate autofocusing is an essential step in the actual experimental measurement of lensfree super-resolution microscopy.

In the past decades, various autofocusing methods have been proposed for digital holography [21–31]. Automatic evaluation function is the primary consideration of image definition, which is mainly determined from the spatial domain and the frequency domain. Compared with the defocused blurred image in the spatial domain, the focused image has obvious sharpened edges. Based on the concept, the Sobel operator [26], Laplace operator [27], and the total sum of gradient [23] have been used as evaluation function. In the frequency domain, the focused image has more high frequency components than the blurred image, so the high frequency component value can be used as the focus evaluation standard, such as bandpass-filtered power spectrum [27]. In addition, evaluation functions based on other models have appeared, such as differential critical function (DIF) [23], self-entropy [28], spectral L1 norms [29] etc. However, the above algorithms are difficult to directly apply to the autofocusing of multi-height pixel-super-resolved lensfree on-chip imaging. The main problems are as follows: (1) Due to the use of lensfree microscopy, the sharp edge of the focused image is not obvious, so it is difficult to judge the focus directly. (2) The lensfree on-chip microscopy is inevitably interfered by twin-image, which affects the accuracy of evaluation function. (3) In super-resolution imaging, each hologram of different heights needs to be accurately reconstructed, which requires high accuracy of the focusing distance of each plane. Currently, there is no specific and effective technology to achieve high-precision autofocusing under the influence of twin-image for lensfree on-chip imaging.

In this paper, a high-precision autofocusing method is proposed based on the multi-height pixel-super-resolved lensfree on-chip microscopy. The proposed method can be divided into two steps: individual preliminary estimation and global precise estimation. First, an improved differential critical function (SDIF) has been proposed to obtain the approximate focus distances of different height planes, which combines differential critical function and frequency domain autofocus. In order to solve the problem that the DIF value will remain flat near the peak or valley, we introduced frequency domain autofocus to improve the sensitivity of DIF. Then, the intensity or phase image of different heights is synthesized into a high-resolution reference without twin-image. we regard a series of holograms of different heights as a whole, and a high-resolution reference image can be obtained by consistently varying the reconstructed distances of the holograms at different heights. we transform the problem of focusing on different planes into a problem of solving the optimal solution of the overall system. Last, by searching for the extremum of the synthesized image, we can determine the overall offset and get the final reconstruction distance sequence. Through the proposed method, we can more accurately determine the focus distances of different plane heights and improve the accuracy of super-resolution based on the multi-height pixel-super-resolved lensfree on-chip imaging. The structure of the paper is as follows: Basic introduction of lensfree on-chip holography imaging and theoretical knowledge of proposed methods are carried out in section 2. Simulations are carried out in section 3. The section 4 shows the experimental setup and experimental results for amplitude-contrast or phase-contrast objects. Conclusions are given in the in section 5.

2. METHODOLOGY

2.1. The Basic Principle of Lensfree On-Chip Holography

First, we introduce the basic recording and numerical reconstruction principles of lensfree on-chip holography, which is essentially in-line digital holographic imaging. When the light source with sufficient spatial and temporal coherence illuminates the sample, the hologram $H(x, y)$ is formed by the interference between the scattered light $O(x, y)$ on the sample and the unscattered background light $R(x, y)$, which can be

expressed as:

$$\begin{aligned} H(x,y) &= R(x,y) + O(x,y) \\ &= r(x,y) + o(x,y)\exp[-j\phi(x,y)] \end{aligned} \tag{1}$$

Where, $r(x,y)$ and $o(x,y)$ are the amplitude information of the reference light and the object light, respectively, and $\phi(x,y)$ is the phase information of the object light wave. Through the angular spectrum algorithm, the light intensity and phase information of the object light wave can be obtained, which can be expressed as:

$$U(x,y,z) = F^{-1}\{F[H(x,y)] \times G(f_x,f_y,z)\} \tag{2}$$

$$G(f_x,f_y,z) = \begin{cases} \exp[j\frac{2\pi z}{\lambda}\sqrt{1-(\lambda f_x)^2-(\lambda f_y)^2}] & f_x^2+f_y^2 < 1/\lambda^2 \\ 0 & f_x^2+f_y^2 \geqslant 1/\lambda^2 \end{cases} \tag{3}$$

$$I(x,y,z) = \left|U(x,y,z)\right|^2 \tag{4}$$

$$\phi(x,y,z) = \arctan\{\frac{\mathrm{Im}[U(x,y,z)]}{\mathrm{Re}[U(x,y,z)]}\} \tag{5}$$

Where F and F^{-1} denote the Fourier transform and the inverse Fourier transform, respectively. $G(f_x,f_y,z)$ is the optical transfer function in the frequency domain. λ is the wavelength of the light source, z_1 is the distance from the sample to the sensor plane. For lensfree on-chip microscopy, in order to expand the field of view and improve the resolution, the distance between the sample and the sensor is very small ($z_1 \ll z_2$) as shown in **Figure 1A**. The typical distance of sample-to-sensor is 400–1,000 μm. Since the system does not have a microscope objective, it is necessary to propagate the hologram back to the focal plane. In actual operation, the distance between the sample and the sensor is usually obtained by the autofocusing algorithm. Based on that, the maximum field of view is similar to the working area of the image sensor, and the maximum image resolution is approximately the resolution of the image sensor. Due to the limitation of the pixel size of the sensor, the resolution of lensfree on-chip holography is insufficient. Reconstruction based on multiple heights is an effective super-resolution reconstruction method, which can also remove twin-image at the same time. The triangle, ellipse, and pentagram in **Figure 1B** represent grid points of captured holograms on different planes, respectively, and each of the low-resolution images contains similar and complementary information. The super-resolution reconstruction combines all these new information into one image to obtain a high-resolution image. The most common matrix notations used to formulate the general super-resolution model in the pixel domain can be defined as [32]:

$$Y_k = D_k H_k F_f X + V_k, k = 1,2,3,...,N \tag{6}$$

Where, the matrix F_k is the geometric motion operator between the high-resolution (HR) frame X and the low-resolution (LR) frame Y_k. The camera's point spread function (PSF) is modeled by the blur matrix H_k, and matrix D_k represents the decimation operator. V_k is the system noise and N is the number of available LR frames. Based on this, the problem of obtaining a high-resolution image from a set of low-resolution images can be attributed to the solution of the following equation:

$$X = argMin\{\sum_{k=1}^{N} \|D_k H_k F_k X - Y_k\|_p^p\} \tag{7}$$

In the process of super-resolution, we need to get a series of low-resolution holograms with different distances of sample-to-sensor. However, the reconstruction distance of each hologram is difficult to determine accurately in actual experiments, which directly affects the resolution of the final super-resolved image. Therefore, accurate autofocusing is an essential step in the lensfree on-chip super-resolution imaging.

2.2. The Proposed Critical Function

First, we initially determine the reconstruction distances for different height holograms. In the autofocusing algorithm, the key issue is to find a high-precision critical function, which directly affects the subsequent resolution accuracy problem. Considering the influence of twin-image, the differential critical function could be more suitable as the critical function. By making a difference between adjacent reconstructed images, the influence of noise such as twin-image can be reduced to a certain extent. The plane in focus can be determined by searching for the minimum value of differential critical function for amplitude-contrast objects or the maximum value for amplitude-contrast objects. Therefore, the reconstruction distance can be preliminarily determined by searching the extreme value in the initial interval $[z_1, z_2]$ with the step size Δ, as shown in the following formula:

$$\Delta\bar{U}(x,y,l) = \left|\bar{U}(x,y,z_1+(l+1)\Delta) - \bar{U}(x,y,z_1+l\Delta)\right| \tag{8}$$

$$\bar{U}(x,y,l) = \begin{cases} I(x,y,l), & amplitude-contrast\ \ object \\ \phi(x,y,l), & phase-contrast\ \ object \end{cases} \tag{9}$$

where $l = 0,1,...,(z_2-z_1)/\Delta - 1$. $\Delta\bar{U}$ is the light intensity or phase depending on the type of object. It should be emphasized that for traditional the differential critical function, usually only rely on the intensity. The initial reconstruction distance can be determined by finding the minimum value for the amplitude-contrast object or the maximum value for the phase-contrast object. When the need for focusing accuracy is not very high, the position in focus can be approximated by the above method. However, when the need for focusing accuracy is high, it is more accurate to use intensity as the evaluation data for amplitude-contrast objects, and phase as evaluation data for phase-contrast objects. Although noise interference can be reduced to a certain extent through the critical function of differential, this discriminant factor is insufficient for high-precision focusing sensitivity. Especially when the step size Δ is very small, it is easy to have multiple extreme values.

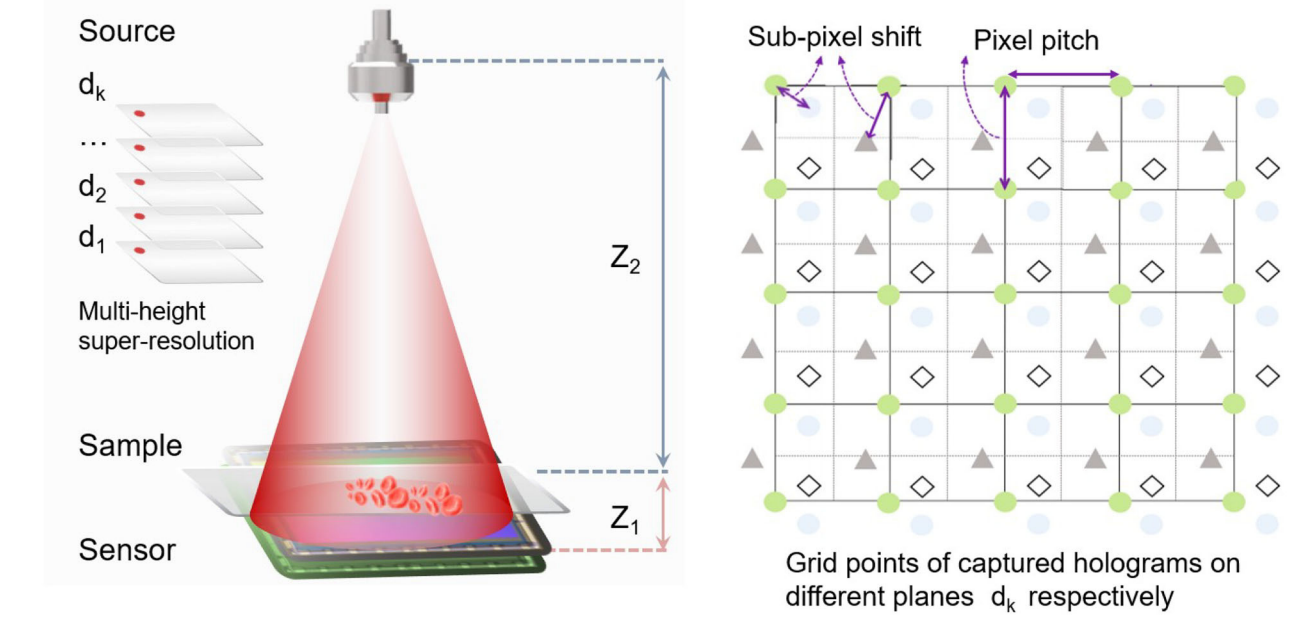

FIGURE 1 | (A) The schematic diagram of the lensfree on-chip holography with multi-distances of sample-to-sensor. **(B)** Sub-pixel shifts among captured images on multi-height planes.

The corresponding simulations and experiments are in the following sections.

In order to solve this problem, the frequency domain critical factor is introduced. The main reasons can be attributed to the following aspects: The critical factor in the frequency domain is more sensitive to high-frequency information. However, if the hologram is directly reconstructed, the high-frequency information generated by the noise will make the frequency domain critical factor unstable or make errors. When the interference of twin-image is weakened, the frequency domain focusing has higher accuracy and stability. Actual simulations and experiments below verify the reliability and stability of the proposed critical factor. Therefore, we can define the criteria function SDIF as shown in the following formula:

$$SDIF(l) = \frac{\sum\sum (x+y) \times \left|DCT(\Delta \bar{U}(x,y,l))\right|}{M \times N} \tag{10}$$

Where *DCT* is the Fast Cosine Fourier Transform. *M*,*N* are the size pixels of the image. By calculating the value of SDIF at different position intervals, we can preliminarily determine the focus distances of different holograms based on the extreme value of SDIF.

2.3. Individual Preliminary Estimation and Global Precise Estimation

According to sections 2.1, 2.2, the reconstruction distances for different height holograms can be initially obtained. However, the resulting reconstructed image still has the effect of the twin-image and it is difficult to further determine the focal distance by a single evaluation factor. Therefore, to ensure the overall resolution of the reconstructed images, we synthesize the reconstructed images of different heights into a single reconstructed image. Based on this, the problem of focusing on different planes is transformed into the problem of solving the optimal solution of the whole system. There are two main issues that need to be addressed. Firstly, when combining reconstructed images of different heights into a whole, consideration must be given to eliminating the effects of twin-image and increasing the resolution of the reconstructed image. Secondly, the current process is not the same as the super-resolution algorithm. It is simply a pre-processing process for super-resolution to obtain the exact reconstructed distance. Therefore, this process should not take too much time. In this paper, we use the weighted average method, which can be expressed as:

$$\begin{cases} \bar{U}s_{k+1} = (1-a) \times \bar{U}s_k(x,y,d_k) + a \times \bar{U}(x,y,d_{k+1}) \\ \bar{U}s_1 = \bar{U}(x,y,d_1), \qquad a = 1/k \\ k = 1,2,3,.....,K-1 \end{cases} \tag{11}$$

Where K is the number of hologram sequences with different heights and d_k is the corresponding initial reconstruction distance based on sections 2.1, 2.2. In the actual operation of multi-height lensfree super-resolution, the defocus range of the reconstruction distance is very small, and the high-frequency detail information of the reconstructed image will change significantly. On the whole, by summing and averaging the reconstructed images of different heights, the noise such as twin-image can be quickly reduced and the high-frequency

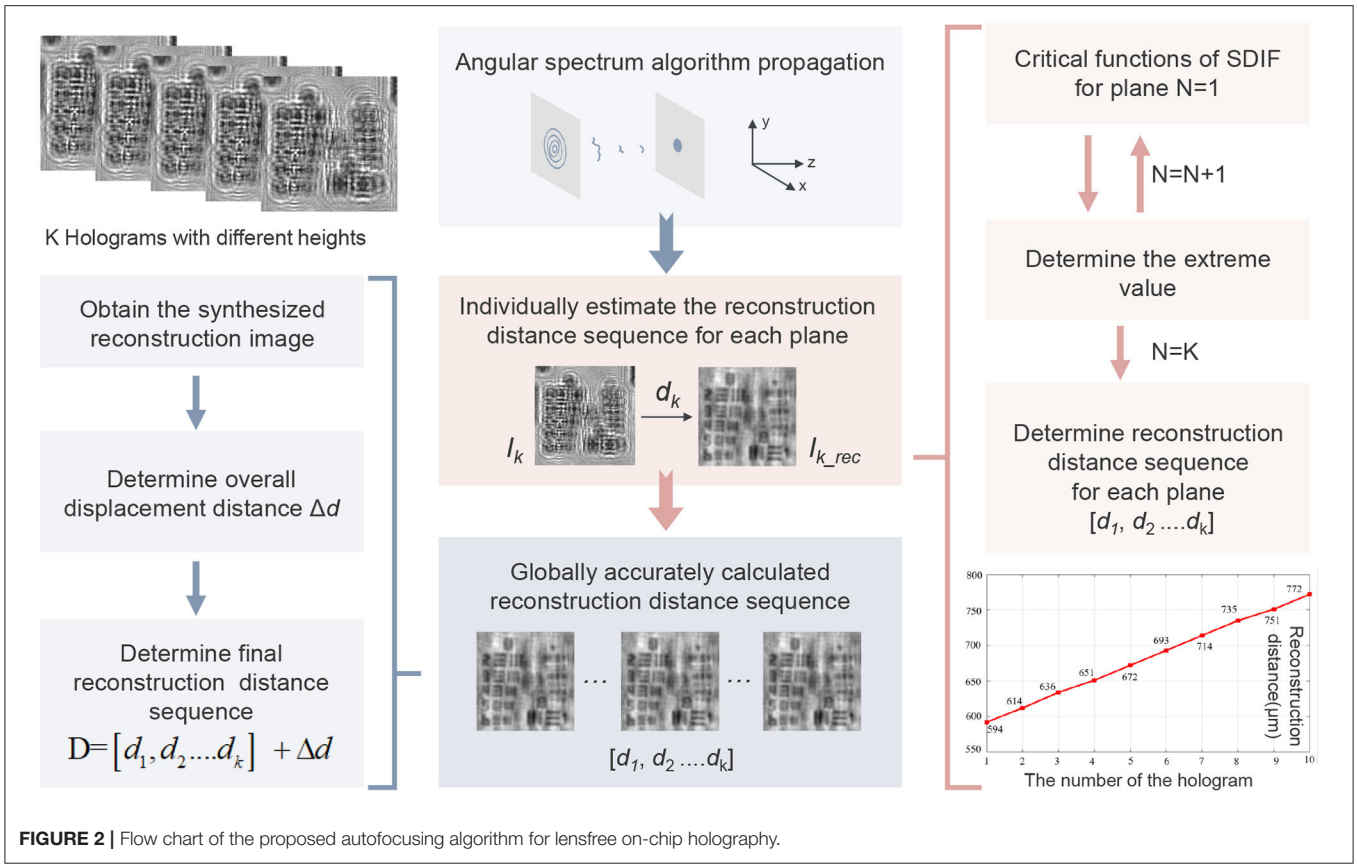

FIGURE 2 | Flow chart of the proposed autofocusing algorithm for lensfree on-chip holography.

information of the reconstructed image can also be improved. In actual operation, there are two problems that need special attention. On the one hand, it should be emphasized that in the actual operation of lensfree on-chip holography, the smaller the distance between the sample and the sensor, the more high-frequency information of the object. Therefore, in the summation process, α is introduced as a weighting factor. In this article, α is set to $1/k$ for simplicity, and theoretical relationships are more complex. On the other hand, when the sample or sensor is displaced in the axial direction, lateral displacement will inevitably occur in the X-Y plane, which will cause serious spatial domain aliasing. In this article, the cross-correlation sub-pixel shift method [33] is applied to correct lateral position errors. The reconstructed image closest to the sensor is used as the initial position reference. The reconstructed image after correction $\bar{U}_{cor}(x_{shift}, y_{shift})$ can be expressed as:

$$\bar{U}_{cor}(x_{shift}, y_{shift}) = F^{-1}\{F\{\bar{U}(x_{shift}, y_{shift}) \exp[-j2\pi(\frac{f_x \times x_{shift}}{M} + \frac{f_x \times y_{shift}}{N})]\}\} \quad (12)$$

Where, (x_{shift}, y_{shift}) is the sub-pixel shift calculated by the cross-correlation method. (f_x, f_y) is the frequency domain coordinates.

Therefore, Equation (11) can be rewritten as:

$$\begin{cases} \bar{U}s_{k+1} = (1-\alpha) \times \bar{U}s_k(x, y, d_k) + a \times \bar{U}_{cor}(x, y, d_{k+1}) \\ \bar{U}s_1 = \bar{U}(x, y, d_1), \qquad a = 1/k \\ k = 1, 2, 3, \ldots\ldots, K-1 \end{cases} \quad (13)$$

So far, we have obtained a preliminary set of reconstructed distance sequences of holograms and synthetic reconstructed images with less noise and more detailed information. We will then evaluate the synthetic reconstructed images to further determine more accurate reconstructed distances. The reconstructed distance sequence $[d_1, d_2, \ldots\ldots, d_k]$ will also be processed as a whole. Now we can further narrow the interval to $[z_3, z_4](z_1 < z_3 < z_4 < z_2)$with a smaller step size Δ_1. Every time the reconstruction distance sequence changes as a whole, a new synthetic reconstruction image can be obtained. Then, based on sections 2.1, 2.2, the focused position of synthetic reconstruction image can be determined by searching the extreme value in the interval $[[z_3, z_4]]$ with the step size Δ_1. Assuming that the overall moving distance sequence is $[d_1, d_2, \ldots\ldots, d_k]$, the final reconstructed distance sequence D can be expressed as:

$$D = [d_1, d_2, \ldots\ldots, d_k] + \Delta d \quad (14)$$

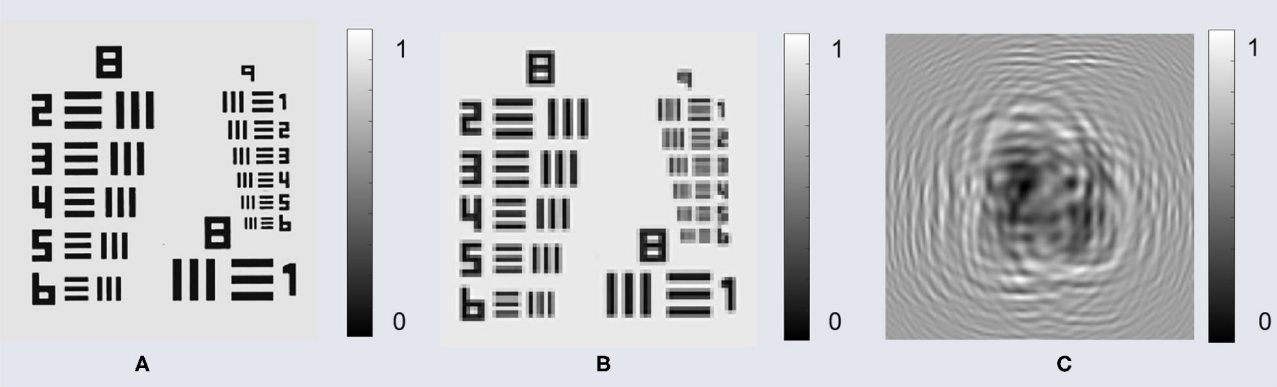

FIGURE 3 | Simulation sample and corresponding hologram. **(A)** Original high-resolution intensity. **(B)** Low-resolution intensity after down sampling. **(C)** Simulated hologram based on the low-resolution intensity.

3. SIMULATIONS

In this section, we will perform simulation experiments to verify the principles of the proposed algorithm. According to the proposed algorithm as shown in **Figure 2**, the whole simulation is divided into two parts: the individual preliminary estimation of the reconstructed distance sequence and the global precise estimation. The simulation procedure is described as follows. First, we simulate an object with amplitude contrast which has a size of 520×520 pixels. The object is propagated to 10 planes by an angular spectrum algorithm. The closest distance between the hologram and the sensor is 500 μm, and the distance interval of each hologram is set to 20 μm. In the actual lensfree on-chip holography, the resolution is limited by the pixel size, so in the simulation experiment, the object light wave is also down-sampled [34] with a down-sampling factor of 4 as shown in **Figure 3**.

3.1. The Individually Preliminary Estimation

In this section, we need to initially calculate the reconstruction distances for holograms of different heights. To verify the accuracy of the proposed critical functions, we used the closest hologram to the sensor to calculate the reconstruction distance ($d_1 = 500$ μm). We calculated the critical functions for DIF and SDIF separately. The initial reconstruction distance range is [485, 515] μm with the interval of $\Delta_2 = 0.5$ μm as shown in **Figure 4A**. By calculating the minimum value of critical functions, we can see that the reconstruction distance is about 500 μm for the critical functions of DIF and the SDIF. In order to determine the reconstruction distance more accurately, we shorten the interval and step size with the reconstruction distance range of [498, 503] μm, the interval of $\Delta_2 = 0.5$ μm. As can be seen from **Figure 4B**, critical functions of DIF changes smoothly in the range of [499, 501] μm, and has no obvious minimum value. However, the critical functions of SDIF can also clearly determine the minimum value of 500.5 μm in the range of [500, 501] μm.

3.2. The Global Precise Estimation

For lensfree on-chip holography, the reconstruction distance accuracy directly affects the resolution of high-frequency information. **Figure 4C** shows the reconstructed intensity at different reconstruction distances. The system has no lens, and the reconstructed image is affected by the twin-image. At this point, it is difficult to directly determine the focus distance of the high frequency information based on a single low-resolution hologram.

Based on section 3.1, we can get the reconstruction distance sequence [500.5, 520.5, 540.5, 560.5, 580.5, 600.5, 620.5, 640.5, 660.5, 680.5] μm corresponding to different height holograms. Then, the synthesized intensity can be obtained by Equations (12) and (13) as shown in **Figure 5A**. It can be clearly seen that the synthesized intensity has clearer detailed information compared with the low-resolution light intensity. Every time the entire distance sequence moves Δd, a new synthesized intensity image can be obtained. In this case, the proposed method transforms the problem of focusing on different planes into a problem of solving the optimal solution of the overall system. By calculating the minimum value of SDIF for synthesized intensity images, the overall displacement distance Δd can be obtained as shown in **Figure 5B**. In the global precise estimation, the range of Δd is [−5.0, 2.0] μm and the interval is 0.5 μm. It is easy to obtain the overall displacement distance minimum $\Delta d = -0.5$ μm. Therefore, the final reconstruction distance sequence can be determined $D = [d_1, d_2.....d_k] + \Delta d$ = [500.0, 520.0, 540.0, 560.0, 580.0, 600.0, 620.0, 640.0, 660.0, 680.0] μm. Last, the high-resolution intensity image can be obtained by the APLI algorithm as shown in **Figure 5C**.

4. EXPERIMENT

4.1. Experimental Setup

To identify the robustness and adaptability of the proposed method, we respectively conducted experiments on an amplitude-contrast object and a phase-contrast object, respectively, based on the lensfree on-chip holography system

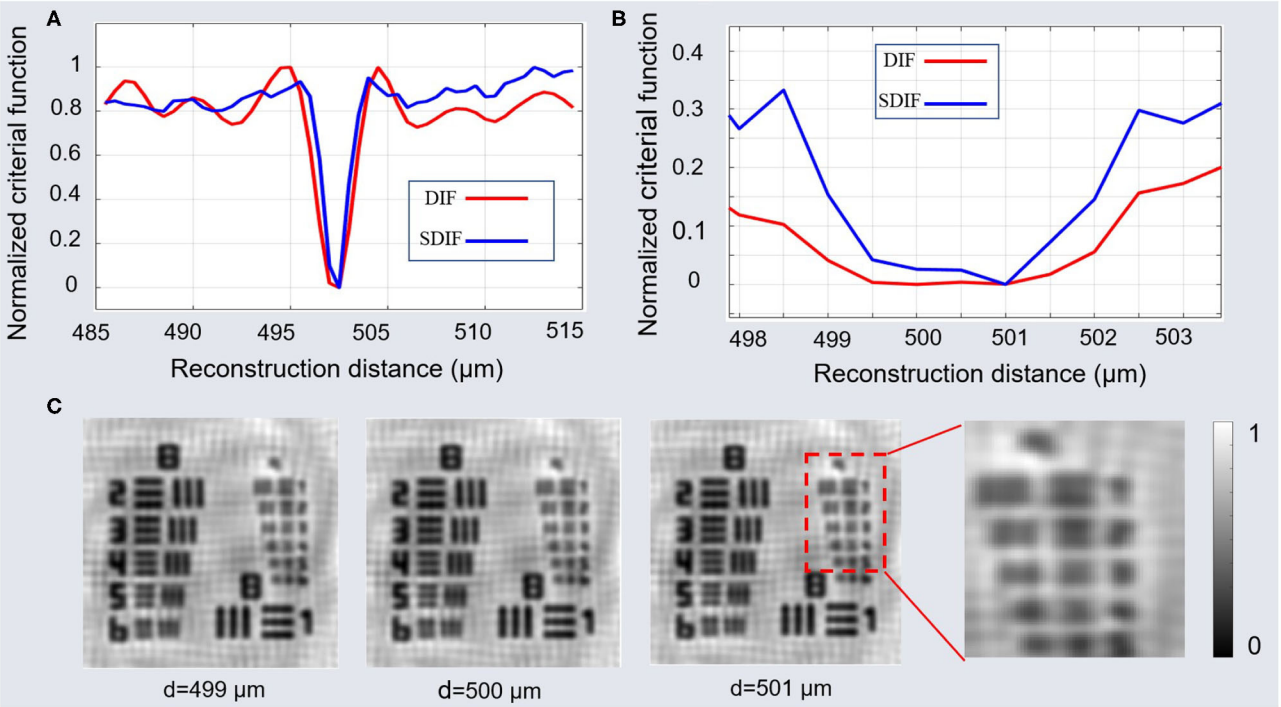

FIGURE 4 | Individually simulation results: **(A)** Normalized criterial function with step of 10 μm. **(B)** Normalized criterial function with step of 0.5 μm. **(C)** Reconstructed intensity at different reconstruction distances.

as shown in **Figure 6**. The system mainly contains four parts: a single mode fiber-coupled light source with the wavelength of 661.5 nm (LP660-SF20, Thorlabs, the United States), a monochrome imaging device with 3,872×2,764, and pixel size of 1.67 μm (DMM 27UJ003-ML, the imaging source, Germany), displacement platform for sample and the motor drive hardware. In the system, the distance between the light source and the sample is about 20 cm. The distance between the sensor and the sample is between 500 and 1,000 μm, and the distance can be adjusted by the motor drive hardware. M1, M2, M3 are fixed reflecting prisms and M4 is a reflecting prism that can be moved around the x and y axes. The sensor is fixed to a displacement table that can be moved precisely vertically by means of a motor drive. However, in actual experiments, when the z-axis distance is adjusted by the motor drive hardware, there is usually a deviation between the preset distance and the actual distance. In addition, during the movement of the z-axis, there will usually be horizontal displacement due to mechanical vibration. It should be emphasized that only the z-axis height needs to be adjusted in our experiments, and there is no need to change the x-axis and y-axis distances.In the following experiment, we will set the hardware program to raise the sample stage by 20 μm in turn and collect 10 low-resolution holograms as experimental samples.

4.2. Amplitude-Contrast Objects

In the first experiment, a standard $2'' \times 2''$ positive 1951 USAF resolution test target is regarded as amplitude-contrast objects to verify our proposed method. Through the hardware drive setting 10 times in the Z-axis direction, 10 raw holograms at different sample-to-sensor distances can be obtained. The first hologram captured by the camera as shown in **Figure 7A**. In order to verify that the algorithm automatically focuses on high-frequency information, we mainly analyze the information of the rectangular frame as shown in **Figures 7B,C**. We will compare the proposed SDIF with three typically existing critical functions, namely DIF, Sobel, SPEC as shown in **Figure 7D**. It is clearly seen that four methods almost locate the focal plane range of [585, 600] μm. In the focal plane, the critical functions of Sobel and SPEC search for the maximum value of the critical function, while functions DIF and SDIF search for the minimum value of the critical function. However, the critical functions of Sobel, SPEC, and DIF have multiple extremes near the focal plane, which has not a good sensitivity. In high frequency information, reconstruction distance errors of a few microns will directly affect the focusing accuracy. As can be seen in **Figures 7B,C**, when the reconstruction distance is in the range of [580, 610] μm, the resolution is essentially the same for group 7, However, the reconstruction distance has a large impact on the resolution of groups 8 and 9. Thus, when the resolution is not high, the method described above allows a better focus plane to be determined; but when the resolution is high, especially when pixel super-resolution is performed, the focus distance must be determined accurately. We can see that the SDIF has one of the sharpest valleys, indicating a better sensitivity than the traditional method. Based on the critical function of SDIF, the sequence of

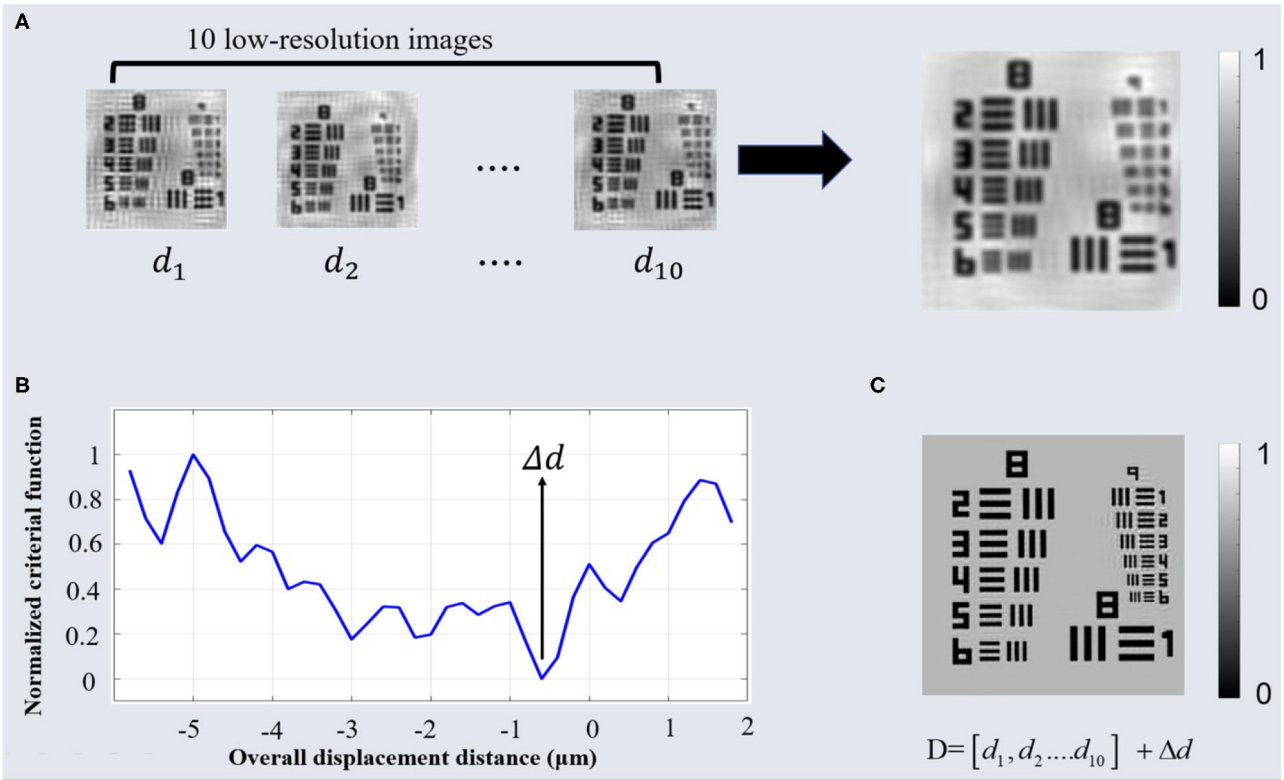

FIGURE 5 | Global simulation results: **(A)** The synthetic intensity based on low-resolution intensity with the reconstructed distance sequence [$d_1, d_2 .....d_{10}$]. **(B)** Normalized criterial function for the synthetic intensity with different overall displacement distance. **(C)** The high-resolution intensity based on APLI algorithm by the reconstructed distance sequence D.

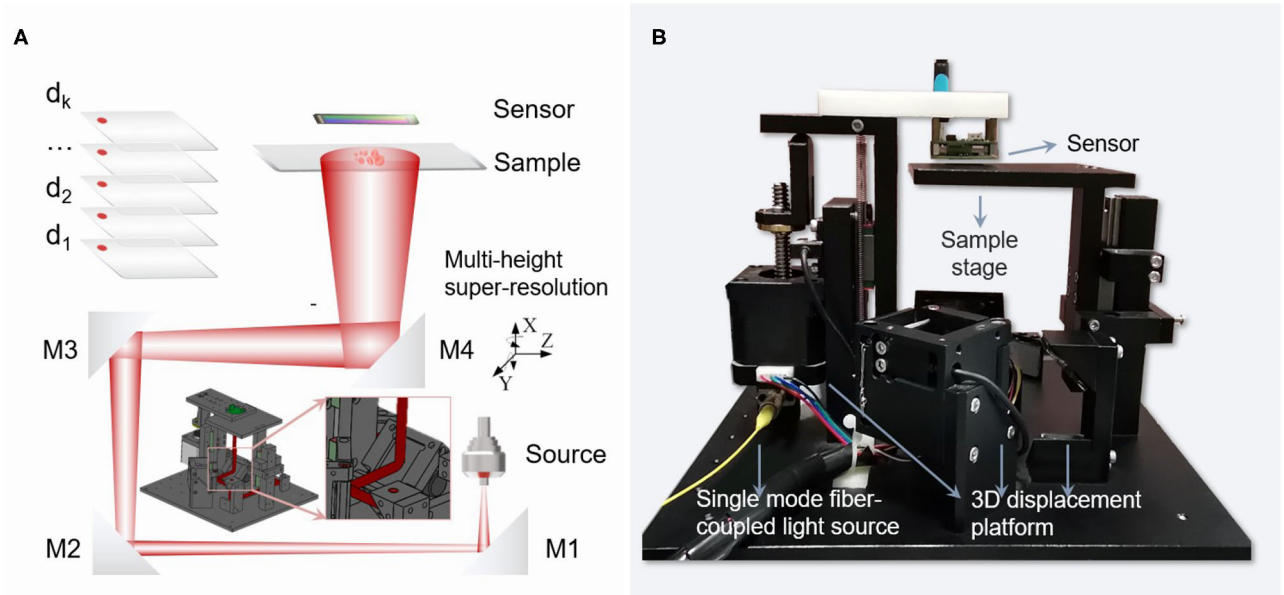

FIGURE 6 | Lensfree system setup based on hardware-driven three-dimensional movement: **(A)** Schematic diagram of the optical path. **(B)** Photographs of experimental equipment.

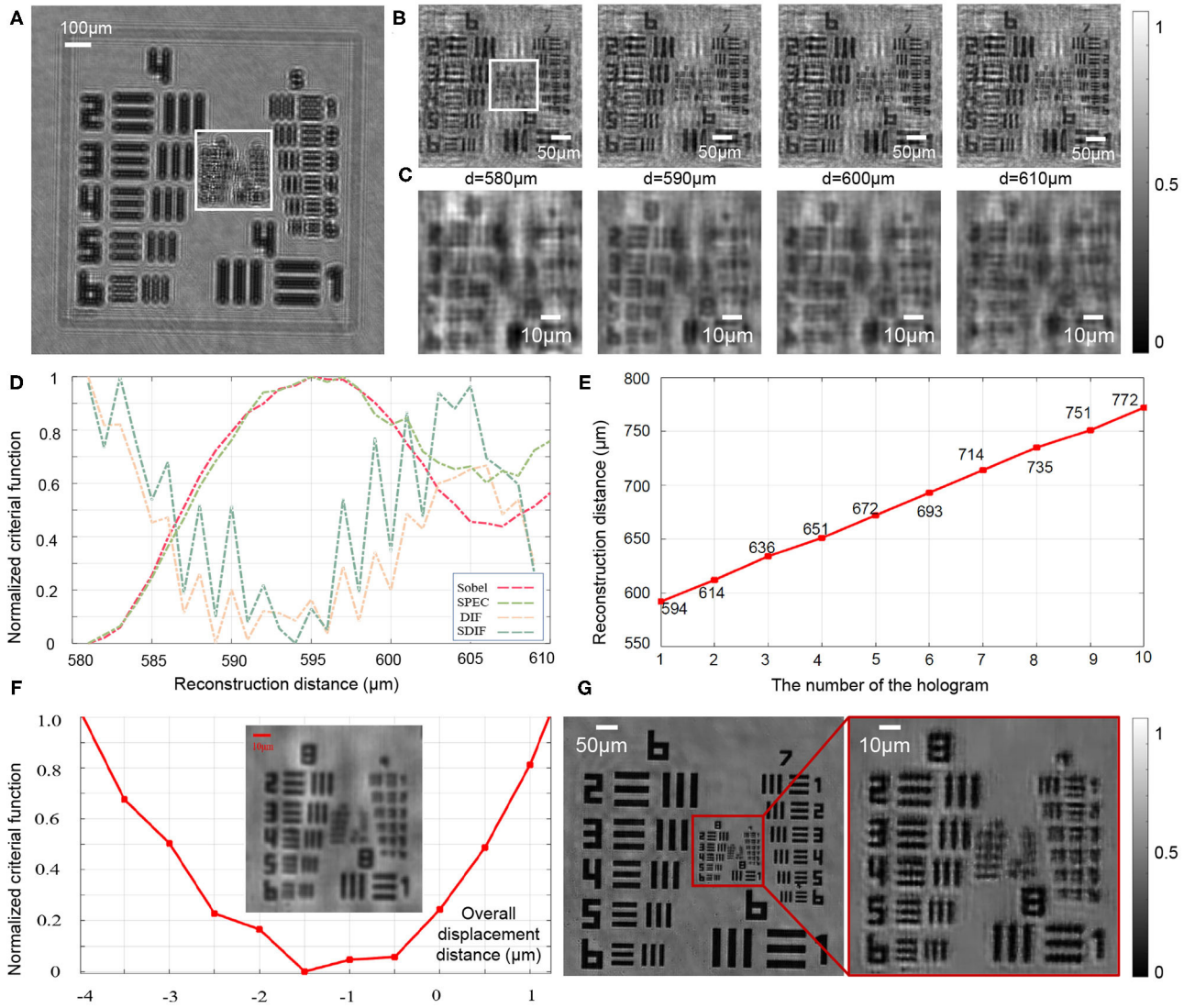

FIGURE 7 | Experimental results for the autofocusing of the amplitude-contrast object. **(A)** The first hologram captured by the camera. **(B)** The enlarged region corresponding to the white rectangle area in **(A)**. **(C)** The enlarged region corresponding to the white rectangle area in **(B)**. **(D)** The criterion curve of SDIF, DIF, Sobel, SPEC. **(E)** The reconstruction distance sequences of different planes by SDIF. **(F)** The synthesized intensity image and the corresponding overall displacement curve. **(G)** Pixel super-resolution intensity images by APLI.

reconstructed distances for the different planes can be uniquely determined, as shown in **Figure 7E**.

To determine the reconstructed distances in each plane more accurately, the 10 reconstructed intensity images were transformed into one synthetic intensity image according to Equations (12) and (13), as shown in **Figure 7F**. It can be clearly seen that the synthesized intensity image has fewer twin-image and clearer detail information. Then, by finding the minimum value of the SDIF critical function, the optimal distance for the overall shift of the reconstructed distance sequence can be determined, as shown in **Figure 7F**. Therefore, the final reconstruction distance sequence can be determined:D = [594, 614, 636, 651, 672, 693, 714, 735, 751, 772]-1.5 = [592.5, 612.5, 634.5, 649.5, 670.5, 691.5, 712.5, 733.5, 749.5, 770.5] μm. Last, the **Figure 7G** shows the high-resolution intensity image obtained by the APLI algorithm, which proves the effectiveness of the proposed algorithm.

4.3. Phase-Contrast Objects

In order to evaluate the capability of the proposed method to detect the pure phase object as shown in **Figure 8A**, we have taken the second experiment. The sample is a benchmark quantitative phase microscopy target, which is completely transparent and can be considered as the phase-contrast sample. The first hologram captured by the camera as shown in **Figure 7A**. In order to verify that the algorithm automatically focuses on high-frequency information, we mainly analyze the information of the rectangular frame as shown in **Figures 8B,C**.

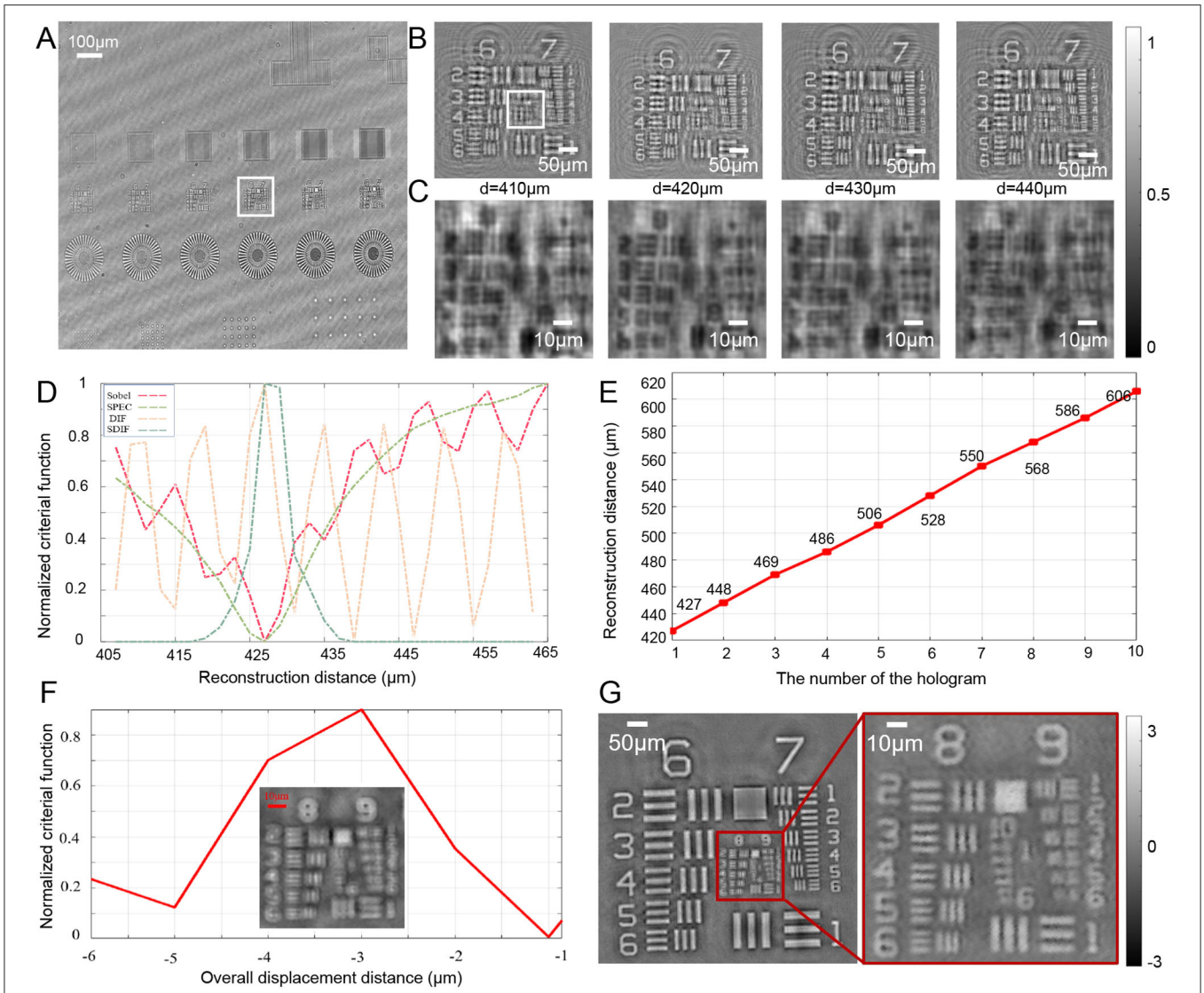

FIGURE 8 | Experimental results for the autofocusing of the phase-contrast object. **(A)** The first hologram captured by the camera. **(B)** The enlarged region corresponding to the white rectangle area in **(A)**. **(C)** The enlarged region corresponding to the white rectangle area in **(B)**. **(D)** The criterion curve of SDIF, DIF, Sobel, SPEC. **(E)** The reconstruction distance sequences of different planes by SDIF. **(F)** The synthesized phase image and the corresponding overall displacement curve. **(G)** Pixel super-resolution phase images by APLI.

Figure 8D shows the criterion curve of SDIF, DIF, Sobel, and SPEC. It is clearly seen that the critical function of DIF is the form of approximate cosine oscillation, which is difficult to determine the focus position by searching extreme values. The critical functions of Sobel, SPEC, and SDIF could locate the focal plane range of [425, 435] μm by searching the minimum value of the critical functions. For phase-contrast objects, the focus position corresponds to the maximum point of the SDIF critical function. Based on the critical function of SDIF, the initial reconstruction distance sequences of different planes can be uniquely determined [427, 448, 469, 486, 506, 528, 550, 568, 586, 606] μm as shown in **Figure 8E**. By calculating the maximum value of SDIF for synthesized phase images with a series of overall displacement distance as shown in **Figure 8F**, the final reconstruction distance sequence can be determined: D = [427, 448, 469, 486, 506, 528, 550, 568, 586, 606]-3 = [424, 445, 466, 483, 503, 525, 547, 565, 583, 603] μm. Last, the **Figure 8G** shows the high-resolution phase image obtained by the APLI algorithm. It can be clearly seen that the resolution of the phase image has been significantly improved, which proves the effectiveness of the proposed algorithm.

5. CONCLUSIONS

In this paper, we present an autofocusing method for multi-height pixel super-resolution lensless on-chip holography. In order to eliminate the influence of twin-image and improve the sensitivity of the critical function, the proposed method

is divided into two steps: individual preliminary estimation and global accurate estimation. First, an improved critical function, named SDIF, is proposed to obtain approximate focal distances in different height planes by combining the differential critical function and frequency domain autofocus. To further obtain more accurate reconstructed distance sequences, the intensity or phase images of different heights are synthesized into a high-resolution reference image without twin-image. We transform the focusing problem on different planes into the problem of solving the optimal solution of the whole system, where we consider a series of holograms of different heights as a whole. By shifting the whole of the distance sequence, we can obtain a high-resolution reference image. With the proposed method, we can determine the focal distance at different plane heights more accurately and improve the super-solution accuracy of the imaging. Compared with conventional methods, the proposed method is more sensitive to the accurate reconstruction of distances for high frequency information and is less disturbed by twin-image. Simulations and practical experiments demonstrate the correctness and stability of the proposed algorithm for amplitude-contrast and phase-contrast objects. Considering that the proposed algorithm performs the estimation of individual reconstruction distances and the estimation of overall reconstruction distances, the time spent by the algorithm will increase. In the experiments, the time consumption for 10 images was around 50 s, and how to further reduce computational complexity is the next step of our research.

DATA AVAILABILITY STATEMENT

The original contributions presented in the study are included in the article/supplementary material, further inquiries can be directed to the corresponding author/s.

AUTHOR CONTRIBUTIONS

YW conceived the idea. LL and ZL did the experiments. JZ provided Super-resolution algorithm support. CZ supervised the project and provided Technical Support. All the authors contributed to discussion on the results for this manuscript.

FUNDING

This work was supported by the National Natural Science Foundation of China (61722506, 61905115), Leading Technology of Jiangsu Basic Research Plan (BK20192003), National Defense Science and Technology Foundation of China (2019-JCJQ-JJ-381), Youth Foundation of Jiangsu Province (BK20190445), The Key Research and Development Program of Jiangsu Province (BE2017162), 333 Engineering Research Project of Jiangsu Province (BRA2016407), Fundamental Research Funds for the Central Universities (30920032101, 30920032101), and Open Research Fund of Jiangsu Key Laboratory of Spectral Imaging & Intelligent Sense (3091801410411).

REFERENCES

1. Mölder A, Sebesta M, Gustafsson M, Gisselson L, Wingren AG, Alm K. Non-invasive, label-free cell counting and quantitative analysis of adherent cells using digital holography. *J Microsc*. (2010) 232:240–7. doi: 10.1111/j.1365-2818.2008.02095.x
2. Zuo C, Sun J, Li J, Zhang J, Asundi A, Chen Q. High-resolution transport-of-intensity quantitative phase microscopy with annular illumination. *Sci Rep*. (2017) 7:1–22. doi: 10.1038/s41598-017-06837-1
3. Zuo C, Li J, Sun J, Fan Y, Zhang J, Lu L, et al. Transport of intensity equation: a tutorial. *Opt Lasers Eng*. (2020) 135:106187. doi: 10.1016/j.optlaseng.2020.106187
4. Wu Y, Cheng H, Wen Y. High-precision rotation angle measurement method based on a lensless digital holographic microscope. *Appl Opt*. (2018) 57:112–8. doi: 10.1364/AO.57.000112
5. Li J, Matlock A, Li Y, Chen Q, Zuo C. Resolution-enhanced intensity diffraction tomography in high numerical aperture label-free microscopy. *Photon Res*. (2020) 8:1818. doi: 10.1364/PRJ.403873
6. Bishara W, Su TW, Coskun AF, Ozcan A. Lensfree on-chip microscopy over a wide field-of-view using pixel super-resolution. *Opt Exp*. (2010) 18:11181–91. doi: 10.1364/OE.18.011181
7. Greenbaum A, Zhang Y, Feizi A, Chung PL, Luo W, Kandukuri SR, et al. Wide-field computational imaging of pathology slides using lens-free on-chip microscopy. *Sci Transl Med*. (2014) 6:267ra175. doi: 10.1126/scitranslmed.3009850
8. Zhang J, Sun J, Chen Q, Li J, Zuo C. Adaptive pixel-super-resolved lensfree in-line digital holography for wide-field on-chip microscopy. *Sci Rep*. (2017) 7:1–15. doi: 10.1038/s41598-017-11715-x
9. Zhang J, Chen Q, Li J, Sun J, Zuo C. Lensfree dynamic super-resolved phase imaging based on active micro-scanning. *Opt Lett*. (2018) 43:3714–7. doi: 10.1364/OL.43.003714
10. Garcia-Sucerquia J, Xu W, Jericho M, Kreuzer HJ. Immersion digital in-line holographic microscopy. *Opt Lett*. (2006) 31:1211–3. doi: 10.1364/OL.31.001211
11. Zhang J, Sun J, Chen Q, Zuo C. Resolution analysis in a lens-free on-chip digital holographic microscope. *IEEE Trans Comput Imaging*. (2020) 6:697–710. doi: 10.1109/TCI.2020.2964247
12. Luo W, Zhang Y, Göröcs Z, Feizi A, Ozcan A. Propagation phasor approach for holographic image reconstruction. *Sci Rep*. (2016) 6:22738. doi: 10.1038/srep22738
13. Luo W, Greenbaum A, Zhang Y, Ozcan A. Synthetic aperture-based on-chip microscopy. *Light: Sci Appl*. (2015) 4:e261. doi: 10.1038/lsa.2015.34
14. Bishara W, Sikora U, Mudanyali O, Su TW, Yaglidere O, Luckhart S, et al. Holographic pixel super-resolution in portable lensless on-chip microscopy using a fiber-optic array. *Lab Chip*. (2011) 11:1276–9. doi: 10.1039/c0lc00684j
15. Gohshi S, Hiroi T, Echizen I. Subjective assessment of HDTV with superresolution function. *EURASIP J Image Video Process*. (2014) 2014:11. doi: 10.1186/1687-5281-2014-11
16. Hardie RC, Barnard KJ, Armstrong EE. Joint MAP registration and high-resolution image estimation using a sequence of undersampled images. *IEEE Trans Image Process*. (1997) 6:1621–33. doi: 10.1109/83.650116
17. Woods NA, Galatsanos NP, Katsaggelos AK. Stochastic methods for joint registration, restoration, and interpolation of multiple undersampled images. *IEEE Trans Image Process*. (2005) 15:201–13. doi: 10.1109/TIP.2005.860355
18. Zheng G, Lee SA, Yang S, Yang C. Sub-pixel resolving optofluidic microscope for on-chip cell imaging. *Lab Chip*. (2010) 10:3125–9. doi: 10.1039/c0lc00213e
19. Coskun AF, Nagi R, Sadeghi K, Phillips S, Ozcan A. Albumin testing in urine using a smart-phone. *Lab Chip*. (2013) 13:4231–8. doi: 10.1039/c3lc50785h
20. Luo W, Zhang Y, Feizi A, Göröcs Z, Ozcan A. Pixel super-resolution using wavelength scanning. *Light Sci Appl*. (2016) 5:e16060. doi: 10.1038/lsa.2016.60
21. Gao P, Yao B, Rupp R, Min J, Guo R, Ma B, et al. Autofocusing based on wavelength dependence of diffraction in two-wavelength digital holographic microscopy. *Opt Lett*. (2012) 37:1172–4. doi: 10.1364/OL.37.001172

22. Wen Y, Wang H, Anand A, Qu W, Cheng H, Dong Z, et al. A fast autofocus method based on virtual differential optical path in digital holography: theory and applications. *Opt Lasers Eng*. (2019) 121:133–42. doi: 10.1016/j.optlaseng.2019.04.006
23. Lyu M, Yuan C, Li D, Situ G. Fast autofocusing in digital holography using the magnitude differential. *Appl Opt*. (2017) 56:F152–7. doi: 10.1364/AO.56.00F152
24. Ilhan HA, Doğar M, Özcan M. Fast autofocusing in digital holography using scaled holograms. *Opt Commun*. (2013) 287:81–4. doi: 10.1016/j.optcom.2012.09.036
25. Yu L, Cai L. Iterative algorithm with a constraint condition for numerical reconstruction of a three-dimensional object from its hologram. *JOSA A*. (2001) 18:1033–45. doi: 10.1364/JOSAA.18.001033
26. Dubois F, Schockaert C, Callens N, Yourassowsky C. Focus plane detection criteria in digital holography microscopy by amplitude analysis. *Opt Exp*. (2006) 14:5895–908. doi: 10.1364/OE.14.005895
27. Langehanenberg P, Kemper B, Dirksen D, Von Bally G. Autofocusing in digital holographic phase contrast microscopy on pure phase objects for live cell imaging. *Appl Opt*. (2008) 47:D176–82. doi: 10.1364/AO.47.00D176
28. Gillespie J, King RA. The use of self-entropy as a focus measure in digital holography. *Pattern Recogn Lett*. (1989) 9:19–25. doi: 10.1016/0167-8655(89)90024-X
29. Li W, Loomis NC, Hu Q, Davis CS. Focus detection from digital in-line holograms based on spectral l 1 norms. *JOSA A*. (2007) 24:3054–62. doi: 10.1364/JOSAA.24.003054
30. Memmolo P, Paturzo M, Javidi B, Netti PA, Ferraro P. Refocusing criterion via sparsity measurements in digital holography. *Opt Lett*. (2014) 39:4719–22. doi: 10.1364/OL.39.004719
31. Yang Y, Kang Bs, Choo Yj. Application of the correlation coefficient method for determination of the focal plane to digital particle holography. *Appl Opt*. (2008) 47:817–24. doi: 10.1364/AO.47.000817
32. Tian J, Ma KK. Stochastic super-resolution image reconstruction. *J Vis Commun Image Represent*. (2010) 21:232–44. doi: 10.1016/j.jvcir.2010.01.001
33. Riha L, Fischer J, Smid R, Docekal A. New interpolation methods for image-based sub-pixel displacement measurement based on correlation. In: *2007 IEEE Instrumentation & Measurement Technology Conference IMTC 2007*, Warsaw: Instrumentation & Measurement Magazine IEEE. (2007). p. 1–5. doi: 10.1109/IMTC.2007.379183
34. Park SC, Park MK, Kang MG. Super-resolution image reconstruction: a technical overview. *IEEE Signal Process Mag*. (2003) 20:21–36. doi: 10.1109/MSP.2003.1203207

Conflict of Interest: The authors declare that the research was conducted in the absence of any commercial or financial relationships that could be construed as a potential conflict of interest.

frontiers in Physics

BRIEF RESEARCH REPORT
published: 29 March 2021
doi: 10.3389/fphy.2021.650353

Applications of Super Resolution Expansion Microscopy in Yeast

Liwen Chen[1], *Longfang Yao*[2], *Li Zhang*[3], *Yiyan Fei*[2], *Lan Mi*[2]* *and Jiong Ma*[1,2,3]*

[1] *Institute of Biomedical Engineering and Technology, Academy for Engineer and Technology, Fudan University, Shanghai, China,* [2] *Key Laboratory of Micro and Nano Photonic Structures (Ministry of Education), Department of Optical Science and Engineering, Shanghai Engineering Research Center of Ultra-Precision Optical Manufacturing, Green Photoelectron Platform, Fudan University, Shanghai, China,* [3] *Shanghai Engineering Research Center of Industrial Microorganisms, School of Life Sciences, Multiscale Research Institute of Complex Systems, Fudan University, Shanghai, China*

Super-resolution microscopy includes multiple techniques in optical microscopy that enable sub-diffraction resolution fluorescence imaging of cellular structures. Expansion microscopy (EXM) is a method of physical expansion to obtain super-resolution images of a biological sample on conventional microscopy. We present images of yeast organelles, applying the combination of super-resolution and ExM techniques. When preparing pre-expanded samples, conventional methods lead to breakage of dividing yeast cells and difficulties in studying division-related proteins. Here, we describe an improved sample preparation technique that avoids such damage. ExM in combination with Airyscan and structured illumination microscopy (SIM) collected sub-cellular structural images of nuclear pore complex, septin, and a-tubulin in yeast. Our method of expansion in yeast is well-suited for super-resolution imaging study of yeast.

Keywords: expansion super-resolution, yeast, nuclear pore complex, septin, tubulin

OPEN ACCESS

Edited by:
Vicente Micó,
University of Valencia, Spain

Reviewed by:
Yongxin Zhao,
Carnegie Mellon University, United States
Michael Hausmann,
Heidelberg University, Germany
Jae-Byum Chang,
Korea Advanced Institute of Science and Technology, South Korea

***Correspondence:**
Lan Mi
lanmi@fudan.edu.cn
Jiong Ma
jiongma@fudan.edu.cn

Specialty section:
This article was submitted to Optics and Photonics, a section of the journal Frontiers in Physics

Received: *07 January 2021*
Accepted: *02 March 2021*
Published: *29 March 2021*

Citation:
Chen L, Yao L, Zhang L, Fei Y, Mi L and Ma J (2021) Applications of Super Resolution Expansion Microscopy in Yeast. Front. Phys. 9:650353. doi: 10.3389/fphy.2021.650353

INTRODUCTION

Optical microscopy is one of the most important tools in the fields of biology and medicine. However, owing to diffraction limits, the resolution of conventional optical systems is limited to roughly 250 nm. In recent years, different methods have emerged to achieve optical super-resolution imaging, breaking the limits of diffraction. These super-resolution microscopy techniques can be divided into two categories—light source modulation and single-molecule modulation.

A classic example of the former is stimulated emission depletion (STED) [1], in which a physical process is used to reduce the spot size of the excitation light, thereby directly reducing the half-height width of the spot diffusion function to improve resolution. However, compared to general optical microscopes, STED causes more damage to the sample owing to the higher excitation light power used [2]. Super-resolution microscopes belonging to this type of technology also include structured illumination microscopy (SIM) [3–5] and Airyscan microscopy [6]. SIM applies a modulated illumination light to the sample to obtain images with different phases and orientations, which are then reconstructed to a super-resolution image. An obvious advantage of SIM is the improved imaging speed, and the technique has been applied for measuring gene sizes with high precision [7]. Airyscan microscopy is a new detector design that optimizes classic components, consisting of 32 elements acting as its own small pinhole in an Airyscan with positional information. This design increases the contrast of the high spatial frequency information but extends the imaging time [8]. Single-molecular-based techniques such as STORM [9], can

achieve multicolor super-resolution images. But STORM method requires random activation of single fluorophores, making experiments difficult to perform. Each of the aforementioned super-resolution techniques have its own advantages and disadvantages, which are applicable to different types of samples for increased resolution.

In addition to microscopy, resolution can be improved from the perspective of the sample. For example, the sample can be magnified by expansion microscopy (ExM) to visualize the finer cellular sub-organ structures [10]. By immobilizing the fluorescent molecules of a labeled protein in a polyacrylamide hydrogel, the molecular structure of the sample is also spatially amplified as the hydrogel physically expands isotopically, thus indirectly improving resolution. In just a few years, many studies have optimized the ExM from the Edward S. Boyden's group to obtain a series of new expansion technologies based on different experimental needs. For example, combined with existing super-resolution microscopy systems, protein-retention expansion microscopy (proExM) [11] has been validated in different cells and tissues to achieve imaging at the nanoscale by retaining the target molecule (e.g., antibody tags, fluorescent proteins) [12]. The magnified analysis of the proteome (MAP), partially optimizes the experimental procedure to control the distance between proteins in the gel for expansion of tissue [13]. Additional methods include ExFISH, with *in situ* hybridization labeled probes for fluorescent RNA imaging [14], iExM, which further expands the resolution through iterative sample swelling [15], and ExPath, for the medical study of human specimen expansion [16]. The combination of ExM and different super-resolution techniques such as SIM and Airyscan has made an outstanding contribution to the study of biological structures and provides good examples of the compatibility of ExM [17–19].

There are many techniques available to apply ExM to different types of cells and tissues, even to bacterial and fungal spores [18, 20]. However, it has not been described in yeast. Yeast has many similarities with some of the functional structures of mammalian cells, and it is convenient to cultivate as a model microorganism, although the smaller size of its functional structures hinders imaging at the nanoscale. Fortunately, ExM is suited for super-resolution imaging of yeast. As a classical model microorganism, many studies have reported on the various functional structures of yeast. The integrated structure of the yeast nuclear pore complex (NPC) was determined by electron microscopy (EM) [21], with the diameter of rings and the distance between the bilayer being observed. However, few articles ever collected the dimensional data directly on single nuclear pores *via* light microscopy. In addition, septins are essential GTP-binding proteins that are found in almost all eukaryotes and are involved in the process of cytokinesis. From polarization data, it is inferred that septins polymerize into filaments and form an ordered array that can polymerize into long filaments and bundle laterally [22, 23]. Previous studies indirectly speculated that septin is linearly aligned [24]. Finally, α-tubulin plays a crucial role in a variety of cellular processes including cell division, motility, and vesicle transport [25].

In conventional yeast immunofluorescence methods [26], the fixed yeast walls are usually processed into individual protoplasts by special digestion and then collected by centrifugation. Next, the protoplasts are adhered to slides coating with poly-L-lysine, followed by the conventional immunofluorescence steps. The protoplasts obtained by this method may break up the dividing cell, thereby destroying the division-related structures. Therefore, although this approach enables fluorescent labeling of proteins in yeast, it is not suitable for studying the relevant proteins located at the division site. For this reason, we improved the immunofluorescence procedure by immobilizing cells on concanavalin A (ConA) coated slides prior to digestion [27]. Combined with ExM and super-resolution microscopy, our methods allow for the study of a wider range of protein structures.

In this study, we applied our improved ExM method to the structural components of NPCs, septin and α-tubulin, of yeast using an expansion Airyscan imaging database of Nup84, an essential scaffolding component of the NPC containing 16 copies and two rings [21], a GFP fusion protein of CDC12, an indispensable part of septin filament formation [24, 28], and z-stack images of antibody-labeled α-tubulin with 3D-SIM. Our results indicate that ExM technology can be applied for imaging of different structures in yeast.

MATERIALS AND METHODS

Materials

The *Saccharomyces cerevisiae* strains of Nup84-GFP used were generated by Huh et al. [29]. The septin CDC12-GFP yeast strain was a gift from the Juntao Gao group. The GFP-tag was added at the C-terminus of the target protein [30].

Cultivation of Yeast Cells

In the first pre-culture, cells were incubated in a fresh YPD Agar media (YPD Agar, A507023, Sangon Biotech, Shanghai, China) for 16 h at 30°C. Cells were then inoculated in a second pre-culture in 6 mL YPD-media (YPD broth, A507022, Sangon Biotech, Shanghai, China) and cultured to the logarithmic phase of growth at 30°C and 220 rpm of agitation. Yeast cell culture was centrifuged at 3,000 × g for 5 min, followed by washing three times with sorbitol buffer and resuspending in sorbitol culture medium (1 M sorbitol solution in YPD broth). The sorbitol buffer was composed of 1.2 M sorbitol solution (D-Sorbitol, A100691, Sangon Biotech, Shanghai, China) in 0.1 M KH_2PO_4 (Potassium dihydrogen phosphate, A100781, Sangon Biotech, Shanghai, China).

Preparation of Coverslips

Coverslips were sonicated in acetone at 30°C for 30 min, washed more than three times with double-distilled H_2O (ddH20), and dried to remove residual solvents. Next, coverslips were washed in 10 mg/mL ConA (ConA, 11028-71-0, Sigma-Aldrich, St. Louis, MO, USA) more than three times and then submerged in the same solution for 10 min. After drying for 2 h, coverslips were washed in nuclease-free water (Water nuclease-free, B300591, Sangon Biotech, Shanghai, China) and dried again to uniformly distribute the ConA.

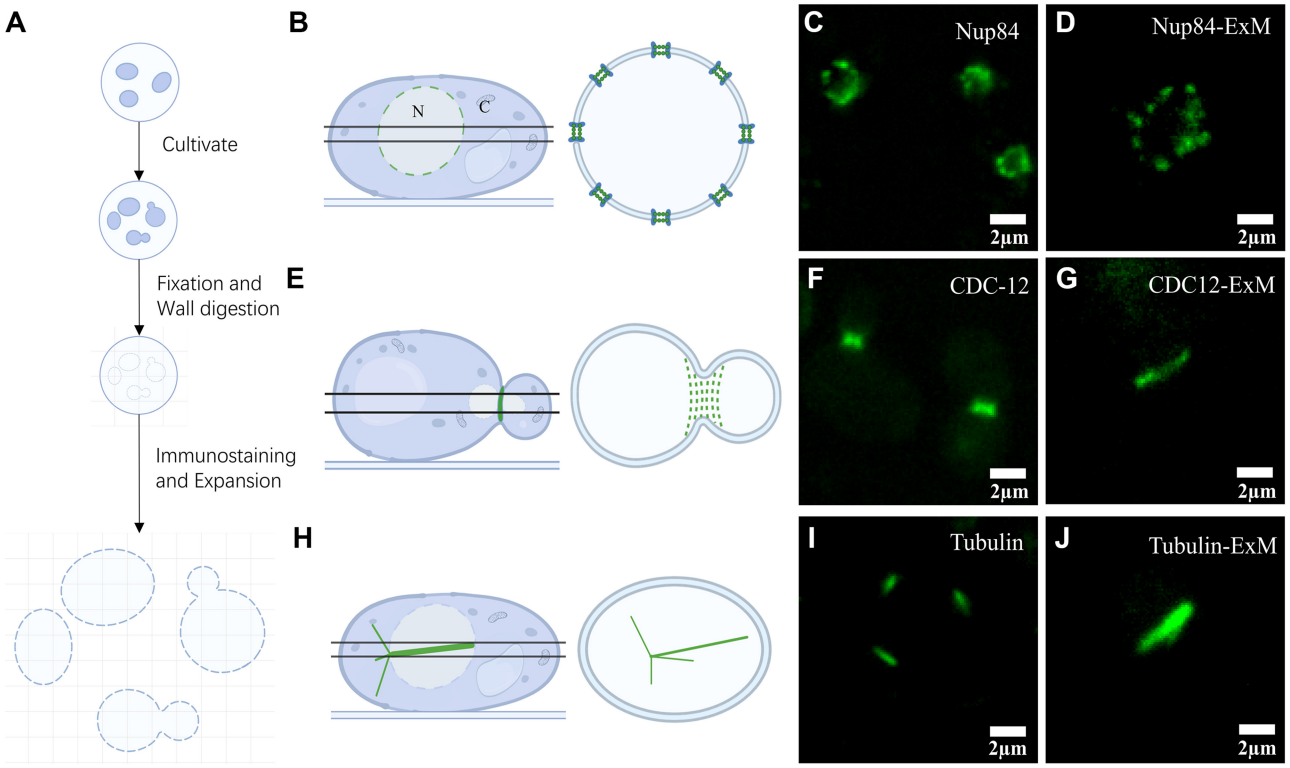

FIGURE 1 | Expansion microscopy of yeast. **(A)** Schematic diagram of the steps in the yeast expansion protocol. **(B)** Illustration representing axial imaging with views of Nups located at the equator. **(C)** Pre-expansion wide-field imaging of Nup84. **(D)** Post-expansion wide-field imaging of Nup84. **(E)** Diagram of septin structural illumination during division. **(F)** Pre-expansion wide-field imaging of septin CDC12. **(G)** Post-expansion wide-field imaging of septin CDC12. **(H)** Graphical demonstration of α-tubulin in yeast. **(I)** Pre-expansion wide-field imaging of α-tubulin. **(J)** Post-expansion wide-field imaging of α-tubulin. Scale bars, 2 μm **(C, D, F, G, I, J)**. All bars were physical scales before correction with expansion factor.

Cell Fixing and Digesting

Yeast culture in sorbitol medium was placed on ConA-coated coverslips and incubated for 30 min at room temperate. After washing with PBS, the coverslip with the sample was fixed for 30 min in 4% formaldehyde (157-8, Electron Microscopy Sciences, Hatfield, PA) at 4°C and unbound cells were removed by washing more than three times with phosphate-buffered saline (PBS, 311-010-CL, Wisent, Quebec, Canada). Add 50 μL of digestion solution containing Lyticase (Lyticase, L2524, Sigma-Aldrich, St. Louis, MO, USA), 1 M sorbitol, and 50 mM Tris-buffer (Tris, A610195, Sangon Biotech, Shanghai, China) to each sample, and the mixture was incubated for 30 min at 30°C with gentle shaking. Next, the samples were immersed in cold methanol for 5 min to stop the reaction and then incubated in acetone for 30 s. At each step, the sample was gently washed more than three times in PBS. All samples were inspected with microscopy to confirm the number of attached yeast cells before labeling.

Immunofluorescence Staining

Digested cells were immersed in 0.5% v/v Triton X-100 (Triton X-100, A110694, Sango Biotech, Shanghai, China) for 5 min and blocked with 1% bovine serum albumin (BSA, 001-000-161, Jackson ImmunoResearch Laboratories, West Grove, PA) and 0.5% v/v Triton X-100 for 30 min. The blocked cells were carefully washed 3–5 times for 10 min in PBS, taking care not to dry out the cover plate. Samples were incubated with primary anti-GFP antibody (ab13970, Abcam, Cambridge, MA, USA) for 1 h and then with secondary antibody (ab150173, Abcam, Cambridge, MA, USA) for 1 h. After removing the unbounded secondary antibody, the samples were inspected with microscopy. All staining treatments were performed at room temperature.

ExM

Gelation was performed as previously described [31]. Before polymerization, the sample was incubated with 0.25% glutaraldehyde (A600875-0025, BBI Life Sciences, Shanghai, China) for 10 min at room temperature and washed several times in PBS. A monomer solution [8.625% sodium acrylate (w/w) (408220, Sigma-Aldrich), 2 M NaCl (S5886, Sigma), 2.5% acrylamide (w/w) (A4058, Sigma-Aldrich), 0.15% N, N, -methylenbisacrylamide (w/w) (M7279, Sigma-Aldrich), and 1 × PBS] was added with 0.2% (w/w) tetramethylethylenediamine (TEMED, 17919, Thermo Fisher Scientific, Waltham, MA) and 0.2% (w/w) ammonium persulfate (APS, 17874, Thermo Fisher

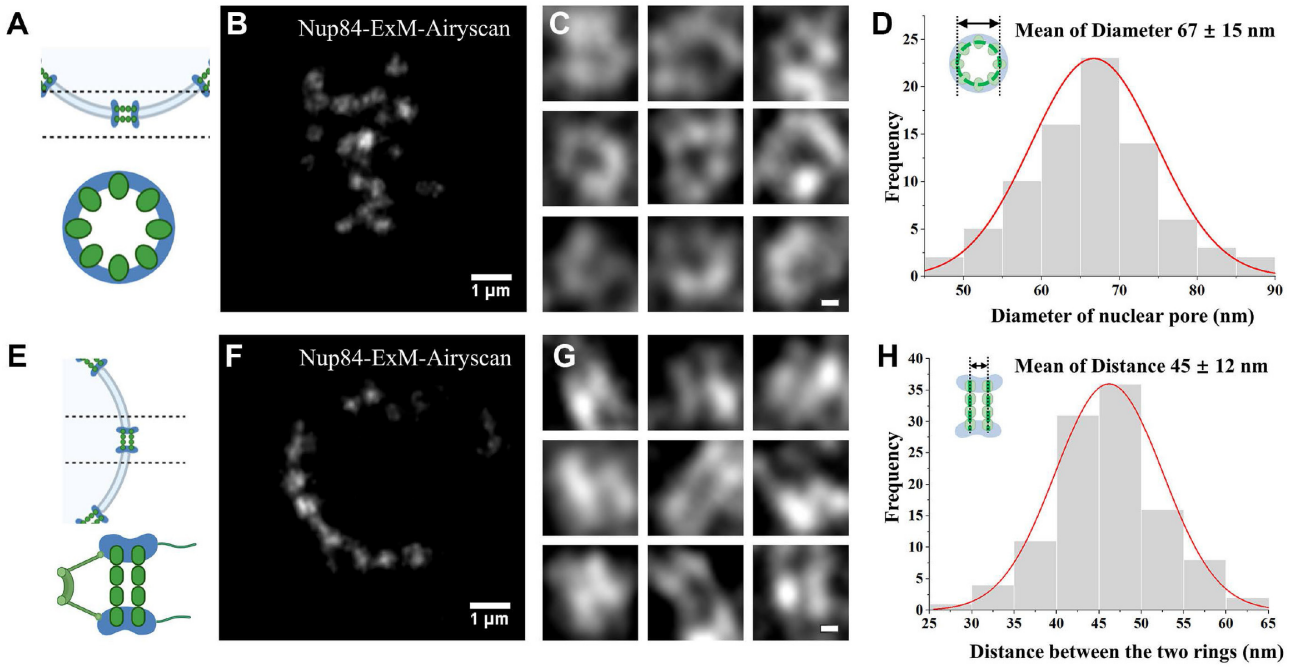

FIGURE 2 | NPC visualized by Airyscan microscopy. **(A)** Diagram of a radial distribution. **(B)** Bottom surface imaging of the expansion in Nup84. **(C)** Images of a radial individual nuclear pore. **(D)** Diameter histogram of the number of Nup84 molecules. **(E)** Schematic diagram of the radial view. **(F)** Post-expanded Nup84 images in the axial view at the equator. **(G)** Images of single nuclear pore in the axis. **(H)** Histogram of the separation between rings. Scale bars, 1 μm **(B,F)** and 0.1 μm **(C,G)**. All bars were physical scales before correction with expansion factor. The expansion factor is 4.0.

Scientific, Waltham, MA) to the coverslip with fixed yeast cells. After 2 h of polymerization, the size of the gelated samples was measured. The gel was digested in 8 U/mL proteinase K (EO0491, Thermo Fisher Scientific, Waltham, MA) in digestion buffer (50 mM Tris pH 8.0, 0.5% Triton X-100, 1 mM EDTA, and 0.8 M guanidine HCl) for isotopical expansion. Digested gels were completely submerged in fresh ddH20 every 0.5 h 3–5 times unless the gel size did not increase. An additional fixation process may be performed for better imaging. This method used 3% agarose (Agarose, A620014, Sango Biotech, Shanghai, China) to immobilize the sample.

Imaging

Wide-field images were collected using an EMCCD camera (Evolve 512 Delta Photometrics) equipped with an oil-immersed objective (150×/1.45, Olympus). The pixel size of wide-field images was ∼106 nm and the exposure time was set at 50 ms. Emissions were passed through the same objective and filtered by a 520 nm band-pass filter (FF01-520/35-25, Semrock) for Alexa 488. Samples stained with Alexa488 were excited using a 488 nm laser. Airyscan imaging was captured with a confocal microscope (ZEISS, LSM880, Germany) and a Plan-Apochromat 63×/1.4NA oil objective (Zeiss; Plan-Apochromat 63×/1.4 Oil DIC M27). Emissions were passed through a 495–550 nm band-pass filter, then through a 570 nm long-pass filter, and collected with a 32-Channel GaAsP area detector. Sim imaging was performed using a SIM Black system (Zeiss ELYRA S.1 SR-SIM) equipped with a 63×/1.4NA oil objective (Zeiss; Plan-Apochromat 63×/1.4 Oil DIC M27).

Image Processing and Analysis

Airyscan and SIM images of the high-resolution acquisition were applied automatically for Alexa Fluor 488 Channel using ZEN software. To correct for imaging drift, the StackReg plugin of the ImageJ software was used to align an image stack with the target image. Next, processed images were measured and analyzed using ImageJ and Origin. The stack of 2D α-tubulin SIM images was reconstructed into a three-dimensional model using Avizo (Version 2019.1), the solution for 3D visualization and analysis of scientific and industrial data.

RESULTS

Optimization of the ExM Method in Yeast

Using ExM, many researchers obtained outstanding outcomes in various organisms except yeast. In this study, we firstly applied ExM to yeast and analyzed some of its structures. The traditional immunofluorescence approach may result in structures such as septin being severely damaged during the preparation of spheroplasts and centrifugation. To solve this problem, we developed an improved method for yeast immunofluorescence combined with ExM as shown schematically in **Figure 1A**. Yeast in a logarithmic growth phase was attached to slides specially treated with ConA, and continued to grow and divide on coated

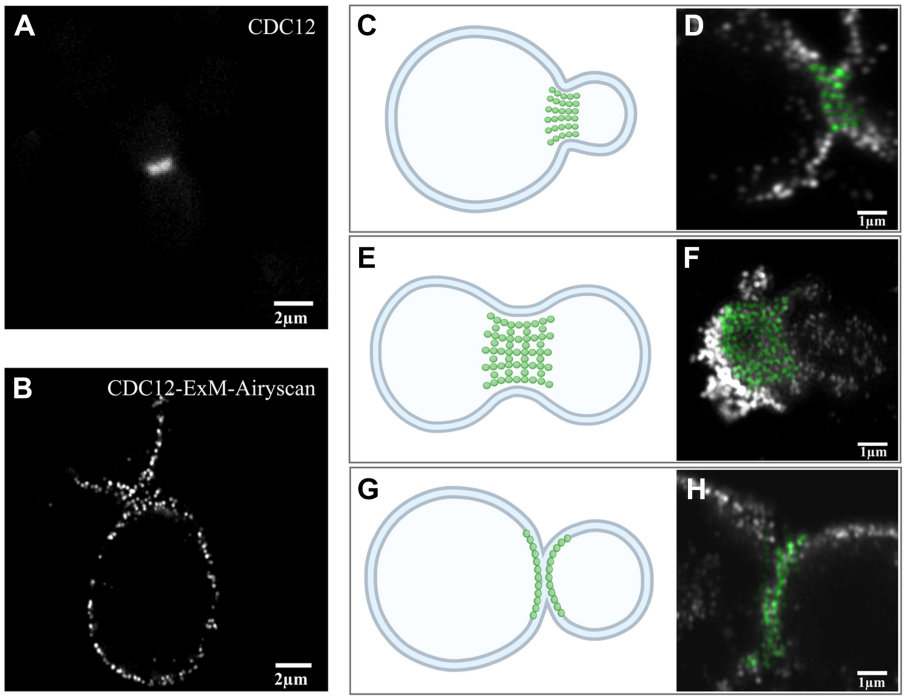

FIGURE 3 | Expansion images of septin-CDC12 in three different stages. **(A)** Pre-expansion wide-field imaging of septin CDC12. **(B)** Post-expansion Airyscan imaging of septin CDC 12. Diagram **(C)** and Airyscan image **(D)** of the early stages of yeast cell division. Graph **(E)** and image *via* Airyscan **(F)** of septin in the transition stage prior to ring splitting. Illustration **(G)** and Airyscan image **(H)** represented septin during the double-ring stage. The green dots in this figure **(D,H)** were pseudo-colors stand for the cdc12 at the division interface. Scale bar, 2 μm **(A,B)** and 1 μm **(D,F,H)**. All bars were physical scales before correction with expansion factor. The expansion factor is 4.1.

slides. After a period of growth, all samples are fixed and wall-digested so that some dividing yeast cells were captured on the slide. Finally, our samples were immunostained and then swelled, and the expansion factor range from 4.0 to 4.1.

ExM Results in Yeast

Using this method, we collected images of three structures: NPC, septin, and α-tubulin (**Figures 1B,E,H**). We illuminated the NPCs located on the equator of the yeast nucleus, which display a circular distribution of nuclear pore spots (**Figure 1B**). Wide-field imaging of GFP-labeled Nups was recognized well by antibodies (**Figure 1C**). The results show that the NPCs' axial view, located at the equator under Nup84 labeling, was observed as a roughly circular pre-expansion. The circular structure of the nucleus in cross-sectional shots post-expansion was more obvious under the same imaging conditions (**Figure 1D**). Using GFP-labeled septin targeted by antibodies, we observed linear septin structures at the junctions of cell divisions (**Figure 1F**). Although the septin size was enlarged after swelling (**Figure 1G**), no further structural information was visible and therefore required imaging in combination with higher resolution microscopy such as Airyscan. Afterwards, we proceeded in the same way with α-tubulin of yeast. After expansion, the needle-like structures with uneven tips observed in the α-tubulin images were more visible than before (**Figures 1I,J**).

Analysis of the NPC

The structure of NPC was analyzed using ExM and Airyscan microscopy. A diagram shows the bottom structure of the nuclear envelope and the radial view of a single NPC (**Figure 2A**). From this view, the yeast NPC complexes normally consist of eight spokes arranged around a central channel. The top view of yeast NPC at the bottom of the cell nucleus was imaged using Airyscan microscopy, which shows some nuclear pores as hollow spaces (**Figure 2B**). Using the Airyscan images, we chose single nuclear pores observed with a clear hollow structure and five points (**Figure 2C**). After center positioning, these nuclear holes with distinct hollow structures were measured and counted. The statistical measurement of the ring diameter data yields a histogram shown in **Figure 2D**. Analysis of the statistical data results in an average diameter of $\sim 67 \pm 15$ nm for the Nup 84-GFP fusion protein labeled with antibody after correction with expansion factor. The axial view of the NPC at the equator of the nuclear envelope was illustrated in a diagram in **Figure 2E**, and two-layer images should be observed in theory [32]. Based on the collected images, two parallel line structures were observed on some nuclear pores (**Figure 2F**). Likewise, the individual nuclear pores with two linear structures clearly apart and arranged in parallel (**Figure 2G**) were selected from the lateral images. From the statistical results, the absolute distance between the two parallel rings was recorded, with an average value of 45 ± 12 nm (**Figure 2H**). We measured 81

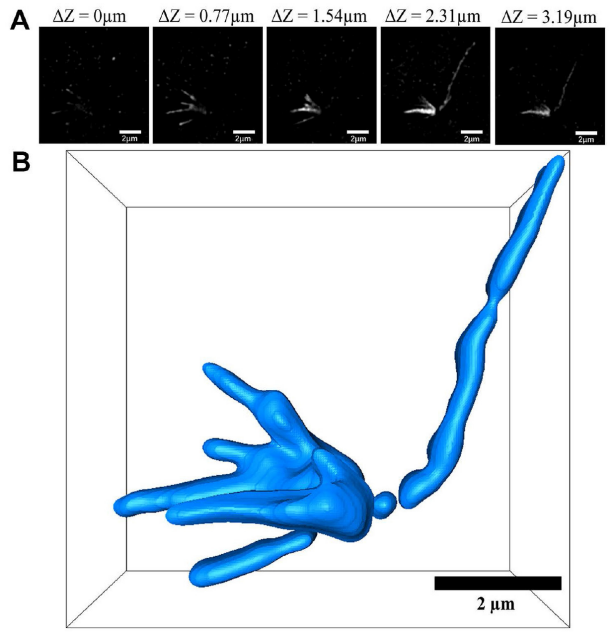

FIGURE 4 | Three-dimensional reconstruction of α-tubulin. **(A)** SIM images views at different z-levels. **(B)** Three-dimensional reconstruction using Avizo software. Scale bar, 2 μm **(A,B)**. All bars were physical scales before correction with expansion factor. The expansion factor is 4.0.

pores for diameter and 109 pores for the distance between the two rings.

Different Septin Stages

As the septin structure (**Figure 3A**) obtained before expansion imaging by wide-field microscopy did not show more detail compared to the pre-expansion sample, the post-expansion sample was photographed in Airyscan mode. From the Airyscan images, septin labeled with CDC12 was found to have a punctuated distribution, which provides additional structural information (**Figure 3B**). The structure of septin is arranged differently depending on the period of division based on EM studies [33]. From the EM results, there are three different periods of yeast budding: (1) the early hourglass stage (**Figure 3C**), (2) the transition stage (**Figure 3E**), and (3) the double-ring stage (**Figure 3G**). In the early stage of yeast division (**Figure 3C**), we found that the fluorescence signals of septin structures were arranged as short parallel lines perpendicular to the division interface (**Figure 3D**). During this period, the short septin filaments supporting the buds appeared to be arranged in parallel. In the transition stage prior to ring splitting (**Figure 3E**), the septin structures were arranged in a grid-like pattern during yeast division (**Figure 3F**), which are supposed to be composed of intersected filaments. The transitional septin complex structure seemed to be made up of horizontally and vertically interwoven septin filaments. At the later, double-ring stage (**Figure 3G**), the signals were also arranged in lines, but parallel to the division interface (**Figure 3H**). Compared with the first stage, septin filaments were reoriented by 90 degrees during the whole transition. This observation is in agreement with the model based on polarized fluorescence microscopy studies [22, 23].

Three-Dimensional Reconstruction of α-Tubulin

After labeling the yeast α-tubulin, we observed the expansion map of the α-tubulin structure. In SIM mode, we obtained images at different z-axis positions. These images represent the same xy interface with z-axis heights of 0, 0.77, 1.54, 2.31, and 3.19 μm (**Figure 4A**). All z-axis heights and bars of **Figure 4** were physical scales. A single long α-tubulin can be seen connecting multiple branches that were indistinguishable with wide-field imaging (**Figures 1I,J** and **Supplementary Figure 2**). However, in SIM imaging, five more clearly detailed branches were visible after inflation (**Figure 4A**). This observation is consistent with previously reported fluorescence images and EM results of yeast α-tubulin [25]. The α-tubulin structure was analyzed using graphs from different levels, and its three-dimensional view was reconstructed using Avizo software (**Figure 4B**).

DISCUSSION

Advances in super-resolution microscopy have overcame the limits of optical resolution, and offer researchers more visual information [34, 35]. However, super-resolution strategies are not based on a single optical technology, and the combination of different methods allowed us to gain insight into the function of the cell. The ExM technology is simple to operate, with a wide range of applications and compatibility with a wide range of super-resolution microscopy systems. As a result, numerous groups have made great strides in their fields by merging ExM with other super-resolution techniques. Here we show that the application of expansion technology is suitable for use in yeast, and that biological structures can be imaged at the single nuclear pore size level using expansion Airyscan and SIM microscopy. Combined with ExM, the standard Airyscan and SIM microscopy achieved an up to 4-fold improvement in resolution, from 120 to 30 nm (**Supplementary Figure 1**). Our method is designed to physically expand the yeast cell by immobilizing it and then digesting its cell walls, followed by conventional sample swelling methods. Using this technique, we carried out a structural analysis of the NPC, septin, and α-tubulin in yeast.

Conventional immunofluorescence procedures, which may lead to rupture of dividing yeast cells or even destruction of associated structures, have been optimized in our method. Typical yeast immunofluorescence methods use poly-L-lysine, a cellular non-specific attachment factor that immobilizes cells onto the slide by enhancing the electrostatic interaction between the cell membrane and the slide surface. However, it does not work for all cells, including yeast. Therefore, in the traditional method, the yeast cell walls need to be digested to obtain spheroplasts before it can be adhered to the slide. In these cases, ConA, a coagulant used as an immobilizer, was tried in our approach. Importantly, it also allows yeast to germinate in these conditions and in the presence of sorbitol. After the yeast cell was successfully attached to the ConA-coated slide and cultured in

YPD growth medium with sorbitol for a short time, the structure of dividing yeast cells was harvested from dividing cells. This approach allowed us to successfully apply the swelling super-resolution technique to septin in yeast to study the structure of the relevant proteins in the splitting position (shown in the schematic diagram of **Figure 1E**). This optimization enabled us to apply ExM to some structures in yeast, including septin, which is a structure located at the division site.

We applied our method to the molecular organization of the yeast NPC scaffold, which is generally assumed to be similar to the organization of the human subcomplex [36]. With ExM, the hollow and double-ring structure of individual yeast nuclear pores was observed *via* Airyscan microscopy. We measured nuclear pores that had a distinctly hollow structure and obtained a mean pore diameter of 67 ± 15 nm. In the same way, the absolute distance between two pore rings in the lateral view was 45 ± 12 nm. More than one factor should be considered regarding the deviation. As resolution increases, the error caused by the size of the antibody itself increases. The error close to the size of the GFP protein and the antibodies is ∼15 nm. However, we located the position of the center of the pore with intensity information over five points from the same nuclear pore, which reduces the error to below 7 nm [37]. For further improvements in resolution, small tags such as nanobody or snap [38] can be used in the future to obtain more accurate data in combination with our protocol.

Applying the ExM method to yeast, we showed that septin had different morphologies at the three stages of the cell cycle when imaged with Airyscan. This observation is consistent with models based on EM studies [33]. According to many traditional optical microscopy studies, the septin organization is presented as a long bar in the side-view throughout the period of division, and a detailed distribution of its structure cannot be visualized. In contrast, our Airyscan imaging of septin enabled us to determine that it was linearly aligned both at the early budding and double-ring stages, but with a 90-degree change of direction (**Figures 3D,H**). This result is consistent with previous polarized fluorescence microscopy studies [22, 39]. In the transition period, however, we observed a grid-like arrangement (**Figure 3F**). Moreover, our protocol allowed for tagging of multiple proteins, and thus it is potentially valuable to address other issues such as septin order. Admittedly, the distance between two septin proteins is hard to measure accurately owing to the loss of fluorescence during expansion processing [11]. The structure of septin could be further explored if the labeling density were increased.

CONCLUSIONS

In summary, the combination of the ExM technique with Airyscan or SIM was suitable to study different yeast structures. As a demonstration, we applied ConA to allow yeast cells to divide on a slide and collected structural images of NPC, septin, and α-tubulin. Our improved method provides access to the analysis of division-related structures located at the placement of the division site, and therefore extends the range of ExM applications in yeast. Compared to conventional optical microscopy, the combination of ExM and super-resolution imaging techniques increase the resolution for observing sub-cellular structures. Because ExM is independent and compatible with many super-resolution microscopes, cutting-edge imaging techniques such as STED and STORM can also be used to solve even smaller biological structural questions in yeast. In addition, ExM can be used flexibly in combination with various techniques, such as small molecule labeling or multiple labeling, to further examine the layout of protein complexes in yeast. Based on our method, other optimized yeast ExM protocols will allow further advances in yeast research.

DATA AVAILABILITY STATEMENT

The original contributions generated in the study are included in the article/**Supplementary Material**, further inquiries can be directed to the corresponding authors.

AUTHOR CONTRIBUTIONS

LC and JM conceived the project. LC performed the experiments, wrote the manuscript and performed imaging processing, and data analysis. LY, LZ, YF, LM, and JM revised the manuscript. All authors contributed to the article and approved the submitted version.

FUNDING

This research was financially supported by the National Natural Science Foundation of China (NSFC; Grants Numbers 11574056 and 61575046), the Ministry of Science and Technology of the People's Republic of China, (China-Serbia Bilateral Project SINO-SERBIA2018002), the Fudan University–CIOMP Joint Fund (Grant Numbers FC2017-007 and FC2018-001), the Pioneering Project of Academy for Engineering and Technology, Fudan University (Grants Numbers gyy2018-001 and gyy2018-002), the Shanghai Key Discipline Construction Plan (2020-2022) (Grant Number GWV-10.1-XK01), and the Shanghai Natural Science Foundation (Grant Numbers 20ZR1405100 and 20ZR1403700).

ACKNOWLEDGMENTS

The authors wish to thank LZ for help with the experiments, LY, Baoju Wang, and Yueyue Jing for help in revising the manuscript, the Juntao Gao group for providing us with the septin CDC12-GFP yeast strain, and Editage (www.editage.cn) for English language editing.

SUPPLEMENTARY MATERIAL

The Supplementary Material for this article can be found online at: https://www.frontiersin.org/articles/10.3389/fphy.2021.650353/full#supplementary-material

REFERENCES

1. Hell SW, Wichmann J. Breaking the diffraction resolution limit by stimulated emission: stimulated-emission-depletion fluorescence microscopy. *Optics Lett*. (1994) 19:780–2. doi: 10.1364/OL.19.000780
2. Jahr W, Velicky P, Danzl JG. Strategies to maximize performance in stimulated emission depletion (STED) nanoscopy of biological specimens. *Methods*. (2020) 174:27–41. doi: 10.1016/j.ymeth.2019.07.019
3. Hausmann M, Schneider B, Bradl J, Cremer C. High-precision distance microscopy of 3D-nanostructures by a spatially modulated excitation fluorescence microscope. *Proc SPIE*. (1997) 3197:217–22. doi: 10.1117/12.297969
4. Gustafsson MG. Surpassing the lateral resolution limit by a factor of two using structured illumination microscopy. *J Microsc*. (2000) 198:82–7. doi: 10.1046/j.1365-2818.2000.00710.x
5. Schermelleh L, Carlton PM, Haase S, Shao L, Winoto L, Kner P, et al. Subdiffraction multicolor imaging of the nuclear periphery with 3D structured illumination microscopy. *Science*. (2008) 320:1332–6. doi: 10.1126/science.1156947
6. Huff J. The Airyscan detector from ZEISS: confocal imaging with improved signal-to-noise ratio and super-resolution. *Nat Methods*. (2015) 12:i–ii. doi: 10.1038/nmeth.f.388
7. Hildenbrand G, Rapp A, Spöri U, Wagner C, Cremer C, Hausmann M. Nano-sizing of specific gene domains in intact human cell nuclei by spatially modulated illumination light microscopy. *Biophys J*. (2005) 88:4312–8. doi: 10.1529/biophysj.104.056796
8. Korobchevskaya K, Lagerholm BC, Colin-York H, Fritzsche M. Exploring the potential of airyscan microscopy for live cell imaging. *Photonics*. (2017) 4:41. doi: 10.3390/photonics4030041
9. Rust MJ, Bates M, Zhuang X. Sub-diffraction-limit imaging by stochastic optical reconstruction microscopy (STORM). *Nat Methods*. (2006) 3:793–5. doi: 10.1038/nmeth929
10. Chen F, Tillberg PW, Boyden ES. Optical imaging. *Expans Microsc Sci*. (2015) 347:543–8. doi: 10.1126/science.1260088
11. Tillberg PW, Chen F, Piatkevich KD, Zhao Y, Yu CC, English BP, et al. Protein-retention expansion microscopy of cells and tissues labeled using standard fluorescent proteins and antibodies. *Nat Biotechnol*. (2016) 34:987–92. doi: 10.1038/nbt.3625
12. Artur CG, Womack T, Zhao F, Eriksen JL, Mayerich D, Shih W-C. Plasmonic nanoparticle-based expansion microscopy with surface-enhanced Raman and dark-field spectroscopic imaging. *Biomed Opt Express*. (2018) 9:603–15. doi: 10.1364/BOE.9.000603
13. Ku T, Swaney J, Park JY, Albanese A, Murray E, Cho JH, et al. Multiplexed and scalable super-resolution imaging of three-dimensional protein localization in size-adjustable tissues. *Nat Biotechnol*. (2016) 34:973–81. doi: 10.1038/nbt.3641
14. Wang G, Moffitt JR, Zhuang X. Multiplexed imaging of high-density libraries of RNAs with MERFISH and expansion microscopy. *Sci Rep*. (2018) 8:4847. doi: 10.1038/s41598-018-22297-7
15. Chang J-B, Chen F, Yoon YG, Jung EE, Babcock H, Kang JS, et al. Iterative expansion microscopy. *Nat Methods*. (2017) 14:593–9. doi: 10.1038/nmeth.4261
16. Zhao Y, Bucur O, Irshad H, Chen F, Weins A, Stancu AL, et al. Nanoscale imaging of clinical specimens using pathology-optimized expansion microscopy. *Nat Biotechnol*. (2017) 35:757–64. doi: 10.1038/nbt.3892
17. Cahoon CK, Yu Z, Wang Y, Guo F, Unruh JR, Slaughter BD, et al. Superresolution expansion microscopy reveals the three-dimensional organization of the Drosophila synaptonemal complex. *PNAS*. (2017) 114:E6857–66. doi: 10.1073/pnas.1705623114
18. Halpern AR, Alas G, Chozinski TJ, Paredez AR, Vaughan JC. Hybrid structured illumination expansion microscopy reveals microbial cytoskeleton organization. *ACS Nano*. (2017) 11:12677–86. doi: 10.1021/acsnano.7b07200
19. Tsai A, Muthusamy AK, Alves MR, Lavis LD, Singer RH, Stern DL, et al. Nuclear microenvironments modulate transcription from low-affinity enhancers. *eLife*. (2017) 6:e28975. doi: 10.7554/eLife.28975
20. Götz R, Panzer S, Trinks N, Eilts J, Wagener J, Turrà D, et al. Expansion microscopy for cell biology analysis in fungi. *Front Microbiol*. (2020) 11:574. doi: 10.3389/fmicb.2020.00574
21. Aitchison JD, Rout MP. The yeast nuclear pore complex and transport through it. *Genetics*. (2012) 190:855–83. doi: 10.1534/genetics.111.127803
22. Vrabioiu AM, Mitchison TJ. Structural insights into yeast septin organization from polarized fluorescence microscopy. *Nature*. (2006) 443:466–9. doi: 10.1038/nature05109
23. McMurray MA, Bertin A, Garcia G, III, Lam L, Nogales E, Thorner J. Septin filament formation is essential in budding yeast. *Dev Cell*. (2011) 20:540–9. doi: 10.1016/j.devcel.2011.02.004
24. Bertin A, McMurray MA, Grob P, Park SS, Garcia G, III, Patanwala I, et al. Saccharomyces cerevisiae septins: supramolecular organization of heterooligomers and the mechanism of filament assembly. *Proc Natl Acad Sci USA*. (2008) 105:8274–9. doi: 10.1073/pnas.0803330105
25. Keck JM, Jones MH, Wong CC, Binkley J, Chen D, Jaspersen SL, et al. A cell cycle phosphoproteome of the yeast centrosome. *Science*. (2011) 332:1557–61. doi: 10.1126/science.1205193
26. Senic-Matuglia F, Visintin R. Localizing MEN components by indirect immunofluorescence analysis of budding yeast. *Methods Mol Biol*. (2017) 1505:135–49. doi: 10.1007/978-1-4939-6502-1_11
27. Syga Ł, Spakman D, Punter CM, Poolman B. Method for immobilization of living and synthetic cells for high-resolution imaging and single-particle tracking. *Sci Rep*. (2018) 8:13789. doi: 10.1038/s41598-018-32166-y
28. Garcia G, III, Bertin A, Li Z, Song Y, McMurray MA, Thorner J, et al. Subunit-dependent modulation of septin assembly: budding yeast septin Shs1 promotes ring and gauze formation. *J Cell Biol*. (2011) 195:993–1004. doi: 10.1083/jcb.201107123
29. Huh WK, Falvo J, Gerke L, Carroll AS, Howson RW, Weissman JS, et al. Global analysis of protein localization in budding yeast. *Nature*. (2003) 425:686–91. doi: 10.1038/nature02026
30. Zhanghao K, Chen L, Yang XS, Wang MY, Jing ZL, Han HB, et al. Super-resolution dipole orientation mapping *via* polarization demodulation. *Light Sci Appl*. (2016) 5:e16166. doi: 10.1038/lsa.2016.166
31. Chozinski TJ, Halpern AR, Okawa H, Kim H-J, Tremel GJ, Wong ROL, et al. Expansion microscopy with conventional antibodies and fluorescent proteins. *Nat Methods*. (2016) 13:485–8. doi: 10.1038/nmeth.3833
32. Mi L, Goryaynov A, Lindquist A, Rexach M, Yang W. Quantifying nucleoporin stoichiometry inside single nuclear pore complexes *in vivo*. *Sci Rep*. (2015) 5:9372. doi: 10.1038/srep09372
33. Ong K, Svitkina T, Bi E. Visualization of *in vivo* septin ultrastructures by platinum replica electron microscopy. *Methods Cell Biol*. (2016) 136:73–97. doi: 10.1016/bs.mcb.2016.03.011
34. Coltharp C, Xiao J. Superresolution microscopy for microbiology. *Cell Microbiol*. (2012) 14:1808–18. doi: 10.1111/cmi.12024
35. Schermelleh L, Ferrand A, Huser T, Eggeling C, Sauer M, Biehlmaier O, et al. Super-resolution microscopy demystified. *Nat Cell Biol*. (2019) 21:72–84. doi: 10.1038/s41556-018-0251-8
36. Szymborska A, de Marco A, Daigle N, Cordes VC, Briggs JA, Ellenberg J. Nuclear pore scaffold structure analyzed by super-resolution microscopy and particle averaging. *Science (New York, NY)*. (2013) 341:655–8. doi: 10.1126/science.1240672
37. Ma J, Kelich JM, Junod SL, Yang W. Super-resolution mapping of scaffold nucleoporins in the nuclear pore complex. *J Cell Sci*. (2017) 130:1299–306. doi: 10.1242/jcs.193912
38. Sun DE, Fan X, Shi Y, Zhang H, Huang Z, Cheng B, et al. Click-ExM enables expansion microscopy for all biomolecules. *Nat Methods*. 18:107–13 (2021). doi: 10.1038/s41592-020-01005-2
39. DeMay BS, Bai X, Howard L, Occhipinti P, Meseroll RA, Spiliotis ET, et al. Septin filaments exhibit a dynamic, paired organization that is conserved from yeast to mammals. *J Cell Biol*. (2011) 193:1065–81. doi: 10.1083/jcb.201012143

Conflict of Interest: The authors declare that the research was conducted in the absence of any commercial or financial relationships that could be construed as a potential conflict of interest.

frontiers in Physics

BRIEF RESEARCH REPORT
published: 01 April 2021
doi: 10.3389/fphy.2021.651147

Programmable Supercontinuum Laser Spectrum Generator Based on a Liquid-Crystal on Silicon Spatial Light Modulator

Pascuala García-Martínez[1]*, *Ignacio Moreno*[2,3], *María del Mar Sánchez-López*[2,4], *Jordi Gomis*[3], *Pedro Martínez*[3] and *Aarón Cofré*[3]

[1] Departamento de Óptica, Facultat de Física, Universitat de València, Burjassot, Spain, [2] Instituto de Bioingeniería, Universidad Miguel Hernández de Elche, Elche, Spain, [3] Departamento de Ciencia de Materiales, Óptica y Tecnología Electrónica, Universidad Miguel Hernández de Elche, Elche, Spain, [4] Departamento de Física Aplicada, Universidad Miguel Hernández de Elche, Elche, Spain

Supercontinuum (SC) lasers combine a broadband light spectrum with the unique properties of single-mode lasers. In this work we present an optical system to spectrally filter a SC laser source using liquid-crystal on silicon (LCoS) spatial light modulators (SLM). The proposed optical system disperses the input laser and the spectrally separated components are projected onto the LCoS-SLM, where the state of polarization of each wavelength is separately modulated. Finally, recombining the modulated spectral components results in an output laser source where the spectrum can be controlled dynamically from a computer. The system incorporates two branches to independently control the visible (VIS) and the near infrared (NIR) spectral content, thus providing a SC laser source from 450 to 1,600 nm with programmable spectrum. This new ability for controlling at will the wide spectra of the SC laser sources can be extremely useful for biological imaging applications.

Keywords: supercontinuum laser, broadband light sources, spatial light modulators, biological applications, microscopy, liquid crystal on silicon

OPEN ACCESS

Edited by:
Ming Lei,
Xi'an Jiaotong University, China

Reviewed by:
Kapil Debnath,
Indian Institute of Technology Kharagpur, India
Junichi Fujikata,
Photonics Electronics Technology Research Association, Japan

***Correspondence:**
Pascuala García-Martínez
pascuala.garcia@uv.es

Specialty section:
This article was submitted to Optics and Photonics, a section of the journal Frontiers in Physics

Received: *08 January 2021*
Accepted: *09 March 2021*
Published: *01 April 2021*

Citation:
García-Martínez P, Moreno I, Sánchez-López MM, Gomis J, Martínez P and Cofré A (2021) Programmable Supercontinuum Laser Spectrum Generator Based on a Liquid-Crystal on Silicon Spatial Light Modulator. Front. Phys. 9:651147. doi: 10.3389/fphy.2021.651147

INTRODUCTION

A wide range of applications from biological and biomedical microscopic imaging requires a use of SC laser sources. They are characterized by an extremely broad spectral coverage from ∼400 to 2,400 nm emitted as a continuum with an integrated power of up to several watts (even tens of watts), and at the same time a perfect Gaussian single-mode beam which can be focused down to the diffraction limit. This gives rise to a brightness that can exceed conventional light sources by more than six orders of magnitude, while staying within the spatial resolution regime of optical microscopy if needed [1]. Those sources have found many applications in a variety of fields of microscopy such as confocal microscopy [2] and STED microscopy [3].

In addition, SLMs are useful devices for advancing microscopy technology and they have been employed to control the imaging performance of many optical microscopes [4, 5]. In fact, a SLM can have different functions in a microscope, going from controlling the illumination by displaying a diffractive optical element (DOE) that structures and shapes the illumination beam, or/and acting on the imaging path of the microscope, by manipulating the Fourier components of the light coming from the sample [4, 6].

In many optical systems, the possibility of controlling light source spectra is an interesting subject. Some efforts have been done in solar simulators using a supercontinuum laser to implement tuning spectra using static opaque masks as mobile elements for spectral shaping [7] or use a programmable liquid crystal (LC) SLMs to rapidly generate an arbitrary spectrum [8]. However, the visible range is lost due to the poor laser emission in this wavelength range.

Some years ago, we presented an optical system based on a LCoS-SLM that acts as a waveplate with a programmable spectral retardance function in the visible wavelength range which is controlled via the voltage signal which depends on the addressed gray level of the LCoS panel [9]. The proposed optical system was probed experimentally through different examples, which include broadband constant phase-shift retarders, and retardance bands of variable bandwidth and variable central wavelength. A great number of applications, such as hyperspectral imaging, spectral polarimetry, ellipsometry, interferometry or colorimetry, among others, can benefit from this control.

In this work, we extend our previous optical system shown in Moreno et al. [9] to a programmable spectra light source generation by extending the spectral range to include also the near infrared (NIR) region and so being able to generate any desired spectra. This spectral extension is accomplished taking profit of the light beam reflected at the beam splitter in the system to include a second arm that is modulated by a second LCoS-SLM operational at the NIR wavelength range. In fact, the extension to NIR light could be very important in different areas, like optical fiber communications, with standard windows operating at 980 nm, 1,330 m, and 1,550 nm [10], or in biomedical imaging, where the conventional therapeutical windows are centered at ranges of 650–950 nm (first window) or 1,100–1,350 nm (second window) [11]. Using techniques like Optical Coherence Tomography (OCT), the penetration in biological tissues has been demonstrated to increase with larger wavelengths, ranging from only hundreds of microns in the shorter wavelength region of the visible spectrum (about 450–550 nm) to about 1–2 mm in the mid infrared (1,300–1,500 nm) [12]. Thus, a broadband laser source system where the spectrum can be designed and tuned in real time can be extremely interesting also for these applications.

The paper is organized as follows: after this introduction, Section "Experimental System" describes the VIS-NIR programmable SC laser spectrum generator system; then Section "Calibration Procedure" explains the explains the adjustments required to achieve good results; Section "Experimental Results" includes experiments that demonstrate the effective generation of different spectral content in the laser source; finally, Section "Conclusions" concludes the work.

EXPERIMENTAL SYSTEM

The optical setup scheme is shown in **Figure 1**. The input light is a supercontinuum laser beam from Fianium (model SC400). This light source emits a broadband laser beam with continuous broadband spectrum from 400 nm to more than 1,800 nm. The beam is first polarized by a Glan-Taylor linear polarizer useful in this complete spectral range (Edmund Optics #89–547), with an orientation of 45° with respect to the horizontal direction in the laboratory framework. Then, it is directed onto a non-polarizing beam splitter (BS) that splits light into two arms. One arm is used to modulate each of the two spectral regions: VIS and NIR ranges, respectively. Then, each arm has the same optical scheme. First, the light beam traverses a blazed grating that disperse the input light. The first diffraction order, where the gratings show the highest efficiency, passes through an achromatic converging lens that produces a collimated beam that projects the dispersed light beam into the LCoS-SLM panel. We use two SLMs from Hamamatsu, models X10468-01 and X10468-08, specifically designed to be used for VIS and NIR, respectively. Both devices are parallel-aligned LCoS devices, i.e., they are pixelated linear retarders whose retardance at each pixel is controlled from a computer [13]. The applied voltage, and hence the retardance, is controlled using grayscale images with 8-bit encoding, allowing 256 levels. The LC director is oriented along the horizontal direction in both SLMs. Because the LC director axis forms 45° with the input polarization, the state of polarization is modulated on the reflected light as a function of the retardance applied by the LCoS-SLM. The modulated reflected beams follow then the reverse path, and the lens and the grating recombine all the spectral components again on the first diffraction order. This recombined beam propagates towards the BS where the two VIS and NIR beams merge again in a single output beam. A second Glan-Taylor linear polarizer is placed at the output, also oriented at 45°, which transforms the polarization modulation induced by the LCoS-SLMs onto irradiance modulation, thus generating a desired spectral filtering on the SC spectrum.

The spectrum of the output beam is registered with two spectrometers, a Stellar-Net Black-Comet STN-BLK-C-SR-25 model that can measure between 200 and 1,080 nm, and another Stellar-Net STE-RED-WAVE-NIR-512-25 model that can measure between 900 and 2,300 nm. A mirror mounted on an adjustable flip platform is used to direct the beam to one or the other spectrometer. A diffuser is placed before the spectrometer entrance, to avoid damaging the detectors.

CALIBRATION PROCEDURE

However, prior to be used, the system must be calibrated, since the SLM retardance depends on the wavelength and on the applied voltage. This means that one must carefully adjust the LCoS array to display the desired retardance for the wavelength illuminating each pixel. Therefore, it is necessary to determine the device retardance $\Phi\left(\lambda, g\right)$ both as a function of the wavelength (λ) and as a function of the addressed gray-level signal $\left(g\right)$. This function follows the typical relation of a single anisotropic LC layer, i.e., $\Phi\left(\lambda, g\right) = (2\pi/\lambda)\,\Delta n \cdot d$, where d is the thickness of the LC layer and $\Delta n(g)$ is its effective birefringence, which depends on the addressed signal.

Since the input polarizer has the transmission axis oriented at 45° with respect to the LC director axis, if the output polarizer is parallel to the first one, the ideal output normalized

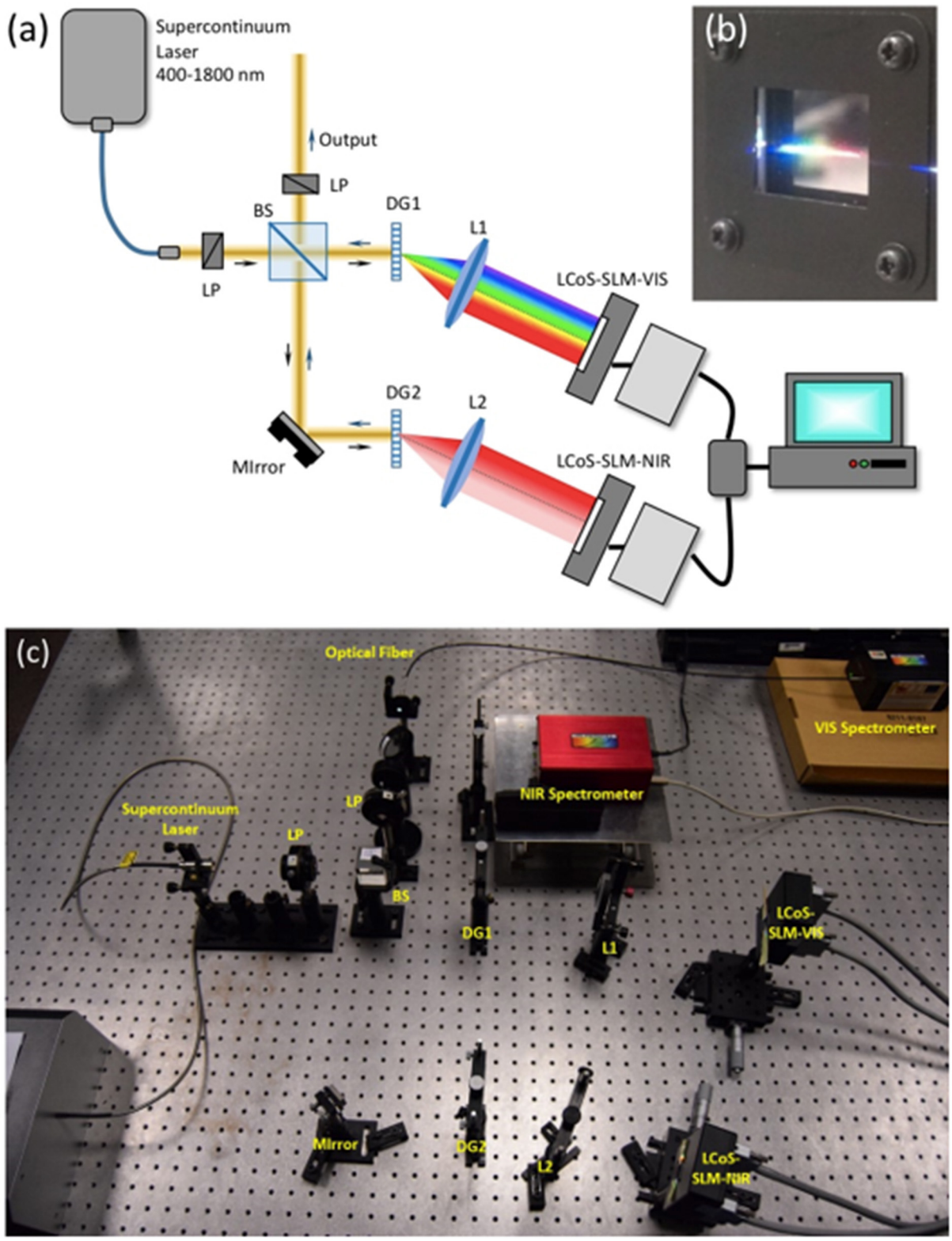

FIGURE 1 | (a) Scheme of the VIS-NIR spectrum generator; LP, linear polarizer; BS, beam-splitter; DG, blazed diffraction grating; L, converging lens. **(b)** Picture of the dispersed visible SC beam projected onto the VIS-LCoS-SLM. **(c)** Picture of the complete system.

irradiance transmission for parallel polarizers would be given by $i = i_{\max}\cos^2(\Phi/2)$ where $i_{\max}$ indicate the maximum transmission [14]. This relation allows calibrating the spectral retardance $\Phi(\lambda)$ in the SLM by measuring transmission $t(\lambda)$. Measurements show a typical oscillating spectrum vs. λ that can be fitted, typically with a Cauchy type relationship, to derive the retardance function for different applied voltages, as detailed in [9, 14]. Some other secondary rapid oscillations typically appear in the spectrum, due to Fabry-Perot type interferences generated at the different layers in the SLM device. Other polarization changes can occur at the different elements in the system. Nevertheless, all these effects can be considered to achieve a better fit, as detailed in [15]. The procedure has been applied successfully in many liquid-crystal devices, for precisely calibrating its modulation properties in the VIS spectral range [16], but also in the NIR range [17].

As a result of this calibration we obtain, for each gray level g addressed from the computer, functions that provide the spectral retardance $\Phi(\lambda, g)$ in the SLM, and the corresponding spectral irradiance $i(\lambda, g)$ at the output beam. Once this information was processed, we obtain a table of correspondence between retardance, wavelength and addressed gray level, which makes possible to define a gray level function $g(\lambda)$ that generates the desired spectral retardance $\Phi(\lambda)$ that provides a desired spectral irradiance $i(\lambda)$ at the output beam [9].

Another second important calibration requirement is an accurate determination of the spatial location on the SLM panels where each wavelength is impinging. As we see in **Figure 1b**, when separating the wavelengths with the diffraction grating and projecting on the SLM screen, a horizontal light beam strikes in which the different wavelengths are separated. Note that this is a requirement to be able to generate any arbitrary desired spectra $i(\lambda)$ since in this way we can control the retardance applied to each wavelength individually. Therefore, another very relevant calibration of the system consists in determining the mapping function $x = f(\lambda)$ that relates the wavelength λ with the pixel location x where this wavelength λ impinges. This calibration is obtained by displaying in the SLM again a uniform gray-level image, but now with a very narrow vertical bar with a different gray level. Such a narrow bar affects only a narrow spectral band, which can be easily identified in the spectrometer measurement.

Finally, as a result, if an output spectrum function defined as $i(\lambda)$ is desired at the output, a corresponding gray-level function $g(x)$ is calculated that must be addressed to the SLM to generate it. Note that the images addressed to the SLM are one-dimensional functions with variations only along the x direction. We refer the reader to our previous works [9, 14–17] to obtain more details about all these calibration procedures, and here we rather concentrate on the obtained results with the VIS-NIR spectral generator.

EXPERIMENTAL RESULTS

In this work we applied this full procedure for both the VIS and the NIR SLMs, so we can extend the range in which the function $i(\lambda)$ can be designed. For that purpose, we generate two gray-level images, one for the VIS-SLM that controls the spectrum between 450 and 800 nm, and another for the NIR-SLM, that controls the spectrum between 900 and 1,400 nm. Note that we have a gap between 800 and 900 nm; these wavelengths lie outside the active area of the two SLMs are therefore are not contributing to the final output beam. However, we selected this configuration to be able to extend the function $i(\lambda)$ to cover most of the AM1.5 solar spectrum [7].

Minimum and Maximum Spectra

The first results, presented in **Figure 2a**, show the spectral functions $i_0(\lambda)$ and $i_1(\lambda)$ that correspond to the minimum and maximum irradiance, respectively. An image $g_0(x)$ like shown in **Figure 2b** is addressed to the VIS-SLM, where the gray-level values at each location has been assigned to provide at the output a polarization as close as possible to be linear and oriented at -45° for all wavelengths. In this way the light is completely absorbed by the output polarizer and a null transmission is expected. Considering that the input polarizer is oriented at $+45^\circ$, this implies that the system must operate as a half-wave retarder for all wavelengths. Note that the pattern $g_0(x)$ in **Figure 2b** is a continuous slow varying gray function along the horizontal direction, where the light spectrum has been dispersed (**Figure 1b**). Since the retardance, for a given gray-level, depends on the wavelength, the gray level mask $g_0(x)$ must show this above-mentioned variation to provide a constant half-wave retardance for all wavelengths. A similar function is addressed to the NIR-SLM, adapted to the modulation characteristics of this SLM.

Similarly, another gray-level image $g_1(x)$ is designed to generate the maximum spectrum $i_1(\lambda)$. In this case, the SLM must retain the input polarization linear oriented at $+45^\circ$ for all wavelengths, so it is fully transmitted by the output polarizer, delivering the maximum irradiance in the full spectrum. Therefore, the system must operate as a full-wave retarder for all wavelengths.

The results in **Figure 2a** verifies the good extinction expected for $i_0(\lambda)$ for all wavelengths, and the generation of a broadband spectrum $i_1(\lambda)$ that represents the upper bound of the different spectra than can be generated in the system. The experimental $i_1(\lambda)$ curve shows a value around 0.10 mW/(cm^{2}nm) in the complete spectrum from 450 to 1,400 nm, except for the non-accessible gap between 800 and 900 nm. A strong peak is entered at 1,064 nm, corresponding to the pump laser originating the SC continuum emission. Some rapid oscillations are also observed for low wavelengths, corresponding to Fabry-Perot interference effects in the VIS-SLM, which are more noticeable in this short wavelength range. These two spectra $i_1(\lambda)$ and $i_0(\lambda)$ are therefore the maximum and minimum bounds where we can control the output light. We measured an average signal-to-noise ratio $SNR = i_1/i_0 > 50$.

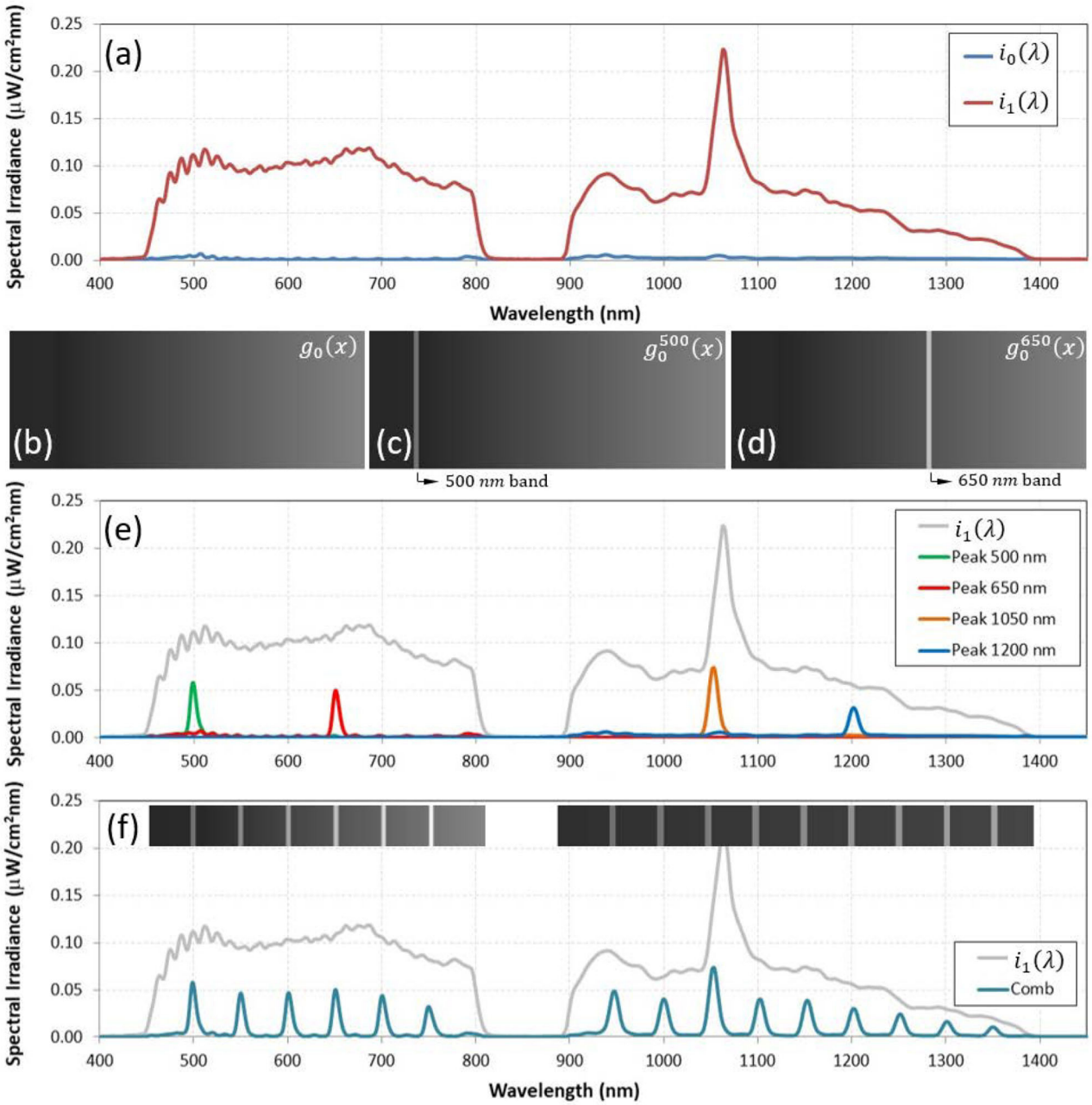

FIGURE 2 | (a) Experimental measurements of the minimum i_0 (λ) and maximum i_1 (λ) spectra. **(b)** Gray level function $g_0(x)$ generating i_0 (λ). **(c)** Gray level function $g_0^{500}(x)$ generating the narrow band at 500 nm. **(d)** Gray level function $g_0^{650}(x)$ generating the narrow band at 650 nm. **(e)** Experimental measurements for narrow bands centered at 500, 650, 1,050, and 1,200 nm. **(f)** Experimental measurements for a wavelength comb spectrum.

Specific Narrowband Wavelength Selection and Wavelength Combs

In many situations it is very interesting to achieve a light source where a narrow spectral band can be selected. This is a typical case in many biological samples that can show certain phenomenon (absorption, changes in their atomic structures, etc.) when illuminated by specific wavelengths. In **Figure 2e** we illustrate the possibilities offered by the developed system showing the spectral measurements when narrow spectral peaks are selected art wavelengths of 500, 650, 1,050, and 1,200 nm, respectively. The figure includes also the i_1 (λ) spectrum for comparison, that reveals that we are not reaching the maximum possible transmission. We attribute this effect to the fact that the laser spot on

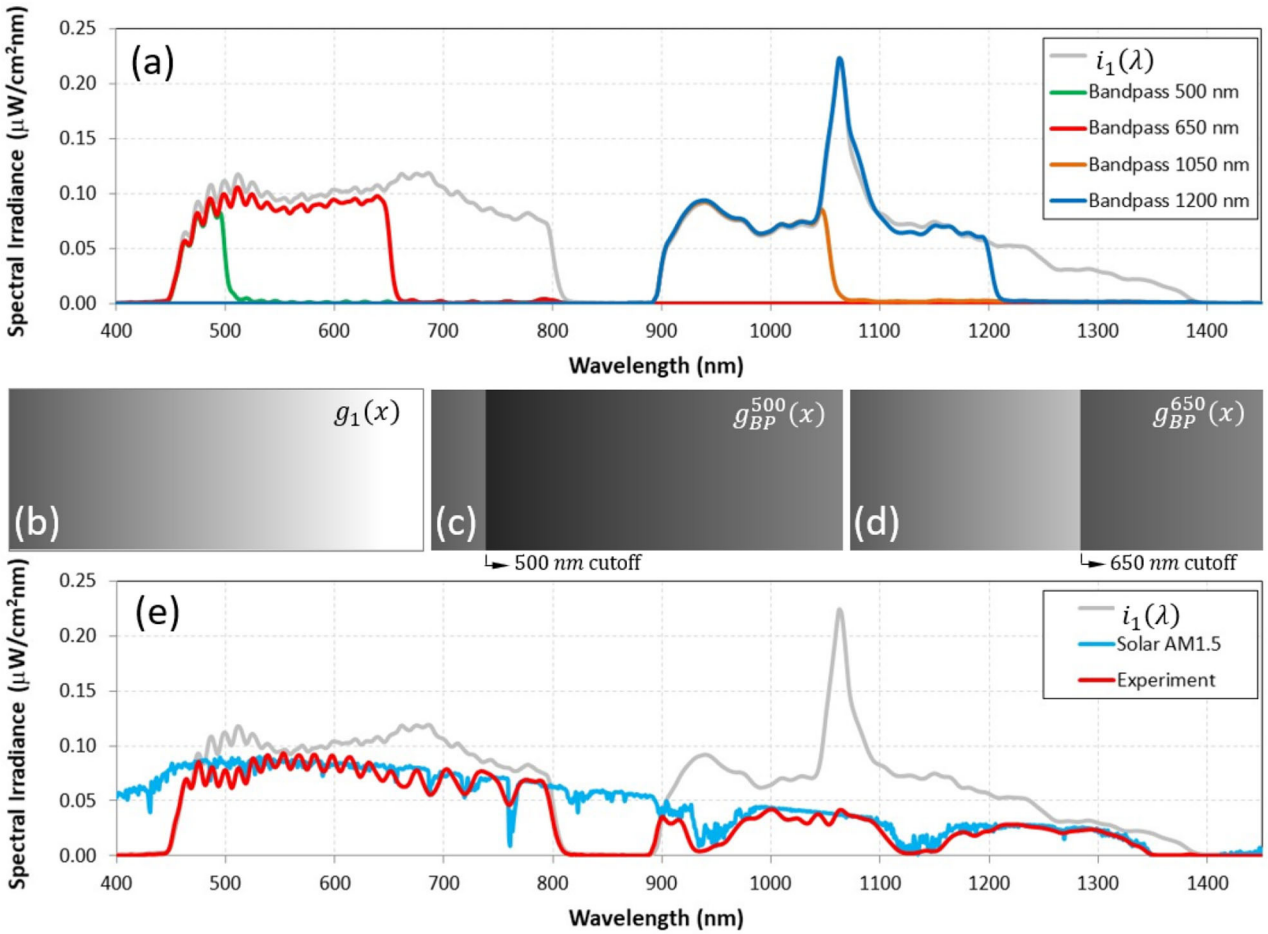

FIGURE 3 | (a) Experimental measurements for low bandpass illumination with cutoff wavelengths at 500, 650, 1,050, and 1,200 nm. **(b)** Gray level function $g_1(x)$ generating $i_1(\lambda)$. **(c)** Gray level function $g_{BP}^{500}(x)$ generating the bandpass at 500 nm. **(d)** Gray level function $g_{BP}^{650}(x)$ generating the bandpass at 650 nm. **(e)** Comparison of the solar AM1.5 spectrum with its experimental reproduction on the supercontinuum laser.

the SLM is larger than the pixel size, and some wavelength crosstalk happens. Nevertheless, the measured spectra show a successful generation of narrow bands centered at the expected wavelengths.

Figures 2c,d illustrate the gray-level masks $g_0^{500}(x)$ and $g_0^{650}(x)$ that are addressed in this case to the VIS-SLM device to generate the peaks at 500 and 650 nm, respectively. In each mask, a narrow vertical band substitutes the original values of $g_0(x)$ by those of $g_1(x)$, thus providing the high transmission in this narrow spectral band. Laterally shifting this band in the gray-level mask provides the wavelength shift in the spectrum. In order to clearly show the effect, these results show narrow bands of 10 pixels width around the central selected wavelength, which give a spectral width on the basis between 10 and 20 nm, depending on the central wavelength. Further reduction in the number of pixels in the band results in narrower but weaker spectral bands.

Figure 2f shows the generation of a wavelength comb spectrum, where one such narrow band peak is added every 50 nm, both in the VIS and in the NIR regions of the spectrum. The inset illustrates the two gray-level masks that are addressed to the two SLMs, each one composed of the corresponding $g_0(x)$ function background with the narrow bands corresponding to each peak in the spectrum.

Spectral Passband Illumination and Solar Spectrum

Spectral bandpass illumination is also interesting in many applications, including fluorescence or colorimetry. **Figure 3a** shows the experimental measurements obtained for different bandpass spectra starting at 450 nm and in 900 nm, respectively, with the cut-off wavelengths centered at 500 and 650 nm in the VIS region, and at 1,050 nm and 1,200 nm in the NIR region. **Figures 3b–d** illustrate the gray-level masks that are addressed to the VIS-SLM. **Figure 3b** shows the mask $g_1(x)$ that generates the maximum spectrum $i_1(\lambda)$. Note that it also presents a continuous gray-level variation, but with different values compared to the function $g_0(x)$ in **Figure 2b**, since $g_1(x)$ must provide a full wave retardance for all wavelengths. **Figures 3c,d** are the gray level

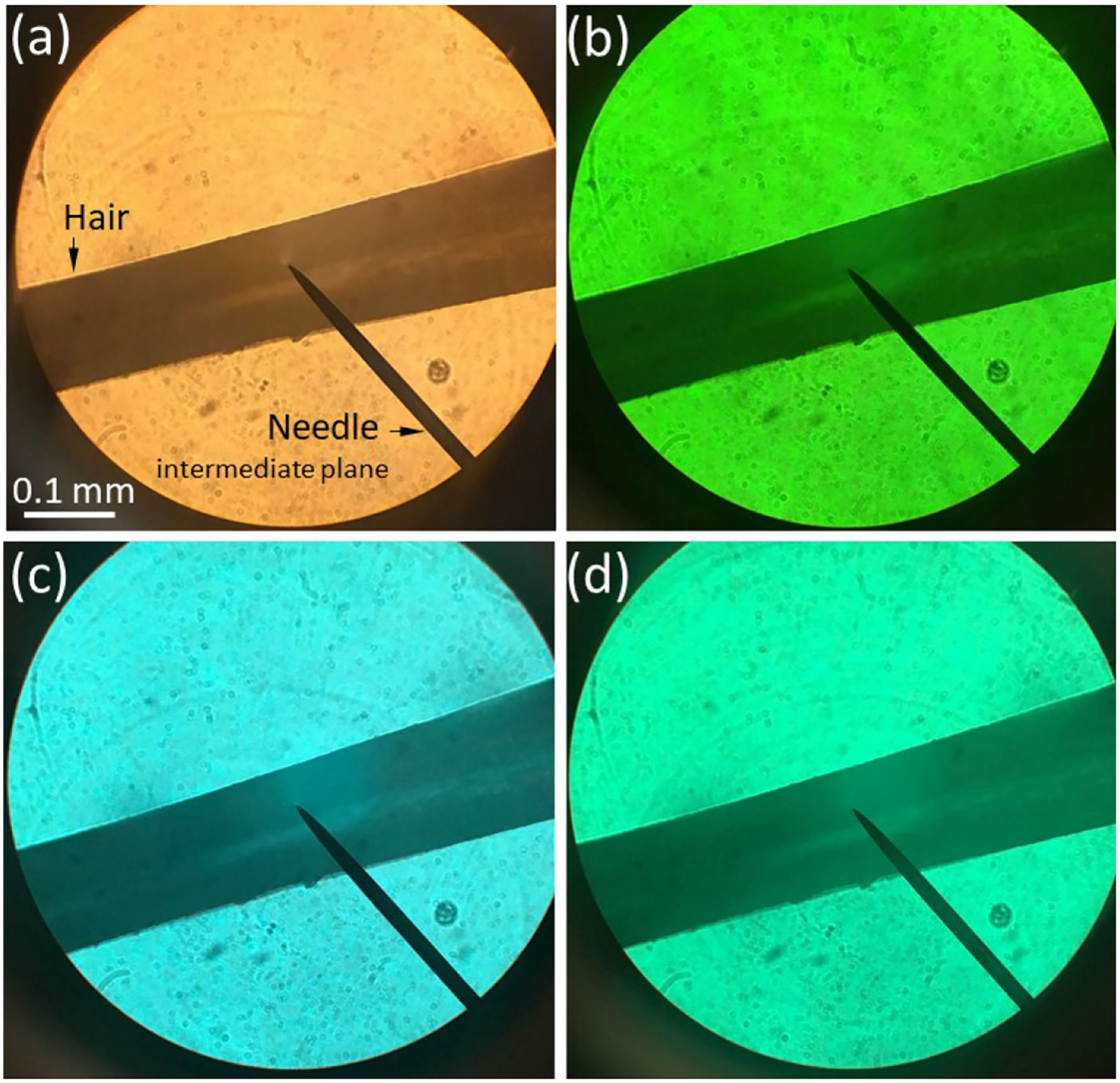

FIGURE 4 | Imaging in a conventional microscope illuminated with light output from the spectrum generator system. **(a)** Solar spectrum. **(b)** Narrowband illumination centered at 500 nm. **(c)** Narrowband illumination centered at 475 nm. **(d)** Lowpass illumination with cut-off centered at 550 nm.

masks $g_{BP}^{500}(x)$ and $g_{BP}^{650}(x)$ that generate the bandpass spectra with cut-off at 500 and 650 nm, respectively. Now, in each mask, the function $g_1(x)$ is used until the spatial location corresponding to the cut-off wavelength, where the mask is selected to the function $g_0(x)$ that provides the null transmission shown in **Figure 2b**. The transitions between the gray level masks $g_1(x)$ and $g_0(x)$ have been marked in **Figures 3c,d** when the cut-off wavelength is selected at 500 and 650 nm, respectively.

As a final example, in **Figure 3e** we have simulated the solar AM1.5 spectrum. Solar simulators are of great interest in photovoltaics [7] or in precision agriculture [18] applications. We have calculated the gray-scale image that best matches this solar spectrum within the limits imposed by the maximum available irradiance $i_1(\lambda)$. The graphs in **Figure 3e** shows the AM1.5 spectrum that we try to reproduce and the effective generation on the supercontinuum laser. Despite the oscillations observed in the visible region, and the bands below 450 nm and the gap between 800 and 900 nm, which are not accessible in the system, the rest of the spectrum shows a rather good reproduction of the solar AM1.5 curve. The ripple in the visible spectrum might be due to the Fabry-Perot effects that this SLM suffers, or to other electronic based effects like the pixel crosstalk caused by fringing in the LC layer. Nevertheless, the solar spectrum is well-reproduced in the VIS and in the NIR ranges, including the characteristic H_2O absorption bands around 940 and 1,140 nm.

To illustrate the possible potential use of this illumination system in microscopy. **Figure 4** shows some images captured in a conventional bright field microscope, where the illumination system has been substituted by the light output of the spectral generator system, which is delivered to the microscope with an optical fiber. A 10X objective is employed and the sample is a hair. The metallic needle that is also present in the image

is located in the microscope intermediate image. The images correspond to illumination of the sample with the solar spectrum (**Figure 4a**), with two narrow band illuminations centered at 500 and 475 nm (**Figures 4b,c**), and finally for a low band-pass illumination with cut-off at 550 nm. In this case, we used a regular RGB camera, so the spectral changes can be visualized in the change of color of the background. These results show the potentials of the system for multispectral, hyperspectral, or even more complicated structured spectral illumination.

CONCLUSIONS

In summary, an optical system for generating laser light spectra with a programmable spectral distribution is presented. One of our main motivation is to implement light sources at will for microscopic and biological imaging. The programmable part of our systems comes from the use of SLMs that can change retardance, and so irradiance, in real time. We proposed a complete system that covers both visible and near-infrared wavelength regions. In fact, there is a great interest in extending to NIR the technique because of its application in bio-samples imaging, where it increases the penetration in biological tissue.

Note that one of the great limitations of our system is the reduced light efficiency, due to the use of diffraction gratings, beam splitters, polarizers, as well as the losses in the SLMs. These limitations can be reduced by optimizing some of the optical elements such as diffracting grating and beam splitters.

DATA AVAILABILITY STATEMENT

The original contributions generated for this study are included in the article/supplementary material, further inquiries can be directed to the corresponding author/s.

AUTHOR CONTRIBUTIONS

JG and PM were two master students that did the optical experiments under the supervision of IM. AC was a doctorate student under the supervision of IM and MS-L. PG-M was a visitors professor at the University Miguel Hernandez of Elche that was collaborating in the experiment. PG-M, MS-L, and IM wrote the paper. All authors contributed to the article and approved the submitted version.

FUNDING

This work has been financed by Generalitat Valenciana, Conselleria d'Educació, Investigació, Cultura i Esport (PROMETEO-2017-154) and by Ministerio de Ciencia, Innovación y Universidades, Spain (RTI2018-097107-B-C33).

REFERENCES

1. Granzow N. Supercontinuum white light lasers: a review on technology and applications. *Photonics Educ Meas Sci.* (2019) 11144:1114408. doi: 10.1117/12.2533094
2. Shi K, Yin S, Liu Z. Chromatic confocal microscopy using supercontinuum light. *Opt Express*. (2004) 12:2096–101. doi: 10.1364/OPEX.12.002096
3. Wildanger D, Rittweger E, Kastrup L, Hell S. STED microscopy with a supercontinuum laser source. *Opt Express*. (2008) 16:9614–21. doi: 10.1364/OE.16.009614
4. Maurer C, Jesacher A, Bernet S, Ritsch-Marte M. What spatial light modualtors can do for optical microscopy? *Laser Photonics Rev*. (2011) 5:81–101. doi: 10.1002/lpor.200900047
5. Martinez J L, García-Martínez P, Moreno I. Microscope system with on axis programmable Fourier transform filtering. Opt. *Laser Eng*. (2016) 89:116–22. doi: 10.1016/j.optlaseng.2016.04.008
6. Micó V, García J, Camacho L, Zalevsky Z. Quantitative phase imaging in microscopy using a spatial light modulator. *Springer Ser Surf Sci*. (2011) 46:145–67. doi: 10.1007/978-3-642-15813-1_6
7. Dennis T, Schlager JB, Bertness KS. A novel solar simulator based on supercontinuum laser or sola cell device and material characterization. *IEEE J Photovoltaics*. (2014) 4:1119–27. doi: 10.1109/JPHOTOV.2014.2321659
8. Dennis T. An arbitrarily programmable solar simulator based on a liquid crystal spatial light modulator. *IEEE 40th Conference Photovoltaic Specialist Conference* (Denver, CO). (2014). p. 3326–30. doi: 10.1109/PVSC.2014.6925647
9. Moreno I, Carrión JV, Martínez JL, García-Martínez P, Sánchez-López MM, Campos J. Optical retarder system with programmable spectral retardance. *Opt Lett*. (2014) 39:5483–6. doi: 10.1364/OL.39.005483
10. Hetch J. *City of Light: The Story of Fiber Optics*. Oxford: Oxford University Press (1999).
11. Sordillo LA, Pu Y, Pratavieira S, Budansky Y, Alfano RR. Deep optical imaging of tissue using the second and third near-infrared spectral windows. *J Biomed Opt*. (2014) 19:056004. doi: 10.1117/1.JBO.19.5.056004
12. Unterhuber A, Povazay B, Bizheva K, Hermann B, Sattmann H, Stingl A, et al. Advances in broad bandwidth light sources for ultrahigh resolution optical coherence tomography. *Phys Med Biol*. (2004) 49:1235–46. doi: 10.1088/0031-9155/49/7/011
13. Rosales-Guzmán C, Forbes A. *How to Shape Light With Spatial Light Modulators*. SPIE Press (2017). doi: 10.1117/3.2281295
14. Vargas A, Donoso R, Ramírez M, Carrión J, Sánchez-López MM, Moreno I. Liquid crystal retarder spectral retardance characterization based on a Cauchy dispersion relation and a voltage transfer function *Opt Rev*. (2013) 20:378–84. doi: 10.1007/s10043-013-0068-4
15. Vargas A, Sánchez-López MM, García-Martínez P, Arias J, Moreno I. Highly accurate spectral retardance characterization of a liquid crystal retarder including Fabry-Perot interference effects. *J Appl Phys*. (2014) 115:033101. doi: 10.1063/1.4861635
16. Marco D, Sánchez-López MM, García-Martínez P, Moreno I. Using birefringence colors to evaluate a tunable liquid-crystal q-plate. *J Opt Soc Am B*. (2019) 36:D34–41. doi: 10.1364/JOSAB.36.000D34
17. Messaadi A, Sánchez-López MM, García-Martínez P, Vargas A, Moreno I. Optical system for measuring the spectral retardance function in an extended range. *J Eur Opt Soc Rapid Pub*. (2016) 12:21. doi: 10.1186/s41476-016-0023-7
18. Yoon HI, Kim JH, Park KS, Namgoong JW, Hwang TG, Kim JP, Son JE. Quantitative methods for evaluating the conversion performance of spectrum conversion films and testing plant responses under simulated solar conditions. *Hort Environ Biotechnol*. (2020) 61:999–1009. doi: 10.1007/s13580-020-00286-y

Conflict of Interest: The authors declare that the research was conducted in the absence of any commercial or financial relationships that could be construed as a potential conflict of interest.

frontiers in Physics

ORIGINAL RESEARCH
published: 12 April 2021
doi: 10.3389/fphy.2021.650108

Deep-Learning-Based Halo-Free White-Light Diffraction Phase Imaging

Kehua Zhang[1], *Miaomiao Zhu*[1], *Lihong Ma*[2,3]*, *Jiaheng Zhang*[2,3] *and Yong Li*[2,3]

[1] Key Laboratory of Urban Rail Transit Intelligent Operation and Maintenance Technology and Equipment of Zhejiang Province, Zhejiang Normal University, Jinhua, China, [2] Institute of Information Optics, Zhejiang Normal University, Jinhua, China, [3] Key Laboratory of Optical Information Detecting and Display Technology in Zhejiang Province, Zhejiang Normal University, Jinhua, China

In white-light diffraction phase imaging, when used with insufficient spatial filtering, phase image exhibits object-dependent artifacts, especially around the edges of the object, referred to the well-known halo effect. Here we present a new deep-learning-based approach for recovering halo-free white-light diffraction phase images. The neural network-based method can accurately and rapidly remove the halo artifacts not relying on any *priori* knowledge. First, the neural network, namely HFDNN (deep neural network for halo free), is designed. Then, the HFDNN is trained by using pairs of the measured phase images, acquired by white-light diffraction phase imaging system, and the true phase images. After the training, the HFDNN takes a measured phase image as input to rapidly correct the halo artifacts and reconstruct an accurate halo-free phase image. We validate the effectiveness and the robustness of the method by correcting the phase images on various samples, including standard polystyrene beads, living red blood cells and monascus spores and hyphaes. In contrast to the existing halo-free methods, the proposed HFDNN method does not rely on the hardware design or does not need iterative computations, providing a new avenue to all halo-free white-light phase imaging techniques.

Keywords: quantitative phase imaging, diffraction phase microscopy, deep learning, halo-free, white-light illumination

OPEN ACCESS

Edited by:
Chao Zuo,
Nanjing University of Science and Technology, China

Reviewed by:
Jiaji Li,
Nanjing University of Science and Technology, China
Zahid Yaqoob,
Massachusetts Institute of Technology, United States

***Correspondence:**
Lihong Ma
zjnumlh@zjnu.cn

Specialty section:
This article was submitted to Optics and Photonics, a section of the journal Frontiers in Physics

Received: *06 January 2021*
Accepted: *16 March 2021*
Published: *12 April 2021*

Citation:
Zhang K, Zhu M, Ma L, Zhang J and Li Y (2021) Deep-Learning-Based Halo-Free White-Light Diffraction Phase Imaging. Front. Phys. 9:650108. doi: 10.3389/fphy.2021.650108

INTRODUCTION

In recent years, quantitative phase imaging (QPI) is a rapidly growing research field, which has been broadly used in cell biological research and disease diagnosis [1]. Quantitative phase imaging can acquire quantitative phase measurement without the need for tagging, investigating optical path delays induced by the specimen at the full field of view. And the optical pathlength data can be further converted into various biologically-relevant information [2–4]. Kinds of QPI techniques, such as optical coherence tomography (OCT) [5, 6], digital holographic microscopy (DHM) [7, 8], diffraction phase microscopy (DPM) [9, 10], transport of intensity equation (TIE) [11, 12], optical diffraction tomography (ODT) [13, 14], and so on, have been developed to help access to this valuable phase information.

Diffraction phase microscopy combines many of the best attributes of current QPI techniques. Its common-path [15], off-axis [16] approach takes advantage of both the low spatiotemporal noise and fast acquisition rates of previous QPI techniques. Diffraction phase microscopy using white-light illumination (wDPM) [17, 18], exhibits lower noise levels than its laser counterparts, although requires more precise alignment. This is a result of the lower coherence, both temporally and spatially, which reduces speckle [19, 20]. Due to the dramatically low spatiotemporal noise, wDPM has been receiving intense scientific interest as a new modality for label-free cell biology studies and medical diagnostics.

However, unfortunately, like all white-light phase contrast imaging systems, when used with insufficient spatial filtering, wDPM exhibits object-dependent artifacts not present in laser counterparts, especially around the edges of the object, referred to the well-known halo effect, which disrupt the accuracy of quantitative measurements. Previous many methods have been proposed to eliminate the halo problem. A possible way is to simply reduce the area of the illumination aperture to improve the spatial coherence of the illumination, thus reducing the halo artifacts [21–25]. It is feasible for wDPM to adopt proper spatial filtering at the condenser and the output Fourier plane to ensure adequate spatial coherence and remove the halo artifacts. The solution introduces a trade-off. Sufficient spatial filtering leads to reducing the illumination power. In turn the exposure time has to be increased, which prevents real-time imaging. Edwards et al. [25] presented the investigated experimental data on the exposure time and the spatial filter diameter in wDPM. Using a standard halogen lamp (HAL 100 Halogen Lamp) and a gain setting of 0 dB on the CCD camera, the exposure time was above about 600 ms when proper spatial filtering was adopted to ensure the halo-free imaging. The second class of approaches involves pure numerical processing [26–28]. A real-time numerical processing approach for removing halos was described in [26], which can remove the negative values around the edge of an object but not correct the underestimated phase values to the accurate measurement. The third method, combining both hardware and numerical processing, relies on an iterative deconvolution algorithm to invert a non-linear image formation model with partially coherent light [29]. While successful for correcting the phase values to the accurate measurement, the approach suffers from poor numerical convergence leading to long computation times, impractical for real-time measurement.

Here, we propose a novel deep-learning-based method for accurately and rapidly removing the halo artifacts. Deep learning (DL) is a machine learning technique for data modeling, and decision making with a neural network trained by a large amount of data [30, 31]. The application of machine learning techniques in optical imaging was first proposed by Horisaki et al. who used the support vector regression (SVR) to recover the image through a scattering layer [32]. In the recent years, the application of DL has been rapidly developed in solving various inverse problems in optical imaging. For example, DL has been used for imaging through thick scattering media [33], ghost imaging with the data under the significant reduction of sampling [34], image reconstruction in the Fourier ptychography [35], image reconstruction and automatic focusing in digital holography [36, 37], image classification and recognition [38, 39], fringe pattern analysis imaging [40] and so on. Although neural networks have been extensively studied for tasks in optical imaging, to our knowledge, it has not been concerned for halo-free phase image processing. We develop a deep neural network (DNN) and thus we term it to accurately correct halo artifacts by an end-to-end learning approach, namely HFDNN. First, the HFDNN architecture is designed. Then through iterative training and self-learning features, the HFDNN is constructed. Last, after any phase image with halo artifacts, captured on our wDPM setup, is sent into the HFDNN, it can be corrected into an accurate halo-free phase image rapidly. In contrast to the existing halo-free methods, the proposed HFDNN method does not rely on the hardware design or does not need iterative computations, resulting in correcting the phase image accurately and rapidly.

EXPERIMENTAL SETUP

Figure 1 shows a schematic of the white-light diffraction phase imaging system. The part in the dotted line frame illustrates the schematic of a bright light microscope, and DPM interferometer is an added-on module to the bright light microscope, created using a diffraction grating in conjunction with a 4*f* lens system. First, a *Ronchi* diffraction grating is precisely placed at the output image plane of the microscope and multiple diffraction orders containing full spatial information about the sample are generated. Then, a filter is placed at the Fourier plane (i.e., the spectral plane) of the first lens, which takes a Fourier transform in the 4*f* configuration, creating a Fourier plane. The design of the filter is as shown in **Figure 1**. It allows the *1st* diffraction order to pass completely through the rectangular hole and the *0th* order is filtered down by the small pinhole. Finally, the second lens takes a Fourier transform again. The *1st* order light forms the imaging field and serves as the object wave field. The *0th* order serves as the reference wave field. The object wave field and the reference wave field are superposed at the CCD plane to form an interferogram.

In wDPM system, the measured quantity is the temporal cross-correlation function of the object wave field and the reference wave field [21, 26, 29]. Because the two fields pass through the same optical components, the time delay between them is evaluated to zero, that is, $\tau = 0$. Therefore, the measured quantity can be written as

$$\Gamma_{s,r}(r, r, 0) = \left\langle U_s(r, t)\, U_r^*(r, t) \right\rangle_t \tag{1}$$

where $U_s(r, t)$ is the object wave field, $U_r(r, t)$ is the reference wave field, the angular bracket denotes ensemble average. Assuming that fields are ergodic and, thus, stationary. Thus, the ensemble averaging in Equation (1) can be replaced by time averaging. As a result of the generalized Wiener-Khintchine theorem, the cross-correlation function $\Gamma_{s,r}(r, r, \tau)$ is the Fourier transform of the cross-spectral density $W_{s,r}(r, r, w)$. Thus, according to the central ordinate theorem, Equation (1) can be

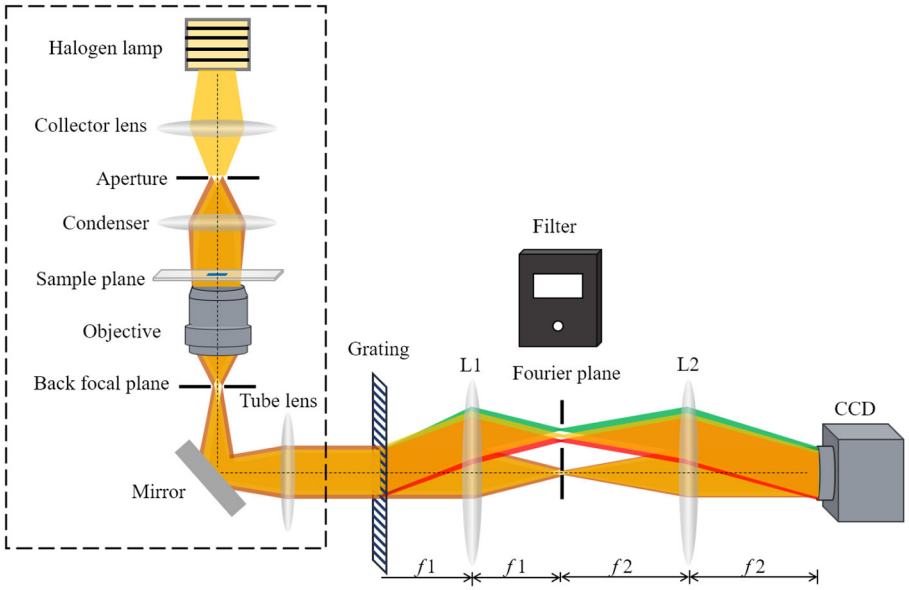

FIGURE 1 | The wDPM add-on module uses a 4-f system coupled to the output port of a bright light microscope. A camera is placed at the output of the module to record the interference intensity.

written as

$$\begin{aligned}\Gamma_{s,r}(r,r,0) &= \int W_{s,r}(r,r,w)\,dw \\ &= \int \left\langle U_s(r,w)\,U_r^*(r,w)\right\rangle dw \end{aligned} \tag{2}$$

where $U_s(r, w)$ and $U_r^*(r, w)$ are the Fourier transforms of $U_s(r, t)$ and $U_r^*(r, t)$, respectively.

In order to establish the model of image formation, we further analyze the object and reference wave fields. The diffraction grating creates copies of the image at different angles, and the filter allows the 1st order to completely pass through the rectangular hole. Thus, the object light field at CCD plane can be written as $U_s(r, w) = T(r)U_i(r, w)$, where $U_i(r, w)$ is the illumination field at the sample plane and $T(r)$ is the transmission function of the measured sample. However, the *0th* order field is filtered by the pinhole, expressed as $U_r(r, w) = [T(r)U_i(r, w)] \otimes h_0(r)$, where $h_0(r)$ is the Fourier transform of the transmission function of the *0th* filter aperture, $\otimes$ denotes the two-dimensional convolution operator. Equation (1) can be written as

$$\begin{aligned}&\Gamma_{s,r}(r,r,0) \\ &= \int \left\langle T(r)\,U_i(r,w)\left[\int\int_{-\infty}^{\infty} T(r')\,U_i(r',w)\,h_0(r-r')\,d^2r'\right]^*\right\rangle dw \\ &= T(r)\int\left[\int\int_{-\infty}^{\infty} W_i(r,r',w)\,h_0^*(r-r')\,T^*(r')\,d^2r'\right]dw \\ &= T(r)\int\int_{-\infty}^{\infty}\Gamma_i(r-r',0)\,h_0^*(r-r')\,T^*(r')\,d^2r' \\ &= T(r)\left[T(r)\otimes h(r)\right]^* \end{aligned} \tag{3}$$

here, $h(r) = \Gamma_i^*(r, 0)h_0(r)$ where $\Gamma_i^*(r, 0)$ is the conjugated term of the temporal cross-correlation function of the illumination source, and $\Gamma_i(r, 0)$ reflects the coherence of the illumination field; $W_i(r, r', w)$ is the cross-spectral density of the illumination field, assuming that fields are stationary, *i.e.*, $W_i(r, r', w)=W_i(r-r', w)$. Equation (3) establishes a relationship between the measured quantity $\Gamma_{s,r}(r, r, 0)$ and the sample transmission function $T(r)$. Solving the phase value from Equation (3), the relationship between the measured phase value and the true phase value can be obtained as:

$$\varphi_m(r) = \varphi(r) - \arg\left[\left(T\otimes h\right)(r)\right] \tag{4}$$

here, $\phi_m(r)$ is the measured phase value, $\phi(r)$ is the true phase value, $\arg[(T \otimes h)(r)]$ indicates that the measured phase distribution is smoothed. The effects of phase underestimation, can be clearly seen, that is, the measured phase value is lower than the true phase value, even causing a negative value around the edges of the object, which is known as the halo effect.

Conventionally, to obtain the true phase distribution, given correlation measurements of the light source $\Gamma_i(r, 0)$ and the filter function $h_0(r)$, Equation (4) is solved by the constrained optimization problem as follows

$$\begin{aligned}\varphi^{\dagger}(r) = \arg\min_{\varphi}\Big\{&\left\|\varphi_m-\varphi(r)+\arg\left[e^{i\varphi(r)}\otimes_r\left(\Gamma_i{}^*h_0\right)(r)\right]\right\|_2^2 \\ &+\lambda TV(\varphi)\Big\}\end{aligned} \tag{5}$$

here, $TV=\int d^2r\sqrt{(\partial\varphi/\partial x)^2(r)+\left(\partial\varphi/\partial y\right)^2(r)}$, is the total variation term, which suppresses the noise effects and enforces the sparsity assumption of the sample phase distribution. $||.||_2$ denotes the l_2-norm. While successful for the phase

values estimation, the approach suffers long computation times, impractical for real-time measurement [29].

THE HFDNN METHOD

Here, we propose a deep learning approach that uses end-to-end learning to reconstruct the true phase from the measured phase. The end-to-end learning approach is to use a set of data, consisting of the measured phase images $(\phi_m)_n$ and their corresponding ground-truth phase images $(\phi(r))_n$, where $n = 1, \ldots, N$, to learn the parametric inverse mapping operator $R(F)$ from the measured phase to the true phase. The inverse mapping operator $R(F)$ can be expressed as:

$$R(F) = \arg\min_F \sum_{n=1}^{N} L\left((\varphi(r))_n, F\left\{(\varphi_m(r))_n\right\}\right) + \lambda J(F) \quad (6)$$

where F denotes the deep neural network model, which contains the two types of parameters. The first type includes the parameters that specify the structure of the network, such as the number of the layers and neurons in each layer, the size of the kernels, etc. This type of parameters needs to be determined before training according to the training data sets and the purpose of learning. The other type includes the internal weights of different convolutional kernels. The weight parameters are adjusted autonomously during the training. L is the loss function to calculate the error between $(\phi(r))_n$ and $F\{(\phi_m)_n\}$. And J is a regularization function, aim of constraining iterations and avoiding overfitting, and λ is the coefficient for balancing the loss and the regularization. Once the inverse mapping has been learned autonomously, the neural network can be used to recover the true phase directly from the measured phase, removing the halo artifacts.

We propose a HFDNN model, which is plotted in **Figure 2**, partially inspired by the autoencoders [41], to realize halo-free white-light phase imaging. The HFDNN architecture is composed of the convolutional blocks, the pooling blocks, and the up-sampling blocks. The convolutional block is a convolutional layer, with an activation function, which is used to extract local features and increase the expression ability of measured data. The pooling block is a max pooling or an average pooling layer, which can selectively extract representative features and reduce parameters. The up-sampling block is an up-sampling layer used to restore high-dimensional features to the reconstructed data with the same size as the input data. There is an apostrophe in the middle of the HFDNN architecture, which means that the number of the blocks can be increased or decreased, according to the size and complexity of the data, which affects the feature representation of the data during the calculation process. It is worth noting that that the compression ratio of the pooling layer should be equal to the expansion ratio of the up-sampling layers, otherwise the data size will have a mismatch.

In the proposed HFDNN architecture, the network first performs a 3 × 3 convolution operation with 3 channels to increase the depth on the input data. Then through three convolutional layers with 3×3 kernel size, whose channel numbers are 8, 16, and 32, respectively, to extract important local features, and each layer is interleaved with a 2 × 2 max pooling layer. By setting the down-sampling process as above, we can avoid extreme compression by increasing the number of channels of the feature map while reducing the size of the feature map. In the up-sampling process, there are also three 3 × 3 convolutional layers with 32,16 and 8 channels, respectively, and each layer is interleaved with a 2 × 2 up-sampling layer. And then we use the concatenation operation on the first convolutional layer and the last up-sampling layer to get a feature map of 11 channels. Each convolutional layer has rectified linear units (ReLU) [42], called an activation function, which allow for faster and more effective training of deep neural architectures on large and complex data sets. However, the final layer uses a depth-reducing 1 × 1 convolutional filter without an activation function to create the reconstructed data. In our network, the measured phase images with 1,024 × 1,024 pixels are used as the input to the HDFNN architecture. The image is calculated by the first 3 × 3 convolutional layer to increase the number of channels. After the following three convolutional and pooling calculations, the size of the data is reduced to 512 × 512 pixels, 256 × 256 pixels, 128 × 128 pixels, respectively, and the number of convolutional channels for extracting local features are 8, 16, and 32, respectively. During the up-sampling process, the data with 128 × 128 pixels is restored to the one with 1,024 × 1,024 pixels by symmetric three up-sampling calculations. Last, the halo-free phase image with the same size is outputted.

After the structure of the network is established, the network will be trained to obtain the internal weights. The process of training the HFDNN network is as shown in **Figure 3**. The input data is calculated by the HFDNN network to generate a reconstructed data every time. And the error is calculated by comparing the reconstructed data with the target data. We used the back-propagation algorithm to back propagate the error into the network, and the Adaptive Moment Estimation (Adam) [43] based optimization to optimize the weights. The weights at when the error remains a constant or reaches a value are saved. And the HFDNN network is established. In the method proposed in this paper, the error is calculated as

$$e_{error} = \frac{1}{M \times N} \sum_{u=1}^{M} \sum_{v=1}^{N} \left(F\left\{(\varphi_m(u,v))_n\right\} - \varphi(u,v)_n\right)^2 \quad (7)$$

where $e_{error}$is the error between the reconstructed data and the target data.

The HFDNN architecture is implemented using Keras [44] with TensorFlow [45] backend. We perform the training and validation on a personal computer with two-core 2.60 GHz CPU, 56 GB of RAM, and Nvidia Quadro K5000. For the training of the model, we select an initial learning rate of 1e-4 for the Adam optimizer and train the network for 200 epochs on a batch of 8 training data with1,024 × 1,024 pixels.

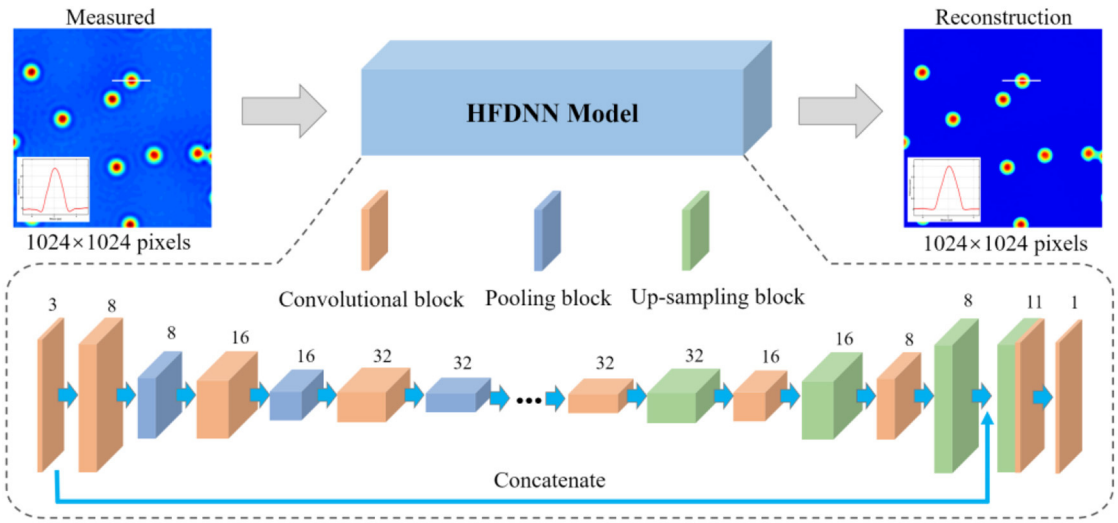

FIGURE 2 | A schematic of the proposed HFDNN architecture. The digits above each layer denote the number of input channels.

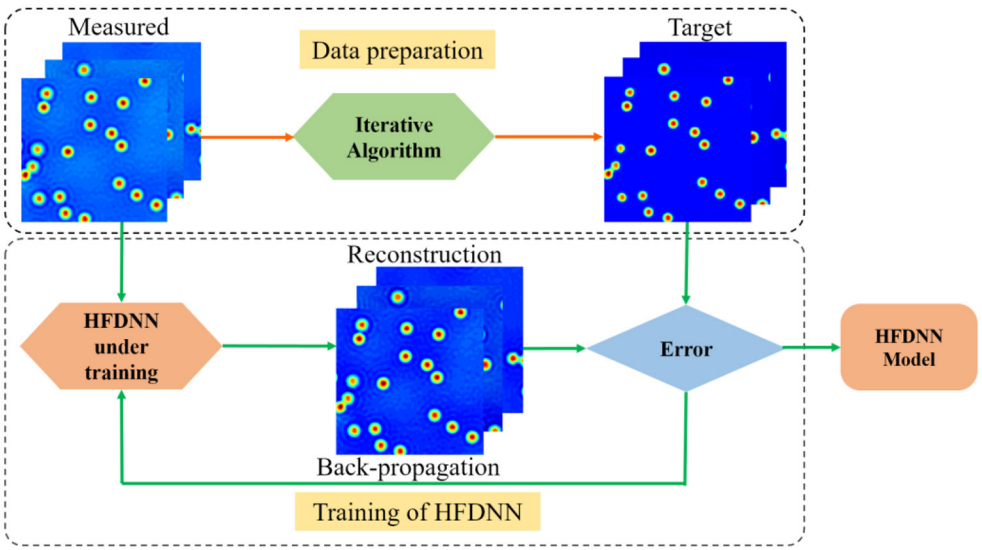

FIGURE 3 | A schematic of the process of the HFDNN training. In the process of data preparation, the measured images are acquired by our wDPM system, which are used as the input data; the measured images are reversed into the halo-free images by the iterative algorithm, which are used as the target data. In the process of the HFDNN training, when the error remains a constant or reaches a value, the training is terminated and the HFDNN model is established.

RESULTS AND DISCUSSION

Experimental Results

In order to verify the feasibility and accuracy of the proposed HFDNN approach, we carry out the experiments on our established wDPM system. In our initial set of experiments, we use 2 μm polystyrene beads as the samples. Its refractive index is 1.59. A small number of beads are taken and scattered on a slide, then the Olympus immersion oil (the refractive index is 1.518) is dropped to immerse the beads, finally the sample is covered with the cover glass. The prepared sample is placed on the stage of the microscope and imaged on the plane of the CCD camera. The interferograms at different field of view are captured. And the phase images are reconstructed by numerical computations. First, the complex amplitude of the object wave is obtained by the frequency domain filtering and inverse Fourier transform. Then, by phase unwrapping [46] and phase compensation operation by the method of the reference interferogram [47], the quantitative phase image is reconstructed. Due to the known refractive indexes and the center wavelength, the thickness image of the polystyrene beads can be further

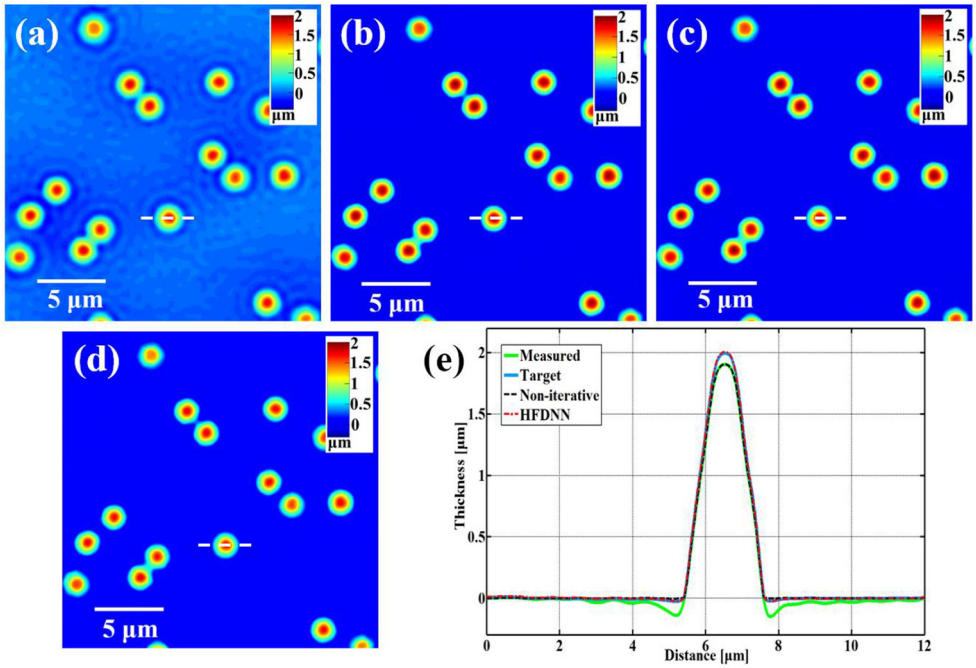

FIGURE 4 | The reconstructed results of standard polystyrene beads. **(a)** The measured image; **(b)** the target data; **(c)** the reconstructed image by our HFDNN; **(d)** the reconstructed image by the non-iteratitave method —"Non-iterative" in [26]; **(e)** the thickness profiles along the same diameter of the same bead drawn in **(a–d)**; the green curve illustrates the profile of the measured data; the blue curve illustrates the profile of the target data; the red dash curve illustrates the profile of the HFDNN output data; the black dash curve illustrates the profile of the non-iterative reconstruction.

obtained from the reconstructed phase values by $h_m(x,y) = \frac{\lambda\varphi_m(x,y)}{2\pi(n_{beads}-n_{oil})}$.

For training the HFDNN network, 1000 interferograms with 1,024 × 1,024 pixels are captured at different fields of view for several samples on our experimental setup. After the reconstructing computation, these measured thickness images are used as the training data set. In order to augment the data set by four-fold, the measured data set are further augmented by rotating them to 0, 90, 180, and 270 deg. The true thickness images, used as the target data set, are recovered using the iterative deconvolution algorithm described in [29] based on the physical parameters of the image formation. As described in [29], the iterative method can successfully eliminate the halo effect to recover the true image. Therefore, the corresponding thickness images after the iterative calculations are taken as the target data set. For training the network, the data set is divided into the training and validation sets with the ratio of 7:3.

After the training, next we blindly test the HFDNN network on the samples that had no overlap with the training or validation sets. **Figure 4** illustrates the success of HFDNN. **Figure 4a** is a measured thickness image of polystyrene beads. It is apparent that there are halo artifacts in the measured image, especially around the edges of the beads. **Figure 4b** is the thickness image calculated by the iterative algorithm in combination with the hardware parameters. It can be seen that the iterative calculation succeeded in eliminating the halo effect. **Figure 4c** is the thickness image calculated by the HFDNN. It clearly illustrates that our end-to-end deep learning method can eliminate halo artifacts like the iterative algorithm. In order to compare the performance with other previous methods, the reconstruction is also performed by the direct non-iterative algorithm based on Hilbert transform [26]. As shown in **Figure 4d**, the halo artifacts around the edges of the beads can be removed but the thickness of the beads is still underestimated than the ones in **Figures 4b,c**. **Figure 4e** is the line profiles along the same diameter of the same bead that further compares the measured data, the target data, the reconstructed data calculated by the HFDNN and by the direct non-iterative algorithm, respectively. Through the comparison of the line profiles, it is more clearly seen that the reconstructed data by the HFDNN is almost identical with the target data but the one by the non-iterative algorithm seems like a non-negative clipping. Therefore, **Figure 4** illustrates that the HFDNN can successfully correct halo effect, that is, the negative values surrounding the beads in the measured data is removed and the thickness of the reconstructed beads converges to our expected value of 2 μm. The HFDNN algorithm is written in Python and optimized by GPU codes. Using the HFDNN, it takes only about 60 ms to achieve a halo-free image reconstruction on our personal computer, which is much more efficient than using the iterative algorithm (also written in Python and optimized by GPU codes), which takes about 600 ms for the same image. Although the non-iterative algorithm can reconstruct an image a little faster than the HFDNN, it can only remove the negative values around the edge of the object but not correct the underestimated values to the accurate measurement.

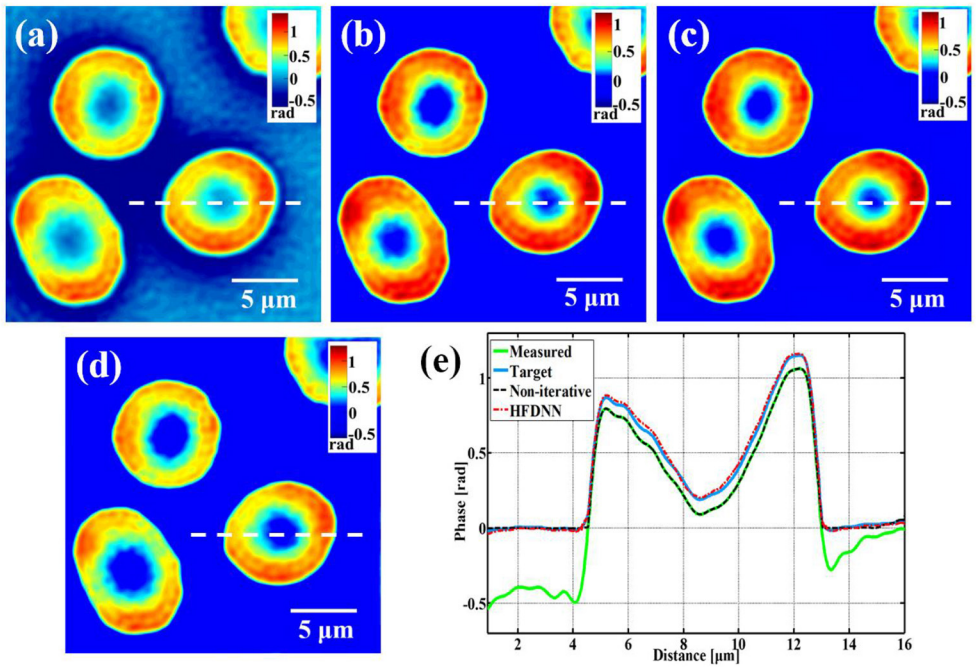

FIGURE 5 | The reconstructed results of living red blood cells. **(a)** The measured image; **(b)** the target data; **(c)** the reconstructed image by the HFDNN; **(d)** the reconstructed image by the non-iteratitave method; **(e)** the phase profiles along the same position of the same cell drawn in **(a–d)**; the green curve illustrates the profile of the measured data; the blue curve illustrates the profile of the target data; the red dash curve illustrates the profile of the HFDNN output data; the black dash curve illustrates the profile of the non-interative reconstruction.

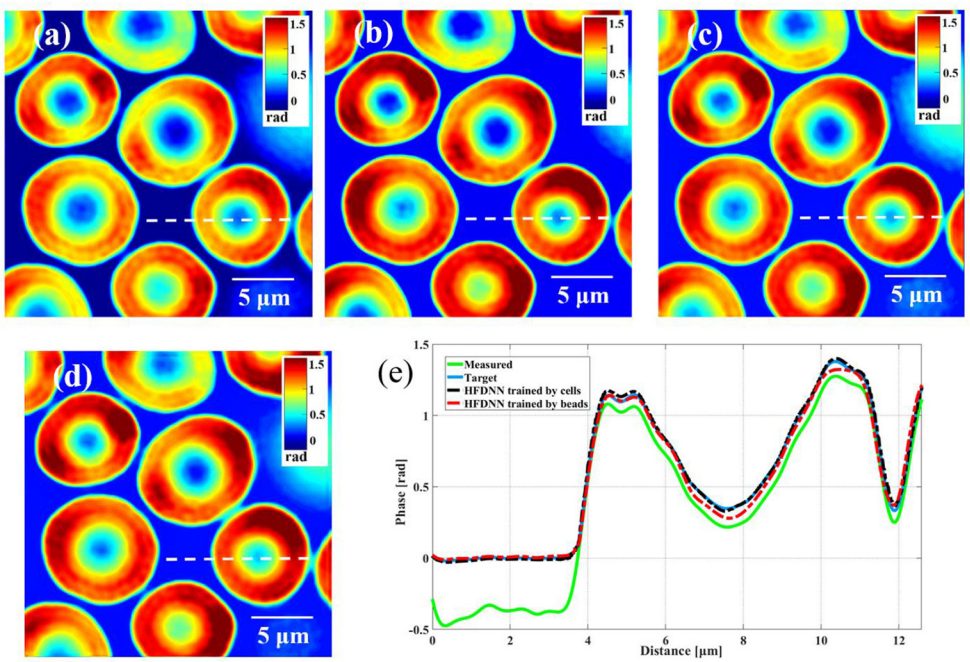

FIGURE 6 | The comparison of the reconstructed results of living red blood cells. **(a)** The measured image; **(b)** the target data by the iteration method; **(c)** the reconstructed image by the HFDNN trained by red blood cells; **(d)** the reconstructed image by the HFDNN trained by beads; **(e)** the phase profiles along the same position of the same cell drawn in **(a–d)**; the green curve illustrates the profile of the measured data; the blue curve illustrates the profile of the target data; the black dash curve illustrates the profile of the HFDNN trained by cells; the red dash curve illustrates the profile of the HFDNN trained by beads.

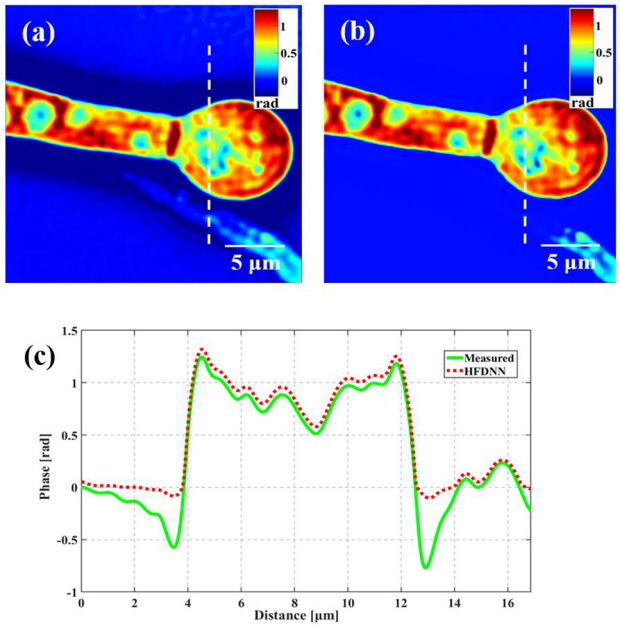

FIGURE 7 | The reconstructed results of the spores in monascus. **(a)** The measured image; **(b)** the reconstructed image by the HFDNN without re-training; **(c)** the phase profiles along the same position drawn in **(a,b)**; the green curve illustrates the profile of the measured data; the red dash curve illustrates the profile of the HFDNN.

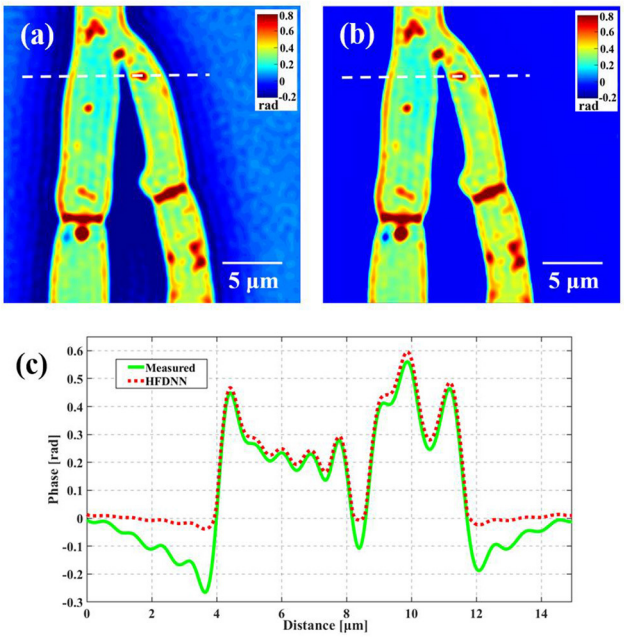

FIGURE 8 | The reconstructed results of the hyphae branches in monascus. **(a)** The measured image; **(b)** the reconstructed image by the HFDNN without re-training; **(c)** the phase profiles along the same position drawn in **(a,b)**; the green curve illustrates the profile of the measured data; the red dash curve illustrates the profile of the HFDNN.

Based on the argument of deep learning, the HFDNN approach should let the network learn halo-effect features by the training, i.e., the deep learning method should be generalized for different types of samples. In order to test this generalization, next we test the HFDNN on the measured phase data of living red blood cells captured by our wDPM system. Still using the HFDNN architecture as shown in **Figure 2**, only the training data set is changed. The red blood cells are obtained from our local hospital using venipuncture and stored in a refrigerator at 4°C. The blood is diluted to a concentration of 0.2% in PBSA solution (0.5% Bovine Serum Albumin in PBS). To prevent cell tilt during imaging, a sample chamber is prepared by punching a hole into a piece of double-sided scotch tape and sticking the tape onto a coverslip. After dispensing a drop of blood into this circular chamber, the drop is sealed from the top by a Poly-L-lysine coated coverslip. The coverslip pair is then turned over and the cells are allowed to settle for 1 h before imaging so that they become immobilized. The prepared samples are placed on the objective stage and focused onto the CCD camera. Also for training the network, we capture 800 interferograms at different fields of view for several samples. The phase image is reconstructed as shown in **Figure 5a**, which is severely affected by halo artifacts. Then by the iterative calculation, halo-free phase images are obtained as shown in **Figure 5b**, used as the target data. And the data set is still augmented by four-fold. The data set is still divided into the training and validation sets with the ratio of 7:3. After the training, the weights of the network are iteratively updated. We blindly test the HFDNN network on the samples that had no overlap with the training or validation sets. The result is shown in **Figure 5c**. It can be seen from the visualization that halo artifacts are successfully corrected. For comparing, we also reconstruct the image by the non-iterative algorithm. As shown in **Figure 5d**, the halo artifacts around the edges of the cells can be removed but the phase values are still underestimated. Through the further comparison of the line profiles in **Figure 5e**, the reconstructed data by the HFDNN is almost identical with the target data by the iterative calculation and the one by the non-iterative algorithm seems like only a negative removing. The results illustrate that the HFDNN model can successfully remove the halo artifacts for other sample types.

DISCUSSION

First, to further quantify the accuracy of our proposed HFDNN method, two evaluation metrics are used to evaluate our reconstructed data. One is the normalized root of mean square error (NRMSE) as follows:

$$NRMSE = \sqrt{\frac{\frac{1}{M\times N}\sum_{u=1}^{M}\sum_{v=1}^{N}\left(\tilde{\varphi}\left(u,v\right)-\varphi\left(u,v\right)\right)^{2}}{\frac{1}{M\times N}\sum_{u=1}^{M}\sum_{v=1}^{N}\varphi(u,v)^{2}}} \tag{8}$$

where $\varphi\left(u,v\right)$ is the target data, and $\tilde{\varphi}\left(u,v\right)$ is the reconstructed data by HFDNN. The smaller the NRMSE, the closer the reconstructed data is to the target data.

The second one is the Structural Similarity Index (SSIM) as follows:

$$SSIM = \frac{\left(2\mu_{\varphi}\mu_{\tilde{\varphi}} + c_1\right)\left(2\sigma_{\varphi,\tilde{\varphi}} + c_2\right)}{\left(\mu_{\varphi}^2 + \mu_{\tilde{\varphi}}^2 + c_1\right)\left(\sigma_{\varphi}^2 + \sigma_{\tilde{\varphi}}^2 + c_2\right)} \tag{9}$$

where φ and $\tilde{\varphi}$ represent the target data and the reconstructed data, respectively, μ is the mean of the data, σ^2 is the variance of the data, and $\sigma_{\varphi,\tilde{\varphi}}$ is the covariance of the two data, c_1 and c_2 are two constants. The range of SSIM is from 0 to 1, and when the reconstructed data is the same as the target data, the SSIM takes a value of 1.

We calculate the NRMSE and the SSIM over the test images as the metric values. For the polystyrene beads, the NRMES and the SSIM are 0.025 and 0.980, respectively. For the red blood cells, the NRMES and the SSIM are 0.073 and 0.941, respectively. For comparing, the NRMSE and the SSIM are also calculated over the reconstructed images by the direct non-iterative method. For the polystyrene beads, the NRMES and the SSIM are 0.085 and 0.863, respectively. For the red blood cells, the NRMES and the SSIM are 0.162 and 0.814, respectively. It can be seen from the two image metric values that the proposed HFDNN can more accurately correct the halo artifacts than the direct non-iterative method.

Second, the generalization of the HFDNN will be further discussed. Although in the experiments of red blood cells, the reconstructed results are calculated by the re-trained HFDNN network. Factually, as shown in **Figure 6** there are almost no differences between the reconstructed results by the re-trained network and by the network without being re-trained. For further comparison, we also analyze the NRMES and the SSIM between the reconstructed results and the target data. Using the network without being re-trained, the NRMES and the SSIM are 0.094 and 0.923, respectively. And using the re-trained network, the NRMES and the SSIM are 0.073 and 0.941, respectively. However, the NRMES and the SSIM between the measured results and the target data are 0.514 and 0.665, respectively. It is clear that using the HFDNN network without being re-trained also can reconstruct high-quality images on red blood cells. Therefore, re-training the network, when a new type of samples is introduced, should be emphasized as a guarantee of the best results. In order to further prove the generalization of the HFDNN, we also applied it to other sample types which are morphologically different. The spores in monascus are imaged by our wDPM system. A small number of spores are diluted in water and dropped into a sample chamber, which is prepared by punching a hole into a piece of double-sided scotch tape and sticking the tape onto a coverslip. After dispensing a drop of the spores into this circular chamber, the drop is sealed from the top by a coverslip. The sample is stored under the room temperature of 25 °C. After about 1 day, the spores grow out the hyphae branches. **Figure 7** is the reconstructed results for the spores and **Figure 8** is the reconstructed results for the hyphae branches. It can be seen from the visualization that halo artifacts are successfully corrected. The results show that the HFDNN approach is generalized to different sample types.

On the other hand, the HFDNN method does not rely on any system parameter, which lets the network learn the features of halo artifacts by the training. There exists the low spatiotemporal noise in wDPM due to its common-path, white-light illumination approach. When the systems are well-established, although in different measurements on the same system or on different systems there are minor differences to some extent between system SNR, alignment, etc., the features of halo artifacts for the same type of samples will be the same. Therefore, it is not necessary to re-train the network when measuring the same type of samples at different measurements on the same microscope or even on different microscopes.

At last, it should be pointed out that the mass measurements are often required for some types of samples in the practical applications. Therefore, even if we have to collect training data (both with halo and halo-free phase images) on that specific type of cells and redo the training process, we still can get the more benefits because the deep-learning-based method can rapidly and accurately remove the halo artifacts in the following mass measurements.

CONCLUSIONS

In summary, we present the HFDNN method, a deep-learning-based approach for halo-free white-light phase diffraction imaging. Unlike the conventional iterative approach, the proposed deep convolutional neural network can be applied to the high-speed elimination of halo effects on various samples. The feasibility of the method is illustrated by the experimental data captured on our wDPM setup. Factually, the HFDNN method provides new avenues in all white-light phase imaging field. The HFDNN can learn the features that the phase images possess due to the halo effects. Thus, it can eliminate halo artifacts for different samples in various white-light phase images. In the future, we aim to validate our algorithm on a larger dataset on more types of objects to make our algorithm more robust to sample variation and to improve the generilizeation.

DATA AVAILABILITY STATEMENT

The raw data supporting the conclusions of this article will be made available by the authors, without undue reservation.

AUTHOR CONTRIBUTIONS

KZ and LM conceived the idea of the HFDNN method. KZ and MZ were involved in the design and construction the HFDNN network. MZ and LM analyzed the data. JZ gathered the experimental data. LM, MZ, and YL wrote the paper. All authors contributed to the article and approved the submitted version.

FUNDING

The Natural Science Foundation of Zhejiang Provincial of China (Grant No. LY17F050002); the National Natural Science Foundation of China (Grant No. 61205012).

REFERENCES

1. Popescu G. Quantitative *Phase Imaging of Cells and Tissues*. New York, NY: McGraw-Hill (2011).
2. Barer R. Determination of dry mass, thickness, solid and water concentration in living cells. *Nature*. (1953) 172:1097–8. doi: 10.1038/1721097a0
3. Uttam S, Pham HV, LaFace J, Leibowitz B, Yu J, Brand RE, et al. Early prediction of cancer progression by depth-resolved nanoscale mapping of nuclear architecture from unstained tissue specimens. *Cancer Res*. (2015) 75:4718–27. doi: 10.1158/0008-5472.CAN-15-1274
4. Ma L, Rajshekhar G, Wang R, Bhaduri B, Sridharan S, Mir M, et al. Phase correlation imaging of unlabeled cell dynamics. *Sci Rep*. (2016) 6:32702. doi: 10.1038/srep32702
5. Huang D, Swanson EA, Lin CP, Schuman JS, Stinson WG, Chang W, et al. Optical coherence tomography. *Science*. (1991) 254:1178–81. doi: 10.1126/science.1957169
6. Izatt JA, Boppart S, Bouma B, Boer JD, Drexler W, Li X, et al. Introduction to the feature issue on the 25 year anniversary of optical coherence tomography. *Biomed Opt Expr*. (2017) 8:3289–91. doi: 10.1364/BOE.8.003289
7. Cuche E, Bevilacqua F, Depeursinge C. Digital holography for quantitative phase-contrast imaging. *Opt Lett*. (1999) 24:291–3. doi: 10.1364/OL.24.000291
8. Colomb T, Cuche E, Charrière F, Kühn J, Aspert N, Montfort F, et al. Automatic procedure for aberration compensation in digital holographic microscopy and applications to specimen shape compensation. *Appl Opt*. (2006) 45:851–63. doi: 10.1364/AO.45.000851
9. Popescu G, Ikeda T, Dasari RR, Feld MS. Diffraction phase microscopy for quantifying cell structure and dynamics. *Opt Lett*. (2006) 31:775–7. doi: 10.1364/OL.31.000775
10. Majeed H, Ma L, Lee YJ, Kandel M, Min E, Jung W, et al. Magnified image spatial spectrum (MISS) microscopy for nanometer and millisecond scale label-free imaging. *Opt Expr*. (2018) 26:5423–40. doi: 10.1364/OE.26.005423
11. Teague MR. Deterministic phase retrieval: a green's function solution. *J Opt Soc Am*. (1983) 73:1434–41. doi: 10.1364/JOSA.73.001434
12. Zuo C, Sun J, Li J, Zhang J, Asundi A, Chen Q. High-resolution transport-of-intensity quantitative phase microscopy with annular illumination. *Sci Rep*. (2017) 7:7654. doi: 10.1038/s41598-017-06837-1
13. Wolf E. Three-dimensional structure determination of semi-transparent objects from holographic data. *Opt Commun*. (1969) 1:153–6. doi: 10.1016/0030-4018(69)90052-2
14. Su L, Ma L, Wang H. Improved regularization reconstruction from sparse angle data in optical diffraction tomography. *Appl Opt*. (2015) 54:859–68. doi: 10.1364/AO.54.000859
15. Zheng C, Zhou R, Kuang C, Zhao G, Yaqoob Z, So PTC. Digital micromirror device-based common-path quantitative phase imaging. *Opt Lett*. (2017) 42:1448–51. doi: 10.1364/OL.42.001448
16. Schnars U, Jüptner W. Direct recording of holograms by a CCD target and numerical reconstruction. *Appl Opt*. (1994) 33:179–81. doi: 10.1364/AO.33.000179
17. Bhaduri B, Pham H, Mir M, Popescu G. Diffraction phase microscopy with white light. *Opt Lett*. (2012) 37:1094–6. doi: 10.1364/OL.37.001094
18. Shan M, Kandel ME, Majeed H, Nastasa V, Popescu G. White-light diffraction phase microscopy at doubled space-bandwidth product. *Opt Expr*. (2016) 24:29033–9. doi: 10.1364/OE.24.029033
19. Kemper B, Stürwald S, Remmersmann C, Langehanenberg P, von Bally G. Characterisation of light emitting diodes (LEDs) for application in digital holographic microscopy for inspection of micro and nanostructured surfaces. *Opt Lasers Eng*. (2008) 46:499–507. doi: 10.1016/j.optlaseng.2008.03.007
20. Farrokhi H, Boonruangkan J, Chun BJ, Rohith TM, Mishra A, Toh HT, et al. Speckle reduction in quantitative phase imaging by generating spatially incoherent laser field at electroactive optical diffusers. *Opt Expr*. (2017) 25:10791–800. doi: 10.1364/OE.25.010791
21. Nguyen TH, Edwards C, Goddard LL, Popescu G. Quantitative phase imaging with partially coherent illumination. *Opt Lett*. (2014) 39:5511–4. doi: 10.1364/OL.39.005511
22. Maurer C, Jesacher A, Bernet S, Ritsch-Marte M. Phase contrast microscopy with full numerical aperture illumination. *Opt Expr*. (2008) 16:19821–9. doi: 10.1364/OE.16.019821
23. Edwards C, Nguyen TH, Popescu G, Goddard LL. Image formation and halo removal in diffraction phase microscopy with partially coherent illumination. In: *Frontiers in Optics 2014*. Tucson, AZ (2014). doi: 10.1364/FIO.2014.FTu4C.5
24. Otaki T. Artifact halo reduction in phase contrast microscopy using apodization. *Opt Rev*. (2000) 7:119–22. doi: 10.1007/s10043-000-0119-5
25. Edwards C, Bhaduri B, Nguyen T, Griffin BG, Pham H, Kim T, et al. Effects of spatial coherence in diffraction phase microscopy. *Opt Expr*. (2014) 22:5133–46. doi: 10.1364/OE.22.005133
26. Kandel ME, Fanous M, Best-Popescu C, Popescu G. Real-time halo correction in phase contrast imaging. *Biomed Opt Expr*. (2018) 9:623–35. doi: 10.1364/BOE.9.000623
27. Yin Z, Kanade T, Chen M. Understanding the phase contrast optics to restore artifact-free microscopy images for segmentation. *Med Image Anal*. (2012) 16:1047–62. doi: 10.1016/j.media.2011.12.006
28. Jaccard N, Griffin LD, Keser A, Macown RJ, Super A, Veraitch FS, et al. Automated method for the rapid and precise estimation of adherent cell culture characteristics from phase contrast microscopy images. *Biotechnol Bioeng*. (2014) 111:504–17. doi: 10.1002/bit.25115
29. Nguyen TH, Kandel M, Shakir HM, Best-Popescu C, Arikkath J, Do MN, et al. Halo-free phase contrast microscopy. *Sci Rep*. (2017) 7:44034. doi: 10.1038/srep44034
30. Lecun Y, Bengio Y, Hinton G. Deep learning. *Nature*. (2015) 521:436–44. doi: 10.1038/nature14539
31. Schmidhuber J. Deep learning in neural networks: an overview. *Neural Netw*. (2015) 61:85–117. doi: 10.1016/j.neunet.2014.09.003
32. Horisaki R, Takagi R, Tanida J. Learning-based imaging through scattering media. *Opt Expr*. (2016) 24:13738–43. doi: 10.1364/OE.24.013738
33. Li S, Deng M, Lee J, Sinha A, Barbastathis G. Imaging through glass diffusers using densely connected convolutional networks. *Optica*. (2018) 5:803–13. doi: 10.1364/OPTICA.5.000803
34. Lyu M, Wang W, Wang H, Wang H, Li G, Chen N, et al. Deep-learning-based ghost imaging. *Sci Rep*. (2017) 7:17865. doi: 10.1038/s41598-017-18171-7
35. Cheng YF, Strachan M, Weiss Z, Deb M, Carone D, Ganapati V. Illumination pattern design with deep learning for single-shot Fourier ptychographic microscopy. *Opt Expr*. (2019) 27:644–56. doi: 10.1364/OE.27.000644
36. Rivenson Y, Zhang Y, Günaydin H, Teng D, Ozcan A. Phase recovery and holographic image reconstruction using deep learning in neural networks. *Light Sci Appl*. (2018) 7:17141. doi: 10.1038/lsa.2017.141
37. Wu Y, Rivenson Y, Zhang Y, Wei Z, Günaydin H, Lin X, et al. Extended depth-of-field in holographic imaging using deep-learning-based autofocusing and phase recovery. *Optica*. (2018) 5:704–10. doi: 10.1364/OPTICA.5.000704
38. Wang P, Di J. Deep learning-based object classification through multimode fiber *via* a CNN-architecture SpeckleNet. *Appl Opt*. (2018) 57:8258–63. doi: 10.1364/AO.57.008258
39. Nguyen TH, Sridharan S, Macias V, Kajdacsy-Balla A, Melamed J, Do MN, et al. Automatic Gleason grading of prostate cancer using quantitative phase imaging and machine learning. *J Biomed Opt*. (2017) 22:036015. doi: 10.1117/1.JBO.22.3.036015
40. Feng S, Chen Q, Gu G, Tao T, Zhang L, Hu Y, et al. Fringe pattern analysis using deep learning. *Adv Photonics*. (2019) 1:025001. doi: 10.1117/1.AP.1.2.025001
41. Hinton GE, Salakhutdinov RR. Reducing the dimensionality of data with neural networks. *Science*. (2006) 313:504–7. doi: 10.1126/science.1127647
42. Petersen P, Voigtlaender F. Optimal approximation of piecewise smooth functions using deep ReLU neural networks. *Neural Netw*. (2018) 108:296–330. doi: 10.1016/j.neunet.2018.08.019
43. Kingma DP, Ba J. Adam: a method for stochastic optimization. *arXiv*. (2017) arXiv:1412.6980.

44. Chollet F. *Keras*. Available online at:https://github.com/keras-team/keras
45. Abadi M, Agarwal A, Barham P, Brevdo E, Chen J, Chen Z, et al. Tensorflow: Large-scale machine learning on heterogeneous distributed systems. *arXiv [Preprint]*.
46. Ma L, Li Y, Wang H, Jin H. Fast algorithm for reliability-guided phase unwrapping in digital holographic microscopy. *Appl Opt*. (2012) 51:8800–7. doi: 10.1364/AO.51.008800
47. Ferraro P, De Nicola S, Finizio A, Coppola G, Grilli S, Magro C, et al. Compensation of the inherent wave front curvature in digital holographic coherent microscopy for quantitative phase-contrast imaging. *Appl Opt*. (2003) 42:1938–46. doi: 10.1364/AO.42.001938

Conflict of Interest: The authors declare that the research was conducted in the absence of any commercial or financial relationships that could be construed as a potential conflict of interest.

frontiers in Physics

REVIEW
published: 12 April 2021
doi: 10.3389/fphy.2021.644450

A Comprehensive Review of Fluorescence Correlation Spectroscopy

Lan Yu[1†], *Yunze Lei*[1†], *Ying Ma*[1], *Min Liu*[1], *Juanjuan Zheng*[1], *Dan Dan*[2] *and Peng Gao*[1*]

[1]School of Physics and Optoelectronic Engineering, Xidian University, Xi'an, China, [2]State Key Laboratory of Transient Optics and Photonics, Xi'an Institute of Optics and Precision Mechanics, Chinese Academy of Sciences, Xi'an, China

Fluorescence correlation spectroscopy (FCS) is a powerful technique for quantification of molecular dynamics, and it has been widely applied in diverse fields, *e.g.*, biomedicine, biophysics, and chemistry. By time-correlation of the fluorescence fluctuations induced by molecules diffusing through a focused light, FCS can quantitatively evaluate the concentration, diffusion coefficient, and interaction of the molecules *in vitro* or *in vivo*. In this review, the basic principle and implementation of FCS are introduced. Then, the advances of FCS variants are reviewed, covering dual-color FCCS, multi-focus FCS, pair correlation function (pCF), scanning FCS, focus-reduced FCS, SPIM-FCS, and inverse-FCS. Besides, the applications of FCS are demonstrated with the measurement of local concentration, hydrodynamic radius, diffusion coefficient, and the interaction of different molecules. Lastly, a discussion is given by summarizing the pros and cons of different FCS techniques, as well as the outlooks and perspectives of FCS.

Keywords: fluorescence correlation spectroscopy, biomolecular dynamics, biomolecular interaction, correlation spectroscopy, FCS variants

OPEN ACCESS

Edited by:
Bodo Wilts,
Université de Fribourg, Switzerland

Reviewed by:
Stefan Wennmalm,
Royal Institute of Technology, Sweden
Nobuhiko Yokoshi,
Osaka Prefecture University, Japan

***Correspondence:**
Peng Gao
peng.gao@xidian.edu.cn

†These authors have contributed equally to this work

Specialty section:
This article was submitted to Optics and Photonics, a section of the journal Frontiers in Physics

Received: *21 December 2020*
Accepted: *12 February 2021*
Published: *12 April 2021*

Citation:
Yu L, Lei Y, Ma Y, Liu M, Zheng J, Dan D and Gao P (2021) A Comprehensive Review of Fluorescence Correlation Spectroscopy. Front. Phys. 9:644450. doi: 10.3389/fphy.2021.644450

INTRODUCTION

Molecular dynamics in biological systems are the foundation of life events. Fluorescence correlation spectroscopy (FCS) is a powerful tool for detecting molecular dynamics through analyzing the intensity fluctuation emitted by biomolecules diffusing in and out of a focused light [1–3]. The local concentration, hydrodynamic radius, diffusion coefficient, and the interaction of different proteins, *etc.* [4–7] can be accurately measured with FCS. Compared with other dynamics orientated approaches, FCS has a broader measurable time range spanning from ~ns to ~ s, and a higher sensitivity that can be up to a single-molecule level.

FCS was first proposed by Magde *et al.* in 1972, which was designed for the measurement of the binding of the fluorescent dye EtBr and DNA [8]. It has become a practical tool for the investigation of molecular dynamics since the 1990s when FCS was firstly implemented with confocal microscopy. Confocal microscopy provides a much-confined observation volume ~0.5 fl, which enhances the signal-to-noise ratio (SNR) of FCS significantly [9].

When investigating diverse dynamic processes in live biological systems, FCS is inevitably complicated with many factors, such as the movement of cells, the photobleaching of fluorophores, and anomalous dynamics in sub-diffraction regions, *etc.* To overcome these difficulties, many advances have been initiated to extend the capability of FCS during the past two decades. To name a few, dual-color FCCS [10] was proposed to measure the interaction of different molecules. Space-multiplexing techniques allow FCS to probe dynamics at different locations [11]. Pair correlation function (pCF) based FCS provides information on the

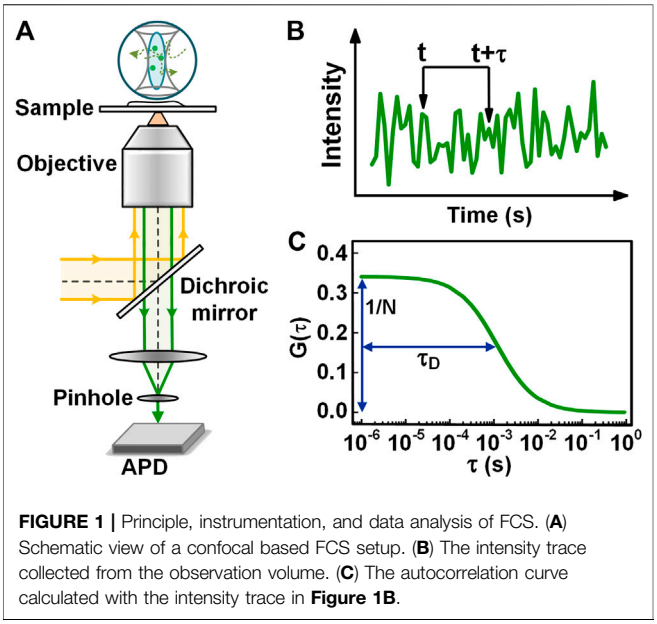

FIGURE 1 | Principle, instrumentation, and data analysis of FCS. (**A**) Schematic view of a confocal based FCS setup. (**B**) The intensity trace collected from the observation volume. (**C**) The autocorrelation curve calculated with the intensity trace in **Figure 1B**.

directional motion of molecules along a certain direction, *i.e.*, between a pair of points [12]. Parallel/perpendicular line-scanning FCS [13] overcomes the photo-bleaching caused by slow diffusion of molecules on the membranes by swiftly scanning the focus on the membrane or perpendicular to the membrane. Moreover, the perpendicular line-scanning FCS overcomes the artificial fluorescence signal fluctuation caused by membrane movements. The combination of stimulated emission depletion (STED) and FCS [14] reduces the detection volume and consequently enables us to detect anomalous diffusion in the nanoscale regions. Single plane illumination microscopy based FCS (SPIM-FCS) [15] combines light-sheet illumination with FCS to acquire molecular information from thousands of pixels simultaneously and reduce the observation volume along the *z*-axis effectively. Inverse-FCS [16] measures the particle volume independent of diffusion dynamics by analyzing the fluctuation of unlabeled particles in the context of a densely labeled surrounding medium. Moreover, the extensions arise in data analysis, such as photon counting histogram (PCH) [17] and fluorescence intensity distribution analysis (FIDA) [18], which are capable of obtaining the molecular brightness that not available in FCS. These above advances extend the capability of conventional FCS in different aspects and make it suitable for measuring the biomolecular dynamics and interactions in complex biological environments.

In this review, the basic principle, the implementation schemes, and data analysis of FCS are elaborated at first. Secondly, the advances in FCS, including dual-color FCCS, multi-focus FCS, pair correlation function (pCF) based FCS, scanning FCS, focus-reducing FCS, inverse-FCS, and PCH are elaborated in both conception or implementation. Thirdly, the applications of FCS in chemistry and biology are outlined. Eventually, the comparison among the different FCS approaches, as well as the outlooks and perspectives of FCS, are discussed.

PRINCIPLE OF FLUORESCENCE CORRELATION SPECTROSCOPY

Experimental Setup

FCS is based on the analysis of time correlations in fluorescence fluctuation emitted when fluorescently labeled molecules are diffusing in and out of a tiny observation volume [2]. In the implementation, FCS is often performed in a confocal system, as illustrated in **Figure 1A**. The fluorescence emitted from the fluorescently-labeled molecules in the observation volume is collected by the same objective, and propagate along the opposite direction to that of the excitation/depletion light. After passing through a long-pass dichroic mirror, the fluorescence is focused through a pinhole onto an avalanche photodiode (APD). The fluorescence emitted in the out-of-focus region is rejected by the pinhole, and therefore, it does not reach the detector. Consequently, the pinhole reduces the axial extension of the observation volume. Such confined observation volume enhances the signal-to-noise ratio significantly and also reduces the measurement time needed to obtain a decent correlation curve. Despite a continuous-wave (CW) laser is available for FCS, the usage of pulsed lasers for excitation and time-correlated single-photon counting (TCSPC) for detection is preferable for the rejection of environmental background and also allows performing dual-color FCCS in a pulsed interleaved excitation scheme [19].

Data Analysis

To perform dynamics measurement with FCS, a sample of the fluorescently-labeled molecules is placed in the focal plane of the confocal microscope. Due to the free diffusion of molecules by nature, an intensity fluctuation $F(t)$ will be induced when the molecules are diffusing in and out of the observation volume. Then, the autocorrelation of $F(t)$ is calculated with:

$$G(\tau) = \frac{\langle F(t)F(t+\tau)\rangle}{\langle F(t)\rangle^2} - 1 \tag{1}$$

$< >$ represents the temporal average, τ is the lag time. $G(\tau)$ is a measure of the self-similarity of a signal in time, *i.e.*, the overlap of a signal with itself at various lag time τ. With the approximation, the observation volume has a 3D Gaussian profile, $G(\tau)$ can be fitted with a 3D diffusion model:

$$G(\tau) = \frac{1}{N}\left(1+\frac{\tau}{\tau_D}\right)^{-1}\left(1+\frac{\tau}{\tau_D}\cdot\frac{r_0^2}{z_0^2}\right)^{-1/2} \tag{2}$$

N is the average molecule number in detection volume, τ_D is the average time of molecules diffusing through the detection volume. r_0 and z_0 are the lateral and axial radial distances over which the intensity decay by $1/e^2$ in the lateral and axial directions, respectively. For 2D diffusions, such as the molecule diffusion on membranes, **Eq. 2** still holds after the substitution of $r_0/z_0 = 0$. Apparently, the amplitude of the correlation curve $G(0)$ is inversely proportional to the average number of fluorescent molecules N in the observation volume, *i.e.*, $G(0) \sim 1/N$. Furthermore, the width of the correlation curve $\tau_D = r_0^2/(4D)$ represents the average time a molecule diffuses

through the waist of the focus laterally. Here D indicates the diffusion coefficient of the molecules. For quantitative analysis, N and τ_D can be obtained by fitting $G(\tau)$) with the model in **Eq. 2**. Then, the diffusion coefficient $D = r_0^2/(4\tau_D)$ can be obtained once r_0 is pre-calibrated. Furthermore, a more meaningful parameter, namely, the hydrodynamic radius R_H, can be obtained from the relationship $R_H = K_B T/6\pi\eta D$. Here, K_B is the Boltzmann constant, T is absolute temperature, and η is solution viscosity which is known for a specific solvent at a certain temperature T.

The correlation in **Eq. 1** can be calculated with a computer-based software or hardware correlator [20–23]. With the software correlator, photon counts and arrival times are imported into the computer and then correlated with relevant programs. The hardware correlators correlate on board the incoming photon arrival times electronically and feed the correlated data [5]. Both of the two approaches employ the multi-tau algorithm, but there are still some differences [5, 24]. Firstly, the hardware correlator works out in real-time mode, allowing adjusting the experimental setting in time, while the software correlator performs the calculation after experiments. Secondly, the speed of the hardware correlator is much faster than that of the software correlator. Thirdly, the hardware correlator can not reserve the raw data and is not capable of handling the issues of photobleaching, clusters, or other disturbances. By contrast, the software correlator can dispose or compensate for the above-mentioned disturbances and enables us to make other analyses such as pulsed interleaved excitation (PIE) to remove the spectrum-crosstalk and time-gated detection to suppress the background once using pulsed excitation. In short, hardware and software correlator both have their own advantages and disadvantages. The choice of each method is determined by the desired property in experiments. Compared with imaging-based dynamic determination approaches, the temporal resolution of FCS can reach the ns range, so it allows detecting molecular diffusion both *in vitro* and *in vivo* [25–27].

ADVANCES IN FLUORESCENCE CORRELATION SPECTROSCOPY

In this section, we will introduce the recent advances on FCS that aim at endowing FCS with new capabilities by concept or adapting FCS for specific applications.

Dual-Color FCCS for Molecular Interaction Investigation

To measure the molecular binding, conventional FCS is only available when the binding lead to a resolvable change in diffusion time, compared to individual molecules. This application will be handicapped when uninteresting molecules are bound to the fluorescently labeled molecules. Compared to conventional FCS, dual-color FCCS is a preferable technique to detect molecular binding without these limitations [4, 10, 28–30]. The concept of dual-color FCCS was first proposed by Eigen and Rigler [30], and was implemented experimentally by Schwille *et al.* [31] In dual-color

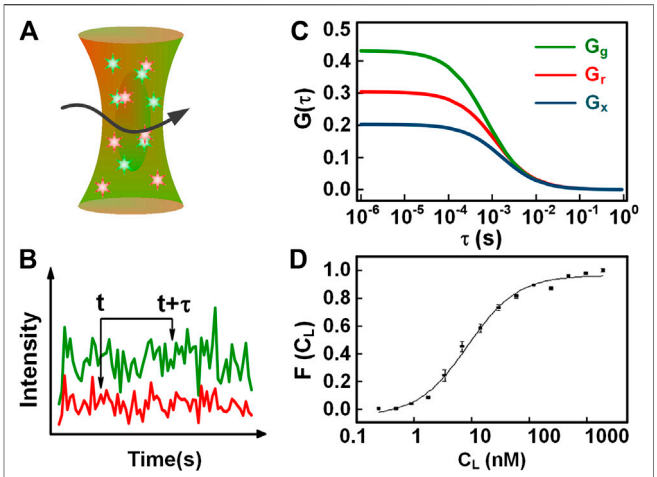

FIGURE 2 | Illustration of dual-color FCCS. (**A**) The detection scheme of dual-color FCCS. (**B**) Two-color intensity traces generated in the red and green channels. (**C**) The autocorrelation and cross-correlation curves of the red and green intensity traces in (**B**). (**D**) The binding curve of the BNP tracer and Ab-BC203, *i.e.*, the fraction of BNP bound complex varying with the free Ab concentration. The fit provides a K_D = 8.9 ± 1.0 nM.

FCCS, two species of interest are labeled with two different types of spectrally distinct fluorophores, indicated with the subscript r (red) and g (green) for simplicity. Upon the excitation of the red and green lights (as shown in **Figure 2A**), the fluorescence from the two-color fluorophores is separated and counted into two detection channels, respectively (**Figure 2B** shows two intensity traces). The autocorrelations of the intensity traces $F_g(t)$ and $F_r(t)$ from the two-color channels are calculated with **Eq. 1**, yielding G_g and G_r for the two channels (as shown in **Figure 2C**). The complexes introduce synchronized intensity fluctuation in the two channels when diffusing into and out of the observation volume. Accordingly, the presence of the complexes can be analyzed with the cross-correlation of the two-color intensity traces:

$$G(\tau) = \frac{\langle F_g(t) F_r(t+\tau)\rangle}{\langle F_g(t) F_r(t)\rangle} - 1 \tag{3}$$

$F_g(t)$ and $F_r(t+\tau)$ are the intensity traces from the two-color channels and have a lag time τ. The proportion of the complex versus the green molecules can be estimated with $G_X(0)/G_r(0)$, where $G_X(0)$ and $G_r(0)$ are the amplitude of the cross-correlation curve and the autocorrelation curve of the red channel. Moreover, a binding affinity K_D is often used to quantify the binding tendency of two kinds of molecules, which can be calculated with $K_D = C_R C_L / C_{RL}$ [32], where C_R, C_L, and C_{RL} refer to the concentration of free receptors, ligands, and the complex, respectively. These three quantities can be obtained with FCS measurement. However, this method determines K_D with a single ligand concentration C_L, and the result can be easily wrong due to the existence of a variety of disturbances in the measurement. As an improvement, a binding curve [33], which represents the fractions of the complex to the total receptors versus different

free-ligand concentrations, is often employed to acquire a more precise K_D. In practice, to calculate the binding curve, dual-color FCCS experiments are performed for a series of C_L spanning in a broad range, yielding $G_r(0)$, $G_g(0)$, and $G_X(0)$ for each C_L. Then, the fractional occupancy $F(C_L) = A_{eff}/A_g \cdot G_X(0)/G_g(0)$ is calculated for each C_L, as shown in **Figure 2D**. Here A_g is the observation area for the green species, and A_{eff} is the effective observation area. Eventually, the value of K_D is determined by fitting the $F(C_L)$ data with the following model:

$$F(C_L) = \beta \cdot (1 + K_D/C_L)^{-1} \quad (4)$$

Compared with the method of determining K_D with $K_D = C_R C_L / C_{RL}$, this approach is more robust since there are much more statistics, which are obtained in a systematic and organized way (at different C_L). In addition to the dissociation constants K_D, the fit can also extract the ratio β between receptors carrying a functional fluorescent domain and all (exogenous or endogenous) receptors capable of specific binding.

Dual-color FCCS labels two species of interest with spectrally distinct fluorophores, and the binding of the two species is analyzed with the cross-correlation. Therefore, compared with the single species, dual-color FCCS is neither limited by the relative size change of the complex compared with single species nor susceptible to binding with other species. Hence, it has been widely used to investigate molecular interactions in cells, small organelles, and many other issues [34–37].

However, there are still some factors affecting the accuracy of the dual-color FCCS. Firstly, spectral crosstalk, *i.e.*, the signal of the green species falling in the red channel, often produces a "false-positive" cross-correlation amplitude. There have been some mathematical approaches to correct the cross-talk mathematically. For instance, a simple and reliable correction approach was proposed to compensate for the cross-talk with the bleed-through ratio, the brightness ratio, and the number ratio [10, 38]. Pulsed interleaved excitation (PIE) [19], which excites and detects interleaved two-color fluorescence in separate time windows, provides a solution for this problem (**Supplementary Material**). Similarly, fluorescence lifetime correlation spectroscopy (FLCS) can also be used to distinguish the fluorescence from two different species that have different fluorescence lifetimes and therefore to remove crosstalk [39].

The second is the imperfect focus-overlap of two excitation lights, which often reduces the cross-correlation amplitude falsely. Fortunately, this artifact reduces the cross-correlation amplitude by a constant ratio. This ratio can be determined by performing dual-color FCCS on one kind of fluorophores with a broad absorption spectrum, and calculating the ratio of the obtained cross-correlation amplitude and the autocorrelation amplitudes. Then, the influence of the imperfect focus-overlap can be compensated by dividing the cross-correlation by this ratio, when measuring the binding of two species. Alternatively, two-photon excitation, which uses one laser to excite two kinds of fluorophores employing respectively single-photon excitation and two-photon excitation regimes, is available to avoid this artifact [40, 41].

The third is the uncorrelated background from the auto-fluorescence of cells, extracellular environment, or stray lights. This uncorrelated background will affect both the autocorrelations and cross-correlation curves. In the general case, the background in the red and green channel, denoted with B_r and B_g respectively, reduces the amplitude of the auto- and cross-correlation curves by [42]:

$$G_{rg}^{meas} = G_{rg}^{true} \frac{F_r}{F_r + B_r} \frac{F_g}{F_g + B_g} \quad (5)$$

F_g and F_r are the means of the green and red fluorescence intensities, excluding the background.

G_{rg}^{meas} and G_{rg}^{true} are the amplitudes of the cross-correlation calculated from the measurement and the cross-correlations in reality, respectively. With **Eq. 5**, the auto-fluorescent background and detector dark counts can be corrected.

The fourth factor is photobleaching. The continual loss of fluorophores in the focus area with time will falsely distort the autocorrelation curves by providing apparently smaller molecule numbers N_r and N_g, and shorter correlation time τ_{Dr} and τ_{Dg}. Interestingly, it was found recently that the amplitude of the cross-correlation is barely influenced by the bleaching of either red or green species [43]. Furthermore, the molecule numbers can be corrected by multiplying N_r and N_g with the coefficients γ_r and γ_g, which is quantified with the raw red and green intensity traces, considering the fluorescence intensity is linear to the molecule number [43]. Nevertheless, it is always preferable to avoid bleaching in both channels, since the lateral shift of the correlation curves induced by the bleaching can never be restored yet.

Dual/Multi-Focus Fluorescence Correlation Spectroscopy and Imaging Fluorescence Correlation Spectroscopy to Acquire Space-Multiplexing Dynamics

Conventional FCS could only detect the dynamics of a single spot. Dual-focus FCS (and multifocal FCS) was developed with their major merit of probing dynamics simultaneously at two separated positions. Meanwhile, in single-focus FCS, the pre-calibration for focus size r_0 is needed for the quantitative analysis of the FCS data [44]. Dual-focus FCS can avoid this pre-calibration procedure when the inter-focal distance is prior-known [45, 46].

In dual-focus FCS, a DIC prism splits two orthogonal linear-polarized pulsed lasers into two laterally shifted foci, as shown in **Figure 3A**. The fluorescence alternatively excited by the two foci is separated by using a time-correlated single-photon counting (TCSPC) module. By applying a global fit to all correlation curves, including the ACF from each focus, and the CCF between both foci, one can extract the absolute values of the diffusion coefficient D and the focus size r_0 when the inter-focal distance is pre-known [45]. Therefore, it is promising for dual-focus FCS to obtain a more accurate diffusion coefficient in experiments [47]. With the dual-focus FCS, Kerstin *et al.* investigated protein diffusion in black lipid membranes, yielding highly accurate diffusion coefficients [48]. In addition, it is also worthy of mentioning that the inter-focal distance was also influenced by specific experimental settings, such as the thickness of the cover-slip and index mismatch. So a pre-calibration is necessary for most of measurements.

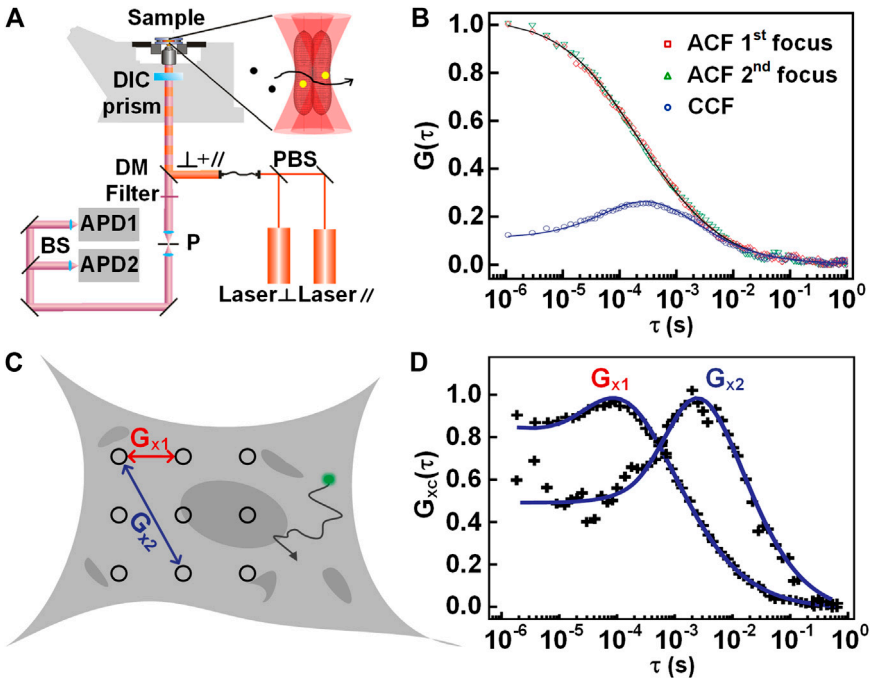

FIGURE 3 | Illustration of dual-focus and multi-focus FCS. (**A**) Schematic setup of dual-focus FCS. (**B**) Autocorrelation and cross-correlation curves of dual-focus FCS. (**C**) Schematic view of multi-focus FCS measurement. (**D**) The correlation curves between two pairs of positions with different distances. Adapted from Refs. [11, 56].

Besides the dual-focus FCS, there exist similar techniques, such as imaging FCS [49], multi-scale FCS [11], and multi-focus FCS [50, 51]. In imaging FCS, a series of images are taken on a certain area of the sample, and then the intensities associated with each pixel are correlated with time. When fitted with a suitable diffusional model, the dynamics at thousands of points can be measured simultaneously [15, 52]. Except for auto- and cross-correlation analysis, spatiotemporal image correlation spectroscopy (STICS) [53, 54] and k-space image correlation spectroscopy (kICS) [55] have been proposed to analyze the dynamics at different locations. STICS allows measurement of diffusion coefficients and velocity vectors of particles by using temporal and spatial correlation on measured image stacks. kICS can quantify molecular dynamics by performing correlation in reciprocal space even in the presence of fluorophore photobleaching and blinking. kICS does not rely on nonlinear curve fitting, or the knowledge of the beam radius of the exciting laser. With the advent of fast and sensitive EMCCD cameras, the potential of the imaging FCS will be further exploited for wide applications in biomedical and chemical sciences. Similarly, multi-scale and multi-focus FCS both detect the signals from multi-points in an extended area, as shown in **Figure 3C**. Then, the spatial information of molecular motion can be analyzed by the autocorrelation or the cross-correlation curves between the different pairs of points (**Figure 3D**). Multi-focus FCS was implemented recently by using a spinning-disk [51] or beam-splitter array [50]. Multi-scale FCS was proposed by Baum *et al.* [11] to characterize the intracellular architecture by employing a line for illumination. As the common disadvantages of imaging FCS, multi-scale FCS, and multi-focus FCS, their temporal resolution is low (in the millisecond range) due to the usage of 2D imaging sensors; meanwhile, these three techniques have a larger observation volume than the confocal based FCS due to the lack of pinhole filtering. In addition, by scanning a wide area across the sample and performing a correlation analysis of relevant subregions within the acquired image, the dynamics can be probed by the analysis of raster image correlation spectroscopy (RICS) [57]. Despite the dynamics can be obtained by scanning one frame, RICS often scans a few frames to compensate for the immobile component in the image. In RICS, the correlation data is calculated with a dozen of pixels that are connected with each other along the line scan. Therefore, the spatial resolution of RICS (a few micrometers) is much lower than the above-mentioned techniques.

Pair Correlation Function Analysis for Directional Diffusion

The conventional FCS detects dynamics at one point or two, and lacks the ability to detect path-related anisotropic diffusion. To acquire directional diffusions or to detect obstacles to molecular diffusion, Digman *et al.* incorporated pair correlation function (pCF) into FCS [12]. pCF was performed by repeatedly scanning a line in a cell (indicated with the white-dash line in **Figure 4A**), and then assembling the acquired lines into a kymography (**Figure 4A**-bottom). In the kymography, when the intensities of a specific pixel assembled are correlated with time, an autocorrelation $G(\tau)$ is generated, the local concentration and

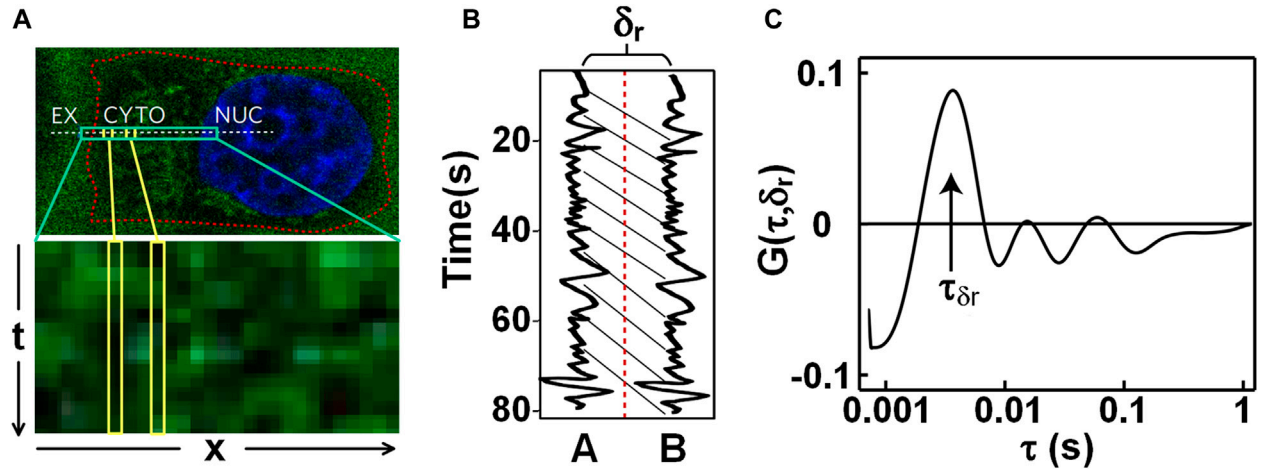

FIGURE 4 | Pair correlation function (pCF) analysis on nanoparticles transmitting in live cells. (**A**) Fluorescence image of nanoparticles and Hoechst-stained nucleus (*Top*) and the kymograph (*Bottom*). The dash-line indicates the scanned line across the extracellular space (EX), the cytoplasm (CYTO), and the nucleus (NUC). (**B**) Fluorescence intensity fluctuations of two pixels with a distance of δ_r in the sample. (**C**) Pair correlation curve $G(\tau, \delta_r)$ calculated with the two intensity traces in **Figure 4B**. Adapted from Ref. [60].

the diffusion coefficient of targeted biomolecules at this pixel can be obtained by fitting $G(\tau)$ with the diffusion model in **Eq. 2**. Furthermore, when the cross-correlation of a pair of pixels (*see* **Figure 4B**) separated by δ_r is calculated, the lag time of the cross-correlation peak characterizes the transmit time a molecule diffusing from point A to point B, as shown in **Figure 4C**. The longer the transit time is, the more the mobility between the two pixels is hindered. Therefore, according to the pCF analysis, the obstacles which hinder the molecular diffusion can be detected from the abnormal migrating time [12, 58]. Recently, Bianchini *et al.* [59] utilized STED-based pCF to investigate local diffusion barriers in living Chinese Hamster Ovary cells. This method provides directional spatial motion information, which is not obtainable with conventional FCS.

There is a certain similarity between pCF and dual-focus FCS [46]. However, dual-focus FCS can only detect dynamics on a fixed pair of points. pCF can obtain information about any pair of points in the detection area or scanned line, which greatly increases the amount of spatial information. In all, pCF is more practical and convenient for biological researchers.

Recently, two-dimensional pair correlation function (2D pCF) was developed as an extension of pCF analysis. 2D pCF probes the anisotropic paths at different spatial locations and maps the intercellular environment [61]. Compared with one-dimension pCF, 2D pCF can provide more information of the intercellular environment. Specifically, correlating the intensity series of each image pixels with its neighboring pixels at a certain distance yields a set of pair correlation functions. Plotting the results of pCFs as a function of time delay and angle, a sub-image for each pixel can be obtained, and then a polar plot for each pixel can be generated. If the molecules move isotropically, the correlation function will be equal in all directions. However, if there are barriers in some directions, a deformed polar plot can be obtained and analyzed by moment analysis [62]. Therefore, the 2D pCF is a fingerprinting tool for the investigation of anisotropic motions and intracellular structures in living cells. Compared with 1D pCF, 2D pCF using a 2D image sensor for the detection trades its temporal resolution for spatial information.

Except for analyzing the fluorescence fluctuation, some researchers applied pCF analysis to sense other parameters such as molecular brightness. For instance, Hinde *et al.* [63] utilized pCF to quantify molecular brightness (pCOMB) and tracked the mobility of different oligomeric species within living cell nuclear architecture.

Scanning Fluorescence Correlation Spectroscopy Targeting Dynamics on Membranes

For static FCS, the observation volume is kept fixed at a specific location in the sample, and therefore, it is not applicable for the studies of rather slow diffusional dynamics in bio-membranes. The reason lies in that the infrequent appearance of fluorophores in the focal spot poses sampling problems, and meanwhile, their long retention in the focus volume enhances the likelihood of photo-destruction. Scanning FCS was proposed to overcome this difficulty by sweeping the focus rapidly across a sample, calculating the autocorrelation of the assembled intensity trace associated with one or multiple positions, and then obtaining the dynamics after applying a fit model [64, 65]. Sorted by the scanning direction with respect to the membrane position, scanning FCS can be classified into two categories: parallel scanning FCS and perpendicular scanning FCS.

Parallel Scanning Fluorescence Correlation Spectroscopy

Parallel scanning FCS scans a focused light along one line [66], two lines (as shown in **Figure 5A**), or a circle [67, 68], (as shown in **Figure 5B**) in the plane of a membrane, acquiring and assembling the photons with pixels and time. After that, the intensities of each pixel from the scanned line or circle are extracted and binned into an

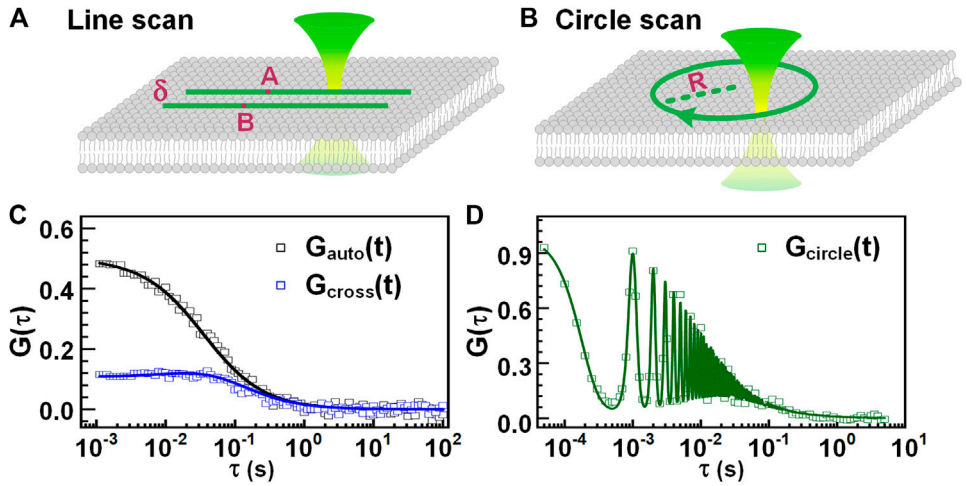

FIGURE 5 | Parallel scanning FCS. Scheme of line-scanning FCS (**A**) and circle-scanning FCS (**B**). (**C**) The autocorrelation curve (black) of a specific pixel and the cross-correlation curve (blue) of two pixels separated by a distance of δ. (**D**) The correlation curve obtained from all the photons assembled with time, regardless of scanning positions.

intensity trace, the autocorrelation of the intensity trace can provide the concentration and diffusion coefficient of the targeted biomolecules. Furthermore, similar to dual-foci FCS, the intensity of two pixels from the two scanned lines or from the scanned circle, which has a known distance, can be auto-correlated and cross-correlated. A global fit on the obtained autocorrelations and the cross-correlation can provide, the focus size, concentration, and diffusion coefficient of measured biomolecules, as shown in **Figure 5C**. This method avoids additional procedures for detection volume calibration. Alternatively, in circle-scanning FCS, the photons collected during the whole scanning process are globally assembled with time, yielding a global intensity trace (regardless of the scanning position). The concentration and diffusion coefficient of biomolecules can be obtained from the calculated autocorrelation curve (*see* **Figure 5D**) with a suitable fit model [67, 69, 70].

In general, parallel scanning FCS alleviates the photobleaching of fluorophore by splitting the light exposure among a set of pixels. Equivalently, the time each fluorophore spends in the focus during measurement is reduced. Scanning FCS has been widely used in the study of biomolecular dynamics on membranes. For instance, Ries *et al.* [66] used line-scanning FCS to measure the diffusion coefficients of lipids accurately, interpreting the diffusion behavior in three phase-separating bilayers and the temperature dependence in several model membranes.

Perpendicular Lateral/Axial Line-Scanning Fluorescence Correlation Spectroscopy

When FCS is used to investigate dynamics on membranes, the movement of the membranes with respect to the observation volume gives rise to strong intensity fluctuations, obscuring those resulting from molecular diffusion in the plane of the membrane. Z-scan FCS tried to solve this problem by measuring a stack of correlation curves at discrete axial positions ("z-scan") and selecting the correlation curve corresponding to the shortest diffusion time and the minimal number of particles [71, 72]. Alternatively, lateral/axial line-scanning FCS (lsFCS) solves this problem by quickly scanning the observation volume perpendicularly through the membrane or GUV [43, 73], as shown in **Figure 6A**. For both lateral and axial lsFCS, the fluorescence collected along the direction is binned into a 2D pseudo image (*see* **Figure 6C**). For data analysis, the photons from the membrane, which is identified with the highest photon counts, are selected and binned into an intensity trace. Then, the intensity trace is correlated and analyzed with 2D diffusional model, yielding useful information, including biomolecular concentration, diffusion coefficient, *etc.* These methods are ideally suited to study dynamics in the membrane [42, 73]. Furthermore, they can be extended to dual-color lateral/axial lsFCS to study the interaction between different molecules, such as ligands and receptors, when tagged with different fluorophores [32].

For comparison, lateral lsFCS is often performed with a galvo-scanner, which limits the time resolution to ~ ms [32]. Nevertheless, the recently reported axial lsFCS performed a resonant axial-scan (*see* **Figure 6B**) by using a tunable acoustic gradient index of refraction lens (TAG lens), providing a time resolution of 0.05 ms, 40 times faster than that the time resolution (2 ms) of lateral lsFCS, as shown in **Figure 6D** [43]. Furthermore, the axial lsFCS has a smaller and more symmetric focal area, and therefore, it can achieve comparable data quality with a remarkably reduced data acquisition time. The reduced measurement time will, in turn, reduces the photobleaching caused. Moreover, compared to the elliptical cross-section in lateral lsFCS, the circular cross-section in the axial lsFCS makes the fit more robust [43].

Reduction of Observation Volume to Probe Nanoscale Dynamics

As we all know, molecules in cells are usually hindered and differ from locations [74]. Also, the anomalous diffusion usually occurs on a small spatial scale with nanoscales [75]. In conventional FCS,

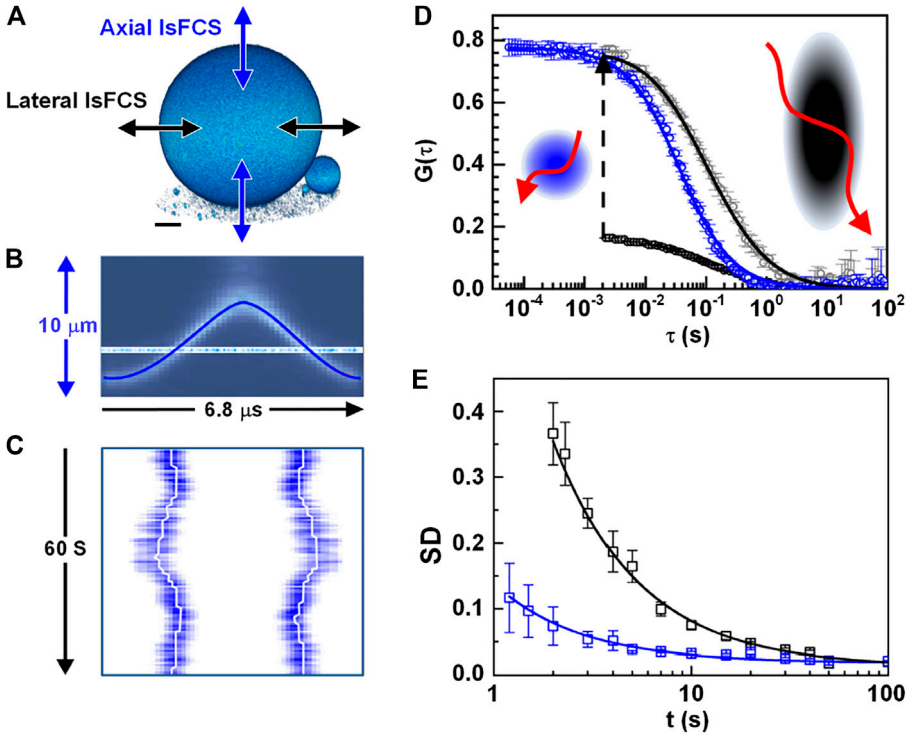

FIGURE 6 | Lateral and axial line-scanning FCS (lsFCS). (**A**) The scanning schemes of lateral and axial lsFCS, which have the observation area A = $\pi\omega_0 z_0$, and A = $\pi\omega_0^2$, respectively. (**B**) Axial focus position during a single oscillation cycle of 6.8 μs in the axial lsFCS using a TAG lens. (**C**) The kymograph during 60s of axial line-scanning in the axial lsFCS. White-lines mark the membrane positions. (**D**) The correlation curve of the lateral (black) and axial (blue) lsFCS. The lateral lsFCS autocorrelation data have also been scaled to the axial ones (gray) for better comparison. (**E**) Standard deviation (SD) of two groups of seven normalized lateral (black) and axial (blue) lsFCS curves. Adapted from Ref. [43].

due to the limitation of the optical diffraction, the observation volume is limited to ~ 0.5 fl [76]. Despite being tiny already, this observation volume can also average out the heterogeneous dynamics happening in the diffraction-limited observation volume. Meanwhile, the diffraction-limited observation volume limits the measurable concentration, not exceeding ~ 100 nM [77]. Otherwise, the fluctuations will be averaged out. However, the concentration of many biomolecules in living cells, especially when induced by an external transfection, is often quite high, usually in the micro-to the millimolar range. Therefore, it is crucial to reduce the detection volume of FCS to measure biomolecular dynamics with much higher concentration or the dynamics happening in the sub-diffraction areas. This section will introduce three techniques that reduce the detection volume, namely, total internal reflection FCS (TIR-FCS), nanofluidic channel-based FCS, SPIM-FCS, and STED-FCS.

Total Internal Reflection-Fluorescence Correlation Spectroscopy and Nanofluidic Channel Based Fluorescence Correlation Spectroscopy

Total internal reflection FCS (TIR-FCS) is a method that can significantly reduce the observation area in the axial direction by utilizing total internal reflection (TIR). TIR-FCS was first proposed by Thompson *et al.* in the 1980s [78]. In TIR-FCS (*see* **Figure 7A**), a laser beam is totally and internally reflected at the surface-solution interface at an angle greater than the critical angle, forming an evanescent wave in a very thin layer with a thickness typically from tens of nm up to a few hundreds of nm. [79, 80] The excited fluorescence is collected by a microscopic objective and used for correlation analysis, from which the quantitative dynamic parameters of the sample can be obtained [81]. In addition to the setup in **Figure 7A**, TIR-FCS can also be realized by epi-illumination. [82] Through total internal reflection, the excitation of fluorophores, which are far away from the surface, is avoided. Therefore, compared with confocal based FCS, TIR-FCS has a much smaller focus volume that contributes to measuring high-concentration molecules and reducing the measurement time. On the other side, molecular diffusion investigated with TIR-FCS is handicapped by the binding of the molecules to the solid surface. Another difficulty in using TIR-FCS is the lack of a valid analysis model. Recently, many researchers have studied mathematical models to enhance TIR-FCS [83–85], taking into account the decay of evanescent waves and many other related problems. TIR-FCS has been widely applied to measuring receptor-concentration near membrane surfaces and the ligand-receptor binding occurring on the membrane [86].

Another way to reduce the observation volume is to use nanofluidic channels in FCS (**Figure 7B**). Foquet *et al.* [87] used nanofabricated channels with dimensions smaller than

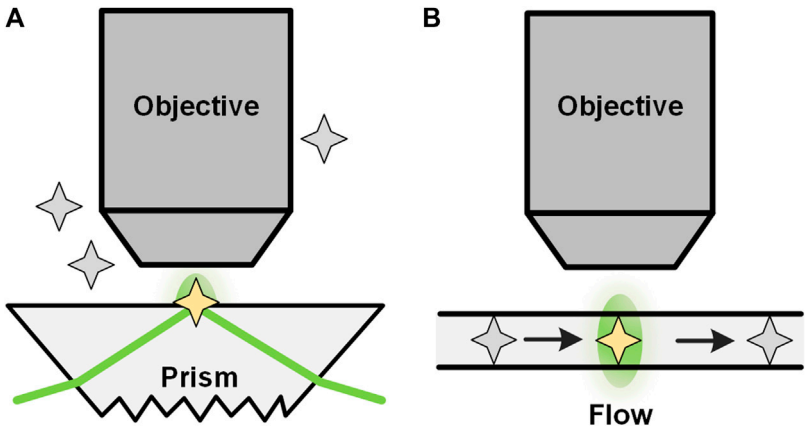

FIGURE 7 | TIR-FCS and nano-channel based FCS. Configurations of total internal reflection (TIRF) based FCS (**A**) and nano-channel based FCS (**B**).

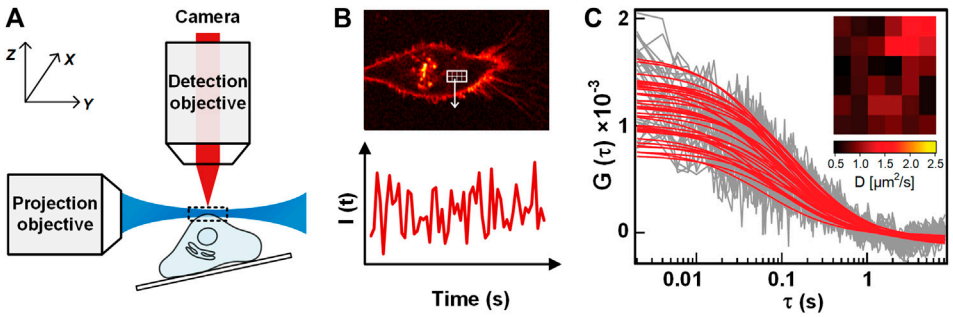

FIGURE 8 | Illustration of SPIM-FCS. (**A**) Schematic of SPIM-FCS measurement on a sample. (**B**) The sectioned image of the sample when illuminated by a light sheet (Top), and the fluorescence intensity trace from one pixel in the image series (Bottom). (**C**) The ACFs of different pixels/locations. The Inset shows the Diffusion coefficient map. Adapted from Ref. [89].

the diffraction-limit as the container of molecules during FCS studies. With such a nano-channel, an effective detection volume of tens of attoliters was achieved. In addition, non-linear or higher harmonics techniques, 4π-alike excitation, near-field techniques, and surface plasmon can also be used to generate an effective focus volume smaller than the diffraction limit [77]. It should be noted that the detection volume of these methods is inherently adjacent to a surface, and consequently, free diffusion is restricted in at least one direction [77]. Another limitation of FCS in microfluidics is the lack of suitable interpretive models under different conditions, especially when measurements are performed in microchannels in which boundary effects cannot be neglected [24].

Single Plane Illumination Microscopy-Based FCS

Single plane illumination microscopy-FCS (SPIM-FCS) is a multiplexed technology that allows simultaneous FCS measurements on thousands of adjacent observation volumes to provide spatial maps of the diffusion coefficient and concentration [15]. In SPIM, a thin light sheet with a typical thickness of 1 ~ 1.5 μm is generated by using a projection objective and a conjugated cylindrical lens, and the emitting fluorescence signal is detected in perpendicular (as illustrated in **Figure 8A**) by a high-speed camera [88]. After that, a series of images are recorded, and the fluorescence intensity trace of each pixel is generated by assembling the intensities of each pixel in the image series (**Figure 8B**). With ACF of the pixelated intensity traces, the quantitative diffusion coefficient and concentration maps are obtained (**Figure 8C**).

Comparing to confocal-based FCS, SPIM-FCS avoids the out-of-focus excitation and hence provides a well-confined observation volume. Moreover, SPIM-FCS can also detect the dynamics of multiple locations simultaneously, providing a diffusion-coefficient map and concentration map [15]. Besides, SPIM-FCS has high flexibility during data analysis. For instance, the observation volume can be controlled during data analysis artificially in SPIM-FCS, which is convenient to adjust the analysis area according to the specific samples. Compared to RICS, which obtains the diffusion coefficient with multiple pixels along the scanning direction, SPIM-FCS excels in the spatial resolution [49]. However, the temporal resolution of SPIM-FCS/FCCS is limited by the performances of cameras. A camera with sufficient quantum efficiency and high speed is needed for SPIM-FCS to measure fast molecular motions with good statics. There are some available cameras such as SPAD, sCMOS, EMCCD,

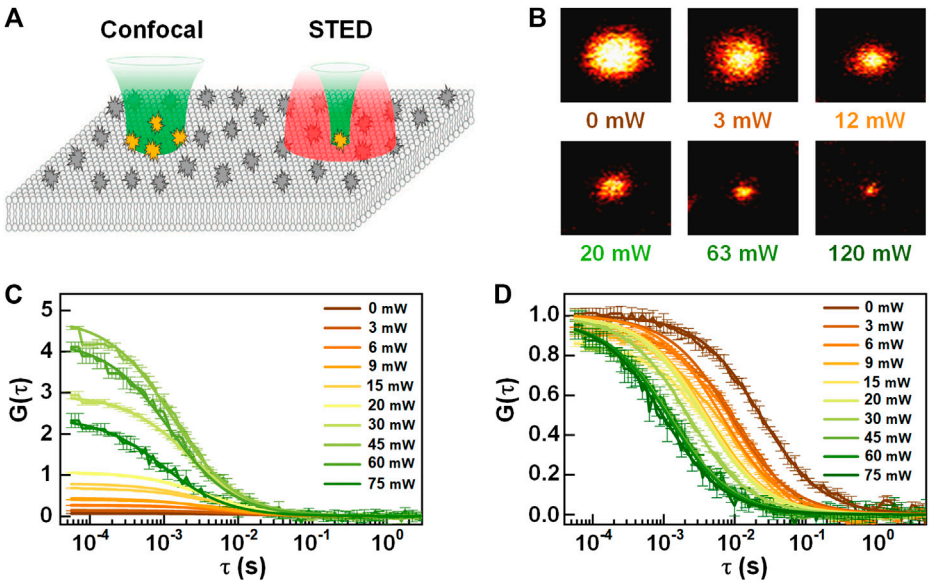

FIGURE 9 | Schematic diagram of STED-FCS. (**A**) The observation volume of confocal **(left)** and STED **(right)**. Adapted from Ref. [100]. (**B**) The effective focus size (STED image of a single particle) at the different intensity of the depletion light. (**C**) Autocorrelation and (**D**) normalized autocorrelation curves of STED-FCS at different depletion intensity.

where EMCCD provides the highest quantum efficiency of more than 90% and the relatively low frame rates of 1000 s^{-1}, which is the most suitable detector with a comprehensive consideration yet [49, 90]. In summary, device advances help to further improve the performance of SPIM-FCS.

SPIM-FCS has played an important role in the detection of molecular diffusion within cells and organizations [89, 91]. Besides dynamics measurement, Krieger *et al.* [92] proposed two-color SPIM-FCS that allows measuring spatially varying molecular interactions. In two-color SPIM-FCS, two light sheets of different wavelengths are used as the excitation, and an image splitter was used to split the detected fluorescence into two separate color channels. Agata *et al.* [93] utilized this method to study the interactions of the molecules Fos and c-Jun in HeLa cells.

Stimulated Emission Depletion-Fluorescence Correlation Spectroscopy

To study the anomalous dynamics of molecules, in 2005, Kastrup *et al.* reduced the FCS detection volume to one-fifth of the conventional confocal volume by using stimulated emission depletion (STED) [14]. In the so-called STED-FCS, a red-shifted doughnut-like depletion light depletes the excited fluorescence in the periphery of the excitation focus, yielding an effective focus much smaller than the diffraction limit (see **Figure 9**) [94]. In principle, the effective focus size of STED-FCS can become infinitely small by increasing the intensity of depletion light, but in actual situations, it is limited by photobleaching of fluorophores and reduction of signal to background ratio. Also, the background fluorescence from the out-of-focus region will directly influence the determination of both the concentration and diffusion coefficient. Recently, stimulated emission double-depletion (STEDD) based FCS (STEDD-FCS) [95] was proposed, which determines the effective fluorescence and background by temporally modulating the effective fluorescence "on" and "off" by applying an additional depletion light and later subtracts the background from the signal in total. Alternatively, time-gated detection was proposed on continuous-wave stimulated emission depletion (CW-STED) to reduce background [96]. As an enhanced approach, Lanzanò *et al.* [97] separates the effective signal and background photons by lifetime tuning (SPLIT-FCS) for reducing anti-stokes fluorescence emission background in STED-FCS. Compared with the gating method, SPLIT-FCS does not need complex fitting procedures such as fluorescence intensity distribution analysis (FIDA). Compared with STED-FCS in solution or cytosol, STED-FCS is more promising to probe membrane-related dynamics. This is due to the fact that the membrane intrinsically provides perfect axial confinement of the focus, no longer suffering from the out-of-focus fluorescence. In 2009, Eggeling *et al.* [98] applied STED-FCS to the study of living cell membranes, and proved that STED-FCS is capable of detecting the anomalous or heterogeneous diffusion in the membrane [75, 99]. Also, STED-FCS, which has excellent spatial resolution, can be combined with other techniques to obtain better consequents and facilitates solving more complex biological problems. For instance, Maraspini *et al.* [69] demonstrated the ability of circle scanning STED-FCS in quantifying spatiotemporal heterogeneities of lipid diffusion in cell membranes.

Inverse Fluorescence Correlation Spectroscopy

Wennmalm *et al.* [16] proposed inverse FCS (iFCS), which analyzes the fluctuation of unlabeled particles in the context of a densely labeled surrounding medium. As illustrated by **Figures 10A–D**, when a nonfluorescent particle transits

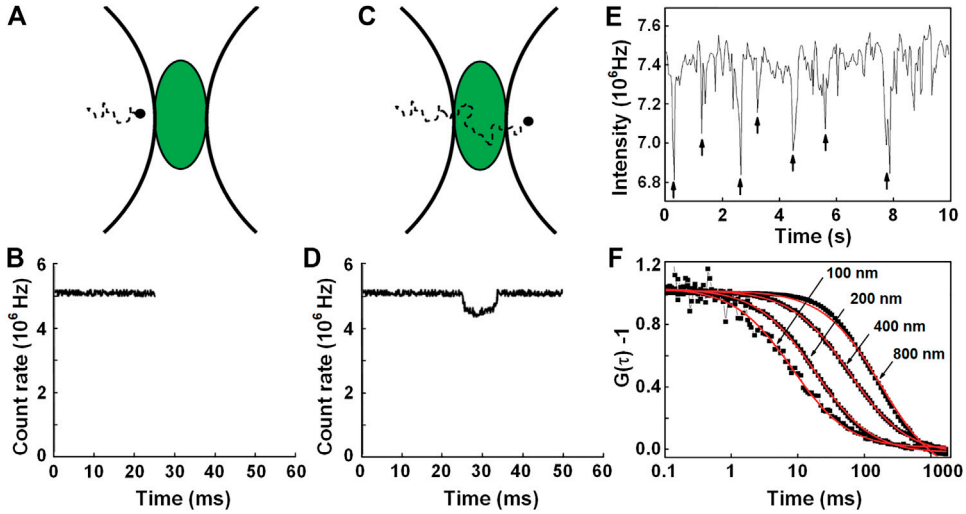

FIGURE 10 | Principle illustration of iFCS. (**A**) ~ (**D**) A fluorescence signal is reduced upon the entrance of a non-fluorescent particle into the detection volume. (**E**) Intensity trace caused by the diffusion of 400-nm beads in 400-μM Alexa 488-medium. (**F**) Normalized iFCS curves from the diffusion of 100, 200, 400, and 800 nm beads in 400 μM Alexa 488. Adapted from Ref. [16].

through the detection volume, a fraction of the fluorescent medium molecules will be replaced by the particle, resulting in a reduction of the fluorescence signal. Therefore, the generated intensity trace $F(t)$ features multiple negative spikes, as shown in **Figure 10E**. To quantify the molecular density and dynamics of the molecule, the autocorrelation of the intensity trace can be calculated and fitted to the following 3D diffusion model (see **Figure 10F**) [16]:

$$G(\tau) = \frac{N}{\left(1/V_q - N\right)^2} \cdot \left(1 + \frac{\tau}{\tau_D}\right)^{-1} \cdot \left(1 + \frac{\tau}{\tau_D} \cdot \frac{r_0^2}{z_0^2}\right)^{-1/2} \quad (6)$$

where N is the average number of molecules in the detection volume. $V_q = V_{\text{particle}}/V_{\text{detection}}$ with V_{particle} being the particle volume and $V_{\text{detection}}$ the detection volume. The fitting model in **Eq. 6** is the same as that in standard FCS, but with the only difference that $1/N$ is replaced by $N/(1/V_q - N)^2$. In iFCS, the average non-labeled molecule number N in the observation volume can be calculated with $1/\sqrt{N} = -\langle(\delta F(t))^3\rangle/\langle(\delta F(t))^2\rangle^{3/2}$, where $\delta F(t)$ is the fluorescence fluctuation ($\delta F(t) = F(t) - \langle F\rangle$), considering the skewness of the fluorescence intensity distribution [101]. Then, the ratio V_q can be determined with N and $G(0)$ solely, irrelevant to the diffusion term. Eventually, the concentration and the volume of the non-labeled particles can be determined after the detection volume $V_{\text{detection}}$ is obtained with standard FCS. Jiang *et al.* [101] used this method to observe the growth of phase domains and study the stages of phase separation in model lipid bilayer membranes. Interestingly, Jiang demonstrated that iFCS could uniquely provide accurate and consistent size of nanodomains while conventional FCS approaches can not. Besides the moment analysis, iFCS can examine the particle volume directly by providing the ratio of the particle to detection volume [102]. Bergstrand *et al.* [103] estimated that the diameter of NPs with iFCS, and provided results that the NPs with a specified diameter of 250 nm was 257 ± 12 nm, and the NPs of 40 nm was 62 ± 26 nm with iFCS.

iFCS has some advantages above FCS. At first, iFCS provides particle sizes directly from $G(\tau = 0)$ without resort to the interpretation of the 3D diffusion model. The diffusion is often influenced by the temperature and viscosity of the medium, and therefore, the obtained diffusion coefficient and particle size are not accurate in a complex environment. Second, in iFCS experiments, the high molecular brightness is not very important, but the total fluorescence signal should be high to improve the signal-to-noise ratio. Thus, the concentration of medium dyes should be high and gives a negligible contribution to ACF. Usually, the concentration of medium used in the experiment is about 10 μM or higher [104].

However, iFCS is limited to the analysis of rather large-volume particles. For instance, Wennmalm's experiments reveal that the lower limit for the particle size that can be analyzed is ~ 100 nm diameter with a detection volume of 0.3 fl [16]; in Jiang's work, the domain which size is five times smaller than the detection area can be detected [101]. To measure the smaller particle, it is necessary for iFCS to perform on the smaller detection volume, such as STED and nanostructured surfaces. The smaller detection volume provides a possibility for iFCS to detect smaller particles. Sandén *et al.* [105] combined iFCS with subwavelength apertures in plasmonic metal layers, which confines the detection volume to 1.2×10^{-4} fl, by which they directly examine the volume of a protein molecules allophycocyanin (APC) as $2.5 \pm 0.6 \times 10^{-7}$ fl in solution. Till yet, iFCS has not been applied in the plasma membranes of living cells [104]. This is mainly because the intercellular environment is very complicated, and different non-labeled cellular organelle are mixed.

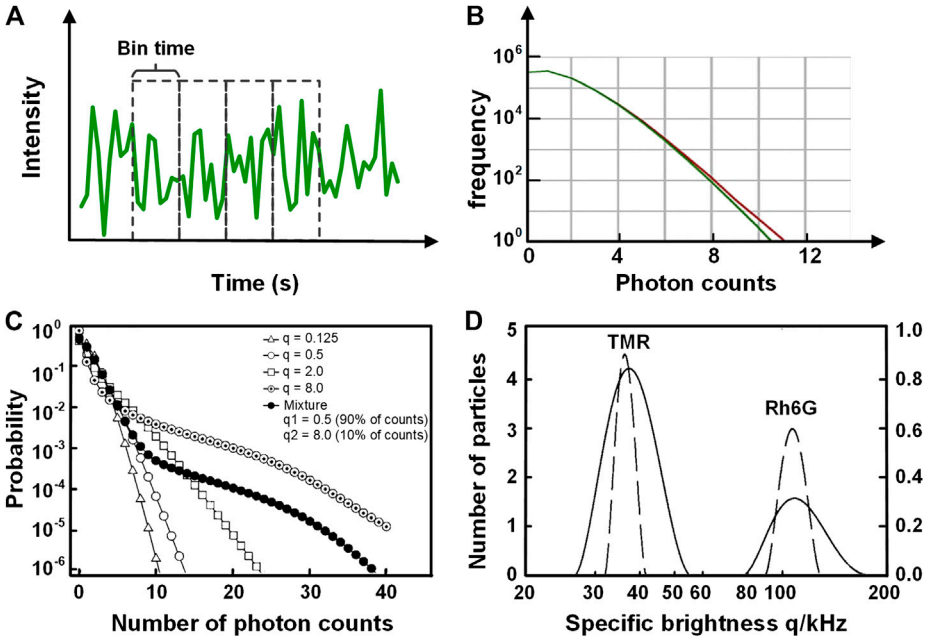

FIGURE 11 | Schematic illustration of the principle of PCH and FIDA. (**A**) The intensity trace used for PCH, which is divided into multiple equivalent time bins. (**B**) The statistics of the photon number per bin (red) for YFP-tagged beta2-adrenergic proteins within the plasma membrane of HEK293 cells. The histogram (red) is fitted with the PCH model (green). The molecular brightness and the average number of molecules can be acquired from the fitting result. Adapted from [106]. (**C**) and (**D**) FIDA analysis on the dyes Rh6G and TMR diffusing in solution (**C**) The probability distribution for five cases featuring different mean count number *q* per particle. The open symbols correspond to solutions of single species. The solid line is calculated for a mixture of two species. (**D**) The brightness histogram of different species obtained from (**C**) with the inverse transformation with regularization (ITR). The dashed lines correspond to the solutions of single dyes (Rh6G and TMR), and the solid line corresponds to their mixture. Adapted from [18].

Photon Counting Histogram and Fluorescence Intensity Distribution Analysis

In addition to FCS which analyzes the fluorescence fluctuation based on the temporal domain, photon counting histogram (PCH) [17] and fluorescence intensity distribution analysis (FIDA) [18] can extract the molecular brightness (photon counts per second per molecule) and the average number of molecules within the observation volume by analyzing the distribution of fluorescence fluctuation amplitude. In PCH, the fluorescence intensity trace is divided into multiple pieces with equivalent time bins, and the photon counts in each piece (**Figure 11A**) are integrated, yielding a photon-counting histogram (red curve in **Figure 11B**). The photon distribution arisen from molecular diffusion in observation volume exhibits a super-Poissonian distribution. The molecular brightness and the average number of molecules can be uniquely extracted by fitting the data with a suitable PCH model, for which Chen *et al.* derived a model [17]:

$$\Pi\left(k;\ \overline{N}_{PSF},\ \varepsilon\right) = \sum_{N=0}^{\infty} p^{(N)}\left(k;\ V_0,\ \varepsilon\right) p_{\#}(N) \tag{7}$$

Eq. 7 describes the probability of observing k photon counts in an open system for a particle solution with a concentration of $c = \overline{N}/(V_0 N_A)p^{(N)}$ is the probability of observing N particles in the observation volume V_0, which is obtained by N-times convolution of single-particle PCH. $p_{\#}(N)$ is the Poissonian probability of observing N particles. Moreover, the PCH for multiple molecular species is generated by successively convoluting the photon distribution of each species with the others. As shown in **Figure 11B**, the green curve is the experimental data, and the red curve is the fitting curve with the PCH model in **Eq. 7**. Finally, the brightness and the average number of molecules can be obtained from the PCH fit [106, 107]. Katharine *et al.* [106] used PCH to study the receptor-receptor interactions in HEK293 cells. The result indicates an average molecular brightness of 17,857 counts per second per molecule. Through comparing the molecular brightness to that of monomer, they found the beta2-adrenergic receptors have a dimeric structure.

Besides PCH, fluorescence intensity distribution analysis (FIDA), firstly proposed by Kask *et al.* [18], is also a useful tool that determines the molecular brightness and the concentration by analyzing the distribution of photon counts. In the FIDA analysis, the observation volume is divided into a great number of spatial sections and calculated the distribution of the photon counts in each spatial section:

$$P_i(n) = \sum_{m=0}^{\infty} \frac{(cdV_i)^m}{m!} e^{-cdV_i} \frac{(mqB_iT)^n}{n!} e^{-mqB_iT} \tag{8}$$

$P_i(n)$ is a double Poissonian distribution, indicating the distribution of the number of molecules with the mean value cdV_i and the photon counts with the mean value mqB_iT, provided

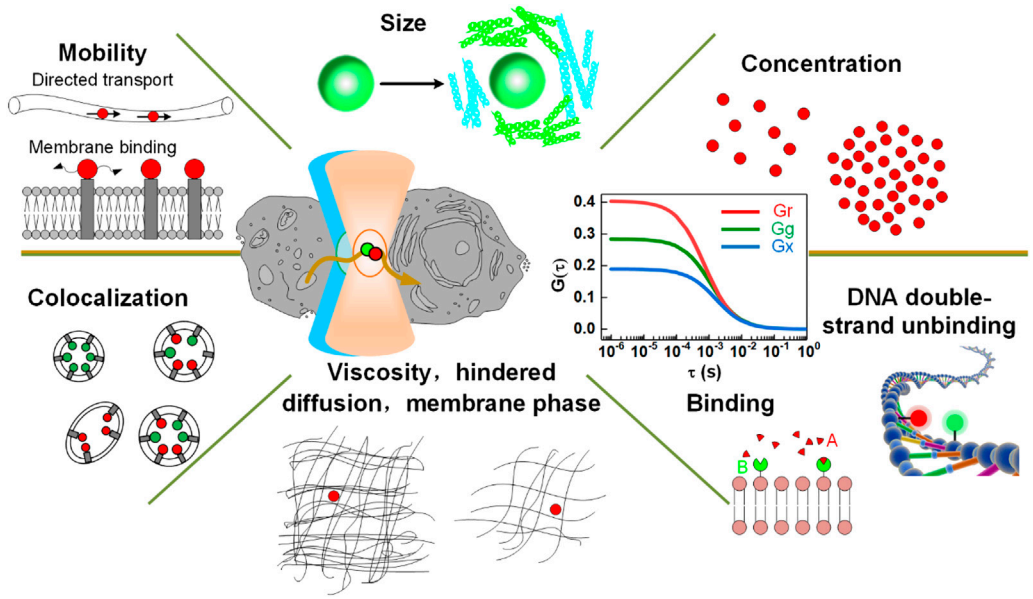

FIGURE 12 | Applications of FCS. Adapted from Ref. [114].

that there are m molecules inside the confocal volume, respectively. The overall distribution $P(n)$ can be obtained by spatial integrals of $P_i(n)$ over the whole observation volume. The measured $P(n)$ is shown in **Figure 11C**, and the brightness and the concentration of the sample (**Figure 11D**) can be acquired by analyzing the data with the FIDA model. The result would be a single δ-peak for the single species and two δ-peaks for the mixture of two species, which offers us an efficient way to distinguish the different species in the sample directly. As shown in **Figure 11D**, the TMR or Rh6G shows one peak in the result (dash lines on the left or right sides); the mixture of two species contains two peaks (solid line). So the different species in solutions can be easily distinguished.

Both PCH and FIDA analyze the molecular brightness and the average number of molecules within the observation volume. They have both similarities and differences. PCH begins with the calculation of the probability associated with fluctuations for a single particle in a reference volume and then convolutes the histogram of a single particle with n times to generate the histogram for n particles; FIDA begins with the calculation of the histogram for all particle numbers in a small volume and then convolutes it over the whole space, which generates the overall photon counts distribution. However, the theoretical formulations of the two in mathematical have been proved to be equivalence [108]. Meng *et al.* demonstrated that the numerical efficiency of PCH is faster than FIDA under the condition of power series expansion being used for the PSFs calculation [108].

FCS, PCH, and FIDA are all the methods for analyzing the fluorescence fluctuation within the observation volume. Compared with PCH and FIDA, FCS can acquire information on dynamics such as diffusion coefficients, and it can distinguish two species with different diffusion coefficients. Nevertheless, PCH and FIDA can analyze heterogeneous samples containing multiple species having different molecular brightness.

APPLICATIONS OF FLUORESCENCE CORRELATION SPECTROSCOPY IN BIOLOGY

Since its invention, FCS has been extensively demonstrated for various applications in chemistry and life science [4–6], as shown in **Figure 12**, of which a few representative applications are listed below.

Diffusion Coefficient

The first important application of FCS is to measure the diffusion coefficient of biomolecules, which is directly related to the molecular size in a certain surrounding medium. For instance, Priest *et al.* [109] used FCS to measure the size of an inert fluorescent tracer inside the nucleus of a living cell. Shang *et al.* [110] utilized FCS to measure the hydrodynamic radius increase of the nanoparticles (NPs) due to protein adsorption. Klapper *et al.* [111] used FCS to quantify the hydrodynamic radius increase of the lipid-coated quantum dots (QDs) when being adsorbed with blood plasma proteins. Negwer *et al.* [112] utilized NIR excitation and emission based NIR-FCS to directly monitor the size and the loading efficiency of drug nanocarriers in human blood. Fu *et al.* [113] implemented multi-photon FCS and detected the dynamics of nanoparticles occurring within the vasculature in the brain of a live mouse. Recently, Struntz *et al.* [91] utilized SPIM-FCS to derive the diffusion maps of peripheral membrane protein PLC1δ1 in the embryo's cytoplasm and on the plasma membrane, and the result shows the spatially varying diffusion coefficients of PLC1δ1 across the embryo. Moreover, FCS can be used to quantify shape-related

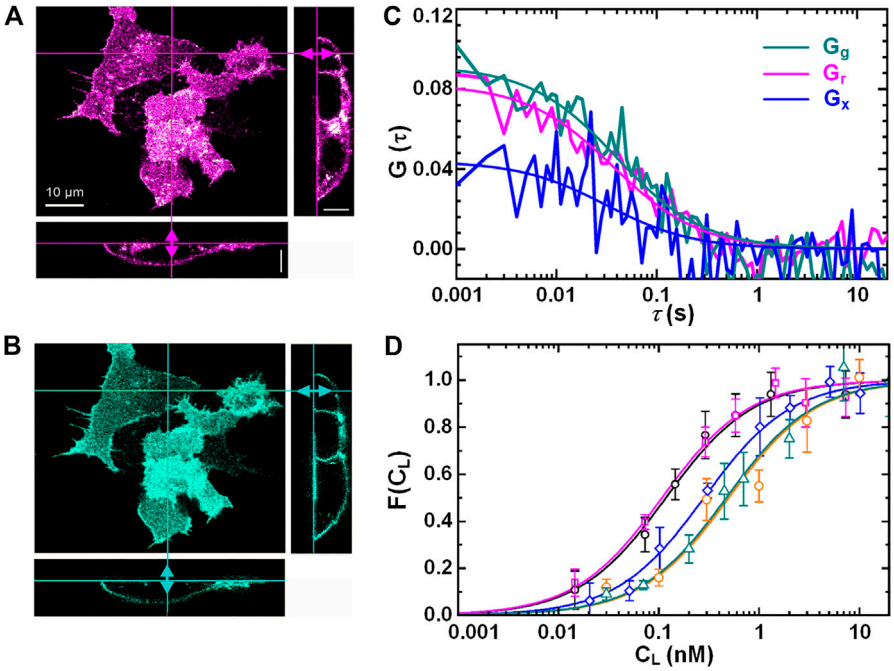

FIGURE 13 | Axial line-scanning FCS measurement on the interactions of ligand (DKK1-eGFP) and receptor (LRP6-mCherry) on cell membranes. Dual-color confocal images of live HEK293 T cells in the red channel (**A**) and the green channel (**B**). (**C**) The autocorrelation curves (G_g and G_r) and cross-correlation curve (G_x) on live NCI-H1703 cells. (**D**) Five binding curves (Fractional occupancies of the receptors) of five different cell-lines with different receptor densities. Adapted from Ref. [43].

diffusional dynamics. In this regard, Hinde *et al.* [60] used FCS to quantify the dynamics of four kinds of polymeric nanoparticles with identical surface chemistries but different shapes. The results turned out that these nanoparticles with different shapes behave differently in diffusional rates when moving across various cellular barriers. This finding is potentially useful for defining the site of drug release and optimizing the shape of drugs for effective release.

Rotational Diffusion

Except for the detection of translational diffusions, FCS can also detect rotational diffusion in the nanosecond to the microsecond time range. For the analysis, an exponential term is added to the FCS autocorrelation function considering the contribution of rotational diffusion [115–118]. Then, the rotational diffusion can be quantified from the fitting result. Jerker *et al.* [118] identified with this method the rotational diffusion of the GFP molecules in the nanosecond time range. Tsay *et al.* [117] studied the translational and rotational diffusion of peptide-coated semiconductor nanorods (pc-NRs) of various sizes and aspect ratios of the nanorods. The result from polarization-dependent FCS reveals that the pc-NRs with the square length of 12 nm have the translational diffusion constant of $40 \pm 10\ \mu m^2 s^{-1}$ and the rotational diffusion constant of $(1.5 \pm 0.5) \times 10^5\ s^{-1}$.

Biomolecular Concentration

FCS can also be used to accurately measure the biomolecular concentration *in vitro* or *in vivo* by analyzing the amplitude of the correlation curve with a known observation volume. In this pursue, FCS is often used to determine the concentration of dye solutions after being diluted from a stock solution. Ries *et al.* [42] used dual-color FCCS to determine the concentration of free ligand Fgf8, free receptors (Fgfr1 and Fgfr4), and the ligand-receptor complexes in the cell membrane of living zebrafish embryos.

Viscosity

Moreover, FCS is capable of quantifying the viscosity of a solution, which can be determined from the diffusion coefficient by using the Stokes-Einstein relation. For example, the viscosity of poly (acrylic acid) grafted onto poly (ethylene terephthalate) films was determined by FCS [119].

Binding of Biomolecules

In addition, dual-color FCCS can be used to monitor the binding or unbinding of two kinds of biomolecules labeled with spectrum-distinct fluorophores. For example, Wenger *et al.* [120] used dual-color FCCS to study the kinetics of enzymatic cleavage reaction at 2-μM DNA oligonucleotide concentration. Verneri *et al.* [121] used FCS to detect impairment of Oct4-chromatin interactions and measured the dynamics changes in transcription factors Oct4 and Sox2 after differentiation was induced. The results are valuable to the studies of embryo development. Chelladurai *et al.* [122] used STED-FCS to provide novel insight on the physics/mechanism nanoparticles show enhanced binding tendency on two-component lipid bilayers compared to single-component membranes. This study also revealed how the binding and the diffusion of nanoparticles are linked to sub-diffraction dynamics and structures. Zhang *et al.* [123] measured by using

FCS the degree of the association and dissociation of mRNAs in the different buffer, such as full human serum and human ascitic fluid. Eckert *et al.* [43] measured the binding of the ligand DKK1 and the receptor LRP6 on cell membranes by utilizing axial lsFCS. In this experiment, the receptor proteins LRP6 were tagged with fluorescent protein mCherry, and the ligand DKK1 with eGFP. **Figures 13A**, **3B** show 3D dual-color images of HEK293T cells with the receptor LRP6-mCherry and the ligand Dkk1 bound on the membrane. Dual-color axial lsFCS were performed at different ligand concentrations spanning from 0.05 to 100 nM. One group of correlation curves are shown in **Figure 13C**. Using the obtained FCS data, a binding curve can be calculated with **Eq. 4**, yielding K_D = 0.22 ± 0.02 nM for the transiently transfected NCI-H1703 cells expressing LRP6-mCherry. Then, the binding of DKK1-eGFP and LRP6-mCherry on cell membranes were measured for five different cell lines that have different receptor densities. The results in **Figure 13D** implies that the binding affinity has a strong dependency on the receptor density.

Intercellular Obstacles

FCS is also capable of probing the diffusion paths of different directions and mapping the intercellular obstacles. Malacrida *et al.* [61] applied 2D-pCF to measure EGFP diffusing in MB231 cells. From the connectivity maps (**Figures 14A**, **4C**), they found obstacles inside the nucleus (**Figures 14B**, **4D**). In 2019, Hidde *et al.* used 2D-pCF to map the environment in cellular synapses perceived by natural killer (NK) cell receptors [62].

Developing Trend in Fluorescence Correlation Spectroscopy Applications

To determine more comprehensive dynamic information, multiple analysis on biomolecular diffusion have been used recently. For instance, Rienzo *et al.* [124] combined 2D pCF with iMSD to generate a fluorescence-fluctuation-based diffusion tensor that contains information on the speed and directionality of the local dynamical processes. Thus, the results provided a fresh insight into the GFP diffusion in the cytoplasm of *E. coli* and the dynamics of a protein diffusing on the plasma membrane of eukaryotic cells. Besides, Scipioni *et al.* [125] combined spot-variation FCS, 2D pCF, and iMSD to provide a comprehensive analysis of free GFP diffusing in live cells at different subcellular compartments.

In recent years, Malengo *et al.* [126] used FCS and PCH to estimate the diffusion coefficient and oligomerization state of GPI-anchored proteins. They showed that the mobile fractions of the two proteins uPAR-G and D2D3-G have comparable diffusion coefficients despite they are constituted by monomers and dimers, respectively. James *et al.* [127] implemented PCH and FCS in a confocal system for single-molecule detection. They found that the detection of single α-synuclein amyloid fibrils with this method has improved sensitivity of more than 10^5-fold over bulk measurements. Scale *et al.* [128] proposed correlated PCH (cPCH), which reflects the probability to detect both a particular number of photons at the current time and another number at a later time. cPCH unifies FCS and PCH to resolve different fluorescent species using the information of their brightness and diffusion. They demonstrated that two species differing in both their diffusion and brightness can be better resolved with cPCH than with either FCS or PCH.

SUMMARY

Being a powerful tool for detecting molecular concentration, hydrodynamic radius, diffusional dynamics, and the interaction of different biomolecules, FCS has been widely applied to different fields. Except for the applications in biology, FCS also has been applied in other fields [129–131]. For instance, FCS has been applied in physics for the study of dynamics/structure of liquid crystal molecules on silicon wafers [131], as well as anomalous diffusion inside soft colloidal suspensions [130]. We believe that, with further developments of lasers and sensors, FCS will become a more and more powerful tool for the study of molecular dynamics in different fields.

FCS has the advantages of high spatial and temporal resolution, short analysis time, and high sensitivity. Recently, novel techniques have been developed as extensions of FCS. Dual-color FCCS was proposed to quantify molecular interactions without the limitation of molecular size but need to correct incomplete overlap of two-color detection volume. Multi-focus FCS can provide spatial information at several points but is limited in time resolution. pCF is performed by calculating the correlation between a pair of points and thus provides spatial

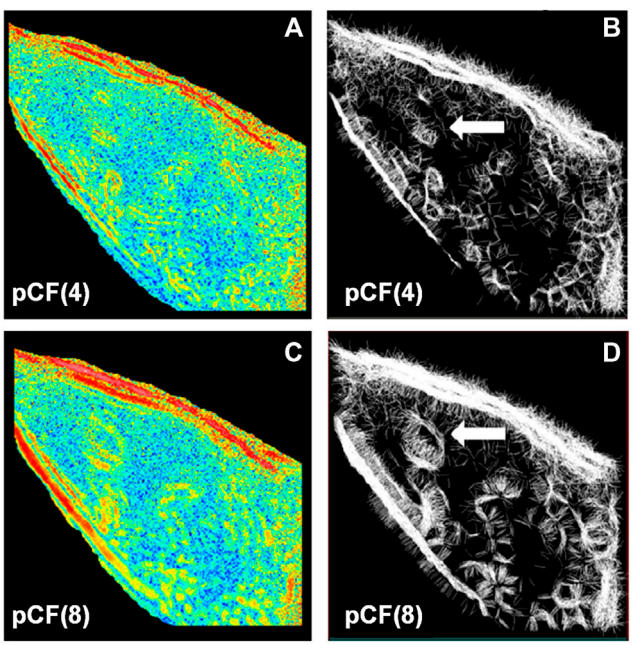

FIGURE 14 | .2D-pCF analysis of EGFP diffusing in MB231 cells. (**A**) and (**C**) The eccentricity of the diffusion calculated by using a pair of locations having a distance of 4 and 8 pixels. (**B**) and (**D**) The connectivity map is calculated by using a pair of locations having a distance of 4 and 8 pixels. The white arrows in (**B**) and (**D**) indicate an obstacle that forces the molecules to go around. Adapted from Ref. [61].

TABLE 1 | Overview of different FCS techniques.

Technique/Methods	Features/Capabilities	References
Traditional FCS	✓ time resolution of sub-μs, enabling fast mobilities to be detected (D up to 300 $\mu m^2 s^{-1}$) ✓ need pre-calibration of focus size ✓ measurable concentration range: 1 pM ~ 100 nM ✓ data collection time, typically 10 ~ 120 s ✓ lack of spatial information ✓ susceptible to photo-bleaching, background noise	[3, 132]
Dual-color FCCS	✓ target the interactions of different molecules ✓ more sensitive to the binding of two-color molecules due to the usage of cross-correlation ✓ susceptible to spectral crosstalk, focus overlap, photo-bleaching, background noise	[10, 114]
Imaging FCSMulti-focus/scale FCS	✓ capable of probing dynamics at different locations ✓ no need to characterize the focus size ✓ time resolution is limited by imaging sensor, typically tens of ms	[11, 45]
Pair correlation function (pCF)	✓ the correlation of any pairs of spots can be analyzed ✓ enables to detect a barrier along a certain path ✓ typical time resolution: 1 ms	[12, 60]
Scanning FCS	✓ reduced photobleaching ✓ limited time resolution, typically, 1 ms ✓ parallel scanning FCS is capable of obtaining location-dependent dynamics ✓ perpendicular scanning FCS compensates for membrane movements	[64, 68]
TIR-FCS	✓ axial resolution ≤100 nm ✓ only applicable to the molecules diffusing at surfaces ✓ capable of measuring samples of higher concentration ✓ diffusion is inevitably influenced by the bottom surface	[81]
SPIM-FCS	✓ enable to detect dynamics at any position in a volumetric sample ✓ less phototoxicity and photobleaching ✓ axial extension of the observation volume is reduced by a light sheet ✓ time resolution is limited by the imaging sensor	[15]
STED-FCS	✓ lateral resolution ~ tens of nm ✓ capable of detecting heterogeneous dynamics ✓ capable of measuring higher concentration samples ✓ susceptible to photobleaching	[75, 97]
Inverse FCS	✓ measure unlabeled particles in fluorescent surrounding medium ✓ requires high-concentration surrounding medium, ≥10 μM ✓ only applicable to relatively large particles to detection volume	[16, 104]
PCH/FIDA	✓ capable of acquiring the concentration and brightness of molecules ✓ capable of analyzing multiple particle species with different brightness ✓ incapable of determining diffusion coefficient	[17, 18]

information. Scanning FCS is suitable for measuring membrane-associated dynamics since it avoids photobleaching and the artifact induced by membrane movement. Of note, the recent axial line-scanning FCS has a significantly enhanced time resolution (~50 μs), targeting the dynamics on time-varying membranes. TIR-FCS measures molecular motion that occurs in the sample surface specifically. SPIM-FCS detects dynamic information from thousands of points simultaneously and avoids the noise from out-of-focus regions. STED-FCS reduces detection volume and allows measuring biomolecular dynamics in nanoscale or with a much higher concentration. Inverse-FCS measures unlabeled particles in a dense fluorescent medium, then provides particle size and concentration independent of the diffusional dynamic. While, this method is only applicable to relatively large particles (preferably with particle radius ≥ 40 nm). While, if being combined with STED, iFCS can detect particles with even smaller diameters. PCH and FIDA, being parallel techniques to FCS, can determine the molecular brightness and is capable of measuring heterogeneous samples with multiple species. The features and capabilities of different FCS technique have been summarized in **Table 1**.

It is worthy to point out that FCS also has some drawbacks. The results of FCS are easily handicapped by many factors in the experimental system or sample preparation. First, The observation volume changes with specific experimental settings, such as the cover-slide thickness variation and index mismatch [44]. Second, the focus volumes of two-color excitation pulses are different in dual-color FCCS, which may decrease the amplitude of cross-correlation. So we must correct it during data processing. Third, FCS is not suited for samples with a tendency to aggregate. When FCS is used to measure aggregating samples, the correlation curves become ill-shaped and poorly reproducible because a few very bright aggregates can distort the entire data set [133]. Therefore, a careful selection of an intensity trace is necessary in this case. Fourth, the photobleaching of fluorophores at high excitation powers is usually unavoidable during the measurements. The photobleaching reduces the fluorescence intensity over time and results in a reduction of the concentration and increase of the diffusion coefficient. So the compensation for the effect of photobleaching on both the intensity trace and the measured amplitude of the correlation curves is important [43]. Fifth, the measurable concentration range is limited to 1 pM ~ 100 nM with FCS. The lower limit is set to guarantee the fluorescence fluctuation is larger than the noise, and the upper limit is set to guarantee the fluctuation is sufficient (more molecules in focus will have a lower fluctuation). Sixth, FCS is, in essence, a statistical method, and the result obtained with FCS presents the average behavior of a large number of molecules. By contrast, single molecular tracking (SMT) enables to provide dynamics for specific molecules by taking image series, leading to insensitivity to single-molecule heterogeneity.

Being driven by the above-mentioned drawbacks of FCS and the existence of essentially complex problems in biology, there is still a need to further improve FCS in the future. First, the experimental setups of FCS can be further improved, *e.g.*, to further enhance the temporal and spatial resolution. Second, the optimization of FCS mathematical models is expected to fit better specific experimental settings. Third, the extension of dual-color FCCS to multi-color FCS is needed to support this scenario where the interactions among multiple species are involved in reality. Fourth, the combination of FCS with other technologies is still in need to fit a complex biological application, considering different methods feature different advantages and limitations.

AUTHOR CONTRIBUTIONS

PG conceived the manuscript. LY and YL wrote the draft of the manuscript; YM, ML, JZ, and DD organized the manuscript; all the authors edited the article.

ACKNOWLEDGMENTS

This work was supported by the National Natural Science Foundation of China (NSFC 62075177); the Natural Science Foundation of Shaanxi Province (2020JM-193, 2020JQ-324); China Postdoctoral Science Foundation (2017M610623); the National Natural Science Foundation of China (91750106), and the Research Fund of State Key Laboratory of Transient Optics and Photonics.

SUPPLEMENTARY MATERIAL

The **Supplementary Material** for this article can be found online at: https://www.frontiersin.org/articles/10.3389/fphy.2021.644450/full#supplementary-material.

REFERENCES

1. Elson EL 40 Years of FCS: how it all began. *Meth Enzymol* (2013) 518:1–10. doi:10.1016/B978-0-12-388422-0.00001-7
2. Elson EL, Magde D Fluorescence correlation spectroscopy. I. Conceptual basis and theory. *Biopolymers* (1974) 13:1–27. doi:10.1002/bip.1974.360130102
3. Elson EL Fluorescence correlation spectroscopy: past, present, future. *Biophys J* (2011) 101:2855–70. doi:10.1016/j.bpj.2011.11.012
4. Moro MM, Silvio DD, Moya SE Fluorescence correlation spectroscopy as a tool for the study of the intracellular dynamics and biological fate of protein corona. *Biophys Chem* (2019) 253:106218. doi:10.1016/j.bpc.2019.106218
5. Mutze J, Ohrt T, Schwille P,Fluorescence correlation spectroscopy: detecting and interpreting the mobility of transmembrane proteins in vivo. *Curr Protoc Toxicol*. Chapter 2 (2011) Laser Photonics Rev p. 52–67. doi:10.1002/lpor.20091004110.1002/0471140856.tx0219s48
6. Macháň R, Wohland T Recent applications of fluorescence correlation spectroscopy in live systems. *FEBS Lett* (2014) 588:3571–84. doi:10.1016/j.febslet.2014.03.056
7. Nienhaus GU, Maffre P, Nienhaus K Studying the protein corona on nanoparticles by FCS. *Meth Enzymol* (2013) 519:115–37. doi:10.1016/B978-0-12-405539-1.00004-X
8. Magde D, Elson E, Webb WW Thermodynamic fluctuations in a reacting system-measurement by fluorescence correlation spectroscopy. *Phys Rev Lett* (1972) 29:705–8. doi:10.1103/physrevlett.29.705

9. Rigler R, Mets U Diffusion of single molecules through a Gaussian laser beam. *Proc SPIE* (1993) 1921:239–48. doi:10.1117/12.146154
10. Bacia K, Schwille P Practical guidelines for dual-color fluorescence cross-correlation spectroscopy. *Nat Protoc* (2007) 2:2842–56. doi:10.1038/nprot.2007.410
11. Baum M, Erdel F, Wachsmuth M, Rippe K Retrieving the intracellular topology from multi-scale protein mobility mapping in living cells. *Nat Commun* (2014) 5:4494. doi:10.1038/ncomms5494
12. Digman MA, Gratton E Imaging barriers to diffusion by pair correlation functions. *Biophys J* (2009) 97:665–73. doi:10.1016/j.bpj.2009.04.048
13. Petersen NO Scanning fluorescence correlation spectroscopy. I. Theory and simulation of aggregation measurements. *Biophys J* (1986) 49:809–15. doi:10.1016/s0006-3495(86)83709-2
14. Kastrup L, Blom H, Eggeling C, Hell SW Fluorescence fluctuation spectroscopy in subdiffraction focal volumes. *Phys Rev Lett* (2005) 94:178104. doi:10.1103/PhysRevLett.94.178104
15. Wohland T, Shi X, Sankaran J, Stelzer EH Single plane illumination fluorescence correlation spectroscopy (SPIM-FCS) probes inhomogeneous three-dimensional environments. *Opt Express* (2010) 18:10627–41. doi:10.1364/OE.18.010627
16. Wennmalm S, Thyberg P, Xu L, Widengren J Inverse-fluorescence correlation spectroscopy. *Anal Chem* (2009) 81:9209–15. doi:10.1021/ac9010205
17. Chen Y, Müller JD, Berland KM, Gratton E Fluorescence fluctuation spectroscopy. *Methods* (1999) 19:234–52. doi:10.1016/s0006-3495(99)76912-210.1006/meth.1999.0854
18. Kask P, Palo K, Ullmann D, Gall K Fluorescence-intensity distribution analysis and its application in biomolecular detection technology. *Proc Natl Acad Sci USA* (1999) 96:13756–61. doi:10.1073/pnas.96.24.13756
19. Müller BK, Zaychikov E, Bräuchle C, Lamb DC Pulsed interleaved excitation. *Biophys J* (2005) 89:3508–22. doi:10.1529/biophysj.105.064766
20. Dong J, Bi R, Ho JH, Thong PS, Soo KC, Lee K Diffuse correlation spectroscopy with a fast Fourier transform-based software autocorrelator. *J Biomed Opt* (2012) 17:97004–1. doi:10.1117/1.jbo.17.9.097004
21. Martinez MM, Reif RD, Pappas D Early detection of apoptosis in living cells by fluorescence correlation spectroscopy. *Anal Bioanal Chem* (2010) 396:1177–85. doi:10.1007/s00216-009-3298-3
22. Li Y, Shivnaraine RV, Huang F, Wells JW, Gradinaru CC Ligand-induced coupling between oligomers of the M2 receptor and the Gi1 protein in live cells. *Biophysical J* (2018) 115:881–95. doi:10.1016/j.bpj.2018.08.001
23. Zou L, Gao N, Xiao Q Research of photon correlation technology. *IOP Conf Ser Mater Sci Eng* (2020) 711:012097. doi:10.1088/1757-899x/711/1/012097
24. Tian Y, Martinez MM, Pappas D Fluorescence correlation spectroscopy: a review of biochemical and microfluidic applications. *Appl Spectrosc* (2011) 65:115A. doi:10.1366/10-06224
25. Günther J-P, Börsch M, Fischer P Diffusion measurements of swimming enzymes with fluorescence correlation spectroscopy. *Acc Chem Res* (2018) 51:1911–20. doi:10.1021/acs.accounts.8b00276
26. Chojnacki J, Waithe D, Carravilla P, Huarte N, Galiani S, Enderlein J, et al. Envelope glycoprotein mobility on HIV-1 particles depends on the virus maturation state. *Nat Commun* (2017) 8:545. doi:10.1038/s41467-017-00515-6
27. Wissner RF, Steinauer A, Knox SL, Thompson AD, Schepartz A Fluorescence correlation spectroscopy reveals efficient cytosolic delivery of protein cargo by cell-permeant miniature proteins. *ACS Cent Sci* (2018) 4:1379–93. doi:10.1021/acscentsci.8b00446
28. Tiwari M, Mikuni S, Muto H, Kinjo M Determination of dissociation constant of the NFκB p50/p65 heterodimer using fluorescence cross-correlation spectroscopy in the living cell. *Biochem Biophys Res Commun* (2013) 436:430–5. doi:10.1016/j.bbrc.2013.05.121
29. Su D, Hou Y, Dong C, Ren J Fluctuation correlation spectroscopy and its applications in homogeneous analysis. *Anal Bioanal Chem* (2019) 411:4523–40. doi:10.1007/s00216-019-01884-1
30. Eigen M, Rigler R Sorting single molecules: application to diagnostics and evolutionary biotechnology. *Proc Natl Acad Sci USA* (1994) 91:5740–7. doi:10.1073/pnas.91.13.5740
31. Schwille P, Meyer-Almes FJ, Rigler R Dual-color fluorescence cross-correlation spectroscopy for multicomponent diffusional analysis in solution. *Biophys J* (1997) 72:1878–86. doi:10.1016/s0006-3495(97)78833-7
32. Dorlich RM, Chen Q, Hedde PN, Schuster V, Hippler M, Wesslowski J, et al. Dual-color dual-focus line-scanning FCS for quantitative analysis of receptor-ligand interactions in living specimens. *Sci Rep* (2015) 5:10149. doi:10.1038/srep10149
33. Ruan Q, Tetin SY Applications of dual-color fluorescence cross-correlation spectroscopy in antibody binding studies. *Anal Biochem* (2008) 374:182–95. doi:10.1016/j.ab.2007.11.007
34. Kaliszewski MJ, Shi X, Hou Y, Lingerak R, Kim S, Mallory P, et al. Quantifying membrane protein oligomerization with fluorescence cross-correlation spectroscopy. *Methods* (2018) 140-141:40–51. doi:10.1016/j.ymeth.2018.02.002
35. Bleicken S, Hantusch A, Das KK, Frickey T, Garcia-Saez AJ Quantitative interactome of a membrane Bcl-2 network identifies a hierarchy of complexes for apoptosis regulation. *Nat Commun* (2017) 8:73. doi:10.1038/s41467-017-00086-6
36. Tiwari M, Oasa S, Yamamoto J, Mikuni S, Kinjo M A quantitative study of internal and external interactions of homodimeric glucocorticoid receptor using fluorescence cross-correlation spectroscopy in a live cell. *Sci Rep* (2017) 7:4336. doi:10.1038/s41598-017-04499-7
37. Padilla-Parra S, Audugé N, Coppey-Moisan M, Tramier M Quantitative study of protein-protein interactions in live cell by dual-color fluorescence correlation spectroscopy. *Methods Mol Biol* (2014) 1076:683–98. doi:10.1007/978-1-62703-649-8_31
38. Bacia K, Petrášek Z, Schwille P Correcting for spectral cross-talk in dual-color fluorescence cross-correlation spectroscopy. *Chemphyschem* (2012) 13:1221–31. doi:10.1002/cphc.201100801
39. Padilla-Parra S, Audugé N, Coppey-Moisan M, Tramier M Dual-color fluorescence lifetime correlation spectroscopy to quantify protein-protein interactions in live cell. *Microsc Res Tech* (2011) 74:788–93. doi:10.1002/jemt.21015
40. Schwille P, Haupts U, Maiti S, Webb WW Molecular dynamics in living cells observed by fluorescence correlation spectroscopy with one- and two-photon excitation. *Biophys J* (1999) 77:2251–65. doi:10.1016/s0006-3495(99)77065-7
41. Berland KM, So PT, Gratton E Two-photon fluorescence correlation spectroscopy: method and application to the intracellular environment. *Biophys J* (1995) 68:694–701. doi:10.1016/s0006-3495(95)80230-4
42. Ries J, Yu SR, Burkhardt M, Brand M, Schwille P Modular scanning FCS quantifies receptor-ligand interactions in living multicellular organisms. *Nat Methods* (2009) 6:643–5. doi:10.1038/nmeth.1355
43. Eckert AF, Gao P, Wesslowski J, Wang X, Rath J, Nienhaus K, et al. Measuring ligand-cell surface receptor affinities with axial line-scanning fluorescence correlation spectroscopy. *eLife* (2020) 9:e55286. doi:10.7554/eLife.55286
44. Dertinger T, Loman A, Ewers B, Müller CB, Krämer B, Enderlein J The optics and performance of dual-focus fluorescence correlation spectroscopy. *Opt Express* (2008) 16:14353–68. doi:10.1364/oe.16.014353
45. Pieper C, Weiß K, Gregor I, Enderlein J Dual-focus fluorescence correlation spectroscopy. *Meth Enzymol* (2013) 518:175–204. doi:10.1016/B978-0-12-388422-0.00008-X
46. Dertinger T, Pacheco V, von der Hocht I, Hartmann R, Gregor I, Enderlein J Two-focus fluorescence correlation spectroscopy: a new tool for accurate and absolute diffusion measurements. *Chemphyschem* (2007) 8:433–43. doi:10.1002/cphc.200600638
47. Loman A, Dertinger T, Koberling F, Enderlein J Comparison of optical saturation effects in conventional and dual-focus fluorescence correlation spectroscopy. *Chem Phys Lett* (2008) 459:18–21. doi:10.1016/j.cplett.2008.05.018
48. Weiß K, Neef A, Van Q, Kramer S, Gregor I, Enderlein J Quantifying the diffusion of membrane proteins and peptides in black lipid membranes with 2-focus fluorescence correlation spectroscopy. *Biophys J* (2013) 105:455–62. doi:10.1016/j.bpj.2013.06.004
49. Krieger JW, Singh AP, Bag N, Garbe CS, Saunders TE, Langowski J, et al. Imaging fluorescence (cross-) correlation spectroscopy in live cells and organisms. *Nat Protoc* (2015) 10:1948–74. doi:10.1038/nprot.2015.100
50. Otosu T, Ishii K, Tahara T Multifocus fluorescence correlation spectroscopy with spatially separated excitation beams. *Bcsj* (2019) 92:1495–502. doi:10.1246/bcsj.20190109
51. Needleman DJ, Xu Y, Mitchison TJ Pin-hole array correlation imaging: highly parallel fluorescence correlation spectroscopy. *Biophys J* (2009) 96:5050–9. doi:10.1016/j.bpj.2009.03.023

52. Capoulade J, Wachsmuth M, Hufnagel L, Knop M Quantitative fluorescence imaging of protein diffusion and interaction in living cells. *Nat Biotechnol* (2011) 29:835–9. doi:10.1038/nbt.1928
53. Hebert B, Costantino S, Wiseman PW Spatiotemporal image correlation spectroscopy (STICS) theory, verification, and application to protein velocity mapping in living CHO cells. *Biophys J* (2005) 88:3601–14. doi:10.1529/biophysj.104.054874
54. Di Rienzo C, Gratton E, Beltram F, Cardarelli F Fast spatiotemporal correlation spectroscopy to determine protein lateral diffusion laws in live cell membranes. *Proc Natl Acad Sci USA* (2013) 110:12307. doi:10.1073/pnas.1222097110
55. Kolin DL, Ronis D, Wiseman PW K-space image correlation spectroscopy: a method for accurate transport measurements independent of fluorophore photophysics. *Biophys J* (2006) 91:3061–75. doi:10.1529/biophysj.106.082768
56. Maffre P, Nienhaus K, Amin F, Parak WJ, Nienhaus GU Characterization of protein adsorption onto FePt nanoparticles using dual-focus fluorescence correlation spectroscopy. *Beilstein J Nanotechnol* (2011) 2:374–83. doi:10.3762/bjnano.2.43
57. Rossow MJ, Sasaki JM, Digman MA, Gratton E Raster image correlation spectroscopy in live cells. *Nat Protoc* (2010) 5:1761–74. doi:10.1038/nprot.2010.122
58. Digman MA, Gratton E Lessons in fluctuation correlation spectroscopy. *Annu Rev Phys Chem* (2011) 62:645–68. doi:10.1146/annurev-physchem-032210-103424
59. Bianchini P, Cardarelli F, Di Luca M, Diaspro A, Bizzarri R Nanoscale protein diffusion by STED-based pair correlation analysis. *PLoS One* (2014) 9:e99619. doi:10.1371/journal.pone.0099619
60. Hinde E, Thammasiraphop K, Duong HT, Yeow J, Karagoz B, Boyer C, et al. Pair correlation microscopy reveals the role of nanoparticle shape in intracellular transport and site of drug release. *Nat Nanotechnol* (2017) 12:81–9. doi:10.1038/nnano.2016.160
61. Malacrida L, Hedde PN, Ranjit S, Cardarelli F, Gratton E Visualization of barriers and obstacles to molecular diffusion in live cells by spatial pair-cross-correlation in two dimensions. *Biomed Opt Express* (2018) 9:303–21. doi:10.1364/boe.9.000303
62. Hedde PN, Staaf E, Singh SB, Johansson S, Gratton E Pair correlation analysis maps the dynamic two-dimensional organization of natural killer cell receptors at the synapse. *ACS Nano* (2019) 13:14274–82. doi:10.1021/acsnano.9b07486
63. Hinde E, Pandžić E, Yang Z, Ng IH, Jans DA, Bogoyevitch MA, et al. Quantifying the dynamics of the oligomeric transcription factor STAT3 by pair correlation of molecular brightness. *Nat Commun* (2016) 7:11047. doi:10.1038/ncomms11047
64. Petrásek Z, Ries J, Schwille P Scanning FCS for the characterization of protein dynamics in live cells. *Meth Enzymol* (2010) 472:317–43. doi:10.1016/S0076-6879(10)72005-X
65. Petrášek Z, Schwille P Scanning fluorescence correlation spectroscopy. In: R Rigler H Vogel, editors. *Single molecules and nanotechnology*. Berlin, Heidelberg: Springer Berlin Heidelberg (2008). p. 83–105.
66. Ries J, Chiantia S, Schwille P Accurate determination of membrane dynamics with line-scan FCS. *Biophys J* (2009) 96:1999–2008. doi:10.1016/j.bpj.2008.12.3888
67. Petrášek Z, Derenko S, Schwille P Circular scanning fluorescence correlation spectroscopy on membranes. *Opt Express* (2011) 19:25006–21. doi:10.1364/oe.19.025006
68. Ruan Q, Cheng MA, Levi M, Gratton E, Mantulin WW Spatial-temporal studies of membrane dynamics: scanning fluorescence correlation spectroscopy (SFCS). *Biophys J* (2004) 87:1260–7. doi:10.1529/biophysj.103.036483
69. Maraspini R, Beutel O, Honigmann A Circle scanning STED fluorescence correlation spectroscopy to quantify membrane dynamics and compartmentalization. *Methods* (2018) 140-141:188–97. doi:10.1016/j.ymeth.2017.12.005
70. Gunther G, Jameson DM, Aguilar J, Sánchez SA Scanning fluorescence correlation spectroscopy comes full circle. *Methods* (2018) 140-141:52–61. doi:10.1016/j.ymeth.2018.01.023
71. Ries J, Schwille P New concepts for fluorescence correlation spectroscopy on membranes. *Phys Chem Chem Phys* (2008) 10:3487–97. doi:10.1039/b718132a
72. Humpolíčková J, Gielen E, Benda A, et al. Probing diffusion laws within cellular membranes by Z-scan fluorescence correlation spectroscopy. *Biophys J* (2006) 91:L23–L5. doi:10.1529/biophysj.106.089474
73. Hink MA, Postma M Monitoring receptor oligomerization by line-scan fluorescence cross-correlation spectroscopy. *Methods Cel Biol* (2013) 117:197–212. doi:10.1016/b978-0-12-408143-7.00011-6
74. Eggeling C STED-FCS nanoscopy of membrane dynamics. In: Y Mély G Duportail, editors. *Fluorescent methods to study biological membranes*. Berlin, Heidelberg: Springer Berlin Heidelberg (2013). p. 291–309.
75. Sezgin E, Schneider F, Galiani S, Urbančič I, Waithe D, Lagerholm BC, et al. Measuring nanoscale diffusion dynamics in cellular membranes with super-resolution STED-FCS. *Nat Protoc* (2019) 14:1054–83. doi:10.1038/s41596-019-0127-9
76. Hell SW Microscopy and its focal switch. *Nat Methods* (2009) 6:24–32. doi:10.1038/nmeth.1291
77. Blom H, Kastrup L, Eggeling C Fluorescence fluctuation spectroscopy in reduced detection volumes. *Curr Pharm Biotechnol* (2006) 7:51–66. doi:10.2174/138920106775789629
78. Thompson NL, Burghardt TP, Axelrod D Measuring surface dynamics of biomolecules by total internal reflection fluorescence with photobleaching recovery or correlation spectroscopy. *Biophys J* (1981) 33:435–54. doi:10.1016/s0006-3495(81)84905-3
79. Grigoriev I, Akhmanova A Microtubule dynamics at the cell cortex probed by TIRF microscopy. In: L Cassimeris P Tran, editors. *Method cell biol*, 97. Academic Press (2010). p. 91–109. doi:10.1016/S0091-679X(10)97006-4
80. Axelrod D Total internal reflection fluorescence microscopy in cell biology. *Traffic* (2001) 2:764–74. doi:10.1034/j.1600-0854.2001.21104.x
81. Thompson NL, Steele BL Total internal reflection with fluorescence correlation spectroscopy. *Nat Protoc* (2007) 2:878–90. doi:10.1038/nprot.2007.110
82. Hassler K, Leutenegger M, Rigler P, Rao R, Rigler R, Gösch M, et al. Total internal reflection fluorescence correlation spectroscopy (TIR-FCS) with low background and high count-rate per molecule. *Opt Express* (2005) 13:7415–23. doi:10.1364/OPEX.13.007415
83. Ries J, Petrov EP, Schwille P Total internal reflection fluorescence correlation spectroscopy: effects of lateral diffusion and surface-generated fluorescence. *Biophys J* (2008) 95:390–9. doi:10.1529/biophysj.107.126193
84. Starr TE, Thompson NL Total internal reflection with fluorescence correlation spectroscopy: combined surface reaction and solution diffusion. *Biophys J* (2001) 80:1575–84. doi:10.1016/s0006-3495(01)76130-9
85. Lieto AM, Thompson NL Total internal reflection with fluorescence correlation spectroscopy: nonfluorescent competitors. *Biophys J* (2004) 87:1268–78. doi:10.1529/biophysj.103.035030
86. Thompson NL, Wang X, Navaratnarajah P Total internal reflection with fluorescence correlation spectroscopy: applications to substrate-supported planar membranes. *J Struct Biol* (2009) 168:95–106. doi:10.1016/j.jsb.2009.02.013
87. Foquet M, Korlach J, Zipfel W, Webb WW, Craighead HG DNA fragment sizing by single molecule detection in submicrometer-sized closed fluidic channels. *Anal Chem* (2002) 74:1415–22. doi:10.1021/ac011076w
88. Langowski J Single plane illumination microscopy as a tool for studying nucleome dynamics. *Methods* (2017) 123:3–10. doi:10.1016/j.ymeth.2017.06.021
89. Ng XW, Teh C, Korzh V, Wohland T The secreted signaling protein Wnt3 is associated with membrane domains in vivo: a SPIM-FCS study. *Biophys J* (2016) 111:418–29. doi:10.1016/j.bpj.2016.06.021
90. Singh AP, Krieger JW, Buchholz J, Charbon E, Langowski J, Wohland T The performance of 2D array detectors for light sheet based fluorescence correlation spectroscopy. *Opt Express* (2013) 21:8652–68. doi:10.1364/oe.21.008652
91. Struntz P, Weiss M Multiplexed measurement of protein diffusion inCaenorhabditis elegansembryos with SPIM-FCS. *J Phys D: Appl Phys* (2015) 49:044002. doi:10.1088/0022-3727/49/4/044002
92. Krieger JW, Singh AP, Garbe CS, Wohland T, Langowski J Dual-color fluorescence cross-correlation spectroscopy on a single plane illumination microscope (SPIM-FCCS). *Opt Express* (2014) 22:2358–75. doi:10.1364/OE.22.002358
93. Pernuš A, Langowski J Imaging fos-jun transcription factor mobility and interaction in live cells by single plane illumination-fluorescence cross

correlation spectroscopy. *PLoS One* (2015) 10:e0123070. doi:10.1371/journal.pone.0123070
94. Hell SW, Wichmann J Breaking the diffraction resolution limit by stimulated emission: stimulated-emission-depletion fluorescence microscopy. *Opt Lett* (1994) 19:780–2. doi:10.1364/ol.19.000780
95. Gao P, Prunsche B, Zhou L, Nienhaus K, Nienhaus GU Background suppression in fluorescence nanoscopy with stimulated emission double depletion. *Nat Photon* (2017) 11:163–9. doi:10.1038/nphoton.2016.279
96. Vicidomini G, Schönle A, Ta H, Han KY, Moneron G, Eggeling C, et al. STED nanoscopy with time-gated detection: theoretical and experimental aspects. *PLoS One* (2013) 8:e54421. doi:10.1371/journal.pone.0054421
97. Lanzanò L, Scipioni L, Di Bona M, Bianchini P, Bizzarri R, Cardarelli F, et al. Measurement of nanoscale three-dimensional diffusion in the interior of living cells by STED-FCS. *Nat Commun* (2017) 8:65. doi:10.1038/s41467-017-00117-2
98. Eggeling C, Ringemann C, Medda R, Schwarzmann G, Sandhoff K, Polyakova S, et al. Direct observation of the nanoscale dynamics of membrane lipids in a living cell. *Nature* (2009) 457:1159–62. doi:10.1038/nature07596
99. Andrade DM, Clausen MP, Keller J, Mueller V, Wu C, Bear JE, et al. Cortical actin networks induce spatio-temporal confinement of phospholipids in the plasma membrane--a minimally invasive investigation by STED-FCS. *Sci Rep* (2015) 5:11454. doi:10.1038/srep11454
100. Hedde PN, Dörlich RM, Blomley R, Gradl D, Oppong E, Cato AC, et al. Stimulated emission depletion-based raster image correlation spectroscopy reveals biomolecular dynamics in live cells. *Nat Commun* (2013) 4:2093. doi:10.1038/ncomms3093
101. Jiang Y, Pryse KM, Melnykov A, Genin GM, Elson EL Investigation of nanoscopic phase separations in lipid membranes using inverse FCS. *Biophys J* (2017) 112:2367–76. doi:10.1016/j.bpj.2017.04.013
102. Wennmalm S, Widengren J Inverse-fluorescence cross-correlation spectroscopy. *Anal Chem* (2010) 82:5646–51. doi:10.1021/ac1006409
103. Bergstrand J, Rönnlund D, Widengren J, Wennmalm S Scanning inverse fluorescence correlation spectroscopy. *Opt Express* (2014) 22:13073–90. doi:10.1364/OE.22.013073
104. Wennmalm S Potentials and pitfalls of inverse fluorescence correlation spectroscopy. *Methods* (2018) 140-141:23–31. doi:10.1016/j.ymeth.2018.01.005
105. Sandén T, Wyss R, Santschi C, Hassaïne G, Deluz C, Martin OJ, et al. A zeptoliter volume meter for analysis of single protein molecules. *Nano Lett* (2012) 12:370–5. doi:10.1021/nl2036468
106. Herrick-Davis K, Mazurkiewicz JE Fluorescence correlation spectroscopy and photon-counting histogram analysis of receptor-receptor interactions. In: PM Conn, editor. *Method cell biol*, 117. Academic Press (2013). p. 181–96. doi:10.1016/B978-0-12-408143-7.00010-4
107. Müller JD, Chen Y, Gratton E Resolving heterogeneity on the single molecular level with the photon-counting histogram. *Biophys J* (2000) 78:474–86. doi:10.1016/S0006-3495(00)76610-0
108. Meng F, Ma H A comparison between photon counting histogram and fluorescence intensity distribution analysis. *J Phys Chem B* (2006) 110:25716–20. doi:10.1021/jp063845r
109. Priest DG, Solano A, Lou J, Hinde E Fluorescence fluctuation spectroscopy: an invaluable microscopy tool for uncovering the biophysical rules for navigating the nuclear landscape. *Biochem Soc T* (2019) 47:1117–29. doi:10.1042/BST20180604
110. Shang L, Nienhaus GU *In Situ* characterization of protein adsorption onto nanoparticles by fluorescence correlation spectroscopy. *Acc Chem Res* (2017) 50:387–95. doi:10.1021/acs.accounts.6b00579
111. Klapper Y, Maffre P, Shang L, Ekdahl KN, Nilsson B, Hettler S, et al. Low affinity binding of plasma proteins to lipid-coated quantum dots as observed by *in situ* fluorescence correlation spectroscopy. *Nanoscale* (2015) 7:9980–4. doi:10.1039/c5nr01694k
112. Negwer I, Best A, Schinnerer M, Schäfer O, Capeloa L, Wagner M, et al. Monitoring drug nanocarriers in human blood by near-infrared fluorescence correlation spectroscopy. *Nat Commun* (2018) 9:5306. doi:10.1038/s41467-018-07755-0
113. Fu X, Sompol P, Brandon JA, Norris CM, Wilkop T, Johnson LA, et al. *In vivo* single-molecule detection of nanoparticles for multiphoton fluorescence correlation spectroscopy to quantify cerebral blood flow. *Nano Lett* (2020) 20:6135–41. doi:10.1021/acs.nanolett.0c02280
114. Bacia K, Kim SA, Schwille P Fluorescence cross-correlation spectroscopy in living cells. *Nat Methods* (2006) 3:83–9. doi:10.1038/nmeth822
115. Yamamoto J, Oura M, Yamashita T, Miki S, Jin T, Haraguchi T, et al. Rotational diffusion measurements using polarization-dependent fluorescence correlation spectroscopy based on superconducting nanowire single-photon detector. *Opt Express* (2015) 23:32633–42. doi:10.1364/OE.23.032633
116. Pieper CM, Enderlein J Fluorescence correlation spectroscopy as a tool for measuring the rotational diffusion of macromolecules. *Chem Phys Lett* (2011) 516:1–11. doi:10.1016/j.cplett.2011.06.091
117. Tsay JM, Doose S, Weiss S Rotational and translational diffusion of peptide-coated CdSe/CdS/ZnS nanorods studied by fluorescence correlation spectroscopy. *J Am Chem Soc* (2006) 128:1639–47. doi:10.1021/ja056162i
118. Widengren J, Mets Ü, Rigler R Photodynamic properties of green fluorescent proteins investigated by fluorescence correlation spectroscopy. *Chem Phys* (1999) 250:171–86. doi:10.1016/s0301-0104(99)00255-4
119. Pan X, Aw C, Du Y, Yu H, Wohland T Characterization of poly(acrylic acid) diffusion dynamics on the grafted surface of poly(ethylene terephthalate) films by fluorescence correlation spectroscopy. *Biophys Rev Lett* (2006) 01:433–41. doi:10.1142/S1793048006000264
120. Wenger J, Gérard D, Lenne PF, Rigneault H, Dintinger J, Ebbesen TW, et al. Dual-color fluorescence cross-correlation spectroscopy in a single nanoaperture : towards rapid multicomponent screening at high concentrations. *Opt Express* (2006) 14:12206–16. doi:10.1364/OE.14.012206
121. Paula V, Camila VE, Camila O, Stortz M, Alejandra G, Levi V Dynamical reorganization of the pluripotency transcription factors Oct4 and Sox2 during early differentiation of embryonic stem cells. *Sci Rep* (2020) 10:5195. doi:10.1038/s41598-020-62235-0
122. Chelladurai R, Debnath K, Jana NR, Basu JK Nanoscale heterogeneities drive enhanced binding and anomalous diffusion of nanoparticles in model biomembranes. *Langmuir* (2018) 34:1691–9. doi:10.1021/acs.langmuir.7b04003
123. Zhang H, De Smedt SC, Remaut K Fluorescence Correlation Spectroscopy to find the critical balance between extracellular association and intracellular dissociation of mRNA complexes. *Acta Biomater* (2018) 75:358–70. doi:10.1016/j.actbio.2018.05.016
124. Di Rienzo C, Cardarelli F, Di Luca M, Beltram F, Gratton E Diffusion tensor analysis by two-dimensional pair correlation of fluorescence fluctuations in cells. *Biophys J* (2016) 111:841–51. doi:10.1016/j.bpj.2016.07.005
125. Scipioni L, Lanzanó L, Diaspro A, Gratton E Comprehensive correlation analysis for super-resolution dynamic fingerprinting of cellular compartments using the Zeiss Airyscan detector. *Nat Commun* (2018) 9:5120. doi:10.1038/s41467-018-07513-2
126. Malengo G, Andolfo A, Sidenius N, Gratton E, Zamai M, Caiolfa VR Fluorescence correlation spectroscopy and photon counting histogram on membrane proteins: functional dynamics of the glycosylphosphatidylinositol-anchored urokinase plasminogen activator receptor. *J Biomed Opt* (2008) 13:031215. doi:10.1117/1.2940570
127. Brown JWP, Bauer A, Polinkovsky ME, Bhumkar A, Hunter DJB, Gaus K, et al. Single-molecule detection on a portable 3D-printed microscope. *Nat Commun* (2019) 10:5662. doi:10.1038/s41467-019-13617-0
128. Scales N, Swain PS Resolving fluorescent species by their brightness and diffusion using correlated photon-counting histograms. *PLoS One* (2020) 14:e0226063. doi:10.1371/journal.pone.0226063
129. Gupta A, Sankaran J, Wohland T Fluorescence correlation spectroscopy: the technique and its applications in soft matter. *Phys Sci Rev*, 4 (2019) 4. doi:10.1515/psr-2017-0104
130. Li H, Zheng K, Yang J, Zhao J Anomalous diffusion inside soft colloidal suspensions investigated by variable length scale fluorescence correlation spectroscopy. *ACS Omega* (2020) 5:11123–30. doi:10.1021/acsomega.0c01052
131. T¨auber D, Radscheit K, von Borczyskowski C, Schulz M Fluorescence correlation spectroscopy in thin films at reflecting substrates as a means to study nanoscale structure and dynamics at soft-matter interfaces. *Phys Rev E* (2016) 94:012804. doi:10.1103/PhysRevE.94.012804

132. Schwille P, Ries J Principles and applications of fluorescence correlation spectroscopy (FCS). In: B Bartolo J Collins, editors. *Biophotonics: spectroscopy, imaging, sensing, and manipulation*. Dordrecht: Springer (2011). p. 63–85.
133. Wang H, Lin Y, Nienhaus K, Nienhaus GU The protein corona on nanoparticles as viewed from a nanoparticle-sizing perspective. *WIREs Nanomed Nanobiotechnol* (2018) 10:e1500. doi:10.1002/wnan.1500
134. Becker W, Hickl H, Zander C, Drexhage KH, Sauer M, Siebert S, et al. Time-resolved detection and identification of single analyte molecules in microcapillaries by time-correlated single-photon counting (TCSPC). *Rev Scientific Instr* (1999) 70:1835–41. doi:10.1063/1.1149677
135. Hendrix J, Lamb DC Pulsed interleaved excitation: principles and applications. *Meth Enzymol* (2013) 518:205–43. doi:10.1016/b978-0-12-388422-0.00009-1
136. Christie S, Shi X, Smith AW Resolving membrane protein-protein interactions in live cells with pulsed interleaved excitation fluorescence cross-correlation spectroscopy. *Acc Chem Res* (2020) 53:792–9. doi:10.1021/acs.accounts.9b00625
137. Jastrzebska B, Comar WD, Kaliszewski MJ, Skinner KC, Torcasio MH, Esway AS, et al. A G protein-coupled receptor dimerization interface in human cone opsins. *Biochemistry* (2017) 56:61–72. doi:10.1021/acs.biochem.6b00877
138. Gao X, Gao P, Prunsche B, Nienhaus K, Nienhaus GU Pulsed interleaved excitation-based line-scanning spatial correlation spectroscopy (PIE-lsSCS). *Sci Rep* (2018) 8:16722. doi:10.1038/s41598-018-35146-4
139. Axelrod D, Koppel DE, Schlessinger J, Elson E, Webb WW Mobility measurement by analysis of fluorescence photobleaching recovery kinetics. *Biophys J* (1976) 16:1055–69. doi:10.1016/S0006-3495(76)85755-4
140. Selvin P Fluorescence resonance energy transfer. *Meth Enzymol* (1995) 246:300–34. doi:10.1016/0076-6879(95)46015-2
141. Qian H, Sheetz MP, Elson EL Single particle tracking. Analysis of diffusion and flow in two-dimensional systems. *Biophys J* (1991) 60:910–21. doi:10.1016/S0006-3495(91)82125-7
142. Lippincott-Schwartz J, Altan-Bonnet N, Patterson GH Photobleaching and photoactivation: following protein dynamics in living cells. *Nat Cel Biol* (2003) Suppl:S7–14. doi:10.1038/ncb1032
143. Jonkman J, Brown CM, Wright GD, Anderson KI, North AJ Tutorial: guidance for quantitative confocal microscopy. *Nat Protoc* (2020) 15:1585–611. doi:10.1038/s41596-020-0313-9
144. Ritchie K, Shan XY, Kondo J, Iwasawa K, Fujiwara T, Kusumi A Detection of non-Brownian diffusion in the cell membrane in single molecule tracking. *Biophys J* (2005) 88:2266–77. doi:10.1529/biophysj.104.054106
145. Müller CB, Loman A, Pacheco V, Koberling F, Willbold D, Richtering W, et al. Precise measurement of diffusion by multi-color dual-focus fluorescence correlation spectroscopy. *Europhys Lett* (2008) 83:46001. doi:10.1209/0295-5075/83/46001
146. Loman A, Müller CB, Koberling F, Richtering W, Enderlein J Absolute and percise measurements of the diffusion of small fluorescent dye molecules across the visible spectrum. *14th Int Workshop Single Molecule Spectrosc Ultrasensitive Anal Life Sci* (2008) 83:1.
147. Peter K, GmbH P *Absolute diffusion coefficients: compilation of reference data for FCS calibration* (2010) Available from: https://www.picoquant.com/scientific/technical-and-application-notes/category/technical_notes_techniques_and_methods/details/absolute-diffusion-coefficients-compilation-reference-fcs-data.
148. Petrásek Z, Schwille P Precise measurement of diffusion coefficients using scanning fluorescence correlation spectroscopy. *Biophys J* (2008) 94:1437–48. doi:10.1529/biophysj.107.108811
149. Gendron PO, Avaltroni F, Wilkinson KJ Diffusion coefficients of several rhodamine derivatives as determined by pulsed field gradient-nuclear magnetic resonance and fluorescence correlation spectroscopy. *J Fluoresc* (2008) 18:1093–101. doi:10.1007/s10895-008-0357-7
150. Culbertson CT, Jacobson SC, Michael Ramsey J Diffusion coefficient measurements in microfluidic devices. *Talanta* (2002) 56:365–73. doi:10.1016/S0039-9140(01)00602-6
151. Müller CB, Weiß K, Richtering W, Loman A, Enderlein J Calibrating differential interference contrast microscopy with dual-focus fluorescence correlation spectroscopy. *Opt Express* (2008) 16:4322–9. doi:10.1364/OE.16.004322
152. Kahya N, Scherfeld D, Bacia K, Poolman B, Schwille P Probing lipid mobility of raft-exhibiting model membranes by fluorescence correlation spectroscopy. *J Biol Chem* (2003) 278:28109–15. doi:10.1074/jbc.M302969200
153. Meacci G, Ries J, Fischer-Friedrich E, Kahya N, Schwille P, Kruse K Mobility of Min-proteins in Escherichia coli measured by fluorescence correlation spectroscopy. *Phys Biol* (2010) 3:255–63. doi:10.1088/1478-3975/3/4/003
154. Braet C, Stephan H, Dobbie IM, Togashi DM, Ryder AG, Földes-Papp Z, et al. Mobility and distribution of replication protein A in living cells using fluorescence correlation spectroscopy. *Exp Mol Pathol* (2007) 82:156–62. doi:10.1016/j.yexmp.2006.12.008

Conflict of Interest: The authors declare that the research was conducted in the absence of any commercial or financial relationships that could be construed as a potential conflict of interest.

frontiers in Physics

ORIGINAL RESEARCH
published: 29 April 2021
doi: 10.3389/fphy.2021.648827

Single-Shot Through-Focus Image Acquisition and Phase Retrieval From Chromatic Aberration and Multi-Angle Illumination

Guocheng Zhou[1], *Shaohui Zhang*[1]*, *Yayu Zhai*[2], *Yao Hu*[1] *and Qun Hao*[1]

[1] School of Optics and Photonics, Beijing Institute of Technology, Beijing, China, [2] Research Center of Ship Quality and Reliability, China Institute of Marine Technology and Economy, Beijing, China

Phase recovery from a stack of through-focus intensity images is an effective non-interference quantitative phase imaging strategy. Nevertheless, the implementations of these methods are expensive and time-consuming because the distance between each through-focus plane has to be guaranteed by precision mechanical moving devices, and the multiple images must be acquired sequentially. In this article, we propose a single-shot through-focus intensity image stack acquisition strategy without any precision movement. Isolated LED units are used to illuminate the sample in different colors from different angles. Due to the chromatic aberration characteristics of the objective, the color-channel defocus images on the theoretical imaging plane are mutually laterally shifted. By calculating the shift amount of each sub-image area in each color channel, the distances between each through-focus image can be obtained, which is a critical parameter in transport of intensity equation (TIE) and alternating projection (AP). Lastly, AP is used to recover the phase distribution and realize the 3D localization of different defocus distances of the sample under test as an example. Both simulation and experiments are conducted to verify the feasibility of the proposed method.

Keywords: phase retrieval, alternating projection, chromatic aberration, single-shot, computational imaging, microscopy

OPEN ACCESS

Edited by:
Chao Zuo,
Nanjing University of Science and Technology, China

Reviewed by:
Yao Fan,
Nanjing University of Science and Technology, China
Jinli Suo,
Tsinghua University, China

***Correspondence:**
Shaohui Zhang
zhangshaohui@bit.edu.cn

Specialty section:
This article was submitted to Optics and Photonics, a section of the journal Frontiers in Physics

Received: *02 January 2021*
Accepted: *03 March 2021*
Published: *29 April 2021*

Citation:
Zhou G, Zhang S, Zhai Y, Hu Y and Hao Q (2021) Single-Shot Through-Focus Image Acquisition and Phase Retrieval From Chromatic Aberration and Multi-Angle Illumination. Front. Phys. 9:648827. doi: 10.3389/fphy.2021.648827

INTRODUCTION

Quantitative phase imaging (QPI) [1] is crucial to label-free microscopic imaging in biomedical fields. In general, for light field passing through a transparent sample, the phase modulation caused by the sample refractive index distribution carries more effective information than the intensity modulation caused by the sample absorption distribution. Nevertheless, instead of phase distributions, we can only obtain intensity distributions with any existing photodetectors due to the extremely fast oscillations of light. Since the early 1900s, a lot of phase imaging methods converting phase to intensity measurement have been proposed [2–7]. It can be roughly classified into two categories. One is contrast phase measurement methods, such as phase-contrast microscopy [8]. Another one is quantitative phase measurement, including interferometry [9], Shack–Hartmann wave front sensor (SHWFS) [10, 11], and so on. The measurement accuracy of interferometry is high, but it is sensitive to environmental noises and suffers from an unwrapping problem. Compared with interferometry, SHWFS and phase-contrast microscopy have relatively simple

system constructions and superior anti-jamming characteristics, but the measurement accuracy of SHWFS is relatively low and phase-contrast microscopy can only achieve a qualitative phase. Therefore, phase imaging with the characteristics of simple structure and strong robustness to noise and environmental disturbances has always been pursued by researchers.

Compared with the conventional methods mentioned above, phase retrieval methods rooting in diffraction have been used widely due to their high anti-jamming capability and good performance, including Fourier ptychographic imaging (FPM) [12–14], ptychographic iterative engine (PIE) [15–18], and so on. PIE aims to retrieve the phase distribution from a series of diffraction patterns corresponding to illumination situations with different positions but a certain overlap ratio between adjacent illumination probes. FPM, sharing its root with phase retrieval and synthetic aperture imaging, can realize a high-resolution (HR), large field-of-view (FOV) amplitude and phase of an object simultaneously. Although PIE and FPM are widely used in quantitative phase imaging, a key problem involved is the time-consuming data acquisition process. In comparison, some phase retrieval methods based on through-focus diversity have also been proposed. Transport of intensity equation (TIE) [19–23] can realize robust phase recovery by constructing the relationship between phase distribution and the differential of light distribution along the optical axis. The axial intensity differential can be equivalent realized by the difference between two through-focus intensity images. Different from the above strategy that calculates phase distribution directly from clear physical models, another kind of phase imaging strategy is realized through the optimization strategy of round-trip iterative constraints between two or more through-focus intensity images. Typical optimization algorithms include the Gerchberg–Saxton (GS) rooting in alternating projection (AP) or projection onto convex sets (POCS), averaged projection, averaged reflection and relaxed averaged alternating reflection (RAAR), etc. [24]. Nevertheless, both TIE and iteration optimization methods need to mechanically scan a camera or sample to obtain the through-focus intensity images, which relies on a precision mechanical moving device.

In order to avoid mechanical scanning and reduce data acquisition time, several methods based on single-shot through-focus intensity image acquisition have been proposed. For example, Waller et al. used chromatic aberration of objective to acquire three raw images simultaneously [25]. Komuro et al. realized TIE phase retrieval with multiple bandpass filters [26] and polarization-directed flat lenses [27, 28]. However, the above methods still require precise mechanical movement calibration of the defocus distance of the system in advance, which is complicated and time-consuming. What is more, the relative distances between each color channel are also related to the overall defocus distance of the sample, which cannot be obtained in a single measurement.

In this paper, we propose a single-shot phase retrieval method based on chromatic aberration and image lateral shift resulting from the multi-angle illuminations of the out-of-focus sample. A sample located at a defocus position is illuminated by light sources of different wavelengths from different incident angles and then imaged with an RGB (red, green, blue) color camera through a microscopic objective. Due to the chromatic aberration of the objective and the different illumination angles, three monochromatic intensity images (red, green, and blue) can be extracted from a single-frame color image. By calculating the lateral shift of each section of the sample, the relative defocus distance between the focus plane and the channel planes can be obtained mathematically. Benefiting from this strategy, defocus distances can be obtained easily without any mechanical moving device and precise measurement. Then, the AP phase retrieval algorithm is utilized to realize phase distribution recovery. Lastly, three-dimensional (3D) localization of the sample can also be obtained. Furthermore, we also improve the Fresnel transfer function (TF) propagator in the AP phase retrieval algorithm in order to accommodate the angle-varied illuminations and out-of-focus samples. This paper is organized as follows: the optical imaging model with angle-varied illuminations is presented in section Oblique Illumination Model. The SAD image registration method used for calculating the image lateral shift is presented in section SAD Image Registration. Color cross-talk in the RGB camera and the AP phase retrieval framework with improved Fresnel TF propagator are presented in sections Color Cross-Talk Elimination and Alternating Projection Phase Retrieval Algorithm, respectively. Section Simulation Experiment presents the simulations to demonstrate the feasibility of the proposed method. We use biological samples in section Experiments to prove the success of phase retrieval experimentally. Finally, the conclusion and discussion are summarized in section Conclusion and Discussion.

PRINCIPLE

Oblique Illumination Model

As shown in **Figure 1**, we build a model to illustrate how the defocus distance and illumination angles affect the image lateral shift in microscopy. If a sample is placed at an out-of-focus position, the images corresponding to illuminations from different angles will have a relative lateral shift between each other. Zheng et al. also realized auto-focusing for microscopic imaging with the lateral shift amount as a defocus distance criterion [29].

A sample is placed at a defocus plane and illuminated by two light beams with the same wavelength, but different incident angles simultaneously, as shown in **Figure 1**. δz is the defocus distance and θ is the angle between two incident light sources. d_1 is the distance between the sensor plane and the theoretical imaging plane. d_2, d_3, d_4, and d_5 are system parameters corresponding to the microscopic system. Assuming there are two points of the sample, a and b. a locates at the optical axis, and the distance between a and b is l_0. b_1' and b_2' are two imaging points corresponding to point b with different incident angles at the theoretical imaging plane. If the sample is placed at the focus plane, both axial points and off-axis points have no lateral shift at the theoretical imaging plane. Thus, b_1' and b_2' will coincide at the theoretical imaging plane. But if the sample is placed at an out-of-focus plane, a lateral shift between b_1' and b_2' will appear. As shown in **Figure 1**, the lateral shift

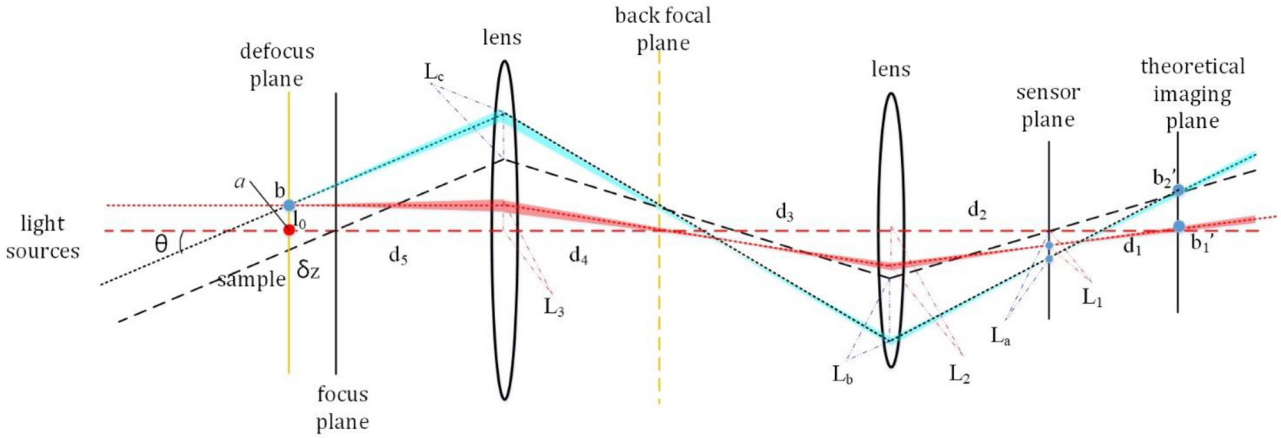

FIGURE 1 | Oblique illumination out-of-focus sample imaging model.

between b_1' and b_2' at the sensor plane is defined as $\delta L = L_a - L_1$. We can derive some equations connecting the above-mentioned variables together.

$$\begin{cases} \frac{L_1}{L_2} = \frac{d_1}{d_1+d_2} \\ \frac{L_2}{L_3} = \frac{d_3}{d_4} \\ L_3 = l_0 \end{cases}, \qquad \begin{cases} \frac{L_a}{L_b} = \frac{d_1}{d_1+d_2} \\ \frac{L_b}{L_c} = \frac{d_3}{d_4} \\ L_c = l_0 + \delta z \cdot tan\theta \end{cases}. \tag{1}$$

Equation (1) can be further organized as follows:

$$\delta \mathrm{L} = L_a - L_1 = \frac{d_1 \cdot d_3}{d_4 \cdot (d_1 + d_2)} \cdot tan\theta \cdot \delta z = \xi \cdot tan\theta \cdot \delta z \tag{2}$$

where $\xi = \frac{d_1 \cdot d_3}{d_4 \cdot (d_1+d_2)}$ is a constant value corresponding to each specific wavelength. It will have different values for different wavelengths due to the chromatic aberration characteristics of the objective. Essentially, Equation (2) aims to calculate the defocus distance δz from d_1. Due to the microscopy and the camera forming an integrated system, the axial defocus distance d_1 is difficult to measure directly. Therefore, we transform calculating d_1 to the lateral distance δL in Equation (2). Given that the AP algorithm framework requires at least two through-focus intensity images to be implemented, we utilize three-wavelength light-emitting diodes (LEDs) corresponding to the three channels of the RGB camera to illuminate the out-of-focus sample from different directions respectively. As shown in **Figure 2**, a red LED is placed at the optical axis, and the corresponding defocus image is used as a reference value because of the characteristic that the defocus image illuminated by normal incidence illumination will not have a lateral shift relative to the focused image. One green LED and one blue LED are placed at the two off-axis positions to provide oblique illuminations, in which the incident illumination angles are θ_{rg} and θ_{rb}, respectively. The defocus distances δz_{fg} and δz_{fb} between the focus plane and the green/blue channel images can be calculated through Equation (3). We should emphasize that benefiting from the normal incidence illumination corresponding to red LED, although the red channel

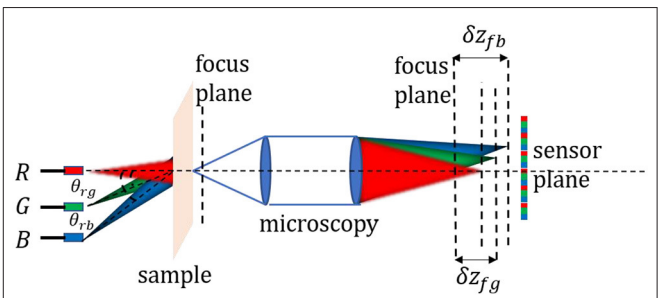

FIGURE 2 | Single-shot oblique illuminations system of our method.

image is located at the out-of-focus position, there exists no lateral shift compared with the focus image. The red channel image can be used as a reference value to calculate the defocus distances between the focus plane and the green/blue channel images. Therefore, we transform calculating the lateral shift between the focus image and the green/blue channel image to calculating the lateral shift between the red and green/blue channel images. Equation (3) indicates that the lateral shifts of the green and blue channels relative to the red image are proportional to the defocus distances between the focus plane and the green/blue channel image, where A_{ri} is a constant value decided by the incident angle and wavelength.

$$\delta \mathrm{L}_{ri} = \xi_{ri} \cdot tan\theta_{ri} \cdot \delta z_{fi} = A_{ri} \cdot \delta z_{fi}, \ (i = g, b) \tag{3}$$

SAD Image Registration

According to the above-mentioned illumination direction and the wavelength multiplexing strategy in section Oblique Illumination Model, we can obtain the defocus distances by calculating the lateral shifts between the red and green/blue channel images. To obtain the precise shifts between different images, we use the sum of absolute differences (SAD) to realize image matching [30, 31]. SAD is a widely used, extremely

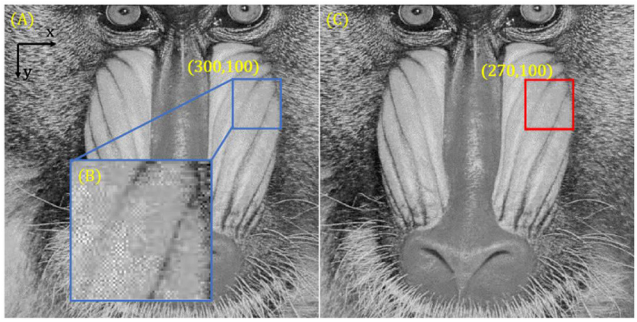

FIGURE 3 | Sum of absolute differences (SAD) image registration examples. **(A)** Original image. **(B)** Window block used for image matching. **(C)** Comparison image in which there is a −30-pixel shift corresponding to the *x* coordinate between **(A)** and **(C)**.

simple video quality metric used for block matching in motion estimation for video compression. It works by taking the absolute value of the difference between each pixel in the original block and the corresponding pixel in the block being used for matching. As shown in Equation (4), $S(i+s-1, j+t-1)$ is one pixel value of the original block and $T(s,t)$ is the corresponding pixel in the block for comparison.

$$\mathrm{D}\left(\mathrm{i},\mathrm{j}\right)=\sum_{s=1}^{M}\sum_{t=1}^{N}\left|S\left(i+s-1,j+t-1\right)-T\left(s,t\right)\right|,\\ \left(1\le i\le m-M+1,\ 1\le j\le n-N+1\right) \tag{4}$$

We show a simulation example of the SAD image registration strategy in **Figure 3**. **Figures 3A,C** are the original and comparison images, respectively. A window block in **Figure 3A** is enlarged, as shown in **Figure 3B**, whose coordinates of the top left corner is (300, 100). Then, we search for window blocks in different positions in **Figure 3C** and calculate the SAD value between them and **Figure 3B**. Finally, we can find the optimal block, whose coordinates of the top left corner is (270, 100). The red boxed sub-region in **Figure 3C**, owning the minimum SAD value with **Figure 3B**, is the best-matched block corresponding to **Figure 3B**. The relative pixel position shift between the matching block pair is (−30, 0), which is consistent with the set value. Assigning a value to pixel size, we can calculate the defocus distance according to Equation (3). Given the discrete sampling process of a digital camera sensor, Equation (3) can be rewritten as follows:

$$\delta \mathrm{L}_{ri}=Ps_{ri}\cdot S_p=A_{ri}\cdot \delta z_{fi},\ (i=g,b) \tag{5}$$

where Ps_{ri} is the pixel shift between the red channel and the green/blue channels and S_p is the pixel size of the RGB camera we used in the following experimental section.

Color Cross-Talk Elimination

Generally speaking, the most common color industrial camera is combined with a Bayer filter and a complementary metal oxide semiconductor (CMOS) sensor. However, due to the color separation performance of the Bayer filter being imperfect, color cross-talk or color leakage will exist among each of the color channels (i.e., red, green, and blue) [32, 33]. Thus, eliminating the color cross-talk among the RGB channels before separating them is important in our proposed method. The imaging process of RGB oblique illumination with a color camera can be mathematically described as follows:

$$\begin{bmatrix}M_R\\M_G\\M_B\end{bmatrix}=\mathbf{W}\cdot\begin{bmatrix}I_r\\I_g\\I_b\end{bmatrix}=\begin{bmatrix}R_r & R_g & R_b\\G_r & G_g & G_b\\B_r & B_g & B_b\end{bmatrix}\cdot\begin{bmatrix}I_r\\I_g\\I_b\end{bmatrix} \tag{6}$$

where **W** is the color cross-talk matrix between the RGB channels. M_R, M_G, and M_B are the RGB channels captured by the color camera, and the subscripts R, G, and B indicate the red, green, and blue channels, respectively. I_r, I_g, and I_b are the illumination intensities in front of the Byer filter corresponding to red, green, and blue colors, respectively. The illumination parameters in the color cross-talk matrix **W** can be obtained experimentally by a spectrometer or calculated using Equation (7), where the superscript "−1" refers to the inverse matrix.

$$\mathbf{W}=\begin{bmatrix}R_r & R_g & R_b\\G_r & G_g & G_b\\B_r & B_g & B_b\end{bmatrix}=\begin{bmatrix}M_R\\M_G\\M_B\end{bmatrix}\cdot\begin{bmatrix}I_r\\I_g\\I_b\end{bmatrix}^{-1} \tag{7}$$

In our experiment, a color camera (FLIR, BFS-U3-200S6C-C) is used for recording images. The matrix ***W*** corresponding to the wavelengths of the RGB LED (470, 517, and 626 nm, respectively) is shown in **Table 1**.

TABLE 1 | Color cross-talk matrix W of our RGB camera.

	626, 517, 470 nm
W	$\begin{bmatrix}1.000 & 0.1462 & 0.0242\\0.0987 & 1.0000 & 0.3292\\0.0414 & 0.2931 & 1.0000\end{bmatrix}$

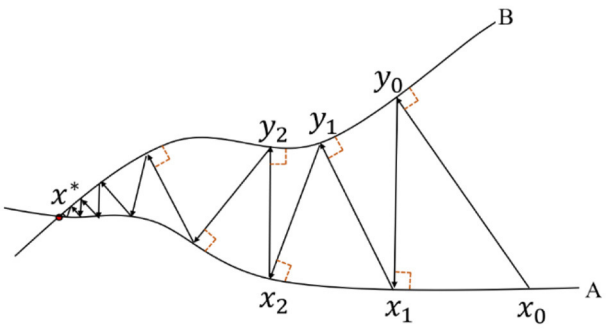

FIGURE 4 | Alternating projection between constraints *A* and *B*.

Alternating Projection Phase Retrieval Algorithm

Alternating projection is a kind of optimization strategy realized by sequentially projecting onto several constraints back and forth multiple times. It has been utilized in performing phase retrieval by means of through-focus intensity images [34, 35]. The simplest case of AP involves two constraints, curves A and B, as shown in **Figure 4**. The intersection point x^* of two constraints indicates the optimal solution of this case. The AP framework can start with an initial guess, x_0, and then projecting x_0 between constraints A and B sequentially. The optimal solution x^* can be found finally as shown in **Figure 4**. Actually, in real experiments, three or more physical constraints can be utilized in the AP process to help improve the possibility of jumping out of the local optimal solution and increase the convergence efficiency, which is also named "sequential projection" or "cyclic projection."

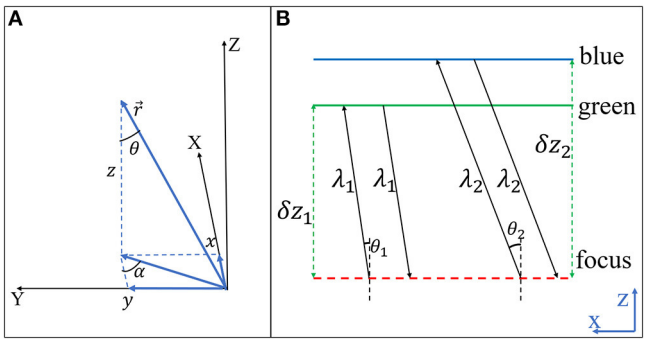

FIGURE 5 | (A) Oblique illumination model in the Fresnel propagation. **(B)** Alternating projection utilized in the proposed method.

The information of a sample under test can be represented by a 3D transmittance distribution, which can be written as Equation (8).

$$U\left(\vec{r}\right) = A_m \cdot e^{j\cdot\vec{k}\cdot\vec{r}} \tag{8}$$

where A_m is the amplitude transmittance of the object and $e^{j\cdot\vec{k}\cdot\vec{r}}$ refers to the phase transmittance part. $k = \frac{2\cdot\pi}{\lambda}$ is the wave vector, where λ indicates the illumination wavelength. Vector $\vec{r}$ denotes the 3D position. Combining with the Fresnel TF propagator, we can propagate the complex light field to different positions and obtain several field distributions corresponding to the different defocus distances [36]. A common propagation routine can be expressed as Equation (9).

$$U_2\left(x,y\right) = I^{-1}\left\{I\left\{U_1\left(x,y\right)\right\}H\left(f_x,f_y\right)\right\} \tag{9}$$

where (x, y) indicates a 2D plane, $U_1(x,y)$ is the original field distribution, and $U_2(x,y)$ is the field in a distance observation plane. The transfer function H is described as Equation (10), where z is the propagation distance from the $U_1(x,y)$ plane to the $U_2(x,y)$ plane.

$$H\left(f_x,f_y\right) = e^{jkz}\exp\left[-j\pi\lambda z\left(f_x^2+f_y^2\right)\right]. \tag{10}$$

The propagator H shown in Equation (10) is applied to a wide range of propagation scenarios that accommodate normal

Algorithm outline

Input: Through-focus image data I_1, I_2; defocus distance δz_1, δz_2;
illumination angels α_1, α_2, θ_1, θ_2; illumination wavelengths λ_1, λ_2;
Output: Updated object $U_{updated}(\mathrm{x},\mathrm{y})$, including amplitude and phase respectively;

The Fresnel propagator: $H_n(\delta z_n,\alpha_n,\theta_n,\lambda_n) = e^{jk_z\delta z_n}e^{j\delta z_n(k_x cos\alpha_n + k_y sin\alpha_n)tan\theta_n}$, $(n = 1,2)$;

Initialize $U_{updated}(\mathrm{x},\mathrm{y}) = Ae^{j\varphi}$ at focus plane, where A and φ are two all ones matrix.

for i= 1: *loopNum*

  for j= 1:2

    project object onto plane j: $U_j(x,y) = \Im^{-1}\{\Im\{U_{updated}(x,y)\}H_j(\delta z_j,\alpha_j,\theta_j,\lambda_j)\} = A_j e^{j\varphi_j}$;

    replace amplitude and keep phase unchanged: $U_{j\_new}(x,y) = \sqrt{I_j}\cdot e^{j\cdot\varphi_j}$;

    project $U_{j\_new}(\mathrm{x},\mathrm{y})$ onto focus plane: $U_{updated}(x,y) = \Im^{-1}\{\Im\{U_{j\_new}(x,y)\}H_j(-\delta z_j,\alpha_j,\theta_j,\lambda_j)\}$;

  end

end

  Amplitude_recovered = abs($U_{updated}(x,y)$);
  Phase_recovered = angle($U_{updated}(x,y)$);

FIGURE 6 | Algorithm outlines of alternating projection in phase retrieval.

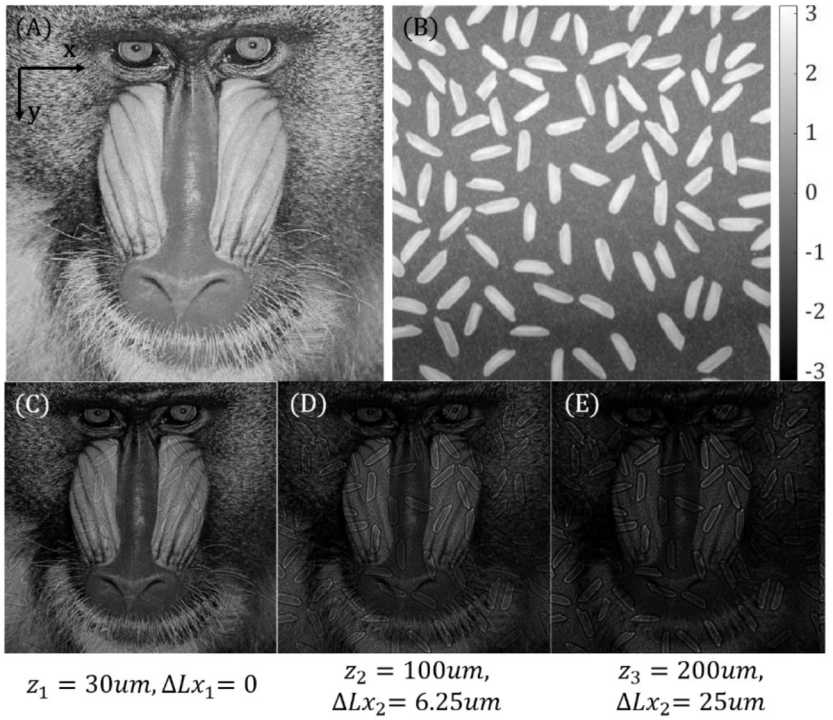

FIGURE 7 | Simulation results. **(A)** Ground truth of amplitude. **(B)** Ground truth of phase. **(C–E)** Raw images with different defocus distances and pixel shifts.

incidence illuminations. However, in angle-varied illuminations, if a sample is placed at the defocus plane, oblique illumination will result in not only a lateral shift in the spatial domain but also a spectrum shift in the Fourier domain. Thus, to solve the spectrum shift, the propagator should be improved.

According to the Fresnel TF propagator with angle-varied illuminations, the phase function can be described as shown in Equation (11), where k_x, k_y are components of the wave vector corresponding to the x-axis and y-axis, respectively.

$$\Phi\left(x, y\right) = k_x x + k_y y \tag{11}$$

As shown in **Figure 5A**, $\left|\overrightarrow{r}\right|$ is the radial distance in the observation plane from the origin to the beam aiming point and z is the perpendicular distance between two planes. Equation (11) can be rewritten as follows, where $\alpha = tan^{-1}\left(\frac{y}{x}\right)$ and θ indicates the illumination angle.

$$\Phi\left(k_x, k_y\right) = z\left(k_x \cos\alpha + k_y \sin\alpha\right) tan\theta \tag{12}$$

The propagator in our strategy should be improved as Equation (13), where $k_z^2 = k^2 - k_x^2 - k_y^2$.

$$H\left(k_x, k_y\right) = e^{jk_z z} \cdot e^{jz(k_x \cos\alpha + k_y \sin\alpha) tan\theta} \tag{13}$$

To obtain several constraints in the optical imaging process, we can propagate the complex light field to different positions by the propagator in Equation (13) and record the corresponding intensity image stack. For instance, as shown in **Figure 5B**, we set $\alpha = 0$. By utilizing the axial chromatic aberration characteristics, we use two channels (green and blue) of the same planar sensor to record the intensity images corresponding to the different propagation distances with different illumination angles. The perpendicular defocus distance δz_n between the focus plane and the green/blue channels can be calculated by Equation (3). Intensity images obtained with a digital image sensor can directly be expressed as Equation (14).

$$I_n = \left|I^{-1}\left\{I\left\{U\left(x, y\right)\right\} H_n\left(k_x, k_y\right)\right\}\right|^2, \quad n = 1, 2, \tag{14}$$

where the intensity images I_1, I_2 that correspond to the green and blue channels form two constraints, respectively. $H_n(k_x, k_y)$ is the Fresnel propagator with different illumination angles and distances. Thus, according to **Figure 5B**, the framework of the alternating projection phase retrieval approach can be expressed as the process shown in **Figure 6**, where *Amplitude_recovered* and *Phase_recovered* are the recovered amplitude and phase of the sample. *loopNum* is an iteration number (typical values are 10, 20, and so on).

SIMULATION EXPERIMENT

Consistent with the systematic parameters in the experiments, the illumination wavelengths are set to 470, 517, and 626 nm in simulation. The pixel size of the RGB camera is 2.4 μm. The distance between the illumination source and the sample plane is 80 mm. According to **Figure 2**, a red LED unit is placed on the

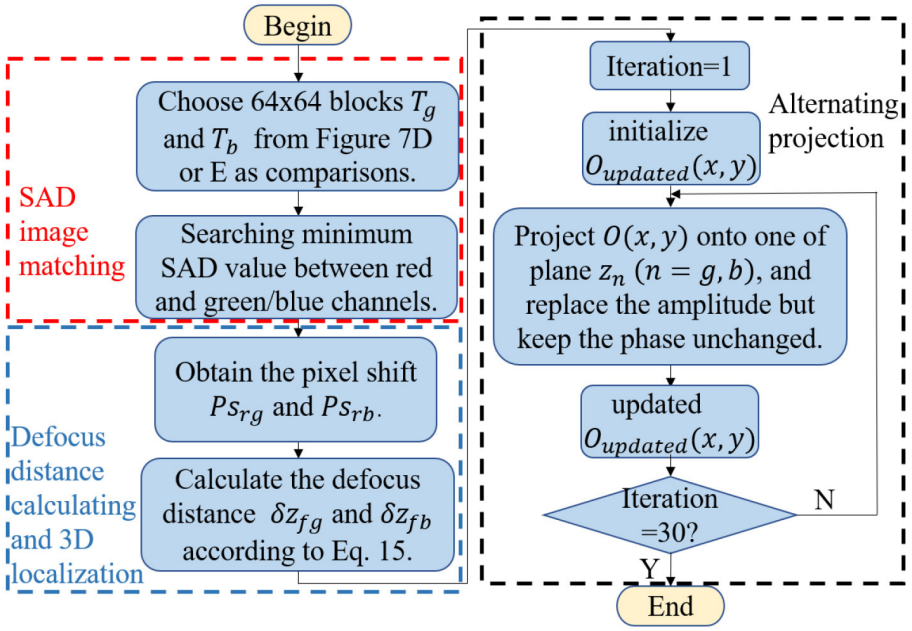

FIGURE 8 | Flow diagram of the proposed method.

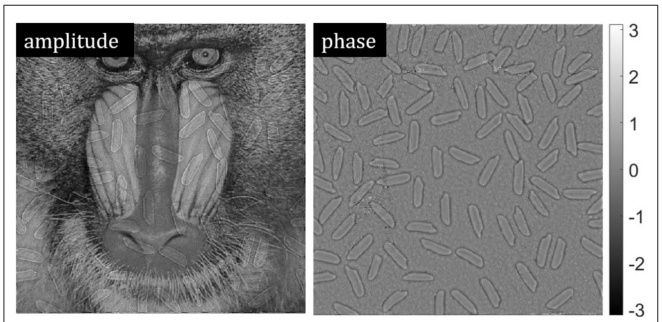

FIGURE 9 | Alternating projection phase retrieval results.

optical axis, in which the corresponding channel image is used as a reference. The x-dimension lateral distance between the red and green LED is set to $Dx_{rg} = 5\ mm$ and the y-dimension distance is set to $Dy_{rg} = 0\ mm$, which means α is set to 0. In a similar way, we set $Dx_{rb} = 10\ mm$ and $Dy_{rb} = 0\ mm$, where r, g, and b indicate the red, green, and blue light source, respectively. Therefore, the tangent functions of the illumination direction angles in **Figure 2** are $\tan\theta_{rg} = \frac{5}{80}$ and $\tan\theta_{rb} = \frac{10}{80}$, respectively. In the simulations, we assume that the scale factor $\xi = 1$. Thus, Equation (3) can be rewritten as follows:

$$\delta L_{ri} = Ps_{ri} \cdot S_p = tan\theta_{ri} \cdot \delta z_{fi},\ (i = g, b) \tag{15}$$

As shown in **Figures 7A,B**, the "baboon" and "rice" images are used as the ground truth of the amplitude and phase parts, respectively. Their image size is set to 512 × 512. By using the Fresnel diffraction equation shown in Equation (14), we obtain three intensity images at different axial positions, as shown in **Figures 7C–E**. As mentioned above, **Figure 7C** belongs to the red channel image, which is illuminated by the normal incidence illumination. Thus, **Figure 7C** is used as the reference to calculate the defocus distances between the focus plane and the green/blue image planes. The equivalent defocus distances between the focus plane and each image plane is set as $z_i = [30,\ 100,\ 200]\ um,\ (i = r, g, b)$. And the x-dimension separation between the focus plane and each channel image can be written as $Lx_i = [0,\ 6.25,\ 25]\ um,\ (i = r, g, b)$, according to Equation (15), while the y-dimension separations are 0. Thus, the relative pixel shifts between the red and green/blue channels can be calculated as $Ps_{ri} = [2.6,\ 10.4]\ pixels\ (i = g, b)$, theoretically. Considering the discrete sampling property of digital cameras, pixel shifts should be rounded as $Ps_{ri} = [3, 10]\ pixels\ (i = g, b)$. In general, **Figures 7C–E** are the final raw data corresponding to the red, green, and blue channels, respectively, which involve different defocus distances and pixel shifts in our simulations.

Figure 8 shows the flow diagram of the proposed method. We chose two 64 × 64 window blocks T_g and T_b as comparisons from **Figures 7D,E**, respectively, which is similar to that in section SAD Image Registration. Then, according to Equation (4), by searching for the optimal window blocks that have the minimum SAD values with T_g and T_b in the red channel intensity image, we can obtain the pixel shifts Ps_{rg}, Ps_{rb} between the red channel and the green/blue channels. The absolute defocus distance between the focus plane and the green/blue channels, δz_{fg}, δz_{fb}, can be calculated by Equation (15). For example, in our simulations, the pixel shifts we calculated are $Ps_{rg} = 3\ pixels$ and $Ps_{rb} = 10\ pixels$, which conform to the parameters we simulated. And according

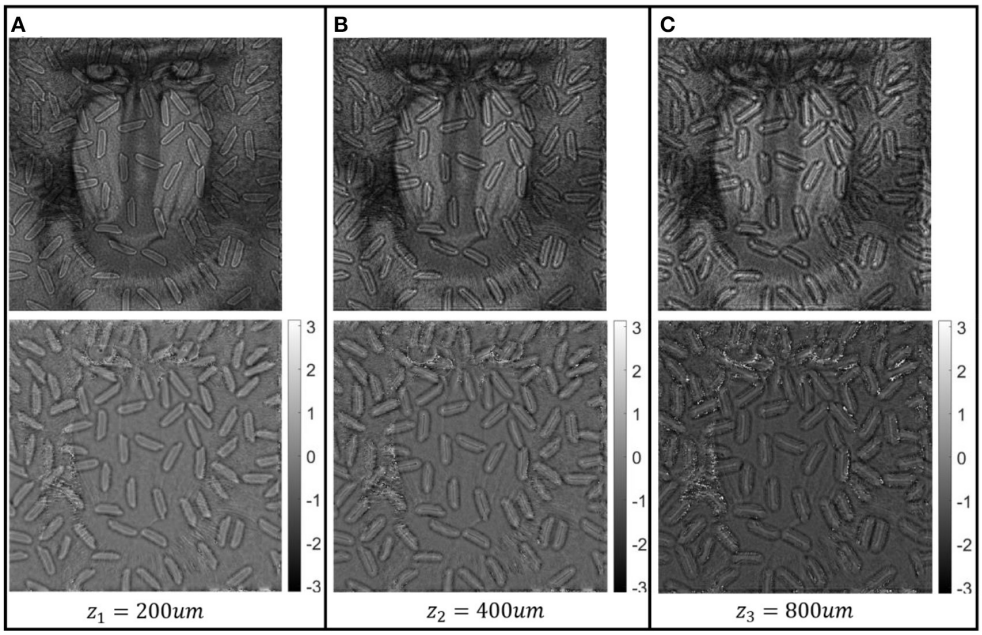

FIGURE 10 | (A–C) Amplitude and phase of the sample corresponding to defocus distances of 200, 400, and 800 μm, respectively.

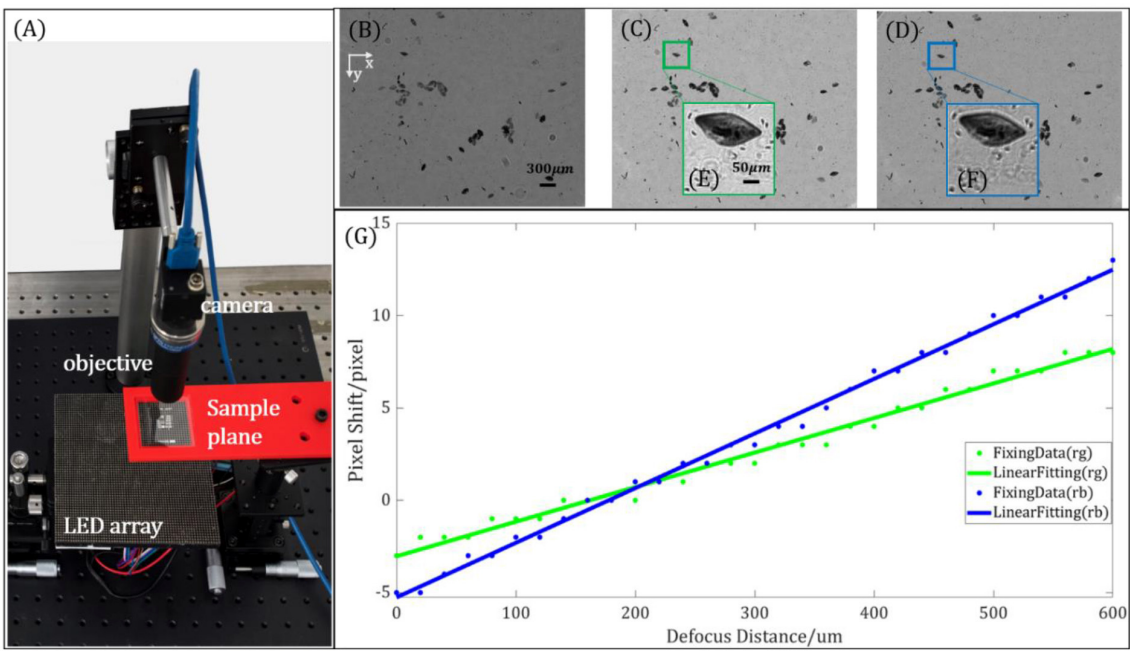

FIGURE 11 | Scale factor calibration results. **(A)** System setup of the proposed method. **(B–D)** Through-focus images corresponding to the red, green, and blue channels, respectively; **(B)** is the reference image for the sum of absolute differences (SAD) image matching. **(E)** Window block from the green channel used for SAD image matching. **(F)** Window block from the blue channel. **(G)** Linear fitting results corresponding to system parameters A_{rg} and A_{rb}.

to Equation (15), the absolute defocus distances we obtained are $\delta z_{fg} = 115\ um$ and $\delta z_{fb} = 192\ um$, which are approximately equal to the ideal values. This error comes from the round-off operation to non-integer pixel data.

In accordance with the defocus distance obtained above, AP phase retrieval approaches are used for phase recovery. According to section Alternating Projection Phase Retrieval Algorithm, two images corresponding to the green and blue

TABLE 2 | Relationship of the defocus distance and pixel shift.

δz/μm	0	20	40	60	80	100	120	140
Pixel shift	−5	−5	−4	−3	−3	−2	−2	−1
δz/μm	160	180	200	220	240	260	280	300
Pixel shift	−1	0	0	1	1	2	3	3
δz/μm	320	340	360	380	400	420	440	460
Pixel shift	4	4	5	5	6	7	8	8
δz/μm	480	500	520	540	560	580	600	
Pixel shift	9	9	10	11	11	12	13	

channels are used as amplitude constraints, which means that the amplitude of the complex light field to be recovered at the same axial position should be equal to the square root of the image intensity value. We give an initial guess of the sample's complex function firstly at the focus plane, and then projecting it onto the green (or blue) plane position, replacing the amplitude part with the measured value while keeping the phase part unchanged, and then projecting it back to the focus plane. By repeating this procedure, we can obtain an updated object complex function. Through multiple projections and amplitude replacements between the focal plane and the corresponding constraints of the blue and green channels, we can obtain a final solution. The amplitude and the phase part recovered with the above approach are shown in **Figure 9**. The cross-talk between amplitude and phase may come from the calculation deviation of the SAD and the following error of defocus distance.

Furthermore, by propagating the recovered object function to the different defocus distances, we can also realize 3D localization in the proposed method. As shown in **Figure 10**, we propagate the recovered object function to 200, 400, and 800 μm with the illumination angle, θ_{rg}, and obtain both the amplitude and phase of the sample corresponding to the different defocus distances, respectively. Compared with the amplitude parts of the sample in **Figures 10A–C**, by changing the different propagation distances but the same incidence illumination angle, we found that our method can be used in refocusing. With the increase of the propagation distance, the lateral shift is clearer in the results. Furthermore, compared with the phase parts of the sample in **Figures 10A–C**, we found that the phase parts also change with the increase of the propagation distance. Generally, the results shown in **Figure 10** demonstrate the feasibility of our method by simulations in 3D localization.

EXPERIMENTS

To demonstrate the feasibility of our method in actual experiments, we use Paramecium and bee wing as samples for parameter calibration, phase imaging, and 3D localization. In our experiment, the optical system consists of an RGB camera (FLIR, BFS-U3-200S6C-C) for recording images, a telecentric objective with certain chromatic aberrations (OPTO, TC23004; magnification ×2, NA ≈ 0.1, FOV = 4.25 mm × 3.55 mm, working distance = 56 mm) for imaging, and an RGB LED array (CMN, P = 2.5, 470, 517, and 626 nm) for providing wavelength and direction multiplexing illumination. The system setup is shown in **Figure 11A**. The distance between the sample plane and the illumination LED plane is adjusted to 90 mm. According to **Figure 2**, red, green, and blue LEDs are used for angle-varied illuminations. Similar to the parameter set in the simulations, the y-dimension lateral distance between the red and green LEDs is set to $Dy_{rg} = 2.5\ mm$ and the x-dimension distance is set to $Dx_{rg} = 0\ mm$, which means α is set to 90°. We set $Dy_{rb} = 5\ mm$ and $Dx_{rb} = 0\ mm$, where r, g, and b indicate the red, green, and blue light sources, respectively. The red illumination light is normally incident onto the sample, while the tangent functions of the illumination angles are $\tan\theta_{rg} = \frac{2.5}{90}$ and $\tan\theta_{rb} = \frac{5}{90}$ for the green and blue lights, respectively. Before implementing Equation (3) to calculate the defocus distance for each channel, we should obtain the scale factors A_{rg} and A_{rb} first. As shown in **Figures 11B–G**, we use a Paramecium biological sample to realize the scale factor calibration. **Figures 11B–D** show the three monochromatic intensity images extracted from the RGB channels of the same image sensor, respectively. **Figure 11B** is the reference image corresponding to the red channel. **Figures 11E,F** are two window blocks we choose to search for the minimum SAD value between the red and green/blue channels, respectively. We change the defocus distance from 0 to 600 μm, in which step the size is set to 20 μm and we record the corresponding through-focus images. By implementing the SAD image registration method, we can calculate the pixel shift between the red and green/blue channels. **Table 2** is a set of SAD image matching results of the reference image and the blue channel image. As shown in **Figure 11G**, by using the linear fitting method, we can obtain the scale factor of the two different wavelengths as follows: $A_{rg} = 0.045$ and $A_{rb} = 0.071$. Then, combining with the results of the scale factor, we can obtain the defocus distance between the focus plane and the green/blue channel planes mathematically. Furthermore, according to **Figure 11G**, we found that the absolute defocus distances at the 0-pixel shift between the green and blue channels are different, which is caused by the chromatic aberration of objectives.

As shown in **Figure 12**, we use the biological sample bee wing to demonstrate the feasibility of our method. **Figures 12A,B** are raw data extracted from the RGB camera corresponding to the green and blue channels, respectively. By utilizing Equation (3), the defocus distances between the focus and the green/blue channel images are 256.6 and 324.6 μm, respectively. Then, as shown in **Figures 12C,D**, we use the AP phase retrieval approach to reconstruct both the amplitude and phase of the biological sample at the focus plane.

Furthermore, similar to the simulations shown in **Figure 10**, we choose several defocus distances as examples to perform 3D localization. As shown in **Figure 13**, after obtaining the recovered object function, we propagate it onto different defocus distances (such as −200, 200, and 400 μm) with the illumination angle θ_{rg}. Both the amplitude and phase of the sample corresponding to the different defocus distances can be obtained by this procedure. As shown in **Figures 13A–C**, the enlarged red boxed sub-regions belong to the same sub-region in the amplitude of the sample while owning different defocus distances. We found that with

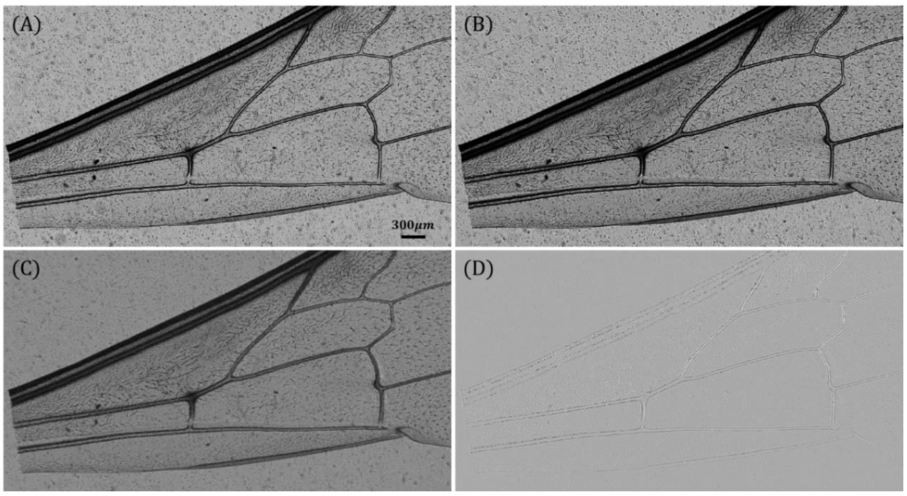

FIGURE 12 | (A,B) Images of the green and blue channels extracted from the RGB camera. **(C)** Amplitude of the recovered object. **(D)** Phase of the recovered object.

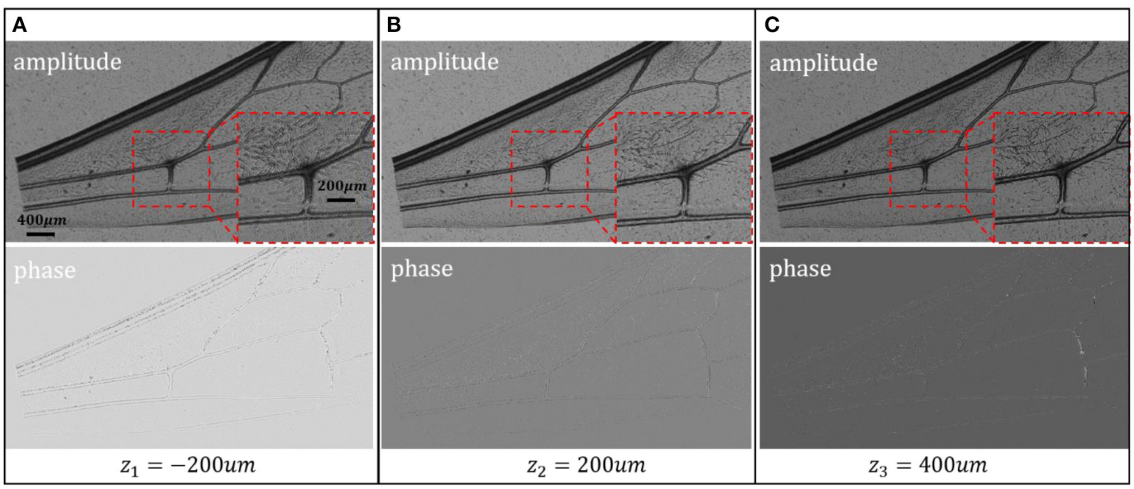

FIGURE 13 | Three-dimensional localization results of the biological sample. **(A–C)** Amplitude and phase of the sample corresponding to different defocus distances.

the change of defocus distance, both the amplitude and phase of the sample will be changed. Generally speaking, **Figure 13** demonstrates the feasibility of the proposed method in realizing a 3D localization in actual experiments.

CONCLUSION AND DISCUSSION

Generally speaking, through-focus intensity image acquisition methods play a critical role in AP and TIE phase retrieval approaches. In this paper, inspired by chromatic aberration of an objective and lateral shift resulting from the multi-angle illuminations of the out-of-focus sample, we proposed a single-shot through-focus intensity image acquisition strategy and realize phase recovery by the AP phase retrieval method. A Fresnel TF propagator corresponding to angle-varied illuminations is utilized in our method to solve the spectrum shift in out-of-focus imaging with oblique illuminations. Three isolated LED units are used for illumination with different wavelengths from different incident angles. Due to the chromatic aberration of an objective, there will be a lateral shift between each color channel. The red channel image is used as a reference in the calculation of the lateral shift between the red and green/blue channel images because there is no lateral shift between the defocus image and the focus image if the sample is illuminated by a normal incidence illumination. Then, the defocus distances between the focus plane and the green/blue planes can be calculated by the lateral shift between the red and green/blue channel images mathematically. Compared with the proposed methods that utilize chromatic aberration while using three normal incidence illuminations, our method can obtain the defocus distances mathematically, avoiding the requirement of accuracy measurement and complex system setup

in conventional methods. Different from the time-consuming process in obtaining the correct defocus distance, our method can obtain the defocus distance quickly on the algorithm. Furthermore, an accurate focusing process is not required in the proposed method. Finally, we use some biological samples and the AP phase retrieval method to demonstrate the feasibility of the proposed method in actual experiments, and a 3D localization corresponding to different defocus distances can be realized.

Although the effectiveness of our method has been proven, there are still some details that can be improved in further works. Firstly, the calculation accuracy of the defocus distance can be increased. In our paper, we use the SAD image registration method to calculate the pixel shift between channels, whose measurement accuracy will be half of a pixel. For further work, the measurement accuracy can be increased by the method proposed in [37]. Furthermore, the sub-pixel image registration method can also be implemented to increase the measurement accuracy. Secondly, theoretically, a larger illumination angle results in a more obvious separation between two channels. However, in actual experiments, considering the effective range of the bright field in oblique illuminations, the largest tangent function between red and blue incident illumination is $\tan\theta_{rb} = \frac{5}{90}$, which results in unobvious separations between the two channels. In further works, we can use some binary lens designed by metamaterial to obtain a more obvious chromatic aberration in experiments.

DATA AVAILABILITY STATEMENT

The raw data supporting the conclusions of this article will be made available by the authors, without undue reservation.

AUTHOR CONTRIBUTIONS

SZ conceived the idea. GZ did the experiments and writing. SZ, YH, and QH supervised the project. All the authors contributed to the review.

FUNDING

This work was supported by the National Natural Science Foundation of China under grants 61875012, 51735002, 61735003, and 61805011.

REFERENCES

1. Barty ANTON, Nugent KA, Paganin D, Roberts A. Quantitative optical phase microscopy. *Opt Lett.* (1998) 23:817–9. doi: 10.1364/OL.23.000817
2. Choi W, Fang-Yen C, Badizadegan K, Oh S, Lue N, Dasari RR, et al. Tomographic phase microscopy. *Nat Methods.* (2007) 4:717–9. doi: 10.1038/nmeth1078
3. Mann CJ, Yu L, Lo CM, Kim MK. High-resolution quantitative phase-contrast microscopy by digital holography. *Opt Express.* (2005) 13:8693–8. doi: 10.1364/OPEX.13.008693
4. Marquet P, Rappaz B, Magistretti PJ, Cuche E, Emery Y, Colomb T, et al. Digital holographic microscopy: a noninvasive contrast imaging technique allowing quantitative visualization of living cells with subwavelength axial accuracy. *Opt Lett.* (2005) 30:468–70. doi: 10.1364/OL.30.000468
5. Millerd J, Brock N, Hayes J, North-Morris M, Kimbrough B, Wyant J. *Pixelated Phasemask Dynamic Interferometers. Fringe 2005*. Berlin, Heidelberg: Springer (2006). p. 640–7.
6. Paganin D, Nugent KA. Noninterferometric phase imaging with partially coherent light. *Phys Rev Lett.* (1998) 80:2586–9. doi: 10.1103/PhysRevLett.80.2586
7. Tan Y, Wang W, Xu C, Zhang S. Laser confocal feedback tomography and nano-step height measurement. *Sci Rep.* (2013) 3:2971. doi: 10.1038/srep02971
8. Zernike F. Phase contrast, a new method for the microscopic observation of transparent objects part II. *Physica.* (1942) 9:974–86. doi: 10.1016/S0031-8914(42)80079-8
9. Allen RD, David GB, Nomarski G. The Zeiss-Nomarski differential interference equipment for transmitted-light microscopy. *Zeitschrift fur wissenschaftliche Mikroskopie und mikroskopische Technik.* (1969) 69:193–221.
10. Thibos LN. Principles of Hartmann-Shack aberrometry. *J. Refractive Surg.* (2000) 16:563–5. doi: 10.1364/VSIA.2000.NW6
11. Platt BC, Shack R. History and principles of Shack-Hartmann wavefront sensing. *J Refract Surg.* (2001) 17:S573–7. doi: 10.3928/1081-597X-20010901-13
12. Zheng G, Horstmeyer R, Yang C. Wide-field, high-resolution Fourier ptychographic microscopy. *Nat Photonics.* (2013) 7:739–45. doi: 10.1038/nphoton.2013.187
13. Zuo C, Sun J, Chen Q. Adaptive step-size strategy for noise-robust Fourier ptychographic microscopy. *Opt Express.* (2016) 24:20724–44. doi: 10.1364/OE.24.020724
14. Bian L, Suo J, Zheng G, Guo K, Chen F, Dai Q. Fourier ptychographic reconstruction using Wirtinger flow optimization. *Opt Express.* (2015) 23:4856–66. doi: 10.1364/OE.23.004856
15. Rodenburg JM, Faulkner HM. A phase retrieval algorithm for shifting illumination. *Appl Phys Lett.* (2004) 85:4795–7. doi: 10.1063/1.1823034
16. Li G, Yang W, Wang H, Situ G. Image transmission through scattering media using ptychographic iterative engine. *Appl Sci.* (2019) 9:849. doi: 10.3390/app9050849
17. Horstmeyer R, Chen RY, Ou X, Ames B, Tropp JA, Yang C. Solving ptychography with a convex relaxation. *New J Phys.* (2015) 17:053044. doi: 10.1088/1367-2630/17/5/053044
18. Maiden AM, Humphry MJ, Zhang F, Rodenburg JM. Superresolution imaging via ptychography. *J Opt Soc Am A.* (2011) 28:604–12. doi: 10.1364/JOSAA.28.000604
19. Gureyev TE, Roberts A, Nugent KA. Partially coherent fields, the transport-of-intensity equation, phase uniqueness. *J Opt Soc Am A.* (1995) 12:1942–6. doi: 10.1364/JOSAA.12.001942
20. Gureyev TE, Roberts A, Nugent KA. Phase retrieval with the transport-of-intensity equation: matrix solution with use of Zernike polynomials. *J Opt Soc Am A.* (1995) 12:1932–41. doi: 10.1364/JOSAA.12.001932
21. Zuo C, Chen Q, Asundi A. Boundary-artifact-free phase retrieval with the transport of intensity equation: fast solution with use of discrete cosine transform. *Opt Express.* (2014) 22:9220–44. doi: 10.1364/OE.22.009220
22. Zhang J, Chen Q, Sun J, Tian L, Zuo C. On a universal solution to the transport-of-intensity equation. *Opt Lett.* (2020) 45:3649–52. doi: 10.1364/OL.391823
23. Wittkopp JM, Khoo TC, Carney S, Pisila K, Bahreini SJ, Tubbesing K, et al. Comparative phase imaging of live cells by digital holographic microscopy and transport of intensity equation methods. *Opt Express.* (2020) 28:6123–33. doi: 10.1364/OE.385854
24. Marchesini S. Invited article: a unified evaluation of iterative projection algorithms for phase retrieval. *Rev Entific Instr.* (2007) 78:229–61. doi: 10.1063/1.2403783
25. Waller L, Kou SS, Sheppard CJ, Barbastathis G. Phase from chromatic aberrations. *Opt Express.* (2010) 18:22817–25. doi: 10.1364/OE.18.022817

26. Komuro K, Nomura T. Quantitative phase imaging using transport of intensity equation with multiple bandpass filters. *Appl Opt.* (2016) 55:5180–6. doi: 10.1364/AO.55.005180
27. Kakei S, Komuro K, Nomura T. Transport-of-intensity phase imaging with polarization directed flat lenses. *Appl Opt.* (2020) 59:2011–5. doi: 10.1364/AO.386020
28. Komuro K, Saita Y, Tamada Y, Nomura T. Numerical evaluation of transport-of-intensity phase imaging with oblique illumination for refractive index tomography. In: *Digital Holography and Three-Dimensional Imaging 2019, OSA Technical Digest (Optical Society of America, 2019), paper Th3A.37.*
29. Guo C, Bian Z, Jiang S, Murphy M, Zhu J, Wang R, et al. OpenWSI: a low-cost, high-throughput whole slide imaging system via single-frame autofocusing and open-source hardware. *Opt Lett.* (2020) 45:260–3. doi: 10.1364/OL.45.000260
30. Guevorkian D, Launiainen A, Liuha P, Lappalainen V. Architectures for the sum of absolute differences operation. In: *Signal Processing Systems. IEEE.* (2002). p. 57–62.
31. Silveira B, Paim G, Abreu B, Grellert M, Diniz CM, da Costa EA, et al. Power-efficient sum of absolute differences architecture using adder compressors. In: *2016 IEEE International Conference on Electronics, Circuits and Systems (ICECS). IEEE* (2016).
32. Lee W, Jung D, Ryu S, Joo C. Single-exposure quantitative phase imaging in color-coded LED microscopy. *Opt Express.* (2017) 25:8398. doi: 10.1364/OE.25.008398
33. Phillips ZF, Chen M, Waller L. Single-shot quantitative phase microscopy with color-multiplexed differential phase contrast (cDPC). *PLoS ONE.* (2017) 12:e0171228. doi: 10.1371/journal.pone.0171228
34. Netrapalli P, Jain P, Sanghavi S. Phase retrieval using alternating minimization. *IEEE Trans Signal Process.* (2015) 63:4814–26. doi: 10.1109/TSP.2015.2448516
35. Fienup JR. Phase retrieval algorithms: a comparison. *Appl Opt.* (1982) 21:2758–69. doi: 10.1364/AO.21.002758
36. Voelz DG. *Computational Fourier Optics: A MATLAB Tutorial.* Las Cruces, NM: SPIE (2011).
37. Zhou G, Zhang S, Hu Y, Hao Q. Single-shot sequential projection phase retrieval and 3D localization from chromatic aberration. *Opt Express.* (2020) 28:9976–87. doi: 10.1364/OE.389260

Conflict of Interest: The authors declare that the research was conducted in the absence of any commercial or financial relationships that could be construed as a potential conflict of interest.

frontiers in Physics

BRIEF RESEARCH REPORT
published: 03 May 2021
doi: 10.3389/fphy.2021.667023

Flipping Interferometric Module for Simultaneous Dual-Wavelength Unwrapping of Quantitative Phase Maps of Biological Cells

*Lidor Karako, Rongli Guo, Itay Barnea and Natan T. Shaked**

Department of Biomedical Engineering, Faculty of Engineering, Tel Aviv University, Tel Aviv, Israel

OPEN ACCESS

Edited by:
Vicente Micó,
University of Valencia, Spain

Reviewed by:
Alexander Khmaladze,
University at Albany, United States
Björn Kemper,
University of Münster, Germany

****Correspondence:***
Natan T. Shaked
nshaked@tau.ac.il

Specialty section:
This article was submitted to Optics and Photonics, a section of the journal Frontiers in Physics

Received: *11 February 2021*
Accepted: *23 March 2021*
Published: *03 May 2021*

Citation:
Karako L, Guo R, Barnea I and Shaked NT (2021) Flipping Interferometric Module for Simultaneous Dual-Wavelength Unwrapping of Quantitative Phase Maps of Biological Cells. Front. Phys. 9:667023. doi: 10.3389/fphy.2021.667023

We present an imaging platform for stain-free quantitative imaging of biological cells using a simultaneous dual-wavelength holographic module. We use this module to experimentally solve the problem of 2π phase ambiguities that occurs in spatial locations where the optical thickness of the sample is larger than the wavelength. Thus, the process does not require using digital phase unwrapping that is computational heavy and impairs real-time processing. The proposed method is not limited to sequential acquisition of two quantitative phase maps in different times, but rather allows optical multiplexing of two off-axis holograms on the camera at once, enabling acquisition of fast dynamic processes. The module is simple and portable, making it attractive for clinical use. We demonstrate using the module for quantitative phase imaging of cancer and sperm cells.

Keywords: quantitative phase imaging, digital holographic microscopy, stain-free cell imaging, synthetic phase imaging, stain-free flow cytometry

INTRODUCTION

Digital holographic microscopy (DHM) can record the optical thickness profile of biological samples, such as cells *in vitro*. This profile, also referred to as the optical path delay (OPD) profile, is defined as the product of the sample thickness and its integral refractive-index (RI) profiles, allowing to visualize transparent or semitransparent samples in high and quantitative contrast, without using cell staining [1]. The OPD profile can be used to calculate the cell dry mass, which is an indicator for the physical density of the cell, as well as other quantitative parameters of biological relevance [2]. The OPD profile can be recorded in a single camera exposure using off-axis holography, where two beams interfere on the camera at a small off-axis angle, one beam interacts with the sample and the other beam is the reference beam that does not contain sample modulation. The resulting off-axis hologram is a cosine pattern, modulated

by the off-axis angle plus the phase difference of the sample, and defined as follows:

$$\Delta\varphi\left(x,y\right)=\frac{2\pi}{\lambda}H_c\left(\overline{n}_c-n_m\right)=\frac{2\pi}{\lambda}OPD\left(x,y\right), \quad (1)$$

where H_c is the sample thickness, $\overline{n}_c$ is the sample integral RI, n_m is the surrounding medium RI, and λ is the illumination wavelength. When creating this profile, 2π phase ambiguities occur in locations where the OPD is larger than the illumination wavelength.

Digital phase unwrapping algorithms can solve this problem [3]. However, they are computational heavy and cannot typically cope with samples which experience more than 2π jumps in neighboring locations. For this reason, two-wavelength phase unwrapping is used [4]. This technique acquires the OPD profile of the sample in two different wavelengths, and creates a new OPD profile at a larger synthetic wavelength, so that the sample is no longer optically thicker than the synthetic wavelength, and 2π phase ambiguities do not occur.

Two-wavelength phase unwrapping is pruned to coherence induced disturbances that may be caused by highly coherent laser light sources and the presence of scattering system components. Typically, this two-wavelength acquisition is done sequentially, in two exposures, which cannot be done for highly dynamic samples that might change between the exposures; Alternatively, if two cameras are used for parallel acquisition, image segmentation problems might occur. Simultaneous, single-camera two-wavelength holography can be used to solve this problem [5]. This can be done by multiplexing two off-axis holograms of the same sample imaged under different wavelengths on the same sensor, providing real-time holographic capabilities without 2π phase ambiguities. In this case, the camera records a multiplexed off-axis hologram composed of two 90°-rotated, or orthogonal, off-axis interference fringes [6–9]. These methods use separate reference beams, independent of the sample beam along most of the optical path, yielding increased temporal noise. Self-interference holography allows decreased temporal noise due to the nearly common-path geometry. A setup that uses a long-distance objective and two beam splitters positioned within the working distance was proposed for two-wavelength phase unwrapping [10]. Alternative approach is generating the reference beam externally, after the image plane of the optical system. Previously, we proposed an external, portable, and nearly common-path interferometric module, which is capable of forming a multiplexed off-axis hologram for two-wavelength phase unwrapping. It externally creates the reference beam using spatial filtering, as implemented by two lenses and a confocally positioned pinhole [11]. This setup requires meticulous pinhole alignment for implementing the spatial filtering, and it also suffers from loss of power in the reference arm, reducing the fringe visibility. To solve this issue, in [12], we proposed the flipping interferometry, which uses half of the optical beam as the reference beam for the other half of the beam; and thus, it does not require pinhole alignment. Since no pinhole is used, the system is not more sensitive to the sample meniscus than in regular holography with external reference beam, provided that half of the optical field of view used as the reference beam is empty and does not any contain a sample modulation such as additional meniscus. Flipping interferometry requires a high spatial coherence source, for obtaining interference in spite of the flipping operation. In addition, a high temporal coherence is preferred to obtain high modulation interference fringes on the entire sensor size. Inexpensive HeNe or many DPSS lasers have both high spatial coherence and temporal coherence and are suitable for flipping interferometry. This system is specifically suitable for acquiring biological cells during flow in a microfluidic channel, since the beam can be easily positioned on the border of the channel to meet the requirement for a half-empty optical beam. Still, in contrast to most shearing interferometers, the off-axis angle, determining the fringe spatial frequency, can be fully controlled, without the requirement for sample sparsity to avoid ghost image overlaps. In [13], we proposed flipping interferometry with doubled imaging area, an external portable module that combines simultaneous acquisition of two fields of view of the sample by spatial off-axis holographic multiplexing, without using a pinhole alignment. It projects two holographic fields of view on the camera at once, where each field of view is encoded into interference fringes of different orientation. Therefore, both fields of view can be reconstructed, while using the same number of camera pixels typically needed for acquiring a single field of view in off-axis holography. The flipping interferometry idea was adjusted for two-wavelength off-axis holographic multiplexing using an interferometric module that contains two lenses, two retro-reflectors, a mirror, and regular and polarizing beam splitters [14]. However, the use of polarizing elements makes the system unsuitable for imaging polarizing samples.

The current paper proposes a new alternative for a module that performs two-wavelength off-axis holographic multiplexing with flipping interferometry. The module uses no lenses and no polarizing elements, making it more portable and suitable even for imaging samples inducing polarization changes. We use this module for simultaneous two-wavelength phase unwrapping and demonstrate dynamic quantitative phase imaging of microbeads, sperm cells and cancer cells.

MATERIALS AND METHODS

The F-2WL Setup

The proposed dual-wavelength flipping interferometry module (F-2WL) setup that allows simultaneous two-wavelength off-axis holography, and therefore two-wavelength phase unwrapping, is shown in **Figure 1**. It is an external interferometric module that is compact, nearly common path, and does not use any lenses or polarizer inside, hence easing its alignment. As in our previous flipping interferometry module that is used for field of view multiplexing [13], here too, the empty half of the optical spot illuminating the sample is used as the reference beam. It is optically flipped over the sample field of view to create an off-axis hologram of the sample on the monochromatic camera. However, in contrast to field of view multiplexing, here two orthogonal fringe patterns of the same sample field of view are acquired at once, each of which under a different wavelength illumination. As shown in **Figure 1**, the system is illuminated by

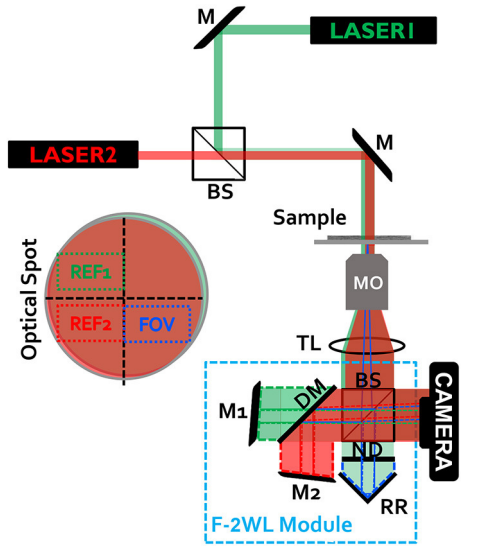

FIGURE 1 | Experimental setup with the simultaneous flipping dual-wavelength interferometry (F-2WL) module, connected to an inverted microscope. M, mirror; BS, beam splitter; MO, microscope objective; TL, tube lens; RR, two-mirror retro-reflector; ND, neutral density filter; DM, dichroic mirror. The optical spot projected on the camera plane is shown on the left. The projected beams create two-wavelength multiplexed off-axis hologram on the camera. Ref_1, reference beam in the green channel; Ref_2, reference beam in the red channel; FOV, field of view containing the biological cells.

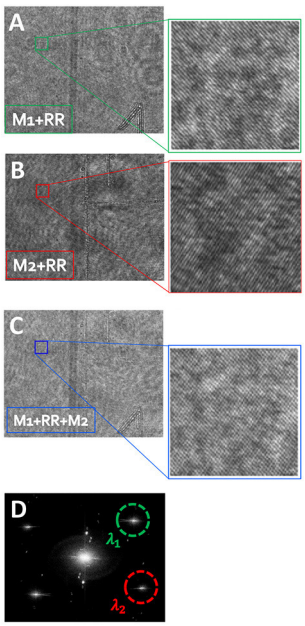

FIGURE 2 | Demonstration of the optical multiplexing operation, while imaging an empty field of view. **(A)** Off-axis hologram at λ_1, comprised of the green beams reflected from M_1 and RR. **(B)** Off-axis hologram at λ_2, comprised of red beams reflected from M_2 and RR. **(C)** The dual-wavelength multiplexed off-axis hologram, containing simultaneous orthogonal-fringe patterns. **(D)** The power spatial spectrum obtained by digital Fourier transforming of the multiplexed hologram. λ_1 and λ_2 are used to denote the selected CC terms of green and red channels, respectively, each of which containing the OPD profile of the sample at a different wavelength.

two temporally coherent lasers 632.8 nm, helium-neon (HeNe) laser (Thorlabs) and 532 nm, diode-pump solid-state (DPSS) laser (Laserglow, Technologies), after being combined by a high-precision plate beam splitter (BSW10R). The sample is illuminated by a plane wave, thus no condenser lens is used. The inverted microscope includes a 1.35-NA microscope objective (UPlanSApo, 60×, oil-immersion, Olympus) and an achromatic lens tube lens ($f = 200$, 2" diameter). The F-2WL module is positioned after the tube lens, wherein the sample is imaged onto the camera. Alternatively, to make the module completely external, a 4f imaging system can be positioned at the exit if the microscope, where the module is located after the second lens, within is focal distance. Inside the module 50:50 beam splitter (BS013, Thorlabs) is used in order to split the beam to reference and sample arms. In the reference arm, one two-mirror retro-reflector is used to flip (mirror) both red and green beams. In the sample arm, a dichroic mirror (cut-off wavelength 567 nm, DMSP567R, Thorlabs) is placed, to split the red and green beams, so that each of them is reflected by a different mirror and is tilted in a different angle, so that each of them create, together with the reference arm from the retroreflector, an off-axis hologram on the CMOS monochrome camera (8 bit depth, 5.2 $\mu m/pixel$, DCC1545M, Thorlabs), so that the two off-axis holograms have orthogonal fringes patterns with respect to each other.

It is assumed that the beam spot projected onto the camera is at least as twice as large as the camera sensor, which is the typical case when using large-magnification objectives. The purpose of the ND filter in **Figure 1** is to balance the intensity levels from each arm of the multiplexing interferometer, enhancing the final multiplexed hologram fringe visibility.

Phase Reconstruction Algorithm

The recorded multiplexed hologram is digitally Fourier transformed, and the resulting spatial spectrum is comprised of a DC term and two non-overlapping pairs of cross-correlation (CC) terms, each pair is from a different wavelength channel. Since the two interference fringe patterns recorded on the camera are orthogonal with respect to each other, the resulting CC terms are located on orthogonal axes in the spatial spectrum. In contrast to field-of-view multiplexing [13], no cross-terms occur between the wavelength channels, since the two different lasers do not create mutual interference resulted in unwanted terms between the useful CC terms.

Figure 2 demonstrates each of the interference channels (regular off-axis holograms) independently, green channel in **Figure 2A** and red channel in **Figure 2B**, indicating the active mirrors each time, as obtained on the monochromatic camera by blocking the other mirror. **Figure 2C** shows both wavelength channels together, creating the multiplexed off-axis hologram on the monochromatic camera.

From the spatial spectrum, we crop one CC from each pairs of CCs, as marked in **Figure 2D**, and then inverse Fourier-transformed them, resulting in the complex wavefronts of the

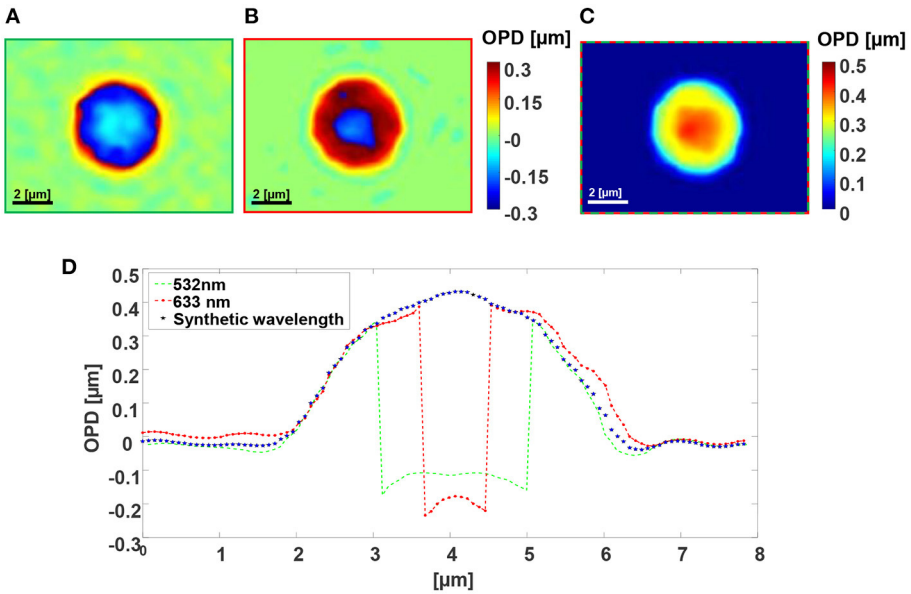

FIGURE 3 | Dual-wavelength OPD reconstruction of a 5 μm silica microbead in water. **(A)** Wrapped OPD profile as obtained in the green channel. **(B)** Wrapped OPD profile as obtained in the red channel. **(C)** OPD profile obtained after using the proposed simultaneous F-2WL module. See dynamics in **Supplementary Video 1**. **(D)** Vertical cross-sections across the center of the cell in **(A–C)**.

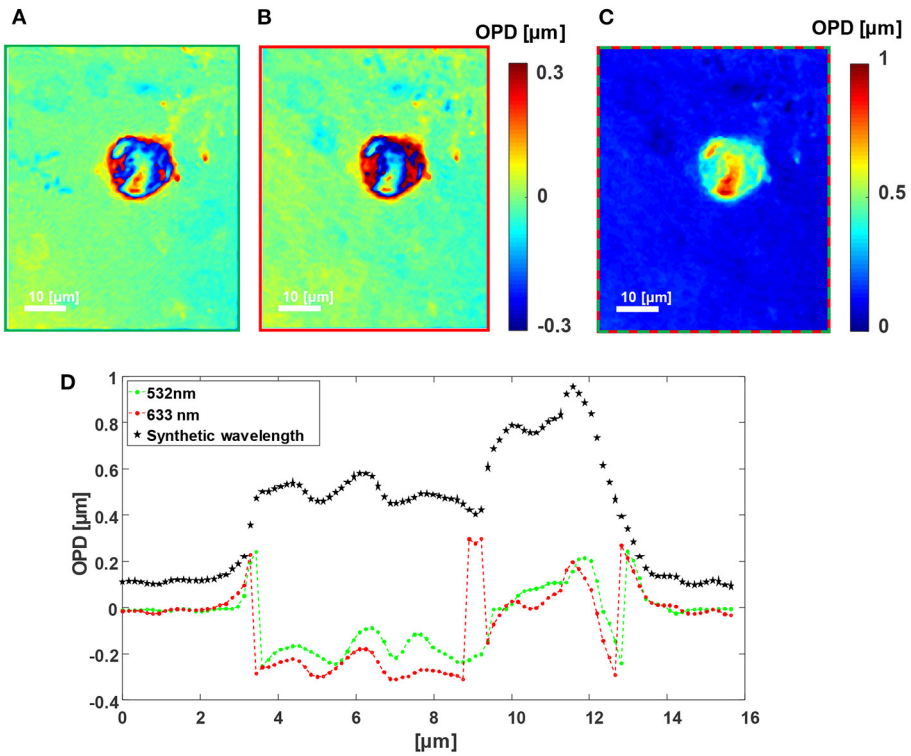

FIGURE 4 | Dual-wavelength OPD reconstruction of a human cancer cell. **(A)** Wrapped OPD profile as obtained in the greed channel. **(B)** Wrapped OPD profile as obtained in the red channel. **(C)** OPD profile obtained after using the proposed simultaneous F-2WL module. See dynamics in **Supplementary Video 2**. **(D)** Vertical cross-sections across the center of the cell in **(A–C)**.

same sample, each acquired under a different illumination wavelength. To reduce stationary coherent noise and beam curvature, we can divide each of the cell sample wavefront by this sample-free background wavefront that does not contain any biological cell sample on the entire beam spot. For this stage, a multiplexed hologram without the sample present is recorded, containing the reference background profiles for both wavelength channels. This stage is not obligatory, but even if performed it does not disturb the recording of the dynamic process since it is done only once, before or after the recording of the dynamic process.

Since the phase arguments of the resulting complex wavefronts are periodically bounded to the range of 0 and 2π, phase ambiguities occur in places where the sample is optically thicker than the illumination wavelength. These ambiguities occur in different spatial locations in each wavelength channel. The setup is designed to resolve this issue by applying the synthetic phase unwrapping process that recovers the true phase values without ambiguities. Hence, it reduces the need for computationally heavy algorithms. The quantitative phase profile extracted from each digitally processed interference pattern is digitally refocused first by assessing the Tamura's coefficient for best refocusing criteria [15].

The two separate illumination wavelengths λ_i, where $i = 1, 2$, record $0 < \varphi_i(x, y, \lambda_i) < 2\pi$, respectively for each wavelength. The synthetic OPD is obtained by simply subtracting the two wrapped phase maps, as follows:

$$OPD_{12}(x,y) = \left[\frac{\varphi_2(x,y,\lambda_2) - \varphi_1(x,y,\lambda_1)}{2\pi}\right]\Lambda, \qquad (2)$$

where $\Lambda = \lambda_1\lambda_2/|\lambda_1 - \lambda_2|$ is the synthetic (beat) wavelength, which, in our case, is equal to approximately 3.37 μm. This synthetic wavelength is larger than both individual wavelengths, and it is also larger than the maximal object optical thickness. Having an object that is optically thinner than the synthetic wavelength ensures no phase unwrapping. For thicker samples, larger synthetic wavelength can be reached by selecting closer illumination wavelengths. On the other hand, the technique is more pruned to noise as result of image subtraction in this case.

Human Colon Cancer Cell Line Preparation

HT-29 human colon cancer cell line was acquired from the ATCC. The growth medium used for these cells was Dulbecco's Modified Eagle's Medium (DMEM) (BI, SN. 01-55-1A) supplemented with 10% fetal bovine serum (FBS) [Biological industries (BI), SN. 04-007-1A], 4 mM L-Glutamin (BI, SN. 03-020-1B) and 1% antibiotics (BI, SN. 03-033-1B). The cell lines were incubated under standard cell culture conditions at 37°C and 5% CO_2 in a humidified incubator. For imaging, the cells were seeded on 24 × 60 mm #1 glass microscope cover-slip placed inside a Petri dish. After 48 h in growth medium, the cells reached about 20% confluence and washed with PBS, and then fixed by methanol for 1 min.

Sperm Cell Collection and Preparation

Upon obtaining the Tel Aviv University's IRB approval, we imaged human sperms. The collected raw semen samples were liquefied at room temperature for half an hour. Standard density gradient based-centrifugation for sperm enrichment was applied for separation of the cells before allowing it to liquefy again. Next, the spermatozoa were cleaned and isolated using the PureCeption Bi-layer kit (Origio, Målov, Denmark). Briefly, upper phases were removed to obtain the leftover pellet, which was resuspended in 5 mL modified human tubal fluid (HTF) medium (Irvine Scientific, CA, USA), and was centrifuged at 500 g for 5 min at 400 RCF in room temperature. Following this, micropipette collection of the sorted sperm cells is performed and the resulted sample is resuspended in 0.1 mL HTF. Ten milliliter of 3:1 methanol to acetic acid solution were then applied on the sample for 5 min. Then, the cells were centrifuged at 800 g for 5 min, the supernatant was discarded, and the pellet was resuspended in 0.2 mL of fixative solution. The sperm was imaged after being dried.

RESULTS

Figures 3, **4** shows the wrapped quantitative OPD profiles of a 5 μm silica microbead in water and a cancer cell, respectively, as obtained while imaged under the green channel (**Figures 3A**, **4A**), under the red channel (**Figures 3B**, **4B**), and under two-wavelength phase unwrapping using the proposed F-2WL module (**Figures 3C**, **4C**), each is obtained in a single camera exposure. Dynamic imaging of the microbead and the cancer cell are shown in **Supplementary Videos 1**, **2**, respectively. **Figure 3D** shows a vertical cross-section through the center of the OPD profile. It demonstrates that after two-wavelength

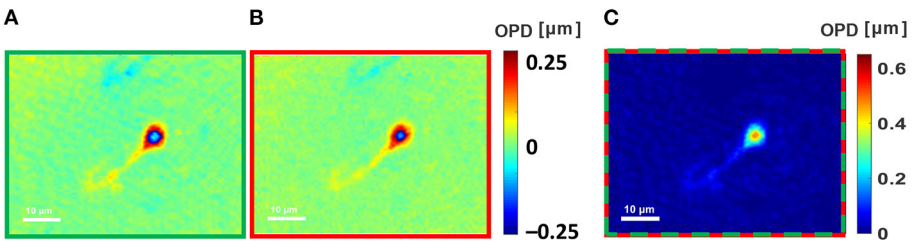

FIGURE 5 | Dual-wavelength OPD reconstruction of a human sperm cell. **(A)** Wrapped OPD profile as obtained in the greed channel. **(B)** Wrapped OPD profile as obtained in the red channel. **(C)** OPD profile obtained after using the proposed simultaneous dual-wavelength module. See dynamics in **Supplementary Video 3**.

unwrapping, the final image is continuous and does not contain large jumps, as apparent in both cross-sections of the OPD profiles obtained under a single-wavelength illumination.

Figure 5A shows the quantitative OPD profile of a human sperm cell as imaged under the green channel, and **Figure 5B** shows the same cell as imaged under the red channel, demonstrating that ambiguities occur in different locations. **Figure 5C** presents the quantitative OPD profile, as imaged by the simultaneous F-2WL module proposed here. Again, no phase ambiguities occur in the latter profile and still the acquisition is done in a single camera exposure. **Supplementary Video 3** shows the cell, scanned while moving the sample stage, demonstrating the capability of the method for dynamic imaging.

CONCLUSIONS

In summary, the F-2WL module is a flipping interferometer, allowing simultaneous acquisition of the complex wavefront of the sample under two different illumination wavelengths. This module is compact and contains only a few and simple components; hence it is accessible, affordable and can fit as a portable device at the output of a routine laboratory microscope, illuminated by two wavelengths of temporally coherent light sources. We used this module for two-wavelength phase unwrapping, using which thicker transparent objects can be acquired without using digital phase unwrapping algorithms that are computationally heavy. Since the module allows the acquisition of a multiplexed off-axis hologram containing the complex wavefronts in the two wavelength channels in a single camera exposure, it is highly suitable for imaging dynamic samples. The method assumes that the sample is empty in three-quarters of the optical field of view. In the fourth quarter, used as the sample beam, the sample can be dense. This is possible by controlling the seeding of the cells, by cleaning cells from the culture before imaging, or by using square chambers and locating the beam at one of the corners of the square. In addition to two-wavelength phase unwrapping, the proposed module can be used for simultaneous interferometric acquisition of two-wavelength channels for other applications, such as interferometric spectroscopy [16] and reduction of coherence-induced disturbances [17, 18]. We expect that in the future, this module will be used for quantitative phase imaging of highly dynamic samples, such as for flow cytometry, while enabling both faster acquisition and processing.

DATA AVAILABILITY STATEMENT

The raw data supporting the conclusions of this article will be made available by the authors, without undue reservation.

ETHICS STATEMENT

The studies involving human participants were reviewed and approved by Tel Aviv University's IRB. The patients/participants provided their written informed consent to participate in this study.

AUTHOR CONTRIBUTIONS

LK designed and built the setup, conducted experiments, designed and implemented the algorithms, processed the data, and wrote the paper. RG designed the algorithms and processed the data. IB prepared the biological samples for imaging. NS conceived the idea, designed the setup and algorithms, wrote the paper, and supervised the project. All authors contributed to the article and approved the submitted version.

FUNDING

This work was supported by Tel Aviv University's Light-Matter Interactions Center.

SUPPLEMENTARY MATERIAL

The Supplementary Material for this article can be found online at: https://www.frontiersin.org/articles/10.3389/fphy.2021.667023/full#supplementary-material

Supplementary Video 1 | Dynamic OPD maps of a 5 μm silica microbead.

Supplementary Video 2 | Dynamic OPD maps of a cancer cell.

Supplementary Video 3 | Dynamic OPD maps of a sperm cell.

REFERENCES

1. Shaked NT, Satterwhite LL, Wax A. Quantitative analysis of biological cells using digital holographic microscopy. In: Rosen J, editor. *Holography, Research and Technologies*. London: InTech (2011). p. 219–36.
2. Girshovitz P, Shaked NT. Generalized cell morphological parameters based on interferometric phase microscopy and their application to cell life cycle characterization. *Biomed Opt Express.* (2012) 3:1757–73. doi: 10.1364/BOE.3.001757
3. Ghihlia DC, Pritt MD. *Two-Dimensional Phase Unwrapping: Theory, Algorithms, and Software.* Hoboken, NJ: Wiley (1998).
4. Gass J, Dakoff A, Kim MK. Phase imaging without 2π ambiguity by multiwavelength digital holography. *Opt Lett.* (2003) 28:1141–3. doi: 10.1364/OL.28.001141
5. Rinehart MT, Shaked NT, Jenness NJ, Clark RL, Wax A. Simultaneous two-wavelength transmission quantitative phase microscopy with a color camera. *Opt Lett.* (2010) 35:2612–4. doi: 10.1364/OL.35.002612
6. Kühn J, Colomb T, Montfort F, Charrière F, Emery Y, Cuche E, et al. Real-time dual-wavelength digital holographic microscopy with a single hologram acquisition. *Opt Express.* (2007) 15:7231–42. doi: 10.1364/OE.15.007231
7. Khmaladze A, Kim M, Lo C-M. Phase imaging of cells by simultaneous dual-wavelength reflection digital holography. *Opt Express.* (2008) 16:10900–11. doi: 10.1364/OE.16.010900
8. Shaked NT, Micó V, Trusiak M, Kus A, Mirsky SK. Off-axis digital holographic multiplexing for rapid wave front acquisition and processing. *Adv Optics Photon.* (2020) 12:556–611. doi: 10.1364/AOP.384612
9. Abdelsalam DG, Kim D. Real-time dual-wavelength digital holographic microscopy based on polarizing separation. *Opt Commun.* (2012) 285:233–7. doi: 10.1016/j.optcom.2011.09.044

10. Guo R, Wang F. Compact and stable real-time dual-wavelength digital holographic microscopy with a long-working distance objective. *Opt Express.* (2017) 25:24512–20. doi: 10.1364/OE.25.024512
11. Turko NA, Shaked NT. Simultaneous two-wavelength phase unwrapping using an external module for multiplexing off-axis holography. *Opt Lett.* (2017) 42:73–6. doi: 10.1364/OL.42.000073
12. Roitshtain D, Turko NA, Javidi B, Shaked NT. Flipping interferometry and its application for quantitative phase microscopy in a micro-channel. *Opt Lett.* (2016) 41:2354–7. doi: 10.1364/OL.41.002354
13. Rotman-Nativ N, Turko NA, Shaked NT. Flipping interferometer with doubled imaging area. *Opt Lett.* (2018) 43:5543–6. doi: 10.1364/OL.43.005543
14. Liu L, Shan M, Zhong Z, Liu B, Luan G, Diao M, et al. Simultaneous dual-wavelength off-axis flipping digital holography. *Opt Lett.* (2017) 42:4331–4. doi: 10.1364/OL.42.004331
15. Tamamitsu M, Zhang Y, Wang H, Wu Y, Ozcan A. A robust holographic autofocusing criterion based on edge sparsity: comparison of Gini index and Tamura coefficient for holographic autofocusing based on the edge sparsity of the complex optical wavefront. *Proc SPIE.* (2018) IV:105030J. doi: 10.1117/12.2291179
16. Turko NA, Shaked NT. Erythrocyte volumetric measurements in imaging flow cytometry using simultaneous three-wavelength digital holographic microscopy. *Biomed Opt Express.* (2020) 11:6649–58. doi: 10.1364/BOE.404368
17. Kosmeier S, Langehanenberg P, von Bally G, Kemper B. Reduction of parasitic interferences in digital holographic microscopy by numerically decreased coherence length. *Appl Phys B.* (2012) 106:107–15. doi: 10.1007/s00340-011-4667-0
18. Larivière-Loiselle C, Bélanger E, Marquet P. Polychromatic digital holographic microscopy: a quasicoherent-noise-free imaging technique to explore the connectivity of living neuronal networks. *Neurophoton.* (2020) 7:040501. doi: 10.1117/1.NPh.7.4.040501

Conflict of Interest: The authors declare that the research was conducted in the absence of any commercial or financial relationships that could be construed as a potential conflict of interest.

frontiers in Physics

BRIEF RESEARCH REPORT
published: 04 May 2021
doi: 10.3389/fphy.2021.653353

Monitoring Human Neutrophil Differentiation by Digital Holographic Microscopy

Maria Augusta do R. B. F. Lima[1,2] *and Dan Cojoc*[2]*

[1] Department of Physics, University of Trieste, Trieste, Italy, [2] Consiglio Nazionale delle Ricerche, Istituto Officina dei Materiali (CNR-IOM), Trieste, Italy

We report on the usefulness of digital holographic microscopy (DHM) for the assessment of human neutrophil differentiation from myeloid cells. The cell and nuclear regions have been designated by image segmentation of the optical phase function, and the changes of the cell nucleus morphology in relation to the whole cell morphology have been examined during the process of granulocytic differentiation into mature neutrophils in PLB-985 cell line. Nucleus phase volume and circularity and the ratios between the nucleus and the cell projected area and volume provide a reliable set of parameters to characterize the maturation process. As control, cell differentiation has been monitored in parallel using standard nucleus staining and fluorescence imaging. From this research, it emerged that DHM can be used as a valid label-free solution, alternatively to the standard staining technology.

Keywords: digital holography microscopy, neutrophil differentiation, PLB-985 cell line, cell and nucleus morphology, label-free

OPEN ACCESS

Edited by:
Vicente Micó,
University of Valencia, Spain

Reviewed by:
Björn Kemper,
University of Münster, Germany
Nirmal Mazumder,
Manipal Academy of Higher Education, India

***Correspondence:**
Dan Cojoc
cojoc@iom.cnr.it

Specialty section:
This article was submitted to Optics and Photonics, a section of the journal Frontiers in Physics

Received: *14 January 2021*
Accepted: *26 March 2021*
Published: *04 May 2021*

Citation:
do R. B. F. Lima MA and Cojoc D (2021) Monitoring Human Neutrophil Differentiation by Digital Holographic Microscopy. Front. Phys. 9:653353. doi: 10.3389/fphy.2021.653353

1. INTRODUCTION

Human neutrophils are central players in innate immunity, a major component of inflammatory responses, and a leading model for cell motility and chemotaxis. The neutrophils are generated from granulocyte-monocyte progenitors (GMPs) in the bone marrow, where they undergo several stages of maturation [1]. Primary, mature blood neutrophils have a short lifetime and lack proliferation and transfection capacity, thus limiting their *ex vivo* experimental use in the laboratory [2]. Therefore, protocols using human myeloid leukemia cell lines, such as HL-60 and PLB-985 (which provides higher differentiation efficiency), have been developed for neutrophil differentiation *in vivo* [3, 4]. In the presence of appropriate inducing agents, these cell lines can undergo granulocyte differentiation into mature neutrophil-like granulocytes [1, 2, 5]. The assessment of the differentiation process is based on cellular morphological parameters, the molecular and functional properties of differentiated cells, defining a neutrophil-like phenotype which closely resembles the mature blood neutrophils [5, 6].

Non-differentiated cells are considered as being at the promyelocytic stage. Activation by chemical agents transforms them along the myeloid pathway into myelocytes (Ms), metamyelocytes (MMs), band neutrophils (BNs) and, lastly, segmented neutrophils (SNs) [1, 2, 7]. This transformation process takes about 4–6 days. Monitoring the changes in nuclear morphology represents one of the most reliable technique to assess different stages and the success of the differentiation process [6, 8, 9]. Thus, cells in SN stage, presenting polymorph nucleus formed usually by two to five nuclear segments, are considered as mature neutrophil-like cells. In the first two stages [promyelocyte (PM) and M], cells have compact ellipsoidal nuclei occupying almost all

of the cell body. Nuclei of the MMs begin to be distorted and present indentations. BNs have more distorted nuclei, often with a "horseshoe" shape, while in the final stage, SNs present multi-lobed nuclei connected between them [6, 8, 9].

In biological laboratories, the current practice to examine the morphology of the nucleus during neutrophil differentiation involves nuclear staining and epifluorescence microscopy [7, 10–12]. Since these techniques require sample preparation and provide relatively poor information, they are mostly used to evaluate the final stage of the differentiation process. Moreover, the labeling methods have a potential risk of altering cellular functions and phototoxicity from repeated excitation of the dye in the imaging process, which limits the duration of the time-lapse imaging [12]. The use of non-quantitative phase microscopy, which has become a pervasive tool for contrast enhancement and qualitative examination of cellular morphology [13], is limited by the low contrast enhancement for these cells.

Label-free quantitative phase imaging (QPI) [14–16], including digital holographic microscopy (DHM) [17–19], has been recently implemented in different setups to study morphology, structure, and dynamics of unstained living cells. QPI is based on the measurement of the optical phase (OP) shift introduced by the sample cell, which allows to calculate the optical path difference (OPD): $OPD = OP \cdot 2\pi/\lambda$, where λ is the wavelength of the laser beam. The OPD combines the physical thickness, h, and the difference between the refractive index (RI) of the cell, n_c, and the RI of the medium, n_m: $OPD = h \cdot \Delta n$, where $\Delta n = (n_c - n_m)$. The RI of the cell represents an important parameter which can be used to correlate with other cell biophysical parameters, such as dry and wet mass, protein concentration, elasticity, and conductivity, and to study certain cell metabolic activities, such as cell division and infection [20]. To isolate the RI from the thickness in OPD, several solutions are possible [21]. Assuming that the RI of the suspension medium is known and that cells in suspension are spherical, the simplest and fastest method to determine the integral RI is to approximate the local thickness [22]. This method has been used to show changes in the subcellular structure and the RI of differentiating myeloid precursor cells within 1 day of differentiation induction [23] and to demonstrate that cell nuclei have lower RI than cytoplasm [24]. Another approach is performing two OPD measurements, each of them with a different surrounding medium [25, 26] or a different wavelength [27], thus obtaining two linear equations with two unknowns which enable the decoupling of the integral RI from the thickness. Other solutions for the thickness-RI coupling problem are thoroughly reviewed in Dardikman and Shaked [21].

Nonetheless, various cell morphological features can also be directly extracted from the OPD, e.g., OPD mean/median, phase volume, phase surface area, dry mass, phase sphericity, phase statistical parameters, and energy [28]. Such features have been successfully combined with machine learning algorithms in cytometric classification of cancer cells and blood cells [29], phenotyping of cell lines [30], classification of leukocytes flowing in microfluidics [31], or automatic detection of *Plasmodium falciparum* [32]. Combining QPI with dye exclusion cell volumetric imaging, the cell volume can be quantified independently of the RI of the cell, enabling high-throughput neutrophil differentiation from other white blood cells flowing in an optofluidic device [33].

Using QPI with a common arrangement for DHM, in this study, we investigate on the usefulness of a set of cell parameters extracted directly from OPD to supervise neutrophil differentiation from the PLB-985 cell line. Since the differentiation protocol includes five stages, namely, PMs, Ms, MMs, BNs, and SNs, and lasts for about 5–6 days, a set of OPD images were taken every day and analyzed. The reconstructed OPD functions for a set of cells in full field were first segmented to separate the cells from the background and then a second segmentation was applied at the single cell level to demarcate the central region with high phase values, designating to the nuclear region. The OPD and a set of nine morphological parameters were calculated for each cell. Comparing the values of the parameters calculated for cells from different stages, we discuss their relevance and show that DHM can be successfully employed to distinguish between different cell stages of neutrophil differentiation.

2. MATERIALS AND METHODS

2.1. Cell Preparation

Neutrophil differentiation from its promyelocytic progenitors was performed following the dimethyl sulfoxide (DMSO) protocol described in Tucker et al. [4]. Briefly, PLB-985 cells (DSMZ, Braunschweig, Germany) were cultured in RPMI 1640 media supplemented with 10% fetal bovine serum (FBS), 1% L-Glutamin, and 100 mg/mL and 100 U/mL (P/S) of streptomycin and penicillin, respectively, at 37°C in a humidified atmosphere with 5% CO_2. Cell cultures were passed three times per week, maintaining cell densities between 10^5 and 2×10^6 cells per mL. The cells were differentiated into a neutrophil-like state by culturing at an initial density of 2×10^5 using RPMI 1640 media supplemented with 10% FBS concentration and 1.3% DMSO for 6 days.

Cell differentiation was monitored every 24 h for 6 days beginning from day 0. For each measurement, 1 mL of cell suspension was taken from the culture flask. The suspension was then centrifuged, and the supernatant was removed to exclude debris and impurities. Then, the sample was resuspended and incubated for 5 min at 37°C. To measure the cells, 50 μL of cell suspension was placed in a 18 mm diameter glass slide. About 2–3 min was required for the cells to sediment before imaging it. For DHM imaging, the sample was resuspended in RPMI 1640 media, while for fluorescence imaging, the sample was resuspended in a Hoechst 33342 solution of 1:1,000 in RPMI 1640 media as described in the study by Chazotte [11].

2.2. Digital Holographic Microscopy

We used a simplified version of a previously developed DHM off-axis configuration, based on a Mach-Zehnder interferometer [34, 35]. The laser beam ($\lambda = 520\,nm$, Thorlabs LP520-SF15) was split into object and reference beams by a fiber optic coupler (Thorlabs TW560R3F1) and recombined by a cube beam splitter

(Thorlabs, BS079) to generate the hologram, which was recorded on a sCMOS camera (Thorlabs CS2100M-USB Quantalux). The power P of the laser was set to $P < 1\,mW$, and the exposure time to $1 < t < 5\,ms$. The magnification of the microscope was 33×, with a lateral spatial resolution $d \sim 600\,nm$. An aspheric lens (Thorlabs C230TMD-A) with the numerical aperture NA = 0.55 was used as the objective lens. The size of the sCMOS sensor was $4.8 \times 4.8\,\mu m$. The inter-fringe, i, of the interference pattern was adjusted to five pixels on the sensor, corresponding to 750 *nm* at the sample plane.

The numerical reconstruction of the optical phase was performed using a method based on the spatial filtering at the Fourier plane from the recorded hologram [36]. Thus, the complex amplitude distribution of the transmitted frequency band-pass was recovered by applying a Fourier transform over the recorded hologram while considering a circular spatial filtering mask located at one of the diffraction orders. After the filtering and centering process at the Fourier domain, the complex amplitude was Fourier transformed again to propagate it to the sample plane and retrieve the wrapped OP. The final step, phase unwrapping, is used to get the reconstructed OP function. Since these issues are of particular significance in the reconstruction process, we defined the parameters for spatial filtering, propagation, and phase unwrapping by calibration with silica microbeads of different diameters ($3 - 30\mu m$) [34]. Microbeads are the perfect sample for calibration purposes since they are microspheres of a single material (silica, polystyerene, etc.) with known value of the RI.

2.3. Segmentation of the OPD Function for Cell and Nuclear Region Designation

In the first step, the OPD map was segmented to isolate the cells from the background by applying the bimodal Otsu's method [37, 38] implemented in MATLAB, using the following two functions, *multitresh* (L = 2 levels) and *imquantize*, from the Image Processing Toolbox. To remove the incongruous cell spots resulting from segmentation, the phase volume of each cell spot was calculated and those spots with the phase volume below a predetermined threshold were discarded.

The designation of the nuclear region was accomplished in a second segmentation applied to each cell, using *multitresh* with ($L = 4$). The number of segmentation levels is supported by the Histogram-based Valley Estimation Method presented in the study by Huang et al. [39], where the number of clusters for an image to be properly segmented depends on the number of

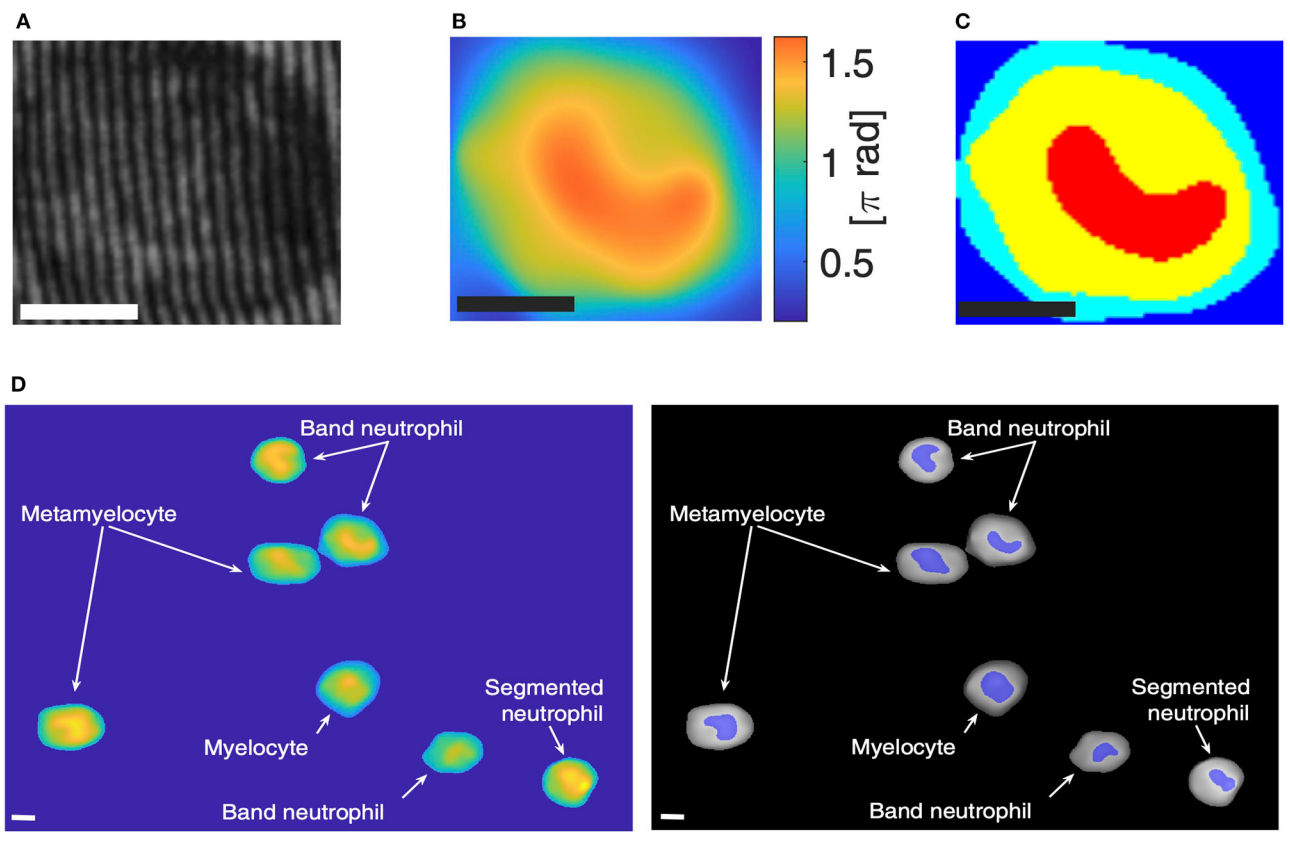

FIGURE 1 | Optical phase (OP) reconstruction and cell selection. **(A)** Recorded hologram, **(B)** reconstructed OP, **(C)** segmentation, **(D)** full field image taken at day 5 showing different types of cells; left: after cell selection, the colors indicate cell height; right: cell and nucleus regions are shown after cell and nucleus selection. Scale bars: 5 μm.

valleys in the histogram of the image. After segmentation, the first level is assigned to the background pixels, the second and the third levels to the cell cytoplasm region, and the fourth level to cell nucleus. The segmentation method is described in detail in **Supplementary Material**.

3. RESULTS AND DISCUSSION

In order to assess Optical phase (OP) imaging by DHM as a free-label technique for characterization and discrimination of the cell stages, we monitored the differentiation of PLB-985 cell line from PMs to SNs and imaged the cells at intervals of 24 h for 6 days during the neutrophil differentiation cycle.

As described in section 2.3, segmentation of the reconstructed OP for an image containing several cells was used to select the cells from the background and delineate the estimated nucleus from the other part of the cell. An example of the image taken at day 5 is illustrated in **Figure 1D**, showing the presence of multiple types of cells as indicated by the morphology of the cell and the designated nuclear regions, characterized by high values of the OPD function. At a first qualitative inspection, using the morphological phenotypes reported in literature and as already mentioned in the "Introduction" section, we can recognize one SN, three BNs, two MMs, one M. BNs are the most frequent, as expected for day 5. The presence of other types of cells is justified by the various biological times employed by different

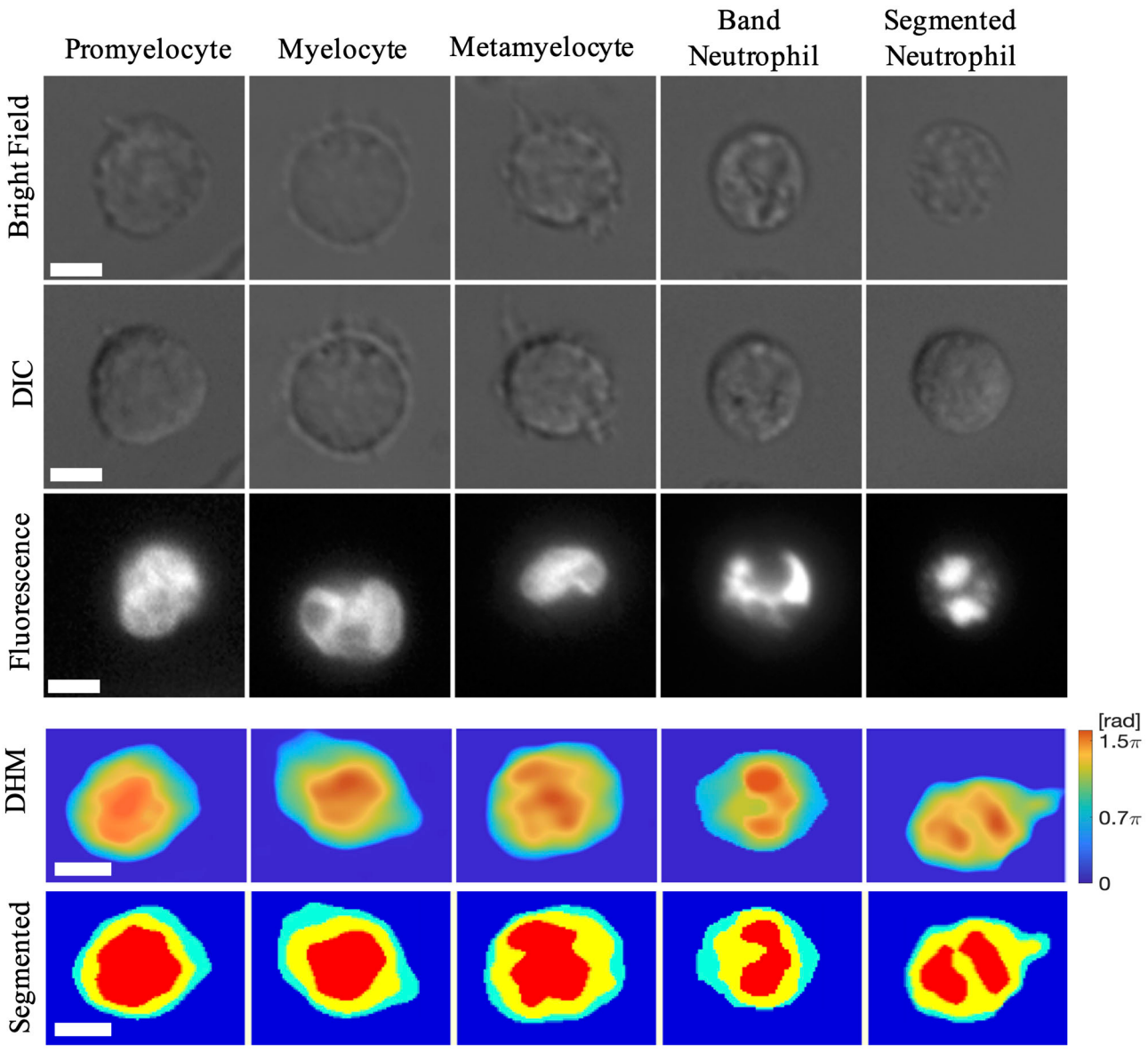

FIGURE 2 | Example of cells in different maturation stages. The first three rows show brightfield, DIC, and fluorescence images, where each column representing the same cell. The last two rows show the reconstructed OP difference (OPD) and cell segmentation. Scale bar: $5\mu m$.

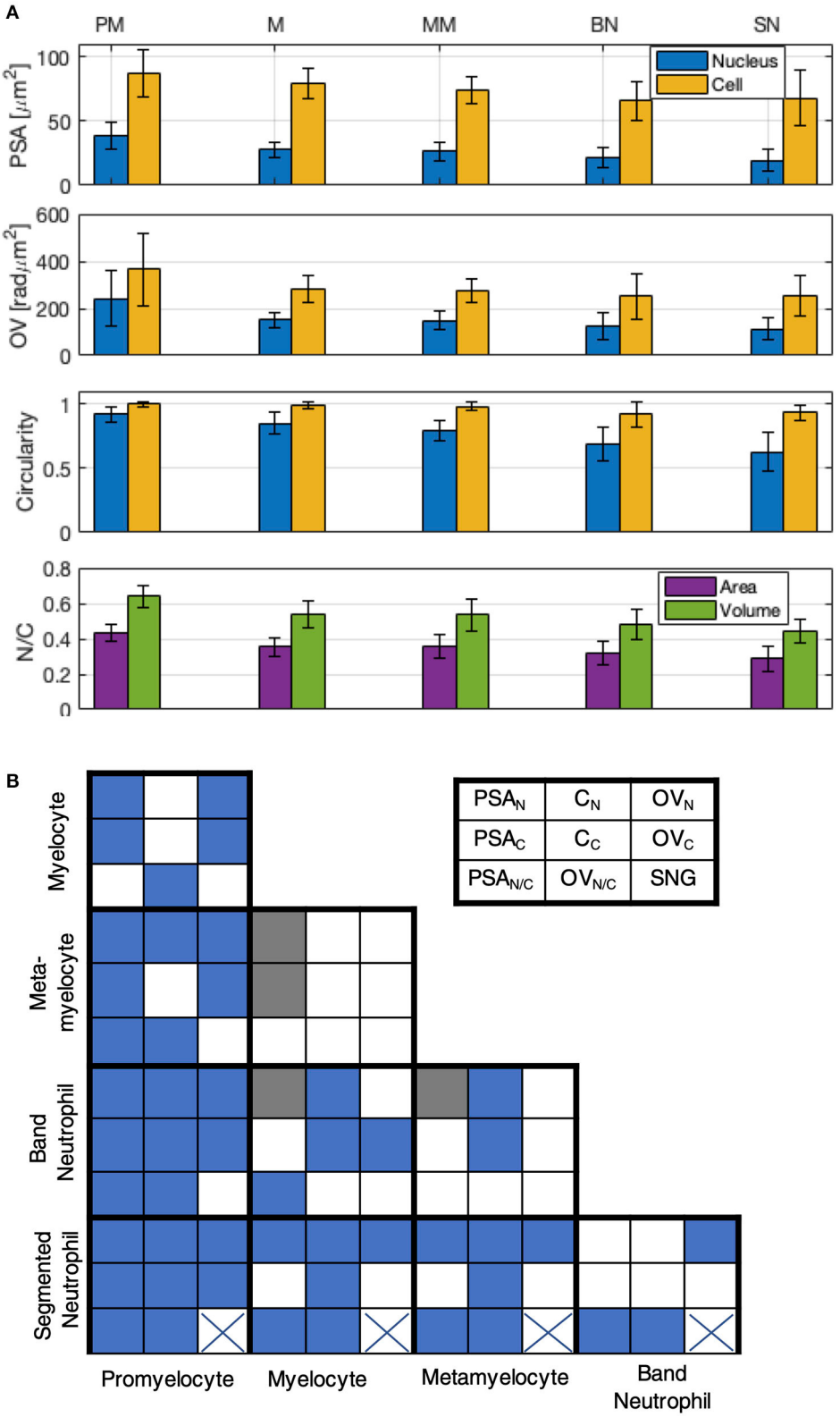

FIGURE 3 | Cell and nucleus morphological parameters. **(A)** Projected Surface Area (PSA), Optical Volume (OV), Circularity (C), and ratios of nucleus to cell, NC, of PSA and OV. Mean and SD values for: promyelocytes (PM, $N = 22$), myelocytes (M,$N = 21$), metamyelocytes (MM, $N = 24$), band neutrophils (BN, $N = 21$), segmented neutrophils (SN, $N = 25$). **(B)** Diagram showing the results of the Mann-Whitney U test calculated for nine parameters, for each class pair. A p-value < 0.05

(Continued)

FIGURE 3 | is indicated by blue color. The legend of the parameters is shown top right: PSA_N, PSA_C—nucleus PSA and cell PSA, respectively; C_N, C_C—nucleus circularity and cell circularity, respectively; OV_N, OV_C—nucleus OV and cell OV, respectively; $PSA_{N/C}$, $OV_{N/C}$—ratio between the cell and nucleus for PSA and OV; SNG—segmented nucleus.

cells to transform [1]. This observation suggests that OPD and the segmented OPD could be used to characterize different stages during neutrophil differentiation.

Since the results reported in the literature are based on nuclear staining and fluorescence imaging, we also performed image analysis of the nucleus morphological changes using Hoechst staining and live cell fluorescence imaging (Nikon TE2003-E inverted microscope, 60X, DAPI fluorescence cube). An example of nuclear morphology changes during the five stages of the neutrophil differentiation is shown in **Figure 2**. The first two rows are brightfield and DIC images, which help to define the cell shape but do not allow to discriminate the nucleus. Complementarily, the fluorescence images illustrated in the third row for the same cell allow the identification of the nucleus. At the beginning of the differentiation, corresponding to PM and M cells, the cell nucleus changes round to oval, occupying more than 50% of the cell projected surface area. The oval shape begins to be preponderant to round shape for M, and the ratio between nucleus and cell area is also slightly smaller than Ms for PMs. As the cell matures, the nucleus begins to be indented and becomes asymmetric with respect to the cell center (MM). A more mature cell presents highly indented nucleus and often a "horseshoes" shape (BN), arriving to the segmentation of the nucleus at the end (SN).

Free-label DHM imaging for the five stages of the cell differentiation is exemplified in the last two rows of **Figure 2**. The OPD and the segmented OPD for an isolated cell from each of the five stages are represented, confirming the observations acquired from brightfield and fluorescence imaging on the cell and nucleus configuration during the differentiation cycle. Moreover, the OPD values in the cell and nuclear regions assigned by segmentation provide additional information on the cell morphological features as the OP volume.

We monitored the neutrophil differentiation recording five DHM image fields/day at intervals of 24 h starting from cell plating. Two different differentiation cycles were completed. The OPD was calculated for each field, and a qualitative inspection was performed as discussed above and showed in **Figure 1**, discarding the cells which did not correspond to the differentiation stage of the respective day. We created then five groups of $N > 20$ cells, corresponding to the five stages: PM, M, MM, BN, and SN, and calculated the parameters defined above for each cell.

Cellular morphologic parameters as projected surface area (PSA), OP volume (OV), and circularity (C) have been effectively used for the characterization of red blood cells [35, 40, 41] in QPI and DHM. In this study, we propose similar parameters for the nucleus, including the ratios between the values for nucleus and cell as parameters. We define the following morphological parameters:

1. Projected surface area (PSA) of the cell and nuclear regions:

$$PSA = N \cdot (ps/M)^2 \tag{1}$$

   where N is the number of pixels within the cell nucleus region, $ps = 4.8 * 4.8 = 23.04\ \mu m^2$ is the area of a single pixel of the CMOS sensor, and M = 33× is the microscope magnification.
2. Optical Phase Volume (OV) of the cell and nuclear regions:

$$OV = PSA \cdot \sum_{i=1}^{N} OPD_i \tag{2}$$

   where *OPDi* is the optical phase difference of cell/nucleus corresponding to the pixel.
3. Circularity (C) of the cell and nuclear regions:

$$C = 4\pi \cdot PSA/Pm \tag{3}$$

   where *Pm* is the perimeter of the cell/nucleus. Circularity expresses the roundness of an object, e.g., $C = 1$ means a perfectly round cell, as a circular disk.
4. PSA and OV nucleus to cell, N/C, aspect ratio:

$$\begin{aligned} PSA_{N/C} &= PSA_N/PSA_C \\ OV_{N/C} &= OV_N/OV_C \end{aligned} \tag{4}$$

   where *N* stays for nucleus, *C* for cell, *PSA* for projected surface area, and *OV* for optical volume.

The mean and SD values for each parameter are presented in **Figure 3A** for each group of cells. This study shows that PSA and OV monotonously decrease as the cells maturate, both for the cell and the nucleus region. The cell C, C_C, is preserved close to $C_C = 1$ for PM, N, and MM, while decreasing slightly for the last two stages, BN and SN ($C_C > 0.9$). As the cells present more protrusions in these two stages, the values for C are also more dispersed. The C values for nucleus, C_N, decrease more than $C_N > 0.8$ for PM and M, $C_N = 0.8 \pm 0.08$ for MM, $C_N = 0.69 \pm 0.13$ for BN and $C_N = 0.63 \pm 0.15$ for SN, indicating that the nucleus undergoes substantial morphological changes during the differentiation process. The relative morphological changes of the nucleus vs. cell are outlined by the N/C ratio for area and volume, respectively, $PSA_{N/C}$ and $OV_{N/C}$, in the last row of **Figure 3A**. Both ratios decrease monotonically during cell maturation, with a more pronounced change in $OV_{N/C}$.

We note that the values between neighboring stages overlap for some parameters, indicating that a set of parameters should be considered rather than a single parameter to characterize the differentiation stages. In order to test the weight of each parameter, we used the Mann-Whitney *U* test (or two-sided Wilcoxon rank sum test) for each pair of classes. The results are

schematically illustrated in **Figure 3B**: $p < 0.05$ (blue box) is considered as a threshold for good distinction between stages, $0.05 < p < 0.1$ (gray) as acceptable, and $p > 0.1$ (white) as non-confident.

It can be seen that all eight parameters are individually suitable to distinguish SN from PM. All parameters except cell PSA_C and cell OV_C are useful to discriminate SN from M and MM. Only three parameters ($OV_{N/C}$, $PSA_{N/C}$, $OV_{N/C}$) are available to distinguish between SN and BN. Note that all of them were extracted from the OPD, which is provided by DHM only. Additionally, the presence of a segmented nucleus, which is confidently detected from OPD, represents another useful parameter which distinguishes SN from all the other stages (crossed box in **Figure 3B**).

All eight parameters are suitable to distinguish BN from PM cells, four of the eight parameters to separate BN from M cells, and only two parameters to discriminate BN from neighboring stage, MM: the nucleus and cell circularity, C_N and C_C. We notice that these two parameters are complementary to the parameters which distinguish BN from the other neighboring stage, SN. Moreover, considering $0.05 < p < 0.1$ for an acceptable discrimination, the nucleus area, PSA_N, becomes an eligible parameter to distinguish between BN and MM or M.

As regards the MM cells, seven of the eight parameters are useful to distinguish MM from PM cells, but none is adequate using the criterium $p < 0.05$ to separate MM from M. However, considering $p < 0.1$, both NA and NC can be used to separate M from MM. Finally, five of eight parameters can be used to separate M from PM cells. These parameters are complementary to the parameters used to distinguish between BN and MM, and only two parameters are in common with the discrimination between BN and SN.

Five parameters can be used to separate M from PM cells. These parameters are complementary to the parameters used to distinguish between BN and MM, and only two parameters are in common with the discrimination between BN and SN.

According to the imposed criterium, $p < 0.05$, the nearest two classes seem to be MM and M cells. However, by relaxing the criterium to $p < 0.1$, two more parameters are indicated as suitable for MM and M cells discrimination.

The analysis of the results show that all these parameters are useful to discriminate between cells in different differentiation stages. Three of these parameters, OV_N, OV_C, $OV_{N/C}$, which have a central role for cell characterization and discrimination between differentiation stages, are extracted from the OPD, which is specific for DHM. These preliminary results suggest that a combination of the parameters derived by means of DHM in a multiparameter testing scheme would enable the characterization and monitoring of the different stages of cell differentiation.

We note that the OPD function was used directly, without decoupling the RI from the cell height. Although, the designation of the nuclear region by segmentation cannot be claimed as precise identification of the nucleus, the method appears useful to monitor the neutrophil differentiation cycle. Considering the recent findings showing that the nuclear RI is lower than the cytoplasm [24, 42], this affects the OV parameter. We calculated the OV of the value which corresponds to a physical volume bigger for the nucleus relative to the same value of the OV for the cell. Although the absolute values of the volume change, the relative differences between stages are not expected to be altered considerably because the changes are uniformly applied.

Another interesting point is the possible change of the cellular RI during the HL60 cells differentiation [23], indicating that the cells become less dense during differentiation. Since we measured only the OPD, we could not confirm that this observation also applied for PLB-985 cells cultured on substrate, but we observed a significant decrease of the $PSA_{N/C}$, which was associated with the decrease in the RI in this study.

4. CONCLUSION

In this study, we performed cell morphological analysis during promyelocytic differentiation into SN for both cell and nuclear regions using DHM as free-label optical imaging technique. We defined a set of eight morphological parameters and investigated their contribution to characterize cells belonging to one of the five maturation stages: PMs, Ms, MMs, BNs, and SNs.

We proved that DHM provides additional information with respect to the standard fluorescence imaging of stained nucleus. This information is related to the volumes of cells and nucleus and allows a better discrimination between different stages of neutrophil differentiation. We believe that DHM has been employed for the first time for monitoring neutrophil differentiation in PLB 945 cells. The results suggest DHM is a suitable free-label technique providing better cell characterization and discrimination between differentiation stages.

DATA AVAILABILITY STATEMENT

The original contributions presented in the study are included in the article/**Supplementary Material**; further inquiries can be directed to the corresponding author/s.

AUTHOR CONTRIBUTIONS

DC and ML conceived the project, analyzed and interpreted the data, and wrote the manuscript. DC designed and implemented the DHM. ML performed the experiments. All authors contributed to the article and approved the submitted version.

ACKNOWLEDGMENTS

The authors thanks Dr. Marta Stefania Semrau and Dr. Valentina Masciotti for the training in cell culture basics.

SUPPLEMENTARY MATERIAL

The Supplementary Material for this article can be found online at: https://www.frontiersin.org/articles/10.3389/fphy.2021.653353/full#supplementary-material

REFERENCES

1. Ng LG, Ostuni R, Hidalgo A. Heterogeneity of neutrophils. *Nat Rev Immunol*. (2019) 19:255–65. doi: 10.1038/s41577-019-0141-8
2. Summers C, Rankin SM, Condliffe AM, Singh N, Peters AM, Chilvers ER. Neutrophil kinetics in health and disease. *Trends Immunol*. (2010) 31:318–24. doi: 10.1016/j.it.2010.05.006
3. Dalton WJ, Ahearn MJ, McCredie KB, Freireich EJ, Stass SA, Trujillo JM. HL-60 cell line was derived from a patient with FAB-M2 and not FAB-M3. *Blood*. (1988) 71:242–7. doi: 10.1182/blood.V71.1.242.242
4. Tucker KA, Lilly MB, Heck LJ, Rado TA. Characterization of a new human diploid myeloid leukemia cell line (PLB-985) with granulocytic and monocytic differentiating capacity. *Blood*. (1987) 70:372–8. doi: 10.1182/blood.V70.2.372.372
5. Boulven I, Levasseur S, Marois S, Paré G, Rollet-Labelle E, Naccache PH. Class IA phosphatidylinositide 3-kinases, rather than p110γ, regulate formyl-methionyl-leucyl-phenylalanine-stimulated chemotaxis and superoxide production in differentiated neutrophil-like PLB-985 cells. *J Immunol*. (2006) 176:7621–7. doi: 10.4049/jimmunol.176.12.7621
6. Shehu S. *Regulation of Apoptosis of Myeloid Immune Cells: Implication for Cancer Therapy and Inflammation*. Liverpool: University of Liverpool (2017).
7. Bjerregaard MD, Jurlander J, Klausen P, Borregaard N, Cowland JB. The *in vivo* profile of transcription factors during neutrophil differentiation in human bone marrow. *Blood*. (2003) 101:4322–32. doi: 10.1182/blood-2002-03-0835
8. Iwasaki H, Akashi K. Myeloid lineage commitment from the hematopoietic stem cell. *Immunity*. (2007) 26:726–40. doi: 10.1016/j.immuni.2007.06.004
9. Lieber JG, Webb S, Suratt BT, Young SK, Johnson GL, Keller GM, et al. The *in vitro* production and characterization of neutrophils from embryonic stem cells. *Blood*. (2004) 103:852–9. doi: 10.1182/blood-2003-04-1030
10. Bezrukov A. Romanowsky staining, the Romanowsky effect and thoughts on the question of scientific priority. *Biotech Histochem*. (2017) 92:29–35. doi: 10.1080/10520295.2016.1250285
11. Chazotte B. Labeling nuclear DNA with Hoechst 33342. *Cold Spring Harbor Protoc*. (2011) 2011:pdb-prot5557. doi: 10.1101/pdb.prot5557
12. Siemann DW, Keng PC. Cell cycle specific toxicity of the Hoechst 33342 stain in untreated or irradiated murine tumor cells. *Cancer Res*. (1986) 46:3556–9.
13. Shaked NT, Zalevsky Z, Satterwhite LL. *Biomedical Optical Phase Microscopy and Nanoscopy*. Amsterdam; Boston, MA; Heidelberg; London; New York, NY; Oxford, Paris, San Diego, CA; San Francisco, CA; Singapore; Sidney: Academic Press (2013).
14. Park Y, Depeursinge C, Popescu G. Quantitative phase imaging in biomedicine. *Nat Photon*. (2018) 12:578–89. doi: 10.1038/s41566-018-0253-x
15. Popescu G. *Quantitative Phase Imaging of Cells and Tissues.* New York, NY; Chicago, San Francisco, CA; Lisbon; London; Madrid; Mexico City; Milan; New Delhi; San Juan; Seoul; Singapore; Sydney, NSW; Toronto, ON: Graw-Hill Education (2011).
16. Ferraro P, Wax A, Zalevsky Z. *Coherent Light Microscopy: Imaging and Quantitative Phase Analysis.* Vol. 46. Berlin: Heidelberg: Springer-Verlag (2011). doi: 10.1007/978-3-642-15813-1
17. Marquet P, Depeursinge C, Magistretti PJ. Review of quantitative phase-digital holographic microscopy: promising novel imaging technique to resolve neuronal network activity and identify cellular biomarkers of psychiatric disorders. *Neurophotonics*. (2014) 1:020901. doi: 10.1117/1.NPh.1.2.020901
18. Micó V, Zheng J, Garcia J, Zalevsky Z, Gao P. Resolution enhancement in quantitative phase microscopy. *Adv Opt Photon*. (2019) 11:135–214. doi: 10.1364/AOP.11.000135
19. Marquet P, Rappaz B, Magistretti PJ, Cuche E, Emery Y, Colomb T, et al. Digital holographic microscopy: a noninvasive contrast imaging technique allowing quantitative visualization of living cells with subwavelength axial accuracy. *Opt Lett*. (2005) 30:468–70. doi: 10.1364/OL.30.000468
20. Liu PY, Chin L, Ser W, Chen H, Hsieh CM, Lee CH, et al. Cell refractive index for cell biology and disease diagnosis: past, present and future. *Lab Chip*. (2016) 16:634–44. doi: 10.1039/C5LC01445J
21. Dardikman G, Shaked NT. Review on methods of solving the refractive index-thickness coupling problem in digital holographic microscopy of biological cells. *Opt Commun*. (2018) 422:8–16. doi: 10.1016/j.optcom.2017.11.084
22. Kemper B, Kosmeier S, Langehanenberg P, von Bally G, Bredebusch I, Domschke W, et al. Integral refractive index determination of living suspension cells by multifocus digital holographic phase contrast microscopy. *J Biomed Opt*. (2007) 12:054009. doi: 10.1117/1.2798639
23. Chalut KJ, Ekpenyong AE, Clegg WL, Melhuish IC, Guck J. Quantifying cellular differentiation by physical phenotype using digital holographic microscopy. *Integr Biol*. (2012) 4:280–4. doi: 10.1039/c2ib00129b
24. Schürmann M, Scholze J, Müller P, Guck J, Chan CJ. Cell nuclei have lower refractive index and mass density than cytoplasm. *J Biophoton*. (2016) 9:1068–76. doi: 10.1002/jbio.201500273
25. Rappaz B, Marquet P, Cuche E, Emery Y, Depeursinge C, Magistretti PJ. Measurement of the integral refractive index and dynamic cell morphometry of living cells with digital holographic microscopy. *Opt Express*. (2005) 13:9361–73. doi: 10.1364/OPEX.13.009361
26. Cardenas N, Mohanty S. Decoupling of geometric thickness and refractive index in quantitative phase microscopy. *Opt Lett*. (2013) 38:1007–9. doi: 10.1364/OL.38.001007
27. Boss D, Kühn J, Jourdain P, Depeursinge CD, Magistretti PJ, Marquet PP. Measurement of absolute cell volume, osmotic membrane water permeability, and refractive index of transmembrane water and solute flux by digital holographic microscopy. *J Biomed Opt*. (2013) 18:036007. doi: 10.1117/1.JBO.18.3.036007
28. Roitshtain D, Wolbromsky L, Bal E, Greenspan H, Satterwhite LL, Shaked NT. Quantitative phase microscopy spatial signatures of cancer cells. *Cytometry A*. (2017) 91:482–93. doi: 10.1002/cyto.a.23100
29. Nissim N, Dudaie M, Barnea I, Shaked NT. Real-time stain-free classification of cancer cells and blood cells using interferometric phase microscopy and machine learning. *Cytometry A*. (2020). doi: 10.1002/cyto.a.24227. [Epub ahead of print].
30. Lam VK, Nguyen T, Phan T, Chung BM, Nehmetallah G, Raub CB. Machine learning with optical phase signatures for phenotypic profiling of cell lines. *Cytometry A*. (2019) 95:757–68. doi: 10.1002/cyto.a.23774
31. Ugele M, Weniger M, Stanzel M, Bassler M, Krause SW, Friedrich O, et al. Label-free high-throughput leukemia detection by holographic microscopy. *Adv Sci*. (2018) 5:1800761. doi: 10.1002/advs.201800761
32. Park HS, Rinehart MT, Walzer KA, Chi JTA, Wax A. Automated detection of *P. falciparum* using machine learning algorithms with quantitative phase images of unstained cells. *PLoS ONE*. (2016) 11:e0163045. doi: 10.1371/journal.pone.0163045
33. Schonbrun E, Di Caprio G. Differentiating neutrophils using the optical coulter counter. *J Biomed Opt*. (2015) 20:111205. doi: 10.1117/1.JBO.20.11.111205
34. Picazo-Bueno JÁ, Cojoc D, Iseppon F, Torre V, Micó V. Single-shot, dual-mode, water-immersion microscopy platform for biological applications. *Appl Opt*. (2018) 57:A242–9. doi: 10.1364/AO.57.00A242
35. Merola F, Miccio L, Memmolo P, Di Caprio G, Galli A, Puglisi R, et al. Digital holography as a method for 3D imaging and estimating the biovolume of motile cells. *Lab Chip*. (2013) 13:4512–6. doi: 10.1039/c3lc50515d
36. Micó V, Zalevsky Z, Ferreira C, García J. Superresolution digital holographic microscopy for three-dimensional samples. *Opt Express*. (2008) 16:19260–70. doi: 10.1364/OE.16.019260
37. Otsu N. A threshold selection method from gray-level histograms. *IEEE Trans Syst Man Cybernet*. (1979) 9:62–6. doi: 10.1109/TSMC.1979.4310076
38. Gonzalez RC,Woods RE. *Digital Image Processing.* 3rd ed. Upper Saddle River, NJ: Prentice-Hall, Inc. (2006).
39. Huang DY, Lin TW, Hu WC. Automatic multilevel thresholding based on two-stage Otsu's method with cluster determination by valley estimation. *Int J Innov Comput Inform Control*. (2011) 7:5631–44.
40. Jaferzadeh K, Moon I. Quantitative investigation of red blood cell three-dimensional geometric and chemical changes in the storage lesion using digital holographic microscopy. *J Biomed Opt*. (2015) 20:111218. doi: 10.1117/1.JBO.20.11.111218
41. Park H, Lee S, Ji M, Kim K, Son Y, Jang S, et al. Measuring cell surface area and deformability of individual human red blood cells over blood storage using quantitative phase imaging. *Sci Rep*. (2016) 6:34257. doi: 10.1038/srep34257
42. Steelman ZA, Eldridge WJ, Weintraub JB, Wax A. Is the nuclear refractive index lower than cytoplasm? Validation

of phase measurements and implications for light scattering technologies. *J Biophoton*. (2017) 10:1714–22. doi: 10.1002/jbio.201600314

Conflict of Interest: The authors declare that the research was conducted in the absence of any commercial or financial relationships that could be construed as a potential conflict of interest.

frontiers in Physics

ORIGINAL RESEARCH
published: 13 May 2021
doi: 10.3389/fphy.2021.665956

Ligand-Free BaF_2: Nd Nanoparticles With Low Cytotoxicity, High Stability and Enhanced Fluorescence Intensity as NIR-II Imaging Probes

Xiaoxia Cui[1,2]*, *Yantao Xu*[1,2], *Shengfei She*[1,2], *Xusheng Xiao*[1,2], *Chaoqi Hou*[1,2] and *Haitao Guo*[1,2]*

[1] State Key Laboratory of Transient Optics and Photonics, Xi'an Institute of Optics and Precision Mechanics, Chinese Academy of Science (CAS), Xi'an, China, [2] Center of Materials Science and Optoelectronics Engineering, University of Chinese Academy of Sciences (UCAS), Beijing, China

Ligand-free BaF_2:Nd nanoparticles (NPs) with a size of 10 nm were fabricated by a novel synthetic route in the liquid phase. A transparent dispersion of the BaF_2:Nd NPs mixed with propanetriol and DMSO-d6 was done. Highly stable and outstanding near-infrared (NIR) fluorescence centered at 1,058 nm was detected using an excitation wavelength of 808 nm laser. Moreover, the dispersion can be found to be stable for over 1 month, and the cytotoxicity of the BaF_2:Nd NP dispersion has also been studied by 3-(4,5-dimethyl-2-thiazolyl)-2,5-diphenyl-2H-tetrazolium bromide (MTT) assay. The superior performance of these NPs exhibits their great potential application in high-contrast and high-penetration *in vivo* imaging.

Keywords: BaF_2:Nd, fluorescence imaging, stability, low toxicity, NIR-II

OPEN ACCESS

Edited by:
Peng Gao,
Xidian University, China

Reviewed by:
Xiaobao Yao,
The First Affiliated Hospital of Xi'an Jiaotong University, China
Zhiguang Zhou,
NewSpec Pty Ltd., Australia

***Correspondence:**
Xiaoxia Cui
cuixx@opt.ac.cn
Haitao Guo
guoht_001@opt.ac.cn

Specialty section:
This article was submitted to Optics and Photonics, a section of the journal Frontiers in Physics

Received: *09 February 2021*
Accepted: *14 April 2021*
Published: *13 May 2021*

Citation:
Cui XX, Xu YT, She SF, Xiao XS, Hou CQ and Guo HT (2021) Ligand-Free BaF_2: Nd Nanoparticles With Low Cytotoxicity, High Stability and Enhanced Fluorescence Intensity as NIR-II Imaging Probes. Front. Phys. 9:665956. doi: 10.3389/fphy.2021.665956

INTRODUCTION

Fluorescence imaging exhibits high sensitivity. Non-invasive and real-time monitoring has been regarded as one of the most promising optical imaging technologies in clinical applications [1]. However, at present, in general, the use of fluorescence imaging is limited due to the strong effect of scattering and absorption of the light by tissues. The image resolution is poor when the visible light-emitting fluorescence probes are employed, since the high scattering loss and autofluorescence observed from the biosamples will reduce the background ratio (SBR) of fluorescence images [2]. The light observed in the near-infrared (NIR) range of 700–950 and 1,000–1,700 nm is considered as the transparency window for bioimaging because the low scattering loss and reduced absorption coefficient are observed from the endogenous molecules [3, 4]. This light can exhibit infrared fluorescence of high brightness, deep tissue penetration, and clear images with high spatial resolution [5–7]. In the NIR imaging system, the fluorescence probe has become the most critical factor to achieve high-quality images. Therefore, the development of the novel NIR probe is becoming important particularly for future clinical applications.

Up to now, various NIR imaging probes (including quantum dots [8, 9], upconversion nanoparticles (NPs) [10–13], and rare earth-doped down-emission NPs [14, 15]) have been reported. However, the high biotoxicity and low quantum efficiency will limit further applications of NPs. Furthermore, for most upconversion NPs based on the $NaYF_4$ matrix, the light with an excitation wavelength of 980 nm causes overheating of tissues due to its matching wavelength with

the absorption of water [16, 17]. The NPs doped with rare earth ions, such as Nd^{3+}, Er^{3+}, and Ho^{3+}, have attracted greater attention because of their emission wavelength in the NIR-II region of 1,000–1,700 nm under the excitation wavelength of 800 nm. Imaing with these probes not only can avoid the heat accumulation in the tissues but also can reduce the biotoxic components and enhance the image quality due to the high penetration depth and spatiotemporal resolution [4, 18, 19].

The ideal fluorescence probe must satisfy the following criteria: First, it should achieve an enhanced emission intensity in the range of 1,000–1,700 nm, long life time, and high luminescence stability. Second, proper size should be fabricated to not only prevent the rapid renal excretion but also reduce the surface quenching effect. Third, it should exhibit high biocompatibility and low biotoxicity. In order to improve the biocompatibility of NPs, the NPs are usually modified by organic surfactants, which may reduce the luminescence intensity because of the quenching effect of the –CH and –OH groups [20]. In this article, BaF_2:Nd NPs were prepared without the use of organic ligand by the solvothermal method to improve the luminescence intensity at 1,058 nm. The BaF_2:Nd NP dispersions in dimethyl sulfoxide (DMSO)/propanetriol were produced with characteristics such as high stability and low biotoxicity. High biocompatibility and the penetration depth of imaging in the pork tissues have been evaluated. Furthermore, the NIR excitation ($\lambda_{ex} = 800$ nm), NIR emission ($\lambda_{em} = 1{,}058$ nm), and high photostability characteristics of the NPs are essential for performing deep tissue imaging in the near future.

EXPERIMENTAL

Material

Ba $(NO_3)_2{\cdot}6H_2O$ (99.9%, Alfa Aesar reagent), Nd $(NO_3)_3{\cdot}6H_2O$ (95%, Alfa Aesar reagent), NaF (99.99%, Alfa Aesar reagent), absolute ethanol (AR, Xian chemical regent Lo.), DMSO, and propanetriol (AR, Alfa Aesar reagent) were used without further purification. Ultrapure distilled and deionized water was used for the preparation of all solutions used in the following experiments.

Synthesis of BaF_2:Nd Nanoparticles

Ligand-free BaF_2:Nd NPs with a doping concentration of 3 mol% were prepared by a modified hydrothermal route [21]: 0.97 mmol of Ba $(NO_3)_2$ and 0.03 mmol of Nd $(NO_3)_3$ were first mixed with 40 mL of water. The solution was stirred thoroughly for 30 min at room temperature, and then 0.08 g of NaF was added to the aforementioned solution under stirring. Finally, 40 mL of ethanol was added and mixed; the mixed solution was again stirred for 10 min and then transferred to a Teflon-lined autoclave. Then, the autoclave was sealed and heated at 170°C for 10 h. The reactor was cooled to room temperature. The products were centrifuged and washed several times by ethanol and acetone. The residual precipitate was dried at 65°C under vacuum for 2 days.

Different concentrations of NP dispersions were prepared by adding 2–15 mg of BaF_2:Nd NPs powder to 0.2 mL of DMSO-d6 solvent. Then, the mixture was subjected to ultrasonication for 15 min, and finally 0.3 mL of propanetriol was added into the abovementioned mixture. The resulting transparent and stable dispersions were fabricated.

Characterization

X-ray diffraction (XRD) patterns of the samples were measured on a Bruker Advance powder X-ray diffractometer *via* a Cu Kα radiation. TEM analysis was performed using JEOL JEM-2100 field emission transmission electron microscope (TEM) at an acceleration voltage of 200 kV. Fourier Transform infrared (FTIR) spectra were determined on a Bruker FTIR spectrometer using transparent KBr wafers. All NPs were dried under vacuum prior to the formation of the KBr wafers and subsequent analysis. The absorption spectra were recorded in the range of 300–1,300 nm by the UV–Vis–NIR spectrophotometer (Shimadzu UV-3600) at room temperature. The fluorescence spectra were measured by a Zolix Omni-k 300 spectrophotometer using 800-nm laser diode pumps. Luminescence decay time of the sample was detected by a 300-MHz Tektronix oscilloscope (Model 3032B). Fluorescence images of NP powders and NP dispersions were captured by an NIR-II imaging system (GuangYingMei Co., Wuhan, China) equipped with InGaAs detector and 808-nm laser diode (the average power density is 80 mW/cm^2). The morphologies of the erythrocytes and platelets were characterized by optical microscope.

Hemolysis Assay

The BaF_2:Nd NP dispersions in phosphate buffer saline (PBS) were prepared with a concentration of 400 μgmL^{-1}. The red blood cells (RBCs) were collected by centrifuging the anticoagulated human whole blood samples at 1,000 rpm for 5 min. Then, RBC suspensions in PBS with a concentration of 2% were prepared. About 2.5 mL of NP dispersions was incubated with 2.5 mL of RBC suspensions (2%) for 2 h at 37°C. The control groups with positive and negative samples were prepared by mixing 2.5 mL of RBC suspensions with 2.5 mL of distilled water and saline water, respectively. After incubation, the samples were centrifuged, and the absorbance of the supernatant was measured at 570 nm. The percentage rate of hemolysis was calculated as follows: Hemolysis rate % $= (OD_{test} - OD_{neg})/(OD_{pos} - OD_{neg})$, where OD_{test}, OD_{neg}, and OD_{pos} are the absorbance of the test sample, absorbance of the negative control (saline), and absorbance of the positive control (water), respectively. All data were obtained based on the average of five replications.

Erythrocyte Morphology

The RBCs were collected by centrifuging fresh anticoagulant human blood and washing it three times with PBS. Then, 20 μL of RBC suspensions was incubated with 1 mL of BaF_2:NP dispersions (100 $\mu g{\cdot}mL^{-1}$) at room temperature for 30 min. Finally, the RBCs were again washed three times with PBS. The morphologies of RBCs were observed under the optical microscope.

MTT Assay

3-(4,5-dimethyl-2-thiazolyl)-2,5-diphenyl-2H-tetrazolium bromide (MTT) assay was performed to measure cell viability after MTT interaction with NPs under different conditions [22].

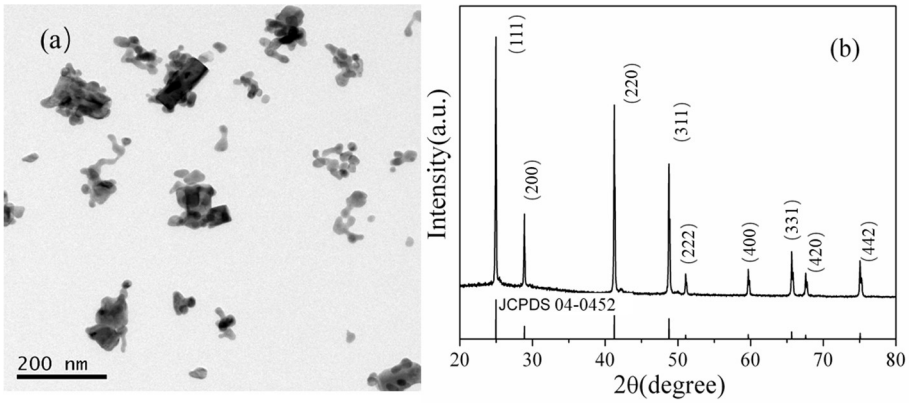

FIGURE 1 | TEM images **(a)** and XRD patterns **(b)** of BaF$_2$:Nd (3 mol%) NPs.

The HeLa cells were placed in 96-well plates and incubated under the atmosphere of 5% CO_2 at 37°C until the monolayer of cell was formed at the bottom of the well (96-well flat plate). After 2 h, different concentrations (50, 100, 150, and 200 μgmL^{-1}) of NP dispersions in PBS were added when the cell adhered to the well. The mixture was incubated in 5% CO_2 at 37°C for 48 h, and 20 μL of the MTT solution (5 mg/mL) was added to each well and cultured for 4 h. After completion of the culture, the medium was carefully discarded and the precipitates were retained. Then, 0.5 mL of DMSO was added to each well and centrifuged at low speed for 10 min to make the crystal dissolve completely. Finally, the solution was transferred into separate wells in a 96-well-plate, and the absorbance values were measured at 540 nm in a spectrophotometer. At the same time, back sample (containing culture medium, MTT, DMSO) and control sample (containing cells, PBS, culture medium, MTT, DMSO) were prepared. The percentage viability of HeLa cells incubated with NPs was calculated as $[A]_{test}/[A]_{control} \times 100$, where $[A]_{test}$ is the absorbance of the tested sample incubated with NPs and $[A]_{control}$ is the absorbance of the control sample.

Imaging in the Phantom and Pork Tissue

The fluorescence imaging was performed by a NIR *in vivo* imaging system equipped with an InGaAs detector. The excitation wavelength of LD laser was 808 nm and the excitation intensity was 80 $mW{\cdot}cm^{-2}$. In order to avoid the interference of excitation lights, 850 nm long-pass filter and 1,060 nm band-pass filter were employed, thus enhancing the image intensity at 1,060 nm. The temperature of detector chip was adjusted as −35°C. Before the imaging technique, the BaF$_2$:Nd NP dispersion was filled to a capillary based on the capillary phenomenon immersed in the dispersions. Then, the capillary was sealed with black glass cement and was inserted into the hole of the phantom and the pork tissues. The fluorescence signals of BaF$_2$:Nd NPs present in the phantom and the pork tissues were captured under the excitation wavelength of 808 nm.

Ethics

The studies involving human participants were reviewed and approved by the Ethics Committee of First Affiliated Hospital of Xi'an Jiaotong University. The A written informed consent was obtained from the patients/participants involved in this study.

RESULTS AND DISCUSSION

Nanoparticle Characterization

Figure 1a shows the TEM images of the obtained NPs. The NPs exhibit an average size of about 16 ± 1 nm and high dispersity. The crystal structural characteristics of the samples were evaluated by the XRD patterns. The diffraction patterns perfectly matched with that of the standard JCPDS Card (No. 04-0452) of the BaF$_2$ crystal, as shown in **Figure 1b**. There were no other impurity peaks found in the diffraction patterns, and the powders were crystallized in a pure face-centered cubic phase.

Figure 2 shows the FTIR spectrum of BaF$_2$:Nd nanopowders. It can be seen that BaF$_2$:Nd NPs show obvious absorption peaks at 3,460, 2,025, 1,675, and 1,207 cm^{-1}. The broad absorption peaks at 3,460 and 1,675 cm^{-1} correspond to the vibration absorption of –OH ions in the water molecules. The absorption bands centered at 1,138 and 1,207 cm^{-1} are attributable to the stretching vibration of the C–O bond. The absorption band centered at 2,025 cm^{-1} is due to the stretching vibration of the C–C bond. Based on the abovementioned results, it can be concluded that the surface of the BaF$_2$:Nd NPs prepared by the hydrothermal method is covered with –OH groups and C–O groups, which greatly improve the hydrophilicity in DMSO-d6/propanetriol solvent.

Figure 3a shows the absorption spectrum of the BaF$_2$:Nd nanocrystal dispersion. All five absorption bands correspond to the Nd^{3+} transitions from $^4I_{9/2}$ ground state to various excited states of the $^4F_3$ electronic configuration. The emission spectrum of the BaF$_2$:Nd NPs was measured at the excitation wavelength of 808 nm (**Figure 3b**). All the observed emission peaks are the principal transitions from the $^4F_{3/2}$ level to the $^4I_{9/2}$, $^4I_{11/2}$, and $^4I_{13/2}$ levels [23]. The bands centered at 894 nm are assigned

to the transitions of $^4F_{3/2} \rightarrow {}^4I_{9/2}$, while the bands centered at 1,056 nm are due to the transitions of $^4F_{3/2} \rightarrow {}^4I_{11/2}$ levels.

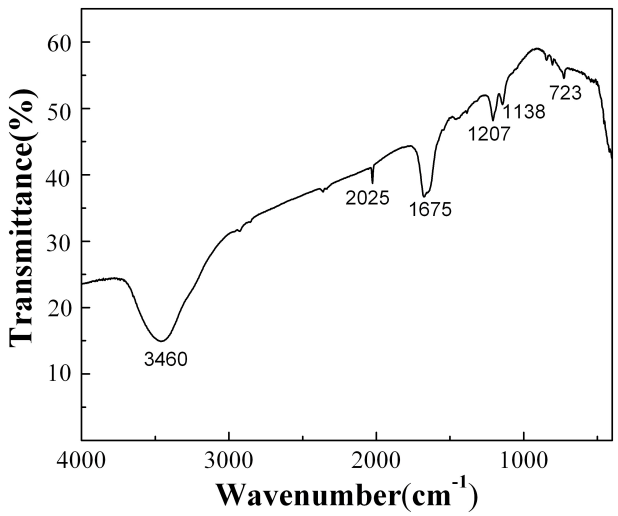

FIGURE 2 | FTIR spectrum of BaF_2:Nd (3 mol%) nanopowders.

Figure 3c shows the decay curve of Nd^{3+} ion for the $^4F_{3/2} \rightarrow {}^4I_{11/2}$ transition in the BaF_2:Nd NP dispersions. A long lifetime was calculated as 135 μs by fitting the decay curve with second exponential function. The long lifetime helps to reduce the imaging noise induced by autofluorescence. **Figure 3d** shows the NIR fluorescence image of the BaF_2:Nd nanocrystal dispersion. The uniform distribution of NP dispersions in terms of optical intensity exhibits their excellent optical and physical stabilities.

To detect the physical stability of the BaF_2:Nd NP probes for NIR-II imaging *in vivo*, the transmittance of the NP dispersion with high mass concentration (30 mg/mL) was monitored for 30 days (**Figure 4**). Obviously, the NPs can form a transparent dispersion in DMSO and propanetriol, which remain uniform and steady for 30 days without any special treatment. These results are consistent with the results of NIR images, as shown in **Figure 3d**.

Biocompatibility Study

Hemolysis Assay

The biotoxicity of the NPs can be characterized by determining the extent of hemolysis. Based on the experimental results of the absorption spectra shown in **Figures 5A–C**, the Hemolysis

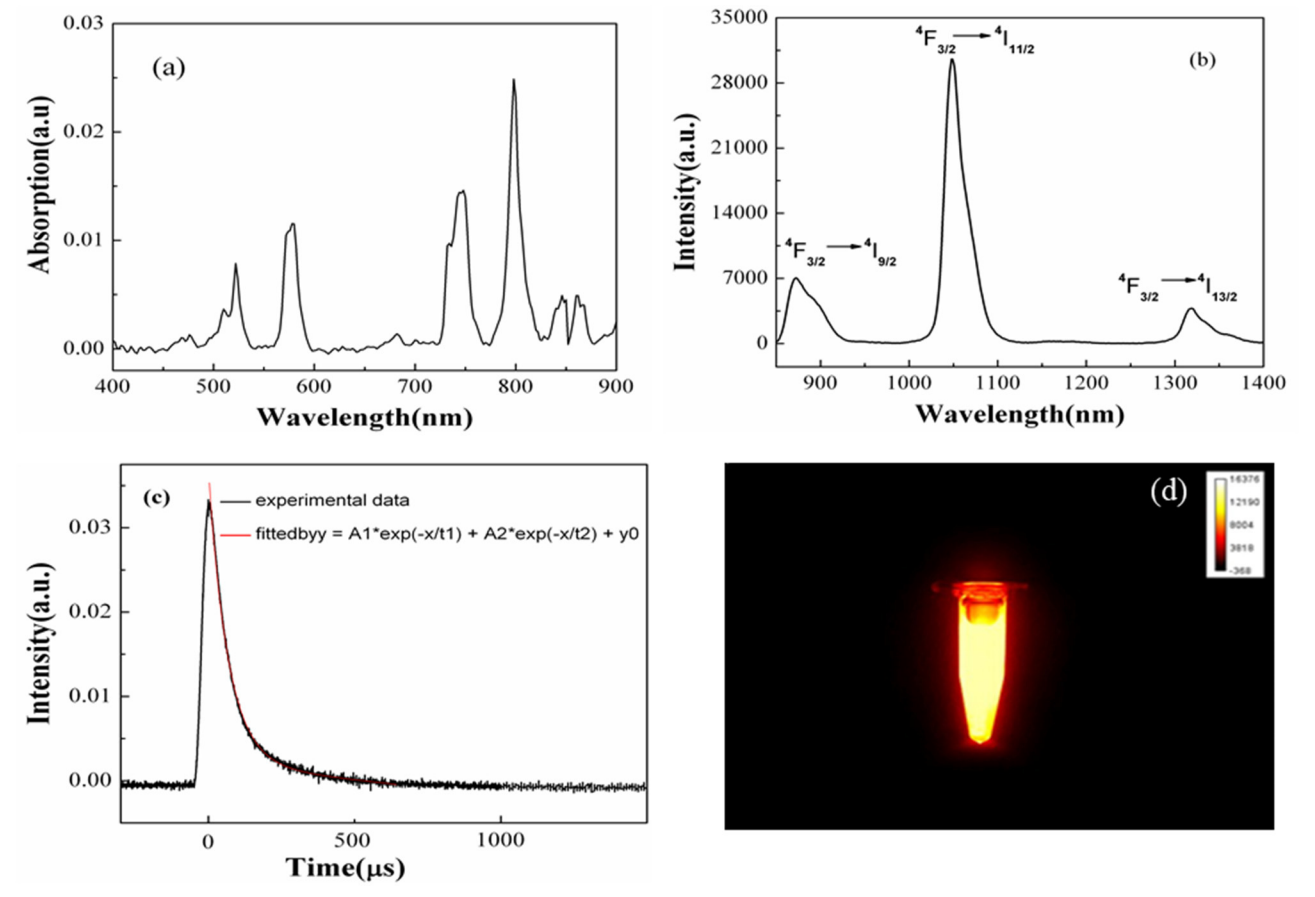

FIGURE 3 | Absorption spectrum **(a)**, emission spectrum **(b)**, decay curve **(c)**, and NIR image **(d)** of the BaF_2:Nd NP dispersion in DMSO-d6/propanetriol solvents (10 mg/mL).

rate (HR) values of the tested specimens were calculated as 3.27%, which is less than the safe value of 5% (ISO10993-4 standard). Such results prove that the BaF_2:Nd NPs are non-hemolytic and that they can be used in future clinical imaging diagnosis.

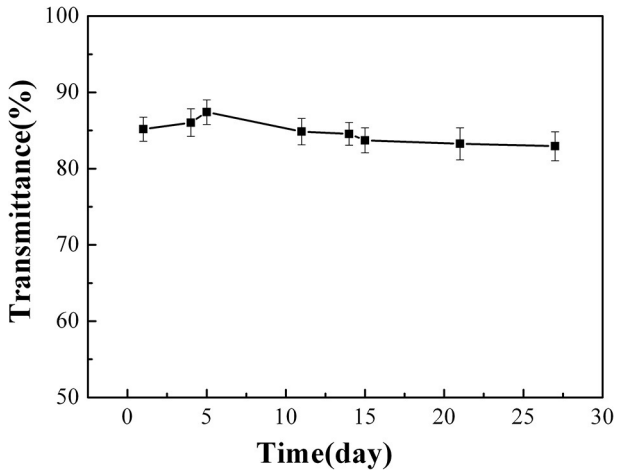

FIGURE 4 | The transmittance of BaF_2:Nd NP dispersions (30 mg/mL) depends on different times.

MTT Assay

The cytotoxicity of the BaF_2:Nd NP dispersions has been evaluated by MTT assay using HeLa cells. Obviously, no cytotoxicity of NP dispersions at a high concentration of 200 μg/mL is observed. As shown in **Figure 5D**, the survival rate of HeLa cells is 91% after incubation with BaF_2:Nd NP dispersions (200 μg/mL) for 48 h. In the case of 50 μg/mL, the survival rate was improved to 97%. These data show satisfactory results on the biocompatibility of the BaF_2:Nd NPs for *in vitro* imaging.

The morphological changes in RBCs are usually used as a marker to analyze the pathological condition of diseases. The normal RBCs are elliptical and sunken on both sides in saline water. When the cells interact with toxic exogenous substances, the morphological changes, such as swelling, spike growth, and even death, in RBCs occur. **Figure 6** shows the morphologies of RBCs before and after incubation with BaF_2:Nd NPs. It can be seen that the RBCs in the experiment do not show additional morphological change (**Figure 6b**) compared with those in the control group (**Figure 6a**). It implies that the BaF_2:Nd NPs possess low toxicity.

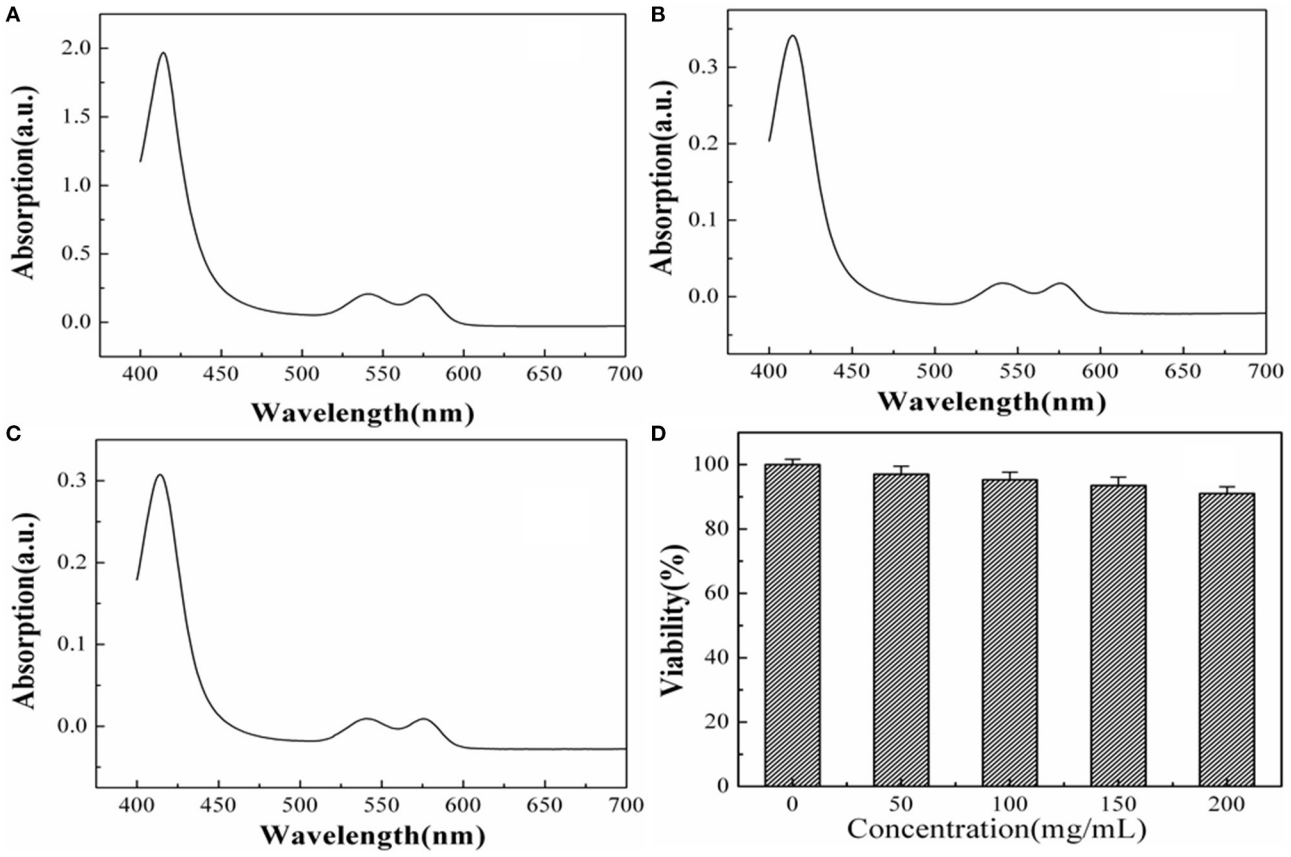

FIGURE 5 | The absorption curves of positive groups **(a)**, experimental groups **(b)**, and negative groups **(c)**. The cell viability of BaF_2:Nd NPs on HeLa cells at the concentration of 50–200 μg mL^{-1} with an incubation time of 48 h **(d)**.

The Images of BaF_2:Nd NP Dispersions in Phantom and Pork Tissues

To measure the luminescence signal of BaF_2:Nd NPs in biological tissues, a standard polyethylene phantom with similar optical parameter to mice muscle was used as a model; the capillary tube with a diameter of 0.2 mm was filled with NP dispersions and inserted into the hole of the phantom, under the excitation wavelength of 808-nm laser (80 mW cm^{-2}), and images with a penetration depth of 10 mm were acquired.

To test the spatial resolution of BaF_2:Nd NPs, two capillary tubes filled with NP dispersions (4 mg/mL) were inserted into two holes of the phantom (**Figure 7a**). Under the irradiation of 808-nm laser (80 mW cm^{-2}), images with a penetration depth of 7 mm were acquired. It can be seen that the two capillaries can be clearly distinguished with an interval of 2 cm inside the phantom (**Figure 7b**). By the same method, two capillary tubes with a diameter of 0.3 mm were inserted into the pork tissue, and images in the pork were recorded with a penetration depth of 5 mm (**Figure 7c**), which is higher than the imaging depth of GdF_3:Nd and LaF_3:Nd NPs (4 mm) [24, 25]. The luminescence intensity dropped to 65% of the original value in phantom due to the light attenuation resulting from the high absorption and scattering of biological tissue and water. When the excitation light penetrates the tissues, they become heavily decayed due to the absorption of water and fat. Therefore, the effective energy for excitation is reduced correspondingly. On the other hand, the attenuation of emission light is also inevitable when it penetrates all the biological tissues and the skin to be detected. A high spatial resolution of 300 μm was visualized, and the fluorescence images with a high signal-to-background ratio of

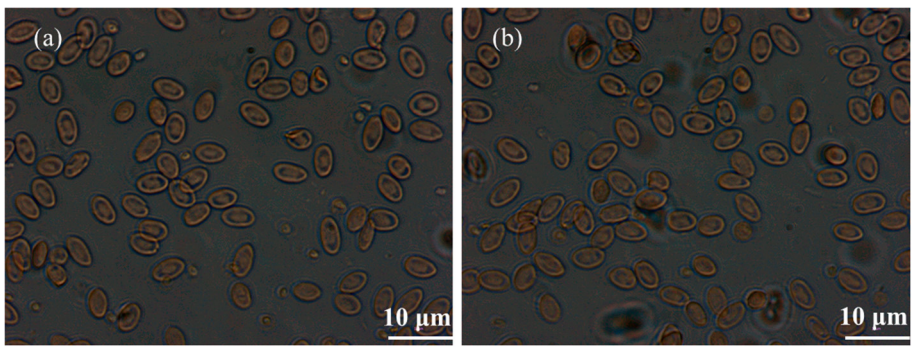

FIGURE 6 | The morphologies of RBCs captured by optical microscope: **(a)** the control group and **(b)** the BaF_2:Nd NP dispersion group.

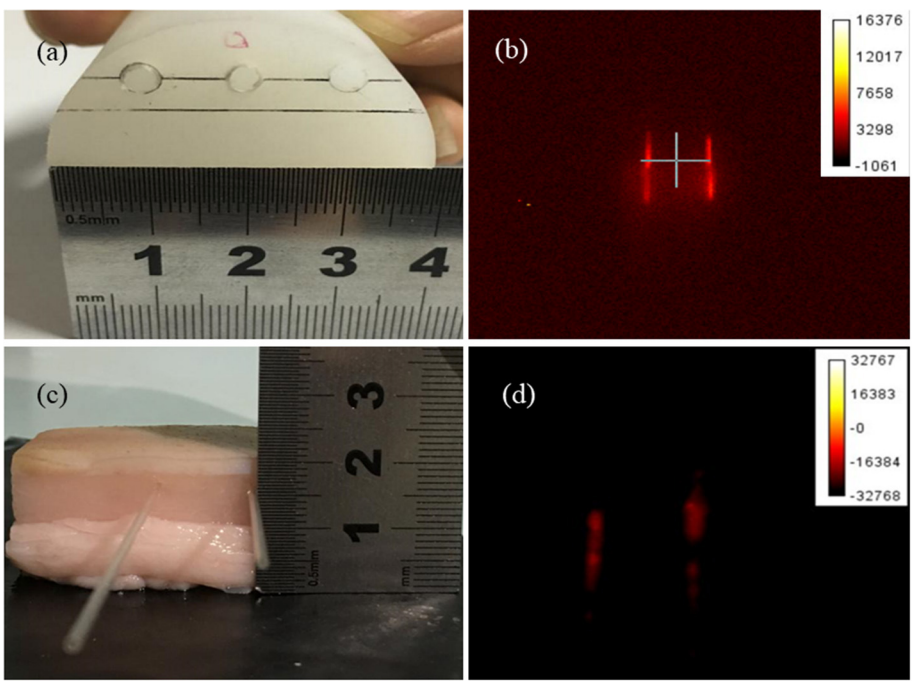

FIGURE 7 | The photographs of the phantom **(a)** and pork tissues **(c)**, and the NIR images of BaF_2:Nd NP dispersion (4 mg/mL) in the phantom **(b)** and pork tissues **(d)**.

18:1 were recorded in the pork tissue (**Figure 7d**). These high-quality images demonstrated the potential for advancement of this type of NP for deep tissue imaging in a living body.

CONCLUSION

A high fluorescence BaF_2:Nd NP without ligand was fabricated with a simple hydrothermal method. The NP dispersions exhibit high superior photostability and physical stability. Furthermore, an imaging depth of 5 mm and a high spatial resolution of 300 μm were found in the pork tissues. The fluorescence image shows a significant SBR of 18:1. Moreover, the BaF_2:Nd NPs show low HR value (3.27%) and high cell viability (91%). These superior performances of these nanoprobes exhibit their great potential application in high-contrast imaging and practical tumor diagnosis.

DATA AVAILABILITY STATEMENT

The raw data supporting the conclusions of this article will be made available by the authors, without undue reservation.

ETHICS STATEMENT

The studies involving human participants were reviewed and approved by the Ethics Committee of First Affiliated Hospital of Xi'an Jiaotong University. The patients/participants provided written informed consent to participate in this study.

AUTHOR CONTRIBUTIONS

XXC and HTG designed experiments. YTX and SFS carried out experiments. XSX and CQH analyzed experimental results. All authors contributed to the article and approved the submitted version.

FUNDING

This work was financially supported by the National Natural Science Foundation of China (Grant Nos. 61205039 and 61475189) and Natural Science Basic Research Plan in Shaanxi Province of China (Grant No. 2014JQ8345).

REFERENCES

1. Lei X, Li R, Tu D, Shang X, Liu Y, You W, et al. Intense near-infrared-II luminescence from $NaCeF_4$: Er/Yb nanoprobes for *in vitro* bioassay and *in vivo* bioimaging. *Chem Sci.* (2018) 9:4682–8. doi: 10.1039/C8SC00927A
2. Weissleder R. A clearer vision for *in vivo* imaging. *Nat Biotechnol.* (2001) 19:316–7. doi: 10.1038/86684
3. Wang X, Shi J, Li P, Zheng SH, Sun X, Zhang HW. $LuPO_4$: Nd^{3+} nanophosphors for dual-mode deep tissue NIR-II luminescence/CT imaging. *J Lumin.* (2019) 209:420–6. doi: 10.1016/j.jlumin.2019.02.028
4. Yang Q, Li X, Xue Z, Li Y, Jiang MY, Zeng S. Short-Wave near-infrared emissive $GdPO_4$:Nd^{3+} theranostic probe for *in vivo* bioimaging beyond 1300 nm. *RSC Adv.* (2018) 8:12832–40. doi: 10.1039/C7RA12864A
5. Fan Y, Wang PY, Lu YQ, Wang R, Zhou L, Zheng X, et al. Lifetime-engineered NIR-II nanoparticles unlock multiplexed *in vivo* imaging. *Nat Nanotech.* (2018) 13:941–6. doi: 10.1038/s41565-018-0221-0
6. Guo B, Feng Z, Hu DH, Xu SD, Middha E, Pan YT, et al. Precise deciphering of brain vasculatures and microscopic tumors with dual NIR-II fluorescence and photoacoustic imaging. *Adv Mater.* (2019) 31:1902504. doi: 10.1002/adma.201902504
7. Feng ZJ, Yang YM, Zhang J, Wang K, Li YX, Xu H, et al. *In vivo* and *in situ* real-time fluorescence imaging of peripheral nerves in the NIR-II window. *Nano Res.* (2019) 12:3059–68. doi: 10.1007/s12274-019-2552-z
8. Cao J, Zhu H, Deng D, Xue B, Tang L, Mahounga D, et al. *In vivo* NIR imaging with PbS quantum dots entrapped in biodegradable micelles. *J Biomed Mater Res Part A.* (2012) 100A:958–68. doi: 10.1002/jbm.a.34043
9. Chinnathambi S, Shirahata N. Recent advances on fluorescent biomarkers of near-infrared quantum dots for *in vitro* and *in vivo* imaging. *Sci Tech Adv Mater.* (2019) 20:337–55. doi: 10.1080/14686996.2019.1590731
10. Ren Y, He SQ, Huttad L, Chua MS, So SK, Guo QY, et al. NIR-II/MR dual modal nanoprobe for liver cancer imaging. *Nanoscale.* (2020) 12:11510–7. doi: 10.1039/D0NR00075B
11. Pan Z, Wen Y, Wang T, Wang K, Teng YJ, Shao K. One-step synthesis of hollow PEI-$NaBiF_4$: Yb^{3+} /Er^{3+} upconversion nanoparticles for water-responsive luminescent probe. *J Rare Earth.* (2019) 38:362–8. doi: 10.1016/j.jre.2019.04.022
12. Liu S, Li W, Gai S, Yang GX, Zhong CN. A smart tumor microenvironment responsive nanoplatform based on upconversion nanoparticles for efficient multimodal imaging guided therapy. *Biomater Sci.* (2019) 7:951–62. doi: 10.1039/C8BM01243A
13. Cho SK, Su LJ, Mao C, Wolenski CD, Flagi TW, Park W. Multifunctional nano-clusters of $NaYF_4$:Yb^{3+}, Er^{3+} upconversion nanoparticle and gold nanorod for simultaneous imaging and targeted chemotherapy of bladder cancer. *Mater Sci Eng C Mater Biol Appl.* (2019) 97:784–92. doi: 10.1016/j.msec.2018.12.113
14. Ma L, Huang S, He SQ, Wang ZX, Cheng Z. Polydopamine-coated downconversion nanoparticle as an efficient dual-modal near-infrared-II fluorescence and photoacoustic contrast agent for non-invasive visualization of gastrointestinal tract *in vivo*. *Biosens Bioelectron.* (2020) 151:112000. doi: 10.1016/j.bios.2019.112000
15. Tan M, Del RB, Zhang Y, Martín RE, Hu J, Zhou ZG, et al. Rare-earth-doped fluoride nanoparticles with engineered long luminescence lifetime for time-gated *in vivo* optical imaging in the second biological window. *Nanoscale.* (2018) 10:17771–80. doi: 10.1039/C8NR02382D
16. Zhang WJ, Yu DC, Zhang JP. Near-infrared quantum splitting in Ho 3+:LaF 3 nanocrystals embedded germanate glass ceramic. *Opt Mater Exp.* (2012) 2:636–43. doi: 10.1364/OME.2.000636
17. Yu DC, Ye S, Huang XY. Enhanced three-photon near-infrared quantum splitting in β-$NaYF_4$:Ho^{3+} by codoping Yb $^{3+}$. *AIP Adv.* (2012) 2:022124. doi: 10.1063/1.4718412
18. Zhao Z, Yuan J, Zhao X, Bandla A, Thakor NV, Tan MC. Engineering the infrared luminescence and photothermal properties of double-shelled rare-earth-doped nanoparticles for biomedical applications. *ACS Biomater Sci Eng.* (2019) 5:4089–101. doi: 10.1021/acsbiomaterials.9b00526
19. Liu G, Sun Z, Jia M, Fu ZL, Zhang AQ, Li PP. One pot synthesis and optimized luminescent intensity of Gd_2 $(WO_4)_3$:Yb^{3+}/Ho^{3+}@SiO_2 nanoparticles for biological application. *J Lumin.* (2019) 206:1–5. doi: 10.1016/j.jlumin.2018.10.039
20. Cui X, Fan Q, Shi S. A novel near-infrared nanomaterial with high quantum efficiency and its applications in real time *in-vivo* imaging. *Nanotech.* (2018) 20:205705. doi: 10.1088/1361-6528/aab2fa
21. Andrade AB, Ferreiraab NS, Valerio MEG. Particle size effects on structural and optical properties of BaF_2 nanoparticles. *RSC Adv.* (2017) 7:26839–48. doi: 10.1039/C7RA01582H
22. Ding Y, Du C, Qian JW, Dong CM. Zwitterionic polypeptide nanomedicine with dual NIR/reduction-responsivity for synergistic cancer photothermal-chemotherapy. *Polym Chem.* (2019) 10:4825–36. doi: 10.1039/C9PY00986H
23. Duan W, Zhang Y, Wang Z. Synthesis and near-infrared fluorescence of $K_5NdLi_2F_{10}$ nanocrystals and their dispersion with high doping

concentration and long lifetime. *Nanoscale.* (2014) 6:5634–8. doi: 10.1039/c3nr06825k

24. Mimun LC, Ajithkumar G, Pokhrel M, Yust BG, Elliott ZG, Pedraza F, et al. Bimodal imaging using neodymium doped gadolinium fluoride nanocrystals with near-infrared to near-infrared downconversion luminescence and magnetic resonance properties. *J Mater Chem B.* (2013) 1:5702–10. doi: 10.1039/c3tb20905a
25. Rocha U, Kumar KU, Jacinto C, Villa I, Sanz-Rodríguez F, Iglesias de la Cruz Mdel C, et al. Neodymium-Doped LaF_3 Nanoparticles for fluorescence bioimaging in the second biological window. *Small.* (2014) 10:1141–54. doi: 10.1002/smll.201301716

Conflict of Interest: The authors declare that the research was conducted in the absence of any commercial or financial relationships that could be construed as a potential conflict of interest.

frontiers in Physics

REVIEW
published: 28 May 2021
doi: 10.3389/fphy.2021.672555

Advances in High-Speed Structured Illumination Microscopy

Tianyu Zhao[1,2,3], *Zhaojun Wang*[1], *Tongsheng Chen*[4], *Ming Lei*[1,3]*, *Baoli Yao*[2,3] *and Piero R. Bianco*[5]*

[1]MOE Key Laboratory for Non-equilibrium Synthesis and Modulation of Condensed Matter, School of Physics, Xi'an Jiaotong University, Xi'an, China, [2]State Key Laboratory of Transient Optics and Photonics, Xi'an Institute of Optics and Precision Mechanics, Chinese Academy of Sciences, Xi'an, China, [3]College of Materials Science and Opto-Electronic Technology, University of Chinese Academy of Sciences, Beijing, China, [4]MOE Key Laboratory of Laser Life Science & Guangdong Provincial Key Laboratory of Laser Life Science, College of Biophotonics, South China Normal University, Guangzhou, China, [5]Department of Pharmaceutical Sciences, College of Pharmacy, University of Nebraska Medical Center, Omaha, NE, United States

Super-resolution microscopy surpasses the diffraction limit to enable the observation of the fine details in sub-cellular structures and their dynamics in diverse biological processes within living cells. Structured illumination microscopy (SIM) uses a relatively low illumination light power compared with other super-resolution microscopies and has great potential to meet the demands of live-cell imaging. However, the imaging acquisition and reconstruction speeds limit its further applications. In this article, recent developments all targeted at improving the overall speed of SIM are reviewed. These comprise both hardware and software improvements, which include a reduction in the number of raw images, GPU acceleration, deep learning and the spatial domain reconstruction. We also discuss the application of these developments in live-cell imaging.

Keywords: fluorescence microscopy, super-resolution, SIM, hardware acceleration of deep learning, image reconstructed algorithm

OPEN ACCESS

Edited by:
Guangcan Guo, University of Science and Technology of China, China

Reviewed by:
Junle Qu, Shenzhen University, China
Nirmal Mazumder, Manipal Academy of Higher Education, India

***Correspondence:**
Ming Lei
ming.lei@xjtu.edu.cn
Piero R. Bianco
pbianco@unmc.edu

Specialty section:
This article was submitted to Optics and Photonics, a section of the journal Frontiers in Physics

Received: *26 February 2021*
Accepted: *11 May 2021*
Published: *28 May 2021*

Citation:
Zhao T, Wang Z, Chen T, Lei M, Yao B and Bianco PR (2021) Advances in High-Speed Structured Illumination Microscopy. Front. Phys. 9:672555. doi: 10.3389/fphy.2021.672555

INTRODUCTION

Fluorescence microscopy is a powerful tool for visualizing biological processes of molecules and intracellular structures in living cells. However, due to the diffraction limit, fine structures within organelles whose dimension is less than ~200 nm laterally and ~500 nm axially are difficult to observe [1]. Over the past several years, exponential growth in using super-resolution (SR) fluorescence microscopy has occurred in the field of biomedical imaging [2]. SR techniques have shattered the diffraction limit, thus researchers are able to investigate fine details of biological structures at the nanometer level. These imaging systems include stimulated emission depletion (STED) microscopy [3–6], photo-activated localization microscopy [7–9], stochastic optical reconstruction microscopy [10, 11], and structured-illumination microscopy (SIM) [12–14] Among these approaches, SIM has attracted considerable interest because of its low light dose and high imaging speed [15]. These characteristics provide a powerful tool in various biological applications including cortical microtubules in Arabidopsis, spine morphology [16], neurotrauma [17], and macrophages in the ischemic tissue [18].

In SIM, the periodic illumination down-modulates the high spatial frequency of the sample information in the Fourier domain. Several raw images with different pattern phases and orientations are captured to undo the frequency modulation. The final high-resolution image is computed after separating and recombining the spectral information [19, 20]. Unfortunately, the capturing of multiple images and post-processing of these images slows down the speed of SIM, resulting in difficulties of SR imaging in real-time *in vivo* [21]. To circumvent these issues, several groups have

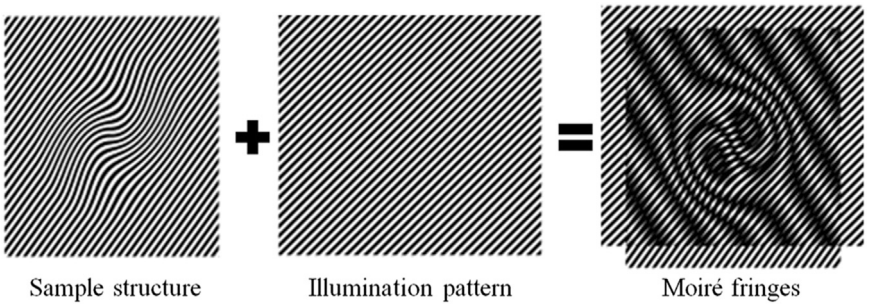

FIGURE 1 | Generation of Moiré fringes. If the sample structure is multiplied by structural light, Moiré fringes will appear.

implemented modifications designed to increase the overall imaging speed of SIM. In this review, we first introduce the basic principle of SIM. Then we focus on the optical configuration of a fast SIM system and compare the different fast SIM implementations that include optimization of the optical configuration as well as improvements in image reconstruction methods.

THE THEORETICAL BASIS OF SIM

The concept behind SIM can be easily understood in terms of the well-known moiré effect. If two fine patterns are superposed multiplicatively, a beat pattern will appear in their product (**Figure 1**). In the frequency domain, there is a cut-off frequency in optical microscopy. The high-frequency information of the sample light is lost after passing through an objective lens, which leads to the diffraction limit of conventional optical microscopy. If the microscope can collect high spatial frequency information, closely spaced molecules can be resolved from each other. In traditional optical microscopy systems, the spatial resolution of the microscope objective depends on the maximum spatial frequency f_0 it can collect. In SIM, the sample is illuminated by the modulated light with a spatial frequency f_1. Thus, the detector receives the moiré fringe including the spatial frequency $|f\text{-}f_1|<f_0$. Because of the moiré effect, high-frequency information moves into the observable region, which is normally unresolvable using conventional microscopy. By resolving the high-frequency information in the moiré fringe, the high-frequency information can be computed, and the resolution enhanced.

Considering a specimen with the fluorescent molecular distribution density $S(r)$ and illumination light $I(r)$, the image collected by the camera $D(r)$ is the convolution of the fluorescent and the point spread function $H(r)$ [22].

$$D(r) = [I(r) \cdot S(r)] \otimes H(r), \tag{1}$$

Where r is the spatial coordinates. In SIM, the illumination is a cosine fringe intensity pattern I(r) with the form

$$I(r) = \left[1 + m \cdot cos\left(2\pi p \cdot r + \varphi\right)\right] \cdot I_0, \tag{2}$$

Where m, p, φ, and I0 are the modulation depth, the spatial frequency, the initial phase of the cosine fringe pattern and the mean intensity, respectively. After combining **Eqs 1**, **2**, the spectrum of the detected image in the frequency domain can be obtained by taking the Fourier transform

$$\tilde{D}(k) = I_0\left[\tilde{S}(k) + \frac{m}{2}\tilde{S}(k+p)e^{-i\varphi} + \frac{m}{2}\tilde{S}(k-p)e^{i\varphi}\right] \cdot \tilde{H}(k), \tag{3}$$

Where $\tilde{S}(k)$ and $\tilde{H}(k)$ are the Fourier transform of the fluorescent distribution and the optical transfer function (OTF), and k is the frequency coordinates. **Eq. 3** shows that the high-frequency features of the sample $\tilde{S}(k+p)$ and $\tilde{S}(k-p)$ are shifted into support areas of the detection OTF by structured light. As the result of diffraction effect, the cut-off frequency k_0 limits the spatial frequency of the system k as $k \in [-k_0, k_0]$ and is enlarged by the structured illumination into $k \in [-k_0 - p,\ k_0 + p]$. Also, since the illumination pattern is generated through the objective lens, the illumination pattern is diffraction-limited as $p \le k_0$. Thus the maximum spatial frequency of SIM is $k \in [-2k_0, 2k_0]$, which means that the maximum resolution enhancement in SIM is two-fold over that of the traditional microscopy [23].

To separate the high-frequency component in the superposing frequency spectrum, three frequency spectrum components $\tilde{S}(k)$, $\tilde{S}(k+p)$ and $\tilde{S}(k-p)$ should be solved. The most usual method is to capture three raw images with different phase shifts between each other and solve the equations as

$$\begin{bmatrix} \tilde{D}_1(k) \\ \tilde{D}_2(k) \\ \tilde{D}_3(k) \end{bmatrix} = I_0\tilde{H}(k) \begin{bmatrix} 1 & \frac{m}{2}e^{-i\varphi_1} & \frac{m}{2}e^{i\varphi_1} \\ 1 & \frac{m}{2}e^{-i\varphi_2} & \frac{m}{2}e^{i\varphi_2} \\ 1 & \frac{m}{2}e^{-i\varphi_3} & \frac{m}{2}e^{i\varphi_3} \end{bmatrix} \begin{bmatrix} \tilde{S}(k) \\ \tilde{S}(k+p) \\ \tilde{S}(k-p) \end{bmatrix} \tag{4}$$

Finally, based on the amplitude and offset of the illumination pattern determined above, the three frequency spectrum components are moved to the correct position and the merged [24]. In order to enhance the isotropic resolution, other images with multiple illumination directions are also required. For example, for 2D SIM, three directions × three phase shifts are needed, which means there are a total of nine original images.

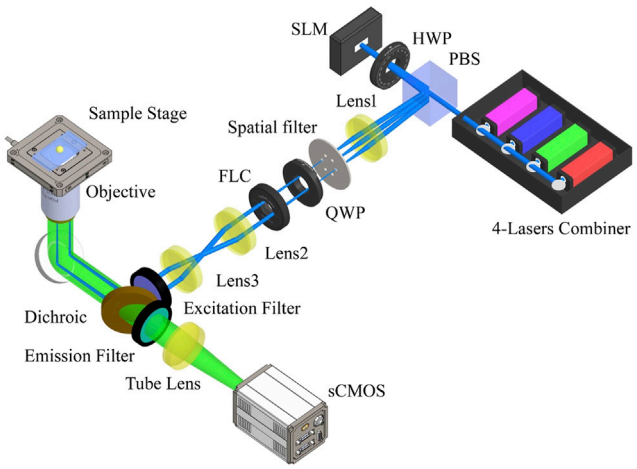

FIGURE 2 | Schematic of a high-speed SIM system. PBS, polarization beam splitter; HWP, half-wave plate; FC-SLM, ferroelectric liquid crystal spatial light modulator; QWP, quarter-wave plate; FLC, ferro-electric liquid crystal phase retarders. The layout is similar to the original SIM presented in [15] but the hardware components have changed over the years.

OPTICAL CONFIGURATION FOR FAST SIM

A basic SIM setup consists of three main elements: the generation of structured light, polarization control, and detection. In common SIM, the interference of multiple laser beams generates a sinusoidal illumination pattern to illuminate samples, which is achieved using a typical, optical layout shown in **Figure 2**. Based on this setup, we introduce several improvements for fast SIM in the following section. In the setup, the expanded and collimated laser beam is modulated by a ferroelectric liquid crystal spatial light modulator (FC-SLM). The laser beam is divided by a diffraction grating generated by the FC-SLM. The ±1 order diffraction beams for 2D-SIM or, the ±1 and 0 order beams for 3D-SIM are selected by a spatial filter. After adjusting the polarization, the laser passes through a 4f system and is focused by the objective. The ±1-order diffraction beams interfere at the focal plane to produce sinusoidal patterns on the specimen. A dichroic mirror reflects the emitted fluorescence signal which is then collected by an sCMOS camera.

Generation of Structured Light

In traditional SIM, cosinoidal illumination is generated by the interference of multiple laser beams. The fringe pattern generation and phase shift control are directly related to the SR image, which are the core technologies of SIM. In 1999, the first generation of SIM used a transmission grating with mechanical devices for moving and rotating [25]. The mechanical movement of the grating was slow and limited the acquisition speed to several seconds per SIM image.

To improve this, the FC-SLM replaced the diffraction grating. The wavefront of the input light is modulated by changing the liquid crystal alignment of the FC-SLM with the desired illumination pattern being generated in less than 1 ms [26]. Consequently, the switching between grating transfers and orientations, which occurs at speeds more than 10 times faster than a motor-based system, greatly improves the temporal resolution of SIM. By using an FC-SLM, Kner et al. and Shao et al. achieved SR imaging of biological samples at ~100 nm resolution at frame rates of 11 and 0.2 frames per second (fps) in 2D- and 3D-SIM, respectively [27, 28]. However, replacing a physical grating with a pixelated SLM has some trade-off. Because of introduced additional unwanted diffraction orders by the SLM display, there are jagged edges in the illumination pattern and loss of laser power. The special filter can block the unwanted frequency spectrum and form a cosinoidal illumination grating, at the expense of light efficiency [29, 30]. A third way to generate the structured light is by scanning the sample with galvanometers (**Figure 3**). Using this approach, an entire U2OS cell with a field of view greater than 40 μm *40 μm was recorded in 4 s at 10 fps [31, 32]. However, this system is more complex than the system shown in **Figure 2** and requires precise adjustment [33].

Polarization Control

To obtain optimal contrast of the fringe pattern in the focal plane of the objective, the polarization of the two interference beams needs to be carefully adjusted [34, 35]. Theoretically, the ±1-order diffraction beams should both be s-polarized to reach the maximum contrast in the fringe pattern [36]. Moreover, SIM imaging requires illumination patterns along at least three different orientations to ensure even resolution improvement. The polarization states of the incident beam also need to be adjusted when switching the orientations of illumination patterns.

Initially, a mechanical rotator with a half-wave plate was used to control polarization, but this method is both slow and unstable [15]. Nine years later, two ferro-electric liquid crystal phase retarders (FLC) were employed to rotate the polarization of the light and illumination pattern synchronously. However, FLCs have a switching time of over 20 ms, which limits the SIM imaging speed to around 50 ms per frame. To avoid the switching time of the FLCs, a passive polarization control scheme was presented where the FLCs were replaced with a quarter-wave plate and a pizza polarizer, which is a custom-made, twelve fan-shaped polarizer (**Figure 4A**) [37, 38]. Unfortunately, the pizza polarizer, which requires an experienced manufacturing setup, causes a 50% reduction in laser power. More recently, Zhao et.al improved this method by making use of the zero-order vortex half-wave retarder, which is a non-uniform half-wave plate whose fast axis distributes as the arrows shown in **Figure. 4B** [39, 40]. It is efficient but only suitable for a single wavelength, which limits its application in multi-color imaging [41].

Detection

For fast SIM systems, sCMOS cameras have significant advantages over EMCCD or CCD cameras regarding field-of-view size and readout speed [42, 43]. When the limiting factor of the system is the camera readout speed, sCMOS detectors combined with a rapid illumination pattern generator like FC-SLM is the superior choice for fast and live-cell acquisition. However, the FC-SLM updates in a synchronous manner,

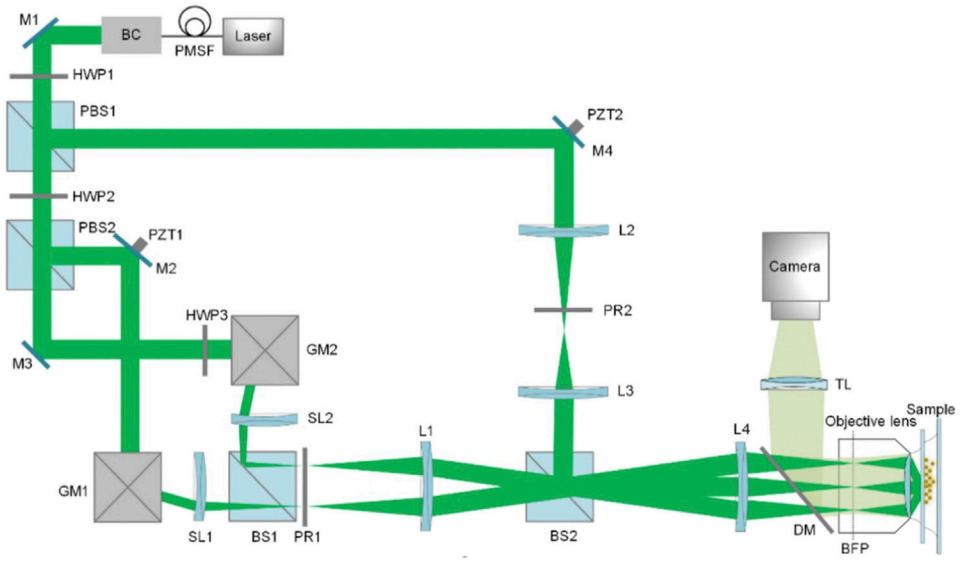

FIGURE 3 | The diagram of 3D galvanometer-based SIM [31]. PMSF, polarization-maintaining single-mode fiber; BC, beam collimator; PBS, polarized beam splitter; GM, scanning galvanometer; PZT, piezoelectric stage; SL, scanning lens; PR, polarization rotator; BFP, back focal plane; DM, dichroic mirror; TL, tube lens. The figure is modified with permission from Ref. (31). Copyright © 2019 The Optical Society.

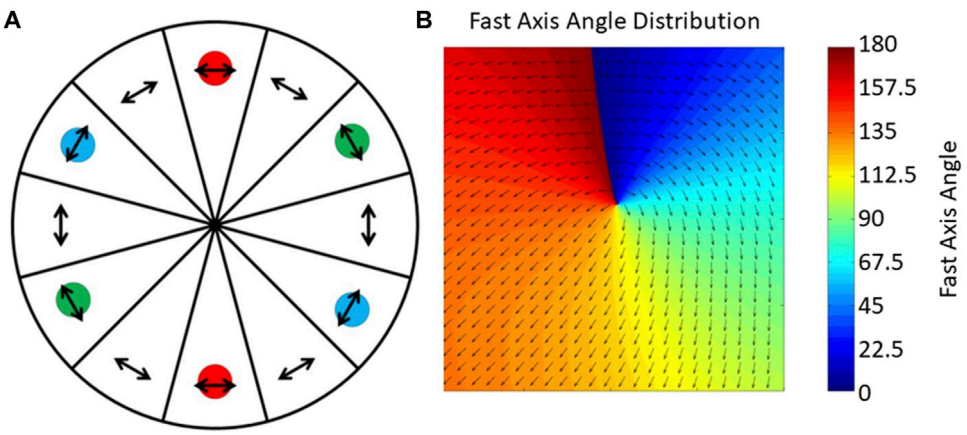

FIGURE 4 | Unique approaches to improving polarization control. **(A)**, The pizza polarizer. The arrows indicate the direction of the transmission axis of each polarizer and the color circles indicate the position of ±1-order diffraction beams on the pizza polarizer [37]. The figure is modified with permission from Ref. (37). Copyright © 2015 IOP Publishing. **(B)**, The zero-order vortex half-wave retarder is a non-uniform half-wave plate whose fast axis distributes in the direction of the arrows shown [39].

whereas the camera used by fast structured illumination systems usually reads the imaging data out in an asynchronous way as a result of rolling shutter mode. This leads to synchronization problems thus limiting the acquisition speed of fast SIM.

To address this, Song *et al* presented a configuration which displayed multiple SLM frames per camera readout cycle by dividing the extremely fast SLM display into several segments along the direction of the rolling shutter of the sCMOS camera (**Figure 5**) [44]. Here, a series of specially designed patterns are used to coordinate the sCMOS. By presenting different SIM patterns during the start exposure and readout line, the SLM maintains the readout line of the camera inside the dark region when the camera runs in continuous rolling shutter mode. This approach reached an acquisition rate of 79 fps with the raw frame rate of 714 fps, the field of view at 16.5 μm × 16.5 μm and the laser illuminating time of 0.5 s.

Adaptive Optics

As with all microscopes, aberrations also detrimentally affect imaging in SIM, resulting in a loss of resolution due to spherical aberration while imaging thick samples [45]. Image quality can be restored using the techniques of adaptive optics (AO), where

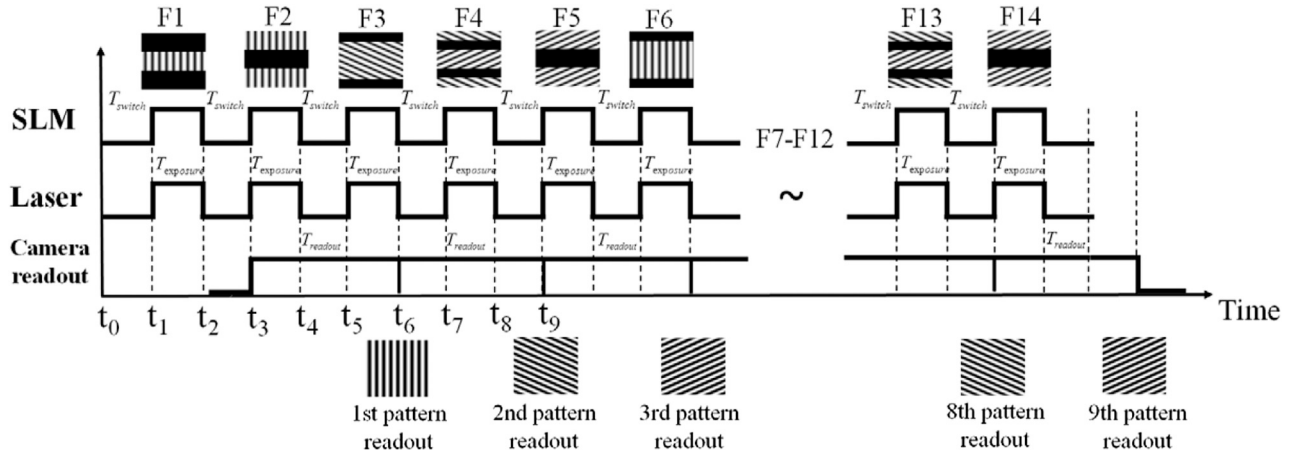

FIGURE 5 | The modified synchronization configuration corresponding to segmented frames [44]. When the camera starts the rolling shutter from the middle of the frame at time t_0, the first segmented F1 is initially uploaded into the SLM. After the SLM finishes uploading F1 at t_1, the laser begins to illuminate for $T_{exposure}$ and the camera detects the emission from the illumination pattern F1. At t_2 the laser is off for T_{switch} and the SLM starts to upload the second frame F2. The camera readout starts at t_3 and the first raw frame receives at t_6. The figure is modified with permission from Ref. (44). Copyright © 2016 IOP Publishing.

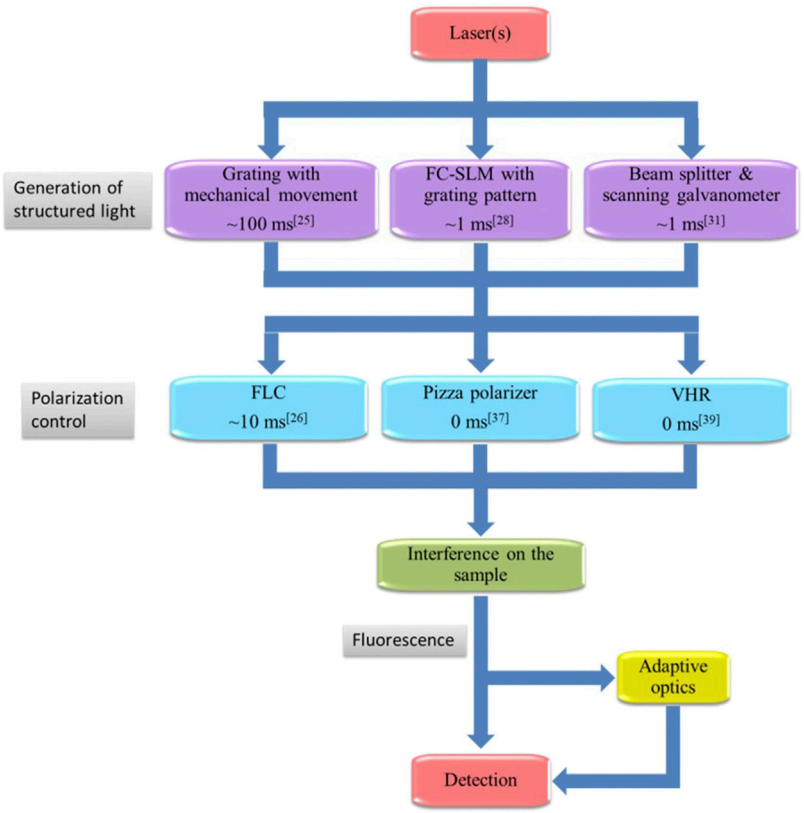

FIGURE 6 | The flowchart for SIM. The majority of SIM systems illuminate samples with one or more lasers. The laser beam is then passed through a pattern-generating system, polarization control system, and interference on the sample. The fluorescence can be optimized by adaptive optics before being detected by the camera.

wavefront sensing and adaptive elements, such as a deformable mirror (DM) or SLM, are used to correct the depth-dependent aberrations [46]. To overcome the aberration and imaging at depth, AO have been an attractive line of research in SIM. The combination of AO and SIM was applied to image through 35 μm of *C. elegans* samples with a resolution of 140 nm [47]. Although

TABLE 1 | Comparison of SIM performance.

Key component	FC-SLM [28]	Scanning galvanometer [31]	FLC [27]	Pizza polarizer [37]	Vortex half-wave retarder [39]	Rolling shutter cameras [44]
Objective	60 × NA1.2	60 × NA1.49	100 × NA1.49	63 × NA1.4	100 × NA1.49	63 × NA1.4
Frame rate	11 Hz@512 × 512 pixel	10 Hz@256 × 256 pixel	11 Hz@128 × 128 pixel	7.6 Hz@1024 × 768 pixel	162 Hz@512 × 100 pixel	79 Hz@512 × 512 pixel
Field of view	25 × 25 μm^2	40 × 40 μm^2	8 × 8 μm^2	19.5 × 13.8 μm^2	36 × 7.2 μm^2	16.5 × 16.5 μm^2
Excitation wave length	Multi	Multi	Single	Single	Multi	Single

the complex adjustment by AO devices takes typically 2–3 min, a one-time wavefront distortion measurement and correction ensure high-quality, hours-long recordings [48]. More recently, Turcotte et al. reported an application of AO to correcting sample-induced optical aberrations *in vivo* with 9.3 fps at a depth of 50 μm, demonstrating the application of SIM in live tissue and *in vivo* imaging [49].

Summary

To permit direct comparisons, we present a comparison flowchart of SIM systems, with more details of the key components of these methods and their performance summarized in **Table 1**. The reader should note that a combination of these methods is feasible, in which the frame rate of SIM images can reach up to 188 fps [50]. However, it will significantly increase the difficulty of building the system. The skillful work by Justin et al [51] and software like SIMcheck [52] provide advanced calibration tools and utilities to create an optimal SIM imaging environment.

RECONSTRUCTION METHODS FOR FAST SIM

Fewer Raw Images

To unmix spatial frequencies along a single direction, conventional 2D-SIM requires three images to be acquired with translated illumination patterns [53]. In order to provide isotropic resolution enhancement, SIM needs to perform this process three times and rotate illumination fringes three times, which yields a total of nine raw images per SR SIM image [54]. Acquiring these nine images to yield a single super-resolution image can be time-consuming. Consequently, reducing the number of raw frames required to produce a SIM image has been an active field of research. It has the potential to increase the acquisition speed and reduce phototoxic effects and bleaching.

In **Eq. 3**, the $\tilde{S}(k)$, $\tilde{S}(k + p)$ and $\tilde{S}(k - p)$ are not independent on one another. This means less than three raw images of a single direction can solve the spatial frequencies and less than nine raw images should be enough for SIM reconstruction. In 2003, Heintzmann realized the redundant data in the SIM algorithm and discussed the potential for substantially decreasing the required number of raw images in SIM. However, **Eq. 4** cannot be solved directly under the condition of fewer raw data, and newer methods were required [55]. In 2015, an alternative imaging strategy was presented, which reduced the number of image acquisitions into four raw images and reconstructed the SR image by a modified, incoherent Fourier ptychographic procedure [56]. Because of the properties of the Fourier transform, there is same information in the ±1 order of the Fourier spectrum of raw images. 0 and π phase shifts illumination fringes can be simply used as the modulating pattern. Thus the method first uses two commentary patterns with the same direction with 0 and π phase shifts, providing a uniform modulation for the sample. A good initial guess is formed by the summation of these two images for the high-resolution sample image. The other two patterns provide different orientations to isotopically double the bandwidth in the Fourier domain. To recover the SR image from the four raw images, the Fourier ptychographic needs the initial guess and the target image as

$$I_{obj} = I_1 + I_2, \;\; I_{tn} = I_{obj} \cdot P_n \tag{5}$$

where $I_n (n = 1,2,3,4)$ is the raw images and P_n $(n = 1,2,3,4)$ is the illumination sinusoidal patterns. Then the initial guess and the target image updates with I_n as

$$I_{tn}^{updated} = I_{tn} + deconvwnr\,(I_n - I_{tn} \otimes H), \tag{6}$$

$$I_{\mathrm{obj}}^{\mathrm{updated}} = I_{\mathrm{obj}} + \frac{P_{\mathrm{n}}}{(\max(P_{\mathrm{n}}))^2}\left(I_{\mathrm{tn}}^{\mathrm{updated}} - I_{\mathrm{obj}} \cdot P_{\mathrm{n}}\right), \tag{7}$$

where H, deconvwnr and max stand for the point spread function, wiener deconvolution and taking the maximum value, respectively. **Eqs 6**, **7** are iteratively repeated for the four measurements. The iteration process is terminated until the difference between two successive recoveries is less than the given limit of error. Although this 4-frame SIM method decreases the data acquisition time greater than two-fold, analysis of each area of the spectra in SIM revealed that there is still an overdetermined equation system in this approach. To overcome this, the authors proposed an underdetermined SIM with three raw images and generated an estimate of the SR image by using a joint Richardson-Lucy deconvolution algorithm [53]. Therefore, it needs only one-third acquiring time compared to the traditional method.

However, both 4-frame SIM and 3-frame SIM utilize iterative algorithms to arrive at the reconstructed image, whereas the conventional 9-frame SIM provides a single-step solution. Over 200 loop numbers are needed to converge the SR image,

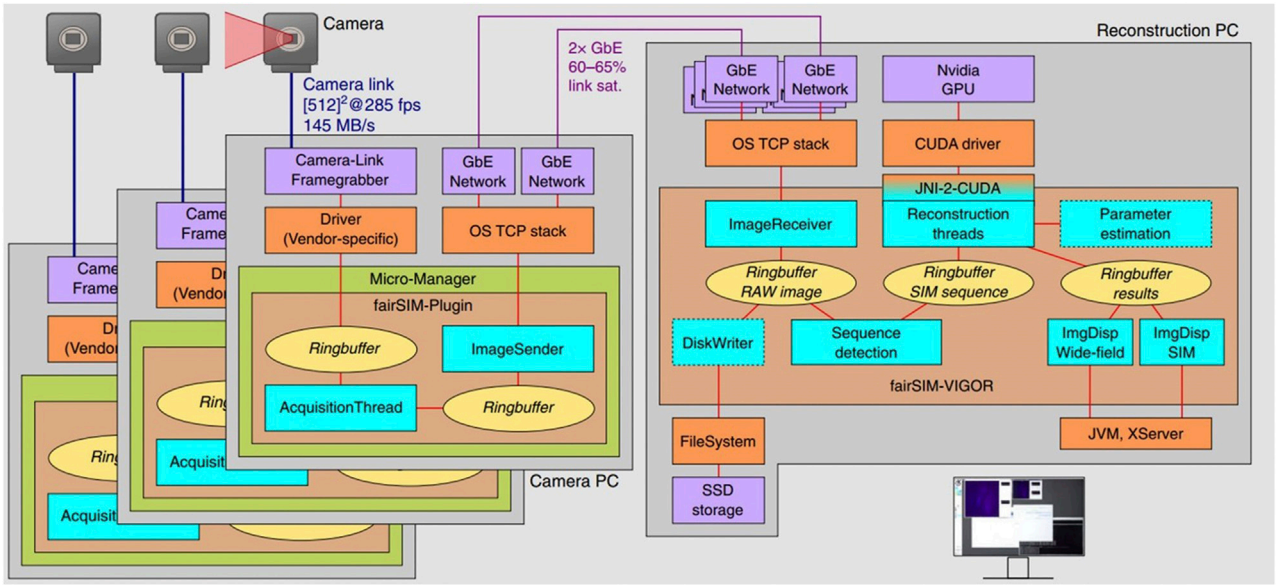

FIGURE 7 | Structure of the real-time reconstruction software fairSIM-VIGOR [62]. These schematics show the data flow of the raw images through the on-the-fly reconstruction pipeline, which from sCMOS to Camera PC is on the left part of the figure (note that there are three of these systems working simultaneously) and from Camera computers to Reconstruction PC is on the right part of the figure. The left part of the image shows the data flow within each camera PC and the right part is flow through the reconstruction PC. The figure is modified with permission from Ref. (62). Copyright © 2019 Springer Nature.

which leads to a significant increase in the amount of time required for post-processing.

GPU Acceleration and Real-Time Display

To reduce the effects of movement in the sample and or the microscope system, image capturing, processing, and the SR image display must occur in rapid succession when imaging live-cells in real-time [57]. The datasets are normally post-processed to speed up the capturing process due to the time-consuming image reconstruction in computational processing. This dilemma has limited the use for real-time evaluation of samples since SR images are not available during image acquisition [58].

To realize the real-time reconstruction, Markwirth et al. utilized a graphics processing unit (GPU) to perform high-speed image reconstruction [59]. GPUs take advantage of executing calculations in a parallel fashion dealing with SIM reconstruction, which is faster than the serial fashion on computer central processing units (CPUs). This follows because the CPU executes calculations sequentially, significantly slowing down the process of images. Using the GPU, a more than 10 fold increase in processing speed was achieved comparing with processing on a multi-core CPU [60].

To display the reconstruction results in real-time, it is necessary to increase the data transmission and processing speed [61]. Continuous reconstruction is achieved by a modularized, networked, and multi-threaded framework (**Figure 7**) [62]. Here, three cameras, each connected to a separate computer were used to capture images (one per laser wavelength). In order to permit the rapid transfer of camera data for nearly instantaneous processing on the GPU, these three systems were connected to a dedicated reconstruction computer by Gigabit Ethernet lines.

It takes ~200 ms to reconstruct a 2D SIM for a typical input image size of 512 × 512 pixels using a current multi-core desktop CPU. Including data transfer to the GPU and back, there is about 20 ms latency to the image processing pipeline in the GPU-assisted SIM reconstruction on a mid-range consumer-level graphics card (Nvidia GTX 1060). Experimental results show 10.4 fps SR imaging speed and less than 250 ms delay between measurement and reconstructed image display, with 512 × 512 pixels and 2 ms illumination time per raw frame. While this approach demonstrates the advantage of GPU-processing, the drawback is the complicated and expensive system which has multiple cameras each with a computer and a fourth PC performing reconstruction.

Deep Learning

Deep learning is a kind of machine learning, which is a powerful tool for increasing the depth of the neural network. It emphasizes looking for increasingly meaningful representations during learning from successive layers [63]. Deep learning methods have been applied to SR microscopy in recent years and could be a solution for high-speed SIM. After training by hundreds of paired training data, the deep learning framework can produce the SR image from fewer raw images and boost the performance of the SIM under low-light conditions. This has the potential to allow for reducing phototoxicity in the imaging process and obtaining the SR imaging at higher speeds [64].

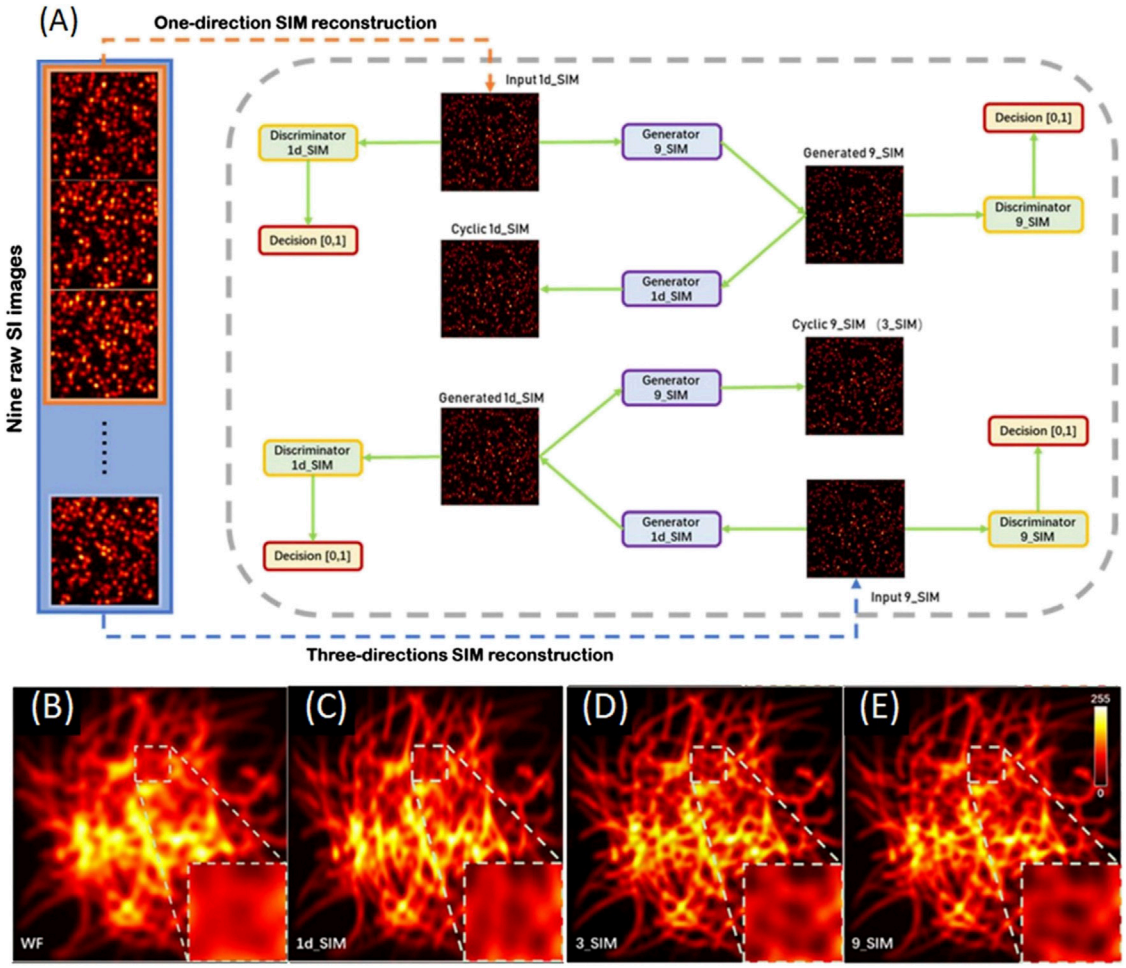

FIGURE 8 | Schematics and results of the deep neural network trained for SIM imaging [65]. **(A)** Deep neural network training cycles. Two training datasets are 1d_SIM and 9_SIM images as the input of two training cycles, following with two generators and two discriminators. These generators and discriminators are trained by optimizing various parameters. This loops until the generated images are accepted by the discriminator. **(B–E)** Deep learning-enabled transformation of images from 1d_SIM to 9_SIM. The 3_SIM image generated by the deep neural network in **(D)** is matched to the 9_SIM image in **(E)**. Figures are modified with permission from Ref. (65). Copyright © 2020 Chinese Laser Press.

To illustrate how this works, one example of a deep neural network trained for SIM imaging is shown in **Figure 8** [65]. Two datasets are needed for training the neural network, which are the SR image in one direction as train A (1d_SIM) and the SR image in three directions as train B (9_SIM). There are two generators and two discriminators featured the deep neural network. Generator 9_SIM transformed images in train A into generated 9_SIM and generated 9_SIM images are transmitted to cyclic 1d_SIM by generator 1d_SIM. Same process subjects to the input images of the 9_SIM dataset. The input of discriminator A and discriminator B are images of the 1d_SIM and 9_SIM datasets, respectively. The loss function is used to train the data, identifying if the output image is generated by the generator or the raw image. This process is repeated until the generated images are accepted by the discriminator. Experimental results in **Figures 8D,E** show that only three raw images in a given direction can generate an SR image in three directions and the resolution of the reconstruction rivals that of the traditional SIM methods.

Reconstruction in the Spatial Domain

The inventor of SIM, Mats G. Gustafsson once said: "I like to think in frequency space, rather than in real space" [66]. Consequently, in traditional SIM systems, the basic workflow to generate the SR image is built on spatial spectrum processing and Fourier domain reconstruction (FDR). The transfer time between spatial and frequency domain slows down the reconstruction speed of SR images inevitably [67, 68]. Since the frequency and spatial domains can be transformed into each other, it should be possible to reconstruct the SR image

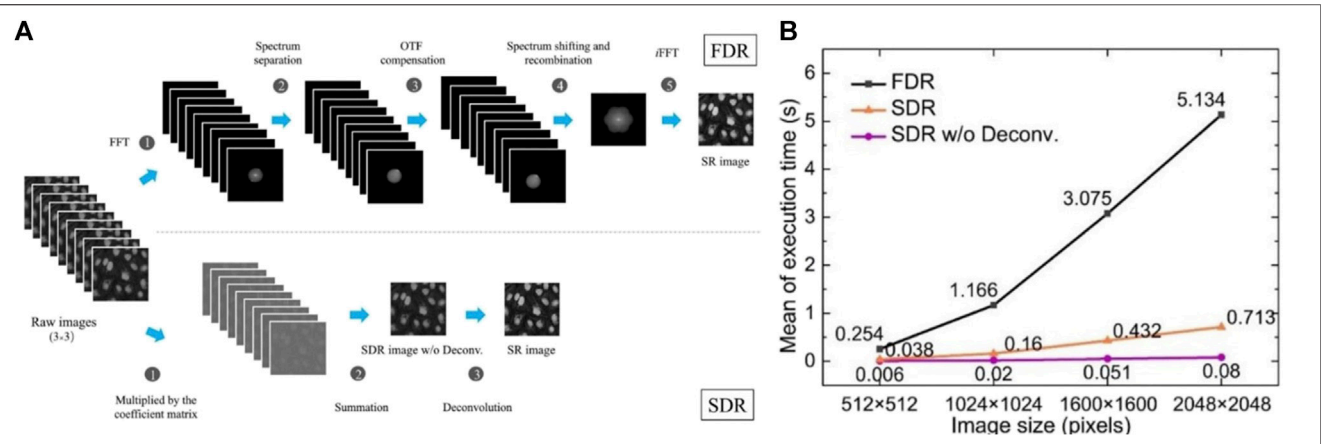

FIGURE 9 | SDR generates SR images 64-fold faster than FDR [71]. **(A)** The comparison of the FDR and SDR image reconstruction schemes. Top line, the FDR workflow needs the five steps to attain a super-resolution image. Bottom line, SDR is intrinsically simpler, which is only 3-step workflow. **(B)** The comparison of the mean execution time between different reconstruction schemes. The mean value of the execution time for SDR without deconvolution is up to 64 times faster than that of FDR.

in the spatial domain. This concept appeared in early works where the theoretical framework was laid down [69, 70]. Recently, the ability to reconstruct the SR image in the spatial domain was demonstrated experimentally by a significantly improved algorithm which is called spatial domain reconstruction or, SDR [71].

The mathematical background of SDR can be described from the perspective of point-spread-function (PSF) engineering, which in SIM generates a composite image with an effective PSF narrower than conventional wide-field microscopy [70]. Thus, the SR image $R_{SDR}(r)$ and its PSF $P(r)$ can be described as

$$R_{SDR}(r) = S(r) \otimes P(r), \tag{8}$$

$$P(r) = \left[1 + cos\left(2\pi p \cdot r\right)\right] \cdot H(r). \tag{9}$$

In the SDR scheme, the patterned illuminated raw images are linear superposition with appropriately weighted coefficients c to attain the SR image. Then the reconstructed SR image is

$$R_{SDR}(r) = \sum_{ja1}^{n} c_j(r)\left[I(r) \cdot S(r)\right] \otimes H(r), \tag{10}$$

where j indicates the several steps shifting of the illumination pattern. It is solvable to the expressions of $c_j(r)$ after expanded into a series of orthogonal complete basis and substituting **Eq. 10** into **Eq. 8**.

In order to perform spectral processing of the images, Fourier transformation are needed with nine raw images (**Figure 9A**, top). After separating the spectra and OTF compensated, the spectra are recombined and enlarged isotropically. Then an inverse fast Fourier transform (iFFT) is used to form an SR image. The multiple operations of iFFT and FFT require significant CPU processing time. In contrast, only three simple steps operate in the SDR scheme, which are image multiplication, summation, and deconvolution (**Figure 9A**, bottom). The multiplied coefficient matrixes can be pre-calculated because they only depend on the sinusoidal light pattern. Consequently, SDR processes one SR image 7- to 64-fold more rapidly than FDR (**Figure 9B**).

The superiority of SDR in producing SR images was demonstrated by imaging fluorescent cells and separately, 100 nm beads in solution (**Figure 10**). The results from cellular imaging show while both FDR and SDR reconstruction approaches produce comparable SR images, SDR is both faster and can discern fine details better than FDR. A further advantage of SDR is revealed when mobile fluorescent beads are imaged. In this example, the Brownian motion of the beads was recorded in real-time with nine raw images reconstructing one frame of the SR image. Importantly, only SDR was sufficiently rapid to produce these movies.

Summary

Considering the growing array of SR-SIM reconstruction methods, picking the "right tool for the job" can be a challenging task. Nevertheless, some general trends become clear when a comparison of the techniques presented in this review is made (**Table 2**). This comparison is qualitative as the actual speed of each system is limited by many factors including the sample used for imaging, the microscope, and the computer hardware and software. As a reference, we use commercial SIM systems and compare acquisition and post-processing speed, and implementation complexity. For acquisition speed, 3-frame SIM and Deep learning methods perform the best and receive the most stars. This makes sense because less raw data are needed for SR image reconstruction and this results in better ways to track sample movement. Deep learning and SDR methods have a faster post-processing speed, which has the benefit of displaying reconstructed SR images of live-cells in real-time. However, these methods are more complex than the commercial ones, especially the deep learning method which requires thousands of pieces of raw data to build the deep neural network.

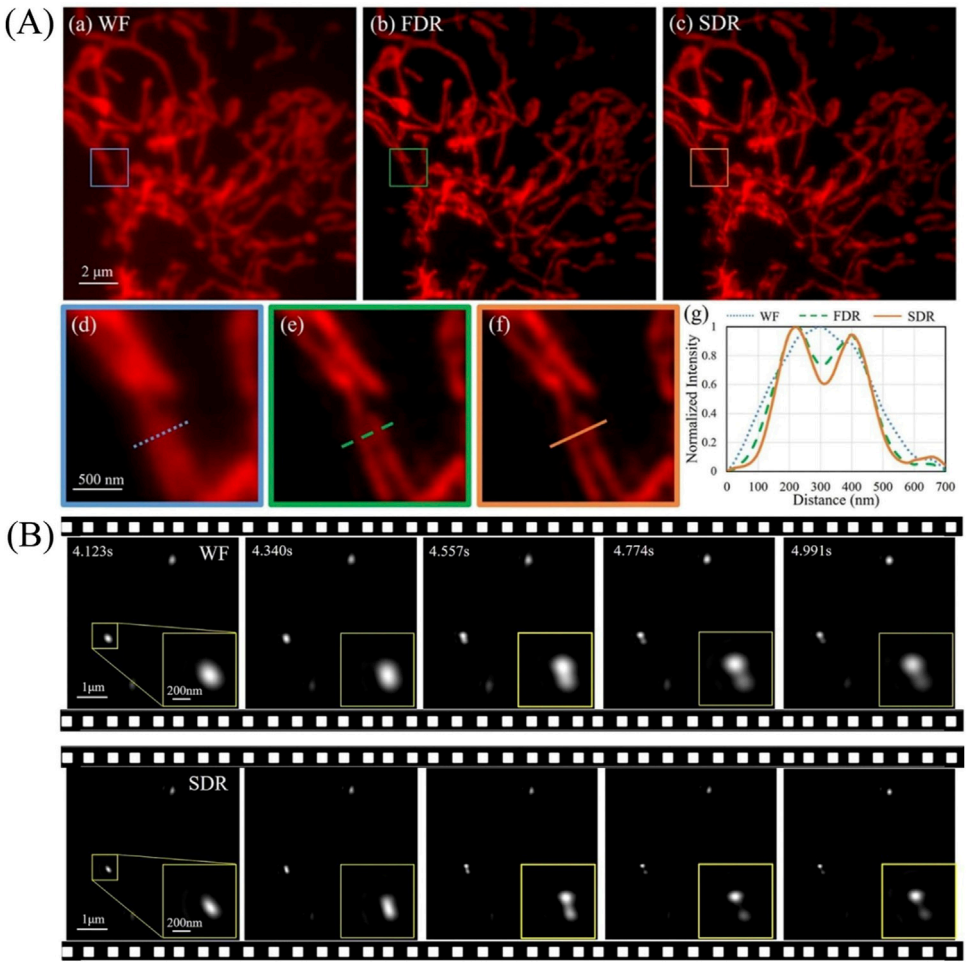

FIGURE 10 | SDR resolves fine details better than FDR in both static and dynamic imaging [71]. **(Ai–iii)** Images reconstructed by wide-field, FDR- and SDR-SIM, respectively. **(Aiv–vi)** The magnified views in the boxed regions in **(Ai–iii)**. **(Avii)** Intensity profiles along the marked lines in **(Aiv–vi)**. **(B)** SDR enables the resolution of beads. Five time-sequential frames in an interval of 217 ms are shown. The zoom-in boxes display the relative position variance of two adjacent beads.

TABLE 2 | Comparison of reconstruction methods for fast SIM.

Component	Commercial	4-frame SIM	3-frame SIM	GPU	Deep Learning	SDR
Acquisition speed	★★★[a]	★★★★★	★★★★★★	★★★★	★★★★★★	★★★★
Post-processing speed	★★★	★★	★★	★★★★	★★★★★★	★★★★★
Implementing complexity	★★★	★★	★★	★★	★	★★★

[a]*More stars indicate that the method performs better.*

CONCLUSION

As one of the super-resolution imaging techniques available, structured illumination microscopy has broken through the diffraction limit and become a powerful tool for studying living cells. As a result of low phototoxicity and high frame rate acquisition, SIM stands alone as the approach to imaging biological transactions at super-resolution and in real-time in living cells. Since its first appearance as an imaging modality 20 years ago, numerous approaches have been presented to increase acquisition speed and improve image reconstruction time. Further advancements in the optical layout such as those seen in fast SIM will further contribute to improvements in image acquisition and quality. The combination of GPU processing and the SDR algorithm will likely push image reconstruction speeds to even greater speeds. When these advances are combined with the use of brighter and more photostable dyes, the anticipated shorter exposure times during image acquisition will result in even lower phototoxicity and increases in imaging speed. Consequently,

this will further establish high-speed SIM as the SR imaging choice for live-cell biological transactions in real-time.

AUTHOR CONTRIBUTIONS

TZ conceived the idea and finished the manuscript. ZW, PB, YB, and ML gave guidance. PB and ML supervised the project. All the authors contributed to the discussion on this manuscript.

FUNDING

This work was supported by Natural Science Foundation of China (NSFC) (61905189, 62005208); China Postdoctoral Science Foundation (2019M663656, 2020M673365); National Key Research and Development Program of China (2017YFC0110100) and National Institutes of Health Grant GM100156 to PRB.

REFERENCES

1. Abbe E. Beiträge zur Theorie des Mikroskops und der mikroskopischen Wahrnehmung. *Archiv F Mikrosk Anatomie* (1873) 9:413–68. doi:10.1007/bf02956173
2. Hedde PN, and Nienhaus GU. Super-resolution Localization Microscopy with Photoactivatable Fluorescent Marker Proteins. *Protoplasma* (2014) 251(2): 349–62. doi:10.1007/s00709-013-0566-z
3. Hell SW, and Wichmann J. Breaking the Diffraction Resolution Limit by Stimulated Emission: Stimulated-Emission-Depletion Fluorescence Microscopy. *Opt Lett* (1994) 19(11):780–2. doi:10.1364/ol.19.000780
4. Klar TA, and Hell SW. Subdiffraction Resolution in Far-Field Fluorescence Microscopy. *Opt Lett* (1999) 24(14):954–6. doi:10.1364/ol.24.000954
5. Klar TA, Jakobs S, Dyba M, Egner A, and Hell SW. Fluorescence Microscopy with Diffraction Resolution Barrier Broken by Stimulated Emission. *Proc Natl Acad Sci* (2000) 97(15):8206–10. doi:10.1073/pnas.97.15.8206
6. Arroyo-Camejo S, Adam M-P, Besbes M, Hugonin J-P, Jacques V, Greffet J-J, et al. Stimulated Emission Depletion Microscopy Resolves Individual Nitrogen Vacancy Centers in diamond Nanocrystals. *ACS Nano* (2013) 7(12):10912–9. doi:10.1021/nn404421b
7. Betzig E, Patterson GH, Sougrat R, Lindwasser OW, Olenych S, Bonifacino JS, et al. Imaging Intracellular Fluorescent Proteins at Nanometer Resolution. *Science* (2006) 313(5793):1642–5. doi:10.1126/science.1127344
8. Hess ST, Girirajan TPK, and Mason MD. Ultra-high Resolution Imaging by Fluorescence Photoactivation Localization Microscopy. *Biophysical J* (2006) 91(11):4258–72. doi:10.1529/biophysj.106.091116
9. Shroff H, Galbraith CG, Galbraith JA, and Betzig E. Live-cell Photoactivated Localization Microscopy of Nanoscale Adhesion Dynamics. *Nat Methods* (2008) 5(5):417–23. doi:10.1038/nmeth.1202
10. Rust MJ, Bates M, and Zhuang X. Sub-diffraction-limit Imaging by Stochastic Optical Reconstruction Microscopy (STORM). *Nat Methods* (2006) 3(10): 793–6. doi:10.1038/nmeth929
11. Huang B, Wang W, Bates M, and Zhuang X. Three-dimensional Super-resolution Imaging by Stochastic Optical Reconstruction Microscopy. *Science* (2008) 319(5864):810–3. doi:10.1126/science.1153529
12. Gustafsson MG. Extended Resolution Fluorescence Microscopy. *Curr Opin Struct Biol* (1999) 9(5):627–8. doi:10.1016/s0959-440x(99)00016-0
13. Gustafsson MGL, Shao L, Carlton PM, Wang CJR, Golubovskaya IN, Cande WZ, et al. Three-dimensional Resolution Doubling in Wide-Field Fluorescence Microscopy by Structured Illumination. *Biophysical J* (2008) 94(12):4957–70. doi:10.1529/biophysj.107.120345
14. Zhou X, Lei M, Dan D, Yao B, Yang Y, Qian J, et al. Image Recombination Transform Algorithm for Superresolution Structured Illumination Microscopy. *J Biomed Opt* (2016) 21(9):096009–15. doi:10.1117/1.jbo.21.9.096009
15. Gustafsson MGL. Surpassing the Lateral Resolution Limit by a Factor of Two Using Structured Illumination Microscopy. SHORT COMMUNICATION. *J Microsc* (2000) 198(2):82–7. doi:10.1046/j.1365-2818.2000.00710.x
16. Kashiwagi Y, Higashi T, Obashi K, Sato Y, Komiyama NH, Grant SG, et al. Computational Geometry Analysis of Dendritic Spines by Structured Illumination Microscopy. *Nat Commun* (2019) 10(1):1–14. doi:10.1038/s41467-019-09337-0
17. Phillips JK, Sherman SA, Cotton KY, Heddleston JM, Taylor AB, and Finan JD. Characterization of Neurite Dystrophy after Trauma by High Speed Structured Illumination Microscopy and Lattice Light Sheet Microscopy. *J Neurosci Methods* (2019) 312:154–61. doi:10.1016/j.jneumeth.2018.12.005
18. Zhao T, Liu Y, Wang Z, He R, Xiang Zhang J, Xu F, et al. Super-resolution Imaging Reveals Changes inEscherichia coliSSB Localization in Response to DNA Damage. *Genes Cells* (2019) 24(12):814–26. doi:10.1111/gtc.12729
19. Wicker K, Mandula O, Best G, Fiolka R, and Heintzmann R. Phase Optimisation for Structured Illumination Microscopy. *Opt Express* (2013) 21(2):2032–49. doi:10.1364/oe.21.002032
20. Zheng X, Zhou J, Wang L, Wang M, Wu W, Chen J, et al. Current Challenges and Solutions of Super-resolution Structured Illumination Microscopy. *APL Photon* (2021) 6(2):020901. doi:10.1063/5.0038065
21. Young LJ, Ströhl F, and Kaminski CF. A Guide to Structured Illumination TIRF Microscopy at High Speed with Multiple Colors. *JoVE* (2016) 3568(111): e53988–e97. doi:10.3791/53988
22. Chang B-J, Chou L-J, Chang Y-C, and Chiang S-Y. Isotropic Image in Structured Illumination Microscopy Patterned with a Spatial Light Modulator. *Opt Express* (2009) 17(17):14710–21. doi:10.1364/oe.17.014710
23. Gustafsson MGL. Nonlinear Structured-Illumination Microscopy: Wide-Field Fluorescence Imaging with Theoretically Unlimited Resolution. *Proc Natl Acad Sci* (2005) 102(37):13081–6. doi:10.1073/pnas.0406877102
24. Shroff SA, Fienup JR, and Williams DR. Phase-shift Estimation in Sinusoidally Illuminated Images for Lateral Superresolution. *J Opt Soc Am A* (2009) 26(2): 413–24. doi:10.1364/josaa.26.000413
25. R Heintzmann and CG Cremer, editors. *Laterally Modulated Excitation Microscopy: Improvement of Resolution by Using a Diffraction Grating.* Optical Biopsies And Microscopic Techniques III. Stockholm, Sweden: Proceedings of SPIE (1999).
26. Fiolka R, Beck M, and Stemmer A. Structured Illumination in Total Internal Reflection Fluorescence Microscopy Using a Spatial Light Modulator. *Opt Lett* (2008) 33(14):1629–31. doi:10.1364/ol.33.001629
27. Kner P, Chhun BB, Griffis ER, Winoto L, and Gustafsson MGL. Super-resolution Video Microscopy of Live Cells by Structured Illumination. *Nat Methods* (2009) 6(5):339–42. doi:10.1038/nmeth.1324
28. Shao L, Kner P, Rego EH, and Gustafsson MGL. Super-resolution 3D Microscopy of Live Whole Cells Using Structured Illumination. *Nat Methods* (2011) 8(12):1044–6. doi:10.1038/nmeth.1734
29. Fiolka R, Shao L, Rego EH, Davidson MW, and Gustafsson MGL. Time-lapse Two-Color 3D Imaging of Live Cells with Doubled Resolution Using Structured Illumination. *Proc Natl Acad Sci* (2012) 109(14):5311–5. doi:10.1073/pnas.1119262109
30. Schermelleh L, Carlton PM, Haase S, Shao L, Winoto L, Kner P, et al. Subdiffraction Multicolor Imaging of the Nuclear Periphery with 3D Structured Illumination Microscopy. *Science* (2008) 320(5881):1332–6. doi:10.1126/science.1156947
31. Liu W, Liu Q, Zhang Z, Han Y, Kuang C, Xu L, et al. Three-dimensional Super-resolution Imaging of Live Whole Cells Using Galvanometer-Based Structured Illumination Microscopy. *Opt Express* (2019) 27(5):7237–48. doi:10.1364/oe.27.007237
32. Chen Y, Cao R, Liu W, Zhu D, Zhang Z, Kuang C, et al. Widefield and Total Internal Reflection Fluorescent Structured Illumination Microscopy with Scanning Galvo Mirrors. *J Biomed Opt* (2018) 23(4):046007–16. doi:10.1117/1.jbo.23.4.046007
33. York AG, Chandris P, Nogare DD, Head J, Wawrzusin P, Fischer RS, et al. Instant Super-resolution Imaging in Live Cells and Embryos via Analog Image Processing. *Nat Methods* (2013) 10:1122–6. doi:10.1038/nmeth.2687
34. Pawley J. *Handbook of Biological Confocal Microscopy*. Madison, WI: Springer Science & Business Media (2006).

35. Li D, Shao L, Chen BC, Zhang X, Zhang M, Moses B, et al. Extended-resolution Structured Illumination Imaging of Endocytic and Cytoskeletal Dynamics. *Science* (2015) 349(6251):aab3500–aab10. doi:10.1126/science.aab3500
36. O'Holleran K, and Shaw M. Polarization Effects on Contrast in Structured Illumination Microscopy. *Opt Lett* (2012) 37(22):4603–5. doi:10.1364/OL.37.004603
37. Lu-Walther H-W, Kielhorn M, Förster R, Jost A, Wicker K, and Heintzmann R. fastSIM: a Practical Implementation of Fast Structured Illumination Microscopy. *Methods Appl Fluoresc* (2015) 3(1):014001–9. doi:10.1088/2050-6120/3/1/014001
38. Förster R, Lu-Walther H-W, Jost A, Kielhorn M, Wicker K, and Heintzmann R. Simple Structured Illumination Microscope Setup with High Acquisition Speed by Using a Spatial Light Modulator. *Opt Express* (2014) 22(17):20663–77. doi:10.1364/oe.22.020663
39. Zhao T, Zhou X, Dan D, Qian J, Wang Z, Lei M, et al. Polarization Control Methods in Structured Illumination Microscopy. *Acta Phys Sin* (2017) 66(14):148704–15. doi:10.7498/aps.66.148704
40. Guo Y, Li D, Zhang S, Yang Y, Liu J-J, Wang X, et al. Visualizing Intracellular Organelle and Cytoskeletal Interactions at Nanoscale Resolution on Millisecond Timescales. *Cell* (2018) 175(5):1430–42. doi:10.1016/j.cell.2018.09.057
41. Brunstein M, Wicker K, Hérault K, Heintzmann R, and Oheim M. Full-field Dual-Color 100-nm Super-resolution Imaging Reveals Organization and Dynamics of Mitochondrial and ER Networks. *Opt Express* (2013) 21(22):26162–73. doi:10.1364/oe.21.026162
42. Peng X, Huang X, Du K, Liu H, and Chen L. High Spatiotemporal Resolution and Low Photo-Toxicity Fluorescence Imaging in Live Cells and In Vivo. *Biochem Soc Trans* (2019) 47(6):1635–50. doi:10.1042/bst20190020
43. Gao P, and Nienhaus GU. Confocal Laser Scanning Microscopy with Spatiotemporal Structured Illumination. *Opt Lett* (2016) 41(6):1193–6. doi:10.1364/ol.41.001193
44. Song L, Lu Walther HW, Förster R, Jost A, Kielhorn M, Zhou J, et al. Fast Structured Illumination Microscopy Using Rolling Shutter Cameras. *Meas Sci Technol* (2016) 27(5):055401–7. doi:10.1088/0957-0233/27/5/055401
45. Sahu P, and Mazumder N. Improving the Way We See: Adaptive Optics Based Optical Microscopy for Deep-Tissue Imaging. *Front Phys* (2021) 9:138. doi:10.3389/fphy.2021.654868
46. Débarre D, Botcherby EJ, Booth MJ, and Wilson T. Adaptive Optics for Structured Illumination Microscopy. *Opt Express* (2008) 16(13):9290–305. doi:10.1364/oe.16.009290
47. Thomas B, Wolstenholme A, Chaudhari SN, Kipreos ET, and Kner P. Enhanced Resolution through Thick Tissue with Structured Illumination and Adaptive Optics. *J Biomed Opt* (2015) 20(2):026006. doi:10.1117/1.jbo.20.2.026006
48. Li Z, Zhang Q, Chou S-W, Newman Z, Turcotte R, Natan R, et al. Fast Widefield Imaging of Neuronal Structure and Function with Optical Sectioning In Vivo. *Sci Adv* (2020) 6(19):eaaz3870. doi:10.1126/sciadv.aaz3870
49. Turcotte R, Liang Y, Tanimoto M, Zhang Q, Li Z, Koyama M, et al. Dynamic Super-resolution Structured Illumination Imaging in the Living Brain. *Proc Natl Acad Sci USA* (2019) 116(19):9586–91. doi:10.1073/pnas.1819965116
50. Huang X, Fan J, Li L, Liu H, Wu R, Wu Y, et al. Fast, Long-Term, Super-resolution Imaging with Hessian Structured Illumination Microscopy. *Nat Biotechnol* (2018) 36(5):451–9. doi:10.1038/nbt.4115
51. Demmerle J, Innocent C, North AJ, Ball G, Müller M, Miron E, et al. Strategic and Practical Guidelines for Successful Structured Illumination Microscopy. *Nat Protoc* (2017) 12(5):988–1010. doi:10.1038/nprot.2017.019
52. Ball G, Demmerle J, Kaufmann R, Davis I, Dobbie IM, and Schermelleh L. SIMcheck: a Toolbox for Successful Super-resolution Structured Illumination Microscopy. *Sci Rep* (2015) 5(1):1–12. doi:10.1038/srep15915
53. Ströhl F, and Kaminski CF. Speed Limits of Structured Illumination Microscopy. *Opt Lett* (2017) 42(13):2511–4. doi:10.1364/ol.42.002511
54. Zhanghao K, Chen X, Liu W, Li M, Liu Y, Wang Y, et al. Super-resolution Imaging of Fluorescent Dipoles via Polarized Structured Illumination Microscopy. *Nat Commun* (2019) 10(1):1–10. doi:10.1038/s41467-019-12681-w
55. Heintzmann R. Saturated Patterned Excitation Microscopy with Two-Dimensional Excitation Patterns. *Micron* (2003) 34(6-7):283–91. doi:10.1016/s0968-4328(03)00053-2
56. Dong S, Liao J, Guo K, Bian L, Suo J, and Zheng G. Resolution Doubling with a Reduced Number of Image Acquisitions. *Biomed Opt Express* (2015) 6(8):2946–52. doi:10.1364/boe.6.002946
57. Wicker K. Non-iterative Determination of Pattern Phase in Structured Illumination Microscopy Using Auto-Correlations in Fourier Space. *Opt Express* (2013) 21(21):24692–701. doi:10.1364/oe.21.024692
58. Chu K, McMillan PJ, Smith ZJ, Yin J, Atkins J, Goodwin P, et al. Image Reconstruction for Structured-Illumination Microscopy with Low Signal Level. *Opt Express* (2014) 22(7):8687–702. doi:10.1364/oe.22.008687
59. Descloux A, Müller M, Navikas V, Markwirth A, Van den Eynde R, Lukes T, et al. High-speed Multiplane Structured Illumination Microscopy of Living Cells Using an Image-Splitting Prism. *Nanophotonics* (2019) 9(1):143–8. doi:10.1515/nanoph-2019-0346
60. Lefman J, Cheuk T, Metaferia B, Scott K, Khan J, and Stranick S. Super-resolution Imaging of Drug Delivery to Live Cells Using Real-Time Structured Illumination Microscopy. *Microsc Microanal* (2010) 16(S2):666–7. doi:10.1017/s1431927610060265
61. Müller M, Mönkemöller V, Hennig S, Hübner W, and Huser T. Open-source Image Reconstruction of Super-resolution Structured Illumination Microscopy Data in ImageJ. *Nat Commun* (2016) 7(1):1–6. doi:10.1038/ncomms10980
62. Markwirth A, Lachetta M, Mönkemöller V, Heintzmann R, Hübner W, Huser T, et al. Video-rate Multi-Color Structured Illumination Microscopy with Simultaneous Real-Time Reconstruction. *Nat Commun* (2019) 10(1):1–11. doi:10.1038/s41467-019-12165-x
63. LeCun Y, Bengio Y, and Hinton G. Deep Learning. *Nature* (2015) 521(7553):436–44. doi:10.1038/nature14539
64. Qiao C, Li D, Guo Y, Liu C, Jiang T, Dai Q, et al. Evaluation and Development of Deep Neural Networks for Image Super-resolution in Optical Microscopy. *Nat Methods* (2021) 18:194–202. doi:10.1038/s41592-020-01048-5
65. Ling C, Zhang C, Wang M, Meng F, Du L, and Yuan X. Fast Structured Illumination Microscopy via Deep Learning. *Photon Res* (2020) 8(8):1350–9. doi:10.1364/prj.396122
66. Masters BR. "Structured Illumination Microscopy," in *Superresolution Optical Microscopy*. (Cham: Springer) (2020), 233–60. doi:10.1007/978-3-030-21691-7_13
67. Dan D, Lei M, Yao B, Wang W, Winterhalder M, Zumbusch A, et al. DMD-based LED-Illumination Super-resolution and Optical Sectioning Microscopy. *Sci Rep* (2013) 3(1):1–7. doi:10.1038/srep01116
68. Perez V, Chang BJ, and Stelzer EHK. Optimal 2D-SIM Reconstruction by Two Filtering Steps with Richardson-Lucy Deconvolution. *Sci Rep* (2016) 6(1):1–11. doi:10.1038/srep37149
69. Lukosz W. Notizen: Ein Verfahren zur optischen Abbildung mit einem über die klassische Auflösungsgrenze hinausgehenden Auflösungsvermögen. *Z Nat Forsch A* (1963) 18(3):436–8. doi:10.1515/zna-1963-0330
70. So PTC, Kwon H-S, and Dong CY. Resolution Enhancement in Standing-Wave Total Internal Reflection Microscopy: A Point-spread-function Engineering Approach. *J Opt Soc Am A* (2001) 18(11):2833–45. doi:10.1364/josaa.18.002833
71. Dan D, Wang Z, Zhou X, Lei M, Zhao T, Qian J, et al. Rapid Image Reconstruction of Structured Illumination Microscopy Directly in the Spatial Domain. *IEEE Photon J.* (2021) 13(1):1–11. doi:10.1109/jphot.2021.3053110

Conflict of Interest: The authors declare that the research was conducted in the absence of any commercial or financial relationships that could be construed as a potential conflict of interest.

frontiers in Physics

ORIGINAL RESEARCH
published: 17 June 2021
doi: 10.3389/fphy.2021.666256

Partially Coherent Optical Diffraction Tomography Toward Practical Cell Study

Juan M. Soto, José A. Rodrigo and Tatiana Alieva*

Department of Optics, Faculty of Physical Sciences, Complutense University of Madrid, Madrid, Spain

Optical diffraction tomography (ODT) is a computational imaging technique based on refractive index (RI) contrast. Its application for microscopic imaging of weakly absorbing and scattering samples has been demonstrated by using a specially designed holographic microscope with angular scanning of the coherent sample illumination direction. Recently, an alternative low cost technique based on partially coherent sample illumination (PC-ODT), which is compatible with the conventional wide-field transmission microscope, has been established. In this case, the 3D refractive index distribution of the sample is obtained by deconvolution from a single stack of through-focus intensity images. The performance of PC-ODT has been successfully tested on various fixed specimens (diatom frustule and biological cells) and moving bacteria. Here, we demonstrate that the PC-ODT is an efficient tool for the analysis of living eukaryotic cell dynamics at short- and long-term periods. The COS-7 cells, which hail from the African green monkey kidney, have been chosen for this study. A fast data acquisition setup comprising an optical scanning module can be easily attached to the microscope, and it allows observing cell 3D organelle movements and RI variations, with the required temporal resolution. In particular, a more rapid nucleoli rotation than previously reported has been found. The long-term cell monitoring during necrosis reveals significant changes in cell dry mass concentration obtained from recovered RI contrast.

Keywords: optical diffraction tomography, wide-field transmission microscopy, quantitative imaging, cell imaging, refractive index

OPEN ACCESS

Edited by:
Vicente Mico,
University of Valencia, Spain

Reviewed by:
Kyoohyun Kim,
Max Planck Institute for the Science of Light, Germany
YongKeun Park,
Korea Advanced Institute of Science and Technology, South Korea
Natan Shaked,
Tel Aviv University, Israel

****Correspondence:***
Juan M. Soto
juansoto@ucm.es

Specialty section:
This article was submitted to Optics and Photonics, a section of the journal Frontiers in Physics

Received: *09 February 2021*
Accepted: *21 May 2021*
Published: *17 June 2021*

Citation:
Soto JM, Rodrigo JA and Alieva T (2021) Partially Coherent Optical Diffraction Tomography Toward Practical Cell Study. Front. Phys. 9:666256. doi: 10.3389/fphy.2021.666256

INTRODUCTION

While the theoretical fundamentals of the ODT were developed more than a half of century ago [1], its applications in high-resolution microscopy have been started relatively recently [2–4]. The widely known ODT modality uses spatially and temporally coherent laser light for sample illumination, indicated throughout the article as coherent ODT (C-ODT). It can be implemented in specially designed holographic microscopes [2–4]. Data acquisition consists in angular scanning of sample illumination directions (i.e., illumination beam rotation) and the corresponding hologram recording. The complex field amplitude of the scattered beam is reconstructed from holograms for every illumination direction. Posterior numerical refocusing and deconvolution allow recovering the 3D sample refractive index (RI) distribution. Note that the C-ODT is based on synthetic aperture microscopy extended to 3D case [5, 6]. This angular scanning is a relatively slow process. To improve temporal resolution of 3D RI imaging up to 10 Hz, a non-interferometric C-ODT technique using limited annular illumination has been recently established [7]; however, the demonstrated lateral

(487 nm) and axial (3.4 μm) resolutions are rather low for cell analysis. Another technique which is also based on angular scanning for non-interferometric microscopy has been reported [8], where Kramers–Kronig relations and oblique illuminations are exploited for phase recovery, instead of interferometric measurements. Coherent noise is another limitation of the interferometric C-ODT. Recently, temporally low-coherence light source and a diffraction-based illumination scanning method (using a ferroelectric liquid crystal spatial light modulator for generating the temporally multiplexed sinusoidal patterned beam) have been used to achieve fast (up to 20 Hz) and low-noise 3D RI reconstruction [9].

However, refractive index tomography is also possible to implement in a conventional wide-field transmission microscope obtaining similar results as by C-ODT. It is based on the approach proposed by N. Streibl [10] that allows reconstructing the RI of a studied sample from a stack of through-focus intensity images obtained by simultaneous illumination of the sample from all the directions allowed by the microscope aperture. The experimental implementation of this modality, further referred to as partially coherent ODT (PC-ODT), has been demonstrated in different examples: fibers, spherical particles, diatom frustule, fixed biological cells, and moving bacteria [11–16]. However, probably the main challenge of ODT is the study of cell behavior in its natural environment that has not been reported yet for the case of PC-ODT. Here, we demonstrate the applications of this technique for short- and long-term cell dynamics analysis reaching fast (0.1 s for $60 \times 60 \times 14\ \mu m^3$ volume) 3D RI reconstruction with high lateral (125 nm) and axial (270 nm) resolutions. Note that the 3D RI distribution provides valuable information for biomedical cell studies: its shape, volume, dry mass, and internal structure organization that certainly evolve with time.

This work is organized as follows. First, we shortly review the principle of the PC-ODT technique and describe the experimental setup used for its implementation. We pay special attention to the design of the optical refocusing module (ORM) which has to be attached to the conventional wide-field microscope for fast and easy data acquisition. Note that the ORM is easy to incorporate into any commercial microscope, as for the example the one used in this work (Nikon Eclipse Ti-U inverted). The next section is devoted to the discussion of the experimental results. The work ends with concluding remarks.

PARTIALLY COHERENT-OPTICAL DIFFRACTION TOMOGRAPHY PRINCIPLE, EXPERIMENTAL SETUP, AND SAMPLE PREPARATION

Partially Coherent-Optical Diffraction Tomography Principle

The goal of the ODT [1] is the recovering of the sample scattering potential defined as

$$V(\mathbf{r}) = k_0^2\left(n^2(\mathbf{r}) - n_m^2\right)$$

from a series of intensity measurements. Here, k_0 is the wavenumber in vacuum, $\mathbf{r}$ is a position vector, and $n(\mathbf{r})$ and n_m are the RI of the sample and surrounding media, correspondingly. The scattering potential is, in general, a complex valued function

$$V(\mathbf{r}) = P(\mathbf{r}) + iA(\mathbf{r})$$

with real and imaginary parts, $P(\mathbf{r}) = k_0^2\left(n_{\mathrm{re}}^2(\mathbf{r}) - n_{\mathrm{im}}^2(\mathbf{r}) - n_m^2\right)$ and $A(\mathbf{r}) = 2k_0^2 n_{\mathrm{re}}(\mathbf{r}) n_{\mathrm{im}}(\mathbf{r})$, respectively, that are related to the real (n_{re}) and imaginary (n_{im}) parts of the sample RI ($n = n_{\mathrm{re}} + i\, n_{\mathrm{im}}$) Here, n_m is assumed to be real.

Let us consider that the sample satisfies the first-order Born approximation, which is suitable for weakly absorbing and low scattering samples. Under this approximation, the 3D intensity distribution $I(\mathbf{r})$ measured in a bright-field microscope (e.g., a stack of through-focus intensity images) can be written as the convolution of the point spread function (PSF), $h(\mathbf{r})$, of the microscope and the sample's scattering potential, as demonstrated in Ref [10–14]. By splitting the PSF into its real and imaginary contributions, one obtains the functions $h_P(\mathbf{r})$ and $h_A(\mathbf{r})$ representing the microscope response to a point scatter, $\delta(\mathbf{r})$, and to a point absorber, $i\delta(\mathbf{r})$, correspondingly. Then, $I(\mathbf{r})$ can be understood as the linear superposition of the real and imaginary contributions of the scattering potential, respectively, convolved with $h_P(\mathbf{r})$ and $h_A(\mathbf{r})$, as it follows [11].

$$I(\mathbf{r}) = B + P(\mathbf{r}) \otimes h_p(\mathbf{r}) + A(\mathbf{r}) \otimes h_A(\mathbf{r})$$

with B being the background intensity (un-scattered light). $p(\mathbf{r})$ and therefore $n_{\mathrm{re}}(\mathbf{r})$ can be easily recovered from this equation for the case of a non-absorbing sample. For weakly absorbing sample, it can be supposed that the real and imaginary parts of the RI are proportional $n_{\mathrm{im}} = \varepsilon n_{\mathrm{re}}$, where ε takes a small positive value (in the range 10^{-5}–10^{-3}) [13, 14]. Then introducing the effective point spread function $h_{EFF}(\mathbf{r}) = h_P(\mathbf{r}) + 2\varepsilon h_A(\mathbf{r})$, the expression is linearized with respect to $P(\mathbf{r})$.

$$I(\mathbf{r}) = B + P(\mathbf{r}) \otimes h_{EFF}(\mathbf{r})$$

The deconvolution process is usually carried out in the Fourier space [13, 14]. The analytical expressions for the phase and absorption optical transfer functions (which are the 3D Fourier transform of $h_P(\mathbf{r})$ and $h_A(\mathbf{r})$, respectively) can be found in Ref [17]. However, better results are obtained using numerically calculated transfer functions, which take into account the experimental sample illumination [18]. The real part of the RI recovered from $P(\mathbf{r})$ is considered for the cell dynamic analysis in *Result and Discussions*.

Experimental Setup

One of the advantages of PC-ODT is that it can be easily implemented in conventional transmission wide-field microscope (e.g., Nikon Eclipse Ti-U inverted) equipped with a quasi-monochromatic LED illumination source filtered with a band-pass filter (depending on the desired working wavelength). In this work, the sample was illuminated with quasi-monochromatic partially coherent light (λ = 560 nm, band-pass filter with FWHM = 30 nm), and a dry condenser

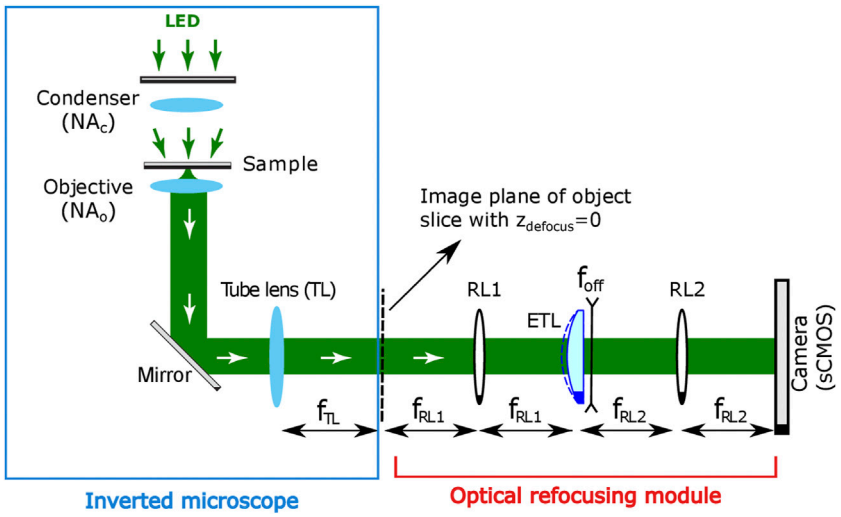

FIGURE 1 | Experimental setup for PC-ODT implementation. Optical refocusing module includes an ETL with an integrated divergent offset lens and additional relay lenses (RL1 and RL2) and the camera.

lens (Thorlabs-CSC200 NA_c = 0.78) and imaged with an oil-immersed objective (Nikon Plan-Apo, 60x, n_{imm} = 1.518, NA_o = 1.45) with a tube lens (f_{TL} = 200 mm). The lateral and axial resolutions of the setup defined as the Nyquist distance [19] are 125 nm and 270 nm, correspondingly.

The 3D through-focus intensity stack required for PC-ODT can be obtained in two different ways: mechanically or optically. The mechanical refocusing consists of changing the distance between the stage of the sample and the objective lenses (for instance, with a motorized piezo stage). However, it is undesirable for high-resolution microscopy (immersed objectives). Conversely, the optical refocusing considered here allows for axial scanning of the sample without moving it physically. It is achieved by incorporation of an optical refocusing module (ORM) after the intermediate image space, as it is shown in **Figure 1**. An electrically tunable lens (ETL) with a variable focal length is a crucial element of this module that enables a fast measuring of a through-focus intensity stack I (**r**).

The high-speed ETL (Optotune EL-10-30-C-VIS-LD-MV device in our case) is located in the Fourier conjugated plane with respect to the central slice, $z_{defocus}$ = 0 μm of the intermediate 3D image. The camera sensor records a 2D image (intensity distribution) corresponding to the transverse xy-object slice located in the microscope's focal plane (defocus distance $z_{defocus}$ = 0 μm). The position of the focused plane is optically shifted according to electric current applied to the ETL, therefore yielding the axial z-scanning of the sample almost in real time. Finally, I (**r**) is acquired by an sCMOS camera (Hamamatsu, Orca Flash 4.0, 16-bit gray-level, pixel size of p = 6.5 μm, in our case) and stored in a computer for its processing.

The shift of the imaged plane ($z_{defocus}$) depends on the magnification M of the considered microscope, as well as the relay lenses projecting the image onto the camera detector. Specifically, the shift distance is given by [20] $z_{defocus} = -n_m f_{RL1}^2 P_{ETL}/M^2$, where f_{RL1} is a focal distance of the relay lens RL1, and P_{ETL} is the power of the ETL lens from the interval of $[P_{ETL}^{min}, P_{ETL}^{max}] = [-1.5, +3.5]$dpt. The total magnification of the system is $M_s = M \times f_{RL2}/f_{RL1}$.

Sample Preparation

The culture and preparation of COS-7 cells (hail from the African green monkey kidney) considered in the next section were conducted as follows. First, the cells were cultured in Dulbecco's modified Eagle medium (DMEM) supplemented with 10% fetal bovine serum (FBS) and incubated at 37°C and 5% CO_2 for 4 days. 12 h before fixation, the cells were trypsinized and transferred to the coverslip. Afterward, the cells are immersed in phosphate-buffered saline (PBS) and sealed between coverslips, to prevent evaporation. The RI of the PBS is similar to water.

RESULT AND DISCUSSIONS

Living cell monitoring is an important source of information in biophysics and medicine. Below, we consider the application of PC-ODT for the analysis of fast and slow cell RI changes.

Study of Rapid Cell Dynamics with 3D Refractive Index Imaging

The fast monitoring of the sample provided by PC-ODT enables the study of cells with fleeting dynamics (wobbling, flickering, etc.), which exhibit noticeable changes in the time scale below 0.5 s. For evaluating the capability of PC-ODT for the study of intracellular motion, we analyze the behavior of living fibroblast-like COS-7 cell for 9 s. The prepared sample has been considered to observe the process of cell attachment to the substrate. The intensity stack comprises 50 2D images acquired with 2-ms camera exposure time (0.1 s for one stack). During 9 s 25 of

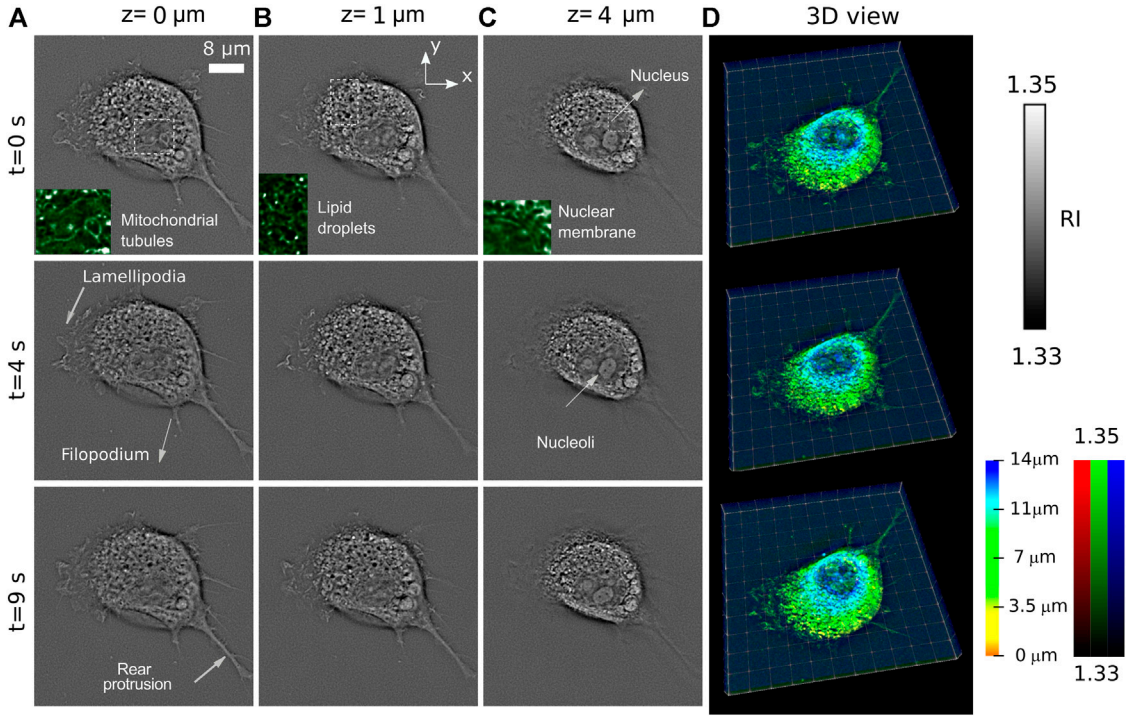

FIGURE 2 | Temporal evolution of cell RI distribution observed at three different axially separated slices z = 0 µm **(A)**, z = 1 µm **(B)**, and z = 4 µm **(C)** of a living COS-7 cell immersed in PBS solution. **(D)** 3D rendering with a color-coded depth and brightness-coded RI applied.

such stacks have been measured. Then, the 3D RI distribution in the volume of 500 × 500 × 50 pixels, corresponding to 60 × 60 × 14 µm^3, has been obtained by applying the PC-ODT deconvolution procedure explained in *Partially Coherent-Optical Diffraction Tomography Principle*. The temporal evolution of two RI tomograms at z = 0 µm (the cell is attached to the substrate) and z = 4 µm is presented in **Supplementary Video S1**. Alternatively, the temporal evolution of 3D RI distribution can be observed in **Supplementary Video S2**, where the dynamic cell is shown as a volumetric reconstruction with a color-coded depth and brightness-coded RI applied for fast and easy cell 3D visualization. We have developed this volumetric reconstruction by using a customized ImageJ macro based on "Z-stack Depth Color Code" and "Clear Volume" plugins [21].

In **Figure 2**, we show the time evolution of RI at three characteristic planes, at z = 0 µm, z = 1 µm, and z = 4 µm. The slices at z = 0 µm and z = 1 µm (**Figure 2A**) and (**Figure 2B**) show intensive activity of lamellipodia, while the indicated filopodium and rear protrusion are immobile. Lamellipodia are a cytoskeletal protein actin projection on the leading edge of the cell. Together with filopodia, they organize process of cell migration. However, while lamellipodia enable an explorative, rather fast random, walk (up to 1.2 µm/s according to Ref [22]), the filopodia promote a more slow ballistic migration guided by external inputs [23]. The sub-second-scale rearrangement of barbed actin filaments of lamellipodia is observed in **Figures 2A,B** (see also **Supplementary Videos S1** and **S2**). The recent comparative fluorescence and RI microscopic study [24] allows easy identification of the cell organelles in the RI images. Thus (see insets of **Figure 2A**), the mitochondria network and lipid droplets can be found. At the slice at z = 4 µm (**Figure 2C**) several organelles including nucleoli immersed in the nucleus are observed. We underline that fibroblast cells often have several nucleoli in the nucleus as in the cases studied in this work. The RI distributions in the plane z = 4 µm demonstrate that the cell exhibits intensive intracellular trafficking, nucleus plication, and counterclockwise rotation.

This cell activity is also reflected in **Figure 2C**, where 3D rendering of the entire cell at different moments of time is shown. The visualization principle is the same as in the **Supplementary Video S2**.

Let us consider now more rapid changes of this cell. In **Figure 3**, four consecutive frames (each pair separated by only 0.36 s) have been analyzed for the planes z = 0 µm and z = 4 µm. Along with RI distributions, we also include speed map plots (see enlarged images, green arrows) of the structures inside the nucleus for studying the rotation motion of its internal organelles. The speed maps have been obtained by using PIVlab plug-in (a digital particle image velocimetry tool) available for MATLAB [25] that performs a multipass window deformation ensemble correlation widely applied in particle velocimetry applications [26]. Thus, by considering the correlation between consecutive image pairs, one can obtain the velocity of each region of the cell. Note that every speed arrow corresponds to a region of 7 × 7 pixels. Thanks to the

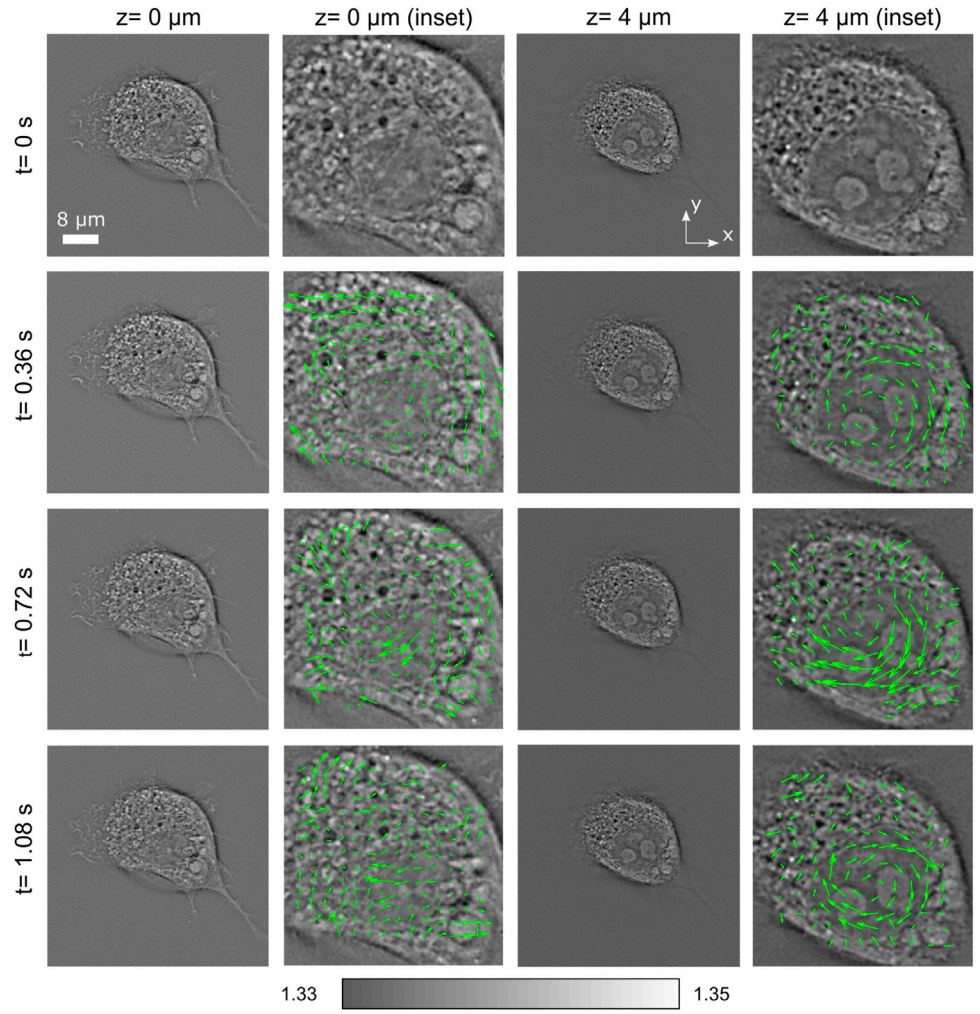

FIGURE 3 | Short-term evolution of RI slices of a living COS-7 cell, along with a speed map plot representing the velocity field of the cell structures. The speed field magnitude is variable within the range 0.18–1.4 µm/s. Certain tendency to vorticity is particularly noticeable at z = 4 µm.

streamlines of this speed vector field, one is able to characterize the motion of organelles inside the entire cell. A higher activity is observed inside the nucleus, in the form of a relatively fast rotation. It is observed that the speed field magnitude is variable within the range 0.18–1.4 µm/s, with certain tendency to vorticity particularly noticeable at z = 4 µm. The nucleus is rotated around an axis perpendicular to the substrate with a speed about 3 degrees/s.

Note that the fibroblast cells often display a high nuclear rotational activity [27]. The nuclear rotation and oscillation are associated with cell movement, mitosis, and necrosis or are induced by external factors, such as mechanical shear stress [28], and have been reported in several publications, but on the larger temporal sampling (minutes). The entire nucleus rotation of the order 10-20 degrees/min (0.2-0.3 degrees/s) has been recently observed using C-ODT [24]. Here, significantly more rapid nucleus rotation (3 degrees/s) is observed (see also **Supplementary Videos S1** and **S2**). This example illustrates the capability of PC-ODT for fast and high-spatial resolution studies of living cells, in particular their behavior under environmental changes, external force applications [22], differentiation, mitosis, etc.

Long-Term Cell Monitoring

Apart from short-term dynamics, long-term processes such as cell mitosis (division) or necrosis (death) are also of great interest in biomedicine. Thus, it is important to prove the applicability of PC-ODT for this type of studies, where the observation can take minutes or even hours. Here, we consider the process of induced necrosis of two COS-7 cells under nutrient deprivation. We scan a field of view ($60 \times 60 \times 16\ \mu m^3$). 3D intensity stack has been measured within 2 hrs in 5-min regular intervals, and the RI has been recovered. The temporal evolution of 3D RI distribution can be observed in **Supplementary Video S3**, as a volumetric reconstruction with a color-coded depth and brightness-coded RI applied for fast and easy cell 3D visualization (as in **Supplementary Video S2**). In **Figure 4A**, two different z-slices for z = 0 µm and z = 4.5 µm of the sample RI are presented, at four different times (t = 0 min, 15 min, 60 min, and 120 min). At z = 0 µm, the cells are attached to the

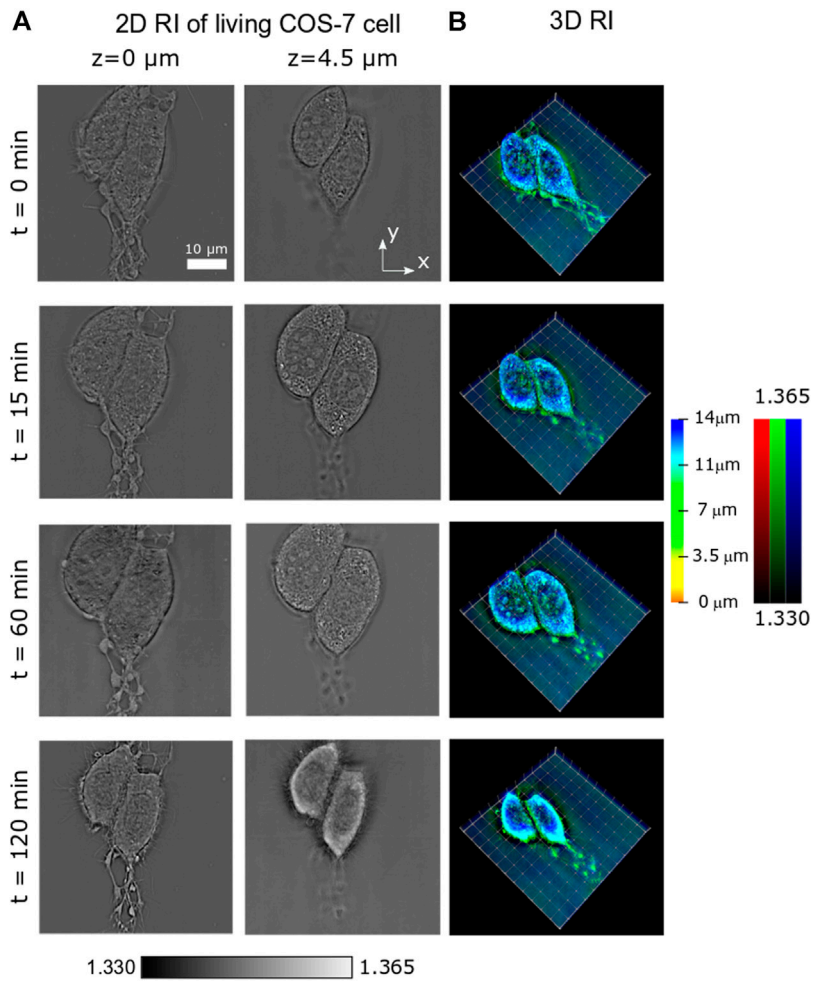

FIGURE 4 | Temporal evolution of the RI of a COS-7 cell undergoing necrosis. **(A)** 2D slices of the RI at two different planes z = 0 µm and z = 4.5 µm. **(B)** 3D rendering of the cell RI in four moments of time.

substrate. At z = 4.5 µm, the cell nucleus with several nucleoli is observed. Also in **Figures 2A,B**, the mitochondrial network and lipid droplets can be identified. Volumetric cell reconstruction with a color-coded depth and brightness-coded RI for different moments of time is shown in **Figure 4B**.

The different phases of the cell cycle have been observed during this long-term study. First, the cell swells progressively (from t = 0 min up to t = 60 min, see **Figures 4A,B**) until a maximum size is reached. Later, the multiple disruption of the outer cell membrane starts, resulting in the efflux of intracellular contents and a dramatic loss of cell volume (compare RI slices in **Figure 4A**). This behavior can be observed in **Supplementary Video S3**.

For quantitative characterization of the observed necrosis process, we analyze the average dry mass concentration (DMC), which can be easily obtained from RI contrast. Indeed, it is widely accepted [29–32] that for biological samples immersed in an aqueous medium, there exists a linear relationship linking the DMC of the sample and the real part of its RI as $\mathrm{DMC}(\mathbf{r})=[n(\mathbf{r})-n_m]/a$, where a represents the so-called specific refractive index increment, n is the sample's RI, and n_m is the water RI. Although the cell chemical composition is variable, an average value around $a = 0.0018$ dL/g is usually used within the light visible range when nucleated cells are considered [30, 32].

To obtain the average DMC, the reconstructed RI stack must be split into cell and background (surrounding medium). The applied segmentation algorithm takes into account the gradient and the absolute value of the sample RI. The 3D image regions that simultaneously satisfy both $|\nabla n(\mathbf{r})| > 0.002$ and $n(\mathbf{r}) > 1.333$ conditions are considered as the cell sample. Only the RI values belonging to those regions are used to obtain the DMC. The temporal evolution of the averaged (mean) DMC is shown in **Figure 5**. During the first hour of experiment, the mean DMC significantly decreases (from 2.422 g/dL at t = 5 min to 1.685 g/dL at t = 60 min). In this period of time, the volume of the cell grows remarkably, but the overall dry mass does not change significantly. After 1 hr of experiment, the DMC reaches a plateau around 1.65 g/dL that can be interpreted in terms of two processes with opposing effects: the outer membrane suffers multiple micro-ruptures and the cell tends to shrink, which should again increase DMC, but at the same time, all the cell contents leak into the extracellular space.

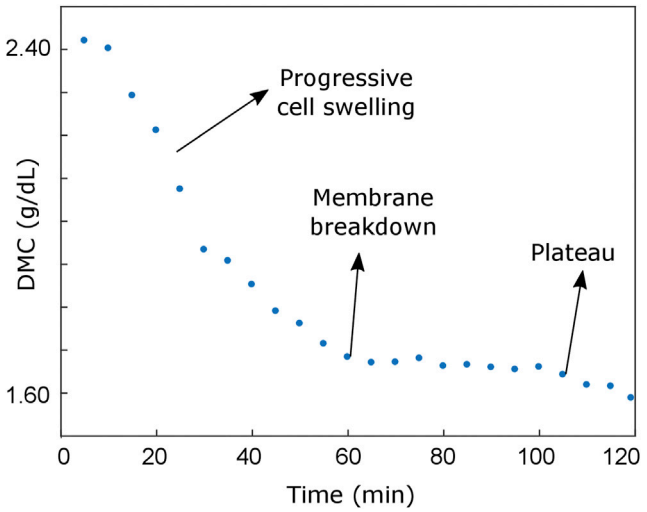

FIGURE 5 | Dry mass concentration evolution during the experiment, which enables the identification of two different cell behaviors during the necrosis: an initial progressive cell swelling (characterized by an approximately linear decrease of the average DMC) and a plateau region corresponding to the cell shrinking process.

The cell death phenomenon is a topic of great interest in biology and medicine [33–36], and PC-ODT seems to be a suitable tool for this study. Note that data for long-term cell temporal evolution observation can be acquired automatically by programmable activation of both ETL and camera sensor.

CONCLUSION

It has been demonstrated in two examples of living eukaryotic cell that by using the 3D RI distribution obtained with PC-ODT, it is possible to study a variety of biological physiological changes in living cells at different time intervals from sub-seconds to hours. We have demonstrated that fast 3D RI monitoring allows revealing sub-second range cell organelle activity (nucleoli rotation and lamellipodia movements), which requires further biological study. The simple relation between the RI and dry mass provides biologically meaningful quantitative information for cell analysis, in particular for the study of cell necrosis, apoptosis, mitosis, and other processes in a natural environment. We conclude that PC-ODT, feasible in the conventional wide-field microscope with an automatized refocusing module, is a viable alternative to C-ODT, realizable in the commercially available holographic microscopes [32, 33], for fast high-resolution quantitative study of living cells.

DATA AVAILABILITY STATEMENT

The raw data supporting the conclusions of this article will be made available by the authors, without undue reservation.

AUTHOR CONTRIBUTIONS

JS performed the experiments. JR and TA supervised the project. All the authors wrote the manuscript and revised the results.

FUNDING

The Spanish Ministerio de Ciencia e Innovación is acknowledged for the project PGC2018-095595-B-I00 (MCI/AEI/FEDER, UE).

ACKNOWLEDGMENTS

The samples were prepared by JS during his stay in the laboratory of nanophotonics, in the Institut d'Optique (University of Bordeaux), under the supervision of Pierre Bon and Laurent Cognet.

SUPPLEMENTARY MATERIAL

The Supplementary Material for this article can be found online at: https://www.frontiersin.org/articles/10.3389/fphy.2021.666256/full#supplementary-material

Supplementary Video 1 | The temporal evolution of COS7 cell refractive index tomograms at z = 0 µm (where the cell is attached to the substrate) and z = 4 µm. Lamellipodia movements (left panel) and nucleus rotation (right panel) are observed during 9 s.

Supplementary Video 2 | The fast dynamics of COS7 cell is shown as a volumetric reconstruction with a color-coded depth and brightness-coded refractive index (different perspectives). Observation time 9 s with an interval of 0.36 s (repeated two times).

Supplementary Video 3 | The slow dynamics of COS7 cell is shown as a volumetric reconstruction with a color-coded depth and brightness-coded refractive index (different perspectives). Observation time 2 hours with an interval of 5 min.

REFERENCES

1. Wolf E. Three-dimensional Structure Determination of Semi-transparent Objects from Holographic Data. *Opt Commun* (1969) 1(4):153–6. doi:10.1016/0030-4018(69)90052-2
2. Haeberlé O, Belkebir K, Giovaninni H, and Sentenac A.Tomographic Diffractive Microscopy: Basics, Techniques and Perspectives. *J Mod Opt* (2010) 57(9):686–99. doi:10.1080/09500340.2010.493622
3. Cotte Y, Toy F, Jourdain P, Pavillon N, Boss D, Magistretti P, et al. Marker-free Phase Nanoscopy. *Nat Photon* (2013) 7(2):113–7. doi:10.1038/nphoton.2012.329
4. Kim Y, Shim H, Kim K, Park H, Heo JH, Yoon J, et al. Common-path Diffraction Optical Tomography for Investigation of Three-Dimensional Structures and Dynamics of Biological Cells. *Opt Express* (2014) 22(9):10398–407. doi:10.1364/oe.22.010398
5. Mico V, Zalevsky Z, García-Martínez P, and García J. Synthetic Aperture Superresolution with Multiple off-axis Holograms. *J Opt Soc Am A* (2006) 23:3162–70. doi:10.1364/josaa.23.003162

6. Zheng G, Horstmeyer R, and Yang C. Wide-field, High-Resolution Fourier Ptychographic Microscopy. *Nat Photon* (2013) 7(9):739–45. doi:10.1038/nphoton.2013.187
7. Li J, Matlock A, Li Y, Chen Q, Zuo C, and Tian L. High-speed *In Vitro* Intensity Diffraction Tomography. *Adv Photon* (2019) 1(6):066004. doi:10.1117/1.ap.1.6.066004
8. Baek Y, and Park Y. Intensity-based Holographic Imaging via Space-Domain Kramers-Kronig Relations. *Nat Photon* (2021) 15(7):354–60. doi:10.1038/s41566-021-00760-8
9. Park C, Lee K, Baek Y, and Park Y. Low-coherence Optical Diffraction Tomography Using a Ferroelectric Liquid crystal Spatial Light Modulator. *Opt Express* (2020) 28(26):39649. doi:10.1364/oe.405418
10. Streibl N. Three-dimensional Imaging by a Microscope. *J Opt Soc Am A* (1985) 2(2):121–7. doi:10.1364/josaa.2.000121
11. Jenkins MH, and Gaylord TK. Three-dimensional Quantitative Phase Imaging via Tomographic Deconvolution Phase Microscopy. *Appl Opt* (2015) 54(31):9213. doi:10.1364/ao.54.009213
12. Chen M, Tian L, and Waller L. 3D Differential Phase Contrast Microscopy. *Biomed Opt Express* (2016) 7(10):3940–50. doi:10.1364/BOE.7.003940
13. Soto JM, Rodrigo JA, and Alieva T. Label-free Quantitative 3D Tomographic Imaging for Partially Coherent Light Microscopy. *Opt Express* (2017) 25(14):15699–712. doi:10.1364/oe.25.015699
14. Soto JM, Rodrigo JA, and Alieva T. Optical Diffraction Tomography with Fully and Partially Coherent Illumination in High Numerical Aperture Label-free Microscopy [Invited]. *Appl Opt* (2018) 57(1):A205–A214. doi:10.1364/ao.57.00a205
15. Soto JM, Mas A, Rodrigo JA, Alieva T, and Domínguez-Bernal G. Label-free Bioanalysis of Leishmania Infantum Using Refractive index Tomography with Partially Coherent Illumination. *J Biophotonics* (2019) 12:e201900030. doi:10.1002/jbio.201900030
16. Rodrigo JA, Soto JM, and Alieva T. Fast Label-free Microscopy Technique for 3D Dynamic Quantitative Imaging of Living Cells. *Biomed Opt Express* (2017) 8:5507–17. doi:10.1364/boe.8.005507
17. Bao Y, and Gaylord TK. Quantitative Phase Imaging Method Based on an Analytical Nonparaxial Partially Coherent Phase Optical Transfer Function. *J Opt Soc Am A* (2016) 33(11):2125–36. doi:10.1364/josaa.33.002125
18. Soto JM, Rodrigo JA, and Alieva T. Partially Coherent Illumination Engineering for Enhanced Refractive index Tomography. *Opt Lett* (2018) 43(19):4699–702. doi:10.1364/ol.43.004699
19. Lauer V.New Approach to Optical Diffraction Tomography Yielding a Vector Equation of Diffraction Tomography and a Novel Tomographic Microscope. *J Microsc* (2002) 205(2):165–76. doi:10.1046/j.0022-2720.2001.00980.x
20. Rodrigo JA, and Alieva T. Rapid Quantitative Phase Imaging for Partially Coherent Light Microscopy. *Opt Express* (2014) 22(11):13472–83. doi:10.1364/oe.22.013472
21. Royer LA, Weigert M, Günther U, Maghelli N, Jug F, Sbalzarini IF, et al. ClearVolume: Open-Source Live 3D Visualization for Light-Sheet Microscopy. *Nat Methods* (2015) 12:480–1. doi:10.1038/nmeth.3372
22. Cojoc D, Difato F, Ferrari E, Shahapure RB, Laishram J, Righi M, et al. Properties of the Force Exerted by Filopodia and Lamellipodia and the Involvement of Cytoskeletal Components. *PLoS ONE* (2007) 2(10):e1072. doi:10.1371/journal.pone.0001072
23. Innocenti M. New Insights into the Formation and the Function of Lamellipodia and Ruffles in Mesenchymal Cell migration. *Cell Adhes Migration* (2018). p. 1–16. doi:10.1080/19336918.2018.1448352 New Insights into the Formation and the Function of Lamellipodia and Ruffles in Mesenchymal Cell Migration*Cel Adhes Migration*.
24. Sandoz PA, Tremblay C, van der Goot FG, and Frechin M. Image-based Analysis of Living Mammalian Cells Using Label-free 3D Refractive index Maps Reveals New Organelle Dynamics and Dry Mass Flux. *PLOS Biol* (2019) 17:e3000553. doi:10.1371/journal.pbio.3000553
25. *PivLab* (2021). Available at: https://www.mathworks.com/matlabcentral/fileexchange/27659-pivlab-particle-image-velocimetry-piv-tool. [Accessed 7 June 2021].
26. Santiago JG, Wereley ST, Meinhart CD, Beebe DJ, and Adrian RJ. A Particle Image Velocimetry System for Microfluidics. *Experiments in Fluids* (1998) 25(4):316–9. doi:10.1007/s003480050235
27. Bard F, Bourgeois CA, Costagliola D, and Bouteille M. Rotation of the Cell Nucleus in Living Cells: a Quantitative Analysis. *Biol Cel* (1985) 54(2):135–42. doi:10.1111/j.1768322x.1985.tb00388.x10.1111/j.1768-322x.1985.tb00388.xM
28. Maninová M, Iwanicki MP, and Vomastek T. Emerging Role for Nuclear Rotation and Orientation in Cell Migration. *Cel Adhes Migration* (2014) 8:42–8. doi:10.4161/cam.27761
29. Barer R.Determination of Dry Mass, Thickness, Solid and Water Concentration in Living Cells. *Nature* (1953) 172(4389):1097–8. doi:10.1038/1721097a0
30. Mahlmann DM, Jahnke J, and Loosen P. Rapid Determination of the Dry Weight of Single, Living Cyanobacterial Cells Using the Mach-Zehnder Double-Beam Interference Microscope. *Eur J Phycology* (2008) 43(4):355–64. doi:10.1080/09670260802168625
31. Popescu G, Park Y, Lue N, Best-Popescu C, Deflores L, Dasari RR, et al. Optical Imaging of Cell Mass and Growth Dynamics. *Am J Physiology-Cell Physiol* (2008) 295(2):C538–C544. doi:10.1152/ajpcell.00121.2008
32. Yakimovich A, Witte R, Andriasyan V, Georgi F, and Greber UF. Label-free Digital Holo-Tomographic Microscopy Reveals Virus-Induced Cytopathic Effects in Live Cells. *mSphere* (2018) 3(6):e00599–18. doi:10.1128/mSphereDirect.00599-18
33. Buendia B, Courvalin JC, and Collas P. Dynamics of the Nuclear Envelope at Mitosis and during Apoptosis. *Cell Mol Life Sci* (2001) 58(12-13):1781–9. doi:10.1007/PL00000818
34. D'Arcy MS. Cell Death: a Review of the Major Forms of Apoptosis, Necrosis and Autophagy. *Cell Biol Int* (2019) 43(6):582–92. doi:10.1002/cbin.11137
35. Tomocube website (2021). Available at: http://www.tomocube.com/ (Accessed June 7, 2021).
36. Nanolive website (2021). Available at: http://nanolive.ch/ (Accessed June 7, 2021).

Conflict of Interest: The authors declare that the research was conducted in the absence of any commercial or financial relationships that could be construed as a potential conflict of interest.

frontiers in Physics

BRIEF RESEARCH REPORT
published: 30 September 2021
doi: 10.3389/fphy.2021.665650

Coherent Anti-Stokes Raman Scattering Microscopy: A Label-Free Method to Compare Spinal Cord Myelin in Different Species

*Gaëtan Poulen[1], Yannick N Gerber[2], Jean-Christophe Perez[2], Khadidja Oubarrahou[3], Nicolas Lonjon[1], Florence Vachiery-Lahaye[4], Hassan Boukhaddaoui[3] and Florence E. Perrin[2,5]**

[1]Department of Neurosurgery, MMDN, EPHE, INSERM, University de Montpellier, Montpellier, France, [2]MMDN, University de Montpellier, EPHE, INSERM, Montpellier, France, [3]Institute for Neurosciences of Montpellier, INSERM, Montpellier, France, [4]Department of Coordination Hospitalière des Dons pour La Greffe, Montpellier, France, [5]Institut Universitaire de France (IUF), Montpellier, France

Many histological techniques are used to identify and characterize myelin in the mammalian nervous system. Due to the high content of lipids in myelin sheaths, coherent anti-stokes Raman scattering (CARS) microscopy is a label-free method that allows identifying myelin within tissues. CARS excites the CH_2 vibrational mode at 2845 cm^{-1} and CH_2 bonds are found in lipids. In this study, we have used CARS for a new biological application in the field of spinal cord analysis. We have indeed compared several parameters of spinal cord myelin sheath in three different species, *i.e.*, mouse, lemur, and human using a label-free method. In all species, we analyzed the dorsal and the lateral *funiculi* of the adult thoracic spinal cord. We identified g-ratio differences between species. Indeed, in both *funiculi,* g-ratio was higher in mice than in the two primate species, and the myelin g-ratio in lemurs was higher than in humans. We also detected a difference in g-ratio between the dorsal and the lateral *funiculi* only in humans. Furthermore, species differences between axon and fiber diameters as well as myelin thickness were observed. These data may reflect species specificities of conduction velocity of myelin fibers. A comparison of data obtained by CARS imaging and fluoromyelin staining, a method that, similar to CARS, does not require resin embedding and dehydration, displays similar results. CARS is, therefore, a label-free alternative to other microscopy techniques to characterize myelin in healthy and neurological disorders affecting the spinal cord.

Keywords: myelinated fibers, g-ratio, CARS, spinal cord, human, lemur, mice

OPEN ACCESS

Edited by:
Peng Gao,
Xidian University, China

Reviewed by:
Nirmal Mazumder,
Manipal Academy of Higher Education, India
Sha AnXian,
Institute of Optics and Precision Mechanics (CAS), China

****Correspondence:***
Florence E. Perrin
florence.perrin@inserm.fr

Specialty section:
This article was submitted to Optics and Photonics, a section of the journal Frontiers in Physics

Received: *08 February 2021*
Accepted: *21 July 2021*
Published: *30 September 2021*

Citation:
Poulen G, Gerber YN, Perez J-C, Oubarrahou K, Lonjon N, Vachiery-Lahaye F, Boukhaddaoui H and Perrin FE (2021) Coherent Anti-Stokes Raman Scattering Microscopy: A Label-Free Method to Compare Spinal Cord Myelin in Different Species. Front. Phys. 9:665650. doi: 10.3389/fphy.2021.665650

INTRODUCTION

Myelin is a lipid-rich protective cover formed by oligodendrocytes that surround and protect axons. Lipids account for about 70% of the myelin and myelin sheaths are characterized by a high lipid-to-protein ratio. Furthermore, myelin displays different lipid compositions when compared to typical plasma membranes [1,2]. Myelin sheaths permit to increase the propagation speed of action potentials along axons [3,4]. Moreover, myelin is a dynamic structure spatially organized in heterogeneous functional domains that provide metabolic support to neurons [5].

Loss and alteration of myelin that results in the reduction of nerve conduction velocity and in the altered transfer of energy metabolites to neurons are reported in various diseases [6,7]. Damage to myelin sheaths

in humans is observed in severe neurological conditions such as multiple sclerosis, idiopathic inflammatory demyelinating diseases, acute disseminated encephalomyelitis, and neuromyelitis *optica* [4,8].

To identify myelin on tissues, on the one hand, classical staining based on the specific lipid composition of myelin, such as Luxol fast blue [9], Sudan Black B [10], Baker's acid hematin method [11], and silver staining [12], had been originally developed. However, these stainings do not always reach a sufficient resolution and contrast to visualize individual fibers [13]. On the other hand, immunochemical methods permit to characterize myelin structure with single fiber resolution and a high reproducibility. Antimyelin protein antibodies most commonly used are myelin basic protein (MBP), proteolipid protein (PLP), myelin oligodendrocyte glycoprotein (MOG), myelin protein zero (MPZ), and myelin-associated glycoprotein [14]. As for all immunohistochemistry approaches, drawbacks are the potential lack of specificity and background noise. Moreover, they only permit a semiquantitative quantification.

Coherent anti-Stokes Raman scattering (CARS) microscopy is a nonlinear optical technique using the endogenous contrast provided by molecules present in the sample [15–17]. The major advantage of this technique is to be done directly on tissues without staining, dehydration, and embedding steps that are detrimental to myelin preservation [18]. Lipid-rich myelinated tissues, such as the spinal cord and brain, appeared to be good samples for CARS imaging [19]. CARS had been used to develop an automated method for the segmentation and morphometric analysis of nerve fibers of spinal cord tissue [20]. CARS had also been used to monitor live myelinated fibers [21], *in vivo* mouse brain [22], and to carry out a longitudinal *in vivo* follow-up of demyelination and remyelination in the injured rats' spinal cord [23]. CARS also permitted to characterize demyelination in mouse models of diseases such as amyotrophic lateral sclerosis [24], experimental autoimmune encephalomyelitis [25], and brain tissues of multiple sclerosis patients [26].

This is the first study using a label-free method to compare myelin sheaths of two separated spinal cord tracts in three different species, i.e., mice, lemurs, and humans. Direct comparison of myelin characteristics between species will not only provide basic data on their similarities but also open the way to compare myelin alterations in animal models and human diseases.

METHODS

Study approval: Experiments were approved by the Veterinary Services Department of Hérault, the regional ethic committee n°36 for animal experimentation, and the French Ministry of National Education, Higher Education and Research (authorizations; mice: n°34118 and non-human primates n° APAFIS#16177-2018071810113615v3). Experiments followed the European legislative, administrative, and statutory measures for animal experimentation (EU/Directive/2010/63) and the ARRIVE guidelines. Human samples collection was done under the approval of the "Agence de la Biomédecine" (PFS-ssNUM-BAUCHET).

Spinal Cord Samples

Animals were injected with a lethal dose of tribromoethanol (rodent; 500 mg/kg, Sigma Aldrich Darmstadt, Germany) or ketamine (non-human primates; 150 mg/kg, Merial, Lyon, France). Animals were perfused intracardially with cold phosphate saline buffer (PBS, 0.1 M, pH 7.2) followed by cold 4% paraformaldehyde (PFA, pH7.2, Sigma Aldrich, Darmstadt, Germany) in 0.1 M PBS. Spinal cords were post-fixed for 2 h in 4% PFA and then incubated in 30% sucrose in 0.1 M PBS, frozen in OCT (Sakura, Alphen aan den Rijn, Netherlands) and stored at −20 °C.

Mice: Three C57BL6/6J male mice of 3 months of age (Charles River, Wilmington, United States) were used. Non-human primates: three adult male lemurs (*Microcebus murinus*, 2 years old) were used. They were born and bred in the animal facility (the University of Montpellier, France (license approval 34-05-026-FS) and housed in cages equipped with wooden nests and an enriched environment. The temperature of the animal facility was constantly kept between 24–26°C with 55% of humidity. All *Microcebus murinus* were fed 3 times a week with fresh fruits and a mixture of cereal, milk, and eggs. Water was given *ad libitum*.

Human: Low thoracic (T11—T12) spinal cords were obtained from three brain-dead organ-donor patients (2 males 45 and 51 years and 1 female 68 years) under the approval of the French Institution for Organ Transplantation. One patient died from cardiac arrest and two from a ruptured aneurysm. Body temperature was lowered and blood circulation and ventilation were maintained until 4 h before spinal cord removal. This short-time interval permitted good preservation of the tissue, as already reported [27]. After organs removal for therapeutic purposes, T8–L5 vertebral bloc was isolated and spinal cord segments were removed and immediately fixed in 4% paraformaldehyde.

Luxol Fast Blue and Neutral Red Staining

14-µm-thick axial spinal cord cryosections (Microm HM550, Thermofisher Scientific, Waltham, United States) were collected on Superfrost Plus© slides. Luxol fast blue staining was done as previously described [28,29]. Briefly, sections were placed 5 min in 95% ethanol and then incubated in 0.1% Luxol fast blue under mild shaking (12 h, room temperature). Slides were then rinsed for 1 min in milli-Q water, then placed for 1 min in lithium carbonate (0.05%), and finally washed in tap water (1 min). Subsequently, slides were incubated for 10 min in 0.5% neutral red solution, 5 min in 100% ethanol, and washed twice for 10 min in xylene. All slides were cover-slipped using Eukitt (Sigma Aldrich, Darmstadt, Germany).

Coherent Anti-Stokes Raman Scattering and Quantifications

We used LSM 7 MP optical parametric oscillator (OPO) multiphoton microscope (Zeiss, Oberkochen, Germany) with an upright Axio Examiner Z.1 optical microscope associated with a femtosecond Ti: sapphire laser (680–1,080 nm, 80 MHz, 140 fs, Chameleon Ultra II, Coherent, France) pumping a tunable OPOs (1,000–1,500 nm, 80 MHz, 200 fs, Chameleon Compact OPO, Coherent, France) to acquire CARS images. We imaged axial spinal cord sections (14 µm) in all species. A x20 water immersion lens (W Plan Apochromat DIC VIS-IR) with the following characteristics: 1024 x 1024 pixels frame size, scan speed of 6 (zoom x1.2) and 8 (mosaic, zoom x3, PixelDwell 3.15 and 1.27 µs/scan, respectively) and either a zoom x1.2 or x3 was

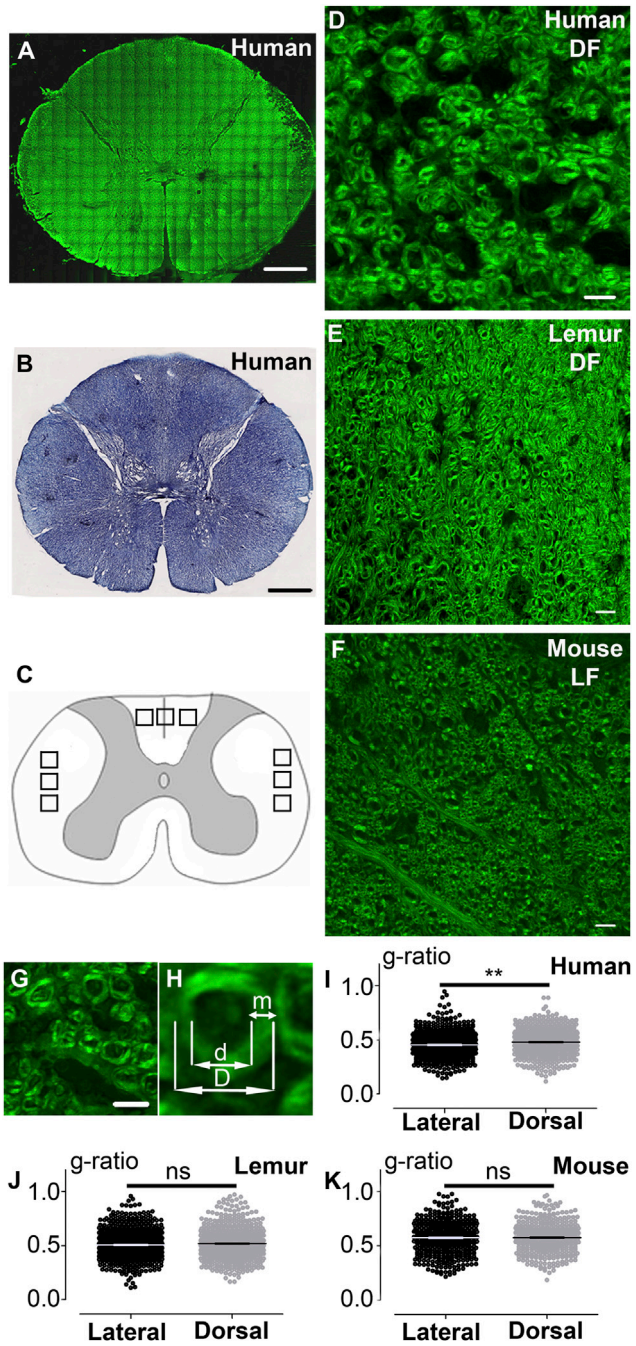

FIGURE 1 | *CARS microscopy, a label-free method to visualize myelin and analyze myelin g-ratio in the spinal cord of humans, lemurs, and mice.* Fast scanning mosaic of axial thoracic section of a human spinal cord imaged with CARS **(A)**; this acquisition allows to locate where higher quality zoomed images were taken for further analysis. Human thoracic spinal cord stained with Luxol fast blue **(B)**. Schematic drawing of a spinal cord, black squares represent locations in the dorsal and lateral *funiculi* of quantified images in all species **(C)**. Humans **(D)** and lemurs **(E)** dorsal *funiculus* (DF), as well as mouse lateral funiculus (LF) **(F)**, were imaged with CARS. Human dorsal *funiculus* **(G)**. Higher magnification of **G** and method used to measure the g-ratio **(H)**. Comparison of the g-ratio in lateral and dorsal *funiculi* in humans **(I)**, lemurs **(J),** and mice **(K)**. Data are mean ± SEM per fibers. $^{**}p < 0.005$; (*Continued*)

FIGURE 1 | paired *t*-test. The number of fibers analyzed: n is at least 432 and up to 681 per group; however, in a given species, the number of fibers in LF and DF is similar. In all graphs, quantification in the lateral *funiculus* is in black and the dorsal *funiculus* is in light grey. Scale bars: **(A**, **B)** 1 mm, **(D**–**G)** 10 µm.

used. CARS excites the CH_2 vibrational mode at 2845 cm^{-1} and CH_2 bonds are found in lipids and thus in myelin sheath [30]. Excitation wavelengths are 836 and 1,097 nm (synchronized Ti-sapphire and OPO, respectively) and the signal is detected at 675 nm (filter from 660-685 nm).

The non-resonant background is reduced due to the use of femtoseconds impulsions [31,32] and EPI-detection [33] [for review see [34]]. We collected CARS signaling in the near-infrared (670 nm) since this wavelength produces rather limited autofluorescence when using biological tissue. Moreover, and as previously reported, before getting a simultaneous scan of both lasers, we switch off sequentially one of the laser beams (either OPO or Ti : sapphire) to confirm a robust intensity decay when compared to the CARS signal [30].

Pictures are a stack of 3 µm (3 slices) and were taken in six locations within the lateral *funiculus* and three locations in the dorsal *funiculus* (**Figure 1C**). In each picture, a square of 100 µmX100 µm located in the center of the image was quantified. Imaris 9.6.0 software was used (Bitplane AG, Zurich, Switzerland) for quantifications using numeric x3 zoom applied to the original image (**Figure 1G**). Only fully identifiable fibers were quantified, and diameters were randomly selected and measured through unidirectional length, without selection criteria (shortest or longest diameter). For some acquisitions, a quick fluoromyelin (20 min, 1: 200, Invitrogen Carlsbad, United States), (rinsed 3 × 10 min in PBS) staining was added to observe eventual co-localization.

Fluoromyelin Staining

We imaged 14 µm-thick axial spinal cord cryosections of the same individuals as for CARS analysis for all species. Sections were incubated 20 min with fluoromyelin (1:200, Invitrogen, Carlsbad, United States), rinsed 3 × 10 min in PBS and mounted with fluorosave (Dako, Glostrup, Denmark). Images were acquired with THUNDER Imager 3D (Leica, Wetzlar, Germany; lens x 63). For all species, one field of 600 µmX400 µm was acquired in the lateral *funiculus* and one field of 600 µmX200 µm in the dorsal *funiculus*. In each field, a picture of 200 µmX200 µm located in the center of the image was taken for quantification, and 40 fibers were randomly selected and measured per location and sample. ImageJ software was used (National Institutes of Health, United States) for quantifications using numeric zoom to reach 300% of the original image. Diameter measurements were done for CARS analysis.

Three-Dimensional Illustration

3D image processing software Imaris x64 7.2.2 (Bitplane AG, Zürich, Switzerland) was used for illustration (**Supplementary Figure S1**).

Statistics

For CARS analysis, at least 432 fibers were quantified per anatomical location and species (3 individuals per species) [number of fibers analyzed: mice (DF = 432; LF = 481);

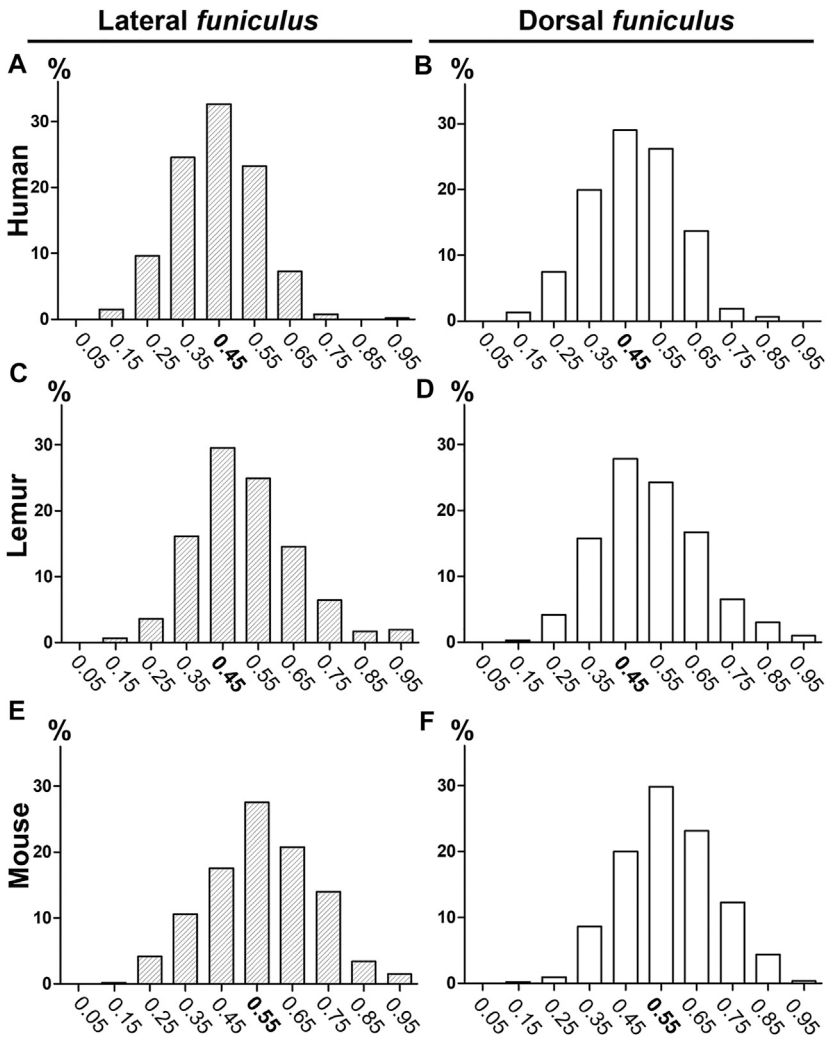

FIGURE 2 | *Histograms of g-ratio distribution in humans, lemurs, and mice using CARS microscopy*. Distributions of g-ratio in lateral **(A**, **C**, **E)** and dorsal (**B, D**, **F**) *funiculi* were quantified in humans **(A**–**B)**, lemurs **(C**–**D),** and mice **(E**–**F)**. The number of fibers analyzed: n is at least 432 and up to 681 per group.

Microcebus murinus (DF = 643; LF = 681); human (DF = 544; LF = 580)]. Significance was accepted at $p \leq 0.05$. Results are expressed as mean ± standard error of the mean. Student's paired (comparison within a given species) or unpaired (comparison between species) *t*-tests with Welch's correction were used. For fluoromyelin analysis, 120 fibers (40 for each individual) per anatomical location and species were quantified.

RESULTS

Coherent Anti-Stokes Raman Scattering Imaging Allows Discriminating Myelin Across Species Through G-Ratio Measurement

We first compared coherent anti-stokes Raman scattering (CARS) imaging (**Figure 1A**, fast scanning mosaic) with standard histological methods to detect myelin, including Luxol fast blue staining (**Figure 1B**). The dorsal (**Figures 1C–E**) and lateral (**Figures 1C, F**) *funiculi* were analyzed on axial sections of the thoracic spinal cord of humans (**Figures 1A, D**; **Supplementary Figure S1A–D**), lemurs (*Microcebus murinus*) (**Figure 1E**), and mice (**Figure 1F**). We then calculated the g-ratio on numerically zoomed images (ratio of the inner-to-outer myelinated fiber diameter, **Figures 1G–H**) in the lateral (LF) and in dorsal (DF) *funiculi* in each species. No significant difference in between *funiculi* was observed in lemurs ($p = 0.0565$; **Figure 1J**) nor in mice ($p = 0.34$; **Figure 1K**). Conversely, in humans, the g-ratio was higher in dorsal than in lateral *funiculus* ($p = 0.0029$, mean g-ratio DF = 0.48 ± 0.005; mean g-ratio LF = 0.45 ± 0.005; **Figure 1I**), that may reflect differences in conduction speed in between *funiculi*. For each species, no major difference in the distribution of the g-ratio between the lateral and the dorsal *funiculi* was observed (**Figure 2**). However, g-ratio between 0.4 and 0.5 (0.45) was the most prevalent in both *funiculi* in humans (**Figures 2A,B**) and lemurs (**Figures**

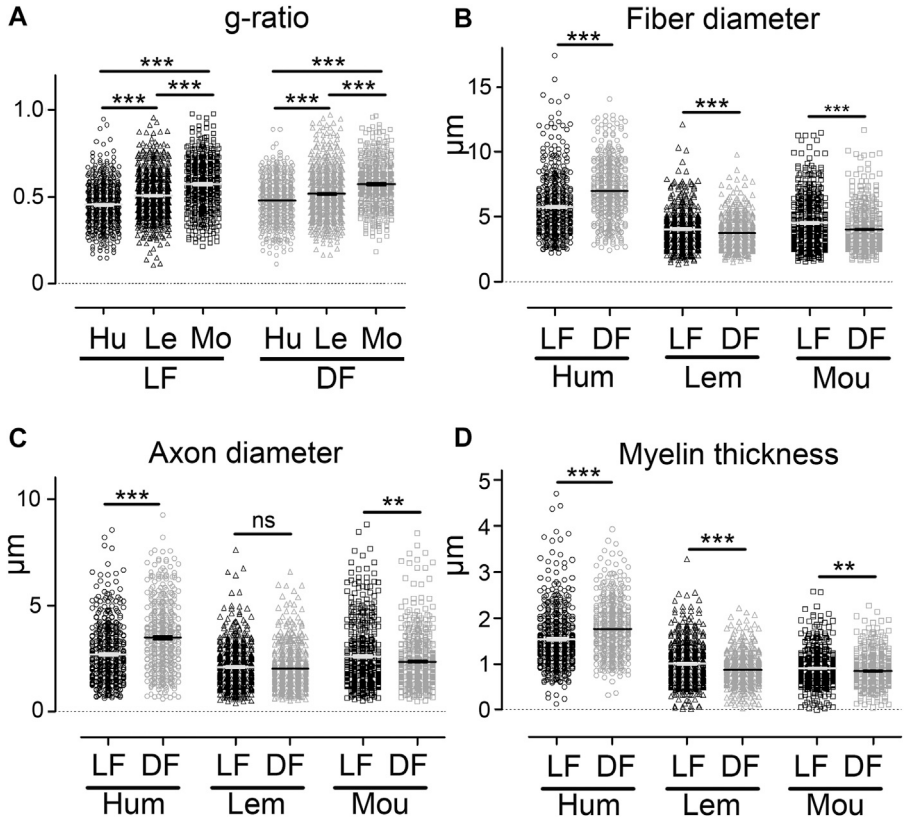

FIGURE 3 | *Comparison of g-ratio, fiber diameter, axon diameter, and myelin thickness between species using CARS microscopy*. Comparison of g-ratio in the lateral and dorsal *funiculi* in between humans, lemurs, and mice **(A)**. Comparison of fiber diameter in the lateral and dorsal *funiculi* in humans, lemurs, and mice **(B)**. Comparison of axon diameter in the lateral and dorsal *funiculi* in humans, lemurs, and mice **(C)**. Comparison of myelin thickness in the lateral and dorsal *funiculi* in humans, lemurs, and mice **(D)**. Hu: human, Le: lemurs, and Mo: mice. Data are mean ± SEM per section. ***$p < 0.001$, **$p < 0.01$ ns: non-significant; unpaired *t*-test with Welch's correction. Number of fibers analyzed: n is at least 432 and up to 681 per group.

2C,D) contrariwise to mice (**Figures 2E,F**) where the peak was observed for g-ratio between 0.5 and 0.6 (0.55).

Spectra of G-Ratio, Fiber Diameter, Axon Diameter, and Myelin Thickness in the Three Species

Comparison of g-ratio, fibers, and axons diameters (**Figure 1J**) in the lateral and dorsal *funiculi* (**Figure 3**) also highlighted species specificities. In both *funiculi*, g-ratio was lower in humans than in lemurs than in mice (**Figure 3A,** $p < 0.001$ for all comparisons); that may reflect differences in conduction speed in between species. Moreover, in humans, fiber and axon diameters, as well as myelin thickness, were higher in the dorsal (fiber diameter: 6.99 ± 0.09 µm, axon diameter: 3.47 ± 0.07 µm and myelin thickness: 1.77 ± 0.03 µm) as compared to the lateral *funiculus* (fiber diameter: 5.78 ± 0.10 µm, axon diameter: 2.69 ± 0.06 µm and myelin thickness: 1.54 ± 0.03 µm) (**Figures 3B-D**, $p < 0.001$ for all parameters). In mice, all parameters were lower in the dorsal *funiculus* (fiber diameter: 4.03 ± 0.07 µm, axon diameter: 2.35 ± 0.06 µm and myelin thickness: 0.85 ± 0.02 µm) as compared to the lateral *funiculus* (fiber diameter: 4.52 ± 0.09µm, axon diameter: 2.59 ± 0.07 µm and myelin thickness: 0.91 ± 0.018 µm) (**Figures 3B-D**, $p < 0.001$ for all parameters). In lemurs, fiber diameter (DF: 3.75 ± 0.05 µm and LF: 4.04 ± 0.06 µm) and myelin thickness (DF: 0.87 ± 0.014 µm and LF: 1.00 ± 0.02 µm) were lower in the dorsal as compared to the lateral funiculus; no difference was detectable in axon diameter between *funiculi* (DF: 2.01 ± 0.04 µm and LF: 2.09 ± 0.04 µm) (**Figures 3B-D**).

Taken together, these data demonstrate that using CARS to compare fiber and axon diameters as well as myelin thickness allows interspecies discrimination of three healthy mammal spinal cords.

Fluoromyelin Analysis Display Similar G-Ratio Values as Coherent Anti-Stokes Raman Scattering Imaging

To confirm the accuracy of CARS imaging, we then carried out in the same samples, g-ratio analysis using fluoromyelin staining; another method that, similar to CARS, does not require resin embedding and dehydration and permits to visualize myelin (**Figure 4**). In the first step, we acquired simultaneously CARS (**Figure 4A**) and fluoromyelin staining (**Figure 4B**), both signals partly co-localized (**Figure 4C**). We then used a Thunder imager with computational clearing to obtain images without out-of-focus

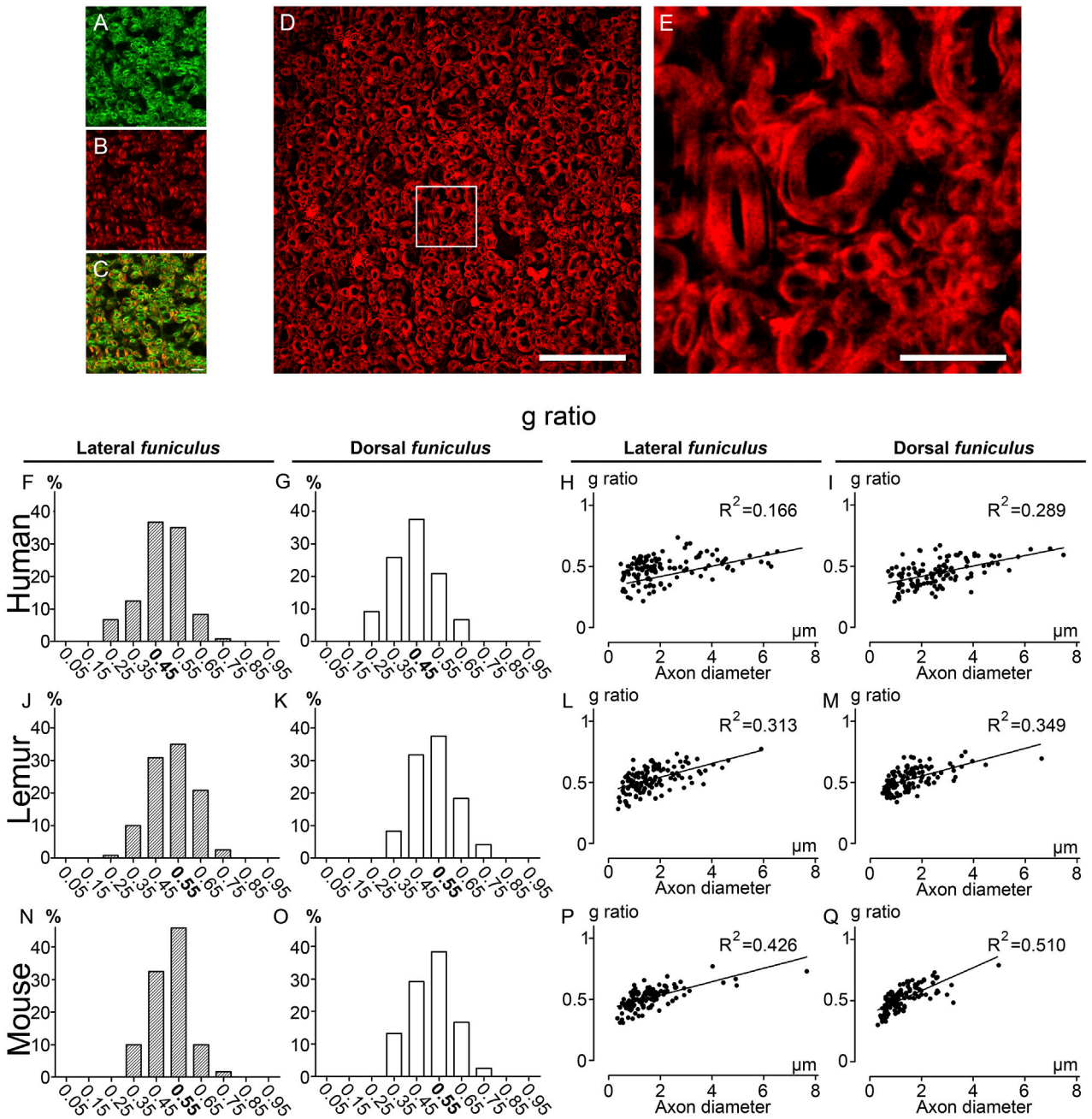

FIGURE 4 | g-ratio *distribution* in *humans, lemurs, and mice using fluoromyelin staining* CARS image of an axial section of the human thoracic spinal cord showing the lateral *funiculus* **(A)** stained with fluoromyelin **(B)**. Merge of both signals **(C)**. Axial section of the human thoracic spinal cord showing the lateral *funiculus* stained with fluoromyelin and imaged with Thunder Imager **(D)**. Higher magnification of the white box presented in D **(E)**. Distributions of g-ratio in lateral **(F**, **J**, **N)** and dorsal **(G**, **K**, **O)** *funiculi* were quantified in humans **(F**, **G)**, lemurs **(J**–**K),** and mice **(N-O)**. Scatter plots of g-ratio against axon diameter in the lateral **(H**, **L**, **P)** and dorsal **(I**, **M**, **Q)** *funiculi* in humans **(H-I)**, lemurs **(L**–**M),** and mice **(P**–**Q)**. Correlation between g-ratio and axon diameter is expressed by the linear correlation coefficient (R^2) of the linear regression curve. Each group included three individuals. The number of fibers analyzed: 120 per group. Scale bars: **(A-C, E)** 10 μm, **(D)** 50 μm.

blur (**Figures 4D,E**; **Supplementary Figures 1E–H**) and to measure g-ratio in the same samples used for CARS analysis. We confirmed for each species the absence of difference in g-ratio distribution between both *funiculi* (**Figures 4F, G**, humans; **J**&**K**; lemurs and **N**&**O**; mice). Moreover, similarly to CARS quantifications, a g-ratio in between 0.4 and 0.5 (0.45) was the most prevalent in both *funiculi* in humans (**Figures 4F, G**); for lemurs, the g-ratio in both *funiculi* was predominantly at 0.55 (however, the proportion of fibers presenting a g-ratio of 0.45 was almost identical) (**Figures 4J, K**); finally, in mice, the peak was observed for g-ratio at 0.55 (**Figures 4**). Linear regression curves of g-ratio against axon's diameter highlighted that lemurs display characteristics (**Figures 4L–M**; LF

R^2 = 0.313 and DF R^2 = 0.349) in between human (**Figures 4H–I**; LF R^2 = 0.166 and DF R^2 = 0.289) and mice (**Figures 4P–Q**; LF R^2 = 0.426 and DF R^2 = 0.510). Taken together, these data demonstrate that CARS is a label-free alternative to other microscopy techniques that allow to discrimination of myelinated fibers across species in the mammal spinal cord *funiculi*.

DISCUSSION

Here, we present the first CARS analysis of spinal cord myelin in two white matter tracts (lateral and dorsal *funiculi*) of three different species, i.e., mice, lemurs, and humans. We identified species specificities in particular regarding values of the g-ratio and thus confirmed the accuracy of CARS imaging as an alternative to other microscopy techniques to assess and compare myelin across species.

G-Ratio Coincides with Species Evolution and Myelin Fibers Differ within the Same Species According to Their Location

Myelin fibers g-ratio of both *funiculi* was higher in mice than in lemurs than in humans and thus inversely coincides with species evolution. This may partly reflect differences in fiber conduction speed across species. Indeed, a few studies have demonstrated that the g-ratio is not only a key determinant for the conduction velocity of a fiber [3,35,36] but also optimized for speed of signal conduction, cellular energetics, and spatial constraints [37]. The distribution of the g-ratio within lateral or dorsal *funiculi* in the three species highlighted a similar repartition in humans and in lemurs by opposition to mice. Moreover, we identified a higher g-ratio in dorsal as compared to the lateral *funiculus* only in humans. Conversely, no difference in g-ratio is observed between the lateral and the dorsal *funiculus* in mice and lemurs. Fibers and axons diameters, as well as myelin thickness, are higher in the dorsal *funiculus* in humans. This observation certainly mirrors anatomical differences in fiber tracts displaying sensory motor functions and may reflect species-specificities of conduction velocity of myelin fibers.

Taken together, structural similarities between humans and lemurs central nervous system confirms the necessity to develop non-human primate models to study CNS diseases such as demyelinating disease, traumatic brain injury, and spinal cord injury. This is particularly important when studying spinal cord disorders since closer anatomical and functional characteristics of the motor systems, including the corticospinal tract, is observed between human and non-human primate as opposed to rodent [38].

Coherent Anti-Stokes Raman Scattering Microscopy, an Alternative Method to Analyze Myelin

A neuroimaging method, termed multi-component-driven equilibrium single-pulse observation of T1 and T2 (mcDESPOT), allows to examine myelin water fraction (MWF) as an *in vivo* metric of myelin integrity and content [39,40]. It has been demonstrated that a combination of magnetic resonance (MR) markers that are sensitive to the myelin volume fraction (MVF) and to the intra-axonal volume fraction (AVF) is sufficient to compute a g-ratio for each voxel (aggregate g-ratio). However, it does not allow estimating axon diameter, myelin sheath thickness, and pitfalls of g-ratio imaging such as MR artifacts, lack of specificity, low spatial resolution, and long acquisition times remain [37]. Thus, as suggested recently [18], the emergence of exhaustive databases of myelin fibers structure using several modalities of investigation tools will facilitate further validation of non-invasive methods such as magnetic resonance imaging.

The overall lower g-ratio values (about 0.5) that we obtained using both CARS and fluoromyelin staining as compared to those obtained using electron microscopy may result from variation in factors such as fixative, embedding, and dehydration steps. As recently reviewed, methods that do not require staining, embedding, and dehydration, which are all critical steps for myelin damage, may provide accurate measurement of parameters such as g-ratio and myelin sheath thickness [for review see [18]]. Slight differences in g-ratio repartition that we observed when using CARS imaging and fluoromyelin; in particular with lemurs, may thus also reflect differences in tissue processing. Indeed, even if both techniques do not require resins embedding and dehydration, conversely to CARS, fluoromyelin is not a label-free method and requires mounting.

In conclusion, this study compared the first-time spinal cord myelin sheath in three different species using a label-free method and thus represents a new biological application of a label-free method in the field of spinal cord analysis. We identified species differences between axon and fiber diameters, myelin thickness, and g-ratio that may reflect species-specificities of conduction velocity of myelin fibers. The combination of several imaging techniques, including CARS, will thus permit to better characterize myelin structure in healthy conditions and its alterations in diseases.

DATA AVAILABILITY STATEMENT

The raw data supporting the conclusion of this article will be made available by the authors without undue reservation.

ETHICS STATEMENT

The studies involving human samples collection were reviewed and approved by the "Agence de la Biomédecine" (PFS-ssNUM-BAUCHET). Written informed consent for participation was not required for this study in accordance with the national legislation and the institutional requirements. The animal study was reviewed and approved by the Veterinary Services Department of Hérault, the regional ethic committee n°36 for animal experimentation, and the French Ministry of National Education, Higher Education and Research (authorizations; mice: n°34118 and non-human primates n° APAFIS#16177-2018071810113615v3). Experiments followed the European legislative, administrative, and statutory measures for animal experimentation (EU/Directive/2010/63) and the ARRIVE guidelines.

AUTHOR CONTRIBUTIONS

GP participated in the design of the project and in human samples collection, analyzed the data, and contributed to the writing of the manuscript; YG contributed to the design of the project as well as acquisition and analysis of the data; J-CP participated in the acquisition and analysis of the data; KO participated in the quantification of the data; NL participated in human samples collection; FV-L coordinated human samples collection; HB designed CARS acquisition and participated in the analysis, and FP conceptualized the research, designed the project, participated in the analysis and data interpretation, drafting the work and final approval.

FUNDING

This work was supported by the patient organizations "Demain Debout Aquitaine" (to YG and FP) and "Verticale" (to YG and FP). The funding sources were not involved in study design, collection, analysis, and interpretation of data and the writing of the report and in the decision to submit the article for publication.

ACKNOWLEDGMENTS

We thank the "Agence de la Biomédecine" for organization of human samples collection. We thank Fabrice Bardin and the "Montpellier Ressources Imagerie" for advices in CARS acquisition. We also thank Nadine Mestre-Frances for her expertise in non-human primates.

SUPPLEMENTARY MATERIAL

The Supplementary Material for this article can be found online at: https://www.frontiersin.org/articles/10.3389/fphy.2021.665650/full#supplementary-material

REFERENCES

1. O'brien JS, and Sampson EL. Lipid composition of the normal human brain: gray matter, white matter, and myelin. *J Lipid Res* (1965) 6:537–44. doi:10.1016/s0022-2275(20)39619-x
2. Harayama T, and Riezman H. Understanding the diversity of membrane lipid composition. *Nat Rev Mol Cel Biol* (2018) 19:281–96. doi:10.1038/nrm.2017.138
3. Rushton WAH. A theory of the effects of fibre size in medullated nerve. *J Physiol* (1951) 115:101–22. doi:10.1113/jphysiol.1951.sp004655
4. Marangon D, Boccazzi M, Lecca D, and Fumagalli M. Regulation of Oligodendrocyte Functions: Targeting Lipid Metabolism and Extracellular Matrix for Myelin Repair. *J Clin Med* (2020) 9(2):470. doi:10.3390/jcm9020470
5. Saab AS, and Nave K-A. Myelin dynamics: protecting and shaping neuronal functions. *Curr Opin Neurobiol* (2017) 47:104–12. doi:10.1016/j.conb.2017.09.013
6. Morrison BM, Lee Y, and Rothstein JD. Oligodendroglia: metabolic supporters of axons. *Trends Cel Biol* (2013) 23:644–51. doi:10.1016/j.tcb.2013.07.007
7. Micu I, Plemel JR, Caprariello AV, Nave KA, and Stys PK. Axo-myelinic neurotransmission: a novel mode of cell signalling in the central nervous system. *Nat Rev Neurosci* (2017) 19:58. doi:10.1038/nrn.2017.128
8. Stimmer L, Fovet C-M, and Serguera C. Experimental Models of Autoimmune Demyelinating Diseases in Nonhuman Primates. *Vet Pathol* (2018) 55:27–41. doi:10.1177/0300985817712794
9. Klüver H, and Barrera E. A method for the combined staining of cells and fibers in the nervous system. *J Neuropathol Exp Neurol* (1953) 12:400–3. doi:10.1097/00005072-195312040-00008
10. Meier C. Some observations on early myelination in the human spinal cord. Light and electron microscope study. *Brain Res* (1976) 104:21–32. doi:10.1016/0006-8993(76)90644-2
11. Hori SH. A Simplified Acid Hematein Test for Phospholipids. *Stain Tech* (1963) 38:221–5. doi:10.3109/10520296309061182
12. Gallyas F. Silver staining of myelin by means of physical development. *Neurol Res* (1979) 1:203–9. doi:10.1080/01616412.1979.11739553
13. Thetiot M, Freeman SA, and Desmazières A. Immunohistochemical Analysis of Myelin Structures. *Methods Mol Biol* (2018) 1791:15–23. doi:10.1007/978-1-4939-7862-5_2
14. Fluri F, Ferracin F, Erne B, and Steck AJ. Microheterogeneity of anti-myelin-associated glycoprotein antibodies. *J Neurol Sci* (2003) 207:43–9. doi:10.1016/s0022-510x(02)00359-3
15. Zumbusch A, Holtom GR, and Xie XS. Three-Dimensional Vibrational Imaging by Coherent Anti-Stokes Raman Scattering. *Phys Rev Lett* (1999) 82:4142–5. doi:10.1103/physrevlett.82.4142
16. Evans CL, and Xie XS. Coherent anti-stokes Raman scattering microscopy: chemical imaging for biology and medicine. *Annu Rev. Anal. Chem.* (2008) 1:883–909. doi:10.1146/annurev.anchem.1.031207.112754
17. Bégin S, Bélanger E, Laffray S, Vallée R, and Côté D. In vivooptical monitoring of tissue pathologies and diseases with vibrational contrast. *J Biophoton* (2009) 2:632–42. doi:10.1002/jbio.200910071
18. Saliani A, Perraud B, Duval T, Stikov N, Rossignol S, and Cohen-Adad J. Axon and Myelin Morphology in Animal and Human Spinal Cord. *Front Neuroanat* (2017) 11:129. doi:10.3389/fnana.2017.00129
19. Brideau C, Poon KWC, Colarusso P, and Stys PK. Excitation parameters optimized for coherent anti-Stokes Raman scattering imaging of myelinated tissue. *J Biomed Opt* (2019) 24:1–8. doi:10.1117/1.jbo.24.4.046502
20. Bégin S, Dupont-Therrien O, Bélanger E, Daradich A, Laffray S, De Koninck Y, et al. Automated method for the segmentation and morphometry of nerve fibers in large-scale CARS images of spinal cord tissue. *Biomed Opt Express* (2014) 5:4145–61. doi:10.1364/boe.5.004145
21. Wang H, Fu Y, Zickmund P, Shi R, and Cheng J-X. Coherent anti-stokes Raman scattering imaging of axonal myelin in live spinal tissues. *Biophysical J* (2005) 89:581–91. doi:10.1529/biophysj.105.061911
22. Fu Y, Huff TB, Wang H-W, Cheng J-X, and Wang H. *Ex vivo* and *in vivo* imaging of myelin fibers in mouse brain by coherent anti-Stokes Raman scattering microscopy. *Opt Express* (2008) 16:19396–409. doi:10.1364/oe.16.019396
23. Shi Y, Zhang D, Huff TB, Wang X, Shi R, Xu X-M, et al. Longitudinal *in vivo* coherent anti-Stokes Raman scattering imaging of demyelination and remyelination in injured spinal cord. *J Biomed Opt* (2011) 16:106012. doi:10.1117/1.3641988
24. Picardi G, Spalloni A, Generosi A, Paci B, Mercuri NB, Luce M, et al. Tissue degeneration in ALS affected spinal cord evaluated by Raman spectroscopy. *Sci Rep* (2018) 8:13110. doi:10.1038/s41598-018-31469-4
25. Fu Y, Frederick TJ, Huff TB, Goings GE, Miller SD, and Cheng J-X. Paranodal myelin retraction in relapsing experimental autoimmune encephalomyelitis visualized by coherent anti-Stokes Raman scattering microscopy. *J Biomed Opt* (2011) 16:106006. doi:10.1117/1.3638180
26. Poon KWC, Brideau C, Klaver R, Schenk GJ, Geurts JJ, and Stys PK. Lipid biochemical changes detected in normal appearing white matter of chronic multiple sclerosis by spectral coherent Raman imaging. *Chem Sci* (2018) 9:1586–95. doi:10.1039/c7sc03992a
27. Perrin FE, Gerber YN, Teigell M, Lonjon N, Boniface G, Bauchet L, et al. Anatomical study of serotonergic innervation and 5-HT1A receptor in the

human spinal cord. *Cell Death Dis* (2011) 2:e218, 2011 . e218. doi:10.1038/cddis.2011.98
28. Gerber YN, Saint-Martin GP, Bringuier CM, Bartolami S, Goze-Bac C, Noristani HN, et al. CSF1R Inhibition Reduces Microglia Proliferation, Promotes Tissue Preservation and Improves Motor Recovery after Spinal Cord Injury. *Front Cel Neurosci* (2018) 12:368. doi:10.3389/fncel.2018.00368
29. Noristani HN, Saint-Martin GP, Cardoso M, Sidiboulenouar R, Catteau M, Coillot C, et al. Longitudinal MRI analysis and histological characterization after spinal cord injury in two mouse strains with different functional recovery: gliosis as a key factor. *J Neurotrauma* (2018).
30. Mytskaniuk V, Bardin F, Boukhaddaoui H, Rigneault H, and Tricaud N. Implementation of a Coherent Anti-Stokes Raman Scattering (CARS) System on a Ti:Sapphire and OPO Laser Based Standard Laser Scanning Microscope. *J Vis Exp* (2016). doi:10.3791/54262
31. Dudovich N, Oron D, and Silberberg Y. Single-pulse coherently controlled nonlinear Raman spectroscopy and microscopy. *Nature* (2002) 418:512–4. doi:10.1038/nature00933
32. Lim S-H, Caster AG, Nicolet O, and Leone SR. Chemical imaging by single pulse interferometric coherent anti-stokes Raman scattering microscopy. *J Phys Chem B* (2006) 110:5196–204. doi:10.1021/jp057493k
33. Volkmer A, Cheng J-X, and Xie XS. Vibrational Imaging with High Sensitivity via Epidetected Coherent Anti-Stokes Raman Scattering Microscopy. *Phys Rev Lett* (2001) 87. doi:10.1103/physrevlett.87.023901
34. Cheng J-X, and Xie XS. *Coherent Anti-stokes Raman Scattering Microscopy: Instrumentation, Theory, and Applications*, 108 (2004). doi:10.1021/jp035693v
35. Goldman L, and Albus JS. Computation of impulse conduction in myelinated fibers; theoretical basis of the velocity-diameter relation. *Biophysical J* (1968) 8:596–607. doi:10.1016/s0006-3495(68)86510-5
36. Chomiak T, and Hu B. What is the optimal value of the g-ratio for myelinated fibers in the rat CNS? A theoretical approach. *PLoS One* (2009) 4:e7754. doi:10.1371/journal.pone.0007754
37. Campbell JSW, Leppert IR, Narayanan S, Boudreau M, Duval T, Cohen-Adad J, et al. Promise and pitfalls of g-ratio estimation with MRI. *Neuroimage* (2018) 182:80–96. doi:10.1016/j.neuroimage.2017.08.038
38. Friedli L, Rosenzweig ES, Barraud Q, Schubert M, Dominici N, Awai L, et al. Pronounced species divergence in corticospinal tract reorganization and functional recovery after lateralized spinal cord injury favors primates. *Sci Transl Med* (2015) 7:302ra134, 2015. 302ra134. doi:10.1126/scitranslmed.aac5811
39. Deoni SCL, Rutt BK, Arun T, Pierpaoli C, and Jones DK. Gleaning multicomponent T 1 and T 2 information from steady-state imaging data. *Magn Reson Med* (2008) 60:1372–87. doi:10.1002/mrm.21704
40. Denic A, Macura SI, Mishra P, Gamez JD, Rodriguez M, and Pirko I. MRI in rodent models of brain disorders. *Neurotherapeutics* (2011) 8:3–18. doi:10.1007/s13311-010-0002-4

Conflict of Interest: The authors declare that the research was conducted in the absence of any commercial or financial relationships that could be construed as a potential conflict of interest.

Publisher's Note: All claims expressed in this article are solely those of the authors and do not necessarily represent those of their affiliated organizations, or those of the publisher, the editors and the reviewers. Any product that may be evaluated in this article, or claim that may be made by its manufacturer, is not guaranteed or endorsed by the publisher.

Advantages of publishing in Frontiers

OPEN ACCESS
Articles are free to read for greatest visibility and readership

FAST PUBLICATION
Around 90 days from submission to decision

HIGH QUALITY PEER-REVIEW
Rigorous, collaborative, and constructive peer-review

TRANSPARENT PEER-REVIEW
Editors and reviewers acknowledged by name on published articles

Frontiers
Avenue du Tribunal-Fédéral 34
1005 Lausanne | Switzerland

Visit us: www.frontiersin.org
Contact us: frontiersin.org/about/contact

REPRODUCIBILITY OF RESEARCH
Support open data and methods to enhance research reproducibility

DIGITAL PUBLISHING
Articles designed for optimal readership across devices

FOLLOW US
@frontiersin

IMPACT METRICS
Advanced article metrics track visibility across digital media

EXTENSIVE PROMOTION
Marketing and promotion of impactful research

LOOP RESEARCH NETWORK
Our network increases your article's readership